Solid Freeform Fabrication Symposium 1994

DTIC
ELECTE
FEB 21 1994
S
F
D

Proceedings
August 8-10, 1994

Edited by
Harris L. Marcus, Joseph J. Beaman
Joel W. Barlow, David L. Bourell
and Richard H. Crawford

This document has been approved for public release and sale; its distribution is unlimited.

The University of Texas at Austin
Austin, Texas

19950210 112

Solid Freeform Fabrication Proceedings

September, 1994

Solid Freeform Fabrication as an important and totally integrated approach to design, materials processing and manufacturing research results related to it is contained in this proceedings of the SFF Symposium held in Austin, Texas on August 8-10, 1994.

SFF Topics covered in the Symposium include:

Machine Design
Computer Sectioning
Reverse Engineering
Materials Processing:
Metals
Ceramics
Polymers
Waxes
Composites
Applications

Accesion For	
NTIS CRA&I	☒
DTIC TAB	☐
Unannounced	☐
Justification	
By N00014-94-1-0829	
Distribution /	
Availability Codes	
Dist	Avail and / or Special
A-1	

Harris L. Marcus, Joseph J. Beaman,
Joel W. Barlow, David L. Bourell,
and Richard H. Crawford, Editors

© 1994 The University of Texas at Austin

All rights of reproduction in any form are protected by U.S. Copyright Laws.

Permission to copy all or portions of the proceedings contents must be obtained from the authors and The University of Texas at Austin.

Library of Congress ISSN 1053-2153

DTIC QUALITY INSPECTED 1

Table of Contents

Preface v

Shape Deposition Manufacturing 1
Merz, R., Prinz, F. B., Ramaswami, K., Terk, M.,and Weiss, L. E., Carnegie Mellon University

Multiphase Jet Solidification - A New Process Towards Metal Prototypes and a New Data Interface 9
Geiger, Martin, Steger, Wilhelm, Fraunhofer-Institut-IPA; Greul, Matthias, Sindel, Manfred, Franhofer-Instut-IFAM

Solid Freeform Fabrication of Functional Ceramic Components Using a Laminated Object Manufacturing Technique 17
Griffin, Curtis, Daufenbach, JoDee, and McMillin, Scott, Lone Peak Engineering, Inc.

Production of Metal Prototypes Using a High Powered Laser Machining Center 25
Pridham, M. S.,Thomson, G. A., University of Dundee; Menon, U., and Koch, M., California Polytechnic State University

Video Microscopy of Selective Laser Sintering 34
Melvin, III., Lawrence S., Das, Suman and Beaman Jr., Joseph J., The University of Texas at Austin

FDM® Technology Process Improvements 42
Comb, James W., Priedeman, William R., and Turley, Patrick W., Stratasys, Inc.

Extrusion Methods for Solid Freeform Fabrication 50
Calvert, Paul, Crockett, Robert, Lombardi, John, O'Kelly, John, University of Arizona and Stuffle, Kevin, Advanced Ceramics Research

Surface Texture By 3D Printing 56
Sachs, E., Curodeau, Alain, Gossard, D., Jee, H., and Cima, M., MIT; Caldarise, S., Johnson & Johnson Professional Inc.

Densification of Selective Laser Sintered Metal Parts by Hot Isostatic Pressing 65
Agarwala, Mukesh K., Bourell, David L., and Beaman, Joseph J. The University of Texas at Austin

Sprayed Metal Shells for Tooling: Improving the Mechanical Properties 74
Fussell, P. S., Aluminum Company of America; Kirchner, H. O. K., Université Paris-Sud; and Prinz, F. B., Carnegie Mellon University

LAPS - Laser Aided Powder Solidification - Technology for the Direct Production of Metallic and Polymer Parts 82
Eyerer, P., Shen, J., and Keller, B., University of Stuttgart

Direct Selective Laser Sintering of Metals and Metal Melt Infiltration for Near Net Shape Fabrication of Components 94
Sindel, M., Pintat, T., Greul, M., Fraunhofer- IFAM; Nyrhila, O., Electrolux, Finland; and Wilkening, C., EOS, München

SLS™ Prototypes From Nylon 102
Forderhase, Paul, McAlea, Kevin, Michalewicz, Mary, Ganninger, Mark and Firestone, Kent, DTM Corporation

Rapid Prototyping: A Global View 110
Campbell, R.I., and Dickens, P.M., The University of Nottingham

A World Wide Assessment of Rapid Prototyping Technologies 118
Aubin, Richard F., United Technologies Research Center

Benchmarking of Rapid Prototyping Systems - Beginning to Set Standards 146
Jayaram, Dureen, Bagchi, Amit, Jara-Almonte, Cynthia C., Clemson University; and O'Reilly, Sean, Ford Motor Company

QuickCast™ & Rapid Tooling: A Case History at Ford Motor Company 154
Denton, Karl R., and Jacobs, Paul F., 3D Systems Corporation.

Integration of Numerical Modeling and Laser Sintering with Investment Casting 175
Pintat, T., Sindel, M., Greul, M., Burblies, A., Fraunhofer-IFAM; and Wilkening, C., EOS, München

Computer-Derived Microstructures by 3D Printing: Bio- and Structural Materials 181
Cima, M.J., Sachs, E., Cima, L.G., Yoo, J, Khanuja, S., Borland, S., MIT; Wu, B., MIT and Harvard School of Dental Medicine; and Giordano, R.A., Boston University Goldman School of Dental Medicine

Selective Laser Sintering of Calcium Phosphate Powders 191
Lee, Goonhee and Barlow, J.W., The University of Texas at Austin

A Histogram - Based Algorithm for Semiautomated Three-Dimensional Craniofacial Modeling 198
Levy, Richard A., The University of Michigan Hospitals

Stereolithography Epoxy Resins SL 5170 and SL 5180: Accuracy, Dimensional Stability, and Mechanical Properties 204
Pang, Thomas H., 3D Systems Corporation

A Simple Polymer Shrinkage Model Applied to Stereolithography 225
Flach, Lawrance and Chartoff, Richard P., University of Dayton

Multi-Layered Composites Using Photolithography 234
Bagchi, Amit, and Beesley, Robert, Clemson University

Reducing Warpage in Stereolithography Through Novel Draw Styles 242
Ullet, Jill S., Chartoff, Richard P. Lightman, Allan J. , Murphy, J.P, University of Dayton; and Li, Jinghong, 3D Systems, Inc.

Studies in Stereolithography: Influence of Process Parameters on Curl Distortion in Photopolymer Models 250
Jayanthi, Suresh, Keefe, Dr. Michael, University of Delaware; and Gargiulo, Dr. Edward P., E.I. Du Pont de Nemours & Co.

On the Computation of Part Orientation Using Support Structures in Layered Manufacturing 259
Allen, Seth, Dutta, Deba, University of Michigan

Product Model Driven Direct Manufacturing 270
Carleberg, Per, Department of Manufacturing Systems, KTH

Temperature-Controlled Selective Laser Sintering 277
Benda, J. A., United Technologies Research Center

Shape and Topology Structural Redesign by Large Admissible Perturbations 285
Bernitsas, Michael M., Suryatama, Danet, Kang, Byungsik and Karr, Dale G., University of Michigan

Structural Design for Freeform Fabrication Using Composite Materials 293
Johanson, Roy, Kikuchi, Noboru, and Papalambros, Panos, University of Michigan

Modeling of Selected SFF Process Limits 299
Mendez, Patricio and Brown, Stuart B., MIT

Applications of 3D Laser Digitizing and Surfacing Technologies 307
Winkelman,Wayne, Digibotics, Inc.

New Developments in Processing and Control of Selected Area Laser Deposition of Carbon 311
Thissell, W. Richards and Marcus, Harris L., The University of Texas at Austin

Measurement and Prediction of the Thermal Conductivity of Powders at High Temperatures 321
Sih, Samuel S. and Barlow, Joel W., The University of Texas at Austin

Anisotropy in Properties of Alumina Processed by SLS 330
Subramanian, P.Kamatchi, Vail, N.K., Barlow, J.W., and Marcus, H.L., The University of Texas at Austin

Selective Laser Sintering of Alumina-Boron Oxide Composites 339
Lee, I, Manthiram, A. and Marcus, H.L., The University of Texas at Austin

Silicon Carbide Shapes By Selected Area Laser Deposition Vapor Infiltration 348
Birmingham, Britton, Tompkins, J.V. and Marcus, H.L., The University of Texas at Austin

Selective Laser Sintering of Polycarbonate at Varying Powers, Scan Speeds and Scan Spacings 356
Childs, T.H.C ., Cardie, S. and Brown, J.M., The University of Leeds

Selective Laser Pyrolysis of Polycarbosilane for Solid Free Form Fabrication of Silicon Carbide 364
Jakubenas, K.J. and Marcus, H.L., The University of Texas at Austin

Manufacture of Injection Molds Using SLS 371
Badrinarayan, B. and Barlow, J.W., The University of Texas at Austin

Fundamentals of Liquid Phase Sintering Related to Selective Laser Sintering of Metals 379
Bunnell, David, Bourell, David, and Marcus, Harris, The University of Texas at Austin

Modeling of Polymer Degradation in SLS 387
Vail, N. K., and Barlow, J.W., The University of Texas at Austin

Ultraviolet Curing of Highly Loaded Ceramic Suspensions For Stereolithography of Ceramics 396
Griffith, Michelle L. and Halloran, John W., The University of Michigan

Adaptive Slicing of Solid Freeform Fabrication Processes 404
Suh, Yong Seok, Rensselaer Polytechnic Institute and Wozny, Michael J., National Institute of Standards Technology

Advances in Selective Area Laser Deposition of Silicon Carbide 412
Tompkins, J.V., Laabi, R., Birmingham, B.R., and Marcus, H.L., The University of Texas at Austin

Keyword Index 422

Author/Attendee List 425

PREFACE

This Proceedings of the Fifth Solid Freeform Fabrication Symposium, held at The University of Texas in Austin on August 8-10, 1994, was the best attended and continued the dynamic nature of the first four. Intense interest was shown by researchers for the latest in the basic aspects of Solid Freeform Fabrication (SFF) that highlighted the papers presented at this Symposium. The speakers addressed problems in computer software, machine design, materials synthesis and processing, and SFF in integrated manufacturing. The continued growth in the research, application and development of SFF approaches was readily apparent from the additional papers presented and the attendees from industrial users, SFF machine manufacturers, universities, and government. There was a very large international involvement in the meeting, both as attendees and as contributors. Research presented in the Symposium showed the continued movement forward toward the goal of structurally sound parts using a wide range of SFF techniques. This continued advancement in the state-of-the-art of SFF and the drive for continually improving and reaching out for standardization of the technology will continue to drive its exponential growth and cooperative efforts. The excitement generated at the Symposium reflects the participants' total involvement in SFF and the future technical health of SFF. The Symposium organizers look forward to its being a continued forum for technical exchange among the expanding body of researchers involved in SFF.

The Symposium was again organized in a manner to allow the multi-disciplinary nature of the SFF research to be presented coherently, with various sessions emphasizing computer aspects, machine topics, and the variety of materials aspects of SFF. Application-related efforts were scattered throughout the Symposium. To avoid parallel sessions, a poster session was organized, and a panel session on SFF was held. The dynamic, loosely organized panel discussion on "Where does SFF go in the Next Five Years?" was led by Joel Barlow, Michael Cima, Thomas Pang, Fritz Prinz, Sean O'Reilly, and Michael Wozny. The written versions of the presented papers are incorporated into these Proceedings. The editors would like to thank the speakers for their timely delivery of the manuscripts. We believe that documenting the constantly changing state of the SFF art as represented by these Proceedings will serve both the people presently involved in this fruitful area as well as the large flux of new researchers and users entering the field of SFF. The evenings were highlighted with Texas-style vittles and entertainment featuring the Geezinslaws.

The editors again would like to extend a warm "Thank You" to Renee Loyless-May for her extensive efforts in the detailed handling of the logistics of the meeting and the Proceedings and the support efforts of Vicki Lehmeier and Cindy Pflughoft throughout. We would also like to thank the organizing committee, the speakers, the session chairmen, panel members, and the attendees for their enthusiastic contributions. We look forward to the continued close cooperation of the SFF community in organizing the Symposium. We also want to thank ONR through Grant No. N00014-94-1-0829, ARPA, and The Minerals, Metals and Materials Society for co-sponsoring the Symposium with the Mechanical Engineering Department and the Center for Materials Science and Engineering at the University of Texas at Austin. The editors.

Organizing Committee:

Dick Aubin, United Technologies
Joel W. Barlow, The University of Texas at Austin
Joseph J. Beaman, The University of Texas at Austin
David L. Bourell, The University of Texas at Austin
Robert L. Brown, The Gillette Company
William Coblenz, ARPA
Richard Crawford, The University of Texas at Austin
Samuel Drake, University of Utah
Steven Fishman, Office of Naval Research
Harris L. Marcus, The University of Texas at Austin
Fritz Prinz, Carnegie Mellon University
Emanuel Sachs, Massachusetts Institute of Technology
Susan Smyth, General Motors Corporation
Sean O'Reilly, Ford Motor Company
Ralph Wachter, Office of Naval Research
Michael Wozny, Rennselaer Polytechnic Institute

Shape Deposition Manufacturing

Merz, R., Prinz, F.B., Ramaswami, K., Terk, M., Weiss, L.E.

The Robotics Institute and
The Engineering Design Research Center
Carnegie Mellon University

Abstract

One challenge for solid freeform fabrication has been to develop the capability to directly create functional metal shapes which are dense, metallurgically bonded, geometrically accurate and with good surface appearance. Shape Deposition is a manufacturing paradigm which attempts to address these issues. It incorporates the advantages of several processes including solid free-form fabrication (complex geometries, rapidly planned), 5-axis CNC machining (accuracy, smooth surfaces), shot-peening (for stress relief) and 'microcasting' (a high-performance, weld-based material deposition process). These processes are integrated within a CAD/CAM system using robotic automation. This paper will present the current research in this effort.

Introduction

While functional metal shapes have been built with solid freeform fabrication (SFF) through postprocessing and/or conversion methods [1], it remains a goal to be able to *directly* build high performance metal shapes. Metal parts which are fully dense, metallurgically bonded, have accurate dimensions and good surface appearance are often required for such applications as fabricating custom tooling (e.g. injection molds) and functional production-ready prototypes (e.g. engine components). An early system, called MD* [2], built prototype metal shapes directly with thermal spraying. While the MD* approach incorporates a versatile material deposition process, it has several limitations which are also common to several other SFF processes. The parts exhibit a stair-step surface texture and it is difficult to achieve the accuracy, precision and resolution which can be achieved with traditional shaping methods such as CNC machining. Sprayed material also exhibits porosity, and the mechanical strength is poor compared to cast or welded materials. In addition, the buildup of residual stress through thermal gradients during layered solidification can lead to warpage and delamination [3].

Other incremental material deposition approaches which are based on welding, such as Shape Melting [4] and 3D-Welding [5], produce superior material properties, but have been limited in geometric complexity and require finishing machining operations. In our experience, no single SFF or conventional fabrication process will satisfy all the requirements for rapidly and *directly* creating high performance metal parts. To address this challenge we are investigating an approach called Shape Deposition Manufacturing (SDM) [10 - 14] which combines the benefits of SFF (i.e., quickly planned, independent of geometry), CNC milling (i.e., accuracy and precision with good surface quality), weld-based deposition (i.e., superior material properties) and shot peening (i.e., control of internal stress buildup). This paper describes the concept of Shape Deposition, a

novel, weld-based deposition process called microcasting and thermal and stress related issues. Further, a testbed implementation of SDM is discussed and examples are presented.

Shape Deposition

The basic steps for building parts with Shape Deposition is depicted in Figure 1. To form each layer the growing shape is transferred to several processing stations. First, the material for each layer is deposited as a near-net shape using a novel weld-based deposition process called microcasting [7] (Fig. 1a). The part is then transferred to a shaping station, such as a 5-axes CNC milling machine, where material is removed to form the net shape (Fig. 1b). In the next step the part is transferred to a stress-relief station, such as shot-peening, to control the buildup of residual stresses (Fig. 1c). The part is then transferred back to the deposition station, where complementary shaped, sacrificial support material is also deposited. Each of these operations are described in detail below.

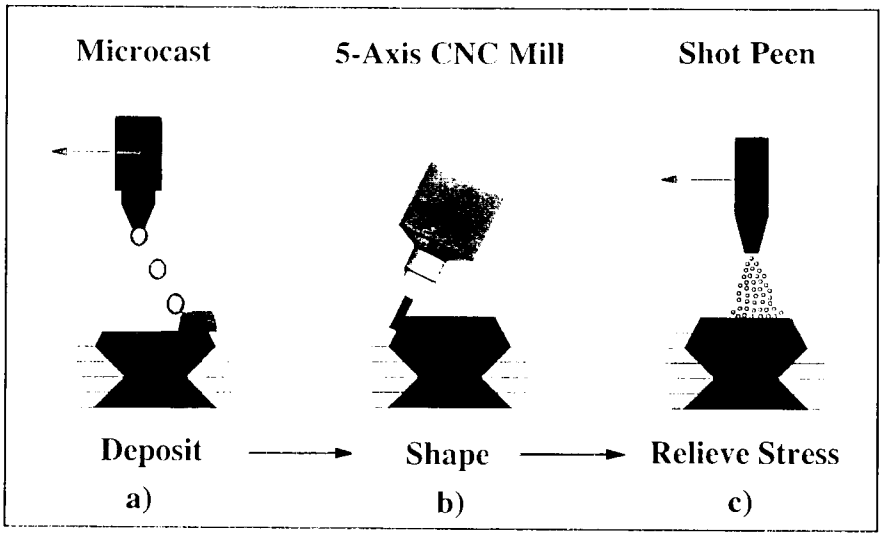

Figure 1: Creation of a layer using SDM

In contrast to SFF processes, Shape Deposition decomposes the CAD model of the part into slices which maintain the full three-dimensional geometry of the outer surface. The total layer thickness and the sequence for depositing the primary and support materials depends upon the local surface geometry. Consider the shape in Figure 2 which represents three fundamental features which can be found in a layer; non-undercut (relative to the build direction), undercut, and a combination of both.

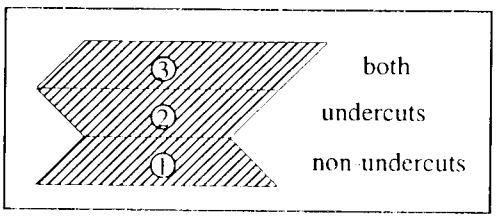

Figure 2: Cross-section of example shape

This shape can be formed as follows:

• In the first layer, which contains only non-undercut features (Fig. 3), the primary material is deposited (Fig. 3a) and shaped (Fig. 3b) first. This layer is completed by depositing the support material (Fig. 3c) and planing the to surface (Fig. 3d).

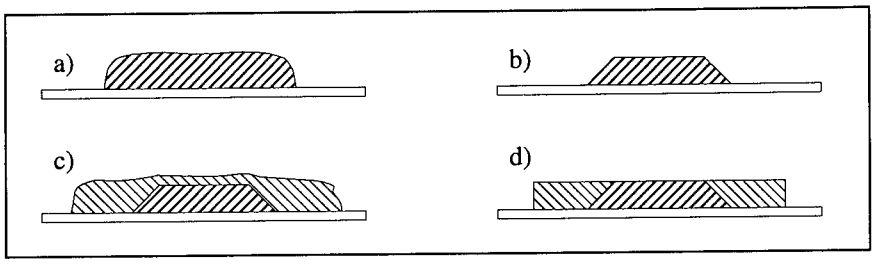

Figure 3: Manufacture of non-undercut features

• The second layer, which contains only undercut features (Fig. 4), is created by depositing (Fig. 4a) and shaping (Fig. 4b) the support material first. This forms a molding cavity into which the primary material is then deposited (Fig. 4c) and the layer is finished by planing the top surface (Fig. 4d).

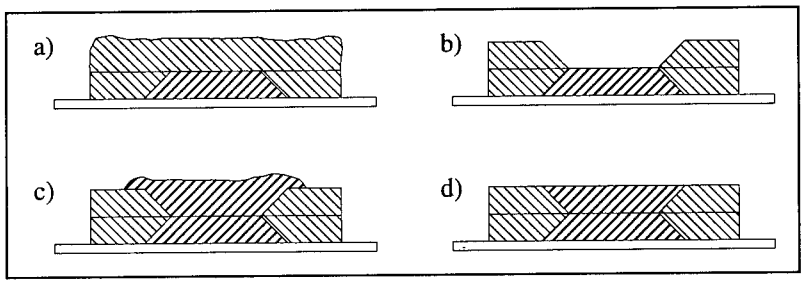

Figure 4: Manufacture of undercut features

• For the third layer the support material must be subdivided (Fig. 5). The section of the support material with no undercuts is deposited and shaped first (Fig. 5a). Next, the primary material is deposited and the non-undercut surfaces are shaped (Fig. 5b). Finally the remaining portion of the support material is deposited and the layer is planed (Fig. 5c). In general, for layers containing a combination of undercut and non-undercut surfaces, the individual materials have to be split into smaller segments. Each segment contains undercut surfaces only in those areas which are adjacent to previously deposited segments of the layer.

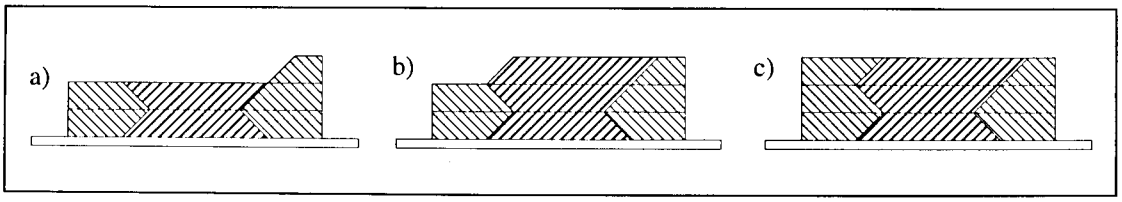

Figure 5: Manufacture of arbitrary layers

Figure 6 shows a comparison of cross-sections of the part manufactured with SFF techniques and Shape Deposition. While SFF needs a relatively large number of layers Shape Deposition can produce thicker layers and eliminates the stairstep texture of the surface.

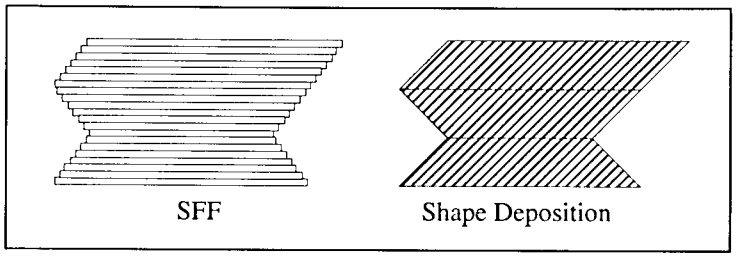

Figure 6: Comparison between SFF and Shape Deposition

Microcasting

Thermal deposition technologies have been investigated in SDM in order to produce high quality material. However, conventional deposition approaches including thermal spraying and welding have several limitations. The molten droplets created by thermal spraying are relatively small (order of magnitude 50 μm) and therefore do not contain enough heat to remelt the underlying surface. Instead, mechanical bonds are predominately formed, and adhesive and cohesive strength are relatively low. While this leads to undesirable material properties, the low heat transfer into the substrate preserves previously shaped layers. In contrast, weld-based deposition approaches, such as MIG or plasma welding, locally remelt the substrate where the feedstock material is deposited, thus forming metallurgical bonds. However, the relatively large heat transfer will affect the shape of underlying material.

A compromise between thermal spraying and welding is required to achieve metallurgical bonding without destroying underlying geometries. Microcasting is a droplet-based deposition process which addresses this challenge. In contrast to the droplets produced with thermal spraying, microcast droplets are relatively large (1 to 3 mm dia.). They contain sufficient heat to remain significantly superheated until impacting the substrate, and rapidly solidify due too significantly lower substrate temperatures. The microcasting apparatus can be implemented with conventional welding equipment configured in a non-transferred mode [11]. Microcasting creates a stream of individual droplets at a rate between 1 and 5 droplets/second. By controlling the superheat of the droplets and the substrate temperature, conditions can be attained, such that the impacting drop-

lets superficially remelt the underlying material (on the order of 10 μm deep) [6] leading to metallurgical interlayer bonding.

Microcasting is used to deposit not only the primary material but also the material for the support structure. One suitable combination of materials is stainless steel for the main material and copper for the support structure. The copper support structure is etched away with nitric acid after the part has been completed. When the stainless steel is deposited it does not deeply penetrate the copper because of the high thermal conductivity of copper. On the other hand, the copper does not deeply penetrate the stainless steel because of its lower melting temperature [7].

Discussion of Thermal and Stress-Related Issues

Key issues in shape deposition manufacturing originate from temperature gradients caused by fusing molten droplets onto previously deposited layers. As described earlier, for the establishing of a solid bond the molten droplets need to be superheated such that they can remelt a thin surface layer immediately after impact. Heat transfer calculations to determine the conditions for remelting have shown an inverse relationship between minimum droplet temperature versus minimum substrate temperature [6]. Intuitively obvious, if the droplet temperature goes down the substrate temperature needs to be increased accordingly. However, due to the latent heat there is a threshold temperature below which the droplets will crystallize without remelting the underlying solid. Experiments have confirmed these calculations.

Temperature gradients in layered material deposition are always associated with internal stresses or distortions. Imagine bonding a hot piece of material on top of a substrate with a lower temperature. After both pieces have cooled down and converged to the same temperature the material portion which was originally hotter will have contracted more then the colder one. This puts the hotter piece in a state of tension while the colder piece will be equivalently compressed. Unless external forces such as the sacrificial support material or material layers underneath lock the joined material layers in place they will bend upwards until having reached static equilibrium. Problems like this occur in a variety of manufacturing applications ranging from welding or thermal spraying to the fabrication of VLSI chips and other Solid Free Forming processes such as Selective Laser Sintering or Shape Melting. One goal in Shape Deposition Manufacturing is to compensate for the tensile stress in the upper most layer by introducing a compressive stress. In materials which can be plastically deformed such as metals this can be accomplished through shot peening [8]. Ideally, the impacting shots create a plastic shear wave which traverses to the remelted zone eliminating the elastically stored tension energy. In practice, this is difficult to realize and in all likelihood a thin layer of compressively stressed material will overcompensate a layer of residual tension stress right above the remelted zone.

Another means of minimizing temperature gradients during molten droplet deposition is increasing the substrate temperature. However, the overall temperature of the article embedded in the sacrificial support structure needs to be kept below a certain level to prevent melting of the later. For primary/sacrificial support material combinations which have been investigated to date the support material had always a melting temperature well below that of the primary material of the target article. Planning material deposition strategies must take into account these conflicting goals of minimizing temperature gradients versus overheating and possibly melting the support structure. A quantitative understanding of temperature gradient, associated internal stress build

up, and thermal energy accumulation is a prerequisite for generating quality parts in Shape Deposition Manufacturing.

Testbed Facility

In order to have the flexibility to investigate different subprocesses, robotic automation was used to implement the SDM process [9]. The testbed facility (Fig. 7) consists of four processing stations; CNC milling, thermal deposition, shot-peening and cleaning. The growing parts are built on pallets which are transferred from station-to-station using a robotic palletizing system. Each station has a pallet receiver mechanism. The part transfer robot places the pallet on the receiver which locates and clamps the pallet in place.

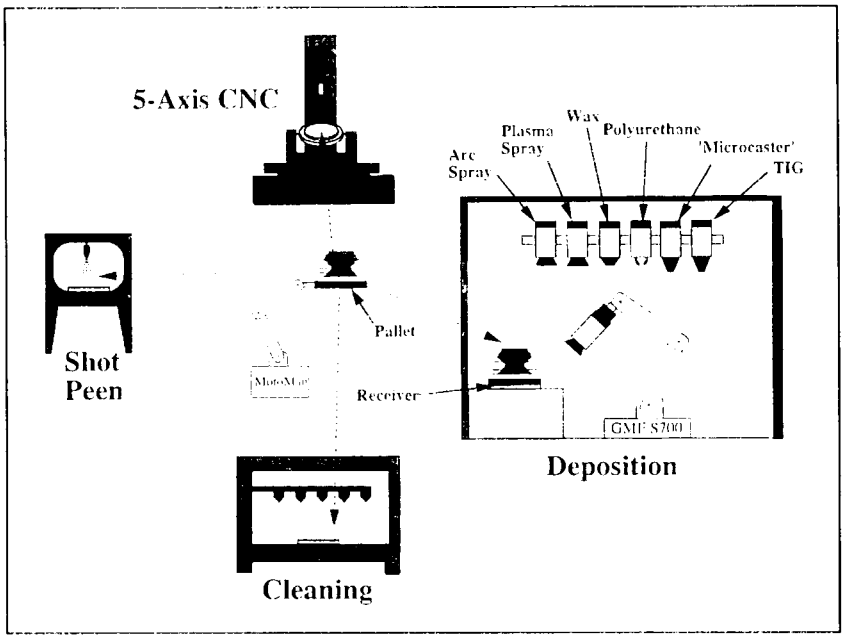

Figure 7: Shape Deposition lab configuration

The deposition station consists of an acoustic chamber (for noise abatement and dust containment), an air handling system (for dust filtration and collection) and a robotic deposition system. The deposition robot is equipped with a tool changing wrist and is able to acquire one of several different deposition torches which are mounted to a docking mechanism. The current sources include arc and plasma sprayers, as well as MIG, plasma and 'microcasting' welders. To deposit material, the robot picks up the appropriate torch and manipulates it over the growing shape.

The shaping station is a 5-axis CNC milling machine with an 21-head tool changer mechanism (i.e., it can automatically acquire one of 21 different end-mills). The hydraulically-actuated receiver used in this station is able to repeatedly locate the pallet within approximately 0.0002 inches. When cutting fluids are used in milling operations, the pallet is then transferred to a cleaning station to remove residuals. The shot peening station, which uses a conventional pressurized media delivery system, also incorporates grit-blasting capabilities for surface preparation prior to conventional spraying operations

Examples

While the Shape Deposition process is at an early stage of development, we have built several test parts. For example, Figure 8 shows a complexly shaped artifact which was made for the IMS (Intelligent Manufacturing Systems) consortium. This is a 308 stainless steel part which was embedded in sacrificial copper support material.

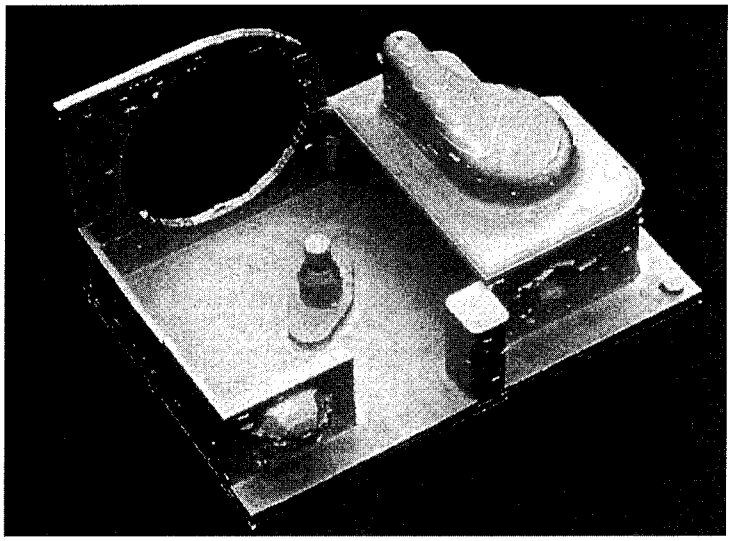

Figure 8: IMS-T2

Data from mechanical testing of this material combination on individual tensile test specimens is shown in Table 1. The tensile strength for 308 weldments is specified at 597.2 MPa (86.6 ksi), the yield point at 399.9 MPa (58.0 ksi) and the elongation at 35%. The average tensile strength of microcast 308 is thus 17% higher, the yield point is 20% higher, and the elongation is 28% higher. While layer to layer bonding strength has not been tested yet, metallographic evidence suggests metallurgical bonding between the layers.

	tensile strength [MPa] ([ksi])	0.2% offset yield [MPa] ([ksi])	elongation [%]
min.	663.2 (96.2)	406.9 (59.0)	34.1
avg.	677.2 (98.2)	481.1 (69.8)	44.8
max.	685.7 (99.5)	499.5 (72.4)	58.4

Table 1: Tensile test results for 308 stainless steel

Conclusions

The implementation of a testbed facility and the creation of several test parts have demonstrated the feasibility of Shape Deposition Manufacturing. However, several issues must be addressed to realize the creation of fully functional shapes. In the current microcasting setup there is no direct control of the temperature of the underlying substrate or of the droplet's temperature,

size and trajectories. This results in several problems which can lead to the existence of voids in the deposited material and excess remelting. To reliably create high quality deposits, a closed loop control system must be developed. The issues involving residual stress buildup during deposition have to be identified, and the influence of shot-peening must be further investigated.

References

[1] Ashley, S., 'Prototyping with Advanced Tools', Mechanical Engineering, June 1994, pp. 48-55.

[2] Weiss, L.E., Prinz, F. B., Adams, D.A., Siewiorek, D.P., "Thermal Spray Shape Deposition", Journal of Thermal Spray Technology, 1(3), Sept. 1992, pp. 231-237.

[3] Amon, C., Beuth, J., Kirchner, H., Merz, R., Prinz, F., Schmaltz, K., Weiss, L., "Material Issues in Layered Forming", Proceedings of the Solid Freeform Fabrication Symposium, The University of Texas at Austin, Texas, August 9-11, 1993, pp. 1-10.

[4] Doyle, T.E., "Shape Melting Technology", Proceedings of The National Conference on Rapid Prototyping, Dayton, Ohio, June 4-5, 1990, pp. 55-62.

[5] Dickens, P.M., Pridham, M.S., Cobb, R.C., Gibson, I., Dixon, G., "Rapid Prototyping using 3-D Welding", Proceedings of the Solid Freeform Fabrication Symposium, The University of Texas at Austin, Texas, August 3-5, 1992, pp. 280-290.

[6] Amon, C.H., Merz, R., Prinz, F.B., Schmaltz, K.S., "Thermal Modelling and Experimental Testing of MD* Spray Shape Deposition Processes", Proceedings of the 10th International Heat Transfer Conference, Brighton, England, August 1994.

[7] Merz, R., "Shape Deposition Manufacturing", Dissertation, Department of Electrical Engineering, Technical University of Vienna, May 1994.

[8] K.I'Anson, et. al., "Use of the Shot Peening process for Surface Modification of Thermal Sprayed Coatings", Proceedings of the ASM Fourth Nat'l. Thermal Spray Conference, Pittsburgh, PA., May 4-10, 1991, pp. 138-145.

[9] Hartmann, K., Krishnan, R., Merz, R., Neplotnik, G., Prinz, F., Schultz, L., Terk, M., Weiss, L., "Robot-Assisted Shape Deposition Manufacturing", Proceedings of the 1994 IEEE International Conference on Robotics and Automation, IEEE, San Diego, CA, May 1994, pp. 2890-2895.

[10] Prinz, F.B., Weiss, L.E., "Method and Apparatus for Fabrication of Three Dimensional Metal Articles by Weld Deposition", U. S. Patent 5,207,371, 1991.

[11] Merz, R., Prinz, F.B., Weiss, L.E., "Method and Apparatus for Depositing Molten Metal", U. S. Patent 5,281,789, 1994.

[12] Weiss, L.E., Prinz, F.B., "Method and Support for Creation of Objects by Layer Deposition", U. S. Patent 5,286,573, 1994.

[13] Prinz, F.B., Weiss, L.E., "Method for Fabrication of Three Dimensional Articles", U. S. Patent 5,301,415, 1994.

[14] Weiss, L.E., Prinz, F.B., "Automated System for Forming Objects by Incremental Buildup of Layers", U. S. Patent 5,301,863, 1994.

Multiphase Jet Solidification – a new process towards metal prototypes and a new data interface

by
Martin Geiger, Wilhelm Steger
Fraunhofer–Institute for Manufacturing Engineering and Automation – IPA
Matthias Greul, Manfred Sindel
Fraunhofer–Institute for Applied Materials Research – IFAM

Abstract

The production of metallic and ceramic parts with RP technologies is requested. Multiphase Jet Solidification (MJS) is a process which reveals good results to develop a commercial system due to this task. Low viscous materials (liquefied substances or powder–binder–pastes) are extruded through an x–y–z–controlled jet and parts of different materials e.g. stainless steel are fabricated layer by layer up to the final extension. The basic principle of the process and the current results will be presented. A slice format was designed for MJS, but it is also usable for other RP technologies. The goal is the development of a general slice interface for RP.

Introduction

Two Institutes of the Fraunhofer Gesellschaft, the Institute for Manufacturing Engineering and Automation in Stuttgart (IPA) and the Institute for Applied Materials Research in Bremen (IFAM) are developing an RP process suitable to produce metallic and ceramic parts directly. The sum of the experiences in manufacturing engineering and information processing at IPA and those in material research at IFAM turned out to build a good team to achieve this aim. After some preliminary examinations of different ideas the working–principle was developed and named "Multiphase Jet Solidification (MJS)". The working–principle will be explained in the first section and the results by producing parts with a first apparatus assembled and tested at IFAM will be shown. Subject of the second section are examinations and developments in information processing. A slice format is, as in most RP systems, base for the computation of the NC code for MJS. Aim of the current work is a slice format suitable for RP processes in general, whereby a first implementation was realized and tested to run MJS. The next task is the coordination of the different contributions to a 'de facto' slice standard. Such a standard is necessary, but its syntax and contents have still to be discussed.

Principle of MJS

The basic idea is to extrude material through a jet, similar to other apparatus such as the 3D Modeler of Stratasys or the Model Maker of Sanders Prototype. In contrast to these techniques the production of metallic and ceramic parts is the main aim of this development. Because of technological limits, pure materials with a high melting point can not be liquefied with the apparatus. Additional to the liquefied pure material, powder–binder–mixtures are used, if the melting point of the material is too high. In any case the material (mixture) is heated above its solidification point and deposited layer by layer. The melted substance solidifies when it gets into contact with the platform or the

previous layer due to temperature, pressure decrease and heat transfer to the part and the environment.

For the present research a simple apparatus is used to test the general feasibility, parameters of the building process and different materials. The main components are an x–y–z–computer controlled positioning system (machine precision +/–0,01 mm, axis traversing 500*540*175 mm^3), a heated chamber and a jet system. The chamber is temperature–stabilized and can be varied within a range of 70 degree to 220 degree Celsius. The material is supplied as powder, pellets or bars. The material flow is controlled by a piston pressing the viscous material through the jet. The first test apparatus is shown in figure 1.

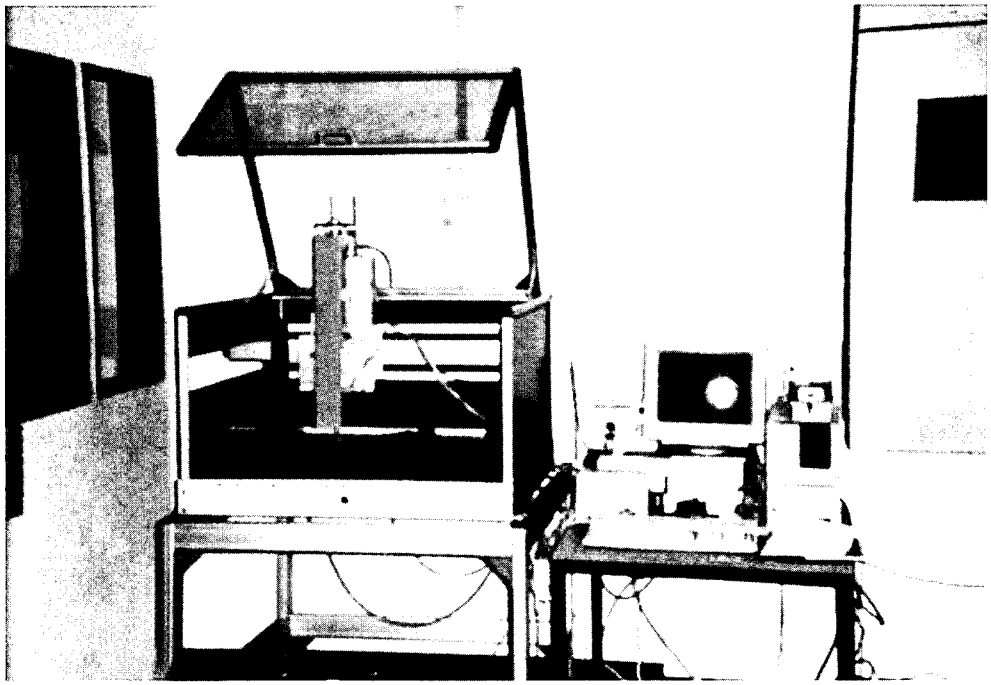

Figure 1: Alpha apparatus of Multiphase Jet Solidification

Production by liquefaction of metals

Metallic parts with a low melting point are directly fabricated by deposition out of the molten phase. The first experiments were accomplished with tin–bismuth alloys (melting temperature up to 180 degree Celsius) which are normally used for mould making and metal spraying. The microstructure of parts shows a good bonding between the layers.

The accuracy of the parts is still limited due to the low viscosity and the surface tension of liquid metal. Therefore, the liquid metal contracts directly after the extrusion before solidification. First experiments by alloying particles into the metal in order to increase the viscosity are very promising.

The melting temperature of industrial relevant materials like metals, e.g. zinc and aluminium, is much higher than this of the tested alloys. Therefore, it is an important task to improve the apparatus towards higher temperatures.

Deposition of powder–binder mixtures

To produce prototypes of materials with higher melting points like ceramics and the most metallic alloys the use of powder–binder mixtures reveals good results. First, prototypes made of stainless steel were fabricated via a powder–binder mixture. At a certain temperature of about 100 degree Celsius the mixture has a suitable viscosity to extrude it via a nozzle. Because of low surface tension the material can be deposited very exactly without contraction. Subsequently the green parts are processed like a metal injection moulded (MIM) part by debinding and sintering to final density. The microstructure and the mechanical properties of the prototypes are comparable to MIM parts.

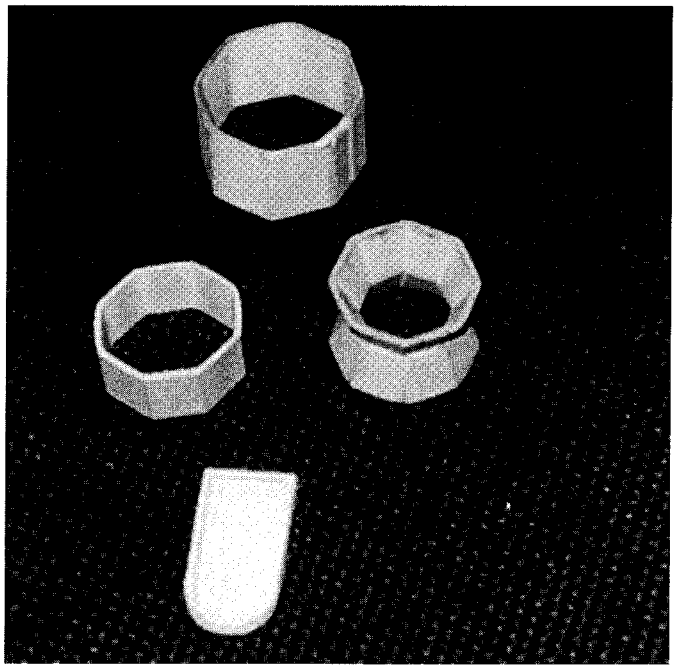

Figure 2: MJS parts in stainless steel

The accuracy of the parts is higher than of the liquefied metal process. The material behaviour of the mixture allows a greater overhang angle. But volume shrinkage of about 30% due to sintering must be taken into account when generating the control data. In MIM, the mixture is pressed with a high velocity into a mould. Powder–binder segregation caused by the different densities of metal powder and binder could often be observed. In MJS, this turned out to be no problem because of the low velocity of the material through the jet in comparison with MIM. A further advantage is, that the green parts can be easily finished to a very smooth surface. Figure 2 displays sintered metallic parts (average diameter is about 60 mm) out of stainless steel.

During sintering, special care has to be taken to avoid distortion by reducing the friction between the part and the support. The wall thickness of the prototypes is currently limited to about 15 mm due to the debinding–process. If thicker areas are necessary, it is possible to use hatches instead of filling the entire contour. Optimization of the binder components is a further task to increase the maximum wall thickness.

Experiments with other powder–binder mixtures in order to achieve titanium and copper parts have been carried out. The process turned out to be practicable for a wide range

of materials. Also the production of ceramic parts like alumina and silicon carbide is in development.

The alternative to the sintering is the infiltration process. The debinded metallic part can be infiltrated by a second metal with a lower melting temperature. This metal is sucked up by the part due to a capillary effect. The benefit of this process is the fact that there is no need to account shrinkage.

Data preparation for RP

For discussions and developments on data handling in RP it is important to consider the present global activities in developing the common, object oriented 'Standard for the Exchange of Product Model Data' (STEP) /1/. In the future, the data describing geometry, topology, features, materials, tolerances, etc. can be used for the planning and rapid production of prototypes. The direct link to different technologies e.g. Virtual Reality, CAM and CAQ with one common throughout data model will become possible. In a common project of several Fraunhofer–Institutes activities to develop a STEP based data handling in RP will start this year. But international standardization needs a lot of time. Until STEP is applicable for RP, the industry needs fast and suitable solutions fitting the different applications best. The data handling, which will be discussed here, could be seen as an interim step until STEP is spread off in industry. Furthermore, the results in developing, using and testing the data format of this interim step will lead to a practical experience which inputs to the development of a STEP Application Protocol.

The exchange of the RP relevant geometry information of parts between CAD systems is based on 3D data, e.g. neutral data models (Initial Graphics Exchange Specification (IGES), interfaces of the 'Verband der deutschen Automobilindustrie' – VDA–FS, VDA–IS – /2/, etc.) or facet formats developed for RP (STL, CFL, etc.). Slice routines exist or all these formats. But the commonly used facet format is STL. Nearly all related CAD vendors offer an STL interface. The disadvantages of the STL syntax are sufficiently discussed. Nevertheless, there is no need for a new 'de facto' facet standard for RP. Time and energy to spread off a new facet format is very high compared with the benefits. Other facet formats, fitting some applications better should be used individually, but should not be used or spread off as an exchange format. Experience made in RP or other areas using facet formats (e.g. Virtual Reality and Finite Element Methods) should be included in the developments of STEP. Nevertheless, benefits of individual facet solutions in special application will be demonstrated later by the example of reverse engineering.

An essential point of the interim data handling is a 'de facto' standard for slice information additional to STL! Direct CAD slice interfaces become even more important. Unfortunately, there is a wide range of variations in slice formats. Nearly every vendor uses its own slice format e.g. SLC, CLI, HPGL. The content of this different slice formats varies from pure geometry information up to machine specific data.

Figure 3 gives an overview of the data handling using one common facet format and one common slice format. The most important benefit of the two 'de facto' standards will be, that users will have the choice to select the data handling (direct slice interface or slicing of STL) depending on which one fits their problems best.

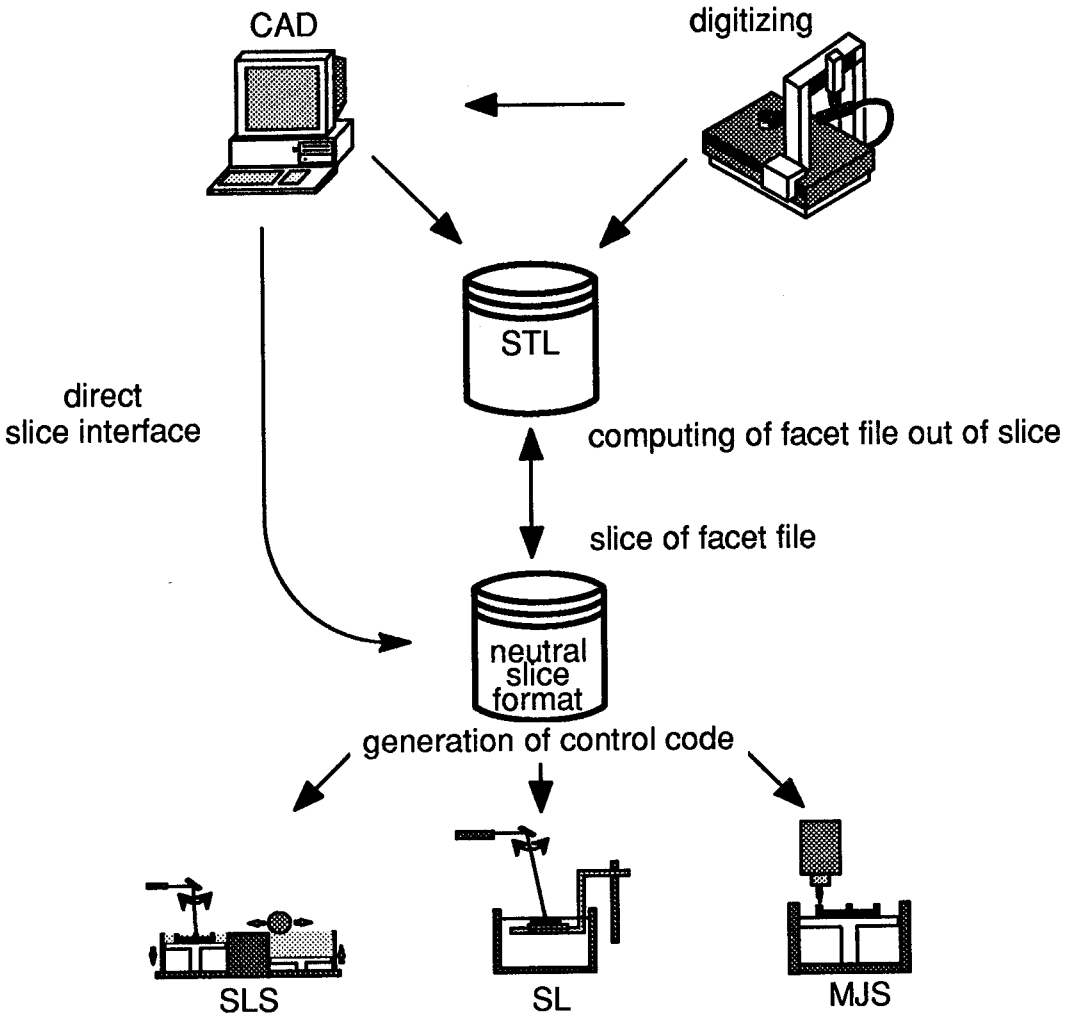

Figure 3 : Data handling in RP

The opinions on direct slicing and on slicing of facets break up in a wide range, dependant on experiences, habits and strategical aims. From a mathematical point of view, there is no difference. The accuracy depends on the quality of the software and not on the choice. The mathematical expenditure to compute a facet format and slice it afterwards is in general equal to the direct slicing. In practise, there are a lot of differences in quality, ergonomics, time and costs dependant on the available software and on the special application. In our opinion, the users should be able to decide themselves. But in fact, the users mostly do not have the choice, because there is a lack of a 'de facto' slice standard and due to this, a lack of software tools supporting direct slicing.

Improved facet description for reverse engineering

Reverse engineering plays an important role in Rapid Product Development. Independant of the individual sensor the result of the digitizing process is point data. Software for automatic detection and computation of regular geometries and freeform surfaces based on a spline description is complex and difficult to realize. The current available solutions are limited in their abilities. As shown in figure 3, an alternative to link

digitizing to RP is to compute a facet presentation of the geometry. A problem is, that a part has to be measured from different views. The result is a number of records with overlapping areas. The hardware installation and software at IPA enables to compute a facet description of the measured areas. Contraction of the point data set and smoothing of the surface is also possible. Furthermore, a software tool to handle, to change and to close the surface according to different applications was developed.

The objective of this tool will become clear with the following example of application. "The hilt of a butcher knife is often designed by manual manufacturing of a physical model. A property of this model is, that one side of the hilt is not the exact reflecting surface of the other. So, the first step to produce a prototype is to determine the better side and to digitize it from selected directions. The point data set leads to a facet file describing the better side of the hilt and due to the measurement process some areas of the other side. To achieve a closed description of the whole hilt the facet file has to be limited by a plane and the mirror image has to be computed."

Data files in reverse engineering do not seldom have millions of facets. Therefore, speed is an important request for the software tools. The STL format turned out to be less suitable to that issue. Access time to selected information is too slow. Therefore we use an own format designed for this demand. Similar to CFL we have a list with the values of all points. The triangles are described using the numbers of the edge points. In addition, we sort the triangles related to the software tools used for special applications. Optional files describing the sorted stock enable very quick algorithms to handle the facet information. If we use our facet format, sort it according to the application and do the mapping to an STL file at the end, it turned out that this way is much faster than handling the STL file.

Neutral slice format

Slices are the lowest common denominator among RP systems. For several reasons the users request for a neutral slice format becomes even higher. The choice between different RP systems in product development increases. Users want to apply the same software for different RP systems as well as they prefer direct slice. Some benefits of a 'de facto' slice format are:

- Software developers have free access to the syntax. The free access simplifies the development of software tools improving the data handling. For the users the choice between different software tools would raise.
- CAD vendors are surely more willing to develop a slice interface, if there is one common format.
- In medical application the output of tomographs is slice information. A common direct link to nearly all RP systems would be available.
- Corrections of failures in the geometry description are easier to make in some cases.
- In developing new RP systems there is no need to develop an individual slicer.

Admittedly, there are a lot of applications where the use of slice information has disadvantages. One is that it is not usable to exchange geometry information for LOM, because the slice thickness varies online during the process. Furthermore, there are disadvantages in manipulating the part e.g. rotating of sliced parts. But once again, it should not replace a facet format but it should supplement it. The decision which one to use for the different applications is task of the users.

Examinations to such a slice format were done in a European project. The format requirements and the results have been published /3/. The format Layer Exchange ASCII Format (LEAF) was developed but has not been realized. It has an object oriented structure where instances of an object of given classes can be created. The only 2D primitive supported by LEAF are polylines. The physical representation of LEAF uses keywords determining the following syntax.

Figure 4 : Object class tree of LEAF /3/

Further work was done in another European project. Recently CLI, the slice format of EOS, has been improved. The new version should be suitable for most RP systems. System dependant information can be presented in the header section. Unfortunately, the latest version is not distributed until now, so a final comment is not possible.

One task of the slice format at IPA is to run MJS as well as a Laser Modeling System of Fockele & Schwarze. The second task is to get experience for the development of the slice part of an RP STEP Application Protocol. Therefore, an object class tree (figure 4) as it is used in LEAF is the basic structure, too. The slice file should describe the product's geometry. However, the geometry of the RP part often deviates from this according to a special application. For investment casting the stereolithography part is produced with the QuickCast build style or only the shell of the part is produced. With MJS it is often of advantage to use special fill strategies due to the following sinter process. E.g. the format must be capable to contain this information.

Regular geometries are often sliced in direct slice processes. Therefore, the slice result is a summary of regular 2D primitives, e.g. lines, arcs, circles and ellipses. These primitives should be handled as primitives and not as a sum of polygon lines due to storage space.

Good experience was maid with a structure that allows a direct link between 'inner' borders to the surrounding 'outer' border (figure 5). The computation of NC code turned out be easier and faster.

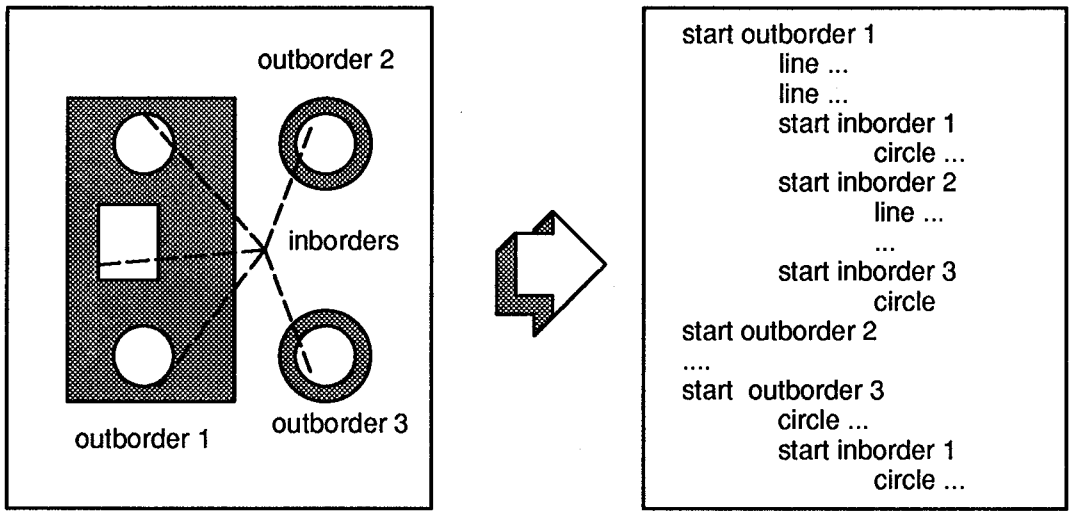

Figure 5: Slice and diagrammatic structure of slice 2D primitives

Efforts to bring the experience of CLI, LEAF and those made during the design of IPA's format together and to coordinate the activities were started. Different questions about contents and syntax of the format have to be discussed. But it will surely be a compromise between the demand to an early available format and the demand to a 'perfect' format. Nevertheless, long term aim is STEP.

Conclusion

The advantage of the MJS–process is the high flexibility of materials, e.g. high melting metals and ceramics, and the simplicity of the apparatus. The future developments will improve accuracy and the number of materials.

The applications of the RP technologies are still increasing. Easy and free choice of RP systems and available software tools fitting to the special equipment and application of the users is required. The acceptance of a 'de facto' slice standard by all RP vendors would probably improve the present situation in data handling. Both a facet and a slice description should be part of a STEP based data handling in RP

References

/1/ Kennicott,P.R.: An Application Reference Model for Layered Manufacturing. In: Proceedings of the IMS International Conference on Rapid Product Development, January 31 – February 2, 1994, Fraunhofer–Institute for Manufacturing Engineering and Automation, Stuttgart, pp 451–473

/2/ Renz, W.: Initiative des VDA zur Verbesserung des CAD Datenaustausches. In: Proceedings of the 8th International Exhibition for Computer Aided Technologies, May 5–8, 1992, Stuttgart, pp. 19–28

/3/ Dolenc, A.: Software Tools for Rapid Prototyping Technologies in Manufacturing. Acta Polytechnica Scandinavia, Mathematics and Computer Science Series No. 62, Helsinki, 1993

Solid Freeform Fabrication of Functional Ceramic Components Using a Laminated Object Manufacturing Technique

Curtis Griffin, JoDee Daufenbach, and Scott McMillin
Lone Peak Engineering, Inc.
12660 South Fort St.
Draper, Utah 84020

ABSTRACT

Lone Peak Engineering (LPE) has demonstrated the feasibility of using solid freeform fabrication to prepare advanced structural ceramics using a laminated object manufacturing (LOM) technique. High purity, high density alumina ceramic components were successfully made using the LOM process. The properties of the laminated object manufactured (LOMed) components were very similar to the physical and mechanical properties of alumina ceramics that were prepared by a conventional pressing process. The LOMed ceramics were also very similar in properties to commercially available alumina ceramics.

INTRODUCTION

A variety of techniques have been developed to produce parts and prototypes directly from a computer-aided drawing (CAD). The overall process is called by a number of names, including desktop manufacturing, rapid prototyping, freeform fabrication and flexible manufacturing. Some of these techniques are being examined for structural ceramics. Lone Peak Engineering has successfully demonstrated the use of one technique, laminated object manufacturing (LOM), to manufacture advanced structural ceramics.

The LOM process and equipment were originally designed to produce parts from paper. Using a modified LOM machine[a], tape-cast ceramic sheets are being used by LPE to manufacture ceramic parts. The LOM machine uses a computer-controlled laser to cut the green ceramic tape. The cutting path of the laser is determined from a computer-generated solid model of the part being manufactured. The solid model is sliced into a number of cross-sections from the bottom of the part to the top. The laser cuts the ceramic tape to create each cross-section. A new layer of green tape is laminated to the previous layers and then the laser cuts the next sheet. The laser cuts only the new layer. The process is repeated layer-by-layer until the parts are finished. Excess material surrounding the part is removed and binder chemicals are removed thermally. The LOMed ceramic parts are then sintered to high density in a conventional sintering furnace.

Lone Peak Engineering has demonstrated that it is possible to produce parts in a matter of days as opposed to the weeks or months that are required by conventional ceramic processing methods. LPE's experience to date indicates that a print-to-part time of seven days is feasible. The process under development is flexible and suitable for ceramic material in virtually any configuration. The

[a]LOM-1015, Helisys, Inc., Torrance, CA.

ability to rapidly prototype ceramic components via the LOM process will expand the range of applications being considered for ceramic materials.

This paper describes a ceramic LOM process currently under development at LPE. The physical and mechanical properties of the LOMed ceramics are compared to ceramics prepared by a conventional pressing technique. The potential to manufacture complex-shaped components by the LOM process is also shown.

EXPERIMENTAL PROCEDURE

Two processes were used to prepare ceramic specimens for this demonstration. One set of specimens was prepared by the laminated object manufacturing process, while the other set was prepared by a conventional powder-pressing process. Most of the specimens prepared in this project were rectangular bars, however, some other more complicated parts were also prepared by the LOM process.

The only difference between the LOM and conventionally-prepared parts was the method used to form the green parts. The same alumina powder (Al_2O_3)[a] was used in both methods. Once the green specimens were formed by the different methods, the binder removal, sintering, and evaluation processes were identical for the LOMed and conventionally-formed specimens. Process steps specific to LOM and to the conventional processes are described in the next sections. Steps common to both processes, binder removal, sintering and evaluation, are described in later sections.

Laminated Object Manufacturing

Prior to manufacturing ceramic parts, CAD drawings of the parts were prepared. A solid model of the part was created and converted to the .STL format. The .STL file was used by the LOM software to control the LOM process.

Thin sheets of alumina were prepared by tape casting using a proprietary process. The alumina powder was mixed with an organic binder system using a ball mill. The resulting slurry was cast into thin tapes. A doctor blade was used to control the tape thickness to approximately 0.015mm. Squares, 10 x 15 cm, were cut from the tape-cast roll.

The LOM procedure to form ceramic parts consisted of several steps. The LOM process was originally developed to make components from paper and plastic. The process is shown schematically in Figure 1. The sheet material is rolled into place and adhered to the previous layer. During this demonstration, LPE used green ceramic tape-casts sheets that were initially placed by hand onto

[a]Grade A-16SG, Alcoa, Inc., Pittsburgh, PA.

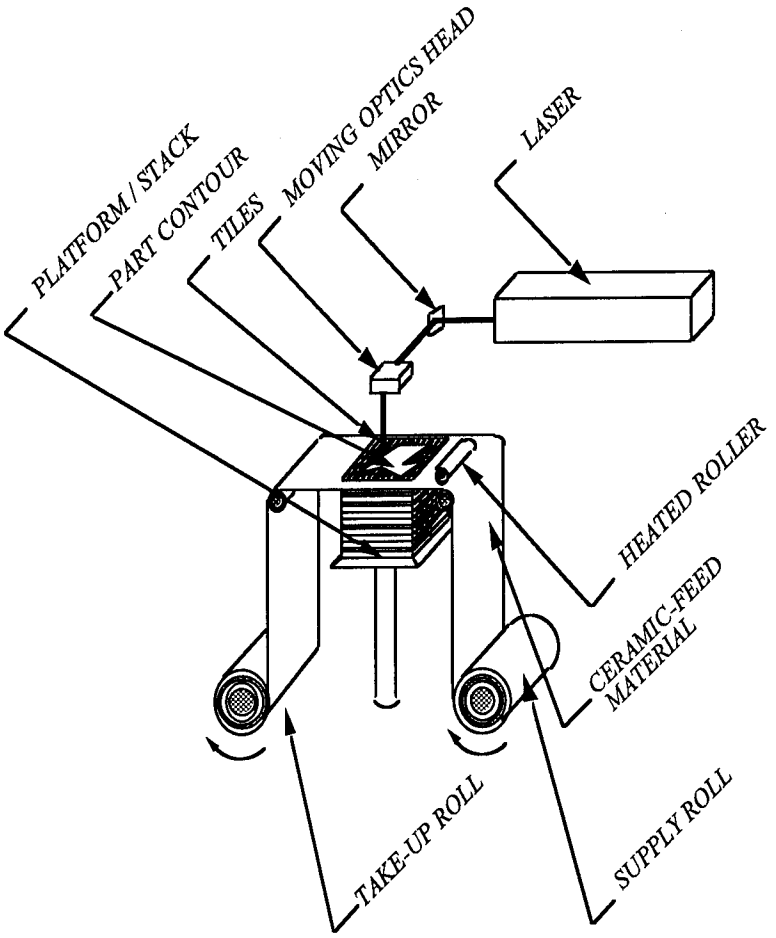

Figure 1. LOM Schematic

the previous layers[a]. The system was modified so that a heated plate and pressure could also be used to assist layer lamination. In the LOM process, a laser cuts only the top sheet material to outline the part. The laser is controlled by a sliced .STL file. "Tiles" are cut into the surplus material to help with removal of the finished component. The table containing the laminated layers is lowered slightly to accommodate the new feed sheet. The process repeats until the part is completed. Eventually, a continuous roll of ceramic tape will be used so that the process can be completely automated for ceramic components.

Excess material was removed from the LOMed parts. The green density of the LOMed parts was determined from the dimensions and mass of the parts when possible. Various alumina parts were made by the LOM process. Bars approximately 6 x 6 x 60 mm in size were prepared. Complex-shaped parts were also made.

---

[a] The initial coated sheet was placed onto a glass plate, whereas subsequent sheets were placed onto the previous layers.

Conventional Processing

The alumina powder was milled in denatured ethyl alcohol with 3 wt% of a polyethylene glycol binder[a] to prepare it for pressing. The milling conditions were similar to the conditions used to mill the alumina slurry for tape casting. The milled alumina was dried and screened to -100 mesh.

Rectangular bars were prepared from the screened powder. The powder was first uniaxially-pressed in a cold steel die to form bars, approximately 6 x 6 x 60 mm. The cold-pressed bars were then isostatically-pressed at 207 MPa (30 Kpsi). The dimensions and weight of the pressed bars were measured.

Binder Removal and Sintering

The binder was removed by thermal degradation in air. The LOMed parts and pressed bars were placed together on alumina setter plates. The setter plates were placed inside a furnace and heated to 600°C to remove the binder. The parts were sintered at 1550°C for 2 hours in air.

Physical Property Evaluations

The density and open porosity of the sintered bars were determined by an immersion technique[b]. The weight loss and shrinkage were determined from the physical measurements of the sintered parts. The data are presented in the Results section.

Mechanical Property Evaluations

The sintered bars were ground using a 320-grit diamond wheel. The grinding was done parallel to the length of the bar. These ground bars were used to determine the flexure strength. Some of the ground bars were polished down to a 1 mm finish. These polished bars were used for the hardness and fracture toughness tests. Bars were prepared so that tests could be conducted either perpendicular or parallel to the direction of lamination or pressing.

The flexure strength was determined in 4-point bending. Outside and inside spans of 40 and 20 mm, respectively, were used. The same conditions were used to test the LOMed and pressed bars. The hardness was measured using a Vickers-type diamond indentor [1]. The hardness (H) was determined from the size of the indentation diagonal (a) and indentation load (P) using the following equation:

$$H = 2P/(2a)^2 \qquad (1)$$

The fracture toughness was determined using the indentation-strength method [1]. In this method, the polished bars were indented with the Vickers indentor and the hardness was determined.

---

[a] Carbowax 20M, Union Carbide, Danbury, CT.

[b] ASTM-STD-C373-56.

The flexure strength (σ_f) of the indented bar was determined in bending. The fracture toughness (K_{ic}) was calculated from the measured hardness, elastic modulus (E), indentation load, and the flexure strength of the indented bar.

$$K_{ic} = 0.59(E/H)^{1/8}(\sigma_f P^{1/3})^{3/4} \qquad (2)$$

The elastic modulus used for these measurements was 375 GPa.

RESULTS AND DISCUSSION

Alumina ceramic components were successfully made by the laminated object manufacturing process described above. The LOMed components were very similar in physical and mechanical properties to alumina ceramics that were prepared by a conventional pressing process during this project. The LOMed ceramics were also very similar in properties to commercially-available sintered alumina ceramics.

Physical Properties

The physical properties of the LOMed and pressed parts are presented in Table 1. The LOMed and pressed parts sintered to very high densities. The sintered densities were about equal regardless of the forming process or the material used to form the parts. The sintered densities of the LOMed and pressed parts shown in Table 1 were similar to densities of a commercially-available 99.5% alumina, 3.89 g/cc [2].

The other physical properties shown in Table 1 are different. The difference in green density, weight loss, and shrinkage can be attributed to the different forming methods. For example, the higher green density of the LOMed parts was due to the higher binder content in these parts, which also resulted in the higher weight loss when the LOMed parts were sintered.

Table 1. Physical Properties of Alumina Parts Made by Laminated Object Manufacturing and by Conventional Pressing.

Forming Process	Material	Density Green g/cc	Density Sintered g/cc	Open Porosity, %	Weight Loss, %	Shrinkage
LOM	Tape	2.55	3.88	1.0	17.6	14.1
Pressed	Powder	2.34	3.89	0.4	3.6	15.8

The higher open porosity of the LOMed parts is probably due to small gaps that were observed at the ends of the bars where the laminating pressures were lower. These gaps have been eliminated in more recent parts by adjusting the lamination conditions.

The microstructure of the LOMed parts are shown in Figures 2. It is difficult to distinguish the individual laminated layers in the microstructure of the LOMed parts. The microstructures perpendicular and parallel to lamination were very similar. The microstructure of the LOMed and pressed parts were similar.

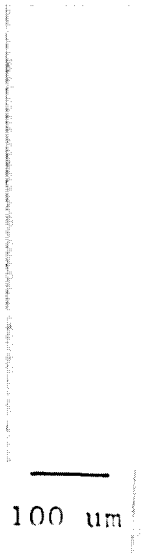

(a) Perpendicular

(b) Parallel

Figure 2. Microstructure of LOMed part

Mechanical Properties

The mechanical properties of the LOMed and pressed bars are summarized in Table 2. Tests were conducted in both the perpendicular and parallel direction to lamination or pressing. The mechanical properties were very similar regardless of the forming method used or the direction the test was conducted.

Table 2. Mechanical Properties of the LOMed and Pressed Alumina Bars.

Forming Process	Direction[1] of Test	Flexure Strength, MPa	Vickers Hardness, GPa	Fracture Toughness, MPa-√m
LOM	Parallel	314	20.2	4.3
LOM	Perpendicular	311	20.1	3.9
Pressed	Parallel	336	21.8	4.0
Pressed	Perpendicular	325	19.8	3.7
Commercial grade[2]		379	14.1[3]	4 to 5[4]

[1]The test direction was either parallel to the direction of lamination (pressing) or perpendicular to it.
[2]Data taken from product data sheet for AD995 (99.5%) Alumina, Data sheet 7164C FP 20K 2/89, Coors Ceramics Company, Golden, CO.
[3]Knoop hardness under a 1000 g load, whereas the other hardnesses shown in the table were measured using a Vickers indentor.
[4]Measured by the single edge notched beam technique.

The mechanical properties of a commercial-grade alumina are included in Table 2 for reference. The flexure strength of the LOMed parts was similar to the strength of commercially available alumina. The hardness of the LOMed parts is higher than the commercial alumina but this probably reflects the different test methods, Vickers versus Knoop. The fracture toughness of the LOMed parts was close to the lower limit of the commercial material. This again may be due to the different test methods used, indentation strength versus the single edge notched beam method, rather than an indication of significant material differences.

Complex-Shapes

The power of the ceramic LOM process comes from the potential to form complex shapes without molds or dies. More complex-shaped parts, such as illustrated in Figure 3, can be manufactured by the LOM process.

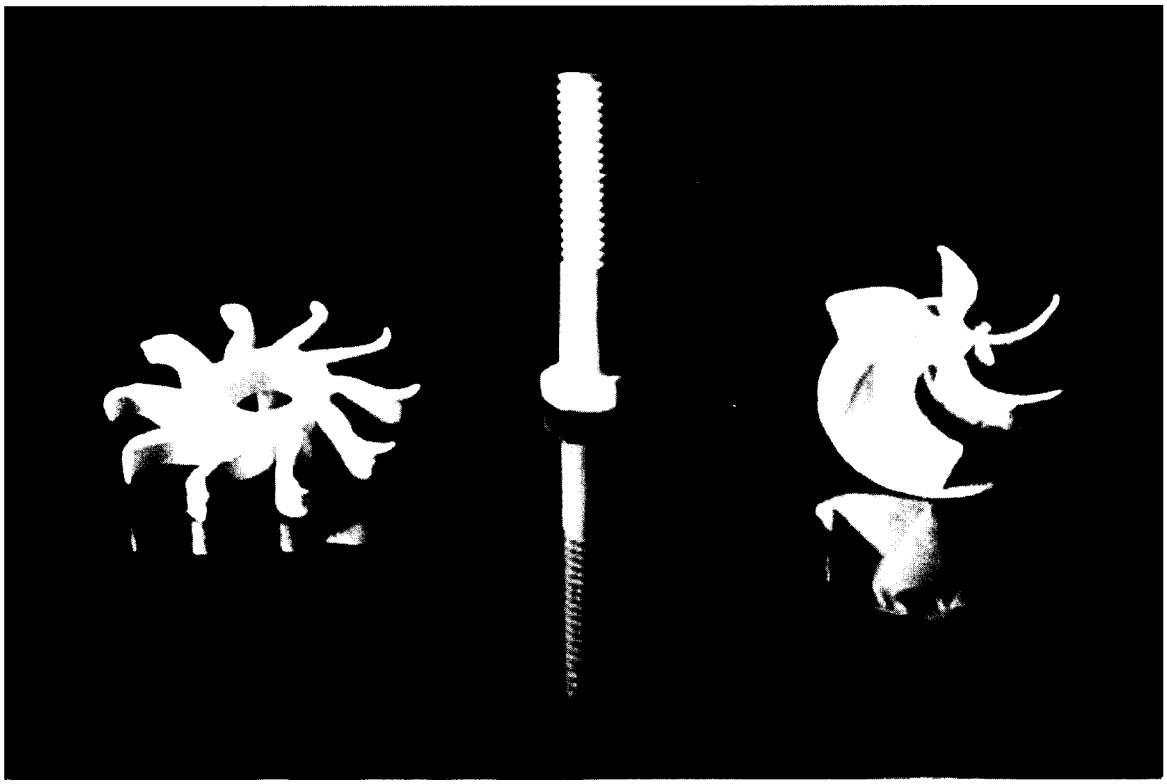

Figure 3. Complex-shaped ceramic components formed by the LOM process

CONCLUSIONS

Advanced structural ceramic parts can be formed by the LOM process. Simple bars and a few complex shapes have been produced. The resulting physical and mechanical properties of the sintered LOMed ceramic bars were similar to ceramics prepared by conventional powder pressing. The properties of the LOMed bars were similar to commercially available alumina.

FUTURE WORK

The ceramic LOM process is still being developed at Lone Peak. The chief goal is to completely automate the LOM process and improve surface finish characteristics.

ACKNOWLEDGMENTS

Lone Peak Engineering thanks the Defense Advanced Research Projects Agency and Dr. William Coblenz for sponsoring this work under contract #DAAHO1-92-C-R244.

REFERENCES

1. J. Am. Cer. Soc., 64[9]: 539-543, 1981.
2. Coors Ceramics Company, Golden, Colorado, Data Sheet 7164C FP20K, 2/89, 1989.

PRODUCTION OF METAL PROTOTYPES USING A HIGH POWERED LASER MACHINING CENTRE

M S Pridham+, G A Thomson+; U Menon* and M Koch*

+ Department of Applied Physics and Electronic & Mechanical Engineering
University of Dundee
Dundee
DD1 4HN
U.K.

*Industrial and Manufacturing Engineering Department
California Polytechnic State University
San Luis Obispo
CA93407
U.S.A.

Introduction

The established commercially available rapid prototyping techniques are now well known throughout the manufacturing community. They are able to produce high quality, accurate prototypes, but are limited largely to processing polymer, wax or paper materials. Where a metal part is required, then a further process step, such as investment casting using the prototype part as a pattern is required. As a further point most of the above systems are high capital cost dedicated pieces of equipment.

This paper describes the use of laser machining centres as rapid prototyping tools in the areas of, laminated prototyping, using both paper and metal, and laser forming.

Laminated Prototyping

For a number of years there has been a considerable amount of work done, particularly in Scandinavia and Japan, in producing laminated tools and dies[1]. The principle is simple and essentially involves assembling a series of laser cut profiles and mechanically fixing them together.

Laminated prototyping is an adaptation of this technique to produce parts rather than tooling and trials have been carried out using both paper and sheet steel.

Laser Forming

Laser forming is a relatively new technique[2]. It involves using a high powered laser to track over the surface of a sheet of metal, the track being defined by the required geometry of the part. The laser parameters are set in order to soften or melt the upper

surface of the metal whilst the lower surface is essentially unaffected. The upper surface is then allowed to cool, cooling may be forced or natural, and as it does so there is a contraction, which causes the sheet to deform. Depending upon the specific laser parameters, it has been found that a fold of 2 degrees from flat is a typical of the deformation that can be expected from a single pass.

Experimental Results

Laminar Prototyping. There are essentially three stages involved in laminar prototyping; laminar geometry generation, profile cutting and joining of laminates.

Work at California Polytechnic State University has been carried out using 1.5kW CO_2 laser machining centre [3] and paper, polymer and sheet steel parts have been produced. One of the first parts processed was a model of a window frame extrusion. As can be seen from Figure 1 the part is relatively complex, the geometry was encoded in CADKEY and SMARTCAM was used to generate the laser tool paths. The component layers were cut from 2.0mm New Board and laminated using a spray on contact cement. Each layer took approximately 30 seconds to cut and a five layer part was manufactured in under 5 minutes. A similar part has also been produced using polymer sheet (see Figure 2).

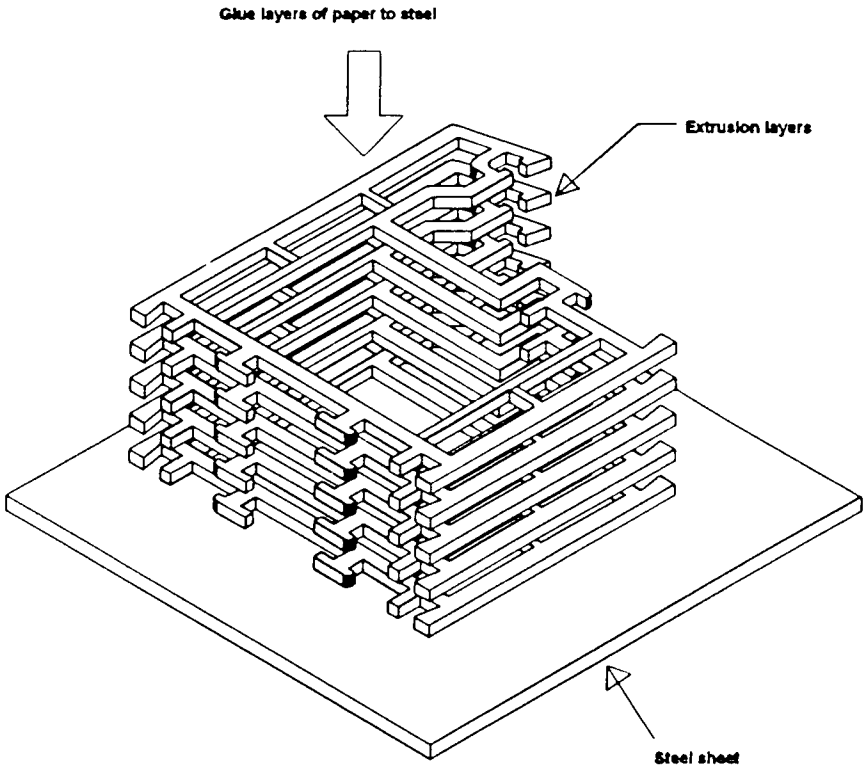

Figure 1 - Window Frame Extrusion

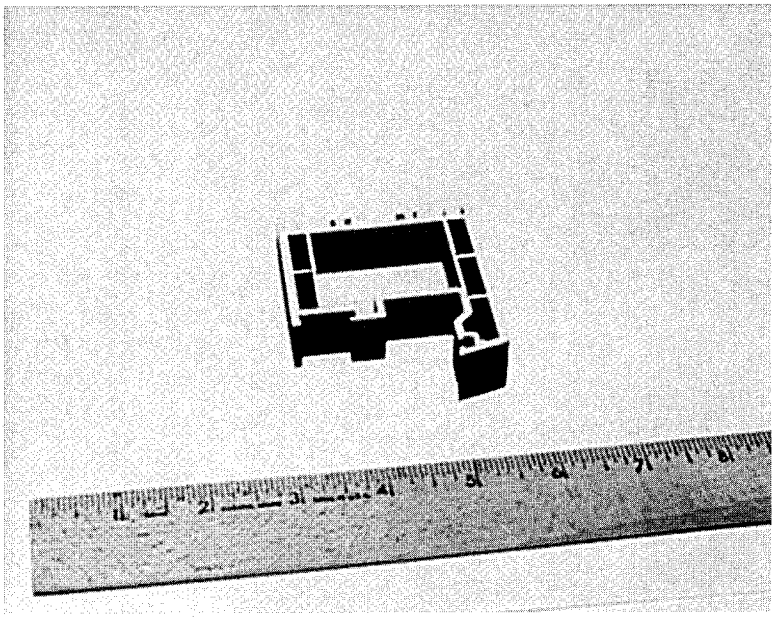

Figure 2 - Window Frame Extrusion Model Produced in Polymer Sheet

A similar technique was used to create a prototype golfclub head, (see Figure 3) the layers of this part were produced in both paper and sheet steel, as yet the steel layers have not been joined, however there are a number of techniques which could potentially be used to do this including laser welding, brazing or soldering and adhesive bonding.

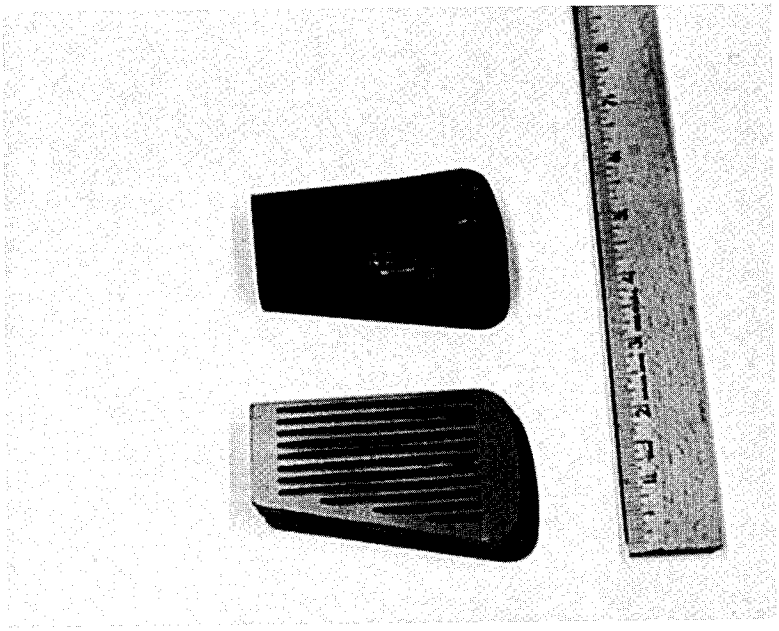

Figure 3 - Golfclub Head

Work at the University of Dundee has shown that in practice conductive laser welding has proved difficult[4]. The main problem being that in small laminae it is extremely difficult to dissipate the excess heat rapidly enough to avoid warping of the part. This problem is exaggerated by the desire to join the laminae, not just at the edge, but all over the surface area. A further problem is the limited power of the laser being used. It is however possible that conventional or laser spot welding may be practical as a joining technique in particular applications.

Figure 4 shows a test component produced from six layers of 2mm thick mild steel. These layers have been joined using a standard electrical grade solder paste in a reflow process. In this instance the paste was applied manually with no special clamping arrangement and hence the solder layers are slightly uneven in thickness. Initial tests on the solder bonds show them to be reasonably strong although the load carrying ability is highly dependent on the integrity of the interface and the bond area.

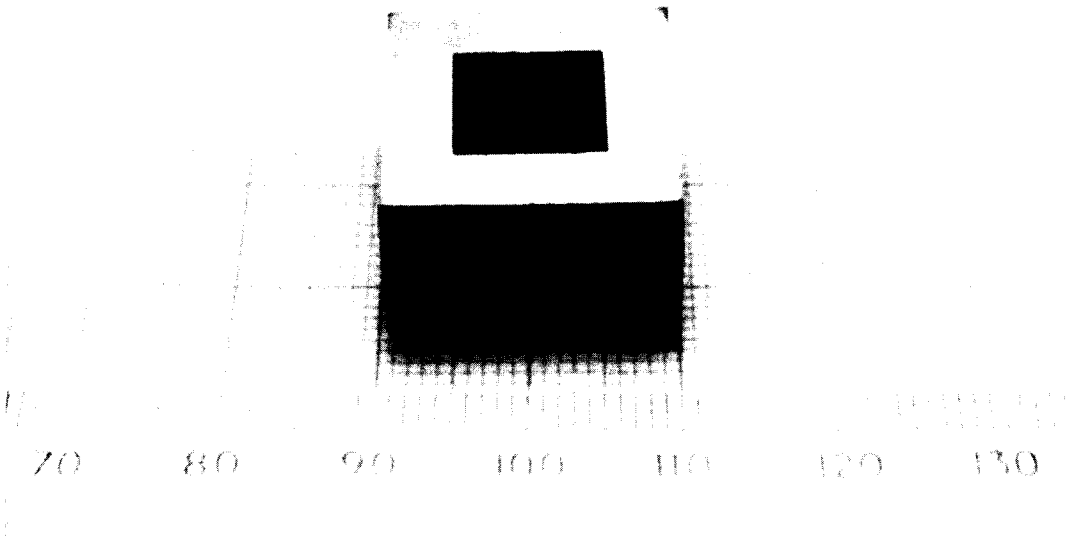

Figure 4 - Soldered Laminate Testpiece

The use of adhesives in engineering and structural applications is a growing area of interest and for certain applications would be viable as a joining technique for metal laminae. As yet only general purpose adhesives have been experimented with and these have produced robust and handleable trial components, Figure 4 shows the component laminae and adhesively bonded structure of a small square based hollow pyramid.

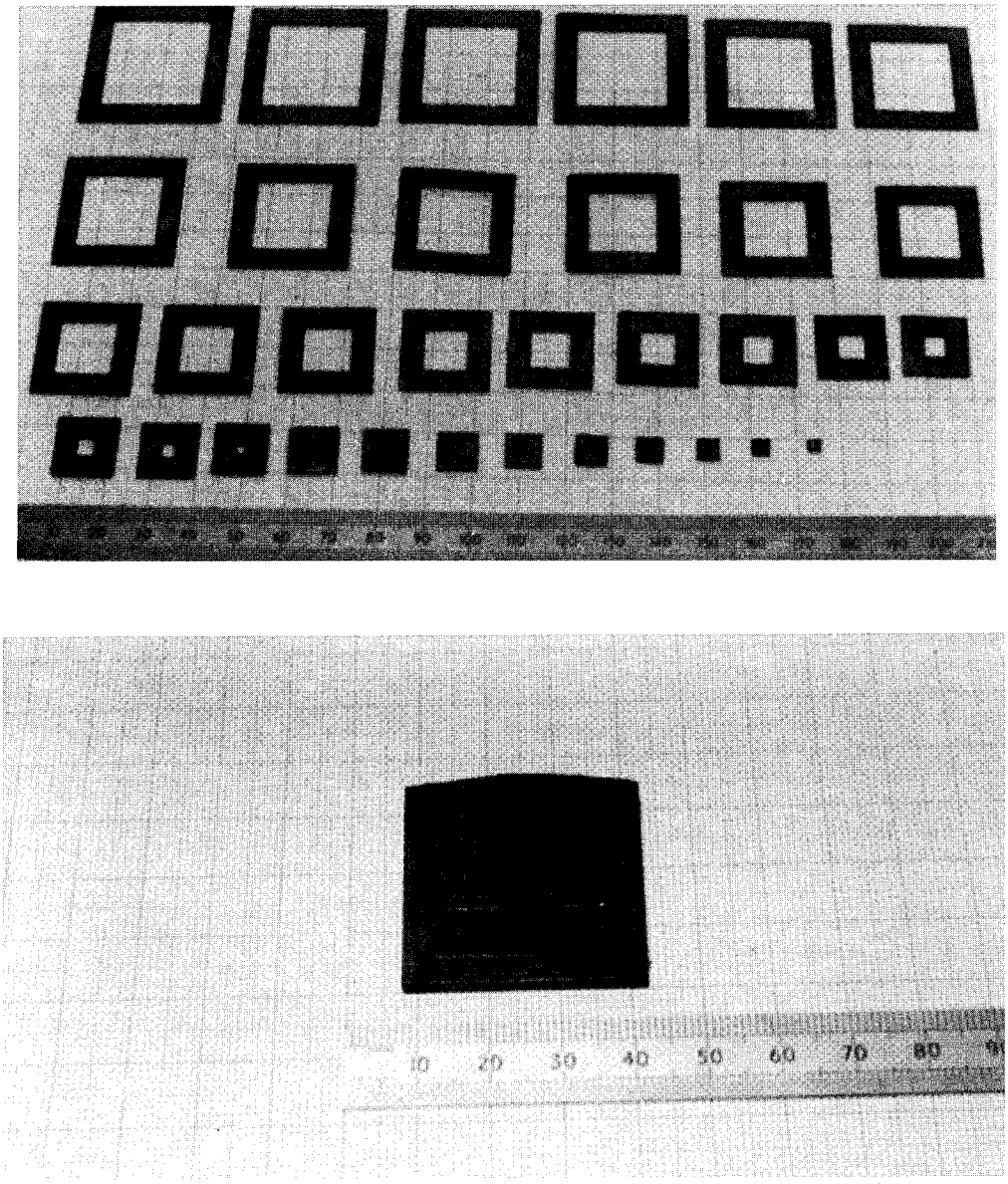

Figure 5 - Individual Laminae and Assembled Pyramid Structure

Laser Forming. Forming trials have been carried out using 1mm and 2mm thick mild steel and 304 grade stainless steel sheet. In order to assess the basic bending behaviour tests were carried out on a 40mm wide strip which was processed from flat to a full 90 degree bend. The strip was passed under the laser beam using an 80mm forward and back double pass action (the 80mm compensates for acceleration and declaration of the XY table.) The deflection against number of double passes was noted in each case. The test was repeated using different values of material thickness, laser power and traverse speed.

An indication of the laser power can be gained from the pulse ratio (which was varied between 20/200 and 20/50) and it was found that the more powerful setting resulted in the 90 degree bend being achieved more quickly. Figure 6 shows the angle of bend against number of passer for various laser pulse settings for 1mm thick stainless steel. Figure 7 shows angle of bend against number of double passes for 2mm thick stainless steel for various traverse feed rates. Figure 8 shows a typical bend produced in 1mm and 2mm thick sheet.

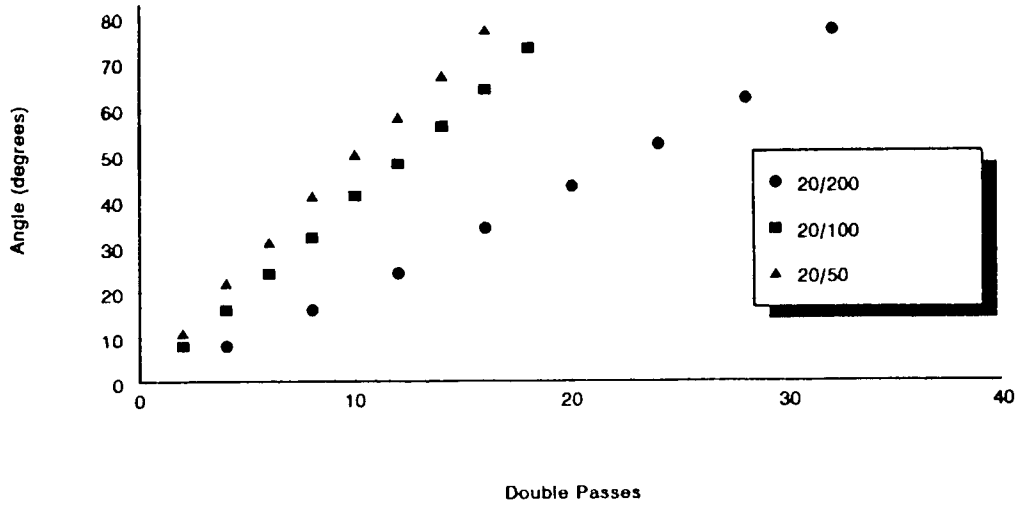

Figure 6 - Angle of Bend Against Number of Double Passes of 1 mm Thick Steel Sheel at Various Laser Pulse Settings

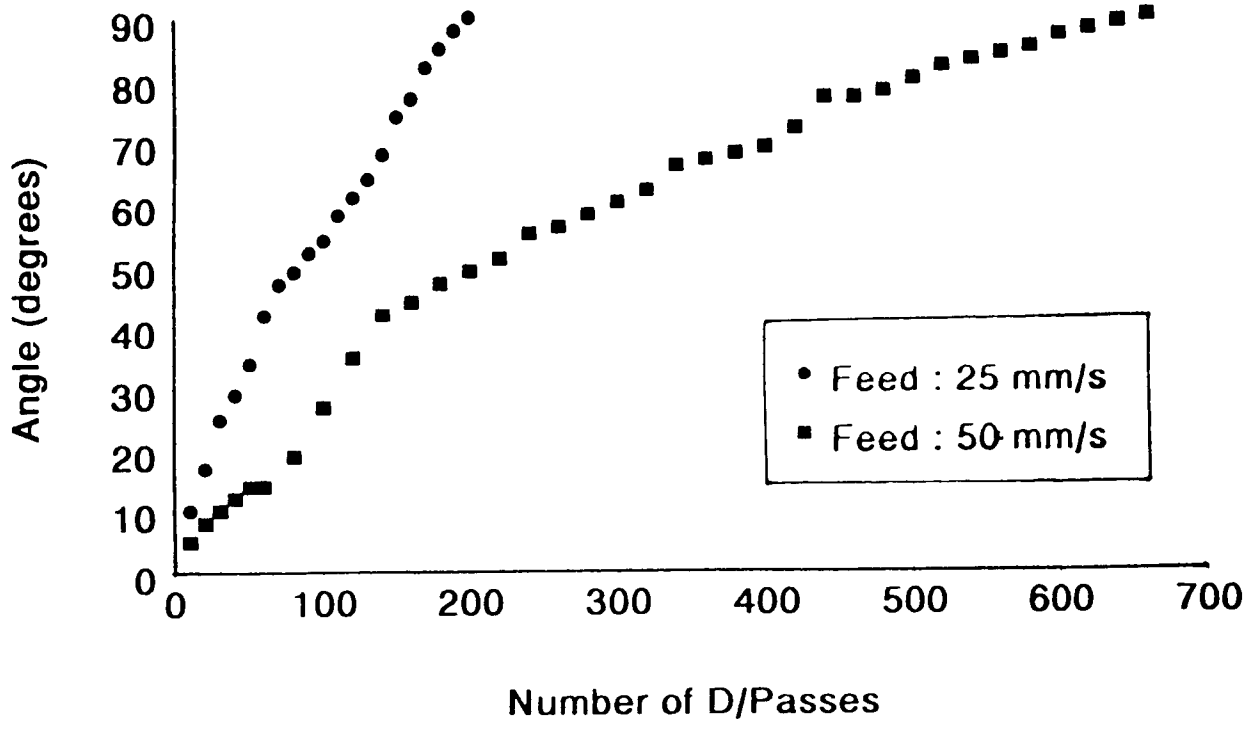

Figure 7 - Angle of Bend Against Number of Double Passes of 2mm Thick Steel Sheet at Various Traverse Feed Rates

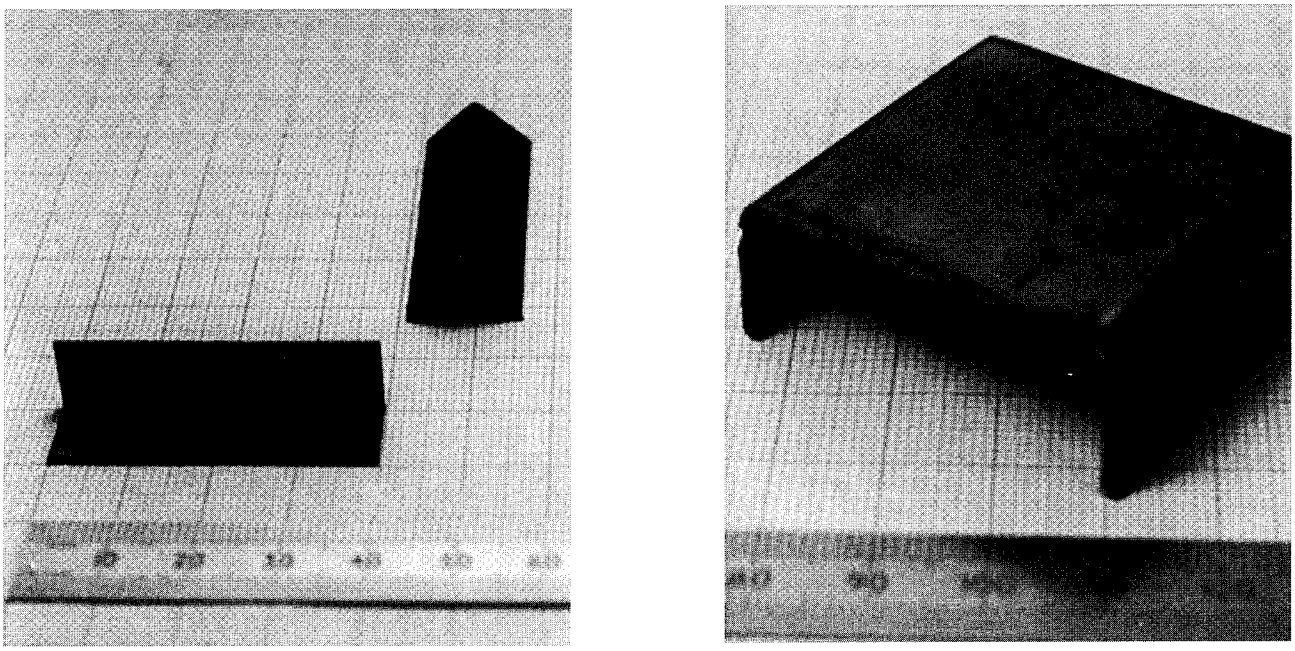

Figure 8 - Typical Bend in 1mm and 2mm Thick Sheet

Most of the current work has concentrated on forming from one side only, it is recognised that in a fully developed working system forming should be possible on both sides of the workpiece. The component shown in Figure 9 was formed from both sides, the flange sections were formed up to 90 degrees from flat pre-cut sheet. The walls were then formed from the other side which then also oriented the flange in the correct position. As more complex parts are produced using this technique it becomes apparent that the order in which particular features are formed may be critical to the success of the processing and this consideration is likely to form a significant part of future work.

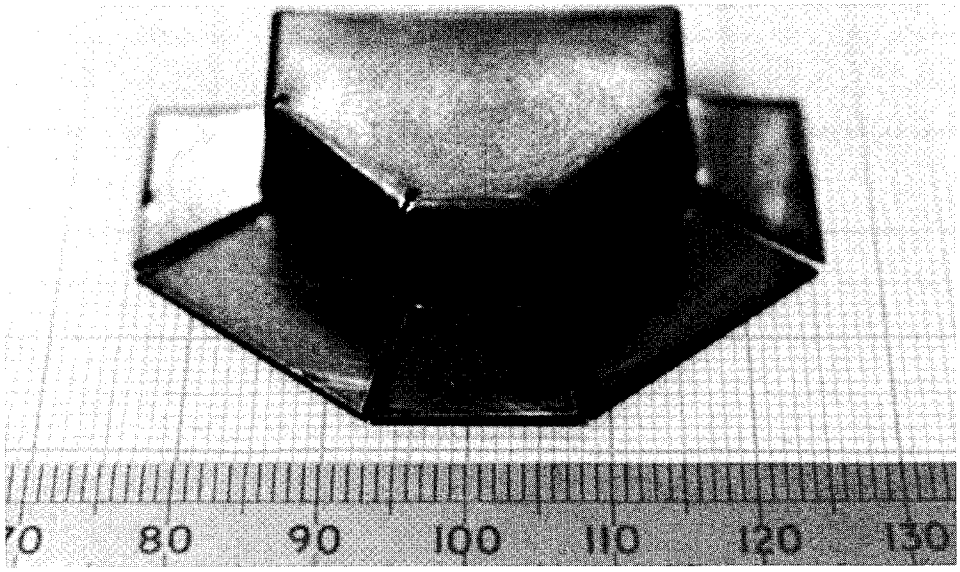

Figure 9 - Laser Forming From Two Sides of the Sheet

As an indication of the potential for systemising the laser forming process, Figure 10 shows the sequential production of a small cube which has been laser cut from sheet, laser formed, and could then be laser welded, it is possible to introduce weld tabs into the geometry to make the welding process more straightforward. The estimated time for the production of the component shown above is five minutes, from raw sheet to welded cube. It is likely that a laser manufacturing system would include a robot manipulator to facilitate the production of more complex geometries.

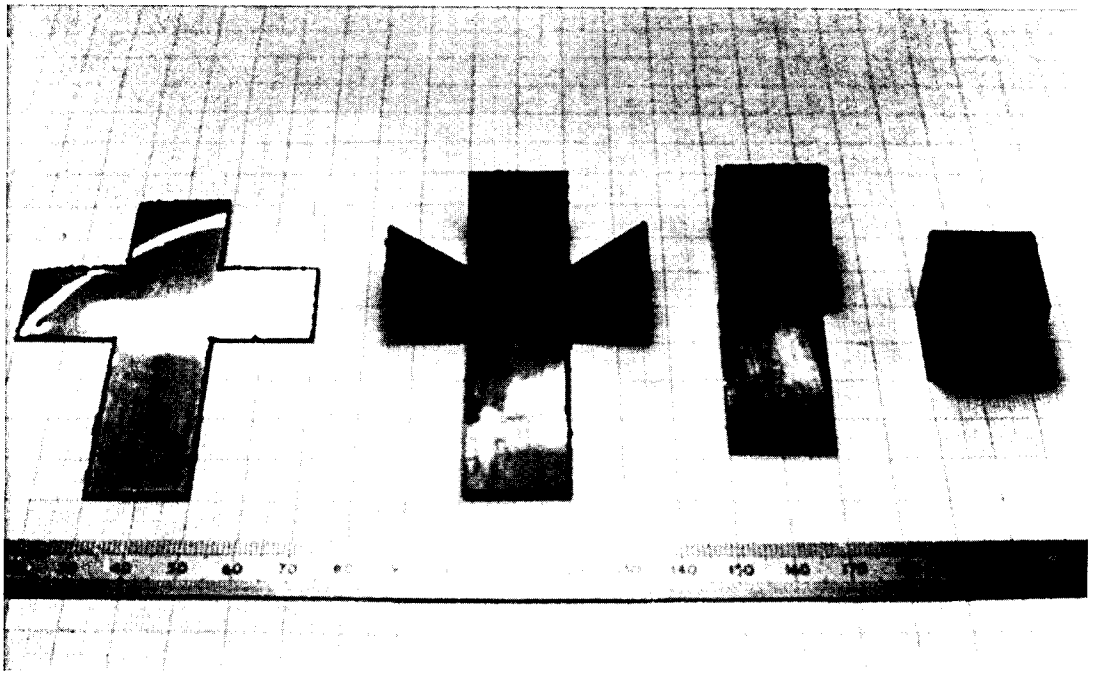

Figure 10 - Sequential Production of a Cube

Further Work

Further areas of investigation are clearly necessary in the work described above before either technique offers a practical production system.

In the case of laminar prototyping, areas of development include the refinement of the methods for joining laminae in order to make this an integral part of the process. Two further areas are currently being investigated namely varying layer thickness so that the build is optimised with respect to the profile geometry, and smoothing the layer steps possibly by using a technique such as laser cladding.

In the area of laser forming an interactive process modelling and empirical test system is being developed.

Results obtained experimentally are being used to gain an understanding of the basic process. It is hoped then to develop a more complete model, compensating for thermal and

internal physical stresses to produce the desired geometry. It is hoped that this will allow more precise control of complex curved profiles.

Conclusions

Both laminar prototyping and laser forming show considerable potential and have distinct advantages. For example laminar prototyping offers potential to produce direct metal prototypes in a single process and with no problems in producing features such as overhangs. However further work is required on methods of joining the laminae.

Laser forming offers promise in a number of industries, perhaps the most obvious is sheet metal processing but other avenues as diverse as specialist electronic devices and aids for reconstructive surgery also show considerable potential. Further work is necessary in dealing with non-linear geometry and thick material, but it is anticipated that with the assistance of computer aided process analysis and monitoring a workable system can be developed.

References

1. Kunieda, M., Nakagowa, T. (1984) *"Development of Laminated Drawing Dies by Laser Cutting"* Bulletin of the Japanese Society of Precision Engineering, Vol. 18, No. 4, pp 353-354.

2. Vaccari, J.A. (1993) *"The Promise of Laser Forming"* American Machinist, June 1993, pp 36-38.

3. Menon, U., Koch, M., Williams, T., Burke, F. *"Using a Laser Machining Centre to Provide R P Services"*. (1993) Proceedings of the 2nd European Conference on Rapid Prototyping and Manufacturing, University of Nottingham, pp 357-361.

4. Pridham, M.S., Thomson, G. (1993) *"Part Fabrication Using Laser Machining and Welding"*. Solid Freeform Fabrication Symposium, University of Texas at Austin, pp 74-81.

Video Microscopy of Selective Laser Sintering

Lawrence S. Melvin III, Suman Das,
and Joseph J. Beaman Jr.
Department of Mechanical Engineering
The University of Texas at Austin

Abstract

This paper presents the design and implementation of a video microscopy system that enables real time observation and archival of selective laser sintering of polymer and metal materials. The design objectives and selection of system components are discussed in the first section of this paper. Experimental results from preliminary experiments conducted on polycarbonate, wax and nylon powders are also presented.

Introduction

Current understanding of the dynamics of the Selective Laser Sintering process is based upon theoretical analysis of the process and macroscopic experimentation in real time. In order attain a better understanding the physics of the sintering process, direct experimental observation of the process is an important tool. To facilitate this observation, a video microscopy system has been designed to observe both polymer and metal materials while they are being laser sintered.

The first part of this paper discusses the design objectives and selection of system components for the video microscopy system. The second part presents experimental results from preliminary work done on video microscopy of the selective laser sintering of polycarbonate, wax and nylon powders. Figure 1 shows a schematic of the video microscope camera assembly.

Video microscopy system design

Magnification

The first parameter of the video microscopy system is its magnification. There are two types of magnification used in this system, optical magnification and pixel enlargement.

Optical magnification is produced by the camera lens and is due to the magnification of the light entering the lens. This magnification is referred to here as 'true magnification'. An increase in true magnification results in a larger on screen image, a need for more illumination of the test area, and an decrease in the focal length [Tipler, P. A., p. 885].

Pixel enlargement, or digital magnification, is the result of the electronic transfer of a discrete image from the small viewing area sized one half inch diameter, of the camera to the large presentation area sized 13 inch diagonal, of the monitor. The camera is comprised of a chip with an array of photosensors. The information each sensor receives is a discrete portion of the picture, known as a pixel. The information from the small viewing area is transmitted to the large viewing area electronically. This results in a digital magnification of 20X. A greater digital magnification of 30X is achieved by viewing the process on a 21 inch diagonal monitor.

The problem with pixel enlargement is that it enlarges each pixel in the magnification process, with no regard for the image as a whole. This phenomenon maybe characterized by stating that the more pixel enhancement present, the more grainy and distorted the final image becomes.

In order to reduce graininess and produce a more clear image, the camera and monitor must be carefully chosen. The grainy image is reduced by increasing the number of pixels in the image. Therefore, a black and white camera with 1000 TV lines of resolution and a monitor with 560 TV lines of resolution were chosen for this system. A household TV set has approximately half this number of lines of resolution.

The total magnification requirement for the video microscope system, i.e. the combined optical and digital magnification was set to a minimum of 100X. In order to maintain a reasonable focal length of least four inches, a zoom lens that could focus between 1X and 6X was chosen.

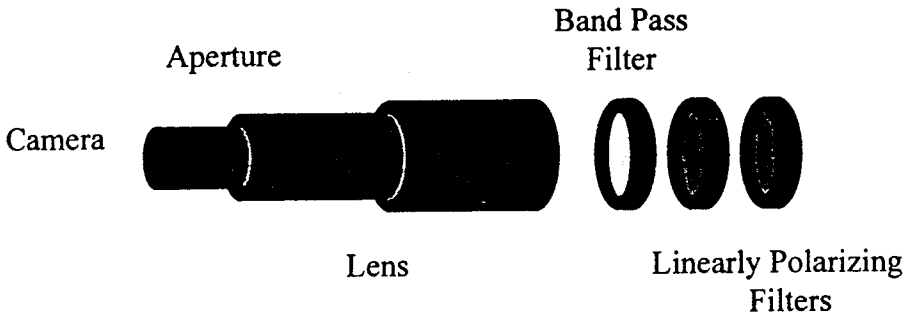

Figure 1
Video microscope camera assembly

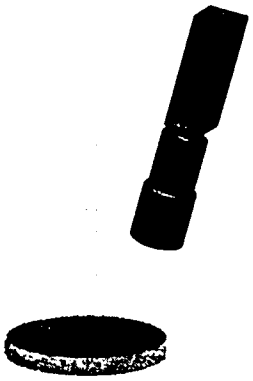

Figure 2
Video microscope viewing position

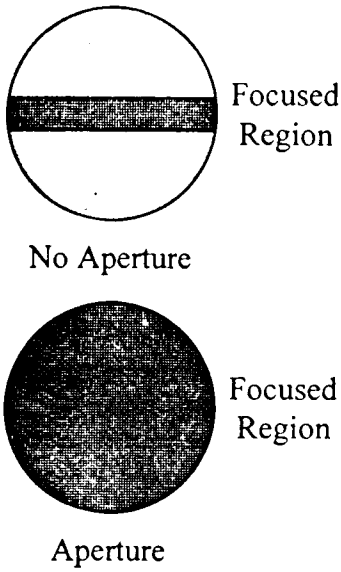

Figure 3
Aperture effect

Aperture

The aperture is one of the most important parts of the video microscopy system. The camera and lens must view the powder bed at an angle to avoid contacting the laser beam as shown in Figure 2 above. The aperture provides depth perception [Reynolds, L.D. and Key, J.F., p. 14], which allows the camera to view the powder bed from an angle. Figure 3 illustrates the difference between an angled system with an aperture, and one without. The system without the aperture can only focus on a narrow band in the field of view, while the system with an aperture can focus on the entire region. The aperture also enables the camera to remain focused on particles which are changing shape in the direction of the camera axis.

The aperture is an adjustable iris shutter placed between the lens and the camera. As the aperture is closed, depth perception of the viewed area increases. However, light is also blocked as the aperture is closed. Therefore, the greater the depth perception, the more illumination required.

Filters

Optical filters are used to clarify the image gathered by the lens. Two types of filters are used, a linearly polarizing filter and a band pass filter. The linearly polarizing filter reduces glare during sintering. This occurs because the glare from a liquid surface is normally polarized [Tipler, P. A., p. 867]. A second linearly polarizing filter is added

when the intensity of the light incident on the sintered surface is very high. The second filter is rotated to reduce the amount of light that reaches the camera.

A band pass filter is used to eliminate thermal radiation when viewing metal sintering. When metals are sintered they have been observed to emit electromagnetic radiation in the red and yellow range and into the infrared spectrum. This radiation disrupts the quality of the video picture [Ogura, A. et. al., p. 753]. Therefore, the lighting system and band pass filter have been designed to observe the system in the 550 nm wavelength range with a wavelength band of 40 nm. This helps eliminate thermal radiation from metals.

In some video microscopy design specifications, the filters and lighting are designed to pass through any vapor phase which is present during the heating process. Voelkel and Mazumder designed a video microscopy system to view laser welding melt pools, and in doing so, the light source was designed to pass through any vaporized metal collecting around the melt pool. However, in the Selective Laser Sintering environment, the metal materials being viewed vary from copper and nickel to iron and steel as well as some ceramic materials. This material variability makes it difficult to tune the lighting and filter systems to the material specific optical properties. For this reason, designing the lighting and filtering systems to eliminate vapor interference was not undertaken. No adverse effects have been observed due to this neglect.

Lighting

The lighting system was also designed to combat the thermal radiation emitted by metals. Mercury vapor lamps were chosen as the illumination source because they emit 50% of their radiation at approximately 545 nm and 25% at 580 nm [Philips]. They are also capable of producing a large amount of light per bulb.

The light which is received by the photoreceptor chip in the camera is drastically reduced by the lens and filters [Reynolds, L. D., and J. F. Key p. 23]. Each of the polarizing filters reduces the incident light by 50%, as does the band pass filter for metals. The aperture also eliminates 50% or more of the incident light. This results in 6.25% of the 75% of useable light being received by the photoreceptor in the case of metals and 12.5% of the incident light being received in the case of polymers.

Multiple light sources were used to provide adequate illumination to the sintering area for viewing and to reduce or eliminate shadows. Three light sources were placed in increments of 120° to reduce the incidence of shadows in the system. If the lighting is not adequate or in the proper position, depth perception is hindered by shadows.

Experimental Results

Introduction

This section of the paper describes a selection of video microscopy experiments performed with the aforementioned system. A number of experiments were run on poly-

carbonate, wax and nylon powders. Stationary laser spots and single scan lines were studied under a variety of laser parameters.

Stationary laser spots were studied at low laser powers of the order of 1 Watt in order to slow down the sintering kinetics for observation. At higher powers, pyrolysis occurred immediately upon turning the laser on. Single scan lines studied were at conditions which allowed us to observe the sintering phenomena in great detail in relatively large time scales. The laser spot size used was approximately 3 mm. A few excerpts from our video presentation are shown below:

1. Figures 4-7 are frames taken from an experiment of a stationary laser spot on polycarbonate powder at a laser power of 1.5 Watts. Melting and collapse is followed by formation of a liquid pool. Bubbles of vapor are seen to form inside the liquid pool. This may be due to trapped air tying to escape. Charring in some regions suggests that pyrolysis is occuring.

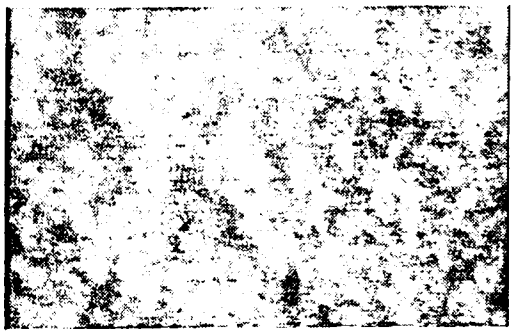

Fig. 4

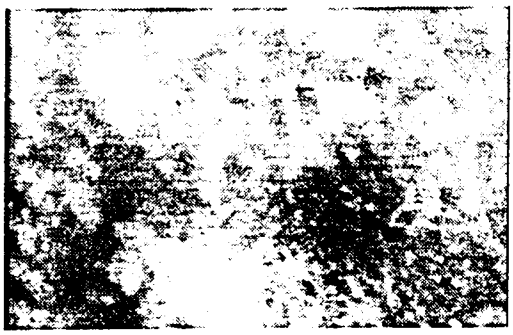

Fig. 5

Fig. 6

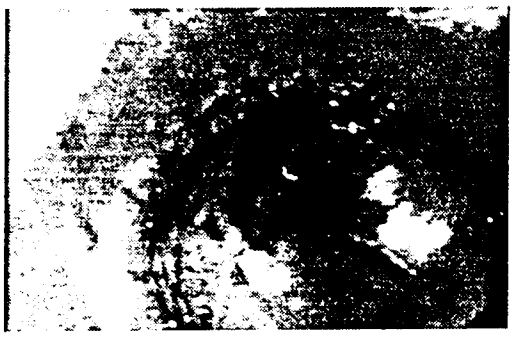

Fig. 7

2. Figures 8-11 are frames taken from an experiment of a stationary laser spot on wax powder at a laser power of 0.8 Watts. Melting is immediate with formation of strong convection currents. Some bubble formation is also observed.

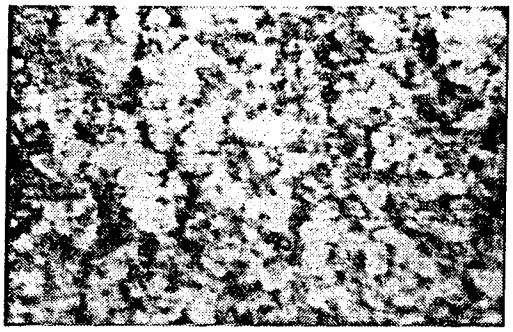

Fig. 8

Fig. 9

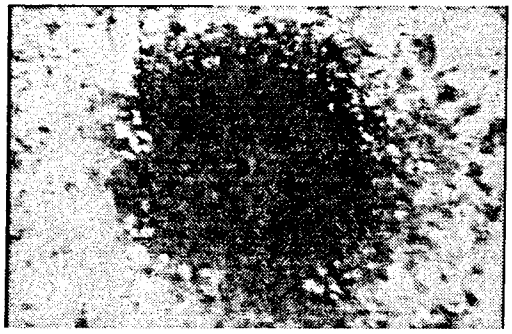

Fig. 10

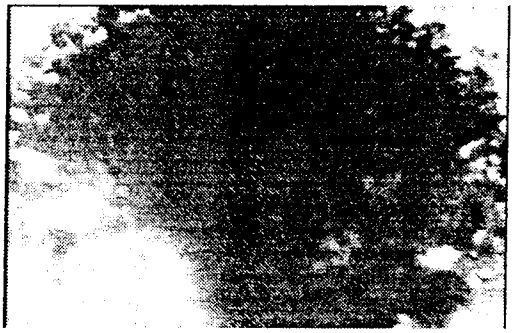

Fig. 11

3. Figures 12-15 are frames taken from an experiment of a single line scan on nylon powder at a laser power of 1 Watt and a scan speed of 0.03 inches/s. Considerable amount of vapor bubbles are formed. Surface solification can be observed quite clearly at the end of line scan.

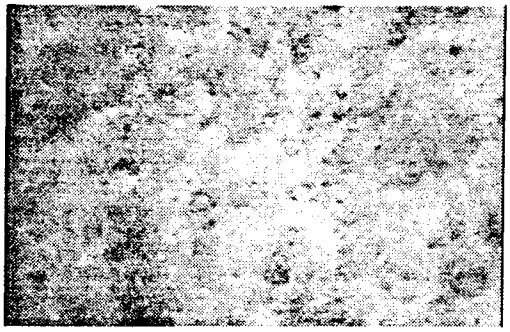

Fig. 12

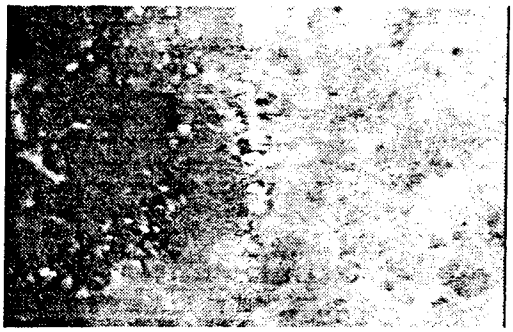

Fig. 13

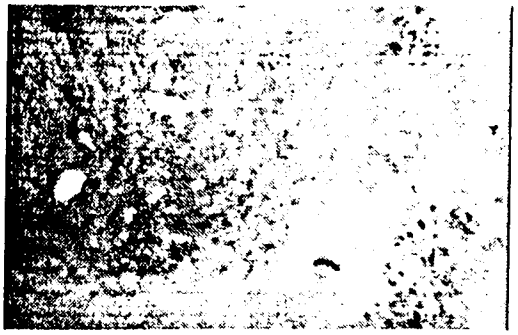

Fig. 14

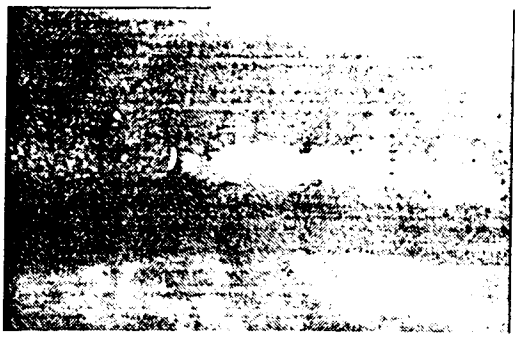

Fig. 15

Summary

The phenomenon of vapor bubble formation and entrapment in the liquid pool needs to be investigated further to determine the vapor content. At present, we believe it is due to air trying to escape; however, it might also be due to steam or gases evolved during pyrolysis. Reduction of vapor bubbles may help improve final part density.

While scanning lines at slow scan speeds, all three materials appeared to receive sufficient energy input to form a liquid layer that flowed and spread well. At higher scan speeds and higher laser fluence, unsintered powder seemed to wrap around the line being scanned. In the case of polycarbonate, this resulted in incomplete sintering of the material and significant depletion of surrounding material. In the case of nylon, there was considerable shrinkage and depletion of surrounding material.

Conclusions

A video microscopy system has been designed and implemented to observe selective laser sintering of polymers and metal materials. Initial experiments conducted with this system have allowed us to observe sintering and flow behavior in greater detail than ever before. This has allowed us to qualitatively evaluate the different sintering characteristics of the materials studied.

The next logical steps in these experiments would be:

1. Perform video microscopy experiments on the Selective Laser Sintering of metals.

2. Examine sintering behavior of spots and lines in these materials with a variety of boundary conditions describing the layer immediately underneath the sintering plane (e.g. conducting layer corresponding to a previously sintered layer).

3. Quantify sintering and densification rates based upon microscopic observation.

References

Ogura, A., et. al., "High-speed Video Observation of a Laser Recrystallization for Semiconductor-on-insulator Fabrication," Journal of Applied Physics, Vol. 65, No. 2, January 15, 1989, pp. 752 to754.

Philips Lighting, "Mercury Vapor Lamps," Sales Brochure, February 1989.

Reynolds, L. D., and J. F. Key, High-Speed Cinematography of Gas-Tungsten Arc Welding - Theory and Application, U. S. Department of Energy, Idaho National Engineering Laboratory, Publication EGG-FM-5051, June 1981.

Tipler, P. A., Physics, Worth Publishers, Inc., New York, NY, 1982.

Voelkel, D. D., and J. Mazumder, "Visualization of a Laser Melt Pool," Applied Optics,Vol. 29, No. 12, April 20, 1990, pp. 1718-1720.

FDM® TECHNOLOGY PROCESS IMPROVEMENTS

James W. Comb

William R. Priedeman

Patrick W. Turley

Stratasys, Inc.
Eden Prairie, Minnesota

ABSTRACT

Since the introduction of rapid prototyping technology as a tool for time compression and concurrent engineering in the design and manufacturing process, many enhancements and refinements have been made based on the experience of users and manufacturers of rapid prototyping equipment. These improvements contribute significantly to faster production of quality output from rapid prototyping systems.

There are diverse control and material selection parameters that affect prototype models built using the Fused Deposition Modeling (FDM®) process. This paper reviews the role of several of these parameters in the process. Data will be presented to help the user choose the appropriate material for specific applications including density, tensile modulus, flexural modulus, tensile strength, flexural strength, impact strength, and hardness.

The integration of material, hardware, and software in the FDM technology begins with the understanding of the basic requirements of the machine and ends with an operating procedure to choose the parameters for optimal model output and efficiency. Some of the variables include: part geometry, deposition geometry, deposition speed, liquefier temperature, material, flow control parameters, etc. Designed experiments are used in material formulation through modeling parameter definition activities.

INTRODUCTION

The fused deposition modeling process for rapid prototyping integrates three key components of the system: software, hardware, and materials. Each component can be analyzed independently for very simple model systems, but for real systems and broad operating conditions, the system complexity and interactions grow. The challenge to develop user-friendly FDM rapid prototyping systems is to define the relationship between the key input variables and the key modeling characteristics, or responses. Designed experiments can begin to identify the key variables and lead to strategies for optimizing the modeling process in a very efficient manner.

PROCESS

The FDM process forms three-dimensional objects from CAD generated solid, wire frame or surface model data through the consistent dispensing of individual layers or thermoplastics materials through a controlled temperature head. The model is built layer upon layer, from the bottom up. The designed object emerges as a solid three-dimensional part without the need for tooling.

The process involved in the development of a three-dimensional model begins with the creation of a conceptual geometric model on a CAD workstation. The model is imported into the ProtoSlice® software program which mathematically slices the conceptual model into horizontal layers and deposition paths are created. The path data is then downloaded to the modeler. The modeler operates in the X, Y, and Z axes, basically drawing the model one layer at a time. Once the build cycle begins, no operator attendance is required.

A spool of thermoplastic modeling material, .070 inches (.18 cm) in diameter, feeds into the temperature controlled FDM extruding head, heating the material to a semi-liquid state. The semi-liquid is extruded and deposited into

A spool of thermoplastic modeling material, .070 inches (.18 cm) in diameter, feeds into the temperature controlled FDM extruding head, heating the material to a semi-liquid state. The semi-liquid is extruded and deposited into ultra-thin layers onto a fixture-less base. Once the material is directed into place by the X-Y controlled FDM head, the material solidifies, creating a precision laminate.

MATERIALS

Users of rapid prototyping technology tend to request models with materials whose properties are similar to materials they might use in their end-use applications, e.g. injection molding. In reality, each rapid prototyping technology rarely brings all the properties of an end-use material to the designer, and FDM is not an exception to this. Materials used in Fused Deposition Modeling must satisfy the requirements of the designer, their subsequent application, and their integration into the FDM process.

As a subset of the universe of thermoplastic materials, FDM materials form strong interlayer bonds at or near their melting points and have appropriate composition and morphology to provide a relatively stress-free, low distortion part once the material has reached room temperature.

An FDM material must also have an adequate flexural modulus and strength to be formed into a filament, spooled, and used as a piston to pump the material through the head, liquefier, and tip. In addition, it must have sufficiently low viscosity to be pumped through the same hardware and also produce well-defined road widths over a broad range of geometries and deposition rates.

These requirements specify the materials which will effectively produce quality models using the FDM process. Some familiar candidate polymer chemistries include polyolefins, polyamides, and polyesters. The four materials currently available from Stratasys have the mechanical properties shown in Table 1. MW01 and ICW04 are wax formulations for use in the investment casting process; and P200 and P300 are plastic formulations (polyolefin and polyamide, respectively) that are stronger and have higher melt points.

Thermal and rheological analysis has been performed on all of the current materials. These data have been important in designing the mechanical components of the FDM head which melt and pump the material. Figures 1-3 show this data for ICW04, the Stratasys investment casting wax. Melt viscosity is measured using a vibratory rheometer. Thermal analysis was performed using differential scanning calorimetry (DSC) and volumetric expansion by thermal mechanical analysis (TMA). ICW04 has the lowest volumetric expansion of the current materials. Table 2 lists the ash content, specific gravity, softening point (R&B), and penetration.

HARDWARE

Figure 4 depicts the mechanical design of the FDM head. The function of this assembly is to heat and pump the modeling material through the tip and onto the modeling surface to produce precise parts. It is a lightweight assembly designed to move at modeling speeds without affecting positioning accuracy.

A small D.C. motor drives a set of feed wheels to provide up to 10 lbs force to push the filament through the liquefier and tip. The feed wheels, which are 1/2" in diameter and covered with an elastomer, are driven in a counter-rotating direction to provide the torque to feed the filament, which acts as a piston. The material must have sufficient column strength to accomplish this task; column strength is a function of the filament diameter, flexural modulus and strength. This provides a positive feed allowing no slippage of the filament.

In the FDM process, material is deposited in layers with rectangular cross-section known as roads, and these have a width (W) and a height (Z). Coupled with the speed of the deposition (S), a volumetric flow rate which the system must provide is defined. The feed mechanism must be able to meet or exceed this flow rate over the full range of viscosities and pressure drops. The design considerations involve the material properties described earlier. The pressure (P) which develops in the liquefier and tip is dependent upon the length and diameter of the liquefier (d_L,L_L) and tip (d_T ,L_T) as well as the material viscosity (h) at temperature (T), and volumetric flow rate ($\dot{V}$). The

tip diameter has a very large impact on the pressure drop because it is much smaller than the liquefier diameter. For Newtonian fluids, the pressure drop can be expressed as[1]

$$P = \frac{128\hat{h}\dot{V}}{\pi}\left[\frac{L_T}{d_T^4} + \frac{L_L}{d_L^4}\right]$$

Because pressure is force divided by area and the area is the cross-sectional area of the filament in FDM, the force is proportional to pressure as well. A force vs. volumetric flow rate curve is shown in Figure 5 for various tip sizes and liquefier combinations. This data was taken using the P200 material with tips of .010", .016", and .052", and liquefier temperatures of 102 and 107^{0}C. As the theoretical equation implies, extrusion force is heavily dependent on tip size. This force is also significantly influenced by liquefier temperature, though to a lesser extent, as material viscosity decreases at higher temperatures. For a given set of operating conditions, the maximum flow rate can be determined by comparing that extrusion force with the column strength of the incoming filament.

A key characteristic of a finished model is the surface finish which is a function of the liquefier viscosity, envelope temperature, deposition speed of the material, and the geometry of the part. The liquefier and tip must heat the material to setpoint and the feed mechanism must pump the material out of the tip at the full range of tip diameters and material viscosities. The required heat transfer is a function of the thermal properties of the liquefier, tip, and modeling materials as well as the diameter of the filament and volumetric flow rate. Whereas it is advantageous to increase the filament diameter to increase the column strength for pumping, the reverse is true for melting the modeling material. The envelope temperature can affect the surface finish (see Figure 6) of the model by softening the material and reducing its flexural modulus. As a new layer is deposited, the previous layer may deflect downward causing preferential flow, due to a lower pressure drop and a poorly defined road width.

SOFTWARE/FIRMWARE

This discussion is limited to the pumping and motion control rather than the slice routines. The software/firmware control the motion of the head assembly on the carriage and also the motion of the feed wheels. The major tasks of feed wheel control can be broken down into two major categories: steady-state and transient behavior; i.e., start/acceleration and stop/deceleration activities. Steady-state pumping requires very accurate carriage and feed wheel control to assure precise geometry and road width. At the start or stop of the road, material flow is inherently different and requires different motor control to accommodate visco-elastic material behavior to precisely begin or end a road.

Before the carriage moves to start a new road, the feed wheels meter a small amount of material in anticipation of the carriage accelerating to the steady-state. When the carriage moves, the flow is slowly turned on based on constant acceleration to the full pumping rate. Likewise, near the end of the road, the pumping rate decelerates prior to the actual end point which creates a "starving" condition at the end point. The deceleration, acceleration, and pre-start metering control values are dependent on the material visco-elastic properties at the application temperature. Each material has its own characteristics which must be programmed into the software/firmware.

SYSTEM INTEGRATION

The integration of material, hardware, and software in the FDM technology begins with the understanding of the basic requirements of the machine and ends with an operating procedure to choose the parameters for optimal model output and efficiency. Some of the variables include: part geometry, deposition geometry, deposition speed, liquefier temperature, envelope temperature, material, flow control parameters, etc. Designed experiments are used in material formulation through modeling parameter definition activities.

In the development process, the sheer number of variables to be considered is overwhelming, and therefore the use of small screening designs has great utility[2,3]. The following example illustrates a material formulation mixture design and shows how it is organized, executed and analyzed. The purpose of this design is to screen, or identify, the critical variables. It is a linear design which allows analysis of individual variables only, and as a four

component mixture, it contains nine unique trials. Table 3 shows the design and uses coded variables to illustrate the two levels (-1 and +1) and a center point (0).

Table 4 contains actual values for this example. Note that the sum of the components for each trial is one. The experiment is executed by preparing the trial mixtures and measuring the responses. Table 5 shows the response matrix of some of the properties that are important to an investment casting wax. These include softening point, density, ash, viscosity and volumetric expansion. Values for all the trials are listed in this table.

Next, regression analysis reveals the relationship between the variables and responses (Table 6), and the significance of each variable. The summary results figure indicates significance with stars - the more stars, the greater the significance. Finally, a graphical representation of the fit (Figure 7) can reveal meaningful trends. In this case, viscosity at 70^{0}C.

Another designed experiment we frequently use is the two variable, two level factorial with the center point (Table 7). An example for this type of experiment would be illustrated by Figure 6 where the liquefier temperature and air (envelope) temperature are variables, and surface finish, delamination and plugging are responses. A robust modeling zone is therefore identified. At this stage, some candidate materials may be eliminated due to lack of lamination, low flexural strength, and/or excessive viscosity.

The goal of the next stage is to expand the variables constrained in the first experiment. These would include tip diameter, deposition speed, deposition geometry, part geometry, liquefier temperature, and envelope temperature. Typically, this is done over a broad range of standard models and test parts. The hard barriers previously described are defined at this stage. Material formulations can be compared to determine which of the initial formulations offered the most desirable characteristics, and can lead to additional designed experiments if the product requirements are not met.

The final stage involves the definition of the flow control parameters in the software/firmware. This is accomplished by iteratively determining the values on test geometries within the modeling parameter envelope.

CONCLUSIONS

The integration of material, hardware, and software/firmware in FDM is accomplished in an efficient manner by understanding the basic independent functions of each system and using designed experiments to lead to optimal results.

REFERENCES

[1]Michaeli, W., 1984, "Extrusion Dies," Hanser, Munich.

[2]Box, G.E.P., Hunter, W.G., and Hunter, J.S., 1978, "Statistics for Experimenters," Wiley, New York.

[3]Wheeler, B., Betsch, R., and Donnelly, T., 1993, "ECHIP User's Guide and Reference Manual," ECHIP, Incorporated, Hockessin, Delaware.

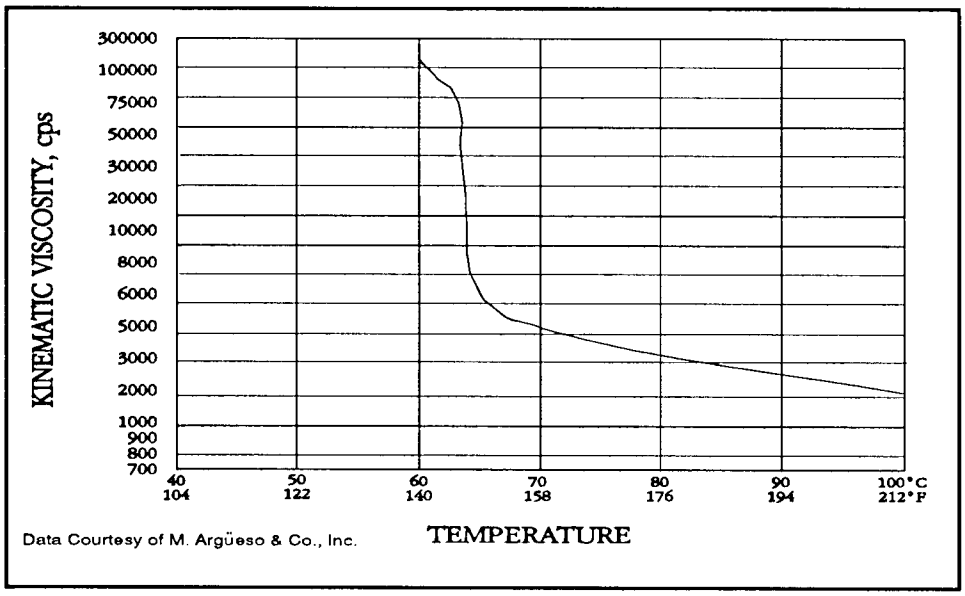

FIGURE 1. MELT VISCOSITY

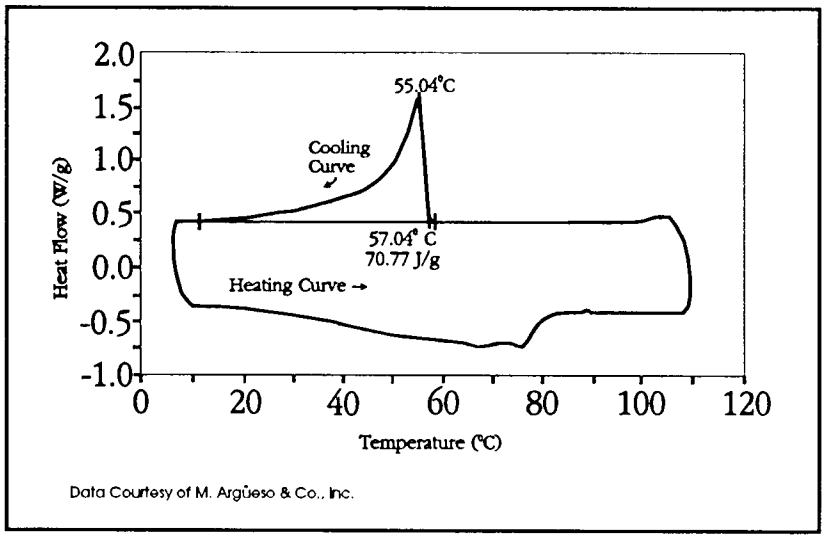

FIGURE 2. DSC THERMAL ANALYSIS

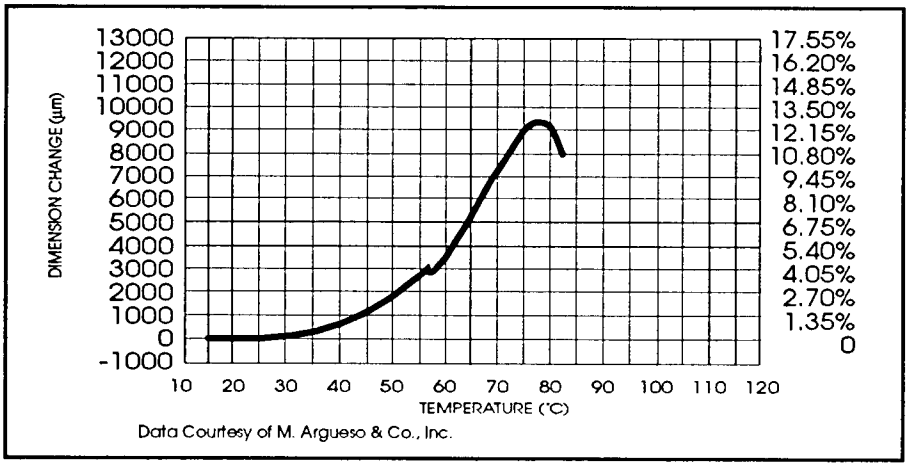

FIGURE 3. TMA VOLUMETRIC EXPANSION

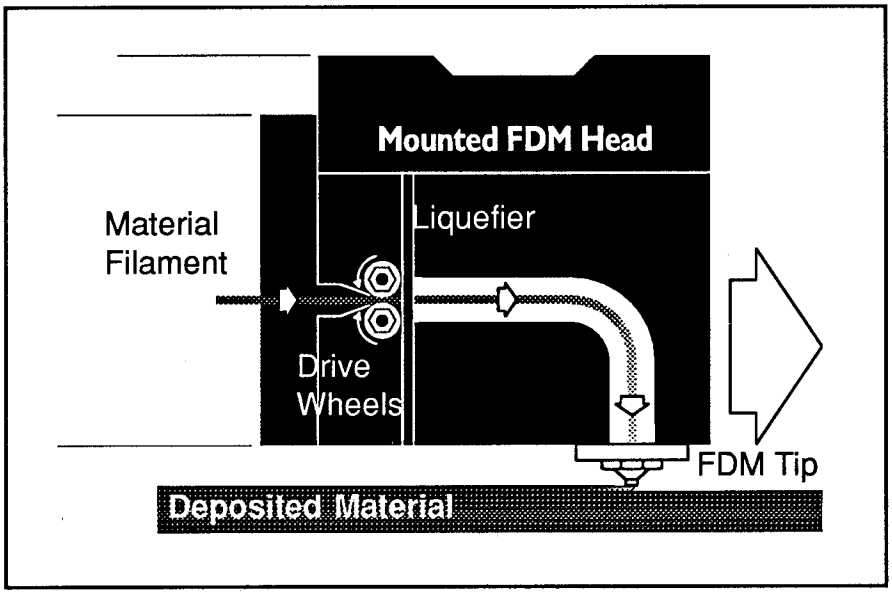

FIGURE 4. FDM HEAD

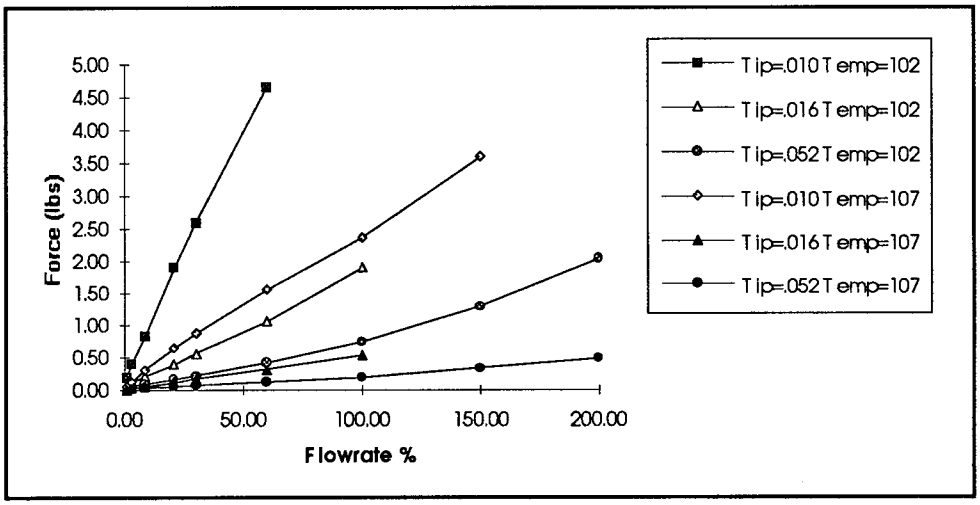

FIGURE 5. FORCE TO EXTRUDE P200 VS. TIP SIZE VS. LIQUEFIER TEMPERATURE

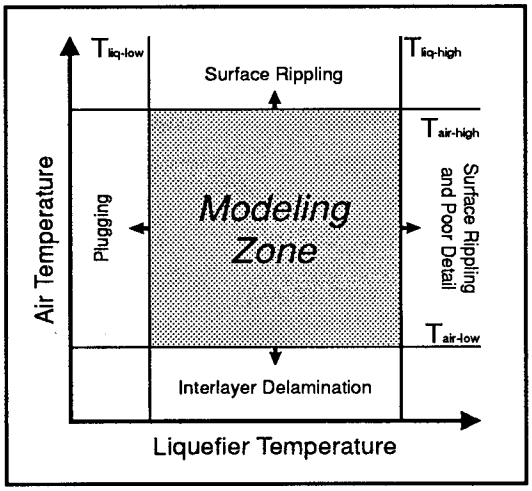

FIGURE 6. TEMPERATURE PARAMETERS

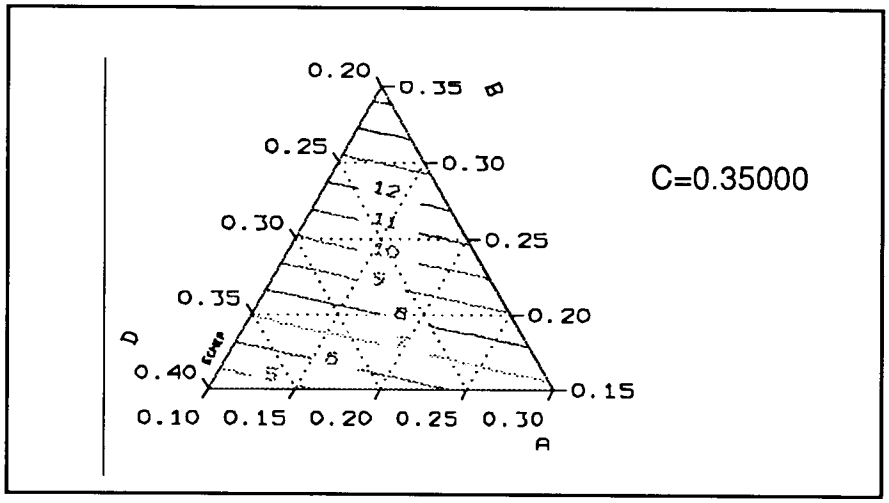

FIGURE 7. RESPONSE CONTOUR PLOT

PROPERTY	ICW04	MW01	P300	P200
Tensile Strength (psi)	509	1,114	1,765	1,324
Tensile Modulus (psi)	40,000	70,000	80,000	90,000
Elongation (%)	10.00+	6.65	3.48	4.68
Flexural Strength (psi)	619	1,293	2,113	1,537
Flexural Modulus (psi)	40,000	50,000	60,000	90,000
Notched Impact (ft*lb/in)	0.32	0.72	0.24	0.17
Unnotched Impact (ft*lb/in)	0.92	12.9	1.46	1.37
Hardness (Shore D)	33	40	70	58
Softening Point (R&B)(F)	177	227	---	---
Melting Point (C)	---	---	100-110	72-108
Specific Gravity (gm/cm³)	1	0.92	1.1	0.9

TABLE 1. MATERIAL PROPERTIES

Softening Point: (Ball and Ring)	177°F
Hardness Penetration: (450 gms., 5 sec., 77°F)	17.0 Dmm
Specific Gravity: (gm/cm3)	1
Ash Content:	0.0075%
Filler Content:	0.00%

TABLE 2. ICW04 ANALYSIS

Trial	A	B	C	D
1	+	-	-	-
2	-	+	-	-
3	-	-	+	-
4	-	-	-	+
5	0	-	-	0
6	-	0	-	0
7	-	0	0	-
8	-	-	0	0
9	0	-	-	0

TABLE 3. DESIGNED EXPERIMENT - FOUR COMPONENT MIXTURE

Trial	A	B	C	D
1	.40	.15	.25	.20
2	.10	.45	.25	.20
3	.10	.15	.55	.20
4	.10	.15	.25	.50
5	.25	.15	.25	.35
6	.10	.30	.25	.35
7	.10	.30	.40	.20
8	.10	.15	.40	.35
9	.25	.15	.25	.35

TABLE 4. SAMPLE MATRIX

Trial	Softening Point (°F)*	Penetration (Dmm)**	Density (gm/cm³)	Ash (%)	Visc. (cps, 70° C)	Volumetric Exp. (%)***
1	167.5	15	1.009	.0055	8250	16.8
2	178.0	19	0.980	.0170	19091	13.5
3	170.0	14	1.003	.0075	8500	16.4
4	179.0	14	0.999	.0135	3556	14.6
5	177.0	14	1.005	.0080	4643	18.1
6	180.5	18	0.992	.0115	13636	21.3
7	174.5	17	0.994	.0280	15909	15.4
8	178.0	16	0.994	.0080	6600	15.8
9	177.0	12	1.001	.0080	4286	14.2

* Ring & Ball method
** 450 gms., 5 sec., 77°F
*** TMA method (M. Argüeso)

TABLE 5. RESPONSE MATRIX

Variables	Softening Point (°F)	Penetration (Dmm)	Density (gm/cm³)	Ash (%)	Visc. (cps, 70° C)	Volumetric Exp. (%)
A	**	-	**	-	-	-
B	-	*	**	-	***	-
C	*	-	-	-	-	-
D	**	-	-	-	**	-

Significance Levels

*	5%
**	1%
***	.1%

TABLE 6. SUMMARY RESULTS

Trial	A	B
1	-	-
2	+	-
3	-	+
4	+	+
5	0	0

TABLE 7. DESIGNED EXPERIMENT -TWO VARIABLE, TWO LEVEL FACTORIAL (WITH CENTER POINTS)

EXTRUSION METHODS FOR SOLID FREEFORM FABRICATION

Paul Calvert[1], Robert Crockett[1], John Lombardi[1&2], John O'Kelly[1], Kevin Stuffle[2]
[1]Arizona Materials Labs. 4715 Fort Lowell Rd., Tucson AZ 85712
[2]Advanced Ceramics Research, 841 E. 47th St., Tucson AZ 85713

INTRODUCTION

It is becoming clear that current SFF methods are members of a potentially very large family. As with current forming methods, it is to be expected that particular materials and objects will lend themselves best to particular methods. Our group has been working for two years on extrusion methods of freeform fabrication where a reactive slurry is extruded into a pattern to form a series of layers that build up a three-dimensional object. A sketch of the apparatus is shown in figure 1. The slurry may cure chemically either as each layer forms or in a postcuring oven.

As a member of the SFF family, this method offers great versatility in the range of materials that can be formed an in control of the material structure and composition within a part. This paper describes our efforts to extend the application of this method from ceramics to polymer composites, thermoplastics and silica-silica composites.

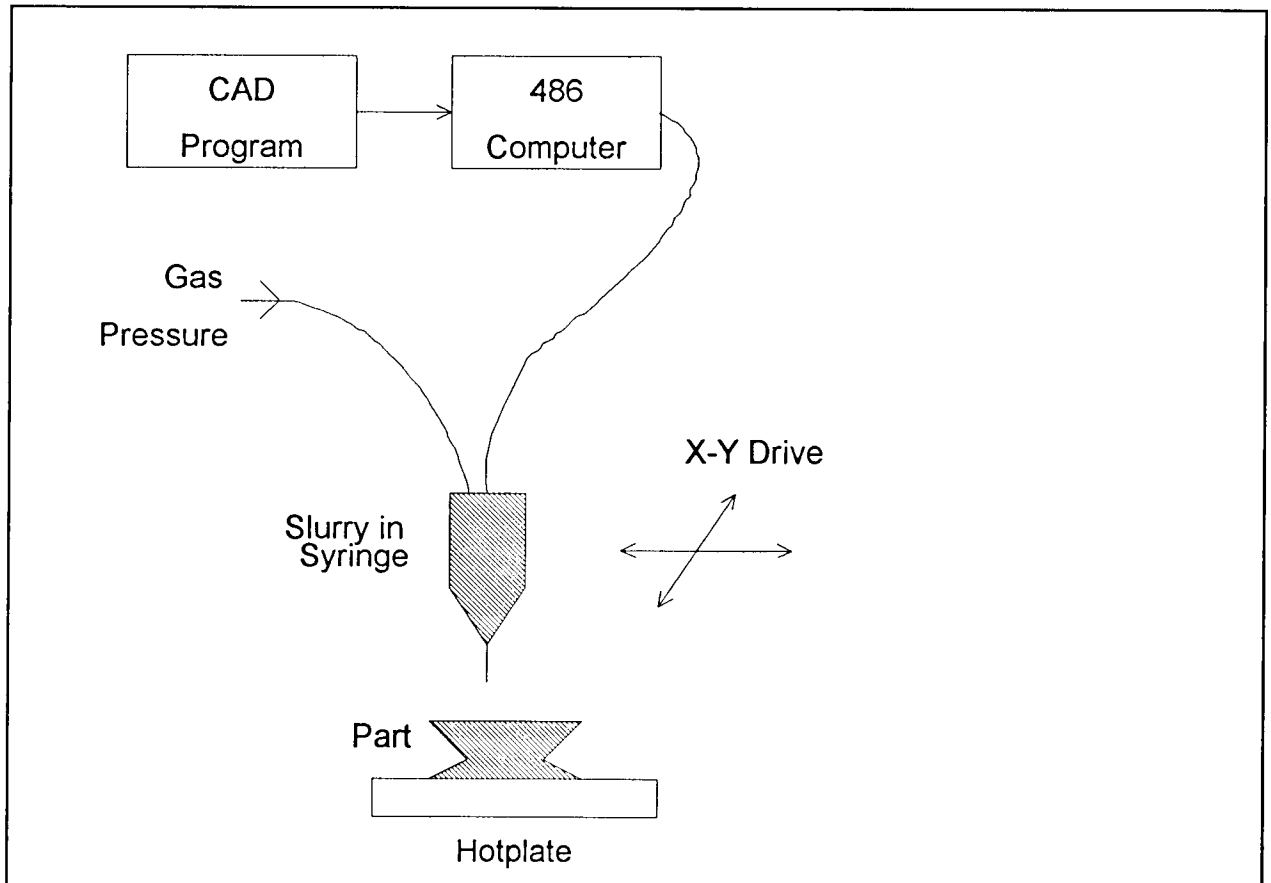

Figure 1: Extrusion SFF Equipment

EXTRUSION SYSTEMS

ACR Systems

The ACR extrusion freeforming equipment comprises a computer-controlled, stepper motor driven and screw-actuated gantry plus a vertical linear slide table. A small positive displacement extruder is mounted on the vertical slide. The extruder is a small stiff piston and cylinder assembly. The piston is actuated by a second linear slide table driven by a stepper motor. Piston and cylinder were originally glass syringes. These have been replaced with epoxy-potted polycarbonate syringes and aluminum pistons. The nozzle (needle) is a shortened Luer-Lok hypodermic needle.

For polymer extrusion, high extrusion pressures increase greatly the weight of the head. To avoid the problems of moving such a large mass a system has been constructed based on a fixed extrusion head and a moving sample table. A computer-controlled massive vertical extruder is mounted above a three-axis table with two orthogonal cross-tables mounted on a vertical stage beneath the extruder. The outlet nozzle of the extruder is a heated block with a machined internal reduction.

AML Dispensing System

Motion control and slurry placement is provided by an Asymtek model 402 benchtop fluid dispensing system. This unit provides an x-y travel of 12" x 12" and z travel of 3.5" with a step resolution of 0.001" on all axes. The maximum head speed is 12 inches/sec, although dispensing is usually limited to 1-4 inches/sec.

Dispensing is through a pinch tube valve connected to a 50 cc syringe. The syringe can be replaced by a feed tube connected to a stationary cartridge allowing a larger supply of slurry. The slurry is pressurized to 5-20 psi from a nitrogen bottle and is dispensed though an 18-25 gauge needle.

Dispensing variables for this system include:
Fluid Pressure
Tip Gauge
Head Velocity
Fill Pattern resolution
Startup delay
Shutoff Distance

The startup delay (time between the opening of the valve and when the head is instructed to move) and shutoff distance (length before the end of a move at which the valve is instructed to shut off) are required to allow the movement of residual fluid in the needle, to avoid blobbing at line ends.

Control is via an IBM PC that handles all aspects of modelling and dispensing in a single integrated package running under Autocad Release 12. The Autocad AME package provides modelling and object slicing, while software routines written in C provide complete control of dispensing operations, converting Autocad data into Asymtek motion commands and issuing machine control statements.

Drawings of an object are prepared as 3-dimensional solid models in Autocad. To fabricate the object, the user manually sets the dispensing tip to the height of the dispensing surface. The control software reads this value, calculates the correct elevation to slice the model and creates a 2-dimensional section. The perimeter of the resulting pattern is dispensed first, then it is filled in a snaking line pattern. After the layer is dispensed, the user is prompted to reset the needle to the new surface height and the process is repeated.

The feedback in the process ensures that the object is fabricated to the highest resolution possible on a layer-by-layer basis, without being subject to additive effects of small changes in dispensing thickness. In principle, surface-sensing equipment could provide this information. Current layer thicknesses are 0.02-0.03 inches.

One promising filling strategy is to dispense the perimeter of three successive layers before filling the interior. The three layers (0.05-0.1" total height) act as a dam, allowing the fill pattern to be dispensed in a much thicker layer without affecting the overall surface resolution. This significantly reduces the total dispensing time and produces flatter, more homogeneous filled regions.

MATERIALS

Ceramic Slurries

Extrusion of slurries of alumina in acrylic monomers was described at the same meeting last year. Slurries could be made with solids contents up to 55% and viscosities of 200 poise. The final parts had good fired density and flexural strength [1].

Filled Resins

Silica-filled acrylic resins could be formed by the same method. In the same way, the slurry cured as each layer was extruded. Table 1 shows the properties of a series of silica-filled acrylics. Ceramic green bodies do not need significant mechanical strength and heavily cross-linking acrylates, such as TMPTA could be used [1]. In the case of composite materials, the high volume fraction of resin places a higher value on good resin toughness. Consequently the highly cross-linked resins based on TMPTA are unsuitable and were replaced by the more flexible urethane acrylates.

Many acrylate and other monomers were investigated before we found a good combination of rapid curing and toughness. Mixtures of a urethane acrylate, hexanedioldiacrylate and N-vinylpyrrolidone were found to give rapid curing (less than 1 minute) and good properties. The resin was reinforced with silica particles plus 1.7 vol.% fumed silica which provided enough viscosity that the larger particles did not settle in the slurry.

We believe that the toughness arises from the polarity of the urethane which allows good bonding to the filler particles. It can be seen that the modulus increases by a factor of three as the filler loading increases to 30 vol.% and that the strength remains high. In many filled polymer systems, where there is poor bonding to the filler, the modulus increases but the strength declines with increasing filler content.

Fiber-reinforced composites

In addition to particulate fillers, short fiber fillers can also be used. As shown in Table

1, 7% carbon fiber (Hercules AS4), chopped to a length of about 100 microns gives a higher modulus but there is some loss of strength. The strength is almost certainly sensitive to the interfacial bonding. Good fiber-resin bonds can be difficult to achieve with carbon fiber.

In situ composites

Other work in our group has been concerned with *in situ* composites where the reinforcing phase grows within the polymer matrix during or after processing. For instance, liquid titanium alkoxides have been blended into polypropylene and co-extruded to form a flexible polymer film. Subsequent treatment of this film in a water bath hydrolyzes the alkoxide and precipitates titania to produce a composite with a very fine titania reinforcement.

Tetraethoxysilane (TEOS) and water, at a 1:4 molar ratio, have been blended with the acrylate monomers to form an extrudable fluid. This both cures and partly hydrolyzes as the layers are deposited to form a composite. A 24-hour steam treatment of the final part was used to complete the hydrolysis to silica. The parts listed in table I contained 7 vol.% silica from TEOS, plus 15 vol.% of silica powder and 1.66 vol.% of fumed silica. The properties are similar to the equivalent 22% silica conventional composite.

These parts show a volume shrinkage of 15% on reaction. For most of these types of *in situ* composites, the shrinkage is a serious problem in forming anything but films and fibers. SFF methods can offer a route to exploitation of this new class of materials since much of the shrinkage can be confined to each layer as it forms, rather than requiring accommodation of the whole part.

Table I: Flexural Tests on Composites

Composition	Flexural Strength, MPa	Flexural Modulus, GPa
Resin	38.3	0.96
Resin + 3.8 vol% Silica	42.8	1.03
Resin + 7.5 vol% Silica	48.8	1.15
Resin + 11.2 vol% Silica	54.9	1.39
Resin + 15 vol% Silica	58.2	1.56
Resin + 22.5 vol% Silica	75.1	2.56
Resin + 30 vol% Silica	61.5	2.89
Resin + 7 vol% Silica from TEOS	50.4	2.10
Resin + 5 vol% Carbon Fiber	27.0	1.24

Ceramic/Ceramic slurries

As part of a program tied to a future lunar base, where polymers would not be available, we have been making ceramic-bonded ceramic materials. A slurry of silica powder, ethylsilicate binder and water is formed in ethanol. Ethylsilicate is related to tetraethylorthosilicate (TEOS) but has been partly hydrolysed under acidic conditions to form linear oligomers. Further hydrolysis and condensation lead to silica which will act as a matrix phase in the final sintered body. The ethanol from the slurry and that released on hydrolysis of the ethylsilicate will be recycled by reaction with silicon derived from lunar sources. The water can also be recycled. Essentially this becomes a process for reforming lunar silica into functional parts.

The hydrolysis and condensation of ethylsilicate can be acid or base catalyzed. Adding catalysts to the slurry produced uneven results as condensation continued in the syringe before dispensing.

Ethylsilicate, water, ethanol and silica are ball milled with alumina balls for 24 hours and then the slurry is poured into the syringe. Particle loadings of 55-58 vol.% dispense well through a 23-gauge needle at 10-15 psi fluid pressure. After dispensing the layer is briefly treated with a heat gun to remove some ethanol and then is sprayed with aqueous ammonia.

The greenbodies are dried slowly and then fired at 1500°C in air. Fired densities have so far only reached 60% of theoretical and fluxes are being explored to enhance the sintering kinetics.

Thermoplastic Resins

Nylon 6 is a tough engineering thermoplastic that is used for many small parts such as gears, cams and bearing housings. For larger parts the high melt viscosity of Nylon causes problems in filling the mold with polymer of high molecular weight. There has been much development work on reaction injection molding (RIM) methods where molten caprolactam monomer is cast or injection molded and polymerized in the mold. The polymerization can be completed in a few minutes. The low viscosity of the monomer allows large molds to be filled and the high molecular weight product has excellent toughness [2,3]. This low viscosity, rapid polymerization system could be readily adapted to SFF extrusion processes.

Molten caprolactam, at 120°C, is pumped through a needle onto a heated platen to cause polymerization. A strongly basic catalyst, sodium caprolactamate, and an activator, N-acetylcaprolactam, initiate the ring opening polymerization [4]. The reaction occurs rapidly above 150°C and typically produces polymer in 95-98% yield.

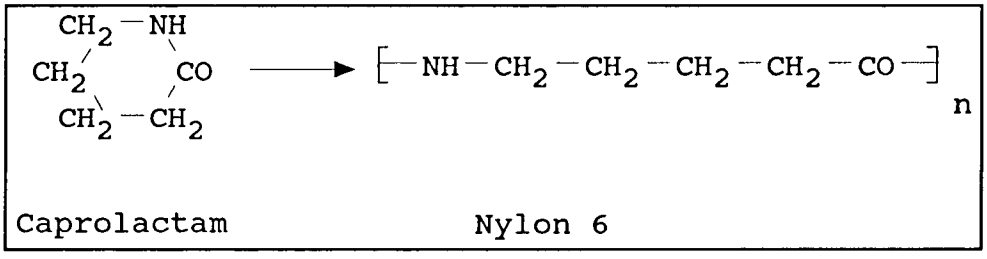

CONCLUSIONS

Extrusion methods of SFF allow considerable versatility in terms of the types of materials that can be formed. Apparatus to carry out this technique is simple and readily constructed. As well as being a manufacturing method, it provides a useful tool for the materials engineer to test the formation of novel materials. In particular the layerwise formation process permits chemical production of materials to final shape without the normal limitations imposed by slow diffusion rates and large shrinkages.

ACKNOWLEDGEMENTS

AML would like to thank NASA for support through the UA SERC. ACR would like to thank DARPA and NASA for support through their SBIR programs.

REFERENCES

1. Kevin Stuffle, Anthony Mulligan, Paul Calvert and John Lombardi, "Solid freebody forming from polymerizable slurry" Solid freeform fabrication symposium proceedings, Univ. of Texas, Austin, 1993, 60-63

2. R. Puff, "Lactam based polyamides" Vol. II, CRC Press, Ann Arbor MI, 1991 pp.145-162

3. C. Macosko, Plastics Engineering, April 1993, pp. 21-25

4. J. Sebenda, J. Macromol. Sci. Chem. A6 1145 (1972)

Surface Texture by 3D Printing

Emanuel Sachs[1], Alain Curodeau[1], David Gossard[1], Haeseong Jee[1],

Michael Cima[2], Salvatore Caldarise[3]

[1] Department of Mechanical Engineering, Massachusetts Institute of Technology, Cambridge, MA

[2] Department of Materials Science and Engineering, Massachusetts Institute of Technology, Cambridge, MA

[3] Applied Research Laboratory, Johnson & Johnson Professional Inc., Raynham, MA

ABSTRACT

Three Dimensional Printing is a solid freeform fabrication process which creates parts directly from a computer model by depositing in layers. Each layer is created by depositing powder and selectively joining the powder with binder applied by a modulated ink-jet printhead. This paper explores the application of 3D Printing to the manufacture of surface textures, where the geometric freedom of 3D Printing is used to create repetitive millimeter and sub-millimeter surface structures with overhangs and undercuts. A related aspect of the work concerns the development of computer representations of these complex structures.

In one investigation, a "mushroom field" surface texture was modeled and printed. Each mushroom consists of a cylinder with a ball on top. These features are printed in a hexagonal array with each feature parallel to the local surface normal of a complex curved surface. In another investigation, textures were printed into ceramic molds. The textures were transferred to metal (tin-lead, CoCr) castings as positive surface features with overhangs and undercuts and typical dimensions of 700 x 350 x 350μm. The application of such cast textures to bone fixation in orthopaedic implants is discussed.

MOTIVATION

Limitations of current methods

Custom surface textures can be produced on cast or forged metal parts by various standard manufacturing processes. Current surfacing methods, such as chemical etching and sintering, are highly specialized and permit little variation over the surface texture characteristics. These processes involve heat or chemical treatments which can alter the crystal structure or create micro-notches on the surface, thereby reducing the fatigue strength of the bulk material. In addition, these methods are all performed as secondary operations and thus represent significant increases in component cost and lead time.

3D Printing introduces fundamental improvements to standard methods. First, it provides an extended choice of geometric shape and surface texture configuration and second, parts can be modified and built directly from a CAD system (see figure 1a &b). Another key attribute is the uniformity of physical properties attained by the simultaneous fabrication of part and texture (see figure 4). In other words, 3D Printing eliminates disruptive intermediate manufacturing steps, such as the surfacing post-processes mentioned above.

Application example

3D Printing (3DP) technology can be used to produce parts by different strategies. For example, 3DP can be used to make molds for investment casting, porous preforms for metal matrix composite, or direct polymer, ceramic, metal and composite objects in whatever shape desired.

In one investigation, a texture printed on a ceramic mold was transferred to a metal casting to create millimeter scale hooks or overhangs (see figure 3), much like "Velcro". This type of 3D texture can be used to improve the fixation strength of two joined surfaces, where the hooks act as anchors for the adhesive material. To illustrate an application of such texture, we intend to use 3D printing to produce functional orthopaedic prostheses with bone ingrowth surface texture. In this case, we wish to firmly attach the orthopaedic implant to the adjacent bone.

Orthopaedic Implant Application

Orthopaedic implants for knees and hips are mainly manufactured from standard processes such as investment casting (lost wax) and forging of cobalt-chrome or titanium alloys. In addition, surface post-processing is required in order to create the necessary mirror finished surface and porous surface texture at selected locations on the prosthesis.

A major issue with orthopaedic joint prosthesis is establishing their permanent fixation to the adjacent bone. The use of porous surface texture for biologic attachment of implants by the ingrowth bone offers a valuable alternative to acrylic bone cement as a means of fixation[1]. Specific surface porosity and pore size are essential conditions for providing bone cells an environment conducive to osseointegration. Numerous surfacing techniques have been designed to attach or carve fine porous surface textures depending on the desired feature geometry, size and material used. For instance, textures can be shaped from fine wax fabrics glued on the prosthesis wax pattern, sintered directly onto the metal part, laser trimmed, electrochemically etched or by electrical-discharge machining (EDM). For example, since forged parts exhibit very hard surfaces, texture need to be carved by EDM or chemical etching which provide a 2 dimensional profile only. More complex texture can be laser trimmed, sintered or even cold formed on cast parts.

However, most of these techniques affect the fatigue strength of material, and are restrained to a specific surface texture with little room for varying surface parameters critical to the performance of the prosthesis. For this reason, a process like 3D Printing, which allows the designers to tailor at will surface characteristics of cast parts, (see figure 2) is considered as a promising alternative method.

PRINTING SURFACE TEXTURE; BASIC CONSIDERATIONS

Two basic factors need to be considered to print accurate surface texture conform to a CAD model. First, the CAD file protocol needs to efficiently handle the geometric complexity associated with the surface texture. Second, the limitation of the fabrication processes must be considered in determining the minimum possible feature sizes.

CAD development

Introduction

Mapped-surface patterns in computer graphics have been widely used for adding visual authenticity to an image since it was first suggested by Catmull in 1974[2]. For example, material recognition is greatly enhanced by wrapping a wood grain pattern image around a rectangular solid to create the impression of a block of wood. In contrast with two-dimensional patterned surfaces, surface textures are three-dimensional features physically made on object surfaces.

Geometric Information Handling

A CAD file representing even a simple repetitive surface texture will have to store the information for thousands of single surface features. However, complication arises since standard CAD systems have not been designed to handle that many small geometric features, resulting in an overflow of CAD information which ultimately overloads the systems. The generally accepted standard CAD model (STL) format reached its limitations with attempts to represent texture information as part of the main CAD model even with the use of efficient tolerance-driven tessellation algorithms[3].

A more effective method has been introduced to model this specific kind of repetitive geometry. This new format currently known as a procedure model[4] does not store the CAD model itself but the *procedure* generating the CAD model which requires much less storage space.

With this new protocol, the geometry of a unit feature forming the surface texture is characterized with the minimal amount of information necessary to keep its conformity and minimize data storage space. For example, the model of a mushroom feature (see figure 1a) composed of a cylinder with a sphere on top, would be built from just a few bytes of parametric information labeled by a given call number. All the mushroom features assembled on the whole surface texture are then represented only by their call number, position and orientation attributes. In other words, since all of the individual features are exactly the same, they could be simply copied from one template CAD model instead of being stored individually.

Control Of Texture Arrangement

Another important issue is the distribution of the texture features on the object surface with the desirable spacing and location. To indicate the specific region on the object surface where the texture features may be located, a texture field should be defined by the user. The various software control actions deciding the final position of all individual texture features are based on distribution rules applied to that particular texture field

boundary. Using this method, the position of thousands of texture features can be precisely defined in order to satisfy predetermined design conditions assuring the desired surface properties.

Cad Implementation Preliminary Results

A first effort to implement a CAD model with surface texture using the procedural method has been made on quadratic object surfaces such as spheres, conic cylinders, and toroids using an IRIS-4D-70GT-Indigo workstation as platform. An example of a CAD model and its physical 3D printed part are shown in figure 1a & 1b. Currently, the texture field is defined as a complex surface bound by an arbitrary NURBS curve user-interactively defined in the (u, v) parametric domain. Once the texture field is defined, each position of single texture feature is carefully computed by considering the desired spacing and size of the texture feature set by the user. Those same position points defined in the parametric domain are then mapped onto the real object domain in order to set the real position of each feature on the object surface. Thereafter, the template CAD model of one feature (mushroom for example) is copied into every single position previously calculated in order to construct the entire surface texture arrangement. The orientation of each feature will exactly coincide with the normal vector pointing outside the object at each particular location. Finally, once the CAD information of a part and texture is well characterized, the model can now be directly translated into manufacturing machine commands necessary to control the 3D Printing machine.

As described before, the CAD model constructed in this example is only for demonstration and verification of the underlying concepts. The next step is to generalize the method for random part shapes described with the STL format, combined with a procedural format to represent the texture characteristics.

Dimensional Limits

As with any manufacturing process, 3D Printing fields of application are partly determined by the resolution, accuracy and minimum feature size it can achieve. In 3D Printing, features can be defined as positive feature (or protrusion) when created by an aggregate of primitives, or negative feature (cavity) when surrounded by a group of primitives. The minimum positive feature size is defined by the primitives size or in other words, the size of single drops and lines of drops forming the building blocks of the parts. The minimum negative feature size can be smaller as it is determined by the need to remove powder to define the feature.

The overall accuracy of the 3D printer is determined by the combination of the errors introduced by each machine component. Printing surface textures is a particularly demanding application and makes a thorough understanding of these errors a crucial step to success.

Minimum Feature Size

3D Printing is a material additive manufacturing process as opposed to a subtractive, forming or phase change process. The material is added, as droplets ejected from a nozzle hits and binds a small region of the powder bed. The primitive size corresponds to the

powder-binder agglomerate formed by a single droplet. The printed ball diameter is determined by various factors including binder drop chemical composition and size, powder chemical composition and size, layer thickness, powder bed density and surface tension. A succession of drop primitives forms lines which will form planes into a solid 3D object on a layer by layer basis. The minimum size of the positive feature (protrusion) forming surface texture is bound by the drop primitive size mentioned above.

For example, a 75μm drop of colloidal silica printed on a 175μm layer thickness of alumina powder will form a 125μm drop primitive . Then, if primitives are overlaid on each other every 20μm, they will form a 200μm wide line. Hence, texture can be produced as protrusion (positive) features as small as 200 μm. On the other hand, cavity or negative features need to be large enough to let the trapped unbound ceramic to be removed easily from cavity. As a rule of thumb, the cavity should be at least as large as four or five ceramic grain size, which is in our case approximately 120-150μm for 30 μm alumina powder.

Figure 5 shows an alumina mold produced for investment casting of a texture. It reveals detailed features in the size range of 375μm, and it should be noted that positive feature size is about twice as big as the primitive size in order to sustain the pouring stresses caused by the liquid metal rushing into the mold. Negative features or cavities are also slightly bigger than the minimum admissible size (≈120μm) to prevent misrun or incomplete mold filling due to metal surface tension.

Machine Accuracy

The ability to reproduce fine textures relies heavily on the machine accuracy. This accuracy depends on the errors introduced in the system by each component of the machine. The final combination of the machine errors, including the controller errors, is done within an error budget. An error budget is a system analysis tool, used for prediction and control of the total error of a system when accuracy is an important measure of performance[6]. To find and organize the different types of error contributors into a budget, one considers the chain of all elements connecting the tool (printhead) to the workpiece (powder bed) through out the machine. This chain consists of all machine elements which provide mechanical support for the printhead and powder bed, and components which measure or control the position of the printhead. This structural chain, referred as a metrology loop[7] is showed for the 3D Printing machine (figure 8). All the error sources are combined selectively for the three axes into a final number representing the achievable accuracy in terms of surface finish, form and size of the produced 3D printed part. A preliminary analysis of the 3D printer error budget showed that a large fraction of errors originate from just a few components of the machine, most notably the electrostatic printhead.

Printhead Accuracy; Simulation and Experiment

One of the major contributors to drop placement error is the electrostatic printhead and the various secondary effects related to it[5]. The electrostatic printhead (figure 6) consists of a continuous jet of droplets printed in either binary or proportional deflection mode. In the binary mode, selected drops can either be fully charged or neutral, in order to be either

deflected away in a drop catcher or printed on the powder. In the proportional deflection mode, droplets are partially charged in order to be positioned proportionally to their charge, on either side of the stream axis (figure 6) .

Potential deflection errors are determined from two basic disturbances affecting the droplet charge and speed; electrostatic interaction between drops and aerodynamic forces[5]. The exact charge carried by each drop determines the final proportionally deflected position. Any secondary effects changing the initial desired charge or speed will generate subsequent droplet positioning error.

As mentioned, positioning error is also caused from drag forces acting on the jet stream by slowing down the initial drop velocity along their path. A simulation of this effect has been conducted to determine the distance from the charging electrode where drag forces make the leading drop merge with the subsequent drops. (figure 7). In this process, merged drops are regarded as unacceptable for accurate printing. Experimentation on a train of drops in still air confirmed the results obtained in the simulation where the first merge occurred at about 15 mm from the charging electrode. Fortunately, most of the drag forces can be counteracted with software compensation by removing problematic drops, modifying charging pattern or printing closer to the powder bed.

Analytically describing the combination of all the drops interaction in the printhead becomes extremely complex. Therefore, most of the error compensations incorporated in a software algorithm will be based on experimental data in the process of being compiled for now.

CONCLUSION

3D Printing has been used to create complex surface textures with overhangs and undercuts. Such textures have been fabricated on ceramic molds and transferred to castings of tin-lead and high melt temperature CoCr alloys. The resulting textures, intended for use as bone ingrowth surfaces for orthopaedic implants, have 40% porosity with an average pore size of 350μm. The 3D printed ceramic molds were generated directly from a CAD model with minimal software error compensation. Research is under way to compile an error compensation scheme that will improve even more the actual accuracy and surface finish of 3D printed parts. This will lead to eventually print a full size ceramic mold to produce functional casting of orthopaedic prosthesis with bone ingrowth surface texture.

The current 3D Printing machine design produces minimum feature size in the range of 175 μm diameter (on alumina powder) which can be positioned on the powder bed with an approximate accuracy of ±5 to 25 μm depending on the part orientation. The formulation of an error budget will help to elucidate the most important factors influencing accuracy and guide future designs and developments of the machine. Research in powder and binder materials is under way in order to better understand and improve our dimensional control over the primitive size.

Many applications will benefit from the use of 3D Printing for its flexibility and fast turnaround time. Moreover, it opens new fields of applications requiring enhanced surface

features, such as protrusions, cavities, overhangs and undercuts in the millimeter or sub-millimeter range. Finally, designers now have access to a new process likely to be used for production, as well as a design of experiment tool. Different conceptual product variations could now be compared to optimize functionality, cost effectiveness or other issues.

ACKNOWLEDGEMENTS

Funding for this research was provided by Johnson & Johnson Inc., National Science Foundation Strategic Manufacturing Initiative, ARPA, and the Three Dimensional Printing Consortium. The authors would like to thank the Johnson & Johnson Professional Inc. team for their expertise and technical support.

REFERENCES

[1] Bobyn, J.D., Pilliar, R.M., Cameron, H.U., Weatherly, G.C., "The optimum Pore Size for the Fixation of Porous-Surfaced Metal Implants by the Ingrowth of Bone", Clinical Orthopaedics and Related Research, p. 263, Number 150, July-August 1980

[2] Catmull,"A Subdivision Algorithm for Computer Display of Curved Surfaces", Ph.D. Thesis, Department of Computer Science, Univ. of Utah, December 1974.

[3] Crawford,"Solid Freeform Fabrication Technologies and Sources of Geometric Data", 3rd SIAM Conference on Geometric Design, Tempe, Arizona, November, 1993.

[4] Peachey, D., "Procedure Texture" SIGGRAPH '93 COURSE 44 NOTES: Procedure Modeling and Rendering Techniques, Chapter 2. 1993

[5] Fillmore, G.L., Buehner, W.L., West, D.L., "Drop Charging and Deflection in an Electrostatic Ink Jet Printer", IBM Journal of research and development, Vol. 21, No.1, p.p 37-47, January 1977

[6] Donaldson R, R., "Error Budget, Large Optics Diamond Turning Machine Project", Lawrence Livermore National Lab., Technology of Machine Tools, Robert J. Hooken (ed), Machine Tool Task Force, U.S. Dept. of Commerce National Technical Information, Service Report UCRL-52960-5, October 1980

[7] Slocum, Alexander H.,MIT, Prentice Hall " Precision Machine Design", chap.2.2 p.61

FIGURES

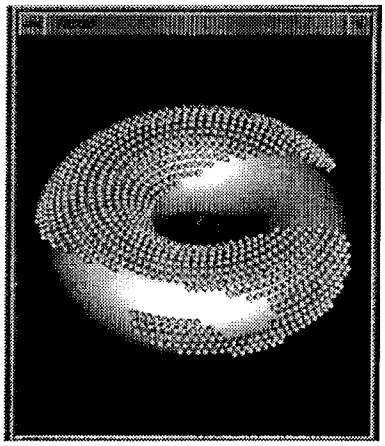

Figure 1a): CAD model of a torus shape with mushroom surface.

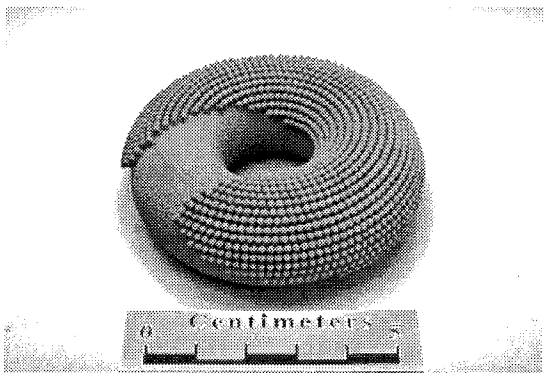

Figure 1b): 3D printed torus of CAD model of figure 1atexture.

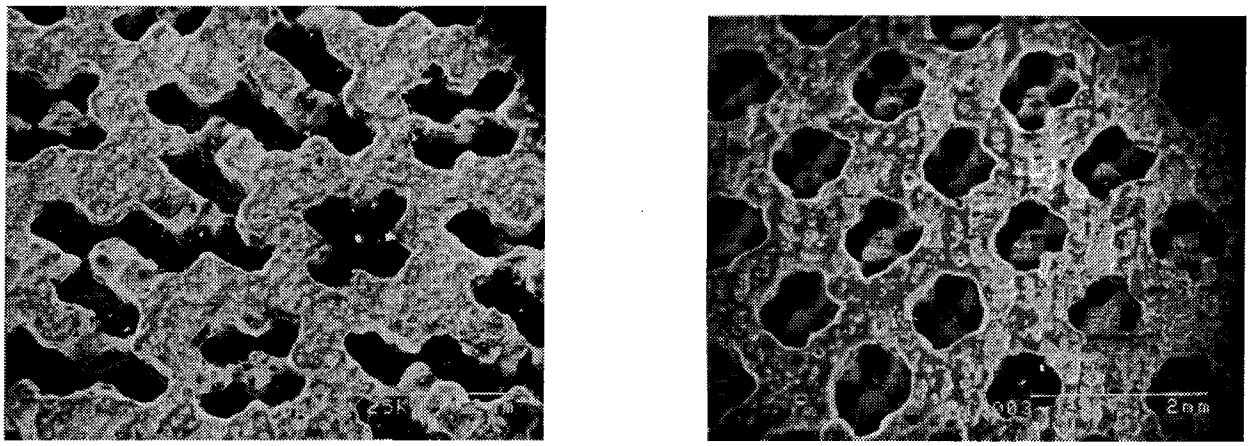

Figure 2: Tin-lead castings of 2 different textures cast from an Aluminum Oxide mold featuring textures (≈400 μm size) generated from macro-cavities directly printed onto the mold surfaces.

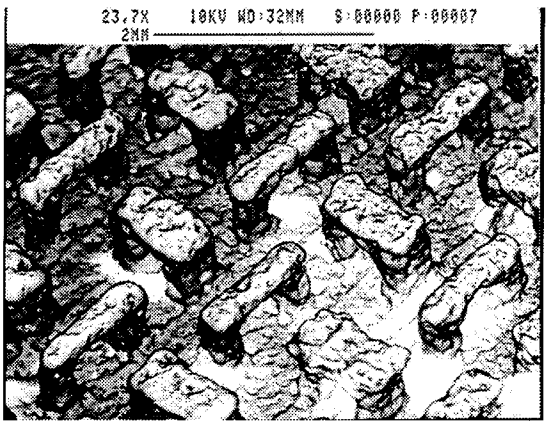

Figure 3: SEM of "Velcro" tin-lead casting. (arches are 1.2mmL x 0.35mmW)

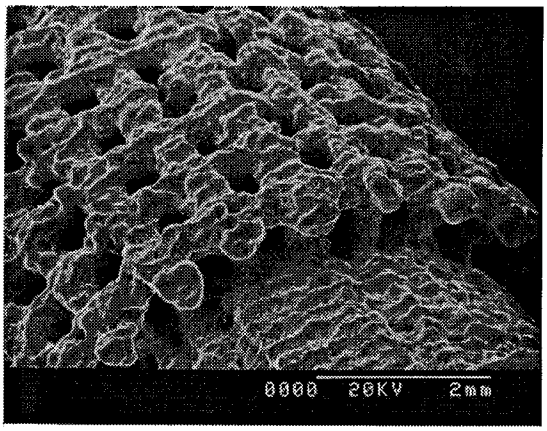

Figure 4: SEM of CoCr texture on a 6mm dia cylinder.

Figure (cont'd)

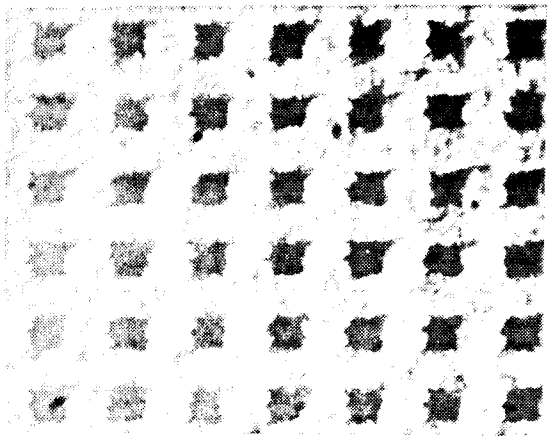

Figure 5: Alumina mold for investment casting of a surface textured part (each line is 350μm wide).

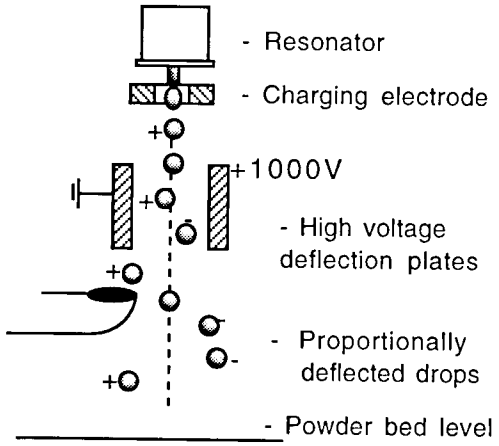

Figure 6: Electrostatic printhead schematic.

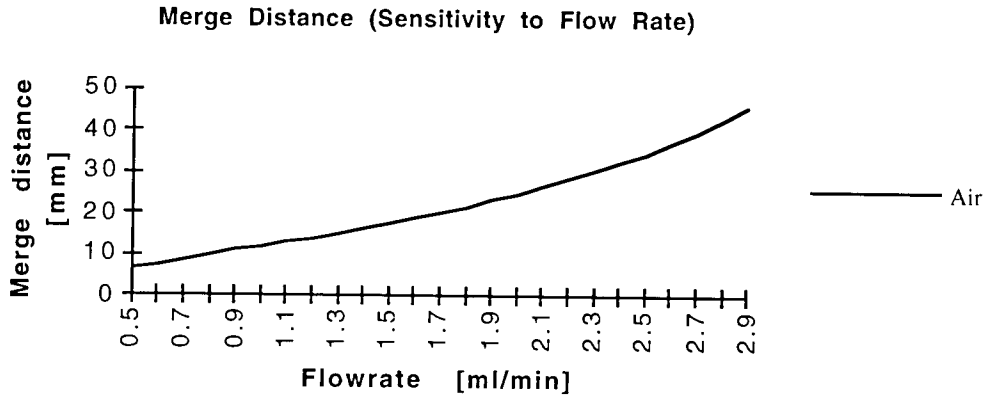

Figure 7: Simulation of drop merge distance in still air as a function of flow rate.

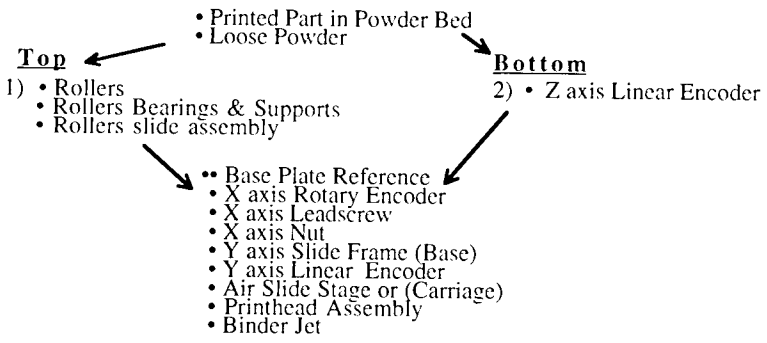

Figure 8: 3D Printing metrology loop.

DENSIFICATION OF SELECTIVE LASER SINTERED METAL PARTS BY HOT ISOSTATIC PRESSING

Mukesh K. Agarwala, and David L. Bourell, Center for Materials Science and Engineering,
Joseph J. Beaman, Department of Mechanical Engineering,
The University of Texas at Austin, Austin, TX 78712.

ABSTRACT

Metal matrix alloy composite parts were made from powders by Selective Laser Sintering (SLS). In this study, partially dense (60%-80%) metal parts made by SLS were densified to full density (>98%) by hot isostatic pressing (HIPping) without any loss of shape. HIPping was done by vacuum sealing SLS samples in glass capsules. HIPping parameters, such as, temperature, pressure, and time, were studied with respect to density, linear shrinkage, and microstructures. Anisotropy in linear shrinkage was correlated to the SLS processing parameters. Densification resulting from HIPping was correlated to microstructures and theoretical HIP densification maps. A detailed analysis of such maps is presented.

INTRODUCTION

The ultimate aim of rapid manufacturing processes is to fabricate three-dimensional fully functional parts directly from metals and ceramic materials, without the use of any intermediate binders or any other materials which may require additional processing steps before or after the rapid prototyping operation. Selective Laser Sintering is one of the few rapid manufacturing processes which possesses the capability of producing such structurally sound parts directly from metals and ceramics [1-4]. Feasibility of producing metal parts directly by SLS has been demonstrated using various metal systems [5-12]. However, SLS parts of metals and ceramics are not fully dense and hence require post processing to obtain near full density. Typically, infiltration and conventional sintering, such as solid state or liquid phase sintering have been employed so far as post-processing steps for SLS parts [1-4]. These post-processing techniques produce near-full density parts, but still leave behind closed pores and result in anisotropic and unpredictable shrinkage during densification. In this study, SLS metal parts have been post processed to full density by **Hot Isostatic Pressing (HIPping)**.

Hot isostatic pressing is a materials processing technique in which high isostatic pressure is applied to a powder part or compact preform at elevated temperatures to produce particle bonding [13-15]. This process usually results in a fully dense body, although partially dense bodies can also be intentionally produced. In hot isostatic pressing, the contact between the particles is increased due to deformation by the external forces and the thermal mobility of the atoms. Therefore, with HIPping it is possible to produce a part with a density approaching the theoretical density and with properties of bulk metal.

Based on certain constitutive equations [16-18], the exact mechanism driving the densification process can easily be determined during HIPping at a given set of process parameters. Using these equations, densification maps are constructed for various material systems. From such maps, shown later for single phase pre-alloyed bronze powders, it can be easily seen that at low temperatures and short time, yielding is the dominant mechanism by which densification takes place. At high temperatures and long times, power-law creep is the dominant mechanism by which densification takes place. Although such maps exist for various single phase metal and ceramic systems, densification maps for multi-phase systems have rarely been studied.

Also, such maps do not take into account the effect of phase transformations on the densification process.

As the pressing temperatures increases, the amount of pressure necessary for compaction decreases. Typically, HIPping temperatures range from 450°C for aluminum alloys to 1700°C for tungsten. Pressures are usually applied using argon gas as the pressure transmitting medium and HIPping pressures range from 20MPa to 300MPa. The duration of the pressing cycle is also important, since at high temperatures lengthy pressing leads to creep. The longer the pressing is done, the greater the density and the better the properties of the pressing at a given temperature and pressure. Lengthy pressing also brings about more complete reduction of oxides, softening and recrystallization, which lead to an improvement in the plastic properties of the part. In addition to temperature, pressure, and time, particle characteristics such as particle size also play an important role in densification during HIPping.

In this study, HIPping was explored as a post processing route for SLS metal parts. SLS bronze-nickel parts, previously used to study the structural integrity and effect of post processing by conventional liquid phase sintering [10-12], were used for HIPping. SLS parts typically have surface connected and interconnected pores. Therefore, such parts require the surface to be sealed or the part to be encapsulated such that the pressure transmitting medium, argon gas, does not flow into the pores in the part. Presence of high pressure gas in the interconnected pores will prevent them from "closing" during the HIP processing. To seal such parts, the parts are encapsulated in an envelope such that the "empty space" in the pores is "squeezed" out during HIPping and the pores close to form a fully dense part.

The basic requirements for the encapsulation material are that it should be relatively strong, gas tight, inert and plastic under the applied temperature and pressure conditions, compatible with the material to be densified so as to minimize diffusion reactions and easily removable. Several materials and techniques are used for encapsulation of powders and compact preforms for HIP processing [13-15].

In this study, the SLS bronze-nickel parts for HIPping were contained in a vacuum-sealed glass capsule. Glass encapsulation has so far been used only on experimental basis. Commercially, sheet metal containers or ceramic containers are commonly used. Glass encapsulation was used instead of sheet metal containers or ceramic containers because of the ease with which glass can be shaped to take the form of SLS parts irrespective of the complex nature of the part. Unlike sheet metal and ceramics, glass becomes vitreous at high temperatures and hence can flow easily and conform to the shape of the preform or in this study, the SLS part.

EXPERIMENTAL PROCEDURE

GLASS ENCAPSULATION OF SLS BRONZE-NICKEL PARTS

SLS bronze-nickel samples of ~70% density were cut from the shoulder section of broken tension test coupons, previously tension tested [10-12], into small sections of 1.5cm x 1.5cm x 0.5cm dimensions. The samples were degassed by annealing them at 450°C in H_2 for 2 hours. Commercial borosilicate glass tubes of O.D. 19 mm and I.D. 15.5 mm were used as the container material. The tube and the sample were thoroughly dried in an oven at 150°C. One end of the glass tube was sealed by a conventional glass blowing method using an oxy-acetylene torch. The SLS sample was then placed in the tube and a small constriction was made in the tube, ~2-4 cm above the sample, by the usual glass blowing technique using a torch. Figures 1A and 1B show schematically the stages involved in vacuum sealed glass encapsulation of the SLS parts. The constriction was as small as possible.

The glass tube with the sample and the constriction was then evacuated using a diffusion pump which was backed up by a mechanical pump, Figure 1B. A liquid nitrogen cold-trap was used in the evacuation to ensure efficient evacuation and prevent any contamination of the diffusion pump. The glass tube with the sample was evacuated to a vacuum of ~10^{-5} torr. Once the desired vacuum level was reached, the constricted part of the tube was sealed completely, using the torch, and removed from the remaining part of the tube.

HOT ISOSTATIC PRESSING OF SLS BRONZE-NICKEL PARTS

HIPping of the vacuum-sealed glass encapsulated SLS bronze-nickel samples was done at three different temperatures of 750°C, 825°C, and 900°C with a pressure of 124MPa (18ksi) for 1, 2 or 3 hours. Similarly, HIPping of SLS bronze-nickel samples of starting density 70% was done with three different pressures of 69MPa (10ksi), 124MPa (18ksi), and 180MPa (26ksi) at 825°C for 1, 2 or 3 hours. Sample dimensions and weight were measured before and after HIPping to determine densification.

RESULTS AND DISCUSSION

SLS bronze-nickel samples exhibited densification at the various HIPping temperatures, pressures and times used in this study. The extent of densification observed varied with these variables. As shown in Figures 2, density increased with increasing temperatures, pressures and times and approached theoretical density at high values of these variables.

Densification of SLS bronze-nickel parts during HIPping was accompanied with phase transformation between bronze and nickel phases, Figures 3 and 4. Bronze, predominantly copper (90 Wt.%), and nickel homogenize at high temperatures by interdiffusion between bronze and nickel to form a homogeneous solid solution. The degree of homogenization depends on temperature and time of sintering or HIPping. As evidenced by (311) peak broadening of copper and nickel, shown in Figures 3, at low temperatures and short times only partial homogenization occurs and complete homogenization occurs at high temperatures and long times. As a result of chemical homogenization, the bronze phase disappears completely leaving behind pores in its place and an expanded solid solution of bronze in nickel. This happens due to a faster diffusion rate of copper into nickel than that of nickel into copper, which results in the Kirkendall effect. Therefore, the pores created at this stage are referred to as Kirkendall porosity. Due to the generation of Kirkendall pores and expansion of nickel phase, the samples may undergo growth or swelling instead of shrinkage, as has been observed in SLS bronze-nickel parts during conventional sintering below 1000°C [10-12]. Although, as shown in Figures 3 and 4, chemical homogenozation between bronze and nickel was observed in the SLS bronze-nickel parts during HIPping also, no overall expansion or growth of the SLS parts was observed during HIPping. Parts processed at lower temperatures and pressures, which exhibit low density, show partial homogenization with Kirkendall pores present at the boundaries of homogenized and non-homogenized phases, Figure 4b. However, parts processed at high temperatures and pressures, which exhibit nearly full density, also show partial homogenization but absence of any Kirkendall pores, Figure 4c.

As a result of chemical homogenization between bronze and nickel, and generation of Kirkendall pores, the densification of the bronze-nickel samples is considerably slower than predicted by theoretical densification maps for single phase pre-alloyed bronze. Figures 5 show the densification of bronze-nickel samples observed in this study relative to theoretical densification curve for pure bronze of 50μm particle size. The theoretical HIP densification map for bronze was

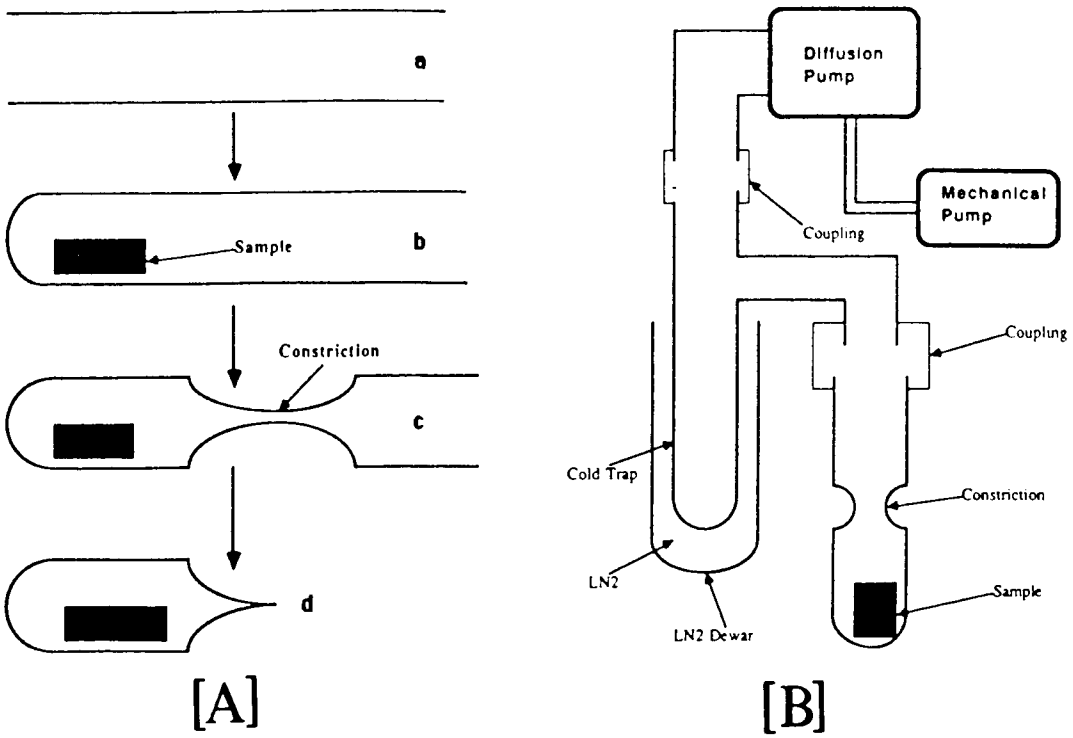

Figure 1: [A] A schematic representation of the glass encapsulation used in this study (a) glass tube with both ends open, (b) glass tube with one end sealed and the sample in the tube, (c) glass tube with the sample in it and a constriction, and (d) vacuum sealed glass capsule with the sample in it, and [B] A schematic representation of evacuation procedure for glass encapsulation of SLS part.

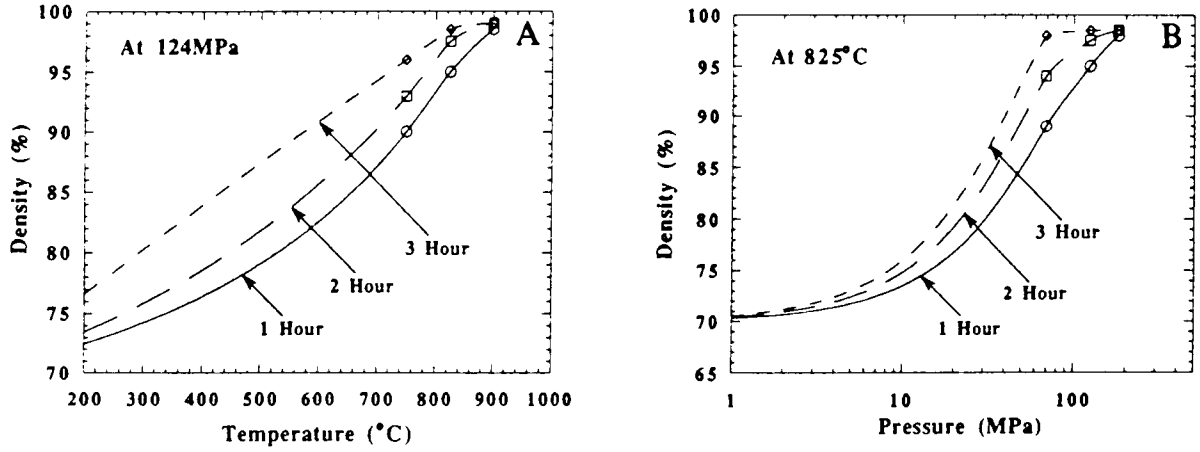

Figure 2: Density of SLS bronze-nickel parts as a function of (A) HIPping temperature and time at a constant pressure of 124MPa, (B) HIPping pressure and time at a constant temperature of 825°C.

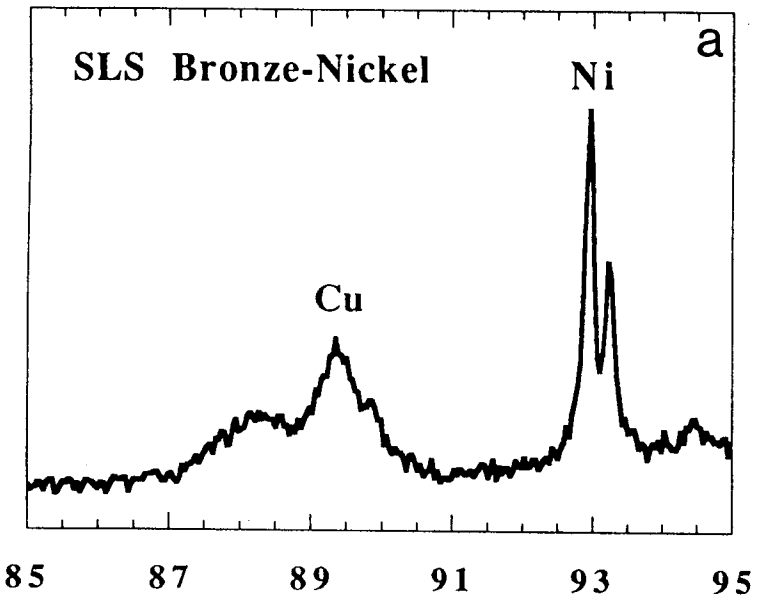

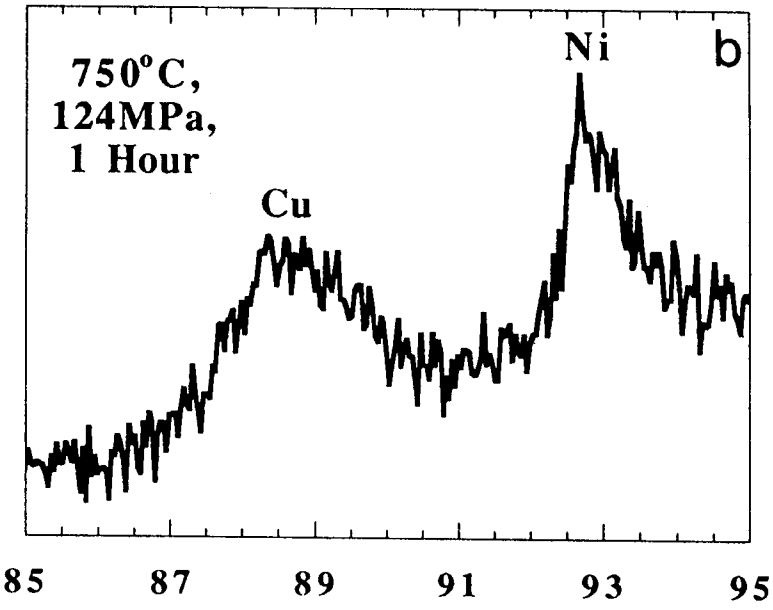

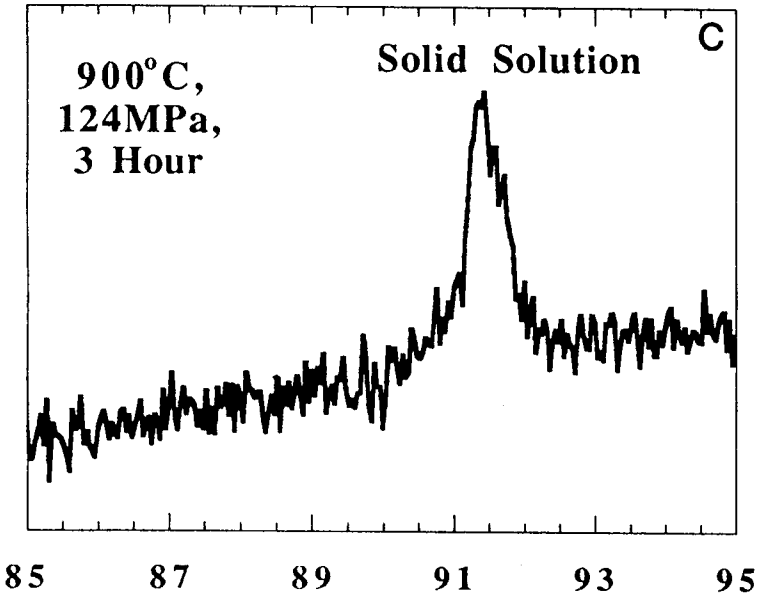

Figure 3: XRD patterns of (311) peaks of Bronze and Nickel showing peak broadening due to homogenization (a) SLS Bronze-Nickel part showing Cu and Ni as separate phases, (b) SLS Bronze-Nickel sample HIPped at 750°C for 1hour at 124MPa, showing partial homogenization, and (c) SLS Bronze-Nickel sample HIPped at 900°C, for 1hour at 124MPa, showing complete homogenization.

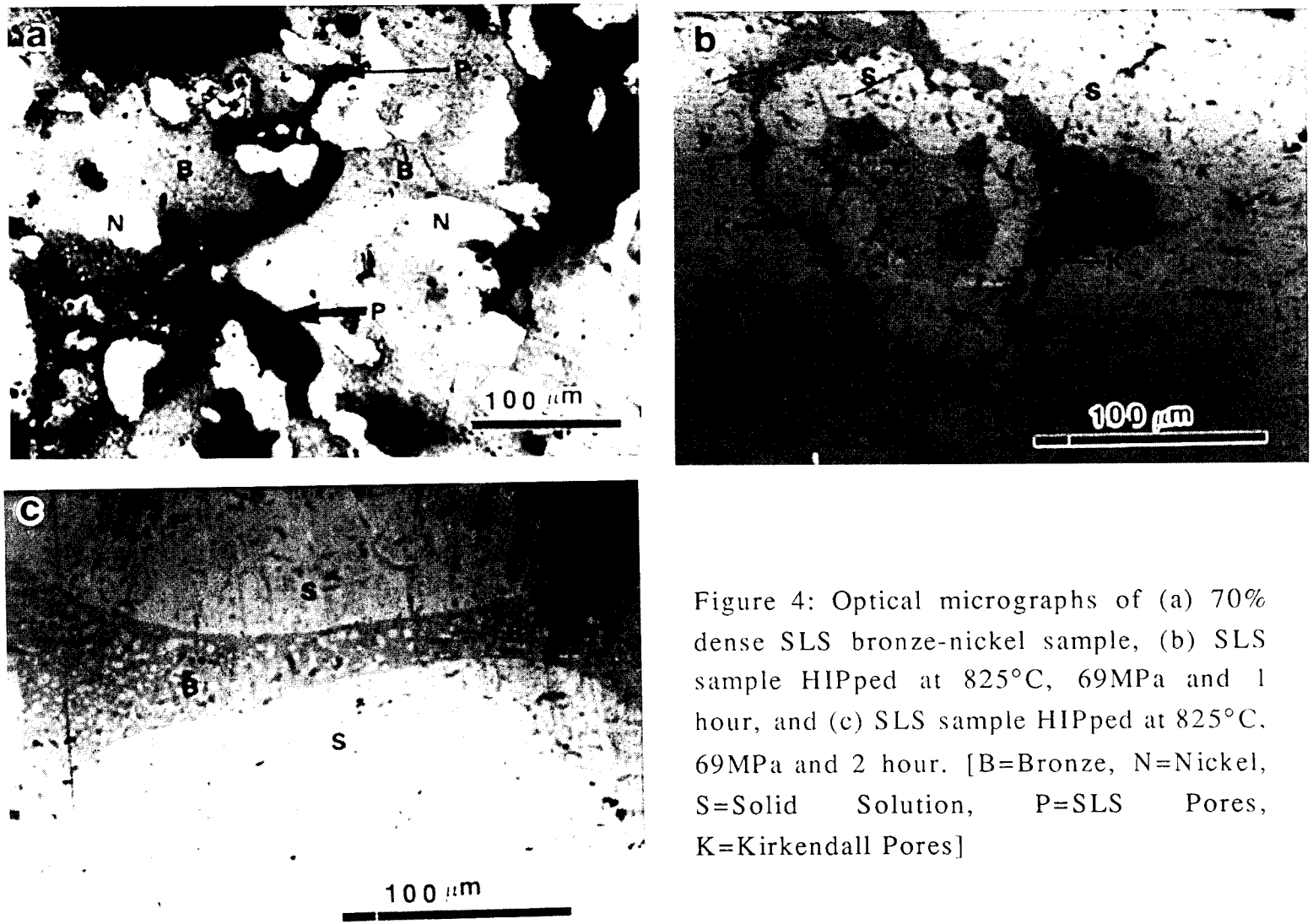

Figure 4: Optical micrographs of (a) 70% dense SLS bronze-nickel sample, (b) SLS sample HIPped at 825°C, 69MPa and 1 hour, and (c) SLS sample HIPped at 825°C, 69MPa and 2 hour. [B=Bronze, N=Nickel, S=Solid Solution, P=SLS Pores, K=Kirkendall Pores]

validated experimentally by HIPping of a single phase pre-alloyed bronze sample at 750°C at 69MPa for 1 hour which yielded nearly full density in accordance with the map. However, the experimental data for SLS bronze-nickel parts are well to the right of the theoretical curves indicating a much slower densification in the bronze-nickel samples. Therefore, densification is slowed down during HIPping of mixed phases, such as bronze-nickel, which form a solid solution at HIPping temperatures resulting in Kirkendall pores which oppose the on-going densification. Theoretical HIP maps do not account for such phase transformations and their effect on densification during HIPping. Low HIPping temperatures and pressures and short time of HIPping cause nearly complete removal of pores present due to SLS but do not result in removal of Kirkendall pores created due to homogenization during HIPping. Therefore, such processing conditions which do not remove the Kirkendall pores completely result in less than full density. However, high temperatures and pressures result in removal of both the pores due to SLS as well as the Kirkendall pores created due to homogenization during HIPping.

Net volume changes (shrinkage) of SLS parts during HIPping was in accordance with the observed density changes. However, the linear dimensional changes, $\Delta L/L_o$, were not the same in all three directions, as observed earlier in conventional liquid phase sintering of such parts. Figure 6A shows the shrinkage in parts HIPped at 825°C and 69MPa for varying times. The linear dimensional shrinkage in these parts was anisotropic with least shrinkage in the scan direction and maximum shrinkage in the thickness or build-up direction. Similar shrinkages have been observed in SLS parts when subjected to conventional liquid phase sintering [10-12]. In either case, maximum shrinkage in thickness direction is observed due to lowest density along that direction due to poor sintering between layers during SLS and minimum shrinkage in the scan direction due higher degree of sintering during SLS along the scan direction. However, the degree of anisotropic shrinkage observed during HIPping is lower than that observed during liquid phase sintering. Comparision of Figures 6A and 6B shows that the difference in shrinkage between thickness and scan direction is lower in HIPped parts. HIPping is done at temperatures well below the liquid phase sintering temperatures, therefore there is little or no liquid phase formed during HIPping. Also, HIPping is done under isostatic pressures, therefore there is minimal effect of gravity aiding the densification or flow of liquid in the direction of gravity which coincides with the thickness or build-up direction during both the HIPping as well as liquid phase sintering processes. Therefore, the anisotropy observed in HIPping of SLS parts represents a more precise picture of density gradient present in parts due to SLS.

CONCLUSIONS

A framework for encapsulation of SLS parts for HIPping has been established using glass containers. Glass encapsulation is an easy, flexible, and economical method for encapsulating complex shapes. Densification studies of SLS bronze-nickel parts by HIPping resulted in higher density parts with increasing temperatures, pressures and times. However, the densification of SLS bronze-nickel parts was slower than that predicted by theoretical HIP densification maps due to generation of Kirkendall pores arising from the chemical homogenization between bronze and nickel phases during HIPping. The anisotropy in linear dimensional changes during HIPping is not influenced by liquid phase or effect of gravity, thus giving a precise picture of anisotropy present in parts due to SLS.

ACKNOWLEDGMENTS

This study was made possible by a research grant from State of Texas Advanced Research Project, ATP-116: Selective Laser Sintering: Direct Metal Fabrication

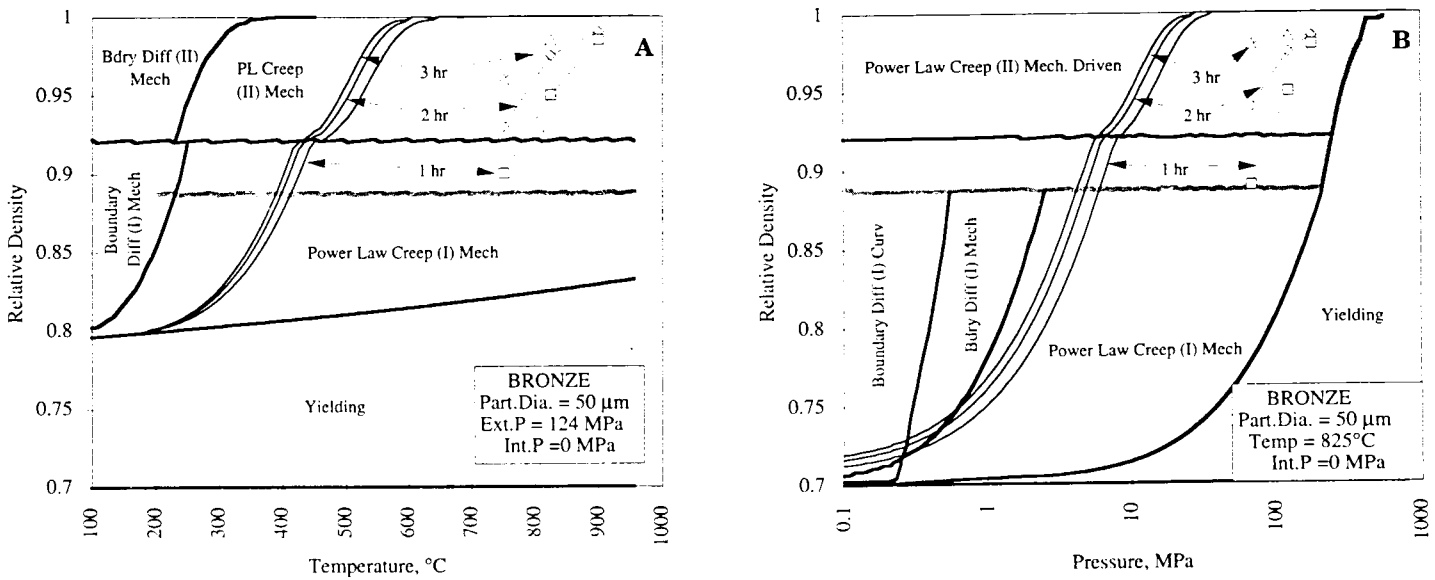

Figure 5: Comparision of densification curves of SLS bronze-nickel samples (symbols) with the theoretical HIP densification curves for single phase pre-alloyed bronze, as a function of (A) HIPping temperature and time, and (B) HIPping pressure and time.

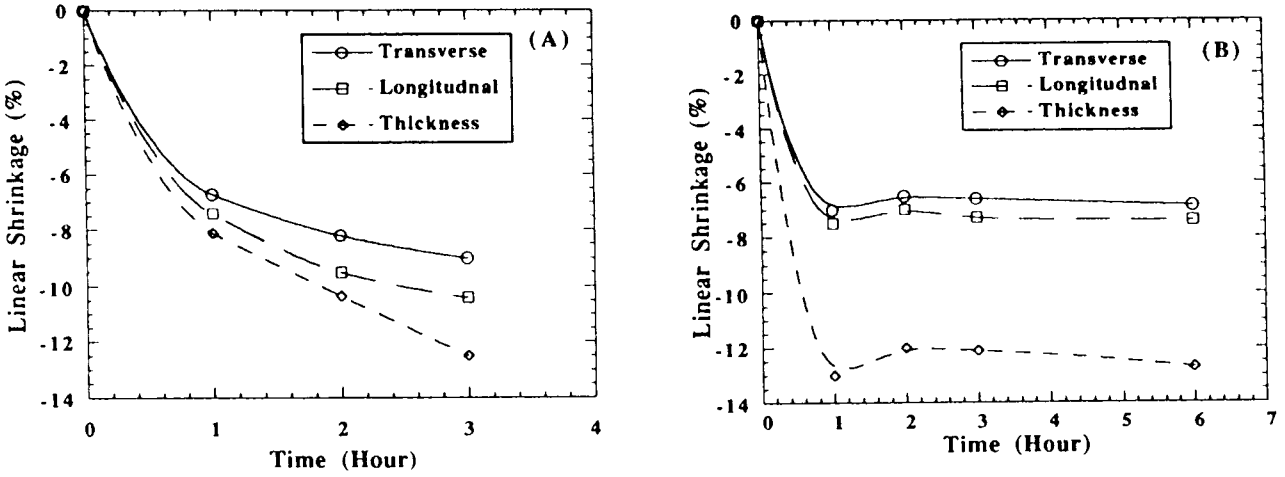

Figure 6: Anisotropic linear dimensional shrinkages observed in SLS bronze-nickel parts subjected to (A) HIPping at 825°C and 69MPa, and (B) Conventional liquid phase sintering at 1030°C.

REFERENCES

1. 1990 Solid Freeform Fabrication Symposium Proc., Edited by J.J.Beaman, H.L.Marcus, D.L.Bourell, and J.W.Barlow, Aug. 6-8, 1990, The University of Texas at Austin, Austin, Texas.
2. 1991 Solid Freeform Fabrication Symposium Proc., Edited by H.L.Marcus, J.J.Beaman, J.W.Barlow, D.L.Bourell, and R.H.Crawford, Aug. 12-14, 1991, The University of Texas at Austin, Austin, Texas.
3. 1992 Solid Freeform Fabrication Symposium Proc., Edited by H.L.Marcus, J.J.Beaman, J.W.Barlow, D.L.Bourell, and R.H.Crawford, Aug. 3-5, 1992, The University of Texas at Austin, Austin, Texas.
4. 1993 Solid Freeform Fabrication Symposium Proc., Edited by H.L.Marcus, J.J.Beaman, J.W.Barlow, D.L.Bourell, and R.H.Crawford, Aug. 9-11, 1993, The University of Texas at Austin, Austin, Texas.
5. J.A.Manriquez-Frayre and D.L.Bourell, "Selective Laser Sintering of Binary Metallic Powder," ibid., Reference #1, pp. 99-106.
6. J.A.Manriquez-Frayre and D.L.Bourell, "Selective Laser Sintering of Cu-Pb/Sn Solder Powders," ibid., Reference #2, pp. 236-244.
7. W.Weiss and D.L.Bourell, "Selective Laser Sintering to Produce Ni-Sn Intermetallic Parts," ibid., Reference #2, pp. 251-258.
8. G.Zong, Y.Wu, N.Tran. I.Lee, D.L.Bourell, J.J.Beaman, and H.L.Marcus, "Direct Selective Laser Sintering of High Temperature Materials," ibid., Reference # 3, pp.72-85.
9. G.Prabhu and D.L.Bourell, "Supersolidus Liquid Phase Sintering of Prealloyed Bronze Powder," ibid., Reference #4, pp.317-324.
10. M.K.Agarwala, D.L.Bourell, B.Wu and J.J.Beaman, "An Evaluation of the Mechanical Behavior of Bronze-Nickel Composites Produced by Selective Laser Sintering," ibid., Reference # 4, pp.193-202.
11. M.K.Agarwala, D.L.Bourell, B.Wu and J.J.Beaman, "Structurally Sound Metal Parts by Selective Laser Sintering," The EPD Congress 1994, Proc. of a symposium sponsored by the Extraction and Processing Division, At the 123rd TMS Annual Meeting, Mar.1994, San Francisco, CA, pp. 833-851.
12. M.K.Agarwala, D.L.Bourell, J.J.Beaman, B.Wu, H.L.Marcus, R.H.Crawford, and J.W.Barlow, "Selective Laser Sintering of a Bronze-Nickel Powder Mixture," Proc. of the IMS Int. Conf. on Rapid Product Development, Feb. 1994, Stuttgart, Germany.
13. P.E.Rice and S.P.Kohler, "Hot Isostatic Pressing of Metal Powders," Metals Handbook, pp. 419-443, Vol.7, 9th Ed., Am. Soc. of Metals, Metals Park, Ohio.
14. H.V.Atkinson, B.A.Rickinson, "Hot Isostatic Pressing," The Adam Hilger Series on New Manufacturing Processes and Materials, Adam Hilger, IOP Publishing Ltd.,New York, NY, 1991.
15. "Isostatic Pressing: Technology and Applications," Edited by M.Koizumi and M.Nishihara, Elsevier Applied Science, London, 1991.
16. M.F.Ashby, "A First Report on Sintering Diagrams," Acta Metall., 22, pp. 275-89, 1974.
17. F.B.Swinkels and M.F.Ashby, "A Second Report on Sintering Diagrams," Acta Metall., 29, pp. 259-81, 1981.
18. A.S.Helle, K.E.Easterling, and M.F.Ashby, "Hot-Isostatic Pressing Diagrams: New Developments," Acta Metall., 33, pp. 2163-74, 1985.

Sprayed Metal Shells for Tooling: Improving the Mechanical Properties

P. S. Fussell† , Aluminum Company of America;
H. O. K. Kirchner, Institut de Sciences des Matériaux, Université Paris-Sud;
F. B. Prinz, Engineering Design Research Center, Carnegie Mellon University.

Abstract

This work describes methods to improve the quality of the metal resulting from thermal spray deposition, including both the mechanical and metallurgical behavior. The engineering context is the production of sprayed metal shells suitable for tooling applications. The sprayed metal shells are mechanically dominated by interparticle interfaces; the particles are largely mechanically interlocked with very little metallurgical bonding. Based on these observations, improvements are made to these interfaces, and the measure of the improvement is shown in mechanical tests.

Rapid Tooling and Sprayed Material

Rapid manufacturing of tooling for injection molding, stamping, composite lay-up, casting, or similar processes where the shape of the tool is critical presents a challenging problem possessing considerable commercial potential (Rothdeutsch 1990; Weiss, Gursoz et al. 1990). The tool, die, and fixture market amounted to about 5 x10^9 US$ in 1989, and prototype to medium life tooling accounts for about 15% or 750 x10^6 US$ of the total. The commercial literature reports the creation of such tooling by arc–spraying zinc and zinc alloys for at least 30 years (MOGUL 1963), and thick sprayed zinc structures have been in the literature for 68 years (Turner and Budgen 1926). Commercially viable, they save as much as 80% to 90% of the time required to make a prototype tool (two weeks for sprayed zinc versus twenty weeks for machined steel), and 75% of the cost (perhaps $4,000 versus $16,000). These alloy systems, however, are relatively soft and prone to wear and loading failure, which limits their usefulness to prototype tooling applications and low pressure applications such as reaction injection molding tooling.

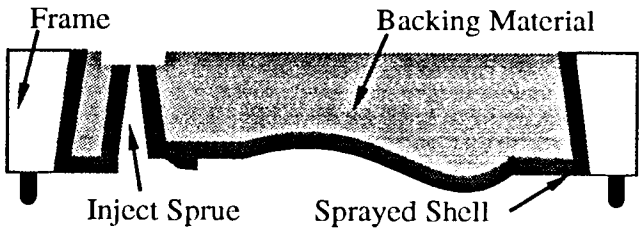

Figure 1. Schematic cross section of a sprayed tool; Angling the frame interior helps support compressive loads on the tool face.

Tools made from ferrous systems(Fussell and Weiss 1990; Fussell, Patrick et al. 1991) are of greater applicability, both for prototyping and limited production. Other possibilities for the materials of the tool face include aluminum bronze (Milovich 1989), which has much greater wear resistance compared to zinc systems.

We describe the part and patterns needed to make the part's mold or die in a CAD system. A solid freeform fabrication process, stereolithography (Hull 1986; Hull 1990) in this case, autonomously creates the pattern in a matter of days. The shells are fabricated by spraying metal using an arc–spray device to create the tooling face and structure. Then, support material fills the back side of the tooling cavity to sustain the compressive service loads. Figure 1 shows a cross section of such a tool. For service at elevated temperatures (~450 °C); it is desirable to match the coefficients of thermal expansion of the sprayed tooling material and the backing material.

The basic fabrication of these sprayed ferrous tools had been described in (Fussell and Weiss 1990; Weiss and Schultz 1992; Weiss, Prinz et al. 1993). There are a number of concerns for a

† to whom correspondence should be addressed:
P. S. Fussell, Alcoa Technical Center, 100 Technical Drive, Alcoa Center, Pennsylvania 15069 USA

tool made in this way. After finishing the arc-spraying, the shell and the substrate still contain considerable internal stress, albeit in equilibrium (Gill and Clyne 1990; Gill 1991). The presence of internal stress in the shell, as well as a mismatch of coefficients of thermal expansion, raise questions of the shell's geometric stability at elevated temperatures, and over long times. Finally, the spray process is poorly suited for spraying into narrow channels and small aspect ratio holes.

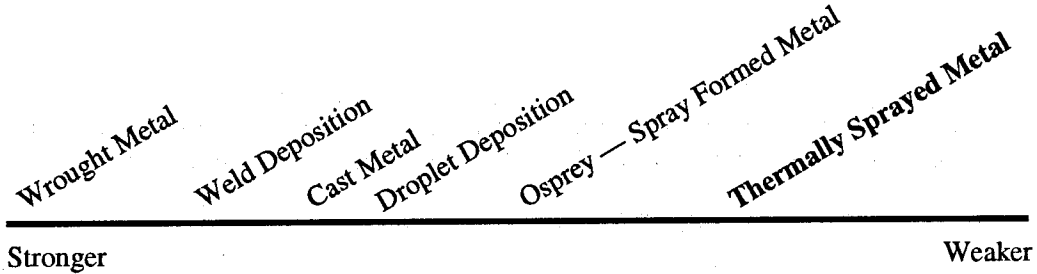

Figure 2. Generalized Continuum of **Material Strength**; (as–formed or as–cast materials).

Sprayed metal is chosen to provide the working surface of the tool for pragmatic reasons: once we have created the pattern's surface geometry, a complete working surface representing that geometry can be created in short order. On a generalized continuum of **material strength**, thermally sprayed metal, one of several alternatives, fits as shown in Figure 2. Poorly thermally sprayed metal has a tensile strength about 5% of wrought material of the same alloy. This is compared to 50% to 80% of normalized wrought materials for droplet deposited steel (Merz 1994).

However, Figure 3, another generalized continuum with respect to the **time** required to form complex geometries, highlights the economic interest in quickly forming complex shapes. The thermally sprayed material can quickly deliver a complex geometry.

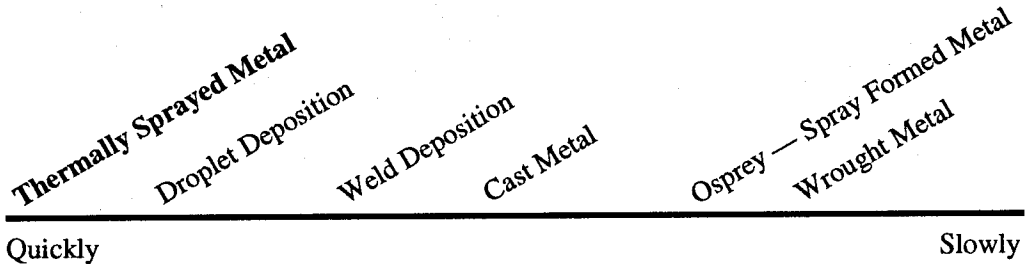

Figure 3. Generalized Continuum of **Time** Required to Form into Complex Shape.

In the same way that a tool's geometry determines much of its function, much of the tool's strength and wear characteristics are determined by the microstructure of the sprayed shell. The work described here is an attempt to find methods to locally, *i.e.*, microstructurally, improve the mechanical properties performance of the thermally sprayed metal. In short, the work here describes ways to move thermally sprayed ferrous and allied materials further up the continuum of strength displayed in Figure 2, while retaining the economic advantages created by speed of manufacture as shown in Figure 3. The methods explored here follow a path: reduce the oxide content, promote metallurgical bonding by permitting diffusion bonding to take place, and attempt to promote metallurgical bonding by adding superheat to the droplets that form the lamella of the shell.

One extremely interesting aspect of the sprayed tool work is its ability to build large tooling structures. Other newly developing rapid prototype systems suitable for manufacturing face the boundaries of either the volume of the tool they are building, or at the best by the surface area of the tool. Thus a doubling of tool volume can amount to an eight fold increase in production time.

The thermally sprayed tool, however, is bound by the area of the working surface. Scaling up from the current tooling experiments of 0.5 m by 0.5 m to tools requiring sizes of 2 m by 0.5 m will be an interesting and immediately addressable problem..

For perspective, other alternatives are being developed to quickly deliver a large prototype tool. The CMU effort to develop tooling structures by layered micro-casting deposition is extremely interesting (Merz, Prinz et al. 1994). The growing number of alternatives for fast production of investment cast tooling also draws attention, especially if someone invents a method for investment casting parts with an accuracy of the order of ±50 μm (±0.002 inches). Similarly, large cast tooling augers well, particularly for those tolerance regimes that accept accuracies of ±0.5 mm (±0.020 inches). However, a leading competitor for this technological niche remains the more traditional CNC cutting of either the tool or the EDM electrodes used to burn the tool.

Experimental Arrangements

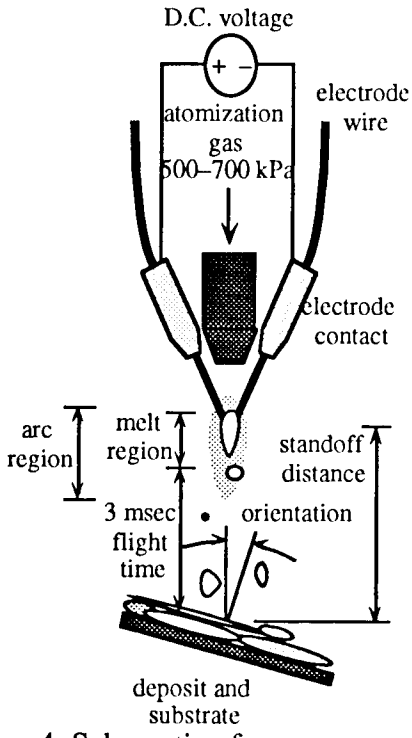

Figure 4. Schematic of an arc–spray gun and deposited particle flight times.

The effort reported here uses an arc–spray system (Cifuentes and Harris 1984; Thorpe 1989). The arc–spray gun is arranged as in Figure 4. Two consumable electrode wires are fed through contact tips to the area of the arc. A D.C. power supply establishes an arc between the wires, melting them in the arc. A column of atomizing gas, ranging from 480 kPa to 690 kPa (70 psi to 100 psi) ablates the molten material from the wires, atomizes the molten droplets and carries them, in a spray, to the substrate. For steel systems, the arc specific energy ranges from 2.6 MJ Kg^{-1} to 3.0 MJ Kg^{-1} giving a temperature of 10^4 K in the arc (Safai and Herman 1981). (Iron requires about 700 kJ Kg^{-1} energy to be melted from ambient temperature.) Deposition rates for an arc–spray system range from 1 kg hr^{-1} to 20 kg hr^{-1}.

Due to the large surface/volume ratio of the sprayed droplets, oxidation in flight and after impingement is a problem. The obvious way to circumvent the detrimental effect of oxidation and avoid the ensuing brittleness of the deposit is to minimize the partial pressure of oxygen in the gaseous atmosphere (Kaiser and Miller

Material	Sintering Temperature	Sintering Time
Fe–36Ni (INVAR)	1400 K (2075 °F)	30 min
Ni–5Al	1400 K (2075 °F)	30 min and 60 min
Fe–0.4C	1400 K (2075 °F)	30 min
50 vol % 308 Stainless & 50 vol % Copper	1170 K (1650 °F)	30 min
50 vol % 308 Stainless & 50 vol % 4043 Al	890 K (1150 °F)	30 min

Table 1. Sintering Schedule for Mechanical Properties Samples

1989). In these experiments, the partial pressure of oxygen was reduced by using a shroud arrangement around the spray region. The shroud gas was argon avoiding potential problems with nitride formation (Milewski and Sartowski 1986).

The samples for this experiment were uniformly sprayed onto a aggressively grit blasted mild steel coupon. After spraying, they were detached from the coupon, and then vacuum sintered with the intention of understanding what metallurgical bonding would develop and how that would affect the material performance. The sintering schedule, reminiscent of that for powder metallurgy sintering (Gall 1985), was as shown in Table 1. The temperature ramp up times from ambient to sintering temperature varied from 30 min to 1 hour. The vacuums were in the range of 5×10^{-6} to 9×10^{-6} bar.

Improving the Properties

Figure 5 shows an SEM view of the sprayed material. This view is typical, and shows that the lamellæ are evidently not metallurgically bound together, or at least very seldomly and with only small cross section bridges (see arrows in Figure 5). In an effort to explore this condition, I mechanically tested the sprayed material in a number of conditions. Specifically:

- INVAR, as sprayed with air atomization (similar to that in Figure 5);
- INVAR, as sprayed in chamber (vacuum purged, backfilled to 0.5 Bar argon, and sprayed with argon atomization);
- INVAR, sprayed under argon shroud cover and then sintered for 30 minutes at 1400 K.
- 308 stainless steel, sprayed using the single wire plasma gun under argon shroud cover.

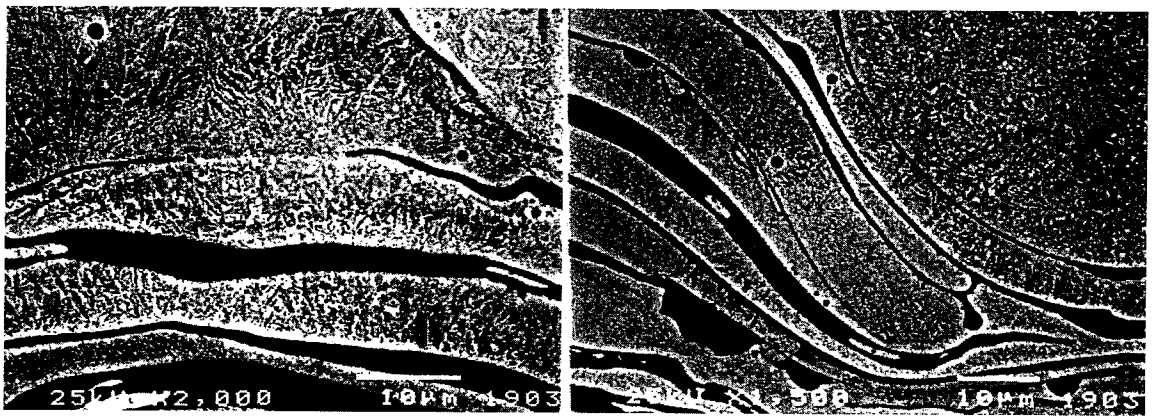

Figure 5. Mechanically linked thermally sprayed lamella.

The first test was the background measurement against which improvements were to be compared. This material is similar to that initially used in making tool shells. The second material was intended to remove the oxide from the material, but there is still substantial void porosity. The third experiment was done to see if the promotion of a diffusion bond would improve the material. The fourth test was to attempt to understand if it was possible to add enough superheat to the individual particles to promote bonding in the as sprayed condition, rather than adding the additional sintering step.

The material tests performed here are limited in scope. Given the nature of these microstructures, it is reasonable to assume that there will be a large measure of variability in the measurement data. I was interested in seeing general trends, rather than detailed statistically significant materials characterization. At best, shades of trends can be extracted from these data.

For the INVAR, the sintering conditions permitted a measure of metallurgical bonding to take place bringing the tensile strength up to nearly half of that expected from wrought material. More importantly, a meaningful amount of elongation has been recovered from the material. This will permit a tool made of such a material to locally adjust (deform) in response to inclusions or other stress risers.

Material	Condition	Tensile Strength	Elongation
Fe–36Ni (INVAR)	*for comparison, typical wrought mat'l*	*500 MPa (75ksi)*	*30 %*
Fe–36Ni (INVAR)	as sprayed, heavily oxidized	12 MPa (1.7 ksi)	0.14 %
Fe–36Ni (INVAR)	sprayed in chamber (Ar backfill, 0.5 Bar)	120 MPa (17 ksi)	0.23 %
Fe–36Ni (INVAR)	sprayed in shroud, sintered	**220 MPa (32 ksi)**	**2.8 %**
308 S.S.	*for comparison, typical wrought mat'l*	*515 MPa (75ksi)*	*40%*
308 S.S.	Sprayed with single wire plasma	**180 MPa (26 ksi)**	**0.3%**
Ni-5Al	sintered	**340 MPa (50 ksi)**	**4.5 %**

Table 2. Summary of Sprayed Material Mechanical Performance.

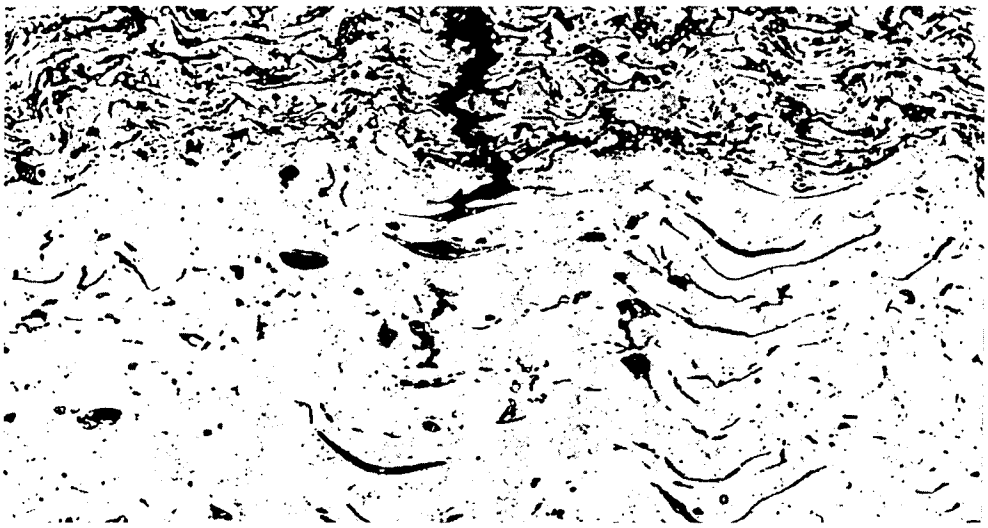

Figure 6. Crack propagation in sintered INVAR ending at the metallurgically bonded material.

The 308 S.S. material that was sprayed with the single wire gun shows considerable strength, but poor elongation. As will be seen in the fracture surface micrographs later on, the material seems to be failing in both the lamellæ regions and along inter-lamella boundaries, but the material is still essentially a rapidly solidified material and therefore it remains a relatively brittle substance.

Figure 6 provides a visual record of the mechanical improvement in an INVAR sample. The upper region of the sample is sprayed with unsatisfactory shielding, and therefore is laden with oxide. The lower region of the sample was sprayed with better inert shielding. The entire sample was sintered at 1400 K (2075 °F) for 30 minutes. The propagating crack was stopped by the metallurgically bonded lamellæ, even though there appears to be a relatively large amount of porosity and oxide still in the microstructure.

The fracture surfaces of the tested samples are illuminating. Figure 7 shows the same region in an Invar sample as Figure 6. This is the sample which was tested to tensile failure in Table 2, and the view is that of the fractured face of the specimen. The top area is the oxide dominated failure region, and the bottom area is the region where the lamellæ have metallurgically bonded. The top area is characterized by the relatively flat fracture surface — the crack was unimpeded by the lamellæ and proceeded along the weak and brittle oxide. However, the lamellæ in the lower portion of 7 clearly increased the difficulty of crack propagation: the surface has much more relief, and the lamellæ are clearly visible.

Figure 7. Sintered INVAR fracture surface.
showing oxide dominated fracture (top) and bonded lamellæ dominated fracture (bottom).

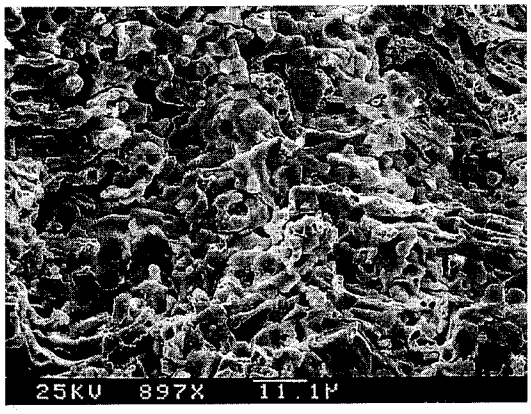

Figure 8. Sintered INVAR oxide fracture surface at higher magnification. (Showing oxide dominated region.)

Figure 8 shows in higher magnification the oxide dominated region of the fracture surface. Two aspects of the view in Figure 8 are noteworthy.

- The field of view is dominated by the small, sharp fractured oxide particles. These are the portion of the material that carried some load until failure and the failure crack propagated through their structure. Figure 8 shows why this oxide laden structure is fairly weak compared to our expectations for an oxide structure (which should be relatively strong if brittle) — the amount of oxide material carrying the load is a relatively small fraction of the total area of the cross section; there is a large fraction of void and the porosity doesn't contribute to the strength of the material.
- Underlying the crystalline fracture in Figure 8 is the relatively smooth surfaces of the undisturbed lamellæ. Where they are visible, there must have been a region of either void porosity or laminar porosity which opened during the fracture.

Figure 9 shows the companion pictures for the region in the sintered Invar where the failure was dominated by the lamellæ themselves. The magnification of 9 is similar to that of 8. Figure 9. shows the lamellæ which have either been cleaved in two, or the failure crack propagated along their boundary. I believe that both mechanisms are present: some of the lamellæ surfaces show characteristics of the wrought material fracture failure such as the graininess of the lamella surface and the small ridge-like surfaces on the lamella in the upper left region of 9. The material in 9 is still a rapidly solidified material that has been sintered for 30 minutes. There are also regions which appear to be boundary failures, particularly the small 15 µm by 20 µm lamella hole in the bottom center of 9. The dark cavern regions on the right side of 9 appear to be void porosity which has been exposed by the fracture.

The fracture face of the single wire plasma sprayed 308 stainless steel sample is shown in Figure 10. This material was sprayed with extra energy being provided to the plasma beyond that needed to melt the wire. The fracture surface shows several species of material condition. First, the lamellar structure is clearly visible in the layered organization of the metal. There are also some regions of apparent inter-laminar porosity visible in the structure. Secondly, there are several broken lamellæ, showing that the crack propagated through at least some of the lamellæ. All of the severed lamellæ in Figure 10 show signs of brittle fracture: there are chevrons on the visible faces. Thirdly, there are smooth lamellæ surfaces visible in the figure. These indicate that the crack was able to propagate along the inter–lamella boundaries in some areas. Notable is what is missing: the regular, crystalline structure of the oxide face is missing from these samples.

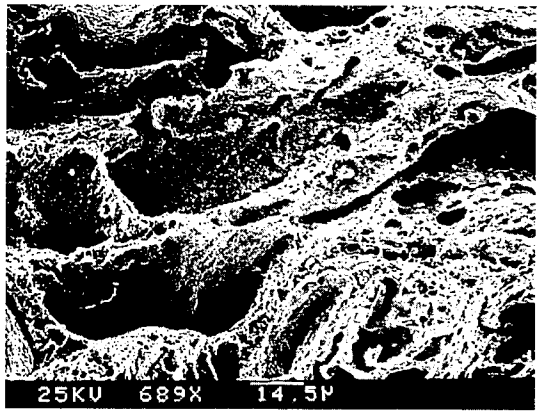

Figure 9. Sintered INVAR metallurgically bonded fracture surface showing fractured lamellæ and inter–lamella regions.

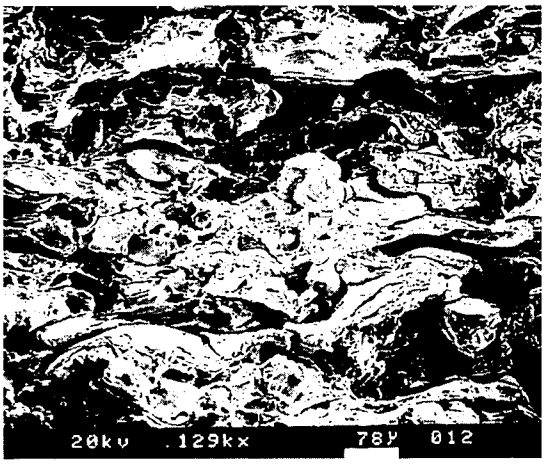

Figure 10. Single wire plasma sprayed 308 S.S. fracture surface, showing fractured lamellæ and inter–lamella regions.

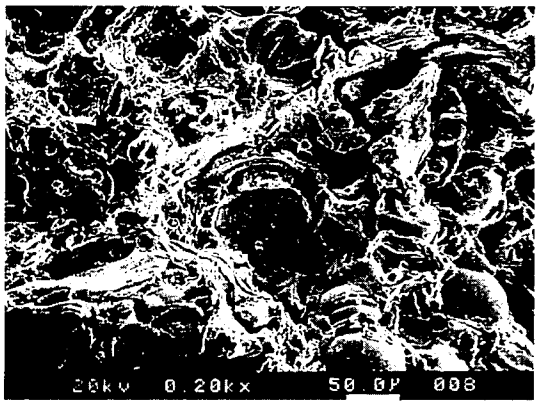

Figure 11. Detail: Single wire plasma sprayed 308 S.S. fracture surface, showing lamella pull–out, and fractured lamella regions.

Figure 11 is a slightly higher magnification micrograph of the same face of tensile tested 308 stainless steel. This picture clearly shows the spherical lamellæ that were formed by particles that solidified, or nearly solidified, in flight prior to impacting the shell. These particles did not, it appears in the figure, contribute to the strength of the shell. Rather, the failure crack propagated along their boundaries. In the center of Figure 11, there is a hole where a spherical lamella was pulled out from the face.

Non-metallurgically Bonded Shells

The current art for making sprayed metal shells results in mechanically bonded lamellæ. A better shell can be made:

- Superheat in the particles will promote fusion with other lamellæ and lower the porosity of the shell — superheat is added to the particles by using a suitable energy source, by spraying with a heated gas stream, and by controlling the radiant heat loss;
- A hot substrate will largely eliminate quench stress, and help reduce porosity — the hot substrate is most easily provided by using a heat castable ceramic substrate;

- The sprayed particles should be of uniform size — the uniform size is a difficult challenge which can be met by a radically different deposition scheme such as the microcast method described in (Merz 1994), or by an extremely carefully managed spray atomizer;
- The partial pressure of oxygen must be minimized — the controlled atmosphere for the spray is easily delivered by a shroud arrangement, and might also be attained by a laminar flow inerting system such as that developed by Praxair or other commercial gas vendors.

Certainly the single-wire plasma device holds promise in delivering a number of these desiderata.

Conclusions

The mechanical performance of thermally sprayed shells can be improved by promoting metallurgical bonding in the microstructure. However, the mechanisms for forming the bonds are defeated if each lamella is coated in an oxide. Further, if the void porosity fraction is too large, the strengths will not be significantly improved and the material will continue to exhibit a measure of anisotropy. Thus oxide control, process control to minimize void porosity, and a mechanism for metallurgical bonding are all simultaneously required to improve the mechanical performance. These microstructural issues will also be valid for other solid freeform fabrication methods which build up metal structures by an accumulation of individual particles.

References

Cifuentes, L. and Harris, S. (1984). "Composition and Microstructure of Arc-Sprayed 13% Cr Steel Coatings." *Thin Solid Films* **118**(4): 515-526.

Fussell, P. S., Patrick, E. P., Prinz, F. B., Schultz, L., Thuel, D. G., Weiss, L. E., Hartmann, K. W. and Kirchner, H. O. K. (1991). *A Sprayed Steel Tool for Permanent Mold Casting of Aluminum.* 1991 SAE Aerospace Atlantic, Dayton, Ohio USA, SAE International.

Fussell, P. S. and Weiss, L. E. (1990). *Steel-Based Sprayed Metal Tooling*. Solid Freeform Fabrication Symposium, Austin, Texas USA, University of Texas — Austin.

Gall, H. E. B. a. T. L., Ed. (1985). *Metals Handbook Desk Edition*. Metals Park, Ohio, ASM.

Gill, S. C. (1991). *Residual Stresses in Plasma Sprayed Deposits.* Ph. D. University of Cambridge, England

Gill, S. C. and Clyne, T. W. (1990). "Stress Distributions and Material Response in Thermal Spraying of Metallic and Ceramic Deposits." *Metallurgical Transactions B* **21B**: 377-385.

Hull, C. W., I. UVP. US Patent 4,575,330 B1. Apparatus for Production of Three-Dimensional Objects by Stereolithography. Dec. 19, 1989.

Hull, C. W., I. 3D Systems. US Patent 4,929,402. Method for Production of Three-Dimensional Objects by Stereolithography. May 29, 1990.

Kaiser, J. J. and Miller, R. A. (1989). "Inert Gas Improves Arc-Sprayed Coatings." *Advanced Materials and Processes* **136**(6): 37-40.

Merz, R. (1994). *Shape Deposition Manufacturing.* Dissertation,. Technische Universität Wien, Institut für Allgemeine Elektrotechnik und Elektronik

Merz, R., Prinz, F. B. and Weiss, L. E., C. M. University. US 5,281,789. Method and Apparatus for Depositing Molten Metal. Jan 25, 1994.

Milewski, W. and Sartowski, M. (1986). Some Properties of Coatings Arc-Sprayed in Nitrogen or Argon Atmosphere. *Advances in Thermal Spraying*. Oxford, Pergamon Press. 467-473.

Milovich, D. (1989). *Metal–Faced Composite Tooling*. Tooling for Composites, Long Beach, California, SME.

MOGUL (1963). *Metallizing Manual.* Metallizing Company of America.

Rothdeutsch, J. G. a. E. (1990). Rapid Tool Manufacturing — Commercial Investigation.

Safai, S. and Herman, H. (1981). Plasma-Sprayed Materials. *Treatise on Materials Science and Technology*. Academic Press. 183-214.

Thorpe, M. L. (1989). *How Recent Advances in Arc Spray Technology have Broadened the Ranges of Applications*. Thermal Spray Technology: New Ideas and Processes, Cincinnati, Ohio USA, ASM International.

Turner, T. H. and Budgen, N. F. (1926). Metal Spraying. *Metal Spraying*. London, Charles Griffin & Co. 162.

Weiss, L. E., Gursoz, E. L., Prinz, F. B., Fussell, P. S., Mahalingam, S. and Patrick, E. P. (1990). "A Rapid Tool Manufacturing System Based on Stereolithography and Thermal Spraying." *Manufacturing Review* **3**(1): 40-48.

Weiss, L. E., Prinz, F. B. and Gursoz, E. L., C. M. University. US Patent 5,189,781. Rapid Tool Manufacture. Mar 2, 1993.

Weiss, L. E. and Schultz, L. L., C. M. University. US Patent 5,079,974. Sprayed Metal Dies. January 14, 1992.

LAPS - Laser Aided Powder Solidification - Technology for the direct production of metallic and polymer parts

P. Eyerer, J. Shen, B. Keller

Institute of Polymer Testing and Polymer Science , Department
of Polymer Engineering, IKP - University of Stuttgart,
Pfaffenwaldring 32, 70569 Stuttgart, FRG

Abstract

The prototypes of today's commercial available RP-Systems (e.g. Stereolithography-Systems) are suitable mainly for designing and, if even, for restricted functional tests. From this it can be concluded that for obtaining functional or technical prototypes one has to use time- and cost-intensive downstream-technologies like investment casting. Because of the economical aspects in industries there is a great demand for direct production of functional and technical prototypes.

The present paper describes the activities and research results on the development techniques based on laser induced solidification of powder materials for the direct manufacturing of metallic parts. Also a various number of polymers, suitable for sintering and remelting, are investigated and presented as functional materials for different applications.

1. Introduction

The technics of **L**aser **A**ided **P**owder **S**olidification have been used to generate metallic and polymer parts. Analogeous to the technics of laser surface treatment, the powder is preplaced onto a substrate and melted or sintered within the laser irradiated zone [1]. The part will be built up with the principle of the well-known Layer Manufacturing Technology (LMT).

With regard to the metal powder application a number of copper-based powder mixtures with different weight percentages of lead and tin were investigated. In this case of applying a mixture of high and low melting materials, a sintering process will be accelerated by generating a liquid phase [2,3]. Therefore the processing temperature, caused by the energy coupling of the laser beam, has to be between both melting points. According to the experimental results described below it is generally necessary to keep the liquid phase as long as possible, because its surface tension will provide the driving force for sintering. Optimization due to the main processing parameters laser power P, beam intensity I and energy density H using the LAPS-testbed is carried out with respect to reduced curl distortion and better interlayer metallurgical bonding.

The LAPS laboratory equipment (low-power laser) is employed to perform optimization on polymer powder analogeous to metal powders. Polystyrene and Polyamid-Copolymer are presented as suitable materials for plaster block mouldings and functional elastomeric parts, respectively.

2. Experimental procedure for metal powder mixtures

The laser used for our experiments is a cw (continous wave) CO_2-laser with a maximum output power of 1500 W (TLF1500). The laser beam has a gaussian intensity distribution and is focused with a parabolic copper mirror (focal length f=300mm). The minimum of the achievable beam diameter is d_L=0.35mm. The test bed with ridgeless layer levelling for metal powder application is fixed onto a 3-axis CNC coordinate machine (figure 1). Although powder heating option was available, the experiments were carried out at room temperature in order to avoid bonding of the entire powder bed. Argon is used as protective gas in an open atmosphere.

The surface temperature of the partially sintered powder during laser processing is detected using an infrared pyrometer. This signal is employed for a closed loop control of the laser power and transformed into a temperature signal for the user control. Therefore a PID control system has been developed in order to transform the desired input signal of the measured temperature and a DC output signal for the direct transmitting control of the laser power. Additional to the pyrometric power control, temperature measurements with thermocouples in different heights of the layers and IR-temperature distribution on the powder surface with a thermography camera were performed.

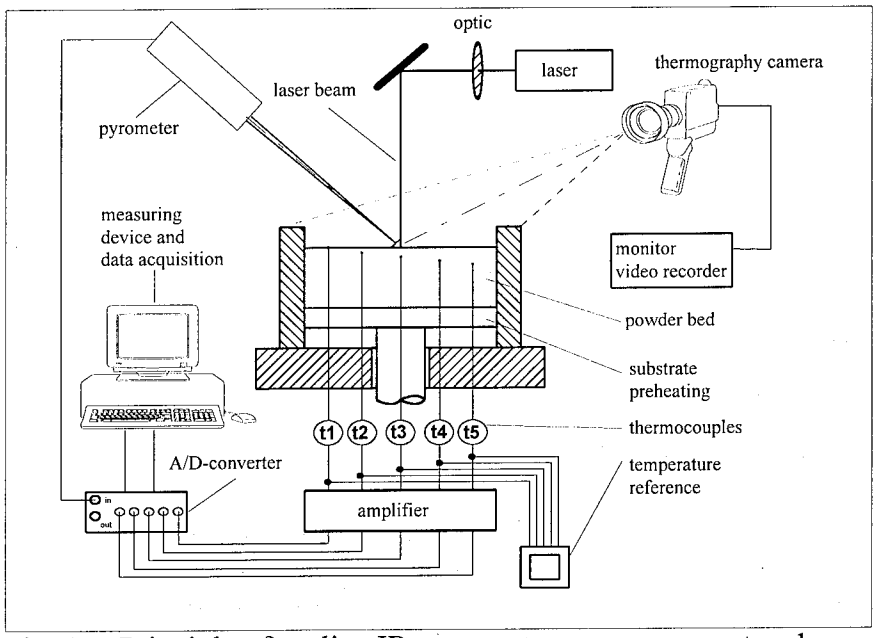

Fig. 1: Principle of on-line IR-temperature-measurement and pyrometric power control during the laser sintering process

All kinds of pulverulent materials used in the overall work are pure metals (Cu, Pb, Sn) or their mixtures (Cu mixed with 10, 20, 30 and 50 wt.-% Pb and Cu mixed with 5, 11, 15, 20 wt.-% Sn). Their particle size is less than 45 µm and the particle shape is chosen approximately spherical because of the good behaviour during the layer levelling. The representation of the results in this paper are focusing on pure copper and copper-lead mixture with 20 wt.-% lead addition but references in the conclusion are given also for other powder mixtures.

$$d_L = \sqrt{\frac{4 \cdot P}{\pi \cdot I}} \quad (1), \text{ and } \quad v = \frac{P}{H \cdot d_L} \quad (2).$$

To classify the results of laser sintering, the width and heights of each sintered track were measured and their strength and faults (oxidation, melting, scale like structure) were registered. Metallographic investigations (SEM and light microscopy) were carried out to get the information about the sintering progress and the microstructure of the sintered tracks.

2.1 Results on pure copper powder

During laser sintering pure copper powders should not be melted. At an elevated processing temperature the bond between the particles can only be established by means of activated diffusion process. A strong bond of the particles, respectively high strength and density, cannot be reached because of the limited interaction time (up to 1,5 s) of laser beam and powder bed.

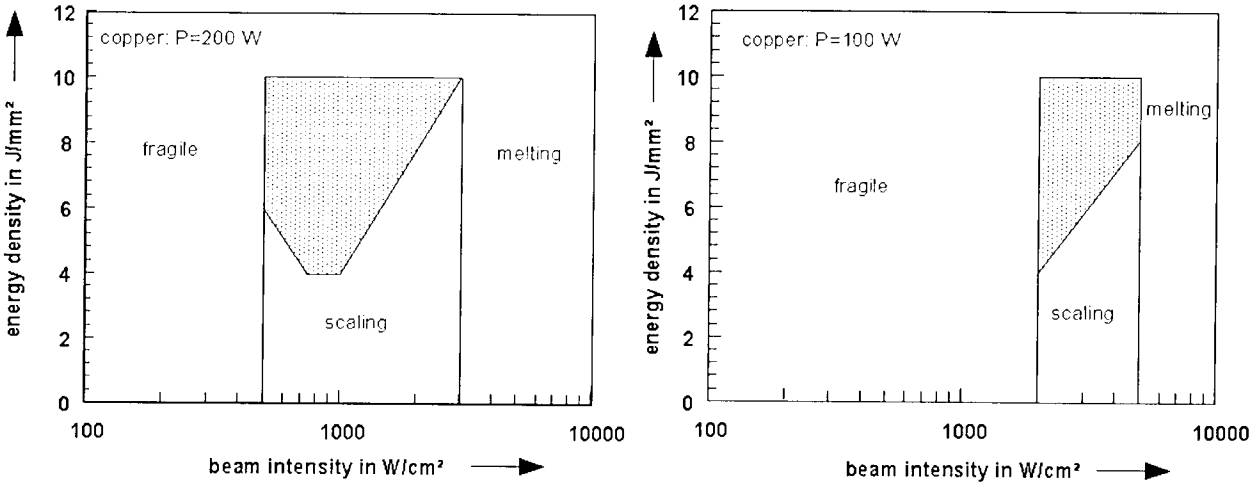

Fig. 2 and 3: Working area (hatched zone) of beam intensity and energy density for laser sintering of copper powder at P=200 W and P=100W

Fig. 2 and 3 show the working areas of energy density as function of beam intensity for different laser powers. Because of extremely short diffusion time the tracks sintered at beam intensities lower than 500 W/cm² are fragile. Higher beam intensity causes an increasing strength of the sintered tracks . Above I=3000 W/cm² the copper powder was molten and chains of metal balls were observed in the middle of the track.

Also the energy density affects the sintering process. In the low range of energy density (H≤4 J/mm²) a scale-like structure occurs on the surface of the track. Because of the thermal tension and the weak powder bond at low energy densities, pieces of powder blocks (scales) rise from the powder bed. Experiments were done at energy densities up to 10 J/mm². If the laser power is reduced from 200 W down to 100 W, the working area shifts to high values of beam intensity (comparing Fig. 2 to Fig. 3). A further reduction of

the laser power (at P=50 W) results fragile sintered tracks at all investigated values of beam intensity and energy density.

Fig. 4 shows a cross sectional SEM micrograph of a sintered track. The bond of laser induced sintering necks between the powder particles is weak, but high enough for depositing from the powder bed (analogeous to green part strength).

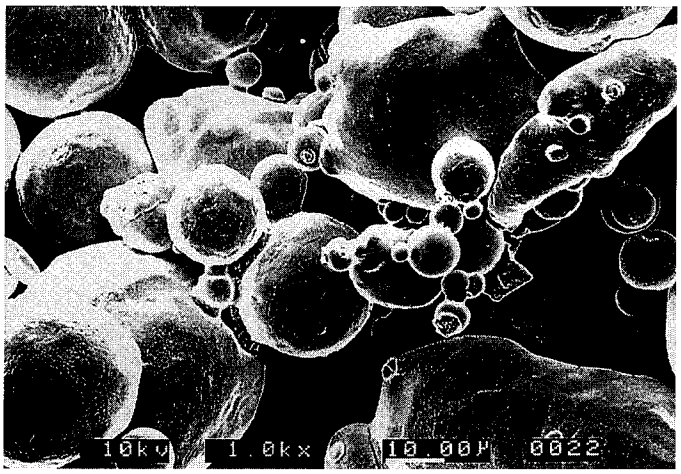

Fig. 4: Cross sectional SEM-micrograph of laser sintered copper powders, showing the sintering necks between powder particles. (P=100 W, I=2000 W/cm², H=8 J/mm²)

The width and the height of laser sintered tracks are illustrated as a function of energy density and beam intensity in Fig.5 and 6. The working areas are hatched. With increasing energy density (though the beam diameter remains constant) the track width rises (Fig. 5). Under the given parameter combination (P=200 W and I=1000 W/cm²) good tracks can be produced only if energy density is more than 4J/mm². The broken line in Fig. 5 marks the layer thickness of the powder bed. Since the track width is linearly proportional to the beam diameter, it drops with increasing beam intensity (Fig. 6).

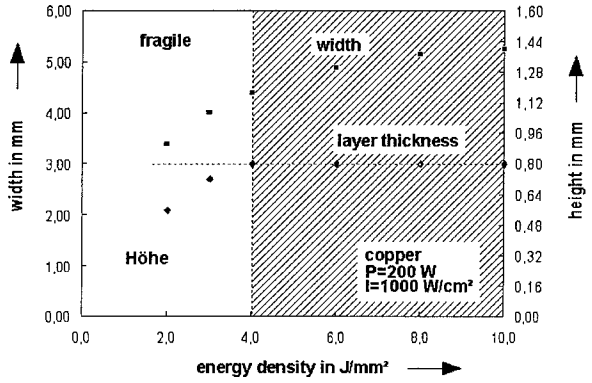

Fig. 5: Width and height of single tracks of copper as a function of the beam energy density. (P=200 W, I=1000 W/cm²)

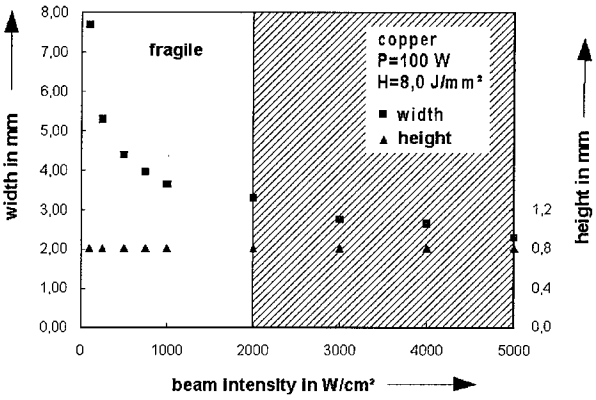

Fig. 6: Width and height of single tracks of copper as a function of the beam intensity. (P=100 W, H=8 J/mm²)

2.2 Results on copper-lead powder mixtures

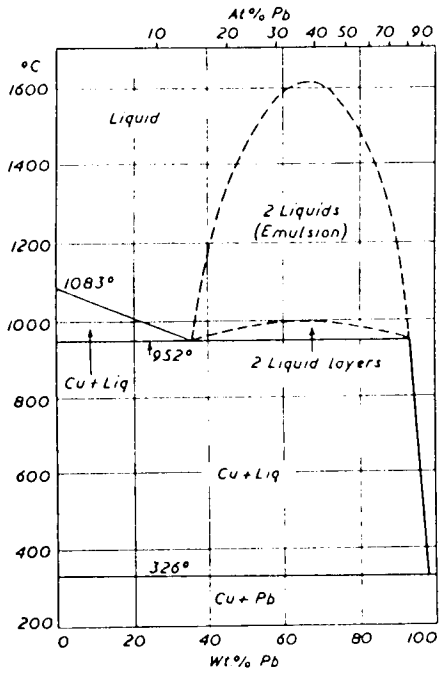

Fig. 7: Binary phase diagram of copper-lead [4]

Corresponding to the copper-lead binary phase diagram in fig. 7 lead does not dissolve in copper. Lead will be melted above T_m=326°C and wets the copper particles. The requirements of liquid phase sintering are fulfilled if the processing temperature is kept below the melting point of copper (T_m=1083°C). It was determined, that an increasing content of lead results in an extending range of parameter variation and a further strengthening of the tracks compared to pure copper. With the minimum achievable constant laser power of P=50 W it was found that the intensity of I=50 W/cm² is high enough for laser sintering Cu-Pb with 30 and even 20 wt.-% lead. However a further increase in lead addition (50 wt.-%) will lead to a strong narrowing of the working area. Fig. 7 shows the working area at P=100 W for Cu-Pb (20 wt.-%) and fig. 8 the corresponding width and heights of the sintered tracks as functions of the beam diameter.

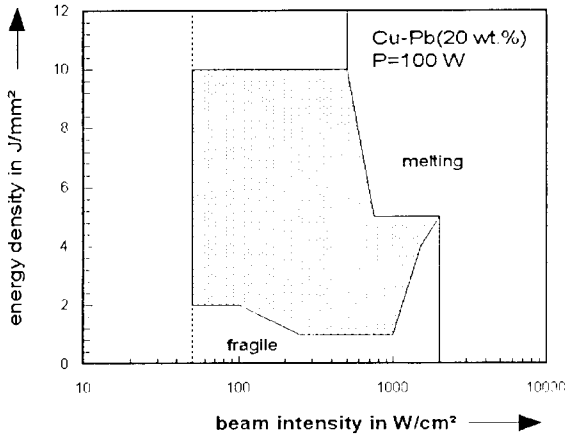

Fig. 7: The working area of laser sintering of CuPb 20 wt.-%.

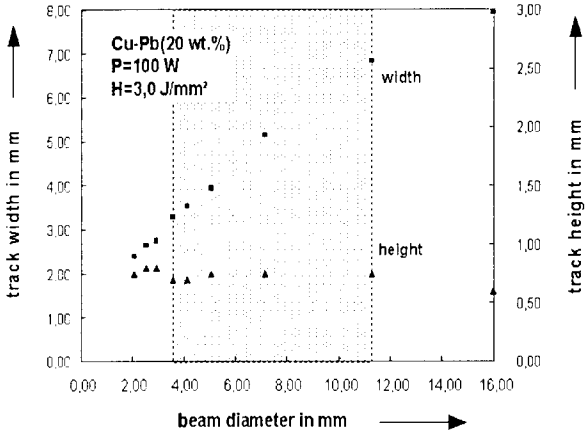

Fig. 8: Corresponding width and height of sintered tracks as function of beam diameter.

The relationship between track geometry and the processing parameters are quite similar to the sintering of pure copper powder (figs. 5 and 6). While the height remains almost constant, the track width rises linearly with increasing beam diameter (hatched zones refer to the working area).

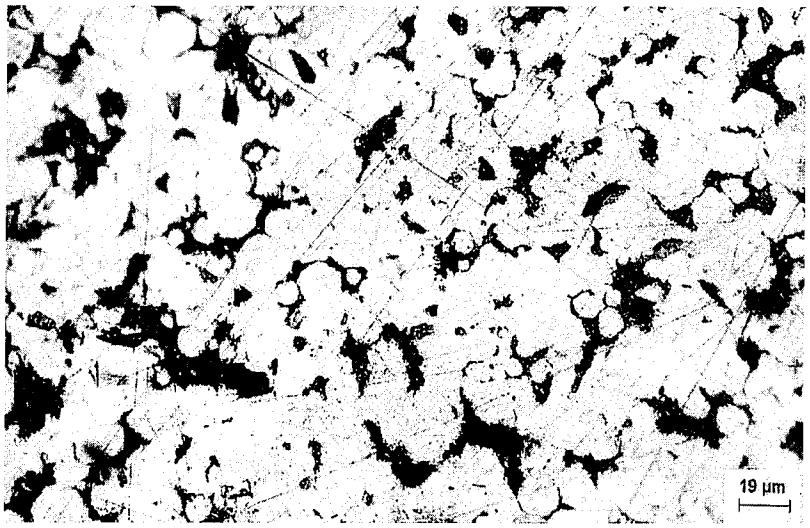

Fig. 9 Cross section of a sintered track (Cu + 20 wt.% Pb). (P=50 W, I=500 W/cm^2, H=10 J/mm^2)

In contrast to the laser sintering of pure copper powders the sintered tracks of copper-lead mixtures don't have the typical copper color. Fig. 9 is a micrograph of the cross section of a laser sintered track of Cu-Pb (20 wt.%). The color of the whole cross section is yellow, indicating that no pure copper powder particles exist anymore. The melted lead powder is distributed in the sintered track homogeneously. The porosity of the sintered track is lower than expected, although the powders were not densified before laser sintering.

2.3 On-line measurement of temperature distribution

The experimental set-up of the temperature measurements in and on the powder bed is shown in figure 1. Specially fabricated Ni-CrNi thermocouples (0,2 mm thickness) covered with a glass layer were arranged in a line at different depths (0, 0.3, 0.6, 0.9 and 1.2 mm) in the powder bed (t1 to t5). Ceramic tubes were used for strengthening and electrical isolation. The laser irradiated zone was measured by the pyrometer and the temperature distribution on the powder surface was recorded by a thermography camera. Both surface temperature measurement devices were fixed constantly versus the laser beam axis. A special program for data acquisition and processing control was developed. These arrangements will allow the time- and point-disintegrated description of the process.

Quantitatve optical temperature measurements require accurate data of emission degrees. They were measured by tailoring the optical devices repeatedly until the temperature measured with the thermocouple were identical. Pure copper showed an absorption rate of 30% and in case with lead addition they rise with increasing lead content, e.g. Cu-Pb (20 wt.-%) has an emission degree of 40%.

Temperature distribution in the powder bed

By modifying the temperature-time curves, derived from the thermocouples, one may get isotherms in the x-z-plane. The derived temperature maintaining time (time interval, where the temperature is kept above the isotherm) enables the quantitative estimation of the sintering progress. In our case a liquid phase sintering is only possible if the processing temperature is at least T=326°C (fig.7). Considering the fast heating speed a isotherm of 350°C is chosen. Figure 10 describes the influence of lead content in the

powder mixture on the 350°C-isotherm. The respective temperature maintaining time is depicted in figure 11.

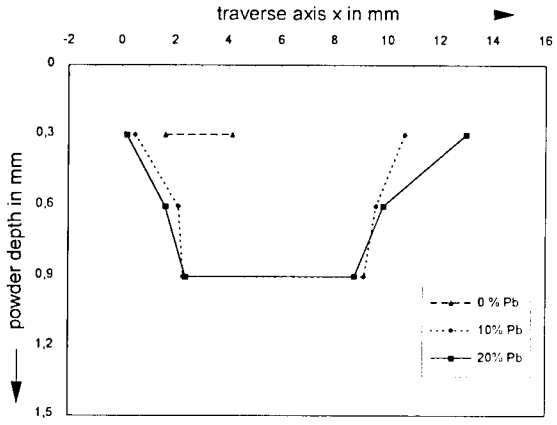

Figure 10: 350 °C isotherms of CuPb powder mixtures. Processing parameters: P=50W;I = 500 W/cm²; H = 6 J/mm²

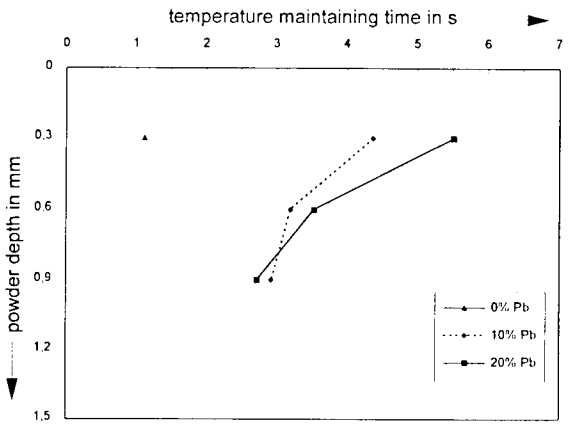

Figure 11: Corresponding temperature maintaining time of CuPb powder mixtures to fig. 10.

The 350°C isotherm of the pure copper powder occures only at 0.3 mm under the powder surface. Temperature maintaining time is about 1 sec. If 10 or 20 wt.% lead is added into the powder the 350°C isotherm reaches a powder depth of 0.9 mm. A significant increase of the temperature maintaining time is observed respectively (figure 10 and 11).

Solid copper has a very poor absorption rate of the CO_2 laser beam. It is about 0.5 % for opaque surfaces. In shape of powder with the applied grain size it rises to a value of about 38% due to increasing surface of powder particles [5]. From the measurements of emission degree we know, that the absorption rate of Cu-Pb (20 wt.-%) powder mixture is about 50% higher than that of pure copper powder. It means that at the same processing parameters the CO_2 laser beam energy coupling of CuPb(20 wt.-%)-powder is about 50% more than of pure copper powder.

It seems the difference of energy coupling is clearly more than 50%. In fact copper-lead powder mixture has a lower thermal conductivity than the pure copper powder (λ_{Cu} = 384 W/mK, λ_{Pb} = 34,7 W/mK). A large part of the laser energy coupled into copper powder is conducted away from the processing area. In the case of Cu-Pb powder mixture heat flow into the powder bed is much lower. The laser heating is more "locally". This explains the larger isotherm area and longer temperature maintaining time

Temperature distribution of the powder bed surface

These investigation were performed for various relevant situations, e.g. single and rectangular tracks, overlappings and overhangings for different layer thicknesses. The results will help describing and understanding the sintering process. Following two figures show some results of Cu-Pb (20 wt.-%), which were received from a rectangular

contour at a corner and the comparison of the surface temperature before and during overlapping.

Figure 12a to 12c represent the temperature distribution at the first corner (1s delay to each other). Although the laser beam stays briefly at the corner (ca. 200ms) while reading a new NC-sentence, neither significant temperature increase nor shift of the distribution was observed.

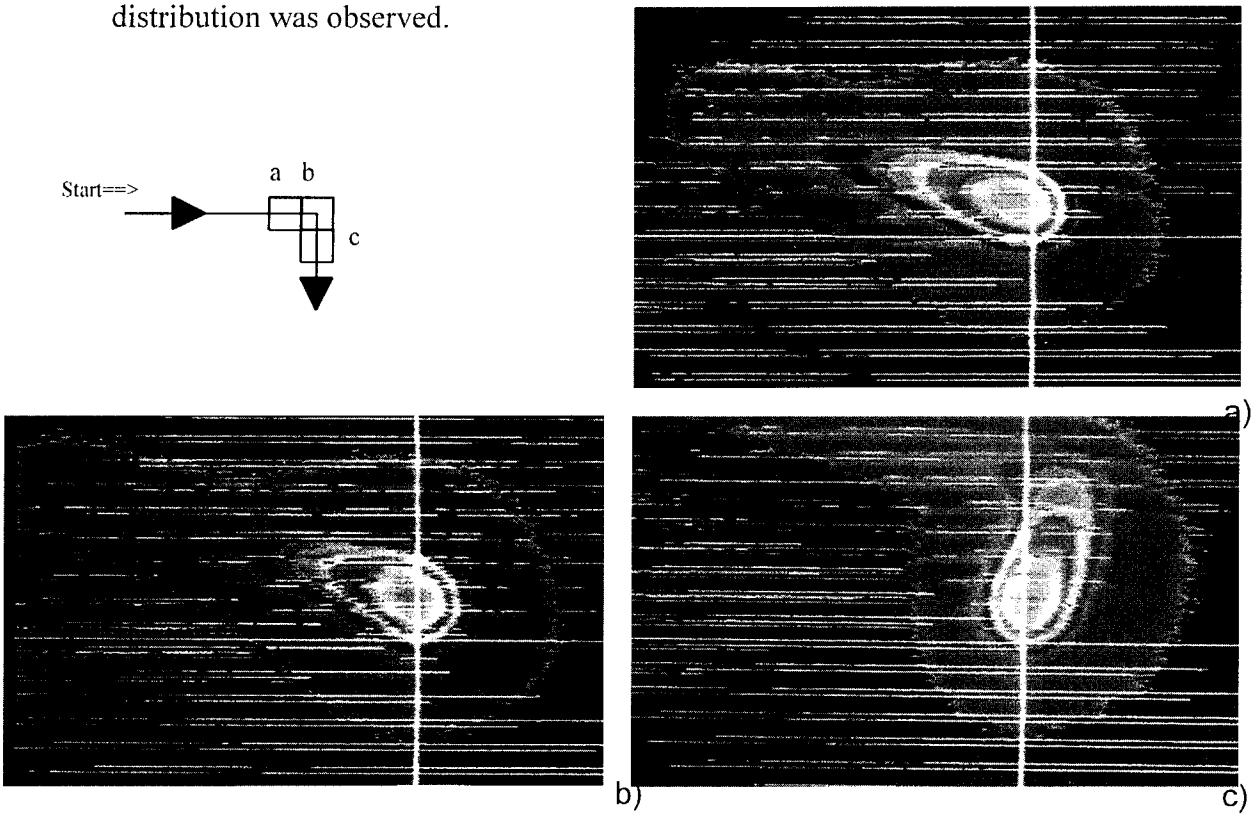

Figure 12: Surface temperature distribution during sintering process. Picture a, b and c have a delay of 1sec. Beam-powder interaction time is 1.5sec.

Figure 13 a and b describe the surface temperature at overlapping a new track on two already sintered tracks (powder depth is 1.2mm). Two effects are evident: the max. temperature in 13 a is is about 70°C higher than in 13 b and the elevated zone behind the laser beam is wider than in 13 b. This behaviour indicates a strong heat flow to the sintered region below. It is comprehensible because in the sintered region the molten lead wets the copper particles and increases the thermal conductivity.

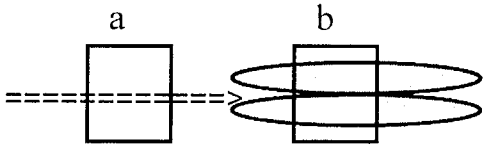

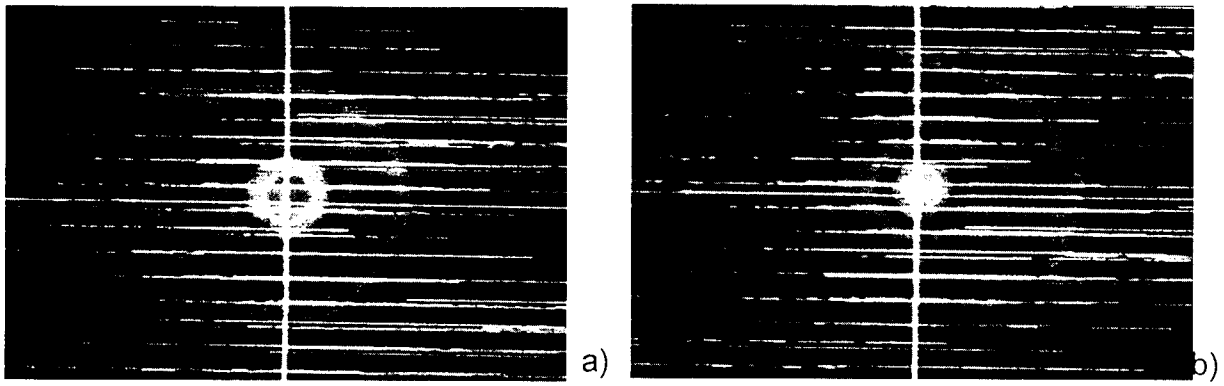

Figure 13: Surface temperature of overlapping a new laser sintering track on two sintered tracks. a) before overlapping, $T_{max.}$ = 563 °C; b) during overlapping, $T_{max.}$ = 493 °C.

3. Experimental set-up on polymer powders

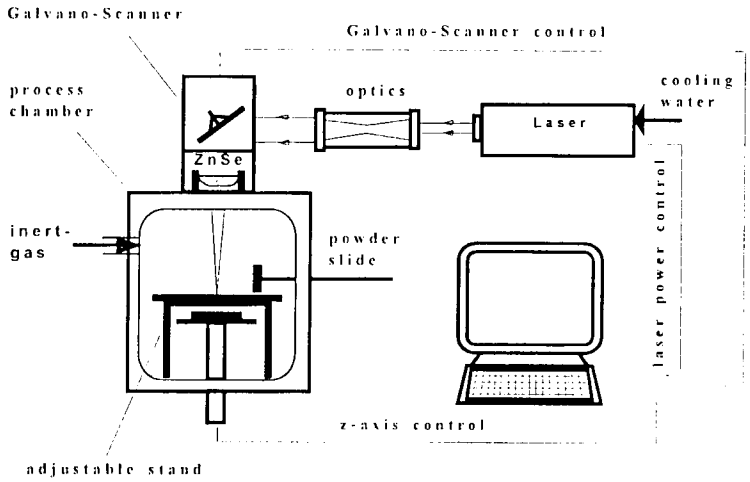

Figure 14: LAPS-laboratory equipment

The LAPS laboratory equipment is assembled consisting of a 50W CO_2-laser, beam recess optics, high speed Galvano-Scanner, ZnSe-focus lense and a temperature controlled (T_{max}=300°C) process-chamber with a ridgeless layer-levelling. The laser power, beam-movement and z-axis are software-controlled. This equipment has been acquired because of its suitability for polymers as well as for metal powders.

Material selection

The selection of polymer materials for our investigations was made in respect to the most employed technical thermoplasts in industries like PA, PE, PP, PVC, PS, ABS, PC and their compatible blends or bimodal powder mixtures. Although comprehensive investigations on these powders, especially for PA 11, showed satisfactory results reffering to the layerwise build-up of complex parts, they are mostly employed for designing and restricted functional tests after postprocessing (infiltration and/or surface finish). However the main application have skilled metal prototypes via investment casting. Polystyrene polymer powder as RP-pattern after laser sintering is investigated for

use of a lost pattern for direct investment casting and elastomeric modificated Polyamid as functional prototype.

3.1 Parameter optimization

The parameter optimization in respect to the polymer powders described below is done in a similar methodical technique as for metal powders but using laser sintered panels with the dimensions of 20mm x 20mm. The assumptions for defining optimal process parameters for working areas (energy density, beam intensity, hatching distance) were taken due to reduced curl distortion, rate of makroscopical sintering (strength of panel), sintering depth (layer thickness) as well as the multilayer behaviour. Following the representation of the results are focused on polysytrene powder with the particle size of less than 100 µm having the shape of shavings.

Figure 15 shows the energy density of a single melted track versus hatch distance for two different intensities, respective laser powers (d_L is 0.35mm). The hatched zones mark the working areas. In respect to the assumptions described above it is clearly to see, that for receiving compact panels an increase in hatching distance is guided by an increase of the required energy density. Regarding the working areas for the two laser powers there is a shift using higher laser power to lower energy densities and smaller areas. This is due to the limited interaction time of laser beam and powder bed.

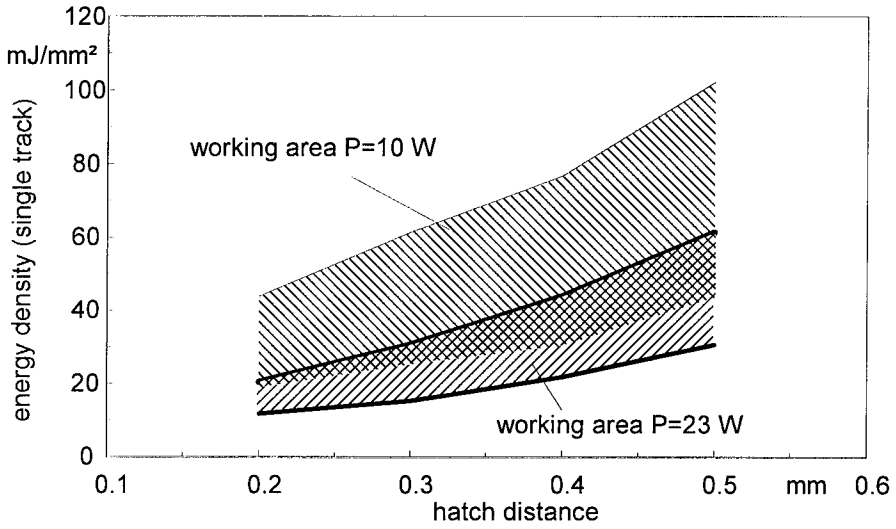

Figure 15: Energy density versus hatch distance for different laser powers.

Within the parameter range various numbers of parts were built using Polystyrene and elastomer modificated Polyamid, respectively to their working areas. No surface finishing or infiltration was performed for postprocessing.. It was proved that there were no geometric restrictions for complex geometries due to both polymers. (see fig. 16-white parts). The Polystyrene parts showed a porous surface (max. surface roughness of 60µm) corresponding to the comparativly big particle size and brittle behaviour while the mechanical behaviour of the PA-Copolymer parts showed their typical properties of 350% elongation at break.

3.2 Investment casting via direct burn-out

The Polystyrene parts were embedded in the plaster block moulding and burnt out afterwards completely. Investment casting of aluminum alloy AlSi10Mg and AlSi9Cu3 was performed. Figure 16 shows an overview of some PS and PA-Copolymer parts with the corresponding aluminum casts. The results present, that PS is very suitable for lost pattern/lost mold to be used for unmodified investment casting. No changes in the normal process chain are necessary. The surface roughness of aluminum parts is as high as the corresponding polymer parts.

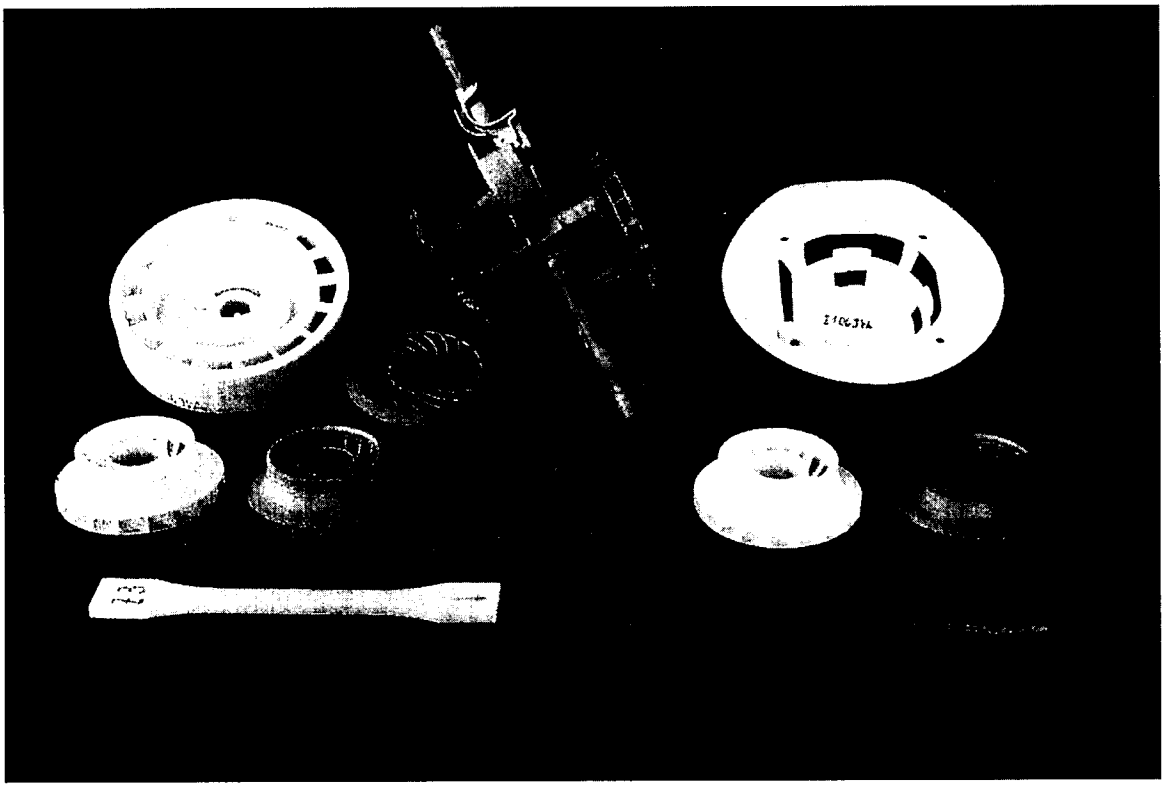

Figure 16: Overview of Polymer parts and corresponding metal parts via investment casting. Bottom: tensile specimen (PS/aluminum); middle: turbine blade housings (left: PA-Copolymer/aluminum, right: PS/aluminum); top: left: turbine (PS); middle: investment casted wax tree (before disassembling); right: loudspeaker housing (PS).

4. Acknowledgements

The authors thank the students for their comprehensive work done on parameter optimization and further development of the LAPS-equipment. The research in respect of metal layer powder application is funded by the European Commission (Programme Brite/EuRam).

The authors thank the partners and endorsers of the project. Also Karl-Heinz Schade from Emil Bucher GmbH&Co, Eislingen/Fils (FRG), who has performed the investment castings and prevented us with relevant datas on casting techniques.

5. References

[1] Zong, G.; Wu, Y.; Tran, N.; Lee, I.; Bourell, B.L.; Beaman, J.J.: Direct Selective Sintering of High Temperatur Materials. In: Marcus, H.Z.; Beaman, J.J.; Barlow, J.W.; Bourell, D.L.; Crawford, R.H.(Hrsg.): Solid Freeform Fabrication Proceedings, Austin, USA, August 1992, pp. 72-85.

[2] Kaysser, W.A.: Sintern mit Zusätzen. Materialkundlich-Technische Reihe 11, Berlin-Stuttgart: Gebrüder Borntraeger, 1992.

[3] Schatt, W.: Sintervorgänge, Grundlagen. Düsseldorf: VDI-Verlag GmbH, 1992.

[4] Massalski, T.B.: Binary Alloy Phase Diagrams Vol. I. American Society for Metals, Metals Park, Ohio 44073, 1986. ISBN 0-87170-262-2

[5] Haag, M: CO_2 Laser Absorption Characteristics of Metal Powders. Institut für Strahlwerkzeuge (IFSW), University of Stuttgart. Diplomarbeit, 1994

Direct Laser Sintering of Metals and Metal Melt Infiltration for Near Net Shape Fabrication of Components

M. Sindel*, T. Pintat*, M. Greul*, O. Nyrhilä**, C. Wilkening***
* Fraunhofer-Institut für Angewandte Materialforschung, Bremen, F.R.G.
** Electrolux, Rusko, Finland
***EOS GmbH, München, F.R.G.

Abstract

Direct laser sintering of metal powders is a great challenge for Rapid Prototyping (RP) because of the high potential of application, for example prototype tooling for polymer extrusion.
Recent development in laser sintering of metal powders use polymer or low melting alloys as a binder phase. Postsintering to strengthen the component produces shrinkage of the part, hence the near net shape capability is limited.
The combination of direct laser sintering and infiltration with metal melts allows the production of strong near net shaped components without shrinkage.
A composite metal powder consisting of Ni, Cu, Sn and P was successfully sintered in a Selective-Laser Sintering unit in ambient atmosphere at room temperature. The influence of laser intensity on microstructure and sintering behaviour is discussed.
Infiltration experiments were done with partially sintered samples. Full density could be achieved without shrinkage. Mechanical properties and microstructural development will be discussed.

Introduction

Currently laser sintering of metal and ceramic powders to manufacture parts is in research. Indirect sintering of polymer coated powders, where the polymer acts as a low melting point binder phase, has been developed to produce metal and ceramic components. Subsequent debinding and sintering is necessary to increase strength /1/.
Direct metal sintering mostly involves the formation of a liquid through a metal phase with low melting point, e.g. Ni/Sn mixture, or by supersolidus sintering of a two phase, e.g. Cu/Sn-alloys /2/. Sintering of high temperature materials without binder phase needs high sintering temperatures. A high temperature laser sintering process (HTSLS) is under development /3/.
Porous components made by SLS need further densification, either by sintering or by infiltrating the component. Further densification by sintering produces shrinkage of the component. Infiltration with liquid metal seems to be more promising, however needs development of the technique for different powder systems. Porous

SiC bodies produced by SLS of coated powder particles have been infiltrated with liquid Al /4/. Also the infiltration of Fe-based porous components with copper alloys is very common /5/.
This paper reports on research work in laser sintering of a multiphase powder mixture in a prototype version of a laser sintering unit. In order to increase density and mechanical properties sintered samples were infiltrated with liquid metal.

Experimental

The powder material used in the experiments contains three different components, Ni and compounds of Cu, Sn and P. A micrograph of the powder is shown in Fig. 1. Laser sintering of test layers was done at ambient atmosphere with a 100 W CO_2 (CW) laser at different laser intensities and a beam scan speed of 200-800 mm/s. Complex parts were built with layer thicknesses of 200 µm. The layers were investigated by SE and optical microscopy. Bulk samples were sintered by laser sintering and for infiltration experiments by conventional sintering in Argon atmosphere.
Infiltration of the porous samples was carried out in air at 500°C, using a PbAg brazing alloy. Different infiltration times were used in order to achieve full density and improved mechanical properties. Tensile strength and hardness were measured from the as sintered and infiltrated samples.

Results and Discussions

Sintering

The thickness of the laser sintered layer was about 100 µm. Single layers were strong enough to be handled without damage. With increasing intensity of the laser beam the powder material goes from sintering to nearly completed melting. The microstructures of the sintered layers of 3 different laser intensities at the same scan rate are presented in Fig. 2 a-c and the corresponding cross sections of the individual layers in Fig. 3 a-c.

low intensity:
Sintering with low laser intensity results in partial melting of the binder phase. The layer is homogeneous over the thickness. Ni-particles, appearing bright in the SEM micrograph, are not wetted.

medium intensity:
At medium intensity wetting of all particles including Ni is observed however the top surface seems to be completely melted, while the lower part still shows individual particles.

SiC bodies produced by SLS of coated powder particles have been infiltrated with liquid Al /4/. Also the infiltration of Fe-based porous components with copper alloys is very common /5/.
This paper reports on research work in laser sintering of a multiphase powder mixture in a prototype version of a laser sintering unit. In order to increase density and mechanical properties sintered samples were infiltrated with liquid metal.

Experimental

The powder material used in the experiments contains three different components, Ni and compounds of Cu, Sn and P. A micrograph of the powder is shown in Fig. 1. Laser sintering of test layers was done at ambient atmosphere with a 100 W CO_2 (CW) laser at different laser intensities and a beam scan speed of 200-800 mm/s. Complex parts were built with layer thicknesses of 200 µm. The layers were investigated by SE and optical microscopy. Bulk samples were sintered by SLS and for infiltration experiments by conventional sintering in Argon atmosphere.
Infiltration of the porous samples was carried out in air at 500°C, using a PbAg brazing alloy. Different infiltration times were used in order to achieve full density and improved mechanical properties. Tensile strength and hardness were measured from the as sintered and infiltrated samples.

Results and Discussions

Sintering

The thickness of the laser sintered layer was about 100 µm. Single layers were strong enough to be handled without damage. With increasing intensity of the laser beam the powder material goes from sintering to nearly completed melting. The microstructures of the sintered layers of 3 different laser intensities at the same scan rate are presented in Fig. 2 a-c and the corresponding cross sections of the individual layers in Fig. 3 a-c.

low intensity:
Sintering with low laser intensity results in partial melting of the binder phase. The layer is homogeneous over the thickness. Ni-particles, appearing bright in the SEM micrograph, are not wetted.

medium intensity:
At medium intensity wetting of all particles including Ni is observed however the top surface seems to be completely melted, while the lower part still shows individual particles.

high intensity:
At high laser intensity the powder is nearly completely remelted at the top surface. Also the lower part of the layer is melted, however individual particles are still visible.

Based on the results of the laser sintering experiments a complex shape of a small turbine, see Fig. 4, could be generated layer by layer. No curling and no distortion occurred during sintering. The component showed no shrinkage during laser sintering.

conventional sintering:
The conventionally sintered microstructure exhibits homogeneous wetting of all particles by the binder phase, as visible in Fig. 5. The material still has open porosity to allow further infiltration of the component. The as sintered density is ~ 70% of theoretical density.

Low laser intensities result in a preferred microstructure in the as sintered state, remelting occurs only at medium and high intensities. Optimisation has to be achieved in improving the bonding at low intensities, for example by altering the atmosphere. Generally remelting should be avoided, because it will cause shrinkage and curling of the sintered layer. Also the microstructure is less homogeneous.

Infiltration

Complete infiltration of the conventionally sintered components with liquid metal was achieved after 45 min total infiltration time. Fig. 6 shows the microstructure of the infiltrated sample. Partial reaction zones could be detected, however these are not generally visible in the material.
Tensile strength of the 45 min. infiltrated material is not improved as compared to the sintered material but hardness is increased. The reason for the unimproved strength lies in the presence of singular large pores in the infiltrated material, as could be observed in the fracture surface. These pores are filled very slowly, because capillary pressure is proportional to 1/r, where r is the radius of the capillary.
Prolonged infiltration time leads to an increase in strength, also hardness is sligthly reduced.

Table 1: Mechanical properties of as sintered and infiltrated material

Material	Tensile Strength (MPa)	Rockwell Hardness
as sintered material	96 - 105	25.2
45 min infiltrated material	92 - 102	89.6
90 min infiltrated material	132	69.5

Conclusions

Direct laser sintering of metal powder mixtures needs careful control of laser intensities to avoid remelting of the powder material and to achieve a homogeneous microstructure of the sintered layer. Using the described powder mixture direct sintering of more complex parts was done at room temperature.
Infiltration of the sintered porous material is practical, however, property improvement is poor at the moment. Further improvement to achieve reasonable strength values of about 200 MPa tensile strength is necessary.

References

/1/ Badrinarayan B. and Barlow, J. W., "Metal Parts from Selective Laser Sintering of Metal-Polymer Powders", Solid Freeform Fabrication Symposium, Austin 1992, 141-146

/2/ Bourell, D.L., Marcus, H.L., Barlow, J.W., Beaman, J.J., "Selective Laser Sintering of Metals and Ceramics", International Journal of Powder Metallurgy (Oct. 1992) 28, (4), 369-381

/3/ J. McWilliams, C. Hysinger, J.J. Beaman, "Design of a High Temperature Process Chamber for the Selective Laser Sintering Process," Solid Freeform Fabrication Symposium, Austin 1992, 110-117

/4/ Deckard, L., Claar, T., D., "Fabrication of Ceramic and Metal Matrix Composites From Selective Laser Sintered Ceramic Preforms", Proceedings of Solid Freeform Fabrication Symposium, Austin 1993, p. 215

/5/ Michaels et al., "Metal Parts Generation by Three Dimensional Printing", Proc. of the fourth internatinal Conference on Rapid Prototyping 1993, p. 25

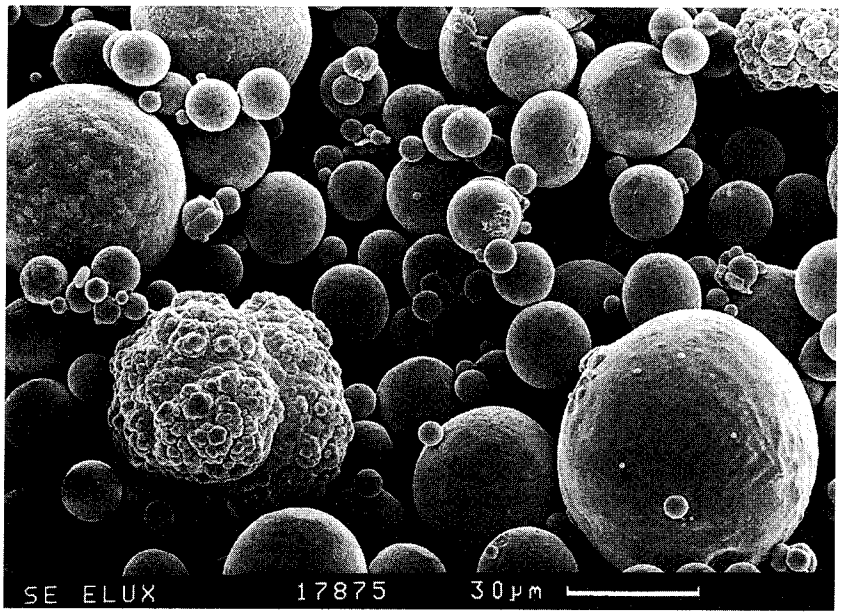

Fig. 1: SEM-micrograph of the composite metal powder used for laser sinter experiments (Ni powder appears bright in the micrograph)

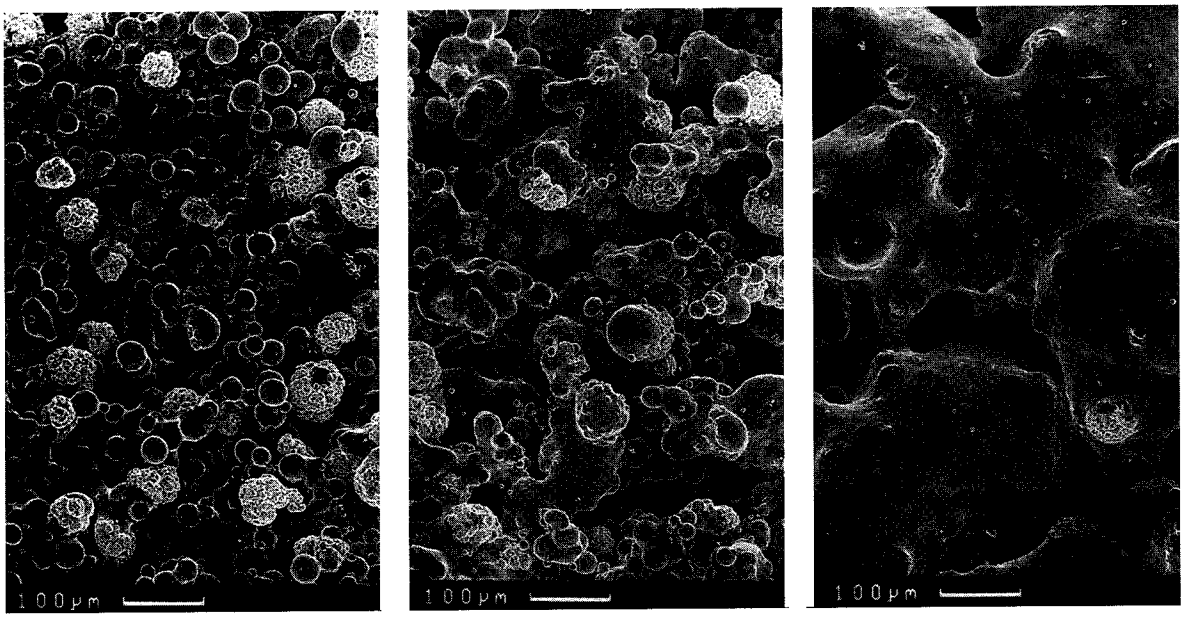

a) b) c)

Fig. 2: SEM-micrographs of the as laser sintered metal powder, low (a), medium (b) and high laser intensity (c), top view

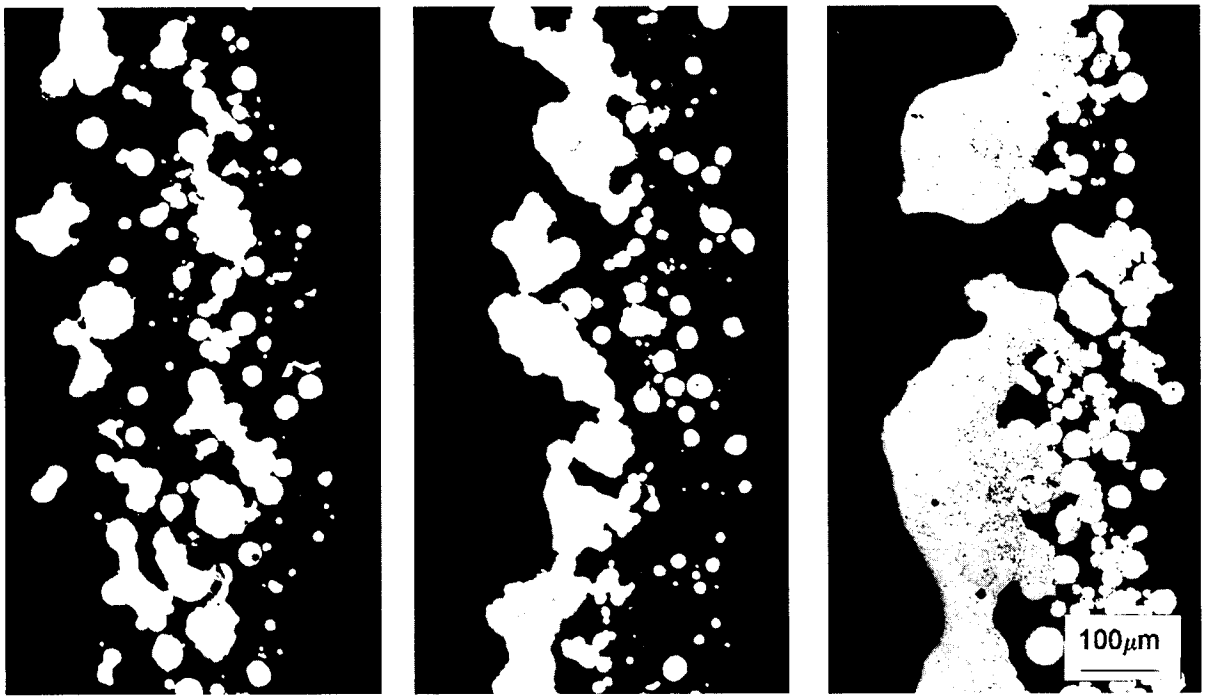

a) b) c)

Fig. 3: Optical micrograph of one individual layer of laser sintered metal material, low (a), medium (b) and high laser intensity (c), cross section (layer thicknes is 100 μm and top of the layer is to the left hand side)

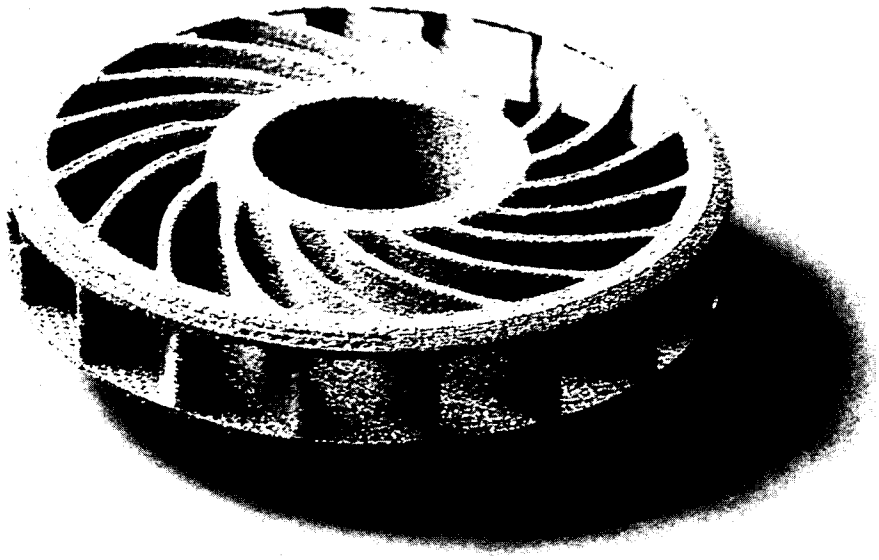

Fig. 4: Laser sintered component out of composite powder

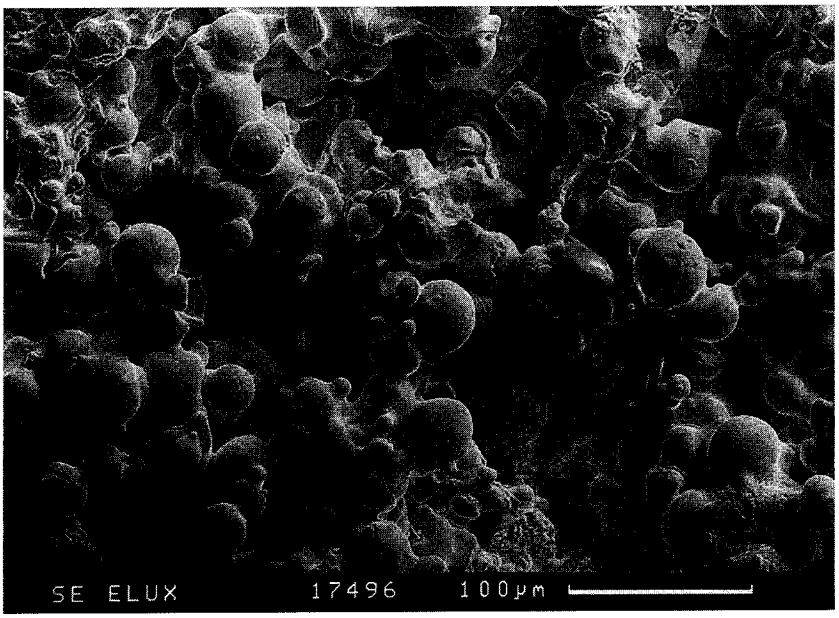

Fig. 5: Microstructure of conventionally sintered composite powder

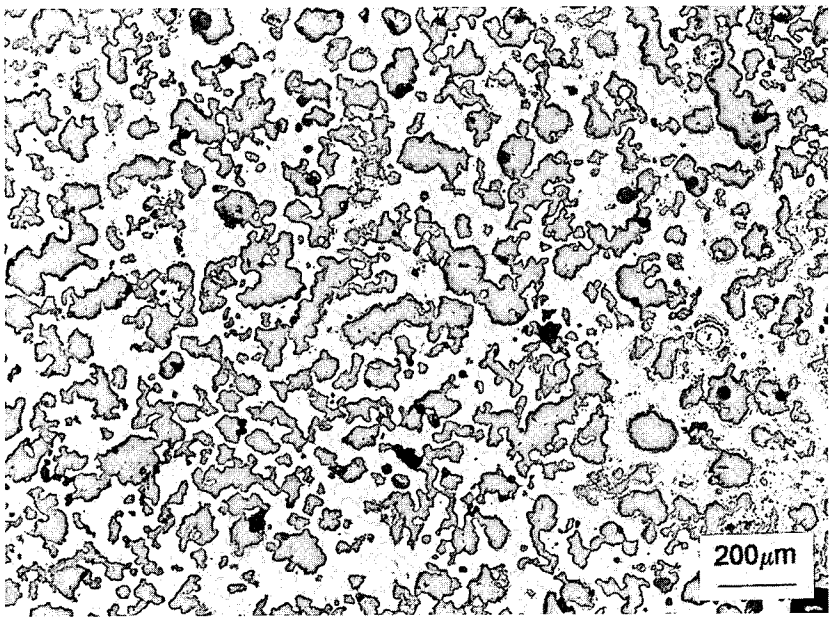

Fig. 6: Microstructure of sintered and subsequently infiltrated material

SLS™ PROTOTYPES FROM NYLON

Paul Forderhase
Kevin McAlea
Mary Michalewicz
Mark Ganninger
Kent Firestone

Introduction

Many rapid prototyping materials and processes produce parts which have relatively low stiffness, strength, and ductility. While such parts are useful for visualization, they have limited value where functional features are necessary or where application testing is required. In order to satisfy these more demanding requirements, rapid prototyping materials which offer part performance representative of molded plastics are required.

DTM has developed and commercialized nylon-based materials (LN-4010 and LNF-5000) for the SLS process which produce strong, durable parts without the use of constraint or support structures. In order to produce dimensionally accurate SLS nylon parts, careful control of the thermal environment is required during the entire process cycle. In this paper, the thermal control elements necessary to achieve this goal are described. Background information concerning SLS nylon part performance and material process behavior is also provided.

SLS Nylon Part Performance

SLS nylon is marketed as two distinct products; the first, LN-4010 has a mean volume-average particle size of 120 microns while the second, LNF-5000, has a mean volume-average particle size of 50 microns. The latter material is used to produce parts with fine detail, strong small features, and smoother surfaces. Examples of parts produced with both versions of this material are shown in Figures 1 and 2.

Figure 1: Functional Nylon (LN-4010) Part

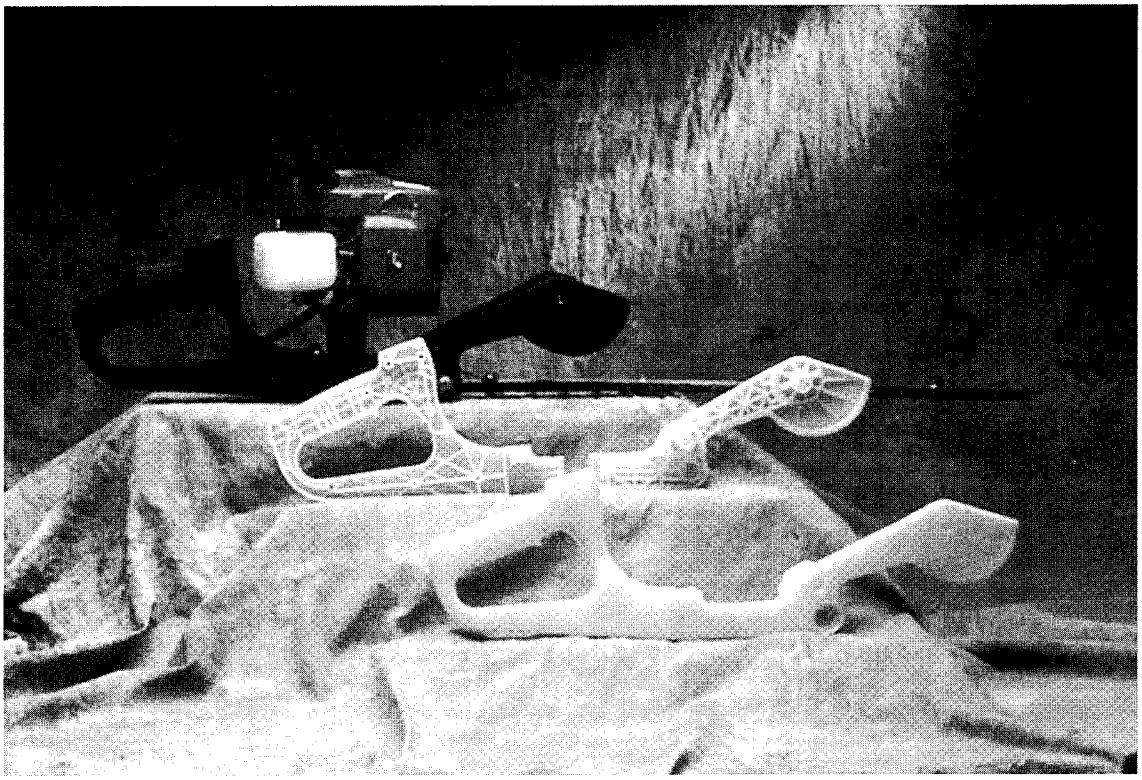

Figure 2: Nylon Part from LNF-5000

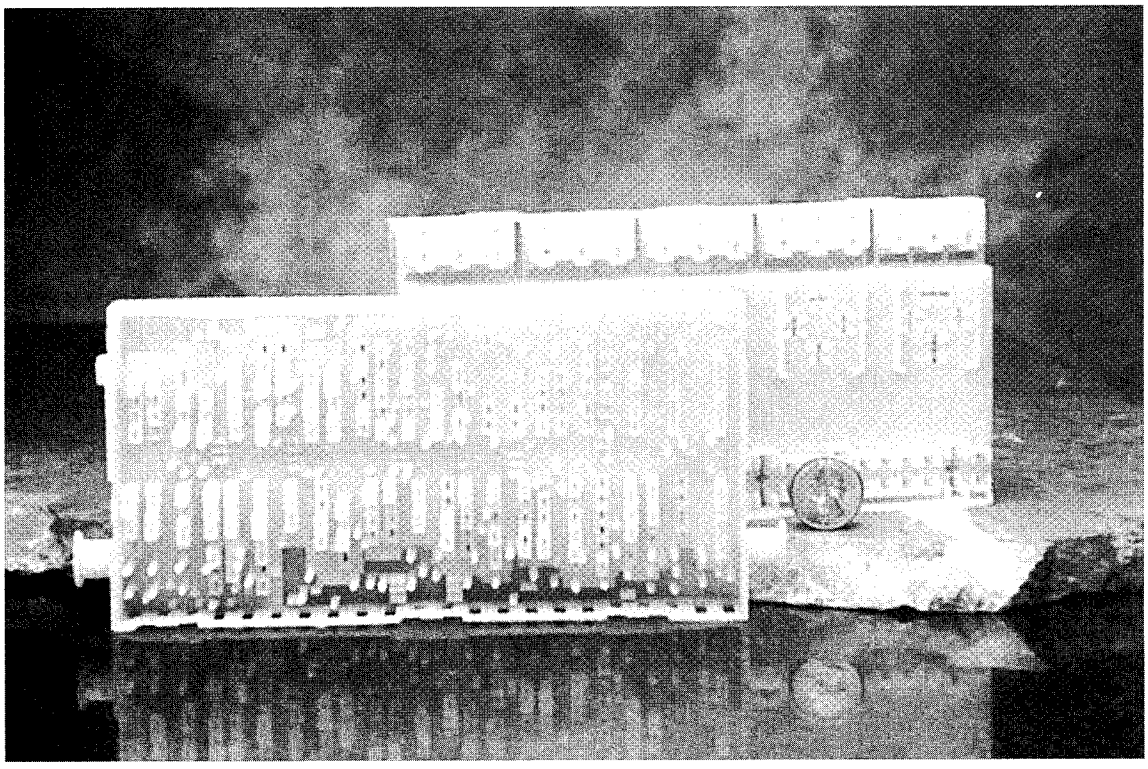

Properties of parts produced with the SLS process and by compression molding are shown in Table 1. Compression molded parts provide a valuable performance baseline since they are fully dense, but lack the orientation effects of injection molded parts.

Table 1: Mechanical Properties of Compression Molded and SLS Parts

PROPERTY	COMPRESSION MOLDED	LN 4010 SLS PARTS
TENSILE STRENGTH (PSI)	6300	5200
TENSILE MODULUS (KSI)	208	202
ELONGATION AT YIELD (%)	30	24
IMPACT STRENGTH (FT-LB/IN)	2.0	1.3
DENSITY (g/cc)	1.03-1.05	0.95-1.00

The densities of the parts produced by both methods are nearly equal, indicating that the SLS parts are substantially void free. This observation is supported by micrographs of polished cross sections of the SLS parts which show only a small number of microvoids. The mechanical properties of both materials are also nearly equal, again consistent with the absence of extensive voiding in the SLS parts. The modulus and yield strength of the SLS nylon parts are characteristic of a number of high volume injection molded materials including polypropylene and ABS. The ultimate failure strain and notched Izod values for the SLS parts are somewhat lower than the compression molded values which probably reflects the greater sensitivity of these ultimate properties to even a small number of microvoids. Nonetheless, the high strength, ductility, and toughness of SLS nylon, particularly compared to other rapid prototyping systems, allow prototypes with greatly enhanced functionality to be fabricated.

SLS Nylon Processing

The excellent mechanical properties of SLS nylon are a direct result of the fact that nearly fully dense parts are produced during processing. Not all materials can be easily processed to full density. Amorphous polymers such as polycarbonate are typically found to produce porous parts. Amorphous polymers exhibit a second order thermal transition (the "glass transition" temperature) and a gradual decrease in viscosity when heated above this temperature as is illustrated qualitatively in Figure 3a.

Figure 3: Qualitative Temperature-Viscosity Curves

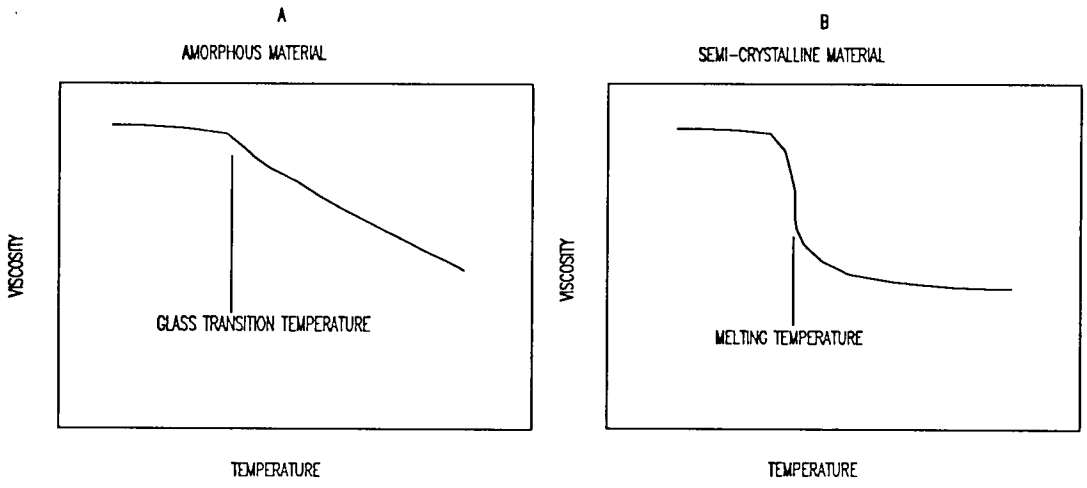

The part bed in an SLS machine can usually be maintained at a temperature near the glass transition temperature for such materials. Since the viscosity controls the kinetics of densification, amorphous polymers must generally be heated with the laser to temperatures well above the part bed temperature in order to produce densified parts. While it is possible in principle to make fully dense amorphous parts, a variety of factors associated with large energy inputs including thermal control, material degradation, and growth make this goal difficult to achieve in practice. Of course, materials with controlled porosity can be very valuable for particular applications such as casting.

Semi-crystalline materials, such as SLS nylon, behave very differently in the SLS process. These materials have both a glass transition temperature and, at a higher temperature, a first order melting point transition. In the SLS process, the part bed temperature can usually be maintained just below the onset of melting. At the melt temperature, the material is transformed from a solid to a viscous liquid over a narrow temperature range as is illustrated qualitatively in Figure 3b. Only a small quantity of energy (the heat of fusion) is required to transform the material to a state where densification can occur and, as a result, the issues associated with high energy inputs are greatly reduced and nearly fully dense parts can be produced if the melt viscosity is sufficiently low. In addition, SLS nylon resolidifies in such a way that no layerwise stress development or warp is observed as the part is constructed and, as a result, no constraint or support structures are required. Part geometry is supported only by unmelted powder.

After the part is built, it is cooled in the unmelted powder from the build temperature (approximately 190° C) to near room temperature. If the cooling rate during this portion of the process is not sufficiently slow, unbalanced stresses and warpage can develop in the parts. Recent work has focused on the thermal control mechanisms necessary to eliminate such warpage.

Control of Long-Term Cooling Rate

The part cooling rate just described above is commonly referred to as the "long term cooling rate" and has a time scale of hours. During layerwise part construction, control of heating/cooling rates and thermal gradients is also important, but the time scale for these events is seconds or minutes rather than hours. The control of long-term cooling rates in the build cylinder or "part cake" is complex. Since parts are supported only by unmelted powder, multiple "layers" of parts are typically produced during a single build as is shown schematically in Figure 4. The first parts made are built directly above the part piston and are referred to as "Layer 1" parts. Subsequent layers of parts are labeled in the order in which they are built and are insulated from the piston by the layers of parts which were previously constructed. If the metal part piston temperature is not controlled, the parts on the Layer 1 and perhaps even Layer 2 may experience a higher cooling rate and greater warpage than the better insulated parts which are subsequently built.

An additional complexity associated with cooling rate control in the part cake is that the available control options are limited. As described above, boundary value temperatures can be controlled, but the insulating properties of polymer powders are such that only parts which are built close to the boundary are affected by this mechanism. A potentially effective means to manage cooling rates in the entire part cake is to percolate gas through the porous cake, a practice referred to as "downdraft". Since radiant heat energy is supplied to the top of the part bed as a means of controlling the temperature of the surface, percolating gas down through the bed will retard cooling of the part within the bed by actively supplying heat to the part. As the gas is drawn through the top of the part bed, the gas is heated by the hot upper region of the part bed.

Control of the long term cooling rate of SLS parts is now accomplished by controlling the temperature of the part piston and by using downdraft. These thermal control mechanisms are used to produce nylon parts with less than 0.010 inch of out of plane warp in the entire nylon build volume.

Figure 4: Cross section of SLS part build area

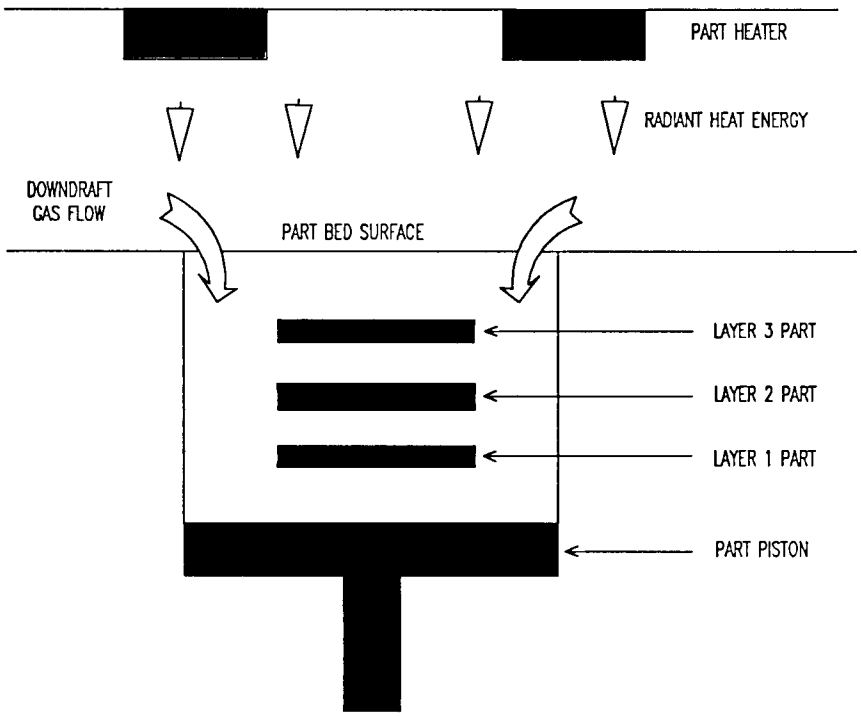

The effectiveness of using piston temperature control and downdraft to control the long term cooling rate of nylon parts was identified by using a design of experiments (DOE) approach. Experimental designs were run with the input variables being piston temperature and downdraft flowrate. Cooling rate within a build is difficult to measure, so the output of the experimental designs was part warp. A sufficiently low cooling rate was inferred when parts were produced with an acceptable degree of warp. Since a high degree of interaction was suspected and few variables were involved, full factorial designs were usually run.

An example of the results from the DOE's is shown below. Figure 5 is a boxplot showing the effect of increasing the piston temperature on Layer 1 parts. The vertical scale is part curvature diameter, in inches. Part curvature is a measure of the diameter of the circle which would pass through the bottom of the part. The higher the part curvature diameter, the less the part is warped; a perfectly flat plane has an infinite curvature diameter. The horizontal line at 200 inches corresponds to a total plane runout of less than 0.010 inch on a 3.5 inch long part. The horizontal scale is the two levels of piston temperature used in the experiment.

Figure 5: Layer 1 Part Curvature as a Function of Piston Temperature

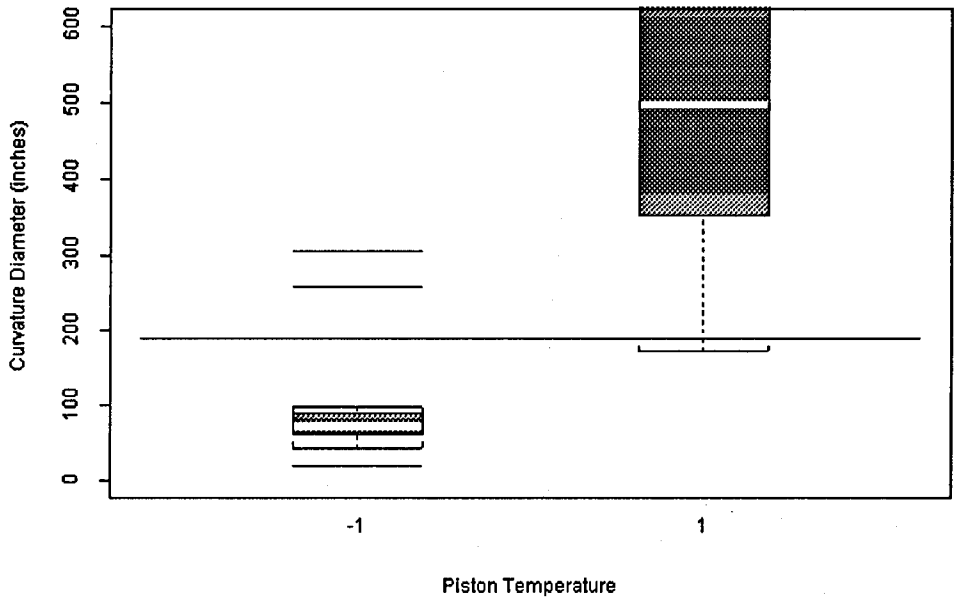

Figure 5 demonstrates the effectiveness of piston temperature control in limiting the warp of parts which are built on Layer 1. The decrease in warp is dramatic. The two piston temperature levels are uncontrolled piston temperature (approximately 55° C) and 120°C (1) Parts built without piston heat on the first layer of the build are visibly warped. When piston heat is used, part warp is greatly reduced. In the case of the test part used to generate the data shown in Figure 5, the use of piston heat reduced the amount of warp to below the target of 0.010 inch of plane runout.

Piston heat dramatically reduces warp of parts on Layer 1 where the most severe warp is generally found. Further improvements in part flatness can be achieved on Layer 1 as well as on subsequent layers when downdraft is used in conjunction with piston heat.

Data from a DOE examining downdraft and piston heat was used to construct a mathematical model showing the effect of the input variables. Tables 3 and 4 show the ANOVA model data derived from a full factorial design. The input variables are downdraft and piston heat. The levels for each are off and 23 lpm (liters per minute) for downdraft, off and 120°C for piston heat. The INTERCEPT column is the average of all part plane forms. Plane form is the measurement in inches of the degree of deviation from a theoretical flat plane. Plane form was used in this experiment set because a part curvature measurement fails when the part flatness approaches the 0.010 inch target. Plane form is a direct measurement of part warp. The aim, therefore, is to minimize the plane form value. The INTERCEPT corresponds to the intercept of a straight line passing through the data. The VALUE column is the coefficient of the half effect in inches of plane form for the particular factor. The VALUE corresponds to a line fit through the data. The P-VALUE is the probability of the observed difference in mean being due to chance as determined by an F-test among the groups. Table 3 is a model of third build layer parts; Table 4 is a model of first build layer parts.

Table 3:
First Layer Form Model (N2LO.AOV)

COEFFICIENT	VALUE	P-VALUE
INTERCEPT	0.009420125	
DOWNDRAFT	-0.001782875	0.03899505
PISTON	-0.001535375	0.07327590
DOWNDRAFT*PISTON	0.001741625	0.04347266

Table 4:
Third Layer Form Model (N2HI.AOV)

COEFFICIENT	VALUE	P-VALUE
INTERCEPT	0.00781475	
DOWNDRAFT	-0.00100075	0.0885140
PISTON	0.00019475	0.7287225
DOWNDRAFT*PISTON	-0.00015375	0.7840782

Note that the coefficients (VALUE) in Table 3 for downdraft and piston heat are negative. This demonstrates that as the input variables are increased from the low setting to the high setting, the warp of the Layer 1 parts is decreased. The P-value is the level of significance of the influence of these features (alpha). The higher the P-VALUE, the more likely the observed difference in mean between the two groups is due to chance. Table 3 shows that the piston heat and downdraft are significant and positive in their effect on part warp. The empirical model of warp for parts which are produced higher in the build is shown in Table 4. Table 4 shows that the effect of piston heat is no longer significant by the Layer 3 parts, but the downdraft does decrease warp for parts not adjacent to the piston.

Figure 6: Effect of Downdraft and Piston Heat on Layer 2 Parts

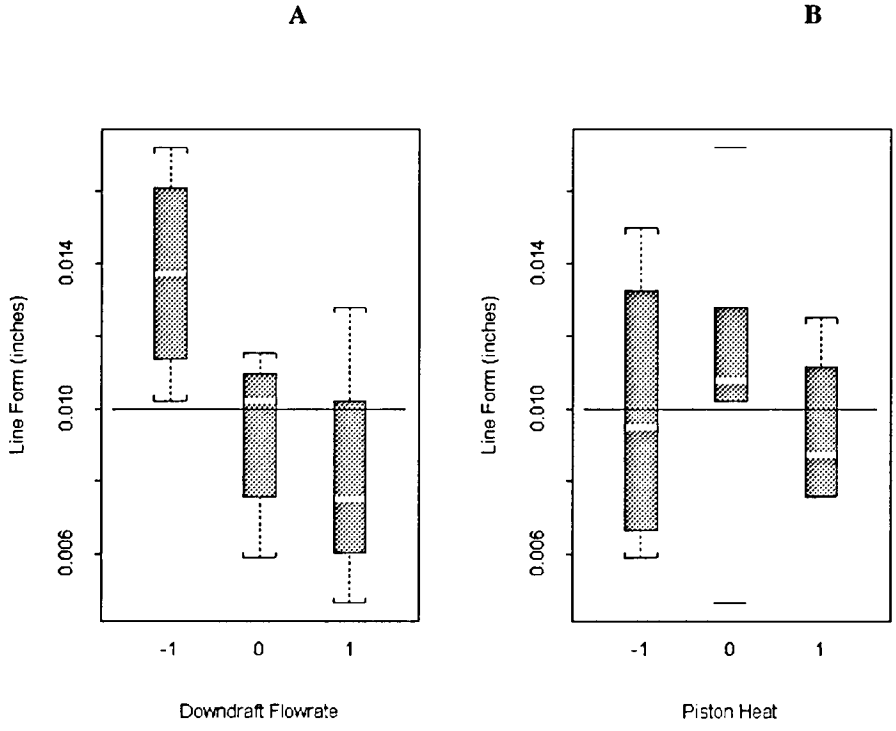

Figure 6 is a set of two boxplots of the line form taken from the open bottom edge of an enclosure part. The data used to generate Figure 6 were gathered from Layer 2 parts. Figure 6a shows a definite decrease in part warp as downdraft flowrate is increased. Figure 6b shows that the effect of piston heat at this position (Layer 2) in the build is less conclusive. At the bottom of the build, the parts which require the most stringent thermal control in order to achieve the correct cooling rate are affected directly by the piston heater. On subsequent layers, the effectiveness of the piston heat in controlling the long-term cooling rate becomes less significant due to the fact that unmelted SLS powder is an excellent insulator. For parts embedded in the part cake surrounded by this thermal insulator, percolation of heated gas is one of the few practical methods to redistribute heat in the part cake.

Summary

- The mechanical performance of prototype parts produced with LN-4010 and LNF-5000 is representative of many injection molded high-volume engineering plastics. These functional prototype parts can be produced in the Sinterstation™ 2000 System without the use of constraint or support structures.

- In order to minimize the development of unbalanced stresses and warpage in SLS nylon parts, it is necessary to limit the rate at which they are cooled from the build temperature to room temperature.

- Moderation of cooling rates in SLS nylon builds is achieved by controlling the part piston temperature and by percolating process gas through the part cake, a procedure referred to as "downdraft". The use of these mechanisms allows SLS nylon parts with less than 0.010" warp to be produced in the entire nylon build volume.

Acknowledgments

The authors would like to thank Lance Shanklin, Gerry Stewart, Phillip Conner, Richard Corden and Steve Barnick of DTM corporation for their tireless effort and support.

References

Kimble, Luke, "A Materials Comparison for Rapid Prototyping Systems", Proceedings of the 1993 SME Rapid Prototyping and Manufacturing Conference, Dearborn, Michigan, Society of Manufacturing Engineers, 1993

RAPID PROTOTYPING: A GLOBAL VIEW

R. I. Campbell and P. M. Dickens
Department of Manufacturing Engineering and Operations Management
University of Nottingham
Nottingham, UK

ABSTRACT

Rapid prototyping technology is advancing at a tremendous rate. Much of this progress is due to research being conducted within academic institutions and industry throughout the world. The USA is leading the research community in this field but a significant contribution is coming from Europe, Japan and elsewhere. The primary aim of this paper is to give a worldwide overview of current research activity and initiatives. Hopefully, this will enable researchers to see where their own work fits into the global picture. If this leads to increased co-operation and a reduction in duplication of effort, then an even faster rate of advance should be attainable.

INTRODUCTION

Rapid prototyping (RP) is one of the fastest developing manufacturing technologies in the world today. In less than ten years it has grown from a single system sold by one company to a point where over a dozen different systems are sold commercially, research is being conducted in virtually every industrialised country and hundreds, if not thousands, of academics and industrialists are actively involved in developing RP technology. This exponential rate of growth makes it virtually impossible to remain informed about research in our own country, never mind the rest of the world.

The aim of this paper is to give a brief overview of what is happening in RP research outside of North America. (The author has assumed that information on North American research is readily available to most symposium attendees.) The majority of the research work discussed in this paper has been conducted in Europe. In Japan, the other major area of activity outside the USA, research is mainly undertaken by system vendors who do not readily publish their work. It cannot be claimed that this paper is an exhaustive review of the subject but it will hopefully cover enough developments to be both informative and useful. The paper begins by looking at various areas of RP research activity, goes on to list research initiatives and finishes with some conclusions that can be drawn from this overview.

RESEARCH ACTIVITIES

Much of the research in the field of RP is the area of applications, i.e. finding new products or industries to which the technologies can be applied. However, this type of research is often at a fairly low level and is considered outside the scope of this review. The research activities reported here are those aimed at advancing RP technology rather than using existing technology for a new purpose.

RP Data Preparation and Verification

This research addresses the "upstream" aspects of the RP process, i.e. preparation and verification of the data within the CAD system and the exchange of data to the RP system. At Helsinki University of Technology in Finland, researchers are developing software to verify and, if necessary correct, STL files that have been created for RP processes[1]. This software searches for incorrectly defined facets and uses topological algorithms to redefine them. This is one method of overcoming problems in what has become the RP industry exchange standard. A RP bureau in Belgium called Materialise have decided to follow a different strategy. They have developed a suite of software modules to work with the alternative exchange formats that use contours or profiles rather than triangulations[2]. These modules can convert data from one format to another, check for errors in contours (e.g. gaps, overlaps) and automatically correct them, allow manual error correction and automatically generate supports for a contour file.

A related area of research is prediction of RP build times. When presented with an exchange file, it would be useful for the RP machine operator to know how long it will take to build the part. At the Queensland University of Technology in Australia a software program called SLICER is being developed to do precisely this for an SLA 250 machine[3]. The program works by loading an STL file, slicing this file into layers and calculating the build time for each layer. The program takes account of laser scanning speed and pattern. The predicted times are currently well below actual build times. This has been attributed to the UV laser irradiance distribution not being truly Gaussian in nature. Work is continuing with the aim of modifying SLICER to take account of this factor.

Photo Polymerisation Process Development

Many research establishments have recognised the limitations of photo polymerisation in terms of part accuracy and distortion. Projects aimed at understanding and overcoming these problems are in progress both in Europe and Japan. The Fraunhofer Institut fur Produktionstechnologie (IPT) at Aachen in Germany has been conducting experiments over the last two years aimed at determining the influence of process parameters upon stereolithography part quality[4]. They have shown that part distortion can be reduced through optimised exposure techniques (e.g. using cells) and scanning strategies (e.g. checker-board scan). A similar investigation has been conducted into the accuracy of parts produced by the solid ground curing process at the SINTEF Institute Trondeim in Norway[5].

In Japan, much of this line of research is conducted by commercial system vendors who keep their results confidential. However, projects on stereolithography part accuracy have been undertaken in Tokyo and Hokkaido Universities. In Hokkaido, many aspects have been investigated including measurement and prediction of solidified unit shape, shape deformation analysis and analysis of laser optics with regard to spatial power distribution[6].

Other interesting photo polymerisation developments include the use of stereolithography for microfabrication. The Kyushu Institute of Technology in Japan have been using an ultraviolet lamp with a spot size of 5μm and positional accuracy of 1μm. They have been able to produce components in polymer and metal (using investment casting) with feature sizes of around 50μm[7].

At Osaka Sangyo University a high power CO_2 laser with a spot size of 50 to 60μm is being used to cure an epoxy-cationic resin loaded with carbon powder[8]. Using this configuration it is possible to obtain a deep and narrow solidified unit shape. This has the potential of delivering a faster and more accurate system than those currently available.

Beam interference or biphotonic polymerisation is a development of standard photo polymerisation. Instead of a single laser beam scanning in 2d to create solidified layers, two laser light sources are directed to interfere with each other anywhere in 3d space within a vat of resin. Thus a 3d object can be built in situ without the need for incrementing a platform between layers. A joint project between the Institut Polytechnique de Sevenans and the Laboratoire Apolo in France aims to develop such a system[9]. The approach they are pursuing is to use a mercury lamp to provide a "layer" of horizontal light and a He-Ne laser to provide a focused vertical beam. The resin used will only polymerise when both light sources are present.

Laser Fusion Process Development

Much of the process development research for laser sintering is aimed at producing metal components. At IPT in Germany a 300W Nd:YAG laser has been used to sinter both high and low melting point metal powders (stainless steel and bronze nickel)[10]. They have also been working with laser generation (see below) and have been drawing comparisons between the two processes. Important differences identified are in surface roughness and internal crystalline structure. To underline the imminent arrival of a commercial metal sintering process, the German company EOS have been using their EOSINT machine to sinter a low melting point alloy powder without polymer coating or pre-heating[11].

Laser generation or laser cladding involves directing a high power laser onto the part being built and, simultaneously, feeding a cladding material in the form of powder or wire directly into the laser spot on the surface of the part. By moving the laser and feed with respect to the part it is possible to lay down tracks and create a 3d shape. IPT have been applying this technique since 1993 and have created a range of fairly simple parts. Using a 700W CO_2 laser with a cobalt-based alloy, accuracies of +/- 0.1mm and surface finishes of 50μm have been achieved[12]. Research into laser fusion is also being

conducted at Stuttgart University in Germany. The Institute for Polymer Testing and Polymer Science have developed a process called laser aided powder solidification (LAPS)[13]. There are two versions of this process, one uses a powder jet and the other a powder bed. The second version is very similar to laser sintering.

Bead Deposition Process Development

Research into use of metals for bead deposition is also in progress. At Nottingham University in England a 3d welding process is being used to create steel and aluminium parts[14]. A MIG welder has been attached to a programmable robotic arm which builds the part one layer at a time. At present, the process creates a poor surface finish but a major EU funded programme commenced in 1993 with the aim of optimising system parameters to resolve this problem.

A joint project between the Fraunhofer Institute for Applied Materials Research (IFAM), Bremen and the Fraunhofer Institute for Manufacturing Engineering and Automation (IPA), Stuttgart in Germany has developed a bead deposition process known as Multiphase Jet Solidification[15]. This process uses a heated extrusion head (70 to 220°C) which can create metal or ceramic parts. For low melting point metals such as tin-bismuth alloys, the material is deposited directly. For high melting point metals and ceramics, a mixture of powder and binder is used. This creates a "green" part which subsequently has the binder removed and is then sintered resulting in around 30% shrinkage. The advantages claimed for the system are the wide variety of possible materials and the simplicity of the apparatus.

Sheet Lamination Process Development

For this technique, once again research into the use of metals is in progress. At Dundee University in Scotland a 1000W CO_2 laser is being used to profile cut sheet steel of 1 or 2mm thickness[16]. Currently, the profiles are manually stacked and bonded using solder or adhesive. Advantages claimed for this process over other proposed metal RP systems are low cost of material and the ability to produce overhangs without supports.

RESEARCH INITIATIVES

There are a number of national, continental and global RP research initiatives that are being funded by governments and/or industry. The general aim of these is to promote collaboration between academic and industrial partners to enable advances in RP technology. Several of these initiatives are outlined below.

Australian Initiative

In 1991, the Queensland Government Department of Business Industry and Regional Development identified RP as a technology that was vital to local industry[17]. As a result, it has set up a network within six educational establishments to encourage research into RP and dissemination of knowledge to local companies. Each institution

has been provided with a CAD/CAM workstation and access to an SLA 250 machine. This facility can be used for the education of undergraduate engineers, for research projects or as a low-cost bureau service for industry. This approach has proved so successful that the network has been able to provide support to industries across the whole of Australia and beyond.

Japanese Initiative

In Japan most research is undertaken by the RP companies and government support has not been extensive. However, this year the Japanese government is expected to begin funding a four year research project concentrating on the areas of data transfer, fundamentals of resin solidification and applications of stereolithography[18]. The total funding for the project will be in the order of 800m YEN. Once again, most of the research will be conducted within industry rather than academia.

European Initiatives

A project entitled the European Action on Rapid Prototyping (EARP) has been initiated by the Danish Technological Institute using funding from the EU Brite EuRam programme. Its partners are drawn from both industrial and academic establishments researching in the field of RP. Amongst the project objectives are the provision of a forum for information exchange, the encouragement of co-operation and the identification of new areas for research and development. EARP has five work areas:-

- Creative Design and Product Development
- Model and Prototyping
- Tooling
- CAD and Software
- Medical Applications

The project commenced in early 1993 and will run for three or four years.

Several other European RP research projects are being funded through the Brite EuRam programme[19]. These include leadtime reduction, spray-forming tooling, RP for the automotive industry, RP models from medical images, RP for short-run injection moulds, development of laser sintering and RP of metal components. Each project involves a consortium of academic and industrial partners with one partner undertaking the role of co-ordinator.

Another EU funded initiative is the SPRINT programme aimed at evaluating the current Europe-wide capability for producing tooling using RP techniques. It takes the form of a survey of all RP facilities in Europe and the result will be a public report detailing the technologies that are available, the organisations using these and the feasibility of creating RP parts in the correct production material.

Nordisk Industrifond has given a grant to a consortium of companies and institutes from Norway, Sweden, Finland and Denmark for a project entitled "Layer Manufacturing as a Tool for Reduction of Product lead Time"[20]. The 2 year project has just started and will concentrate mainly on the impact that RP can have on casting technologies.

Global Initiative

The Intelligent Manufacturing Systems (IMS) programme was established with the aim of conducting international pre-competitive R&D in advanced manufacturing[21]. Six regions are participating in IMS namely Australia, Canada, European Union, European Free Trade Association, Japan and the USA. A test case on Rapid Product Development was initiated during 1993 along with five others to ascertain the feasibility of co-operation on this world-wide scale. Part of the test case was a capability assessment of commercial RP technologies using two test parts. The fact that RP was chosen as one of the key areas to be addressed by this major international programme indicates the high profile it has already gained within manufacturing industry around the world.

Rapid Prototyping Associations

Throughout the world, users of RP technology are recognising the benefits of co-operation and dissemination of knowledge. This has resulted in the formation of RP user associations. Although these associations cannot be classified as research initiatives, they do share some of the same aims. They promote collaboration between academic and industrial partners and provide a forum for sharing information on RP technology and applications. In recent years, several national RP associations have been formed. These include the Japanese Rapid Prototyping Industrial Association, The UK Rapid Prototyping and Manufacturing Association and the Association Francais de Prototypage Rapide. There are also plans to establish an Australian Rapid Product Development Consortium[22] to help co-ordinate RP research activities in that country.

CONCLUSIONS

The activities reviewed in this paper show that researchers outside of North America are making a significant contribution to the advance of RP technology. Centres of excellence are emerging such as the Fraunhofer institutes in Germany. A major theme of research in Europe is the development of RP systems for metal components. In Japan, most work is directed at improving the photo polymerisation technique. The use of lasers figures highly in much of the research, with high power lasers playing an increasingly important role. Governments are recognising the strategic implications of RP technology and are supporting research through various initiatives. This is especially true in Europe where a number of different funding programmes have been established. Finally, world-wide co-operation on RP research has only just begun with the IMS Rapid Product Development test case. The opportunities for developing symbiotic links are there and must be taken if RP technology is to advance at its maximum potential rate.

ACKNOWLEDGEMENT

Financial support of this presentation in the form of a Thomas Andrew Common Grant from the Institution of Mechanical Engineers is gratefully acknowledged.

REFERENCES

1. Dolenc, A. "Design Consideration and Preparing Data for RPT", *EARP Newsletter*, Danish Technological Institute, Denmark, March 1993, p3.
2. Vancraen, W. et al "Contour Interfacing in Rapid Prototyping - Tools that Make it Work", *Proceedings of the 3rd European Conference on Rapid Prototyping and Manufacturing*, University of Nottingham, UK, July 1994, pp25-33.
3. Yu, G.B. and Noble, D. "The Development of a Laser Build-time Calculation Program using Stereolithographic Apparatus (SLA)", *Proceedings of the 3rd European Conference on Rapid Prototyping and Manufacturing*, University of Nottingham, UK, July 1994, pp353-367.
4. Konig, W. et al "Stereolithography Process Technology", *Proceedings of the 3rd European Conference on Rapid Prototyping and Manufacturing*, University of Nottingham, UK, July 1994, pp191-208.
5. Kochan, D. and Hovtun, R. "Precise and Optimised Process Realization for Solid Ground Curing", *Proceedings of the 5th International Conference on Rapid Prototyping*, University of Dayton, Ohio, June 1994, pp77-89.
6. "Precision Machining 1 Laboratory Annual Activity", Dept of Precision Engineering, Hokkaido University, Japan, September 1993.
7. Ikuta, K. et al "Ultra High Resolution Stereo Lithography for Three Dimensional Micro Fabrication", *Proceedings of the 5th International Conference on Rapid Prototyping*, University of Dayton, Ohio, June 1994, pp37-46.
8. Dickens, P.M. "Rapid Prototyping Research - Summary of Visit to Japan", Internal Report, Dept of Manufacturing Engineering and Operations Research, University of Nottingham, UK, September 1993.
9. Clair, J.J. and Lougnot, D.J. "Biphotonic Process for Stereolithography - Which Resins and Which Optics", *Proceedings of the 2nd European Conference on Rapid Prototyping and Manufacturing*, University of Nottingham, UK, July 1993, pp363-367.
10. Konig, W. et al "Rapid Prototyping of Metallic Parts", *Proceedings of the 3rd European Conference on Rapid Prototyping and Manufacturing*, University of Nottingham, UK, July 1994, pp245-256.
11. Shellabear, M. "Optimizing Materials and Process Parameters for Different Rapid Prototyping Applications", *Proceedings of the 3rd European Conference on Rapid Prototyping and Manufacturing*, University of Nottingham, UK, July 1994, pp369-379.
12. Konig, W. et al "Approaches to Prototyping of Metallic parts", *Proceedings of the 2nd European Conference on Rapid Prototyping and Manufacturing*, University of Nottingham, UK, July 1993, pp303-316.
13. Luck, T. et al "Material Research and Development for Rapid Prototyping Techniques at the IKP", *Proceedings of the 3rd European Conference on Rapid Prototyping and Manufacturing*, University of Nottingham, UK, July 1994,

pp309-325.
14. Dickens, P.M. et al "3D Welding", *Proceedings of the 1st European Conference on Rapid Prototyping*, University of Nottingham, UK, July 1992, pp81-93.
15. Greul, M. et al "Multiphase Jet Solidification (MJS) A New Rapid Prototyping Process for Metal and Ceramic Parts", *Proceedings of the 3rd European Conference on Rapid Prototyping and Manufacturing*, University of Nottingham, UK, July 1994, pp257-260.
16. Thomson, G.A. and Pridham, M.S. "The Use of a High Powered Laser Machining Centre in the Production of Metal Prototypes", *Proceedings of the 3rd European Conference on Rapid Prototyping and Manufacturing*, University of Nottingham, UK, July 1994, pp341-352.
17. Riek, A.T. and Roth, R.N. "Government/University Initiatives for Rapid Prototyping in Queensland, Australia", *Proceedings of the 2nd European Conference on Rapid Prototyping and Manufacturing*, University of Nottingham, UK, July 1993, pp317-323.
18. Dickens, P.M. "Rapid Prototyping Research - Summary of Visit to Japan", Internal Report, Dept of Manufacturing Engineering and Operations Research, University of Nottingham, UK, September 1993.
19. Troldhus, E. "Running EC Projects on Rapid Prototyping", *EARP Newsletter*, Danish Technological Institute, Denmark, March 1993, p5.
20. Moos, N. "New Internordic Project", *EARP Newsletter*, Danish Technological Institute, Denmark, January 1993, p12.
21. Aubin, R.F. "A World Wide Assessment of Rapid Prototyping Technologies", United Technologies Research Center Report No. 94-13, January 1994.
22. Loose, S. Private Communication, Queensland Manufacturing Institute, Australia, May 1994.

Richard F. Aubin
United Technologies Research Center
411 Silver Lane MS 129-48
East Hartford, CT 06108
Phone: 203-727-1697
Fax: 203-727-7880

A World Wide Assessment of Rapid Prototyping Technologies

January 1994

Table of Contents

Objectives: 1
Background of Intelligent Manufacturing Systems: 3
Assessment of Rapid Prototyping Technologies: 3
Participating companies in this assessment 4
System and Maintenance Costs 4
Training Duration and Costs 7
System Capacities and Limitations to Feature Sizes 8
Accuracy Issues 8
Specific Part Building Issues for Processing the IMS Test Parts: 10
Pre-Processing Times 10
Part Building Times 11
Post Processing Times 12
Total Time to Fabricate the IMS Test Parts 13
Materials for Rapid Prototyping Systems: 14
University-led Rapid Prototyping Developments: 15
Discussion: 16
Conclusions: 18
Acknowledgment: 20
Appendix A - Photographs of IMS Test Parts 21

This paper describes the results of a worldwide assessment of commercial rapid prototyping technologies that was initiated in the Intelligent Manufacturing Systems IMS Test Case on Rapid Product Development. Additionally, this paper will highlight the development of university-led rapid prototyping technologies.

Objectives:

The objectives of this assessment are:

- Characterize and differentiate the commercially available rapid prototyping technologies by identifying their economic factors and technical capabilities
- Benchmark the pre-processing, building and post processing time to fabricate a common part
- Provide a document on commercially available technologies for potential purchasers to use to compare and contrast the many systems and models available and,
- Provide a brief overview of university-led rapid prototyping research and development.

NOTE: The information contained in this assessment is dated to the Winter of '93-'94. The Rapid Prototyping industry has proven to be dynamic and in continuous improvement.

Table 1 is a listing of commercial organizations that were solicited for participation in this worldwide assessment.

Company	Location	Process
3D Systems	Valencia, CA U.S.	SLA
BPM Technology	Greenville, SC U.S.	Ballistic Particle Manufacturing - Jetting
C-MET	Tokyo, Japan	Solid Object Ultraviolet Plotter SOUP
C-MET	Stuttgart, Germany	Solid Object Ultraviolet Plotter SOUP
Cubital	Raanana, Israel	Solider - Masked Printing
D-MEC	Tokyo, Japan	Solid Creation System
DTM Corp.	Austin, TX U.S.	Selective Laser Sintering
EOS	Planegg, Germany	Electro Optical Systems
EOS	Stuttgart, Germany	Electro Optical Systems
E-Systems	Falls Church, VA U.S.	Jetting Technology
Helisys	Torrance, CA U.S.	Laminated Object Manufacturing
Laser 3D	Nancy, France	Stereophotolithography
Light Sculpting	Milwaukee, WI U.S.	Masked Printing
Mitsui Engr&Ship	Tokyo, Japan	Colamm
Soligen	Northridge, CA U.S.	Direct Shell Production Casting
Sparx AB	Molndal, Sweden	Hot Sparx
Stratasys	Eden Prairie, MN U.S.	Fused Deposition Modeling
Teijin Seiki	Kawasaki, Japan	Soliform
Texas Instruments	Plano, TX U.S.	Protojet - Jetting Technology
Visual Impact	Windham, NH U.S.	Jetting Technology

Table 1. -- Listing of commercial organizations solicited for participation in this assessment.

In order to meet the needs of this assessment, two common test parts were created to provide a variety of geometrical features. Each part measures 6-inches long by 4-inches wide. See figure 1.

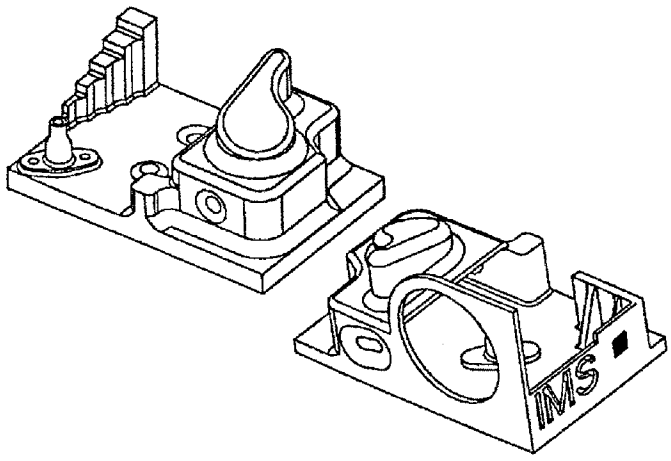

Figure 1 -- Isometric views of the test parts.

Background of Intelligent Manufacturing Systems:

The following background information was sent to the companies in Table 1to provide a basis for their decision to participate.

The principal objective of the IMS program is to conduct international pre-competitive R&D in advanced manufacturing. In 1993, the feasibility of such collaboration was tested by conducting six test cases on selected topics in advanced manufacturing. The organization of the IMS feasibility study has been put in place by an International Steering Committee, Technical Committee, and Intellectual Property Rights Committee, all composed of representatives from the six regions of IMS: Australia, Canada, European Community, European Free Trade Association, Japan and the United States.

Our test case on Rapid Product Development is focused on rapid prototyping, measurement and conversion technologies, the business practices associated with reduced product development cycle time, and multi-media communications. This work was conducted by 22 partners from four regions: Australia, Canada, European Community, and the United States. This project is being led by the following Coordinating Partners: Australia - Swinburne University of Technology, and the Queensland Manufacturing Institute; Canada - Pratt & Whitney Canada and Ecole de Technologie Superieure; European Community - Daimler Benz; and the United States - United Technologies Corporation.

Assessment of Rapid Prototyping Technologies:

We asked the rapid prototyping companies to fabricate four (4) copies of the test part with the IMS-T2 STL (see figure 1), file that was provided to them on 3-1/2" floppy disk. We also provided a fully dimensioned engineering drawing of the test part. In our evaluation, we conducted a dimensional inspection of the parts which they produced and shared the inspection results of their parts with them. However, the inspection results are to be held as proprietary information to the Coordinating Partners of the IMS test case listed above. The inspection results will not be publicized, nor will they be shared with other IMS test case participants. Additionally, we asked that the rapid prototyping companies complete the questionnaire forms and to provide a signature of a company officer in the validation section. The parts and the Rapid Prototyping Technologies Questionnaires were displayed at the IMS International Conference in Stuttgart, Germany on 31 January to 2 February 1994.

We provided the following conditions to maintain consistency among the companies in fabricating the test parts:

1. The 4 parts are to be fabricated directly from the STL files provided - no machining or manual polishing beyond removal of supports, bases, etc.
2. If the companies are required to *calibrate* their rapid prototyping process for the parts by making some iterative trial runs, we asked that they limit them to deliver the best 4 of 6 trials; however, we asked that they identify if and how many trial runs were required.
3. If their processes have "offset" capabilities to compensate for inaccuracies such as material shrinkage, laser beam-width compensation, etc., then we asked that they identify the parameters and numerical amounts (in all directions) used to produce the parts. We also asked that they identify the thickness of each layer.

4. We suggested that if they were unable to fabricate the parts, to please consider completing the questionnaire.

Participating companies in this assessment

Table 2 shows a listing of the responses from the solicited companies with a brief comment if they did not provide full participation.

Company	Location	YES	NO	Comments
3D Systems Inc.	Valencia, CA U.S.			1 test part provided
Helisys Inc.	Torrance, CA U.S.			2 test parts provided
Soligen Inc.	Northridge, CA U.S.			2 molds made at P&W
Stratasys Inc.	Eden Prairie, MN U.S.			
Cubital Ltd.	Raanana, Israel			
Laser 3D	Nancy, France			Questionnaire only
EOS GmbH	Planegg, Germany			Parts paid for by DB
C-MET	Sindelfingen, Germany			By Mercedes-Benz
D-MEC Ltd.	Tokyo, Japan			
Teijin Seiki Co.	Kawasaki-City, Japan			
BPM Corp.	Greenville, SC U.S.			
C-MET	Tokyo, Japan			
DTM Corp.	Austin, TX U.S.			
E-Systems	Falls Church, VA U.S.			
Light Sculpting Inc.	Milwaukee, WI U.S.			
Mitsui Engi&Ship Building	Tokyo, Japan			
Sparx AB	Molndal, Sweden			
Texas Instruments	Plano, TX U.S.			
Visual Impact Corp.	Windham, NH U.S.			

Table 2. -- List of responses from the commercial organizations solicited for participation in this assessment.

System and Maintenance Costs

The major economic factor associated with rapid prototyping is the cost of purchasing and maintaining the equipment. Currently, these rapid prototyping systems range in cost from $75,000 for a Stratasys FDM-1500, to $750,000 for a D-MEC JSC-3000. Table 3 shows a listing of available systems from the participating rapid prototyping companies including their system prices, annual maintenance fees, and training costs.

A series of charts are provided to compare the variety of issues related to these systems. The charts are annotated to assist in identifying the systems. Figure 2 shows a bar chart of the purchasing costs, and figure 3 shows the maintenance fees. Note that most of the companies offer a variety of options. For example, six machine options are available from 3D Systems, 3 from EOS and D-MEC, and 2 from Helisys, Stratasys, Cubital and Teijin Seiki. It should be noted that both Soligen and Laser 3D do not market their devices for purchase, but offer a licensing arrangement. Soligen provides their license in the U.S for $350,000 and for $450,000 in other world regions. Instead of a maintenance fee, they provide for a usage fee

Table 3

Company Name	Systems Available	Price USD	Annual Maintenance	* Notes	Training Days	Training Fees	Warranty Months
3D Systems Inc.	SLA-190/20	135k	5-10k	1	5	Included	12
	SLA-250/30	215k	5-18k		5		12
	SLA-250/40	250k	5-18k		5		12
	SLA-400	425k	5-30k		5		12
	SLA-500/20	495k	5-40k		5		12
	SLA-500/30	540k	5-40k		5		12
Helisys Inc.	LOM-1015	130k	12k	6	5	2.5k	12
	LOM-2030	230k	18k		5		12
Soligen Inc.	DSPC-1	350k	Usage fee	7	12	Included	Unlimited
Stratasys Inc.	FDM 1500	75k	5k	8	5	Included	3
	3D Modeler	198.3k	7k		10		3
Cubital Ltd.	Solider 4600	325k	67k	3	MPM -10	Included	6
	Solider 5600	550k	67k		DFE - 3		6
Laser 3D	SPL 1000/LSA	50k	0	9	5	0	
EOS GmbH	STEROS 300	290k	25k	5	5	Included	12
	STEROS 400	380k	30k		5		12
	STEROS 600	500k	40k		5		12
C-MET	SOUP-600	600k	80k	2	5	4.4k	12
D-MEC Ltd.	SCS-1000HD	500k	15k	4	6	12k	12
	JSC-2000	500k	15k		6	12k	12
	JSC-3000	750k	15k		6	12k	12
Teijin Seiki Co.	Soliform-300	350k	90k	5	3	Included	12
	Soliform-500	500k	90k		3		12

Table 3. Listing of available systems including their costs for annual maintenance and training, and warranty period.
Notes: 1)Variable depending upon coverage level, hotline support, user group meetings, application consulting, modem troubleshooting, 24 hour response time & S/W updates; 2) Incl. Laser, H/W & S/W Support; 3) S/W upgrades, repairs; 4) Laser not incl.; 5) Laser not incl.; 6) Incl. Laser; 7) $40/cm - $12/cm per verticle cm built; 8) H/W maintenance only as an optional purchase; 9) System price includes terminal unit S/W only, annual rental includes laser maintenance, operator and resin.

per vertical cm of shell built on a sliding scale from $40/cm to $12/cm. Laser 3D only provides a terminal unit and software and, for additional fees, builds the actual parts at their facility in Nancy, France.

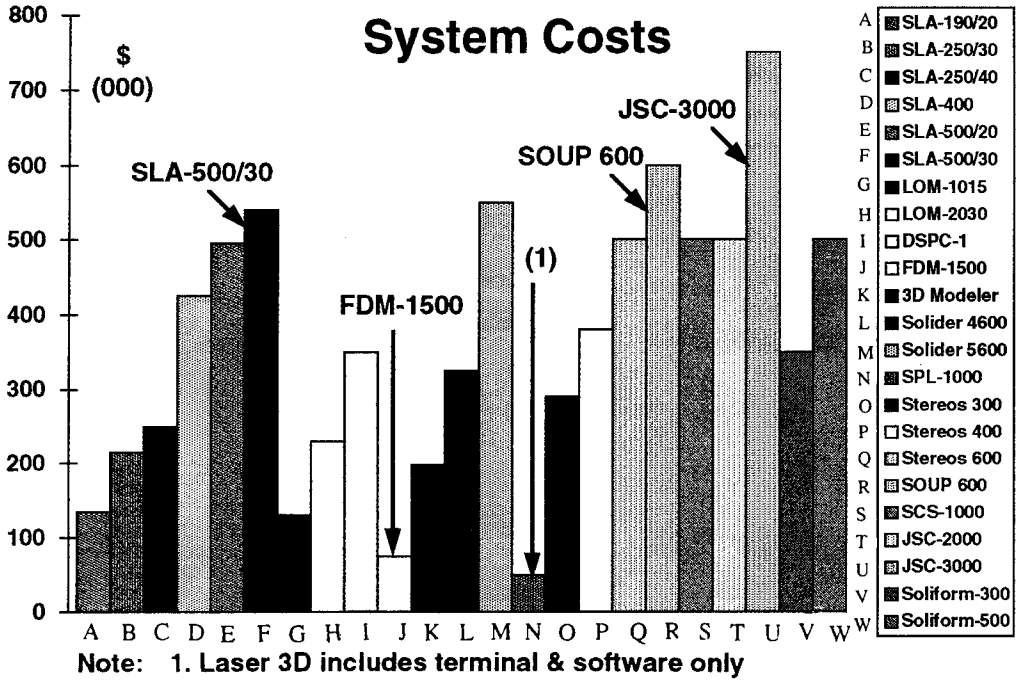

Figure 2 -- System costs are provided in thousands of U.S. dollars.

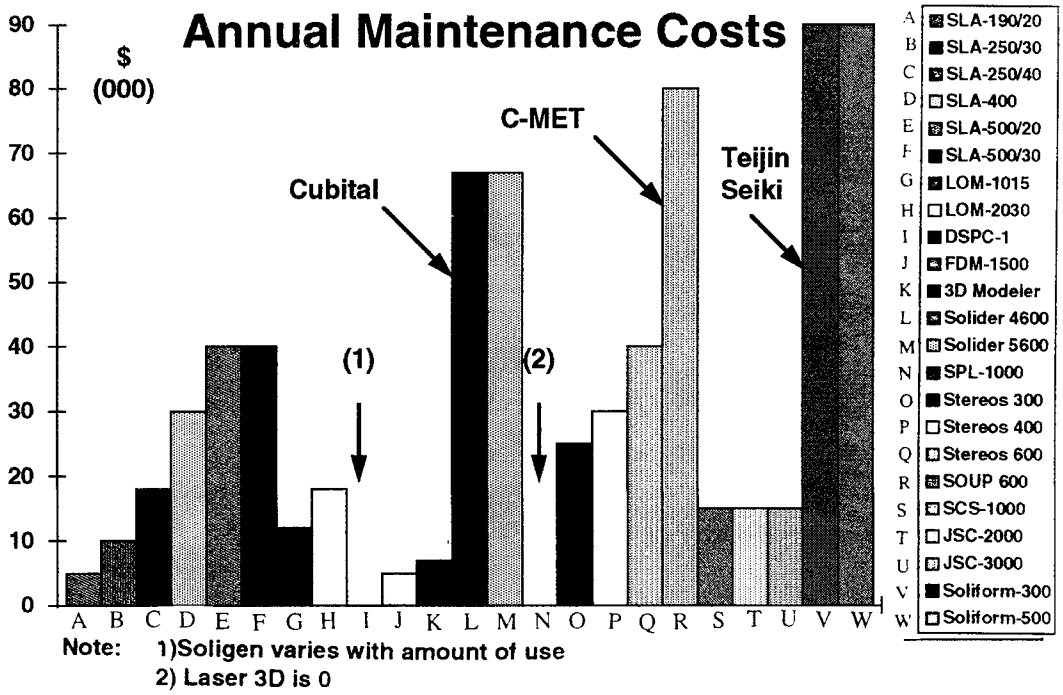

Figure 3. -- Annual maintenance costs.

Training Duration and Costs

Some of these rapid prototyping systems have varying degrees of complexity that impact the time required to understand and efficiently operate the systems. Figure 4 shows the training time required to operate the systems. While a majority of the companies provide training at no additional cost, figure 5 shows which companies require additional fees.

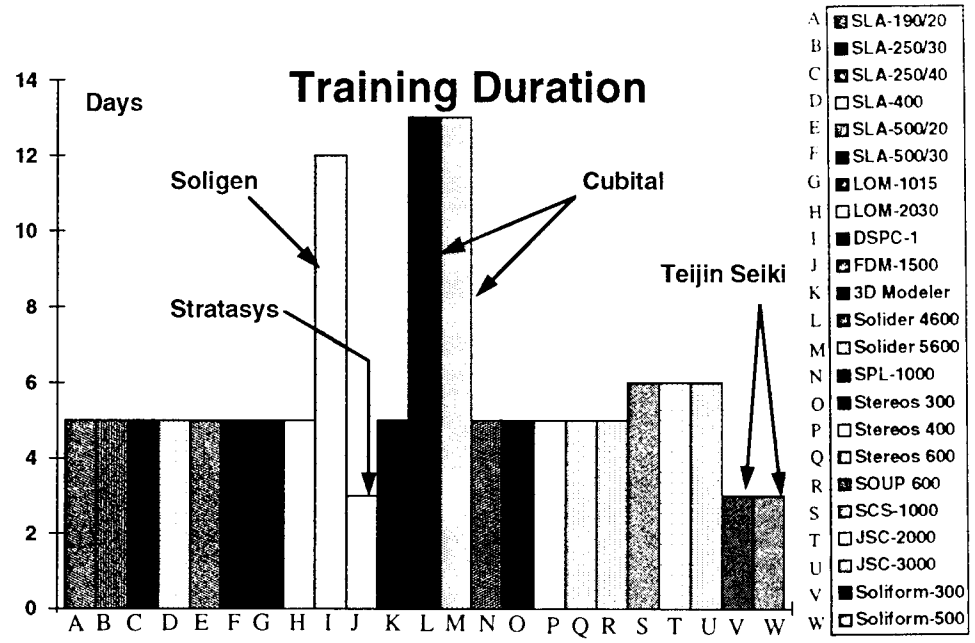

Figure 4. -- Time required for training in days.

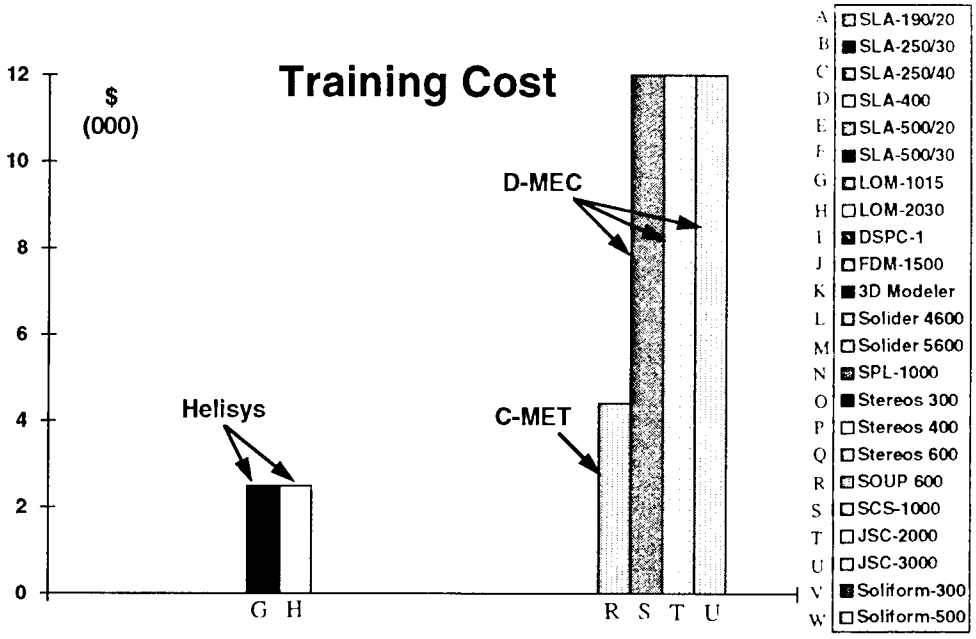

Figure 5. -- Companies requiring additional fees for training.

System Capacities and Limitations to Feature Sizes

The decision to purchase a particular model of a rapid prototyping system is often based on the size of parts it is capable of fabricating. Other factors that impact this decision are the capabilities to produce small internal feature sizes such as slots and holes, and fins or ribs for external features. Table 4 shows the various capacities and limitations to feature sizes for the different rapid prototyping machines. Figure 6 shows a chart of the maximum part building capacity in cubic centimeters.

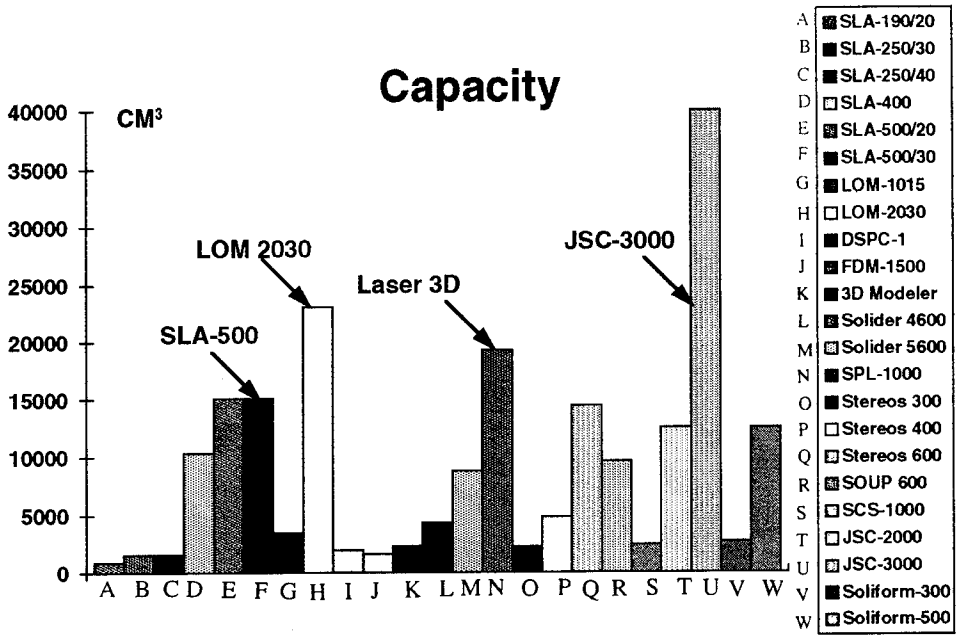

Figure 6. -- Maximum part building capacity.

Accuracy Issues

Accuracy is another key factor in deciding which rapid prototyping system to purchase. Experience has shown that the accuracy attainable in a particular part is often a function of its geometry. As can be expected, relatively small prismatic parts can be fabricated to a higher degree of accuracy than relatively large flimsy parts. The information on accuracy capabilities of the various rapid prototyping systems and models was provided by the manufacturers of the rapid prototyping equipment.

In the charts that follow on accuracy, keep in mind that the questionnaire requested "realistic accuracy expectations" on parts. The questionnaire listed a series of cubes ranging in sizes from small .5-inch, (1.27 cm) to large, 40-inches, (1m). Please note that the accuracies listed are "*claimed*" accuracies and are not related to the IMS test parts. Also note that the accuracy values are depicted in mm.

Figure 7 shows the accuracy expected to be achievable for a .5-inch (1.27 cm) cube part. Figure 8 shows the accuracy expected to be achievable for a 10-inch (25.4 cm) cube part. Note that some companies did not provide accuracy values.

Table 4

Company Name	Systems Available	Maximum Capacity mm	Minimum Ext.Feature Size mm	Minimum Int.Feature Size mm	Layer Thks Min/Max mm	System Resolution mm
3D Systems Inc.	SLA-190/20 SLA-250/30 SLA-250/40 SLA-400 SLA-500/20 SLA-500/30	1250/190/190 250/250/250 250/250/250 508/508/400 584/508/508 584/508/508	XY=.3-.4 Z. 1	XY=.05 Z .1	.1 -.9	XY=.007 Z .005
Helisys Inc.	LOM-1015 LOM-2030	254/381/355 559/813/508	.38	.25	..025 - 1.016	.0254
Soligen Inc.	DSPC-1	305/254/254	.38	.38	.177	.127
Stratasys Inc.	FDM 1500 3D Modeler	254/254/254 228/304/330	.254	.254	.05 - .76	.0254
Cubital Ltd.	Solider 4600 Solider 5600	350/350/350 500/350/500	XY=.6 Z.1	XY=.4 Z.1	.15 .1-.2	XYZ .1
Laser 3D	SPL 1000/LSA	500/550/700	--	--	.015 - .075	--
EOS GmbH	STEROS 300 STEROS 400 STEROS 600	300/300/250 400/400/300 600/600/400	.2x.25x.3 .2x.25x.3 .1x.1x.1	.1x.1x.1	..05 - .5	.01
C-MET	SOUP-600	600/400/400	XY=.2 Z.05	XY=.1 Z.6	.05-.3	XYZ .005
D-MEC Ltd.	SCS-1000HD JSC-2000 JSC-3000	300/300/270 500/500/500 1000/800/500	.1 .2 .3	.1 .2 .3	.03-.4	XY=.1 Z.01
Teijin Seiki Co.	Soliform-300 Soliform-500	300/300/300 500/500/500	.15	.3	.1 - .5	.254

Table 4 -- Listing of systems and their associated capacities for size and limits on feature size, etc.

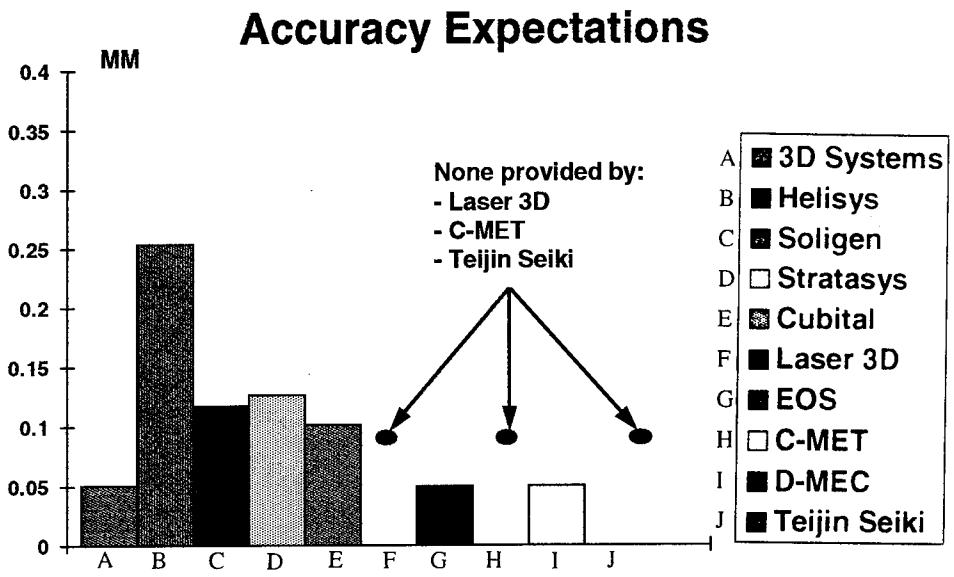

Figure 7. -- Accuracy expectations for a theoretical part measuring .500 inch cube or 12.7 mm cube.

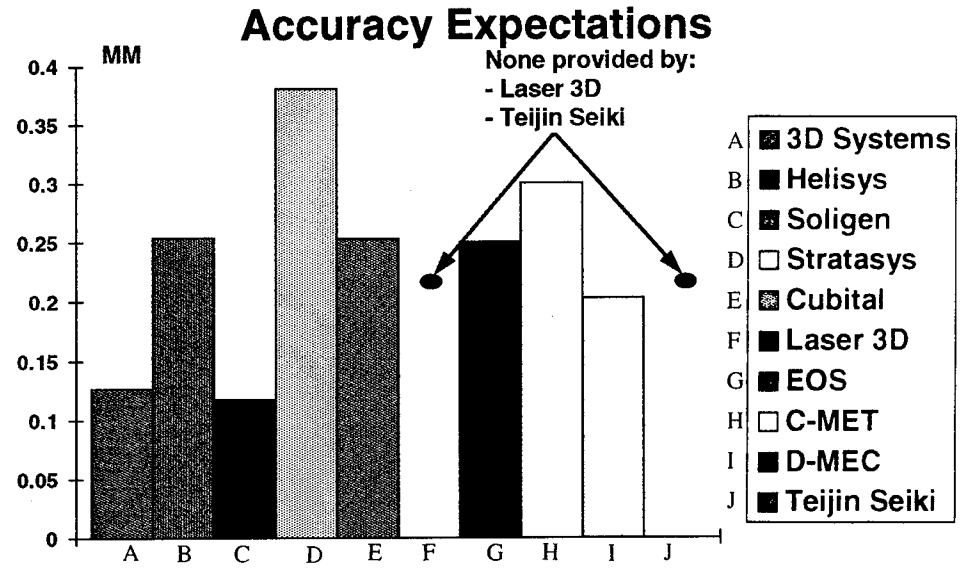

Figure 8. -- Accuracy expectations for a theoretical part measuring 10 inch cube or 254 mm cube.

Specific Part Building Issues for Processing the IMS Test Parts:

Pre-Processing Times

There are typically three phases to processing rapid prototype parts: 1) pre-processing, 2) building, and 3) post processing. During the pre-processing phase, the computer model, usually

rendered in a 3-dimensional tessellated or faceted file format called a "STL file" from the originating CAD system, is read into the rapid prototyping device and reduced to very thin 2-dimensional sliced layers. These sliced layers are then used during the next "build" phase.

The following charts identify the "*actual*" pre-processing, building and post processing times required to fabricate the IMS-T2 test part. The time listed is in hours and the numbers on top of the columns indicate the number of parts processed in the given time. Figure 9 shows the actual pre-processing time. Note that all of the participating companies processed the IMS-T2 test part with the exception of Soligen. Pratt & Whitney processed a ceramic shell (mold) of the IMS-T1 test part at 1/2 scale on their Soligen "alpha" machine for Soligen. Also note that the C-MET time is long because of problems experienced at Mercedes Benz in processing the STL files.

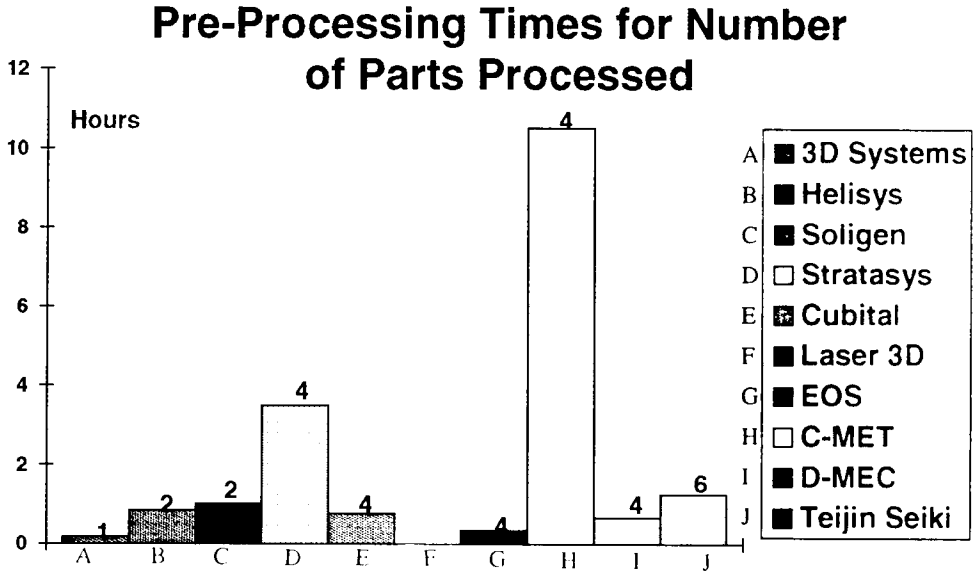

Figure 9. -- Actual pre-processing time for the IMS-T2 test part with the numbers of parts processed indicated on the columns.

Part Building Times

Building time is the time required to physically fabricate the part in the rapid prototyping system from the sliced data generated by pre-processing. In should be noted that in addition to building the part, additional structures such as supports may be required to support cantilevered features or "islands," which are later removed in the post processing phase.

Most of the systems including: 3D Systems (Stereolithography SLA), Laser 3D Stereophoto-lithography); Electro Optical Systems (EOS); C-MET (Solid Object Ultraviolet Plotter - SOUP); D-MEC (Solid Creation System, SCS); and Teijin Seiki (Soliform), produce parts using the computer controlled light from a laser to "draw" the outline of each sliced layer onto a vat of liquid photopolymer, thus causing a chemical reaction in the liquid photopolymer resin to change it to a solid wherever touched by the light, thus producing parts in photopolymer plastics.

The Cubital process also uses photopolymer plastic, but uses an ultraviolet flood lamp as the light source and a computer generated mask to localize the light where it's required. The Cubital process also includes a machining step to mill each layer flat, and uses a layer of wax as a support material for each layer, thus eliminating the need for additional support structures.

Helisys uses the heat from a laser to cut layers of paper in their Laminated Object Manufacturing (LOM) process, thus producing paper parts that look like wooden parts. Because each layer is fully supported, no additional support structures are required.

Soligen incorporates a jetting technology to "print" a liquid binder on a ceramic powder bed in successive layers to produce ceramic shells or molds for the investment casting of metal parts. The Soligen process is called Direct Shell Production Casting (DSPC).

Stratasys uses a heated nozzle to extrude a thermoplastic material in a layer by layer succession. This process lends itself to the use of a variety of materials, but also requires additional supports.

Figure 10 shows the actual building times required to fabricate the IMS-T2 test parts. Note that the wide variation can be due to the number of parts fabricated.

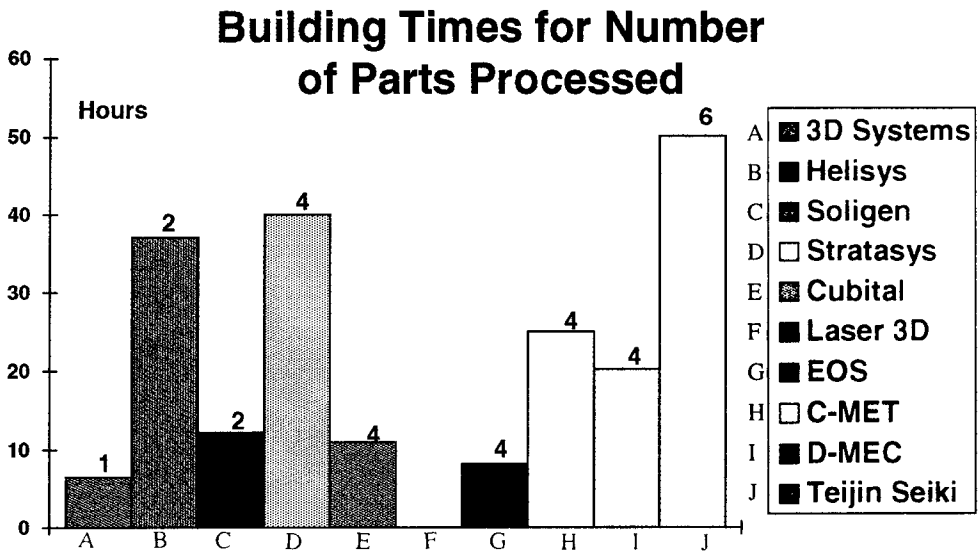

Figure 10. -- Actual building time for the IMS-T2 test part with the numbers of parts processed indicated on the columns.

Post Processing Times

The parts are removed from the rapid prototyping device and processed further during this phase. Typically, this includes the removal of supports that were required during the building of the parts, and can also include further curing, cleaning and perhaps hand finishing and polishing. Figure 11 shows the required post processing time to further cure and/or clean the parts after fabrication. As shown in figure 11, Cubital required more time then the others because of the need to wash away the suporting wax that is used in their process.

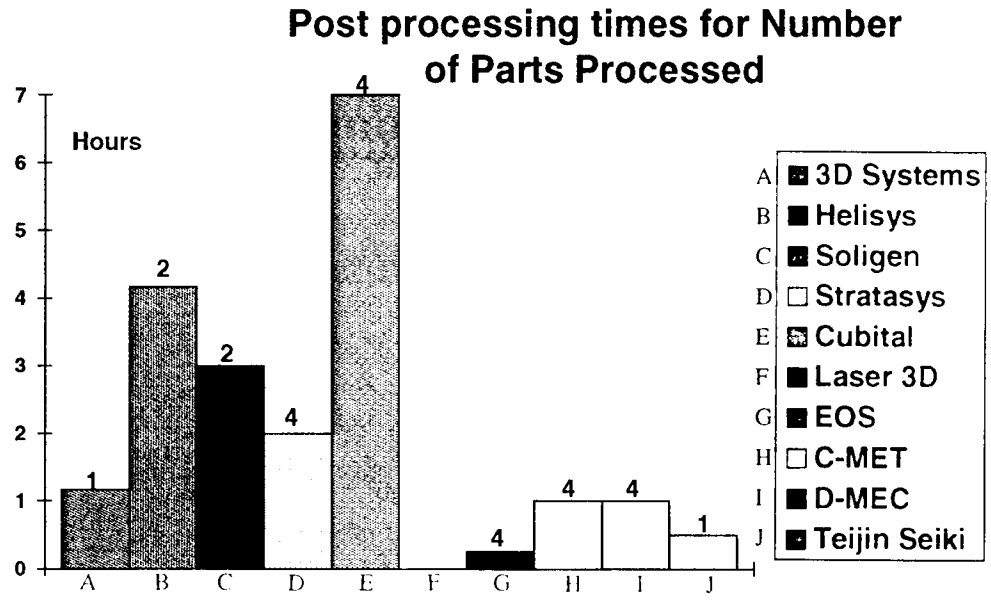

Figure 11. -- Actual post processing time for the IMS-T2 test part with the numbers of parts processed indicated on the columns.

Total Time to Fabricate the IMS Test Parts

Figure 12 shows the actual total time required to fabricate the test parts.

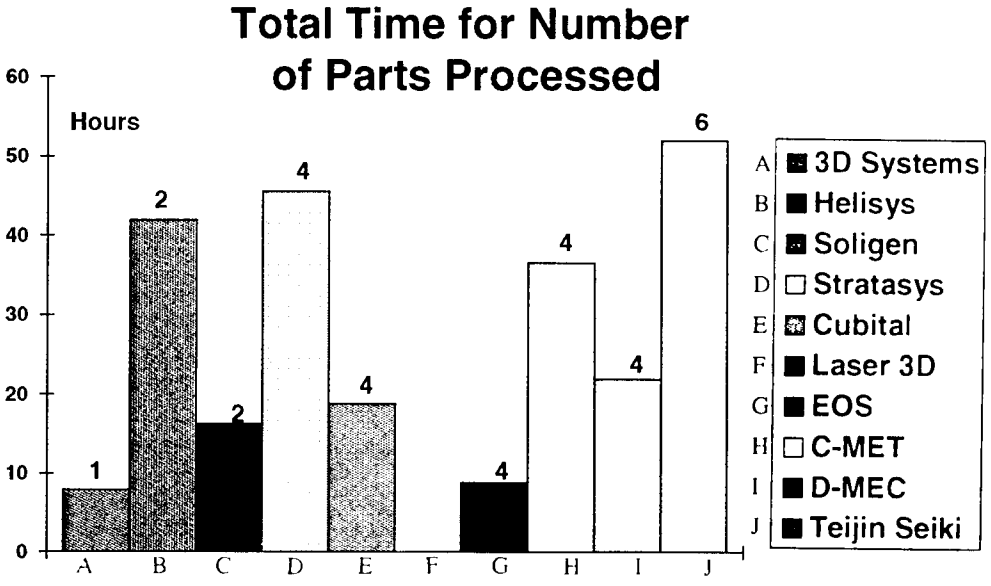

Figure 12. -- Actual total time for the IMS-T2 test part with the numbers of parts processed indicated on the columns.

As highlighted in figure 13, which captures all of the times required for the fabrication of the IMS-T2 test parts, the majority of time is required during the building phase.

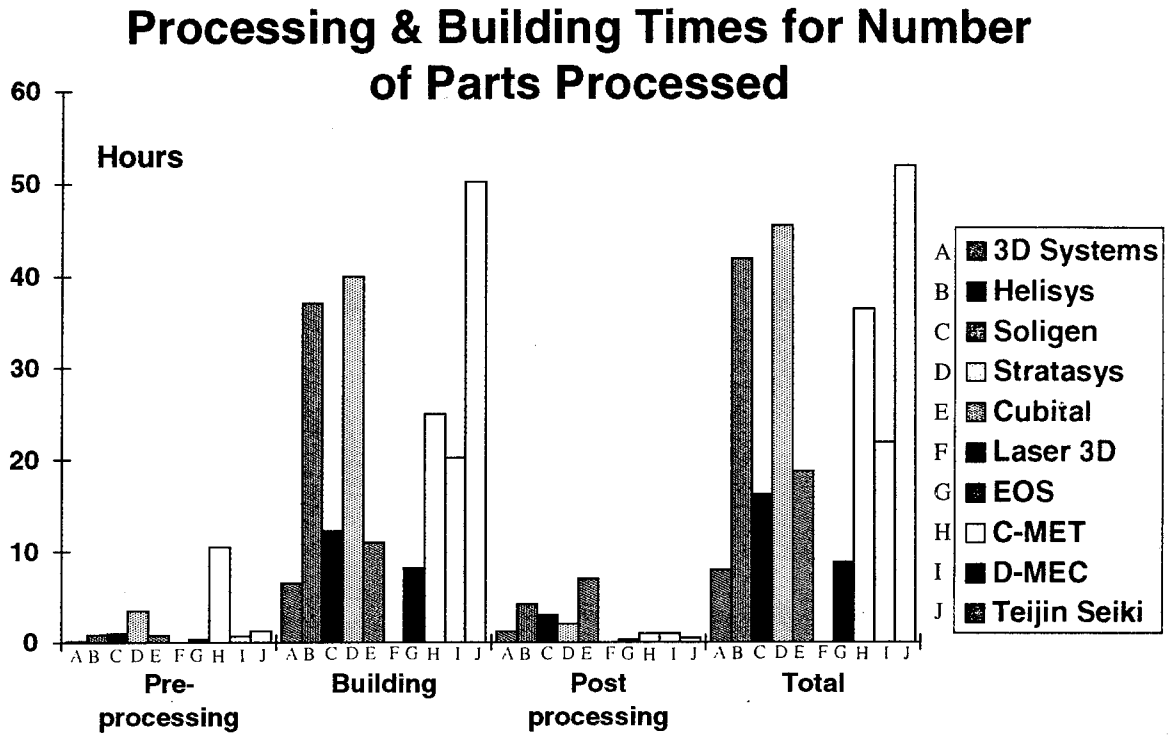

Figure 13. -- Actual pre-processing, building, post processing and total times for the IMS-T2 test parts.

Materials for Rapid Prototyping Systems:

The development of a variety of improved materials for rapid prototyping systems is one of the most significant issues to impact the applications of prototype parts and tooling. The improvements have led to increased accuracy and surface finish, which in turn can be applied to tooling applications in the form of molds and fixtures, or for conversion to make metal castings. Because some rapid prototyping systems can use a variety of materials, the opportunity to build parts that meet the end product material requirements is getting closer to being a reality. Table 5 shows the variety of materials currently available with their respective unit costs.

Company	Material Description	Cost per unit
3D Systems Inc.	XB 5081-1 Photopolymer resins	$145 per kg
	XB 5139	$150 per kg
	XB 5143	$160 per kg
	XB 5149	$165 per kg
	XB 5131	$140 per kg
	XB 5154	$145 per kg
	XB 5170 (epoxy)	$170 per kg
Helisys Inc.	Paper coated with Polyethylene	$2-3 per pound
Soligen Inc.	Ceramic Powder	$10 per Pound
	Liquid Binder	$100 per Gallon
Stratasys Inc.	Machinable wax (MW01)	$175 per spool
	Investment casting wax (ICW04)	$175 per spool
	Polyolefin (P200)	$260 per spool
	Polyamide (P300)	$260 per spool
Cubital Ltd.	General purpose resin (G5601)	$65 per kg
Laser 3D	Dupont 5100 Photopolymer	$138 per kg
EOS GmbH	Dupont SOMOS 2100/3100/5100	$125 per kg
C-MET	Hard photopolymer HS 660	- cost not provided
	Semi rubber HS 661	-
	Rubber HS 662	-
D-MEC Ltd.	SCR-100 Urethane acrylate	$150 per kg
	SCR-200	$150 per kg
	SCR-300	$150 per kg
	SCR-400	$150 per kg
	SCR-500	$250 per kg - SCS-1000 only
Teijin Seiki Co.	SOMOS 2100	$190 per kg
	SOMOS 3100	$190 per kg

Table 5.-- Listing of materials currently available for rapid prototyping.

University-led Rapid Prototyping Developments:

There are three prominent university-led programs in the area of rapid prototyping: Carnegie Mellon University, Massachusetts Institute of Technology (MIT) and the University of Texas. Each of these universities were charged with the challenge to fabricate copies of the IMS test parts using their technologies. The final 3 photographs in Appendix A show the IMS parts that were produced by these university developed technologies. .

Carnegie Mellon University - Shape Deposition

CMU is developing a "Shape Deposition" layered manufacturing process/system which combines the benefits of solid freeform fabrication, CNC milling, and thermal deposition. The strategy is to first slice the CAD model of the shape to be fabricated into layers and then deposit it as a near-net shape using thermal spray and/or molten droplet deposition. The layer is then shaped with a 5-axis CNC milling machine to net shape before proceeding with the next layer. In addition, each layer is shot-peened to control internal stress buildup.

An automated testbed facility has been implemented and a CAD-based process planner/controller has been developed for investigating the Shape Deposition manufacturing paradigm. This testbed configuration consists of four processing stations; CNC milling, thermal deposition, grit blasting/shot peening, and cleaning. The parts are built on pallets which are transferred from station-to-station using a robotic palletizing system. Each station has a pallet receiver mechanism. The part transfer robot places the pallet on the receiver which locates and clamps the pallet in place.

Carnegie Mellon University used their Shape Deposition process to make a Zinc alloy copy of IMS-T1. The part produced demonstrates that the technology is capable of fabricating metal parts directly; however, there is evidence of delamination. See Appendix A.

MIT - 3D Printing

The 3D Printing process under development at MIT creates parts in layers by spreading powder materials on a build platform and selectively joining the powder in the layer by inkjet printing a binder material. The platform lowers and the process is repeated. The process is being applied to the fabrication of expendable molds such as ceramic molds for castings, re-usable dies such as dies for injection molding and end-use parts such as structural metal and ceramic parts.

MIT made several copies of the IMS-T2 test parts in a ceramic material using their 3D Printing process, and also made several ceramic molds of the IMS-T1 test part. These molds were then used at Cercast to mold molten aluminum, thus producing aluminum test parts via a conversion process. The initial trials in making aluminum castings resulted in some "unfilled" areas that can be attributed to air pockets and/or mold temperatures being too cold causing the metal to freeze prematurely.

University of Texas - Selective Laser Sintering:

The University of Texas used their selective laser sintering process to fabricate copper-polymer copies of IMS-T1 test parts. These parts were then baked and infiltrated with an epoxy material for improved density. Although the sintered test parts show signs of warping and "curl," they also demonstrate that the technology has great potential to fabricate metal parts directly.

The results from these university led efforts provide an excellent opportunity to assess the leading-edge capabilities of these emerging technologies. Although further development is indicated, they have all demonstrated that metal parts-making directly from a computer model in a layer-by-layer process is going to be one of the leading approaches of advanced manufacturing.

Discussion:

The rapid prototyping market had evolved from one system availability in 1988, to over 30 systems today. These systems provide part building capabilities in a variety of sizes and materials. At first glance, the casual observer is easily overcome by the confusion of claims that these rapid prototyping developers make in marketing their systems. To date, there are primarily two types of enterprises that have invested in acquiring these rapid prototyping devices: medium to large corporations and service bureaus.

The medium to large corporations have maintained a lead in applying these rapid prototyping technologies to their product development processes. During the initial stages of using these new technologies, a fair amount of experimentation has occurred to find the *best fit* for these technologies. The service bureaus on the other hand have facilitated and promoted these technologies to meet the needs of a wide variety of industries from aerospace and automotive to bio-medical, healthcare and architectural. Further, there has been a growing propensity to apply these technologies to manufacturing and tooling applications.

During the past few years, a differentiation of these rapid prototyping technologies has evolved. In much the same way a typical home owner has a variety of tools for the various seasons, e.g., gardening and lawncare tools for the spring and summer, rakes for the cleanup of leaves in the fall, and snow removal tools during the winter months, today's industries are discovering where rapid prototyping technologies have niche applications. The rapid prototyping devices that are less expensive are also typically less accurate, perhaps not as fast (lower through-put) and build smaller parts. The more expensive equipment is typically more accurate, is faster and has greater through-put, and has larger part building capacities. The leading commercial enterprises that have successfully applied these rapid prototyping technologies can categorize the utility of rapid prototyping technologies in the following applications:

1. **Design verification**: The process of using rapid prototyping to fabricate the first physical object in order to verify the designer's intent. Design flaws often go undetected until the first article is produced. Using traditional approaches to prototyping means that part drawings, fixtures and tools were designed and the parts were then manufactured, days, weeks or months after the design was completed only to discover a design flaw when the first article was produced. With rapid prototyping, these design flaws can be detected very early in the design process without the investment of time and costs in drawings, fixtures and tools. This application simply requires a mock-up of the part with minimal concern for accuracy.

2. **Manufacturing producibility and supplier quoting**: Competition is driving the manufacturing of parts to be faster, have higher quality, and be lower in cost. When manufacturing can have a "say" early in the design cycle, they can provide their input to making the parts easier and at less cost. This insight can lead to significant advantages in the product development life cycle in reducing time to market and lowering costs. Further, when suppliers must quote time and cost to fabricate complex parts from drawings, they typically provide additional "padding" to cushion their quotes for unforeseen problems. However, when a physical article is provided along with the drawings for a quote, the supplier can get the "right" mix of people resources to review the part and drawing to derive a better, more time and cost effective quote. This application also simply requires a mock-up of the part with minimal concern for accuracy.

3. **Conversion technologies**: When a physical article is required that has the same physical and mechanical properties as the final part, a variety of conversion technologies can be employed to convert the rapid prototype article into a "final" article. Typically a rapid prototype model is processes and hand finished to be used as a "master" in a cloning operation such as RTV or silicone tooling, epoxy tooling, etc., where either the final plastic material is injected into the tool, or a wax is injected into the tools and used in the "lost wax" or investment casting process to produce a metal part in a variety of ferrous and non-ferrous metals. This

application requires a part that is more dimensionally accurate and has better surface finish characteristics than the previous applications.

4. **Tooling**: A growing application of rapid prototyping is to use the prototype article as a tool or fixture for the fabrication of a the final parts, e.g., making a rapid prototype mold, or a holding fixture for the machining or inspection of the final part. This application also requires a part that is more dimensionally accurate and has better surface finish characteristics than the previous applications.

Clearly, the most valuable outcome of this assessment is to actually see the IMS T2 test parts that were produced in this effort. The display of these parts provides the viewer with an appreciation for the variety of materials and surface characteristics that each of these different rapid prototyping technologies possess. See Appendix A for photos of these IMS test parts.

Conclusions:

The rapid prototyping industry has been evolving at a fast pace since 1987 when the first Stereolithography SLA-1 System from 3D Systems was introduced. During these past 5 years, significant improvements have been realized in stereolithography and other rapid prototyping systems in accuracy, surface finish and in application development. This proliferation of emerging rapid prototyping systems has, to some degree, created some confusion in the market place. With so many different systems available, it is difficult for potential customers and users to differentiate among the variety of systems. However, with time and users' experience, the analysis of this assessment clearly points to several conclusions:

- The less expensive rapid prototyping systems are an excellent choice for design verification applications that require parts of minimal dimensional accuracy or scaled sizes. These include parts that may be sub scale or oversize that are used to verify the designers intent.
- These less expensive systems can also be used for manufacturing producibility studies to get a "reality check" on the design from a manufacturing point of view.
- The systems that provide greater accuracy are the choice for fabricating "masters" and or "patterns" for conversion technologies such as investment casting and injection molding tooling.
- Tooling applications require "parts" that meet physical property and accuracy needs beyond the capabilities of design verification parts. These applications require stiffness and other characteristics to maintain utility for typical manufacturing applications. Examples include holding fixtures for manufacturing and inspection, and dies and mold halves for both direct and indirect conversion to metal.
- A host of yet-to-be discovered applications in a variety of industries surely exist. The users that are willing to take the "road less traveled" stand to gain much from using and deploying these technologies within their enterprises.

In summary, the tables, figures, charts and the actual IMS test parts provide a wide array of information that can be used to draw a number of conclusions. It is interesting to note that all of these different rapid prototyping developers are continually improving their capabilities. Some of these improvements in accuracy and surface finish are providing a dramatic impact in reducing product development cycle times and costs. Future enhancements to these systems will lead to

even more savings by expanding the use and application of the parts produced by these systems Clearly, the industries that can effectively use and deploy these rapid prototyping technologies for their product lines will have the competitive advantage. The industries that are currently using these rapid prototyping technologies fully appreciate the benefits of "prototyping early and prototyping often."

Acknowledgment:
A special thank you is given to the officers of the participating companies that signed the questionnaires and provided the necessary resources to fabricate the IMS test parts; without their cooperation, this assessment would not have been possible.

Company	Name
3D Systems 26081 Avenue Hall Valencia, CA 91355	Mr. Chuck Hull - President Phone 805-295-5600 Fax 805-257-1200
Helisys, Inc. 2750 Oregon Court Bldg. M-10 Torrance, CA 90503	Mr. Michael Feygin Phone 310-782-1949 Fax 310-782-8280
Soligen, Inc. 19408 Londelius Street Northridge, CA 91324	Mr. Yehoram Uziel - CEO Phone 818-718-1221 Fax 818-718-0760
Stratasys Inc. 14950 Martin Drive Eden Prairie, MN 55344-2019	Mr. Scott Crump Phone 612-937-3000 Fax 612-937-0070
Cubital, Ltd. 13 Hasadna Street, Industrial Zone North Raanana 43650 Israel	Mr. Itzchak Pomerantz - Founder Phone 972-52-906888 Fax 972-52-919937
Laser 3D 6, Allee Pelletier-Doisy 54603 Villers-Les-Nancy CEDEX France	Mr. Claude Medard - Managing Director Phone 83-61-44-76 Fax 83-44-04-82
Electro Optical Systems EOS GmbH Pasinger Str.2 82152 Planegg Germany	Mr. Johann Oberhofer - Vice President Phone 49-89-899-1310 Fax 49-89-859-8402
C-MET C/O Mercedes Benz Werk 50 Postfach 226 7032 Sindelfingen, Germany	Mr. Klaus Scholl - Engineer Phone 49-7031-90-3059 Fax 49-7031-90-7970
D-MEC Ltd. JSR Building 2-11-24, Tsukiji, Chuo-Ku, Tokyo Japan	Mr. Fumio Kurihara - General Manager, Technical Div. Phone 81-3-5565-6661 Fax 81-3-5565-6631
Tegin Seiki Co. Kanagawa Science Park 4Df, 2-1 3-Chome, Sakada Takatsu-Ku, Kawasaki-City 213, Japan	Mr. Kazuo Nakanishi - Office of Corp. Tech. Phone 03-3348-2185 Fax 03-3348-1050

Appendix A - Photographs of IMS Test Parts

The photos on the following pages show the parts produced by the companies and universities that participated in the IMS Rapid Product Development test case:

Company	Material & Description
3D Systems	Photopolymer IMS-T2 test part measuring 6" by 4"
Helisys Inc.	Paper " "
Soligen Inc.	Ceramic mold for half-scale IMS-T1 test part
Stratasys, Inc.	Polyolefin P200 IMS-T2 test part measuring 6" by 4"
Cubital Ltd.	Photopolymer " "
EOS GmbH	Photopolymer " "
C-MET	Photopolymer " "
D-MEC	Photopolymer " "
Teijin Seiki	Photopolymer " "

University	Material & Description
Carnegie Mellon University	Zinc alloy half-scale IMS-T1 test part
MIT	Ceramic 3/4-scale of IMS-T2 test part
MIT	Ceramic mold and Aluminum casting of half-scale IMS-T1
University of Texas	Copper-polymer half-scale IMS-T1 test part

3D Systems Inc.
Stereolithography

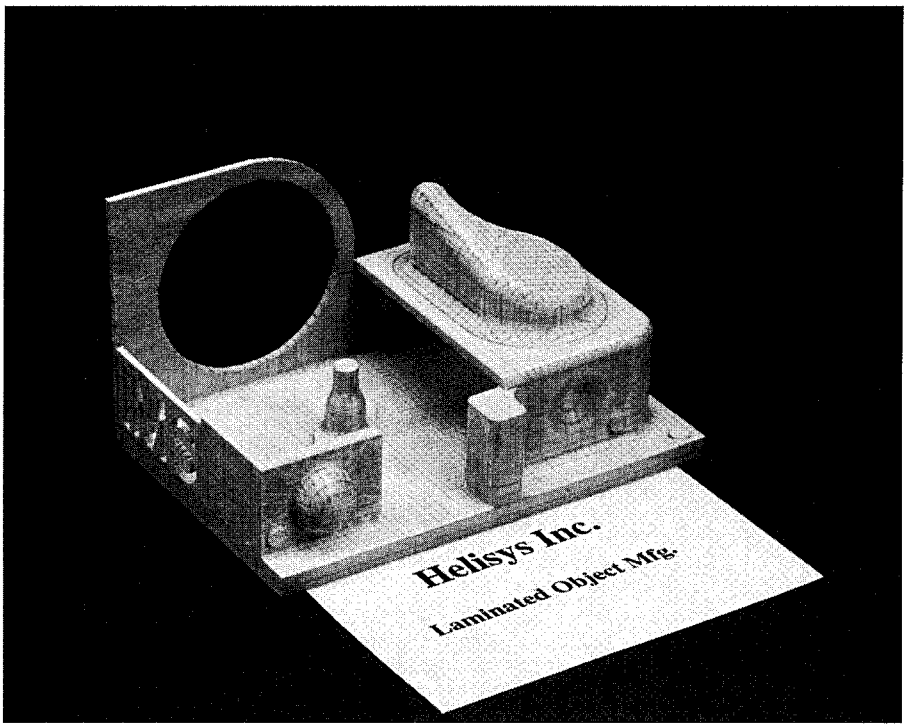
Helisys Inc.
Laminated Object Mfg.

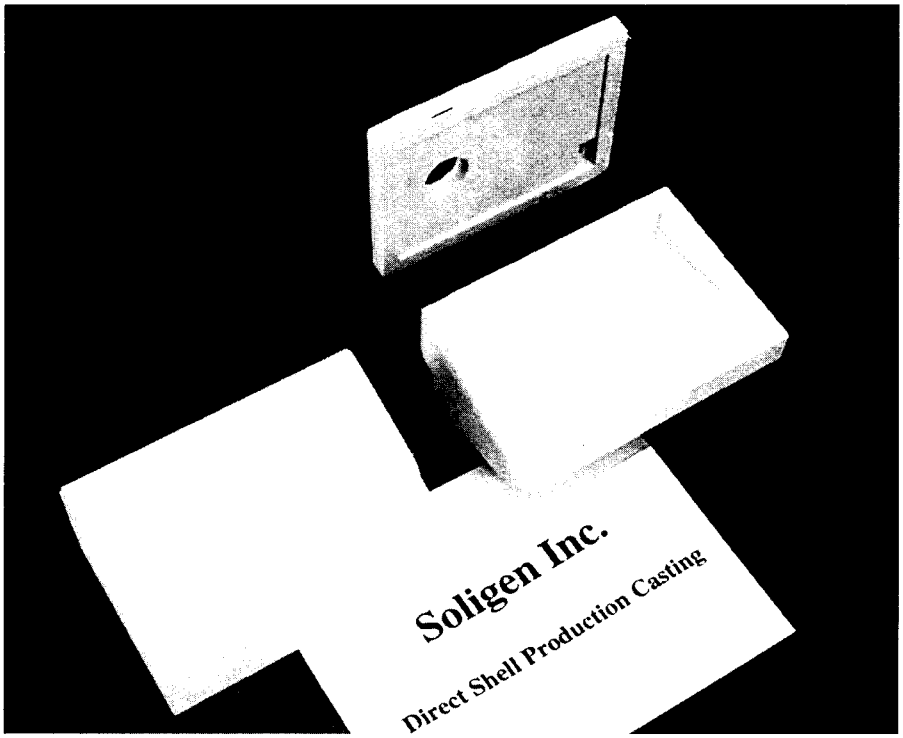
Soligen Inc.
Direct Shell Production Casting

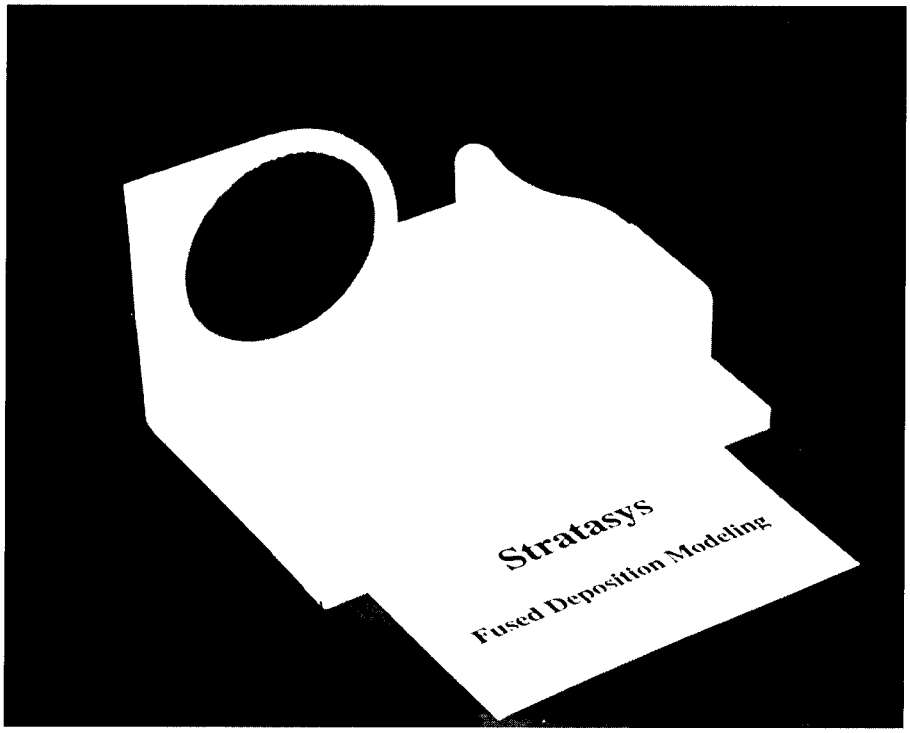
Stratasys
Fused Deposition Modeling

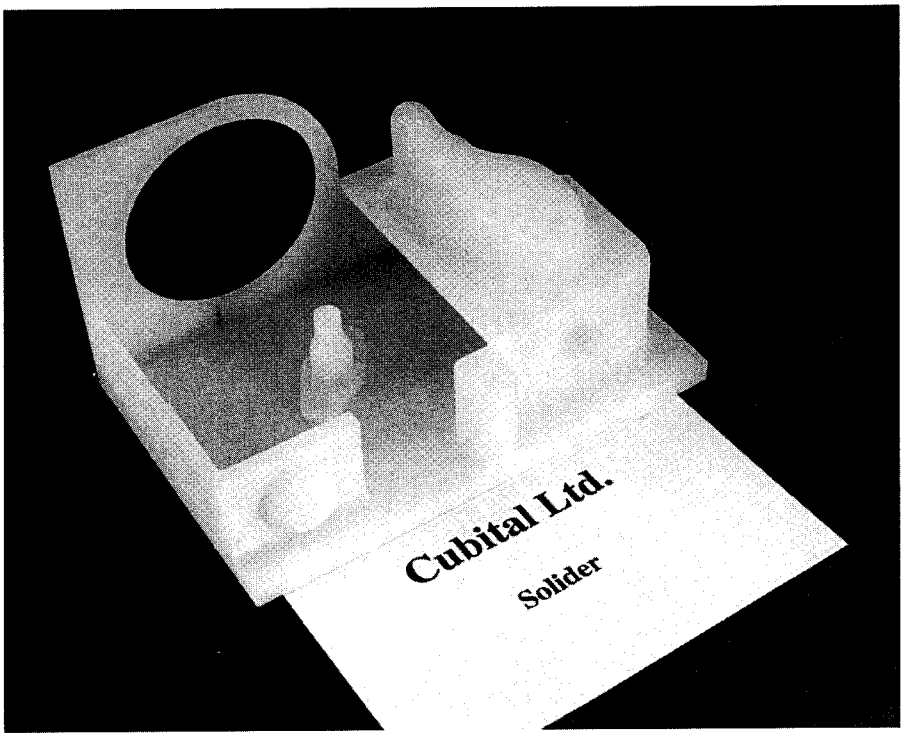
Cubital Ltd.
Solider

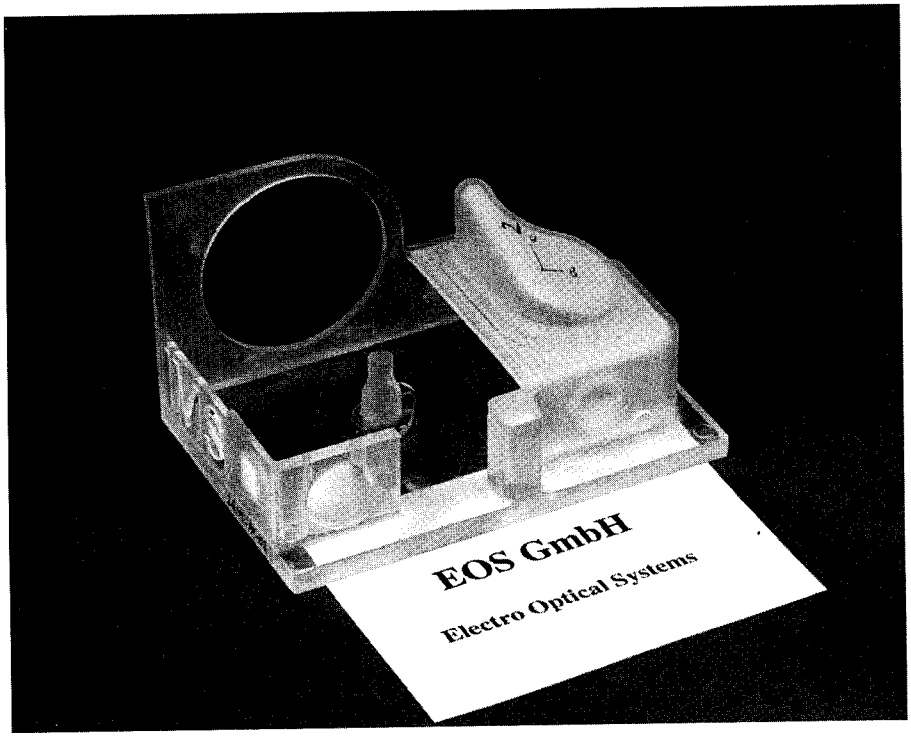
EOS GmbH
Electro Optical Systems

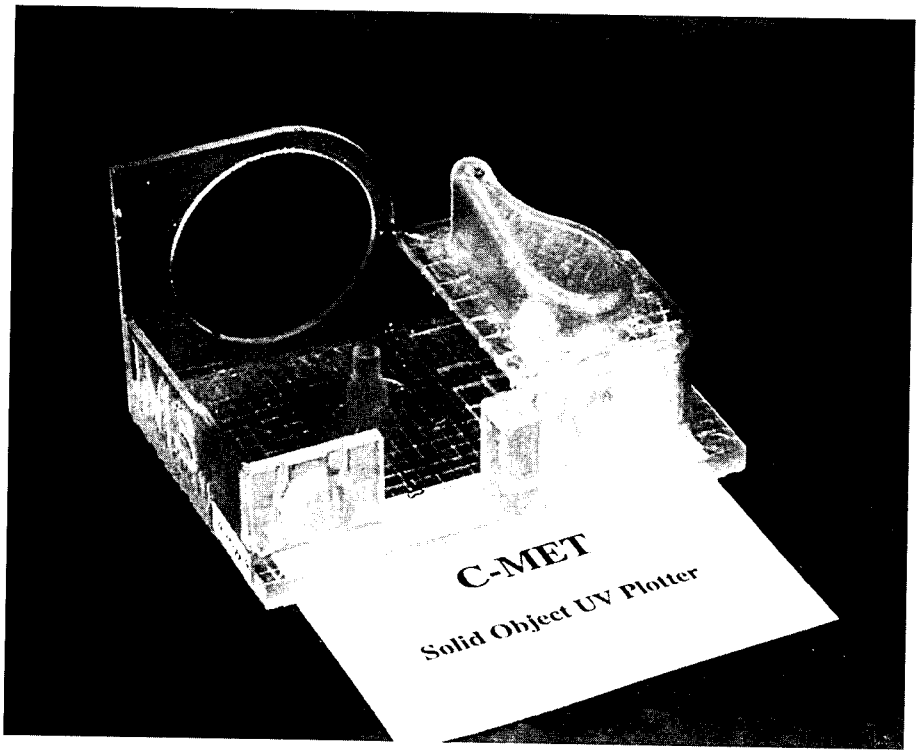
C-MET
Solid Object UV Plotter

D-MEC Ltd.
Solid Creation System

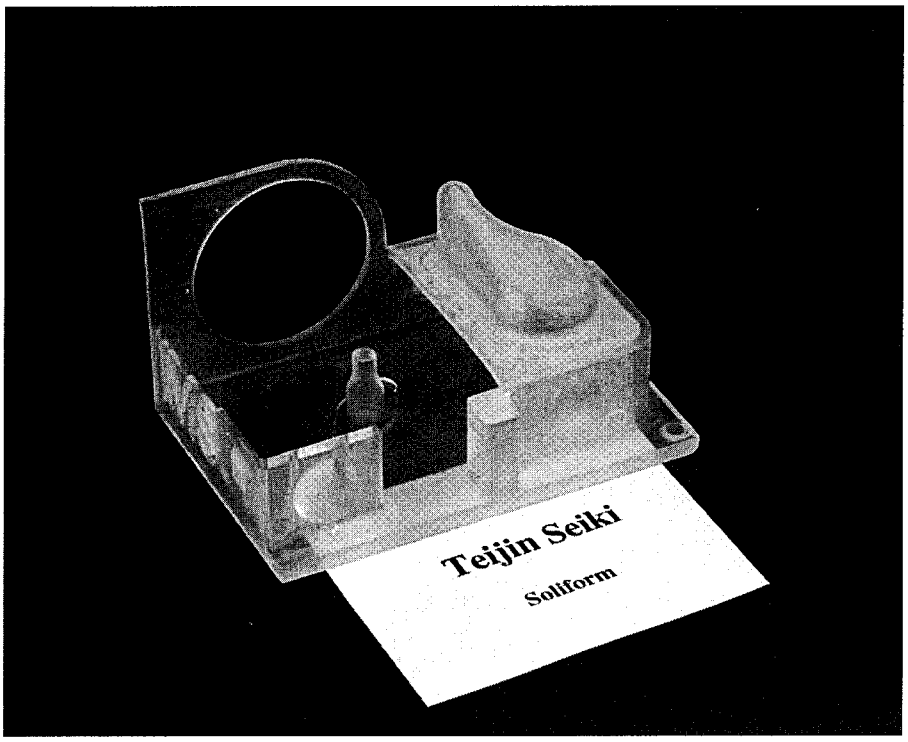
Teijin Seiki
Solform

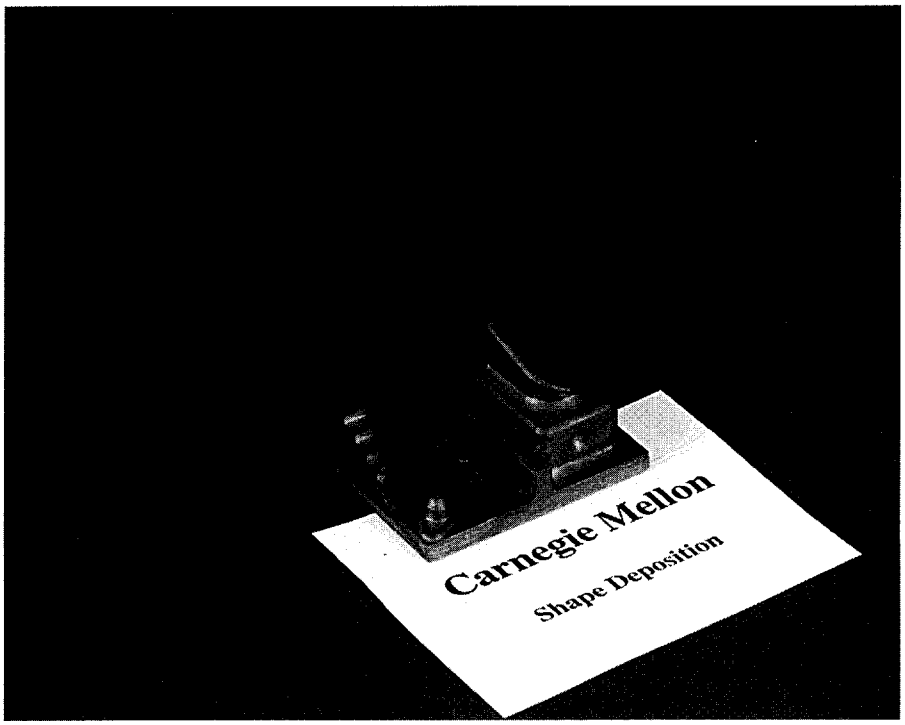
Carnegie Mellon
Shape Deposition

MIT
3D Printing

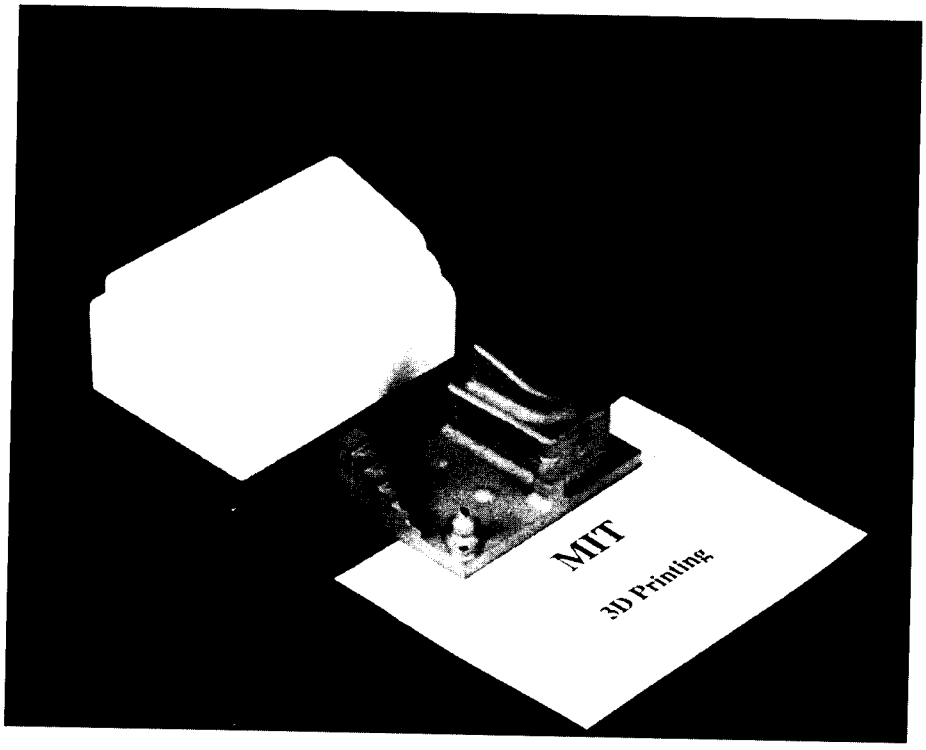
MIT
3D Printing

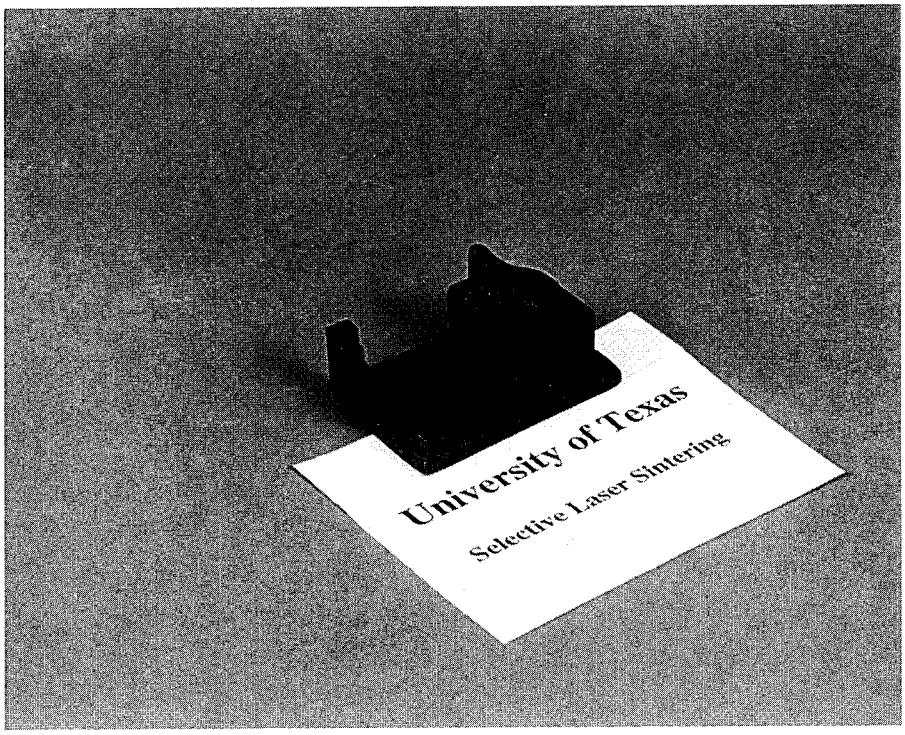
University of Texas
Selective Laser Sintering

Benchmarking of Rapid Prototyping Systems - Beginning to Set Standards

Dureen Jayaram, Amit Bagchi, C.C. Jara-Almonte, Clemson University
Sean O'Reilly, Ford Motor Company

Abstract

Many rapid prototyping (RP) technologies are available today and more are being developed around the world. The absence of benchmarking standards in the RP industry has led manufacturers to use their own standards and make claims about superior performance. The need for testing standards is already felt; standardization will become imperative in the near future. The present work aims to lay the groundwork for the development of standards to measure various performance factors. Issues such as appearance and finish are studied qualitatively; the test part and some findings are presented. Issues such as repeatability, warpage, curl, creep, shrinkage and tensile strength are proposed to be studied quantitatively; test parts designed for studying these are described. Benchmarking standards will help users choose proper systems for their applications and help operators in monitoring machine performance, enabling better control over part building.

1. Introduction

Today's various rapid prototyping (RP) systems have significant differences with respect to their operation and the materials they use. Experimental evidence shows that there are different factors which determine the geometries that build better on each process, the speed of building, the finish and strength of the parts and the accuracy and functionality of the parts. The materials that offer advantages in certain applications may not be suitable for others. The results are also influenced by the expertise of the operators. The effect of some of these factors is known and that of others is not. Figure 1 shows a few of the factors which affect part characteristics.

First time buyers and users often do not understand which system suits their requirements best. Even machine operators usually possess knowledge about one process only. How can a first time user, or a person with limited experience, go about choosing the process that is best suited for his/her requirements? To answer the many questions a potential buyer/user faces, the obvious course of action would be to compare the various processes by studying data on their performance. However, there are no benchmarking standards in the RP industry at the present time.

This paper will address the establishing of systematic benchmarking procedures which may be used to generate useful data on some important material and process characteristics of RP systems.

Qualitative issues such as appearance, form and feel will be important to users with `touch-feel' applications such as design reviews and marketing campaigns. The test part designed to study these will be described here. Some observations about test parts built with four RP technologies, namely, stereolithography (SL), selective laser sintering (SLS), laminated object manufacturing (LOM) and fused deposition modeling (FDM), will be presented.

In investment casting and functional testing, for example, the dimensional accuracy, build defects such as curl and warpage, and the strength of the parts will be important. Test parts have been designed for measuring repeatability, curl, warpage, creep, shrinkage and tensile strength. Detailed measurement plans for collecting useful data are still being developed; the design and results of these experiments will be presented at a later date.

It is important to stress that both the qualitative and quantitative results will indicate the combined capability of each process and the corresponding material, together with the skill of the operator(s). The long term goal of this project is to be able to understand the effects of process_related, material_related and operator_related factors and develop a methodology to study them separately.

2. Previous Benchmarking Studies

An extensive survey of literature, combined with information from manufacturers, users and service bureaus turned up three benchmarking studies whose results have been published. Only two companies, 3D Systems Inc. and DTM Corporation, publish/furnish information on their test parts. These companies use completely different parts for measuring dimensional accuracy. 3D Systems is the only company to have designed tests for studying different part and process characteristics.

Chrysler's Jeep and Truck Engineering conducted a benchmark study [2] in order to decide which system to invest in. A finely detailed speedometer adaptor 1.5"x1.5"x3" in size, shown in Figure 2, was built on six different systems; 3D Systems' SLA 250 and SLA 500, DTM Corporation's SLS 2000, Helisys' LOM 1015, Cubital's Solider 5000 and Stratasys' 3D Modeller. Since Chrysler owned only the SLA 250, they sent the part's STL file to all the manufacturers. For Chrysler, system speed and cost were the most important factors and were studied in detail. Cost was detailed under material, operation, pre and post processing, depreciation and maintenance. The time study included pre-processing, build and post-processing time on each system. Accuracy was not studied in detail, parts were simply measured to ensure that they were within specifications. Nor did Chrysler study the strength or surface finish of the parts.

In 1994, Chrysler sent the same part to RP manufacturers worldwide [4]. The formula for cost comparison was updated but the objective to assist users or purchasers of RP equipment in selecting the fastest and/or cheapest system remained the same. The study concluded that there are no set rules to choose any one RP system over others. It is recommended that each company review factors like end use of models, urgency of turn around time, availability of capital and trained personnel and location of equipment before selecting any technology.

Aubin [3] documents a study of RP technologies from all over the world. The report lists system, maintenance and training costs, build volumes and expected accuracies. Technical capabilities of available systems were characterized and technologies under development were reviewed. A benchmark study was carried out using the Intelligent Manufacturing Systems (IMS) part shown in Figure 3. 4 parts were sought from each company, fabricated from an STL file. The participants were allowed to build a maximum of 6 parts and present the best 4, indicating how many they had built. However, information on the measurements obtained from the parts is proprietary and is not available. The comparison of the pre-processing, building and post-processing times indicates that the processes studied compare differently in these areas.

Van Putte [1] describes a study conducted by Eastman Kodak to study the capability of five RP processes to faithfully reproduce features on a test part. The part, shown in Figure 4, was originally designed to see how various computer-aided design (CAD) / computer-aided manufacturing (CAM) packages could design, alter, analyze and machine typical Kodak components.

Part drawings were made on Pro-Engineer and Aries. The STL files were sent to the service bureaus of five companies: 3D Systems, DTM, Cubital, DuPont and Helisys. The parts were measured using a coordinate measuring machine (CMM), vernier calipers and an optical comparitor. Sixteen X-Y and four Z measurements were taken on each part.

Subtracting the CAD dimensions from the measured ones gave a set of data for each part. Using a statistical software package, the data was analyzed in 2 sets, one for the X-Y plane and the other for the Z-plane, to determine the capability of each process to replicate the original CAD model. A shrinkage correction factor was applied by changing the limits for the capability analysis in such a way as to maximize the performance of each part. A `WAR-PAGE' chart designed by Cubital was used to subjectively assign a warpage value to the base of each part by comparing it to the lines on the chart.

Van Putte himself voices many concerns about the study. Only one part was built by each process. The test part design consisted of features important to Kodak and may have been more favorable to some processes than to others. The same software was not used to generate part drawings. All these factors limit the usefulness of the results to other users who are looking for benchmarking data.

While the Chrysler and Kodak studies are interesting, they are primarily of use only to themselves and the data is of little use to other users of these RP systems whose typical parts may be significantly different, as also the factors critical to their applications. The objective of the present study is to fill this gap by designing experiments which can be used to systematically compare RP systems.

A group of European companies has also conducted a benchmark study [8]. A test part containing thin walls, tapers, slots, holes and free form surfaces was designed and built by 12 vendors. The results are available but have not been reviewed by the authors at this time.

3. Qualitative Issues

A simple test part (shown in Figure 5) which contains only cylinders, cones and prismatic boxes, was designed. Each part has four cylinders, tilted at 0, 30, 60 and 90 degrees from the vertical axis. These were used to study the effect of tilting features. A stepped cone with four sections of different cone angles was used to study stair-stepping. The prismatic boxes were used to study straightness and parallelism of edges and warpage of flat surfaces.

Parts were built with 6 materials on the 4 systems mentioned in section 1. A study of the parts and processes, combined with technical discussions with machine operators [5,6,7], provided an insight into various pre-processing, building and post-processing issues. Such understanding is essential in developing benchmarking standards.

3.1 Pre-Processing Issues

Part building is affected by the inherent errors in converting data from a CAD file to a format acceptable by an RP system. Any benchmarking process will have to ensure that the same CAD software and file format are used. However, this still does not rule out differences in interpretation of the accepted format by the system software.

Build layouts for this study were created as assemblies on Aries by using multiple copies of the test part. This created a concatenation of STL files for each assembly, which the SLS and LOM software found hard to read [6]. Also, in one instance, the FDM software read one cylinder as being separate from the rest of the test part, in spite of the cylinder being `unioned' to the base of the part [6]. Subsequently, the part built without problems.

An important finding is that while the STL format was accepted by all the systems used in the study, the method of constructing the drawing file on a CAD system was found to affect part building on the LOM process. The LOM process is different from the other processes in that it builds parts by cutting away excess material while the others build parts by adding or fusing material where required. The software on the LOM machine recognizes different entities in an STL file and cuts them separately from the sheets of paper. Therefore, on the test part, the cylinders were separated from the base since they were drawn separately and `unioned' into the base. This would not have happened if the drawing had been constructed by subtracting geometry from a block; the test part would then have been treated as one entity [6,7].

Constructing the part drawing with the LOM process in mind will solve this problem but we can only speculate whether the laser on the SL and SLS machines will cure parts differently, based on whether two features were drawn as separate entities or constructed out of one block. If some areas are cured/sintered twice over, parts may be affected in ways not yet known.

3.2 Part Building Issues

Aesthetics: The SL parts (5154, Weave) looked the best, except for `swirls' on some inclined cylinders. The SLS (polycarbonate), FDM (wax), SLS (nylon), SL (5180, Quickcast) and LOM parts rank in order on the basis of appearance. Laser scoring and cross-hatching are causes for the LOM parts to rank low.

Geometric features: All 4 processes appear capable of building cylinders at different angles. The results can be expected to be different if hollow cylinders are built, especially with thin walls.

Stair_stepping was not a problem on any of the cones on any machine. However, only the SLA built all cone tips well. All other processes built some parts where the sharp point was not achieved. Edges were sharpest on LOM parts, followed by SL (5154, Weave), SL (5180, Quickcast), SLS (nylon), FDM (wax) and SLS (polycarbonate) parts.

Material issues: Problems exist with materials on all 4 systems. Building nylon parts on the SLS process requires very tight temperature control [6]. Temperatures even slightly higher than the recommended value harden the loose nylon powder which becomes difficult to remove, affecting appearance and accuracy. In some areas on the test parts, the nylon was so hard that it could not be removed even by sand blasting. A smaller build volume is also recommended for nylon parts [6].

With the LOM process, delamination occurs between layers on some parts. Variation in paper quality, specifically coating inconsistency, is suspected to be the one of the causes for this [7].

The new resin (5180), used on the SLA, has higher surface tension than the old ones. Layers finer than 0.006" are hard to build in styles other than Quickcast. It also increases build time because there is a `pre-dip' delay between layers while the previous layer cures.

While building nylon parts on the FDM process, the nozzle leaves fine "fuzzes" on parts. This can be controlled by using recommended nozzle sizes and velocities, but the problem is still more evident than with investment casting wax [5].

Operation issues: While all four technologies permit build interruption, none of them continue a build successfully after a long delay. Unexpected interruptions occurred on the LOM and SLS machines. A paper jam stopped the build on the former while exhaustion of the nitrogen supply from the supply cylinder was the cause on the latter. An improved paper transport mechanism will help reduce operator monitoring for the LOM process. For large builds on the SLS process, a continuous supply of nitrogen from a plant, as opposed to using a cylinder, may become necessary.

Build time: Although the present study did not involve comparison of build times, some factors which limit process speed are highlighted for interest. The FDM process took the longest time for building a set of parts. Faster builds can be achieved by increasing the space between successive nozzle paths, which determines how densely the material is laid out. However, the mechanical traverse of the nozzle is always slower than the scanning speed of a laser using a set of mirrors. On the LOM process, even though a laser is used, it traverses mechanically, again limiting build speed. Also, since excess material has to be removed after the build is complete, cross-hatching has to be carried out over the entire block. For small parts, a significant portion of build time will be spent on this.

Build failures: In the first set of parts built on the SLS machine with polycarbonate, many of the inclined cylinders and some of the horizontal cylinders broke loose. Some cylinders were also broken into dissimilar sections, appearing to indicate that the sintering had failed to hold material together in those sections. In a subsequent build, parts built with the same material were intact. The cause for the failure is not known.

The first build with the Quickcast style (resin 5180) also failed unexplainably. Fine strands of material were found all over the parts, completely covering them with 'fuzz'. All features were stretched in the Z direction; the parts were 1.5 to 2 times taller than their actual size. The next build was good, though no parameters were changed.

3.3 Post-Processing Issues

All RP processes have recommended procedures which are followed before part building is truly complete. In addition, operators develop their own skills and techniques from experience. To some extent, post-processing is dictated by the end use of the part. Parts for design reviews may be smoothed and painted, Quickcast parts meant for investment casting are carefully drained of uncured resin, and so on. Operator skills influence final part accuracy and finish to varying degrees on different systems. This influence is highest on the LOM parts.

Removing excess material from the LOM parts is difficult where geometries are intricate. Special tools are not available. Operators use suitable wood working tools. Not knowing the

exact geometry can make cleanup even harder, with the danger of accidentally breaking part features being very high for delicate sections. When features are broken, they can be glued back on with wood glue but the effect of this glue on dimensions, especially in the Z direction, needs to be studied. The process is best suited for large, simple parts.

FDM parts require little or no processing. Fine strands of material, which may appear on some parts, can be blown away with an ordinary hair dryer [5]. SLS parts rank second in ease of post_processing, the most difficulty is encountered with cleaning hardened nylon. SLA parts usually require more time than FDM and SLS parts since post_processing involves support removal, draining of uncured resin, curing in an oven and cleaning with chemicals.

4. Quantitative Issues

The factor of greatest interest to this study is repeatability. Repeatability is really a machine issue; two supposedly identical machines, though theoretically of the same capabilities, will still have their differences. It is important for users to understand how consistently a particular machine will build a part when built at different times, platform locations, orientations, by different operators using different materials. It is reasonable to expect variations as mechanical parts wear on the machines. By following a standardized test procedure, it is possible to monitor a machine's capabilities and make adjustments wherever possible to obtain builds that are known to be within the machine's capabilities. A benchmarking procedure will be developed in this light using the test part which was used for the qualitative study described in section 3.

Other factors of interest include build defects such as curl and warpage, material strength (tensile), and part deterioration over time (creep, shrinkage).

Warpage is defined as the out of plane deviation of flat surfaces. The test part is, once again, the one described in section 3. A CMM can be used to measure the coordinates at many points on the top surface of each prismatic box. By fitting a plane through these points, the deviations found at the inspected sections can be used to calculate warpage.

For determining tensile strength, it is proposed that ASTM standard 638-72 flat tensile test bars be built and tested.

Curling is the deformation that occurs in parts with geometries such as cantilever lengths and is due to internal stresses which develop during part building. Creep is defined as the dimensional change that occurs over time due to molecular changes and gravity, that is, the weight of the part. Two types of shrinkage can be studied, linear and bulk shrinkage. Linear shrinkage is defined as the change in part dimensions over time. Bulk shrinkage is defined as the change in volume of a part over time. Test parts and procedures to verify performance of RP systems on these factors will be developed.

Acknowledgements

Ford Motor Co. is thanked for financial support, for the support and cooperation of many staff members in the rapid prototyping laboratory at the Alpha Advanced Manufacturing Division in building all the test parts and for the cooperation extended during one of the authors' (Jayaram's) visit to their facility. The authors also thank Ms. E. Persall at the Product Realization Laboratory, Clemson University, for all her suggestions and help in our 'part cleaning workshop'.

References

1. Van Putte, D.A., "A Brief Benchmarking Study of Rapid Prototyping Processes", Proceedings of the Third International Conference on Rapid Prototyping, Dayton, OH, June 1992,pp. 251-263.
2. Wohlers, T., "Chrysler Compares Rapid Prototyping Systems", Computer-Aided Engineering, October 1992, pp. 84-90.
3. Aubin, R.F., "A World Wide Assessment of Rapid Prototyping Technologies", Report No. 94-13, January 1994, United Technologies Research Center, 411, Silver Lane, MS 129-48,

East Hartford, CT 06108.
4. Schmidt, L.D., "A Benchmarking Comparison of Commercial Techniques in Rapid Prototyping", Proceedings of the Fifth International Conference on Rapid Prototyping, Dayton, OH, June 1994, pp. 333-351.
5. Abramson, R., Alpha Advanced Manufacturing Division, Ford Motor Co., Detroit, MI., Personal Communication, April-July 1994.
6. Newton, D., Alpha Advanced Manufacturing Division, Ford Motor Co., Detroit, MI., Personal Communication, April-July 1994.
7. Sadler, S., Alpha Advanced Manufacturing Division, Ford Motor Co., Detroit, MI., Personal Communication, April-July 1994.
8. Hunwick, J., Delcam International PLC, jph@delcam.co.uk, Electronic Communication, July 1994.

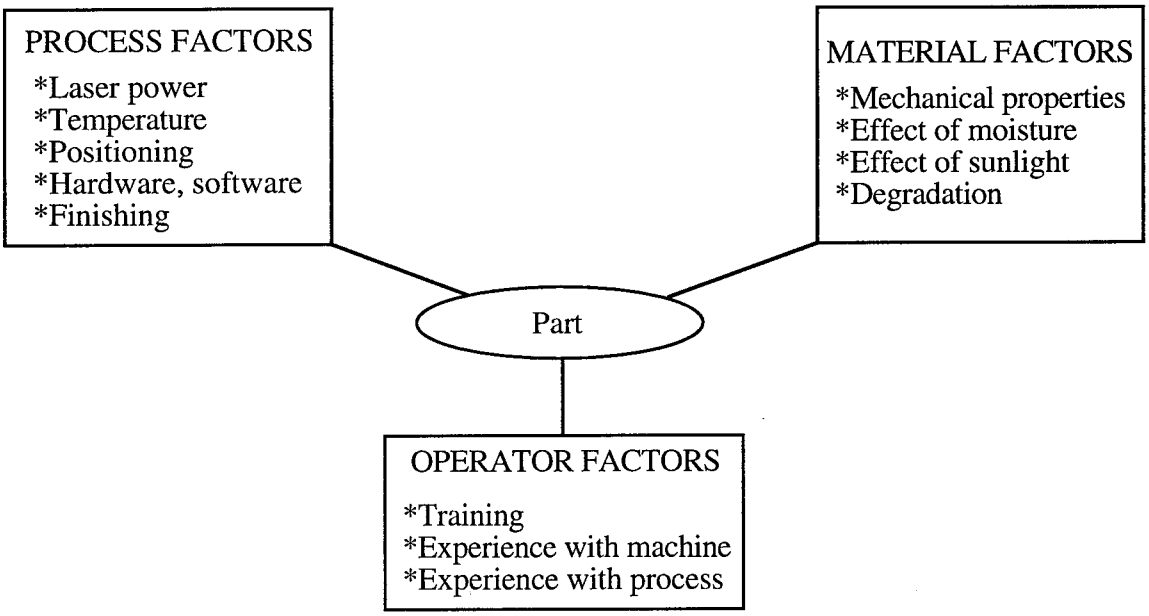

Figure 1. Factors Affecting Performance of RP Systems

Figure 2. Chrysler Benchmark Part

Figure 3. The IMS Benchmark Part

Figure 4. The Kodak Benchmark Part

Figure 5. Part for Qualitative Study

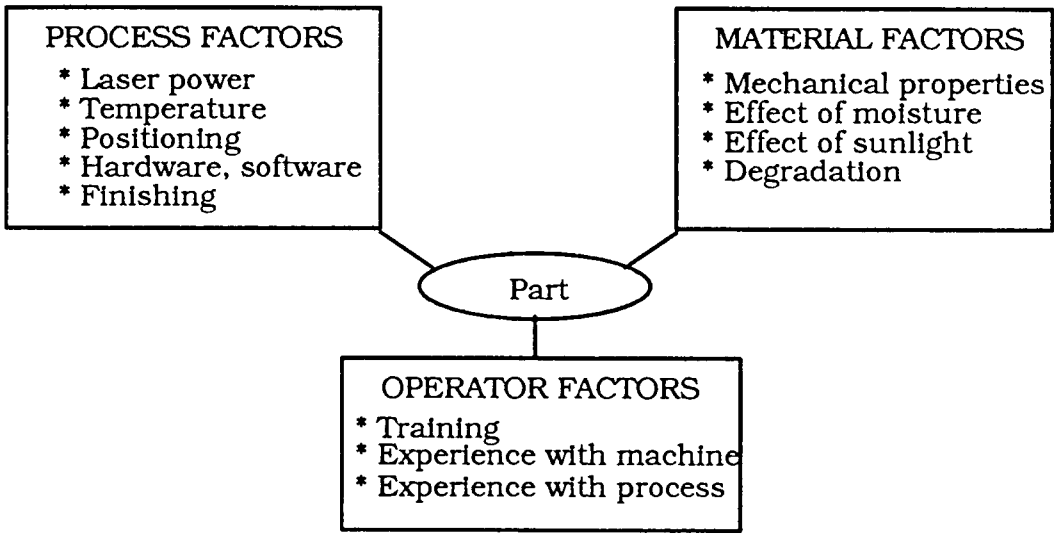

Figure 1. Factors Affecting Performance of RP Systems

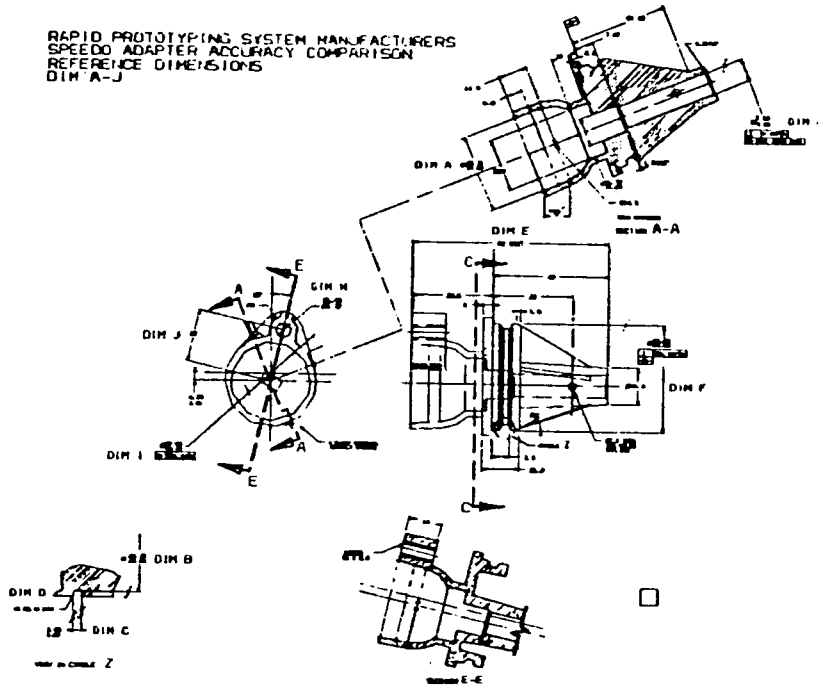

Figure 2. Chrysler Benchmark Part

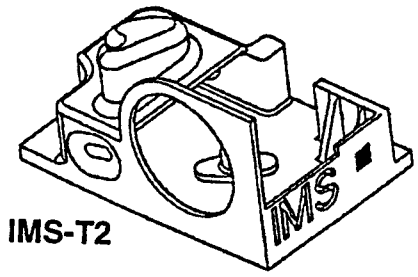

Figure 3. The IMS Benchmark Part

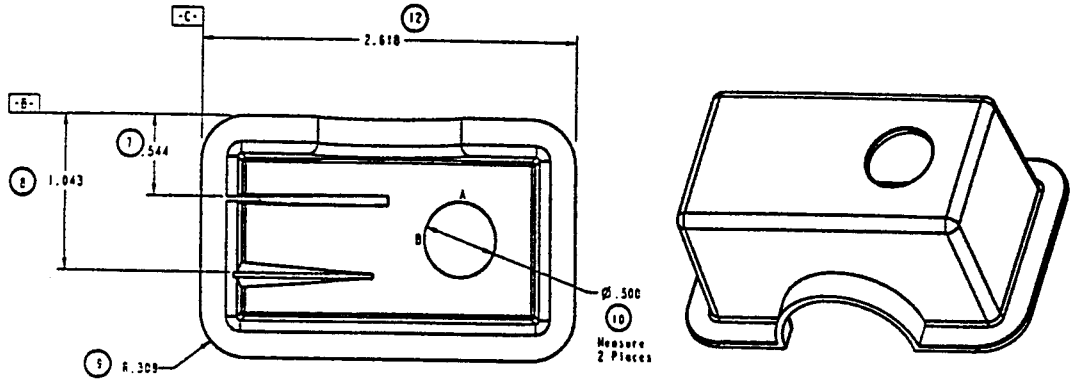

Figure 4. The Kodak Benchmark Part

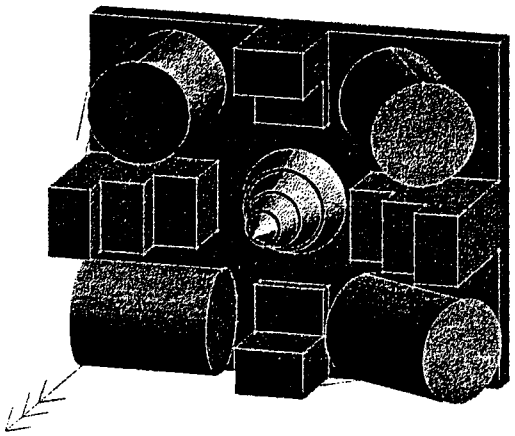

Figure 5. Part for Qualitative Study

QuickCast™ & Rapid Tooling:

A Case History at Ford Motor Company

Karl R. Denton
Ford Motor Company

&

Paul F. Jacobs
3D Systems, Inc.

February 1994

Background:

The technology of Rapid Prototyping & Manufacturing (RP&M) began with Chuck Hull's invention of StereoLithography and the founding of 3D Systems in March, 1986 (Ref. 1). The first StereoLithography Apparatus, the SLA-1, was previewed at AutoFact in November, 1987. The first SLA-250 was announced in March, 1989; followed by the sale of the first SLA-500 only four years ago (Ref. 2).

During 1988 and 1989 many visionary people recognized that StereoLithography (SL) possessed remarkable potential. Nonetheless, from a pragmatic viewpoint the early parts were very brittle, accuracy was mediocre at best, and surface finish was still rather rough. Consequently, the initial parts were really useful only for ***visualization***. However, this capability *alone* was extremely valuable. It enabled designers and engineers to uncover basic errors in a design while inspecting actual, physical, three dimensional objects. These discrepancies were often previously overlooked when reviewing a complex set of two dimensional drawings. As a result, *improved product visualization* was almost certainly the dominant justification for the purchase of an SLA through mid 1990, and *still* remains an important advantage of RP&M.

However, about four years ago a number of key developments in software, hardware, resin formulation and process methods, coupled with a growing understanding of the fundamental science of SL, began to bear fruit. Figure 1 shows the various advances that have been made in SL part accuracy during this period. Here we plot ε (90), ("epsilon ninety") as a function of time. Note that this accuracy metric is defined such that ninety percent of the actual measurements on a part will lie within ε(90) of their intended CAD value. Hence, ε(90) gives the reader an indication of the "90th percentile error" for parts made using StereoLithography. The data shown in this figure were taken from the so-called "UserPart" accuracy test, described in detail in Ref. 3.

Early values of ε(90) were almost 400 micrometers using the original Tri-Hatch build style. When ε(90) was reduced to about 300 micrometers, with the advent of the WEAVE™ build style in June 1990, SL users began to migrate towards applications involving design ***verification*** (Ref. 4). At this point, the parts were "good enough" that engineers and designers could begin to check for component interferences, improperly positioned holes, problems with cable routing paths, etc.

When the values of ε(90) reached about 200 micrometers, after the release of STAR-WEAVE™ in August 1991, SL users began to adopt the technology for applications involving design ***iteration*** and ***optimization***. Stories of designers and engineers building multiple versions of inlet manifolds, impellers, or aerodynamic nose sections, and then performing flow tests to determine the "best" design, became more commonplace (Ref. 5).

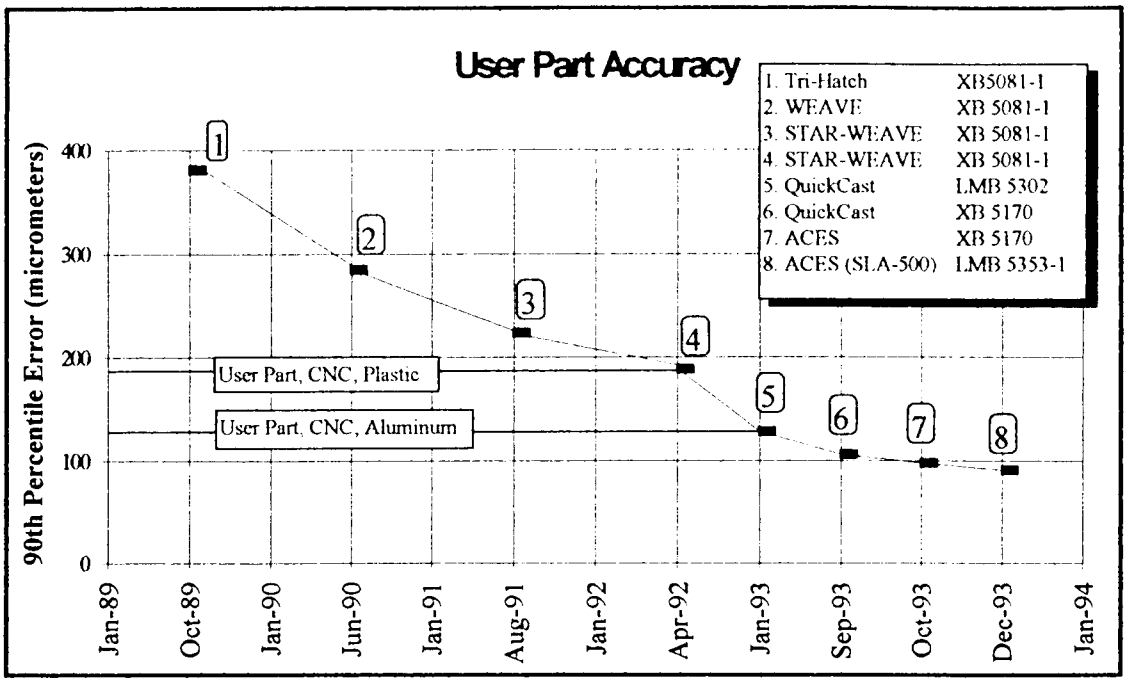

Figure 1

By mid 1993, with the availability of the new epoxy resin XB 5170, the values of $\varepsilon(90)$ began to approach 100 micrometers. When the QuickCast™ build style was also released in July, 1993, it became possible for users to go directly from an accurate SL pattern to a quality shell investment cast *metal prototype*. With this step, designers and test engineers rapidly moved into the realm of ***fabrication*** for functional end-use prototypes. During the past year, dozens of corporations and universities in the U.S. and Europe have followed this path for the production of over a thousand functional prototypes in aluminum, stainless steel, carbon steel, tool steel, ductile iron, inconel, copper, beryllium copper alloys, silicon bronze and titanium. All these functional prototypes were investment cast directly from QuickCast patterns (Refs. 6 - 10).

During December 1993, StereoLithography moved to an improved level of UserPart accuracy, when a value of $\varepsilon(90) = 91$ micrometers was achieved This value was obtained when utilizing the recently developed and released *Diode Leveling Module*, as well as the new *Orion Imaging Technology* now available on the SLA-500/30. As a result, it is now possible for users to advance, albeit cautiously, into the arena of true manufacturing ***production***. This paper describes one of the earliest applications of StereoLithography to be focused on the creation of shell investment cast tool steel *negatives* using QuickCast. These steel negatives then become the basis of core and cavity inserts for Rapid Tooling.

This **"QuickCast Tooling"** process has the potential for truly dramatic cost and time savings. Data presented in this paper document the actual time and money saved by Ford on this project alone. Ultimately, QuickCast Tooling should enable rapid and economical generation of core and cavity inserts for either direct injection molding of

end-use production plastic parts, manufacturing large quantities of *investment casting wax patterns*, or as dies for *direct die casting of production metal components.*

However, in order for this application to provide really substantial cost and time savings, it is essential that the *accuracy* and *surface finish* of the SL generated patterns continue to improve. With ε(90) values currently at 91 micrometers, coupled with the surface finish of the latest QuickCast patterns, we are now moving "into the ballpark" of QuickCast Tooling. As ε(90) is continuously diminished and "stair-stepping" is further reduced, this application will begin to grow rapidly; driven by the remarkable economic and schedule benefits attainable. When ε(90) moves below 40 micrometers and SL pattern surface finish begins to approach that of machined tool steel, we believe that Rapid Tooling will become a dominant growth mechanism of RP&M.

While these levels of pattern accuracy and surface finish may still be a few years away, they are coming. This paper describes a successful project which indicates that we may be closer to the goal of Rapid Tooling than many people realize. Indeed, as shown in the cost and time comparison figures which follow, Ford Motor Company is already beginning to realize significant benefits from this new and important application of SL.

Introduction:

The automotive industry is constantly striving to find ways to produce final products with cost and time savings in the forefront of the designer's, engineer's and manufacturer's minds. Parts constructed more rapidly and economically offer obvious savings. When generated in production materials these parts allow several designs to be tested under real world conditions, enabling selection of the best possible design. The 1994 Ford Explorer "Wiper Module Cover" described in this paper, although a simple part, illustrates the potential of today's technology. Simply stated, the tools created in this project were used to ***injection mold production polypropylene material,*** and equally important, to do so for ***production quantities*** as well.

Process Alternatives:

At the time this project was started, two alternative processes for creating the tools were being considered. The first method involved the possible use of spray metal tooling backed by some sort of composite material. The Wiper Module Cover geometry was simple enough to use spray metal tooling. The primary question was whether the tools would survive the demands associated with production quantities. After some discussion with Ford's Alpha Manufacturing Development Center (Alpha MDC) concerning a project that had previously been accomplished using spray metal (kirksite) tooling with a composite backing, it was clear the tools would almost certainly *not* survive for the required production quantities.

Typical results Alpha MDC were seeing on spray metal tooling were as follows: on the first injection molded part a dimple occurred, although in this case the cause was probably due to excessively rushing the cycle time. At 100 parts, thin intricate sections started to deform. The tool was retired at 300 parts, although part quality was not yet unacceptable. Total production yield was expected to be between 300 and 1,400 parts on that specific spray metal tool. This is consistent with, albeit on the low end of, the results listed in Table 1 below.

Conventional Tooling				
Number of Required Parts	Mold Material Type	Fabrication Cost $(000)	Fabrication Time (weeks)	Mold Life Parts Produced
1 to 30	Silicone	$5	2 to 3	30
30 to 1,000	Epoxy Composite	$9	4 to 5	300
1,000 to 3,000	Kirksite (cast)	$25	12 to 14	1,500
1,000 to 3,000	Aluminum (cast)	$30	12 to 14	2,000
3000 to 250,000	Steel (machined)	$60	16 to 40	250,000
Rapid Tooling				
Number of Required Parts	Mold Material Type	Fabrication Cost $(000)	Fabrication Time (weeks)	Mold Life Parts Produced
1 to 30	Silicone	$5	2 to 3	30
30 to 300	Epoxy Composite	$9	4 to 5	300
300 to 1,400	Arc Metal Spray**	$25	6 to 7	1,000
1,400 to 15,000	Nickel Vapor Deposition**	$30	6 to 7	5,000
3000 to 250,000	Steel (machined)	$60	16 to 18	250,000
3,000 to 250,000*	Steel (cast)	$15	4 to 6	250,000
*Mold life study is still in progress.				
** Composite Assembly				

Table 1

The second process, called Nickel Vapor Deposition (NVD), was a more likely candidate for production tooling requirements. The surface quality of NVD is quite impressive, although estimates of tool life were uncertain. Again, Ford's Alpha MDC group provided some answers based on prior experience. As in the case with spray metal tooling, the NVD process would also require some sort of composite backing material. At the time, Alpha MDC had produced only one mold using the NVD process. That tool was able to withstand very limited injection molding conditions (i.e. 65 psi at 206 °F). These values were far below the requirements of the production tool (viz. 10,000 psi at 450°F - 500°F) as shown in Table 2. Nonetheless, the decision had been made to proceed with limited production quantities in order to establish baseline data for NVD tools.

The NVD tool was stopped at 300 parts, although it held up quite well during use, with little or no degradation evident. Nonetheless, Alpha MDC estimated the yield with the NVD process at between 1,400 and 15,000 parts. While an improvement relative to spray metal tooling, this was still not appropriate for quantities in excess of 100,000 parts.

Tool and Mold Information

Description	Data	Comments
Press	200 Ton	
Tool	12" x 15" Base	DME Cat #1215A-33-17
Pressures	10,000 psi	
Temperatures	450 F - 500 F	
Cooling Line Fittings	1/4" Pipe	DME Cat #JP252
Runner	1/4" Half Round	
Ejector Pins	1/4"	DME Cat #EX-17
Return Pins	5/8"	DME Cat #EX-37
Material to be Molded	Polypropylene	
Shrink Factor	0.018 in/in	
Draft Angle Required	1 degree	
Steel Selected	A2 Tooling Steel	Other possible steels include:
Shrink Factor	2% in all directions	A6 or H13
Mold Inserts Size	CORE - 6" x 8" x 3"	
	CAVITY - 6" x 8" x 3"	

Table 2

Process Selection and Implementation:

Ford Motor Company had been a Beta site for the QuickCast™ process during 1993. Recognizing the limitations of both spray metal and NVD tooling, as described above, Ford decided to try ***"QuickCast Tooling"***. Once the QuickCast Tooling process had been selected, the task of learning how to actually accomplish the desired outcome had begun. The software selected to create the CAD solid model of the Explorer Wiper Module Cover was Parametric Technology Corporation's PRO/Engineer (PRO/E). PRO/E was selected based on the availability of the PRO/Mold software package. PRO/Mold allows the designer or engineer to create ***negative*** molds based on the *positive* of the desired final part geometry. As a starting point, a CAD ***positive*** solid model of the Wiper Module Cover was created in PRO/E and subsequently forwarded to Ford's SLA-250 for creation. A photograph of the QuickCast positive is shown in Figure 2.

As it turned out, the positive of the part allowed the early detection of a packaging interference. A ***second iteration*** was created by altering the PRO/E solid model, and sending the new file to the SLA. This time the positive of the Wiper Module Cover showed no interference, but still required further changes in order for the final assembly to be more easily manufactured. Thus, a ***third iteration*** was generated in PRO/E.

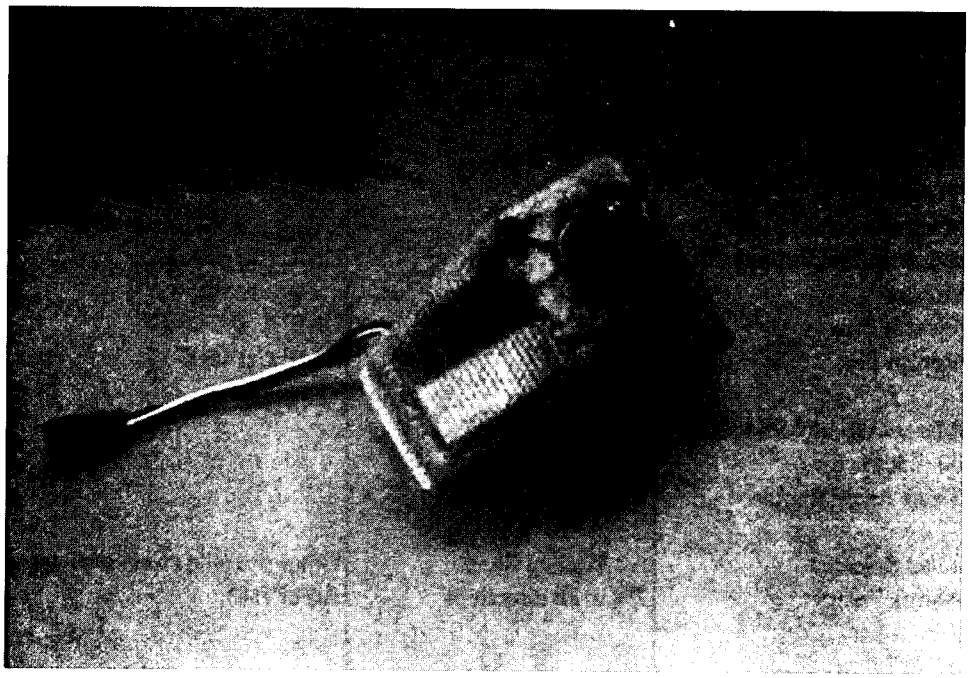

Figure 2: StereoLithography pattern mounted on the wiper module.

When the design, engineering and manufacturing staffs were in concurrence, mold halves were created by initially imbedding the CAD solid model in a block called a "work piece" in PRO/Mold. A parting line was then selected based on the manufacturer's requirements, and the two CAD solid model halves were then "separated." Next, the cooling lines and ejector pin holes were positioned on the PRO/Mold solid models of the mold halves. A schematic of the tooling set-up, showing the mold base, ejector plate, support plate, core and cavity inserts, and top clamping plate, is presented in Figure 3.

However, during a final meeting before actually preparing the STL file, the need for another design change became evident. This ***fourth iteration*** was made to the CAD solid model and was automatically incorporated into the mold halves. The STL files were then generated with the highest accuracy settings in PRO/E in order to obtain the best possible QuickCast pattern surface finish. A photograph of the final QuickCast negative mold insert patterns is shown in Figure 4. It is noteworthy that the classic SL sequence of design visualization, verification, multiple iteration and final optimization was very evident during this project. Had traditional methods been used, significant, expensive, and time consuming tooling rework would certainly have been required. In fact, it is quite possible that a new tool would have been necessary, adding many months to the delivery schedule.

Schematic of Tool

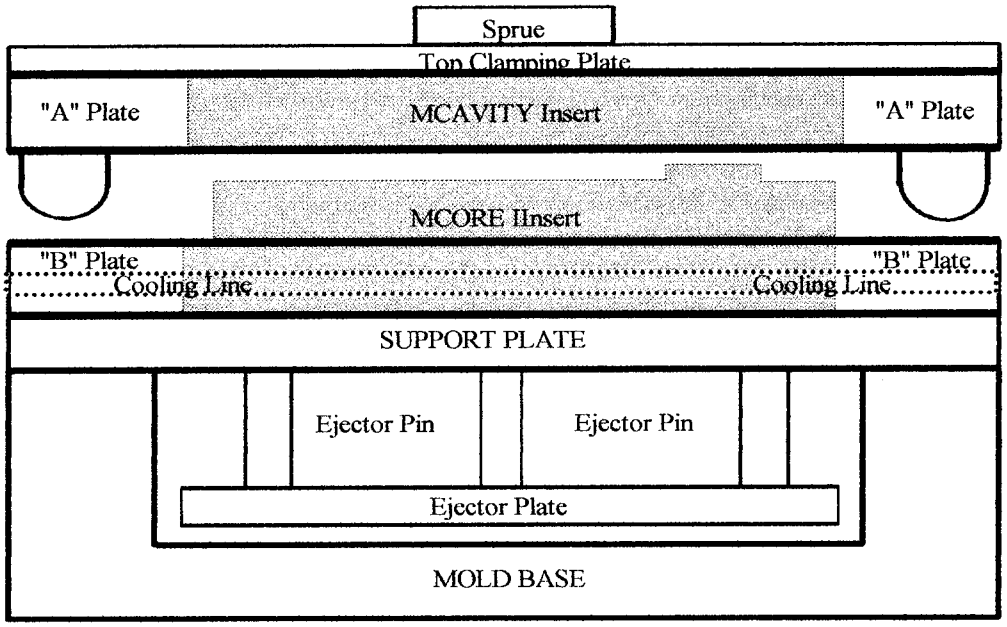

Figure 3

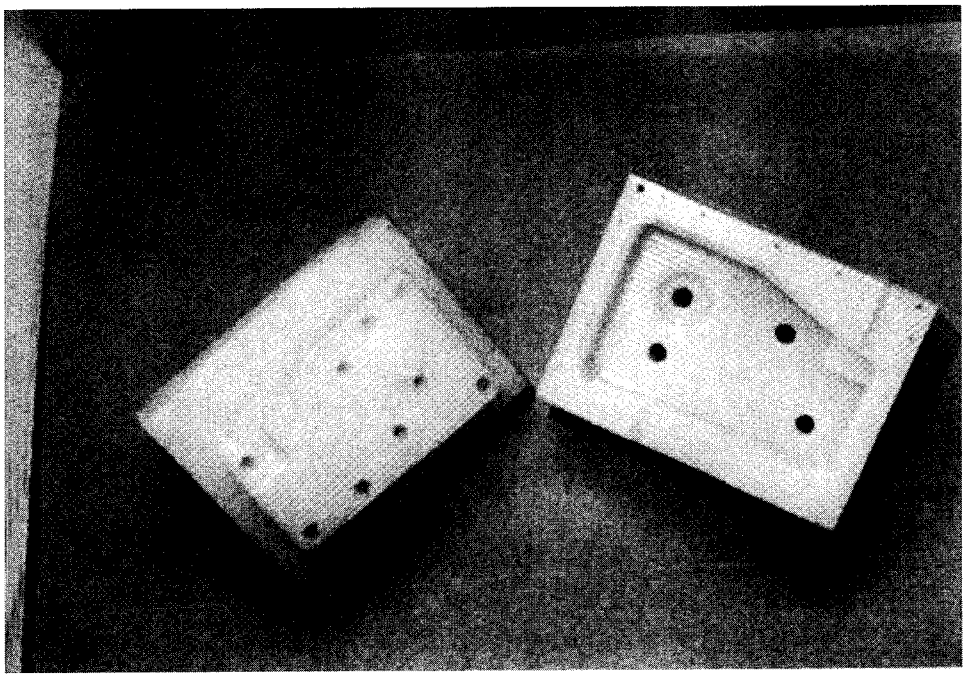

Figure 4: QuickCast core and cavity prior to investment casting.

QuickCast™ Patterns:

Creating the SL patterns was fairly straightforward using 3D Systems QuickCast build style. The build parameters are listed in Table 3. Some details should be mentioned concerning the build process. Three separate shrinkage factors are needed: the shrinkage factor of the final injection molded material (in this case polypropylene), the shrinkage factor of the StereoLithography resin (in this case XB 5170), and finally the shrinkage factor of the A2 tool steel. The latter was the hardest to determine as there was little data to be found on shell investment cast shrinkage factors for A2 tool steel. The best available information suggested a value of about 2% in all directions, although the exact value may be even slightly higher. Ford is currently running samples to determine the shrinkage factors of various tool steels, as well as other data including hardness, after shell investment casting.

Also, the blade gap is an important parameter when working with XB 5170 resin and building parts in the QuickCast style. As can be seen in Figure 5, the horizontal lines perpendicular to the vertical or "Z axis" build direction are a telltale sign of blade contact during the build process. By using the recommended blade gap in conjunction with the new and more accurate Diode Leveling Module, the accuracy of the pattern in the Z direction, as well as the repeatability of the layer thickness, are both greatly improved. Consequently, in this configuration the chances of a blade collision are significantly reduced.

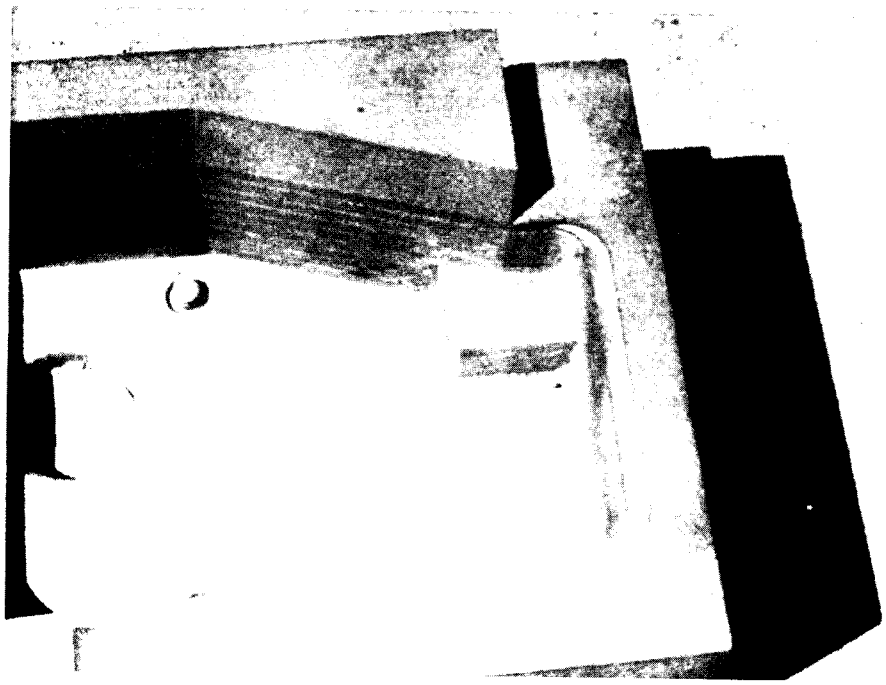

Figure 5: Vertical walls of the steel mold inserts. The layer shift is due to blade contact.

Investment Casting:

The QuickCast patterns were fully drained, cleaned, postcured, checked for the existence of any holes, and then shipped to Howmet Corporation, Whitehall, Michigan. They were then re-checked for holes at Howmet, and any pinholes missed earlier were filled with investment casting wax. The original patterns included the ejector pin holes. However, because this was Howmet's first time shell investment casting A2 tool steel, they felt more comfortable filling the ejector holes with wax; leaving only a small locating dimple. The ejector holes would presumably be drilled after the steel had solidified and cooled.

Subsequent to the patterns being gated and all holes being filled, the QuickCast patterns were cleaned and prepped for dipping. This included an alcohol wipe and a final check for any holes. The QuickCast patterns and their attached gates were then invested in a vat of very fine "face coat" ceramic slurry. After drying, the process is repeated with subsequent layers being sprinkled with refractory sand until the required ceramic shell thickness has been achieved.

On completion of the shell, the patterns, gates and ceramic shell assembly were then placed in a fully aspirated oven and fired at over 1800 °F for one hour, as described in references 6 through 10. This firing cures and strengthens the ceramic shell. It also simultaneously burns out the QuickCast pattern; provided sufficient oxygen is present for the efficient conversion of the hydrocarbon based resin to water vapor and carbon dioxide. After burn out was completed, the shells were checked for any small cracks or fractures. It was determined that in some areas the pattern had "stuck" to the walls of the ceramic face coat, causing some surface imperfections. However, these were relatively minor and could be accounted for in the final polishing of the tool.

Next, the ceramic shells were placed in an oven to preheat them prior to pouring steel. Howmet uses an induction coil to melt ingots of steel and pours the molten metal in a vacuum. After the steel was poured, the shells with the molten steel inside are placed in the open air to cool and harden.

As an interesting and potentially significant sidelight, the low thermal mass and relatively high surface-to-volume ratio of the shell investment casting process resulted in very rapid metal cooling and hence extremely hard tool steel core and cavity pairs. Furthermore, the high hardness was not just at the surface, but rather *it extended through the entire thickness of the mold inserts.* In fact, the resulting A2 tool steel was so hard that five carbide drill bits were dulled and rendered useless while attempting to drill the aforementioned ejector holes. Ultimately, the holes were drilled using diamond tipped bits. Quite obviously, in future QuickCast Tooling projects, any and all registration holes and or ejector pin holes will clearly *not* be filled with wax prior to casting. In fact, Figure 6 shows a hole that was accidentally created as the result of overheating while attempting to cut off the extremely hard A2 tool steel gating.

SLA Build Data

MCORE	
Description	Data
Build Time	48 Hours
Laser Power	
At Start of Build	36 mw
At End of Build	36 mw
X Shrink Comp:	2.06%
Y Shrink Comp:	2.06%
Z Shrink COmp:	2.00%
Part Build Style	QuickCast
	XFILL
Border Overcure	0.0070"
Hatch Overcure	0.0050"
Fill Cure Depth	0.0120"
Part Recoating	
Z Wait	15 Seconds
Pre Dip Delay	0
Post Dip Delay	1
Z Dip Velocity	0.2
Acceleration	0.2
Number of Sweeps	1
Sweep #1 Blade Gap	100%
Period	8
Support Style	Bridge Works
No Hatch	No Fill
All Over Cure Settings	0.0050"
Support Recoating	
Z Wait	9 Seconds
Pre Dip Delay	0
Post Dip Delay	1
Z Dip Velocity	0.2
Acceleration	0.2
No Sweeps	
3dverify information	
Unit	Inches
Volume	145.522
Number of Triangles	4092

MCAVITY*	
Description	Data
Build Time	48 Hours
Laser Power	
At Start of Build	36 mw
At End of Build	36 mw
X Shrink Comp:	2.06%
Y Shrink Comp:	2.06%
Z Shrink COmp:	2.00%
Part Build Style	QuickCast
	XFILL
Border Overcure	0.0070"
Hatch Overcure	0.0050"
Fill Cure Depth	0.0120"
Part Recoating	
Z Wait	15 Seconds
Pre Dip Delay	0
Post Dip Delay	1
Z Dip Velocity	0.2
Acceleration	0.2
Number of Sweeps	1
Sweep #1 Blade Gap	100%
Period	8
Support Style	Bridge Works
No Hatch	No Fill
All Over Cure Settings	0.0050"
Support Recoating	
Z Wait	9 Seconds
Pre Dip Delay	0
Post Dip Delay	1
Z Dip Velocity	0.2
Acceleration	0.2
No Sweeps	
3dverify information	
Unit	Inches
Volume	131.859
Number of Triangles	3510

* The part MCAVITY is a trapped volume and the first attempt at building the part failed. The solution was to place four half inch holes in the bottom of the part and fill them in with wax before casting.
For future tooling inserts more attention will be paid to the recoating parameters.

Table 3

Of potentially greater significance, however, is that the *increased hardness of investment cast tool steel,* relative to conventional billets of the same nominal material, may be of value in *extending the abrasion resistance and hence the life of production tooling.* Furthermore, it is quite possible that extended tool life can be achieved in this manner *without the need for additional heat treatment steps.* Heat treatment further increases tooling cost, extends tooling completion schedules, and can also lead to thermally induced distortion of the mold cavities, thereby requiring subsequent tooling rework and additional cost and time.

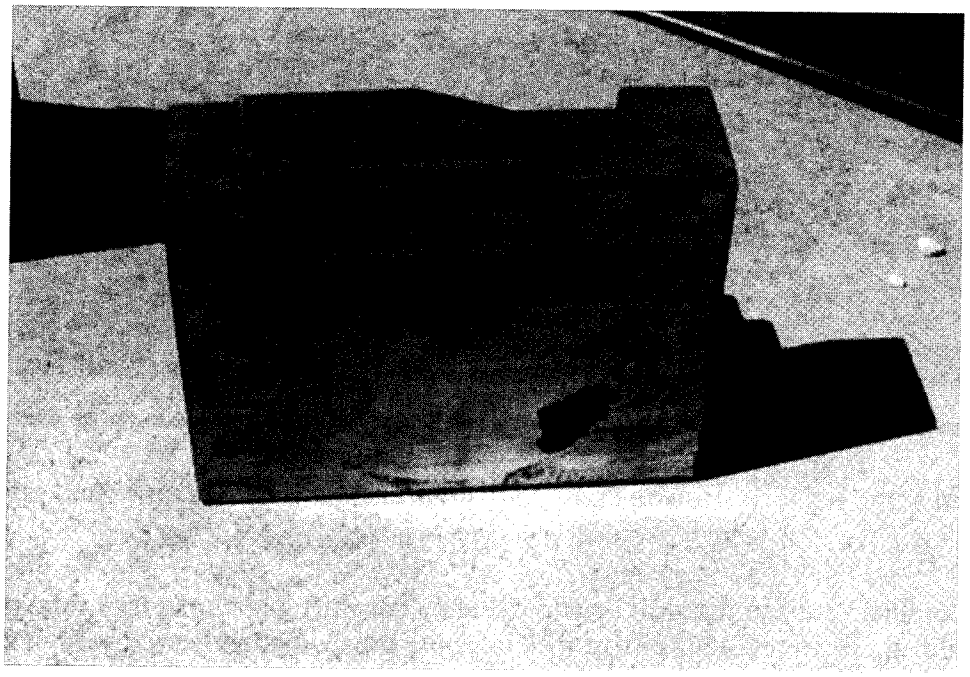

Figure 6: Core half showing a hole that was created while cutting off the pouring cup.

Tool Preparation and Injection Molding:

Upon completion of the investment casting portion of the project, the steel core and cavity inserts were forwarded to ATC Nymold Corporation, Brooklyn Heights, Ohio, for tooling preparation and injection molding of the Wiper Module Covers in polypropylene. Figure 7 is a photograph of the cavity mold insert surface, showing residual signs of the QuickCast triangular structure. This structure was present on the upfacing pattern surface and was later transferred to the tool steel insert during casting.

Further signs of surface degradation are evident in the radii also shown in Figure 7. It has been determined that during autoclave, the superheated steam not only melted out the wax gating and softened the QuickCast pattern as intended, but either the steam, or the alcohol used to clean the patterns, apparently also caused some sort of reaction with the still uncured ceramic shell material. This problem has subsequently been

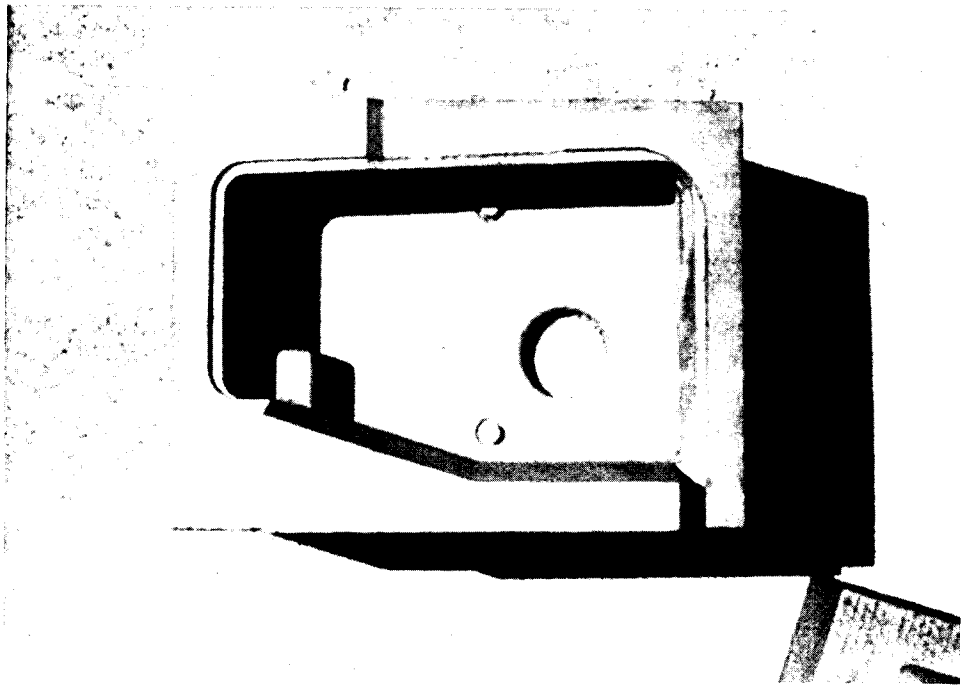

Figure 7: Surface finish of the cast steel inserts. The QuickCast pattern structure can be seen.

addressed at the foundry. Howmet now fully dries and cures the ceramic shell prior to autoclaving.

Another problem that will be addressed by Howmet is the matter of final pattern surface finish. Howmet believes that they can coat the QuickCast pattern with a very thin layer of wax prior to investing the face coat slurry. They believe that this will fill in the residual QuickCast triangulation pattern on the upfacing as well as the downfacing surfaces. However, because the thickness as well as the uniformity of this coating have not been studied at this time, the potential effect of this method on pattern accuracy is presently unknown.

The hardness of the cast pattern is an issue that requires careful attention. ATC Nymold reports that the hardness level of the shell investment castings were about 48 Rockwell C, or a full 18 points higher than the normal value for conventional A2 tool steel. This hardness level, although certainly desirable for the final tool, actually caused some problems in tool preparation. Figure 8 is a photograph of the core and cavity investment cast A2 tool steel mold inserts prior to surface finishing. On the core half a small indentation can be seen where one of the ejector holes was intended to be drilled, as noted earlier. The hole was only about 1/8 inch deep after breaking five carbide drill bits. Even after the holes were finally completed, using diamond tipped drill bits, ATC Nymold reported that these extraordinary hardness levels extended through the entire thickness of the part. They also reported that there were areas of exceptionally hard, brittle material they thought might be slag, although perhaps these regions are pockets of

steel that were super-cooled and are therefore even harder than the remainder of the castings.

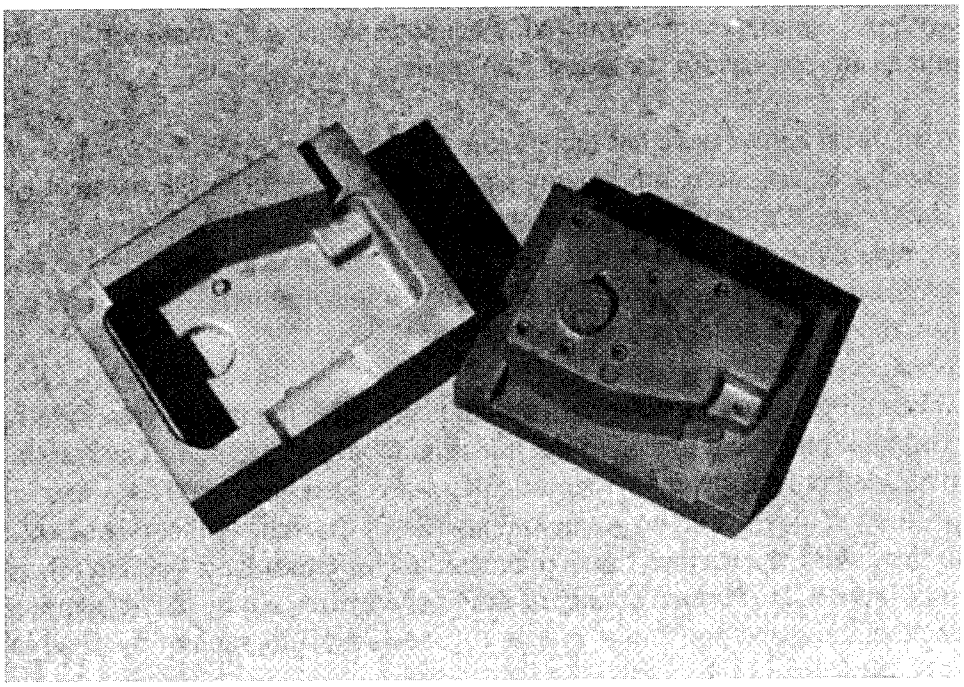

Figure 8: Mold core and cavity prior to surface finishing.

Three possibilities are evident to address the unusual problem of excessive tool steel hardness resulting from shell investment casting. The first, and perhaps the simplest, is to investigate the resulting investment cast hardness of other candidate steel alloys, and then select the optimum choice. Here one would want a material hard enough to insure long tool life, but not so hard as to impose special machining requirements on the finishing operations for the final tooling.

The second approach is to cool the casting in a programmable oven rather than the open air. In this way the casting temperature can be reduced more slowly and in a very controlled fashion to insure the desired metallurgical properties. Finally, one could also anneal the castings after the ceramic shell had been removed. However, this may prove to be the least desirable of the methods as the annealing process itself can lead to warpage of the inserts. Clearly, more work needs to be done to determine the best method of insuring optimal physical properties of the inserts consistent with the highest levels of accuracy in the shortest possible time and at the lowest cost.

Once the hardness issues were dealt with, the tool was fitted to the mold base. This also proved to be somewhat problematic because the two pieces were slightly different in size. The most probable explanation for the size difference was that the core and cavity were built in different orientations relative to the direction of recoater blade travel on the SLA-250. Although this is not normally a concern, the fact that contact

occurred with the recoater blade during build might account for the size difference. A second possibility is that the shrinkage factors for the A2 tool steel might have been geometry dependent and hence not totally uniform. Again, further work is definitely needed with respect to the determination of accurate shrinkage factors for the shell investment casting of various candidate tool steels.

Also, draft angles were not included in the original CAD model or in the subsequent QuickCast stereolithography patterns and the resulting investment cast mold inserts. Rather, the draft angles were subsequently machined after the steel inserts were cast. As a result, the mold inserts had uneven wall thickness values. The obvious answer to this problem is to apply all draft angles, fillets, radiuses, etc. to the CAD design well before the inserts are actually investment cast.

When all these issues were resolved and corrected, the inserts were finally installed on their bases and placed in the injection molding machine. The resultant injection molded polypropylene wiper module covers were then used for water leakage testing. Although they would be going into an area of the vehicle that would not be visible to the public, the surface finish prevented the modules from gaining release status. As seen in Figure 9, the surface quality of the final core and cavity halves required extensive machining and polishing. Figure 10 shows a photograph of the final injection molded polypropylene wiper module cover mounted on an actual wiper module.

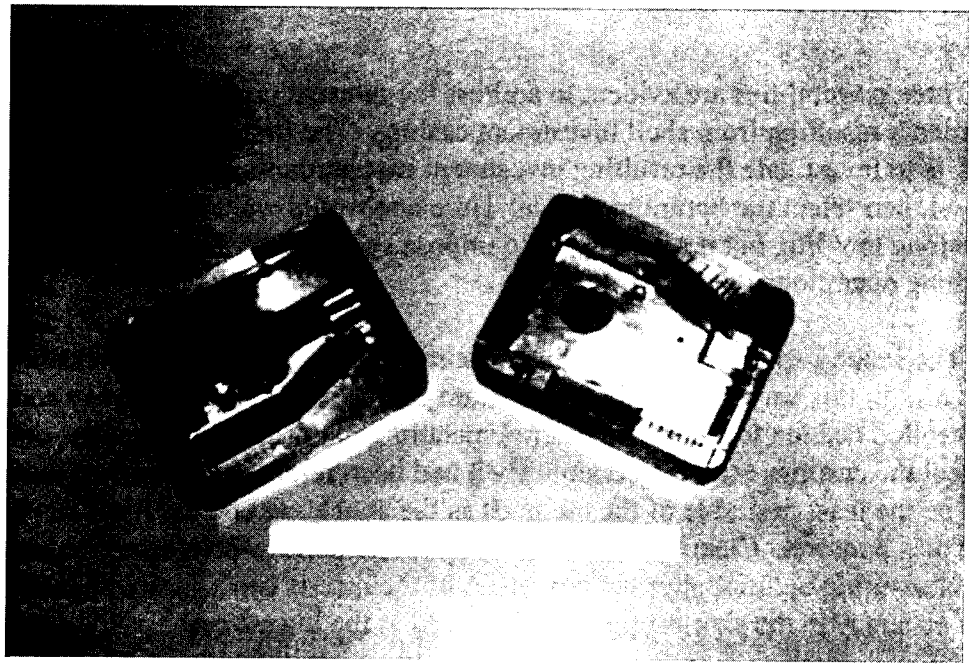

Figure 9: Mold core and cavity after surface finishing. Some areas of the QuickCast pattern were intentionally left unpolished.

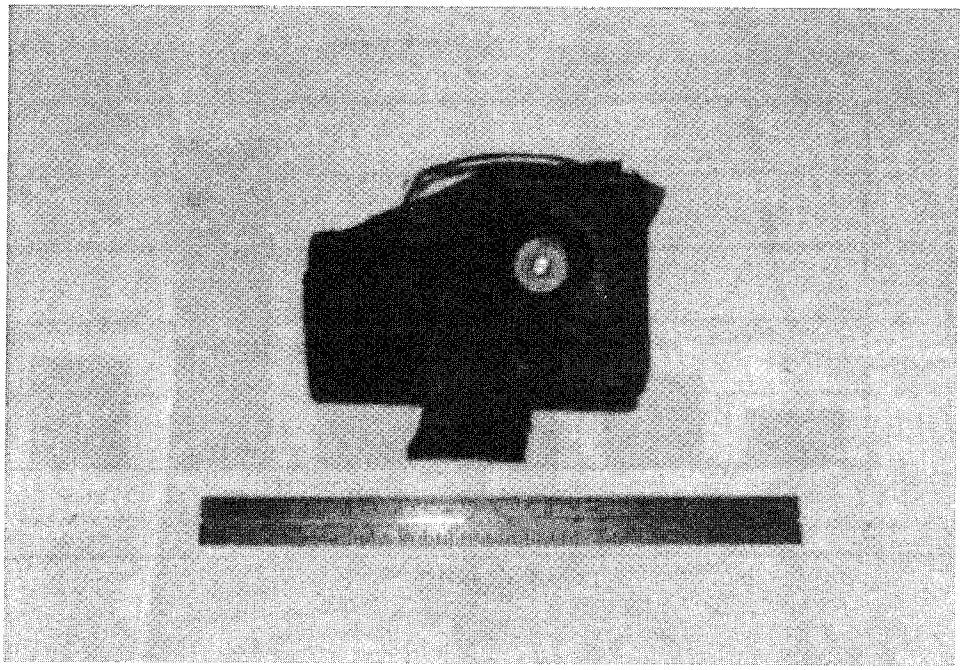

Figure 10: The final injection molded part mounted on a wiper module.

Figures 11 and 12 show Ford's estimates of the cost as well as the fabrication time required for various tooling fabrication techniques. The potential advantages of QuickCast Tooling through investment casting are clearly evident relative to conventional machined steel tooling. Figure 13 shows the actual cost and time comparisons experienced by Ford on this project. Remarkably, this data includes all the various problems associated with ascending the "learning curve" for the first time.

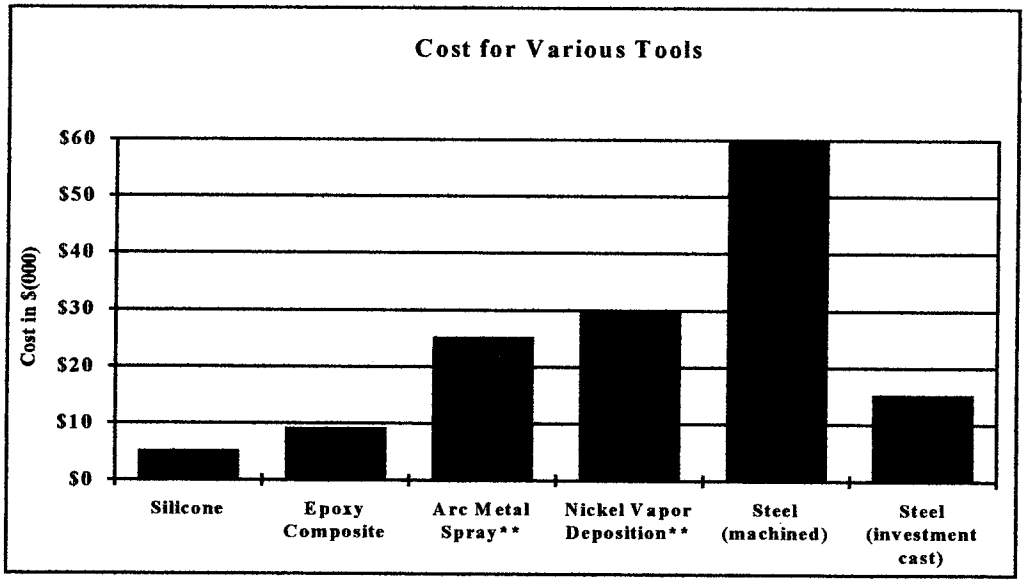

Figure 11

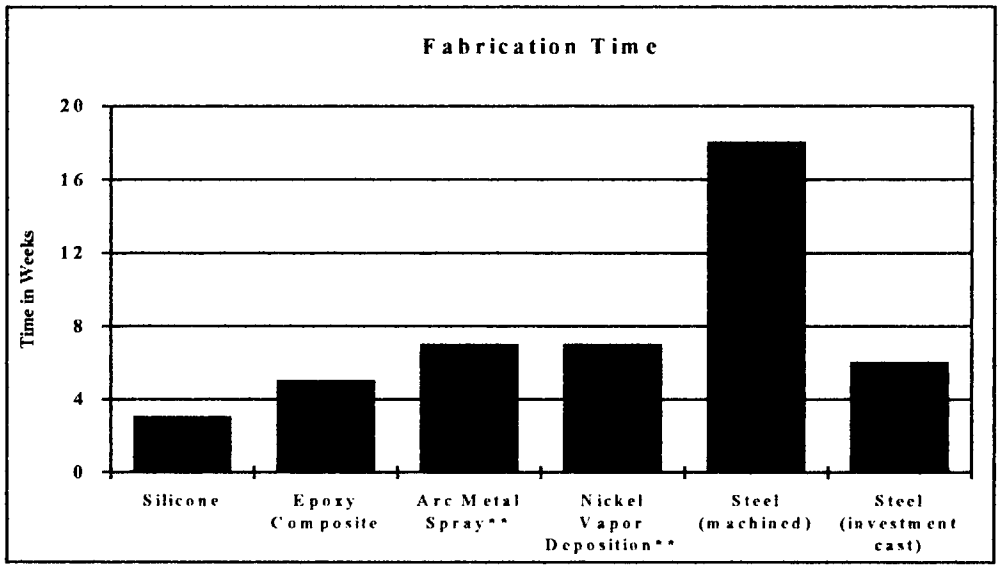

Figure 12

Figure 14 shows Ford's project plan for conventional tooling, while Figure 15 shows the actual results of the QuickCast Tooling project. Again, even with all the various "learning curve" delays, the time savings were noteworthy. Once the process is better defined, and additional information has been generated regarding the hardness as well as the shrinkage factors of various shell investment cast tool steel alloys, the time and cost savings relative to conventional tooling methods should be even more significant. Ford intends to monitor actual cost and time savings on at least two additional future projects, so that the potential advantages of Rapid Tooling can be more accurately assessed.

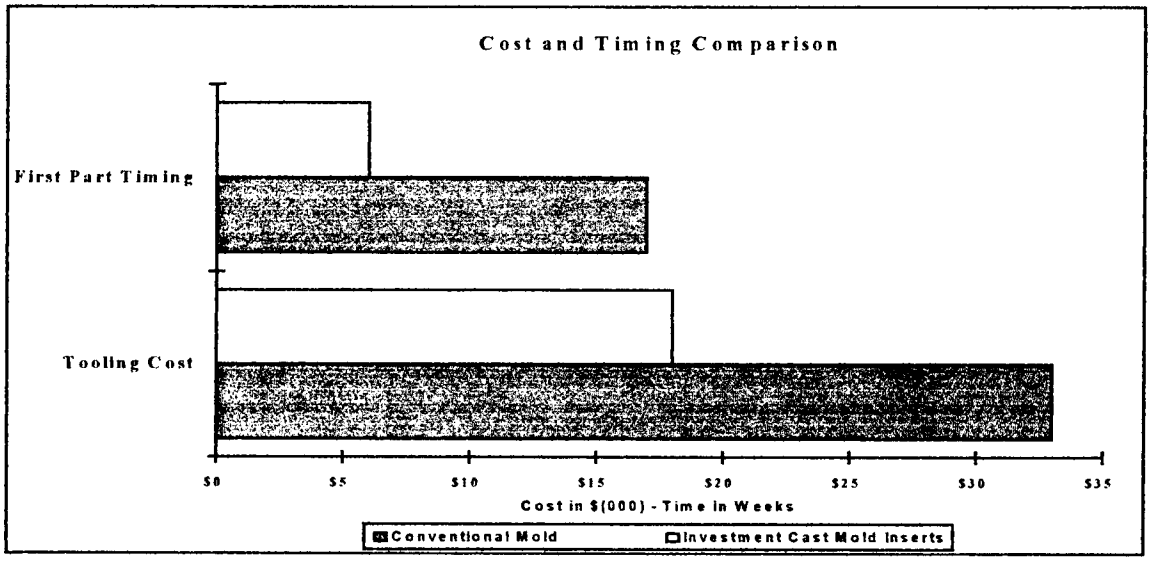

Figure 13

Timing Plan for Explorer Rear Wiper Motor Water Shield
Conventional Tooling

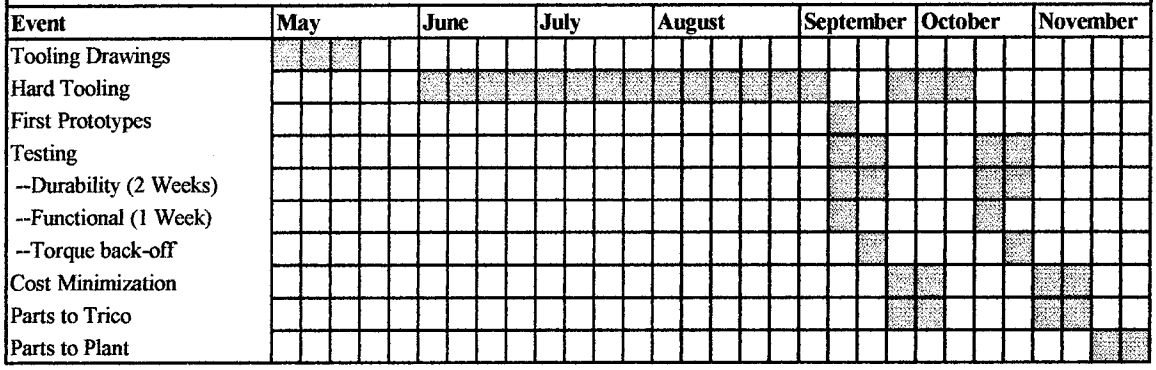

Figure 14

Timing Plan for Explorer Rear Wiper Motor Water Shield
Investment Cast Tooling Inserts

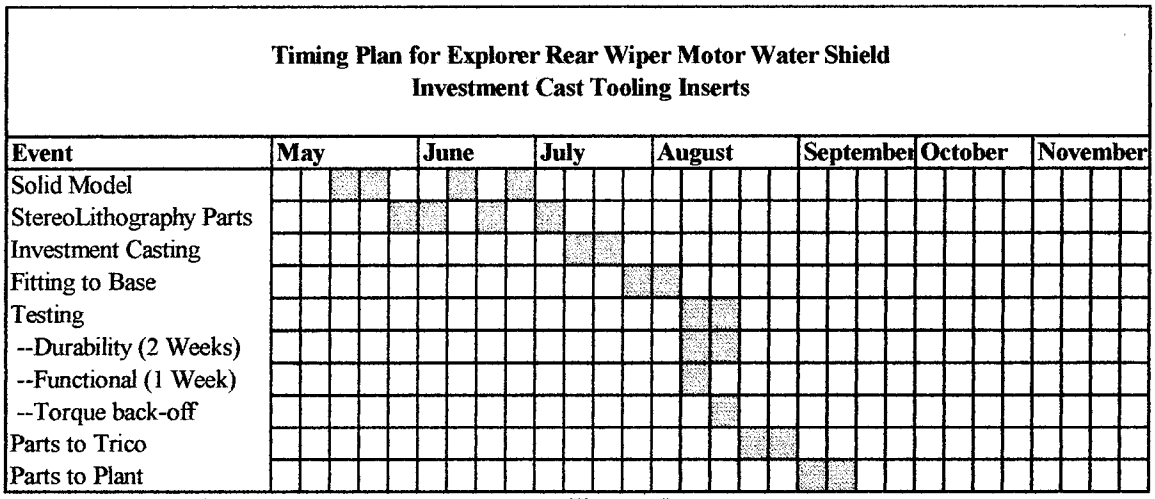

Figure 15

Conclusions:

With all the numbers laid out, and all the photographs, tables and comparison figures in place, the question still comes to mind.....was this project successful? The answer is *most definitely yes!* When the project was started at Ford, the goal was to produce a part capable of being tested under realistic conditions while being fabricated from production material. A secondary goal was the possibility of using the resulting tooling for production run quantities. While we will not use the "first" rapid tool for production, we do intend to use subsequent QuickCast Tooling for actual production. Undoubtedly, the first QuickCast Tool will ultimately become a conversation piece. Nonetheless, its value should not be understated. This project has already changed Ford's thinking about providing parts to our testing facility as well as the way we will

ultimately manufacture production run parts. From this first experience with investment cast tooling, the groundwork has definitely been laid. At this time, Ford has already authorized at least two additional QuickCast Tooling projects.

There are three areas where further research must be completed before we can consistently produce quality rapid tooling. First, the surface finish of the QuickCast patterns as well as the final investment castings must be improved. In this regard, 3D Systems has already developed and is now in the test and evaluation phase of an advanced version of QuickCast that directly addresses the issues of improved upfacing, downfacing and vertical surface quality, as well as the elimination of pinholes during support removal.

Second, is the matter of tool hardness. As discussed above, more data is needed on the hardness of shell investment cast steel alloys as a function of cooling rate. Additional data on shrinkage, tensile properties, abrasion resistance, etc. are also needed to better understand the relationship between cast and cut tool life. Ford and 3D will be actively working with a number of foundries to obtain such data. Assistance from other parties interested in developing a comprehensive data base would certainly be welcome.

Third, we must establish realistic cost and time estimates for QuickCast Tooling. Obviously, the project described in this paper is only the beginning. While we were able to produce these tools in a relatively short time, further reductions are definitely possible. However, because investment casting foundries have been used to the long lead times and large quantities of the aerospace industry, this may be viewed as typical. In the automotive industry we do not produce great numbers of investment castings, but we might use a smaller number of investment cast tools to injection mold very large quantities of mass produced products.

In conclusion, we believe this project has proven that QuickCast Tooling can work. With the creative thinking and energy that has typified the RP&M industry, this project can be considered to be the beginning of a very significant new application. As noted herein, much work remains to be done. However, we also believe that in the future Rapid Tooling will have a major impact upon manufacturing productivity.

Note: QuickCast is a trademark of 3D Systems, Inc.

References:

1. Hull, Charles., Apparatus for Production of Three-Dimensional Objects by StereoLithography, U.S. Patent 4,575,330, March 11, 1986.

2. Jacobs, Paul., Chapter 1 of "*Rapid Prototyping & Manufacturing: Fundamentals of StereoLithography*", SME, Dearborn, MI,. July 1992.

3. Richter, Jan and Jacobs, Paul., Chapter 11, op. cit.

4. Blake, Paul and Baumgardner, Owen., Chapter 12, op.cit.

5. Schmidt, Lavern and Phillips, Lee., Chapter 13, op. cit.

6. Jacobs, Paul and Kennerknecht, Steve., "StereoLithography 1993: Epoxy Resins, Improved Accuracy and Investment Casting", SME Rapid Prototyping & Manufacturing '93 Conference, May 11-13, Dearborn, MI.

7. Jacobs, Paul., "Recommended Foundry Procedure for Shell Investment Casting Using QuickCast™ StereoLithography Patterns", from 3D Systems "Foundry Reports", April 1993.

8. Kennerknecht, Steve., "StereoLithography Based Rapid Prototyping for Aluminum Investment Casting using QuickCast™ ", Ibid., April 1993.

9. Smith, Jeff and Hanslits, Mike., "Allied Signal Impeller Shroud: A Rapid Prototype Pattern Evaluation for Investment Casting", Ibid., April 1993.

10. André, Larry., "QuickCast™, an Adventure", Ibid., April 1993.

Participants:

Ford Motor Company
Karl R. Denton
20000 Rotunda Drive
P.O. Box 2053
Body Engineering Building - Room 2019
Dearborn, MI 48121
(313)322-0960 Fax:(313)845-8216

Laserform, Inc.
David Tait
1124 Centre Road
Auburn Hills, MI 48326
(810)373-4400 Fax:(810)373-4403

Howmet Corporation
Keith Ramthun
Operhall Research Center
1500 South Warner
Whitehall, MI 49461-1895
(616)894-7984 Fax:(616)894-7826

ATC Nymold Corporation
Sanjeev Gaikwad
4626 Spring Road
Brooklyn Heights, OH 44131
(216)741-4735 Fax:(216)741-4308

3D Systems, Inc.
Paul Jacobs
26081 Avenue Hall
Valencia, CA 91355
(805)295-5600 Fax(805)257-1200

Integration of Numerical Modeling and Laser Sintering with Investment Casting

T. Pintat*, M. Sindel*, M. Greul*, A. Burblies* and C. Wilkening**
* Fraunhofer-Institut für Angewandte Materialforschung, Bremen
**EOS, München

Abstract

Industry has a great demand for metallic prototypes to speed up product development. At present there are several RP-technologies for direct fabrication of metal components in development. Today secondary processing of polymer or wax models, like investment casting or sand casting, is a very common way for the production of metallic prototypes.
There are, however, several problems in investment casting resulting from laser sintered models made of wax or polycarbonate.
Recently a polymer mixture consisting of nylon material and a second polymer has been tested with the laser sinter process in a newly developed sinter machine (EOSINT 350 - 60). Shells for investment casting could be prepared easily with the models in a conventional assembly-line. Several castings of laser sintered models in Al were successfully realized.
In future, integration of modeling based on FEM calculations with RP for castings will become more important. Calculations will support the designer to optimize the structure of components and their processing. A viable method will be presented where a new FEM based calculation method to optimize the structure design of a model is integrated with RP. Optimizing castings with FEM will be supported by integration with RP.

Introduction

Investment casting of laser sintered models

Different casting companies have experiences with casting of wax and polycarbonate models, however, there is no systematic report on investment casting of laser sintered models. Generally wax models are fragile and distore easily, hence polycarbonate models are preferred. Investment casting needs special preparations of polycarbonate models using traditional pattern-making techniques to successfully cast the model /1/. Problems can arise from surface penetration of slurry during shell making, hence the surface needs to be completely sealed. Some casting companies have problems with polycarbonate models during the autoclave process. The material can produce foam during the conventional autoclave process which can cause cracking of the shell /2/.

Integration of modeling with Rapid Prototyping

Simulation as a tool for designers is more effective when it is integrated into the design process from the very beginning. This is true for product as well as process design. Integration of modeling with Rapid Prototyping supports concurrent engineering. A concurrent approach is information driven and relies on computer technology. Computer-aided design, mold filling and solidification simulation and finite element stress analysis are means of modeling castings. Interfacing the output of modeling with RP allows the simultaneous production of an optimized model /3/.

Experimental

Laser sintering and casting

The powder material used is a mixture of Nylon 11 and a second componenet. A micrograph of the powder is shown in Fig. 1. The two components were mixed in a conventional tumbling mixer, different compositions were tested.
Sintering was done with the newly developed EOSINT 350 sinter machine, which is capable of building parts as large as 34 x 34 x 59 cm. The machine is equipped with a 50 W CO_2 laser, the focal diameter is < 0,5 mm and the scan rate is up to 2 m/s. Resolution of the laser beam positioning in x and y is 0.015 mm and accuracy 0.1 mm. The vertical positioning accuracy is 0.05 and the resolution 0.01 mm. Layer thickness can be varied between 0.1 and 0.2 mm. Fig. 2 shows the EOSINT unit.
Burning out of the model and casting was realised in the investment casting assembly line of Thyssen-Feinguß. The standard procedure of autoclave processing at 170 °C and subsequent shell firing was followed. Casting was done in Al-alloy. Usually the castings were finished using sand blasting.

Numerical optimization for lightweight castings and integration with RP

Lightweight castings is an option for weight reduction and optimized materials service. A new numerical modeling method was selected to calculate optimized structures. The FEM based calculation, recently developed by Mattheck et al. /4/ and named SKO (soft kill option) method, simulates a biological optimization. It has the potential to refine structures in a lightweight design. The optimization is similar to adaptive bone mineralization. Bones are able to change their degree of mineralization according to a change in their mechanical loading.
Stresses are calculated by FEM in a selected design area with a constant Young´s modulus over the whole area. Then the Young´s modulus is varied as a function of stresses. In a next step a new stress distribution is calculated with the varied Young´s modulus distribution. The repeated application of this procedure leads to distinguished regions of high and low Young's modulus. Eventually non-loaded parts are removed from the structure. The final result is a design with a minimum weight. Fig. 3 shows an application of this method on a rectangular bar with two supports under a single load /5/.
In order to transfer the optimized structure data directly into the STL format special software was developed at IFAM. Optimized components can be subsequently built as a RP models and investment casted.

Results and Discussions

Laser sintering of the nylon/polymer mixture and casting

The powder mixture contains nylon and a second polymer, where the nylon material has a different thermal behavior. Due to this difference one component compensates expansion of the other during heating. This is the key for very successful melting and burning out of the material during the autoclave process for investment casting. Due to special scan strategies of the laser beam the surface can be sealed, while the inner of the component is still porous. A successful investment casting and the laser sintered model is shown in Fig. 4

Numerical modeling and integration with RP

As an example a roof structure was optimized by SKO method. The data of the optimized structure were converted into STL-format and a model was built. The model and the casting are shown in Fig. 5. The casting can be used as a functional prototype to immediately test the feasibility of the new design in service. This example shows how new design concepts can be tested very rapidly by integration with RP. Further development is necessary to transfer the method to real world, i.e. a total integration of the modeling software in a CAD environment.

Acknowledgements

C. Mattheck (KfK, Institut für Materialforschung II, Karlsruhe) kindly provided the FEM calculations and structure data. G. Peter (IFAM, Bremen) developed the software to get the STL-format from the FEM mesh.

References

/1/ Rapid Prototyping Report, 4 (1994), 4, p. 1-2

/2/ Private Communications with U. Schneider, Thyssen Casting, Soest

/3/ K. F. Packer, "Concurrent Engineering in the Casting Industry", Global Cast Metals Newsletter published by The Knight International Cast Metals Practice Committee, Feb. 1994

/4/ C. Mattheck and A. Baumgartner, "CAO & SKO: Fatigue-resistant engineering design by simulation of biological optimization mechanism, Experimental Mechanics, ed by E. G. Little, Elsevier, 1992

/5/ C. Mattheck, "Design in der Natur", Rombach, Freiburg i.B., 1992, S.51

Fig. 1: Polymer powder mixture used for laser sintering for investment casting

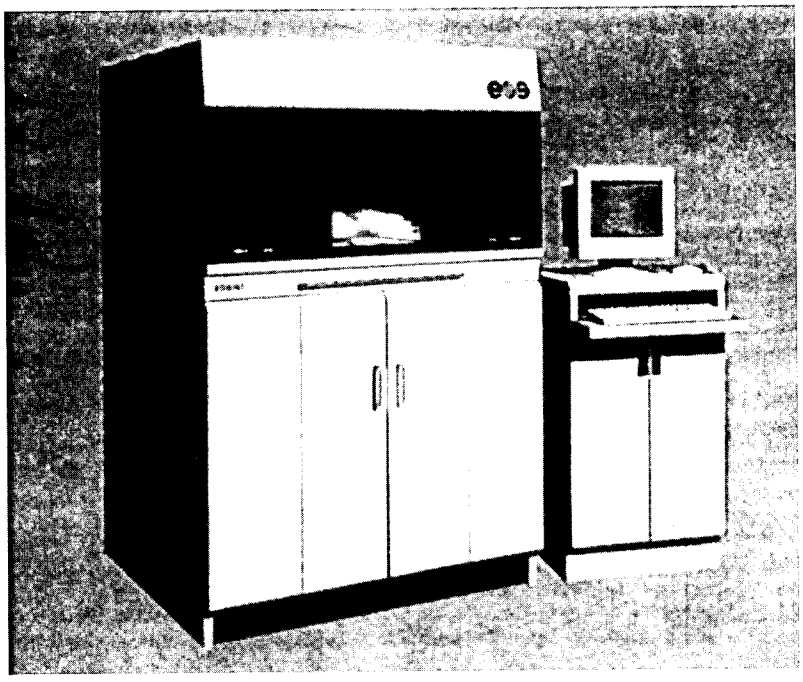

Fig. 2: Laser sinter machine 350-60 from EOS

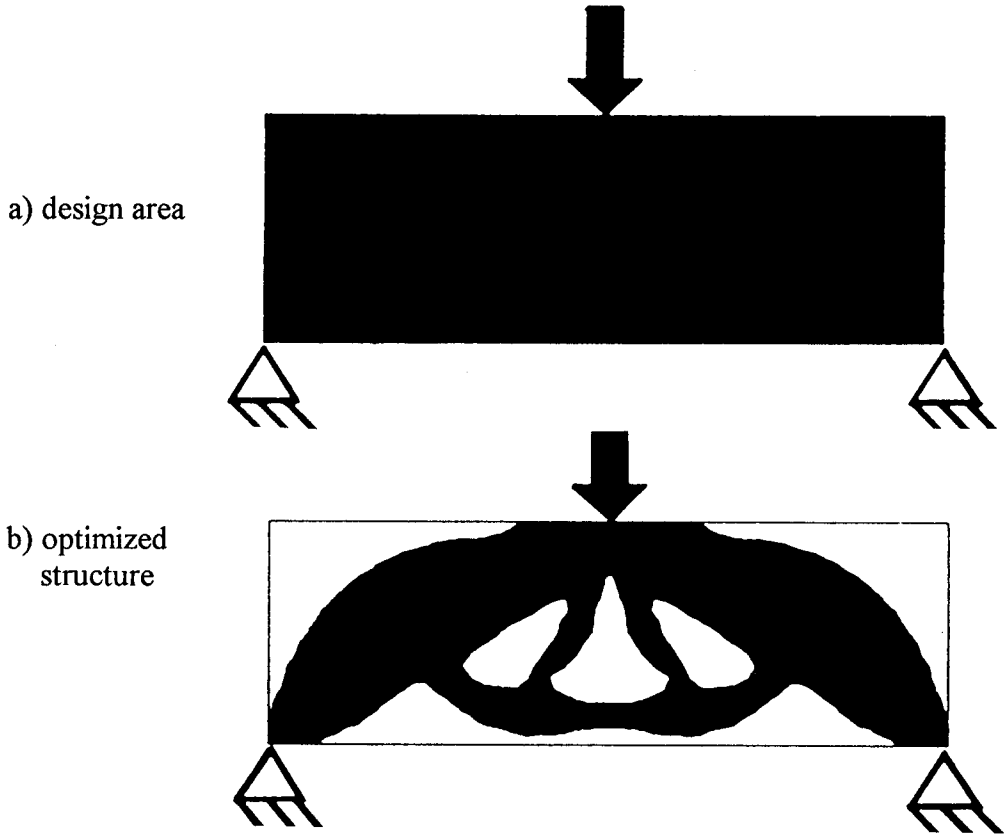

Fig. 3: Rectangular bar with a single load on top (a), and optimized shape after the SKO-calculation (b)

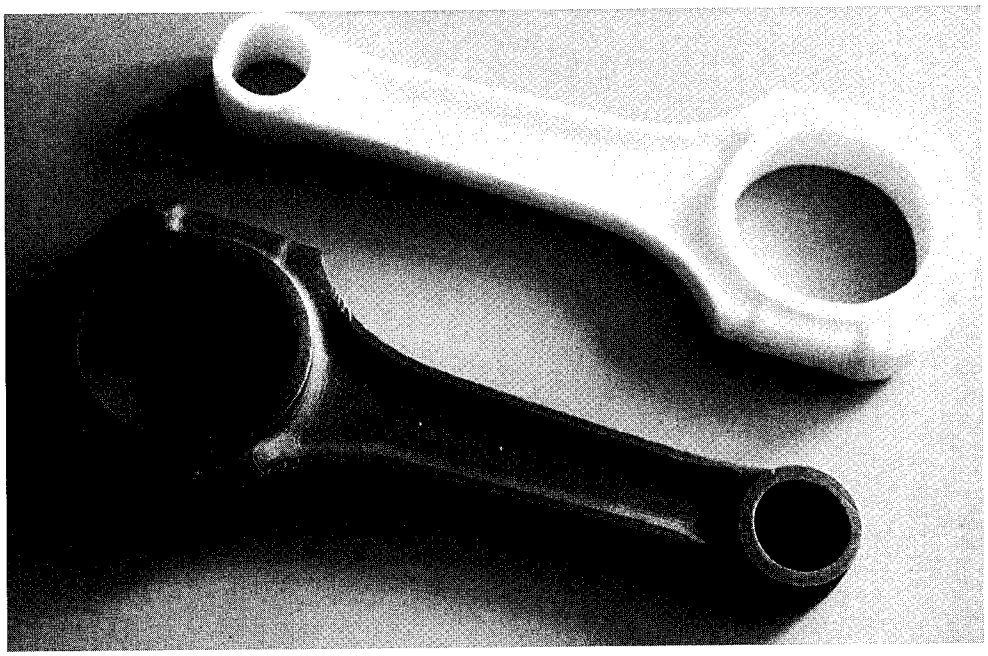

Fig. 4: Laser sintered model of a connecting rod out of the polymer mixture and investmet casting in Al

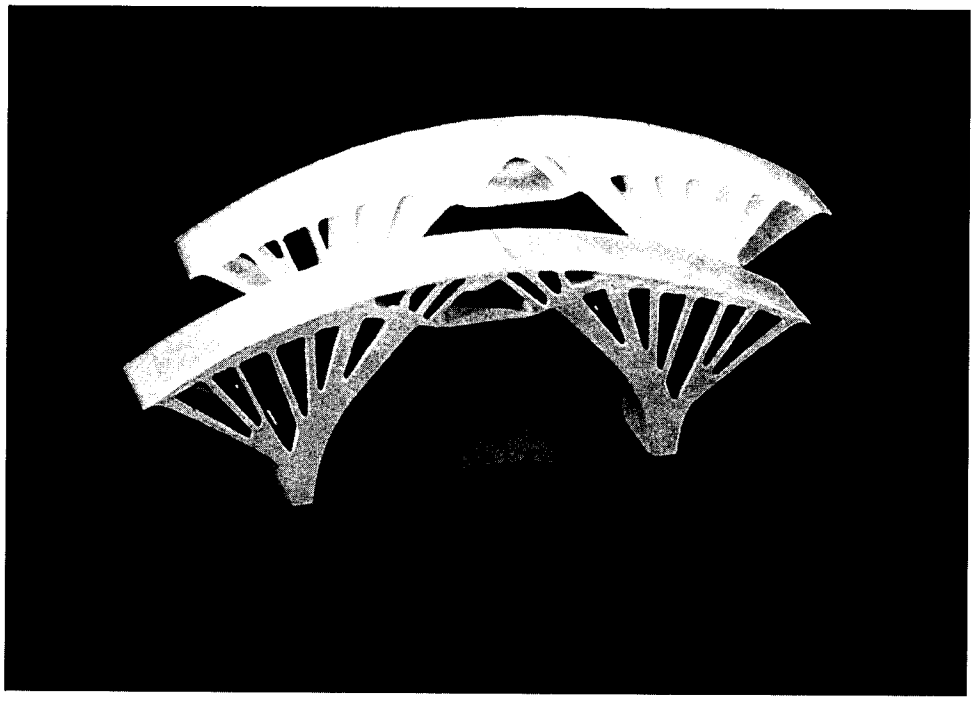

Fig. 5: RP-model built from converted data of the FEM-calculation and investment casting out of Al.

Computer-derived microstructures by 3D Printing: Bio- and Structural Materials

M.J. Cima[1], E. Sachs[2], L.G. Cima[3], J. Yoo[1], S. Khanuja[1], S.W. Borland[3], B. Wu[1,4], and R.A. Giordano[5]

[1] Department of Materials Science and Engineering, Massachusetts Institute of Technology, Cambridge, MA

[2] Department of Mechanical Engineering, Massachusetts Institute of Technology, Cambridge, MA, USA

[3] Department of Chemical Engineering, Massachusetts Institute of Technology, Cambridge, MA

[4] Department of Prosthetic Dentistry, Harvard School of Dental Medicine. Boston, MA

[5] Department of Biomaterials, Boston University Goldman School of Dental Medicine, Boston. MA

Abstract

3D Printing is a rapid prototyping technique to manufacture functional components directly from computer models. The process involves spreading the powder in thin layers and then selective binding of the powder using a technology similar to ink-jet printing. Layers are added sequentially until a part is completed. 3DP has been used to make complex-shaped components from several monolithic materials, including components for use in structural applications. This paper focuses, however, on the ability to control microstructure and local composition by 3DP. We envision cases where computer derived-microstructures can be created by appropriate control of the printing parameters. Thus, one can build components with the desired microstructure independent of the complexity of the desired shape. Examples for both structural materials and biomedical devices are discussed.

Introduction

Three Dimensional Printing (3DP) is a solid free-form fabrication (SFF) method used to create components directly from CAD representations and has been described in several publications[1-3]. Briefly, 3DP creates parts by a layered printing process. The information for each layer is obtained by applying a slicing algorithm to the computer model of the part. An individual two-dimensional layer is created by adding a layer of powder to the top of a piston and cylinder containing a powder bed and the part being fabricated. The new powder layer is selectively joined where the part is to be formed by "ink-jet" printing of a binder material. The piston, powder bed and part are lowered and a new layer of powder is spread out and selectively joined. The layering process is repeated until the part is completely printed. Removal of the unbound powder reveals the fabricated part. The process has been primarily applied to ceramic molds for metal casting. More recently, however, it has been used to make metal parts directly[4], structural ceramic parts[5], and polymer parts[6].

3DP is one of the most flexible SFF technologies. The process can create parts of any geometry, including internal volumes (as long as there is a hole for the loose powder to escape). The support gained from the powder bed means that overhangs, undercuts, and internal volumes can be created. 3D Printing can form any material that can be obtained as a powder. Further, because different materials can be dispensed by different printheads, 3D printing can exercise control over local material composition. Material can be deposited as particulate matter in a liquid vehicle, as dissolved matter in a liquid carrier, or as molten matter. The proper placement of droplets can be used to create surfaces of controlled texture and to control the internal microstructure of the printed part.

The ability to control local composition is a unique feature of 3DP and is the major focus of this article. This type of control permits fabrication of materials with computer derived microstructures or spatially controlled compositions (SCC). These are components in which their microstructure is designed on a computer and built via the 3DP process. 3DP can selectively deposit matter within the structure of a component so that composition can vary from point to point. The macroscopic shape of the component can, however, be specified completely independently. Thus, we envision components where both the macrostructure and microstructure are designed by computer and constructed by 3DP. Potential applications of such a technology are numerous, such as components with anisotropic mechanical properties, microengineered porosity, or constructing composite multilayer modules for electronic packaging. Conventional powder forming technologies cannot provide simultaneous microstructure and macrostructure control. Thus, demonstration of this approach will be a quantum leap beyond current material fabrication and will create a technology that is not unlike the control that photolithography provided the electronics industry.

Structural ceramic components

We have recently modified the 3DP process under ARPA/ONR support to produce alumina components which are greater than 99.3% dense after firing and have average flexural strength of 360 MPa[7]. Sintered silicon nitride parts with average flexural strengths of 570 MPa have also been made by 3DP[8]. The basic elements of the modified process are to spread submicron alumina powder and print latex binder. Green parts are isostatically pressed and sintered to densify the component. The polymeric binder is removed by thermal decomposition prior to sintering.

SCC for structural materials can have many benefits and unusual features. For example, gradual blending of materials with different coefficient of thermal expansion (CTE) is possible with 3DP. Metal parts with surfaces that are ceramic-rich can be made for high temperature applications or for improved wear resistance. Internal residual stresses can be modified with second phases to strengthen or toughen materials. These are just few of the possible applications of 3DP in SCC.

The current 3DP process involves printing of continuous binder jet onto powder bed. Consequently, the ability to prepare a stable dispersion becomes a determining factor for the size and amount of particulate second phase in the final part. Agglomeration in the binder system causes improper nozzle performance and reduces dimensional accuracy and

resolution. Khanuja has established a preparation and filtration scheme for fine alumina dispersion.[9] In his study, electrostatically stabilized submicron alumina dispersions were tested. Alumina slurry with up to 40% in volume has been successfully dispensed through typical nozzle for 3DP. Calculations indicate that the maximum volume fraction of second phase that can have come through nozzle with the current 3DP process is 30 vol% of final parts. However, modifications to the process routes such as the multiple printing cycle per layer and use of porous powder bed may allow the fabrication of parts with larger amounts of second phase.

Zirconia toughened alumina (ZTA) system was chosen as the first model composite system and this system requires only 15 to 20% zirconia dispersed in alumina to attain optimum strength[10]. Fine zirconia particle size and narrow size distribution is also required. These requirements match precisely with the capabilities of current 3DP technology. Simple calculations suggest that one only needs to prepare a zirconia slurry of 12.5 vol% solids loading to fabricate parts with 15 vol% zirconia. Khanuja's success with printing 40 vol% alumina slurries suggest a high probability of success with 15 vol% zirconia system. This makes the ZTA system as a perfect candidate for the first SCC system to be explored by 3DP.

ZTA consists of fine, uniformly dispersed zirconia particles in the matrix of alumina. The unusual phase change in zirconia upon cooling

$$ZrO_{2\ \text{tetragonal}} \Leftrightarrow ZrO_{2\ \text{monoclinic}}\ (1170°C)$$

is the basis of the toughening mechanism in this material system. Three to five percent increase in volume and shear accompanies the tetragonal to monoclinic phase transformation. The high strength and toughness of ZTA are results of absorbed energy during the phase transformation of zirconia particles around the crack tip. The fracture energy required to propagate the crack front increases due to the transformation. Volume expansion of the precipitates also causes strengthening[11]. Expanded monoclinic precipitates cause compressive stress build up on the crack tip. Surface grinding of a ZTA part induces the phase transformation near the surface and leads to residual compressive stress[12]. Various techniques developed to fabricate ZTA with thermally inert compressive surfaces include heat treatments in destabilizing atmosphere and surface coating steps[13-18]. Often these processes require prolonged heat treatments and present manufacturability concerns. 3DP technology can be implemented to fabricate ZTA with built in compressive layer by exercising the spatial control of composition.

3DP can be used to deposit zirconia slurry onto a bed of alumina powder to create a green ZTA part with controlled zirconia distribution. Realization of this concept is illustrated in Figure 1. Cross sections of each line printed with 5 vol% zirconia demonstrates 3DP's ability to control the zirconia content in microstructural level. Although Figure 1 shows the first ZTA part with only one zirconia composition, two or more nozzles can be used to deposit zirconia slurries of different stabilizer contents. For example, pure zirconia slurry can be printed in the regions where spontaneous transformation to monoclinic phase is desired. Yttria doped zirconia may be deposited in the rest of the part where the presence of metastable tetragonal phase is preferred. Thus, ZTA parts with user specified residual stress profile can be fabricated by manipulation of

the 3DP process. such as those with surface compression stresses or with a duplex ZTA microsturcture.

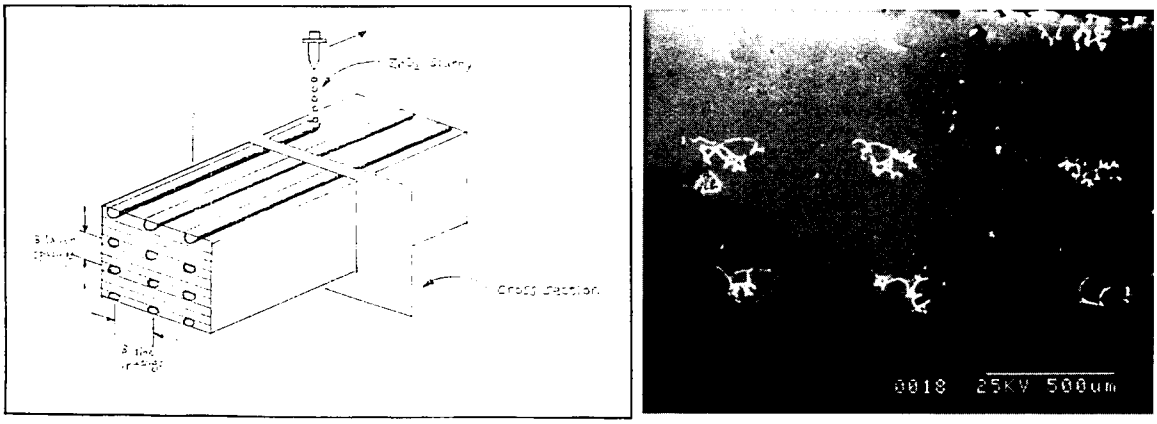

Figure 1: Schematic of the first 3DP-derived ZTA part is shown on left. 5 vol. % ZrO_2 slurry was printed on Al_2O_3 powder. A cross-section of the CIPed and fired sample is also shown. Each bright feature is a cross-section of a printed line.

Advanced materials for medical devices

Computer-derived microstructures such as for SCC and functionally gradient materials (FGM) have several medical applications such as drug delivery devices and structures for tissue regeneration. Our focus has been to demonstrate use of biomedical polymers with the 3DP process for both of these applications[6,19]. Attempts to control drug release rates of implantable and oral drug delivery devices (DDD) by manipulating the geometric structure of the devices have been reported. Cylindrical rods with internal pie shapes, inwardly-releasing hemispheres, and cylindrical donuts, represent attempts to affect release rates by modifying macroscopic shape[20]. These complex shapes are, however, not easily produced by conventional methods. Conventional manufacturing techniques also tend to produce homogeneous blends of the drug and matrix material[21]. The ability to control local composition, microstructure, and spatial distribution of drugs, makes 3DP a viable processing technique for construction of DDD. Prescriptive dosage regime DDD with controlled gradients in drug composition and matrix microstructure can be created by 3DP. The mechanism of resorption can be controlled by selecting the appropriate binder material.

Tissue regeneration devices are structures used as the matrix for tissue growth during healing. These devices are proposed for use in cases where natural tissues have been damaged by disease or trauma. Generally these materials are resorbable and ultimately become natural tissue, such as skin, cartilage, bone, and organ tissue. Medical procedures based on this approach are being developed for a number of applications. Numerous authors[22-25] have reported that optimal devices require control of their structure over several levels of structural hierarchy, including gross macroscopic shape, oriented pores

and channels, and microporosity. The ability to preferentially promote cell migration and angiogenesis, for example, can be accomplished by directing nutrient delivery in a complex cell seeding structure. Precise structural control beyond random microporosity has not been achieved by conventional processing methods. The potential to also intimately control the orientation and placement of porous channels and the overall macroscopic shape of a device makes 3DP an ideal process for producing tissue regeneration devices. Below we describe several devices that demonstrate reticulated structures.

Polyethylene oxide (PEO) and polycaprolactone (PCL) are selected as matrix materials for trial experiments and methylene blue and alizarin yellow were used as drug models. The dye release kinetics is controlled by either specifying the position of the dye within the device or by controlling the local microstructure with the 3DP process. The dye release rates of the devices are characterized by placing single devices into individual beakers filled with 10 ml water at room temperature (20°C). Sample solutions are collected, and fresh 10 ml of water is replaced at appropriate time intervals. Absorbance for methylene blue (664 nm) and alizarin yellow (353 nm) is measured for all samples on a DU-640 spectrophotometer. Spectrophotometric analysis of dye release yielded reproducible results. Three examples are described below.

The model device used for this study is designed to demonstrate regulation of drug release profiles by controlling position, composition, and microstructure. A diagram of the device is shown in Figure 2a. The top and bottom of the tabular device are composed of relatively nonresorbable PCL while the interior layers are composed of PEO bound by printing binders solutions so as to form perpendicular walls in the interior of the device. Dyes are deposited in selected locations within the device during the build procedure. The top and bottom sheets of dense PCL serve as barriers against dye diffusion since hydrolytic degradation of PCL occurs much slower than that of PEO. Therefore dye diffusion during resorption is confined to the plane of the device since the top and bottom are only slowly resorbable. Figure 2b shows the diagram and release profile of a device with symmetrical spatial distribution of the two dyes and uniform matrix gradients. All walls in this device are identical since they are constructed with the same binder composition, under the same printing conditions. As expected, the blue and yellow dyes are released at identical rates to within the statistical error of the experiment.

One of the printing parameters which can be modified to regulate release rates is the inter-line spacing of the lines which make up the walls. The walls of the device in Figure 3a are chemically identical, but physically different. Six solid walls are built in one direction by printing four lines closely together. Then six walls are constructed in the perpendicular direction by printing only two lines, separated from each other by unprinted powder. All walls are constructed to the same total thickness. The device shown in Figure 3a demonstrates that for walls of equal thickness and composition, modification of internal wall microstructure can affect the release rate. Here, the dyes limited by solid walls (4 connected lines per wall) are released at a slower rate than dyes limited by semi-solid walls (2 lines per wall, spaced apart by unprinted PEO powder). It should be noted that other printing parameters, such as printhead traverse velocity, binder flow rate, and layer thickness, can also be controlled to modify release rates. 3D Printing also feature the ability to control the relative position of the dye to the diffusion barrier. In the device

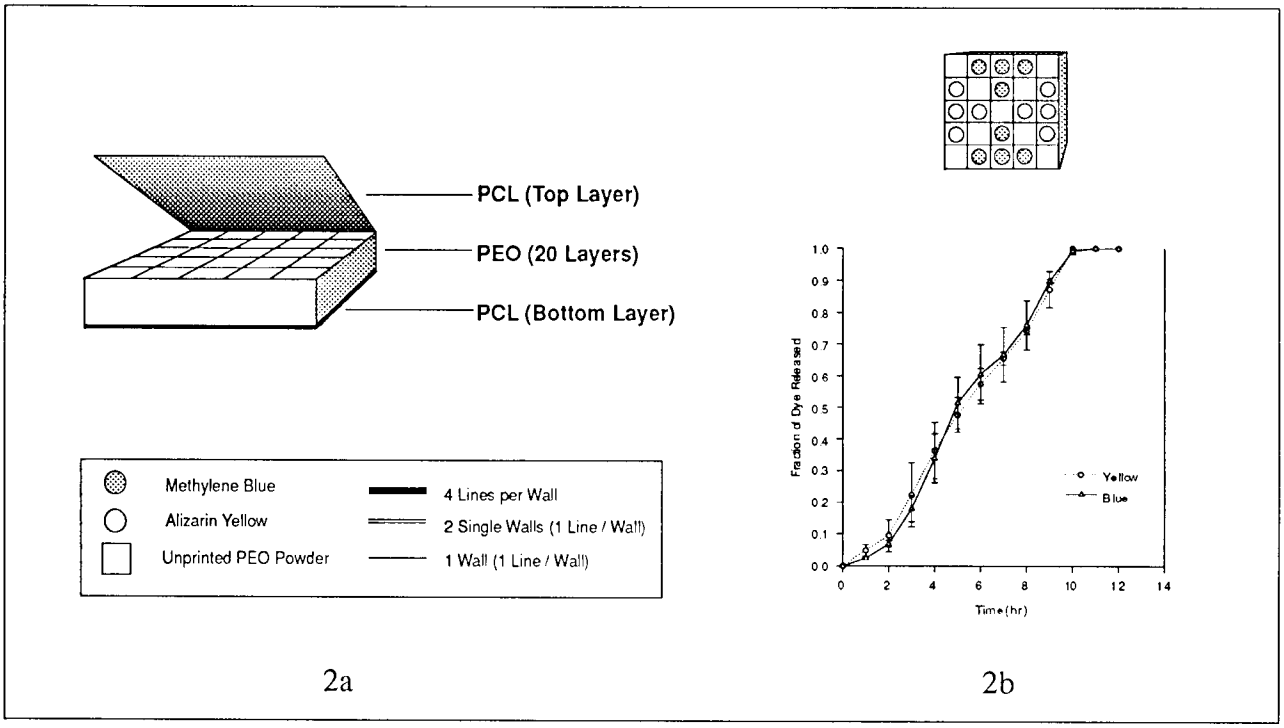

Figure 2a: Diagram of the model drug delivery device.
Figure 2b: Release profile of device with equal spatial distribution of dyes, and identical wall structures.

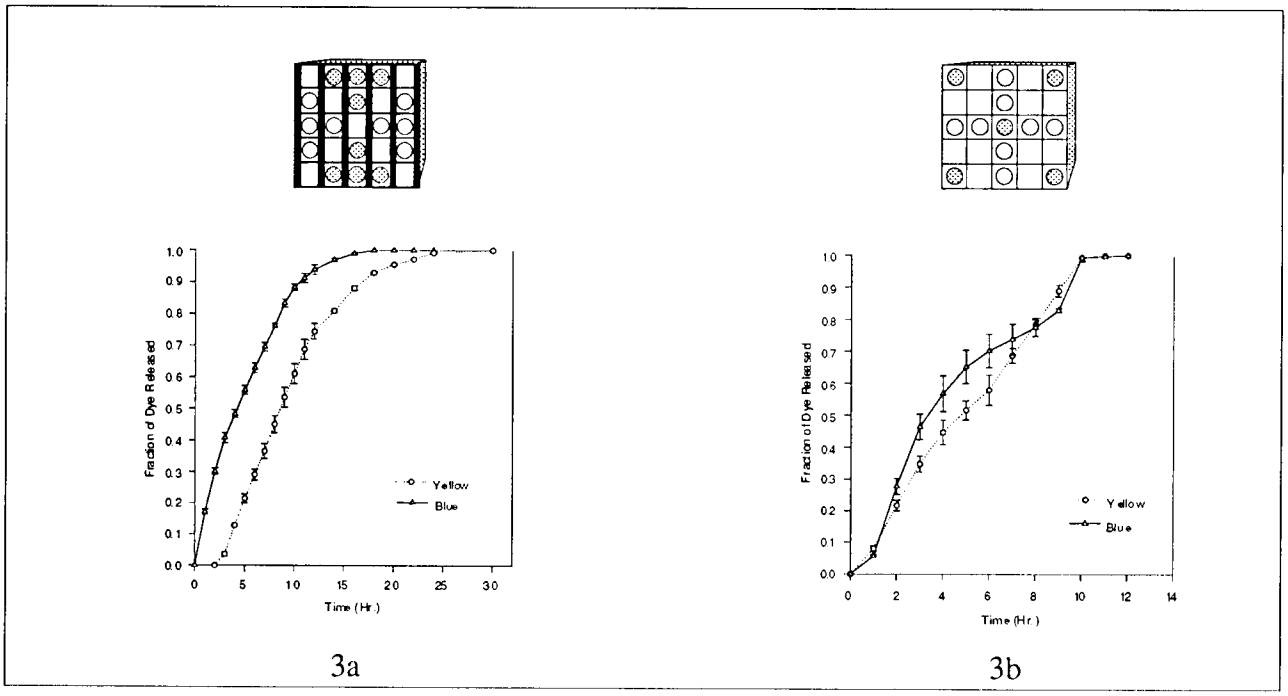

Figure 3a: Release profile is affected by controlling microstructure.
Figure 3b: Release profile is affected by controlling spatial distribution of dyes.

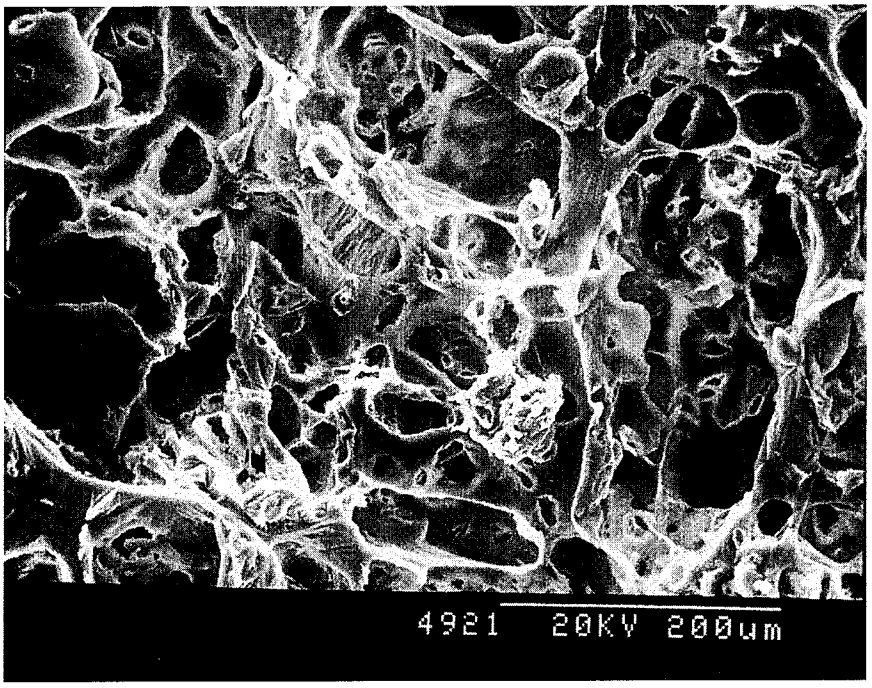

Figure 4: Binder: 30 wt% acid modified PCL in chloroform; Binder per Line Length: 2.85 x 10^{-4} cm^3/cm; Powder: NaCl 75-150 um; Layer thickness: 150 um; These devices were leached in water for 24 hours after printing and drying to produce the microporosity visible.

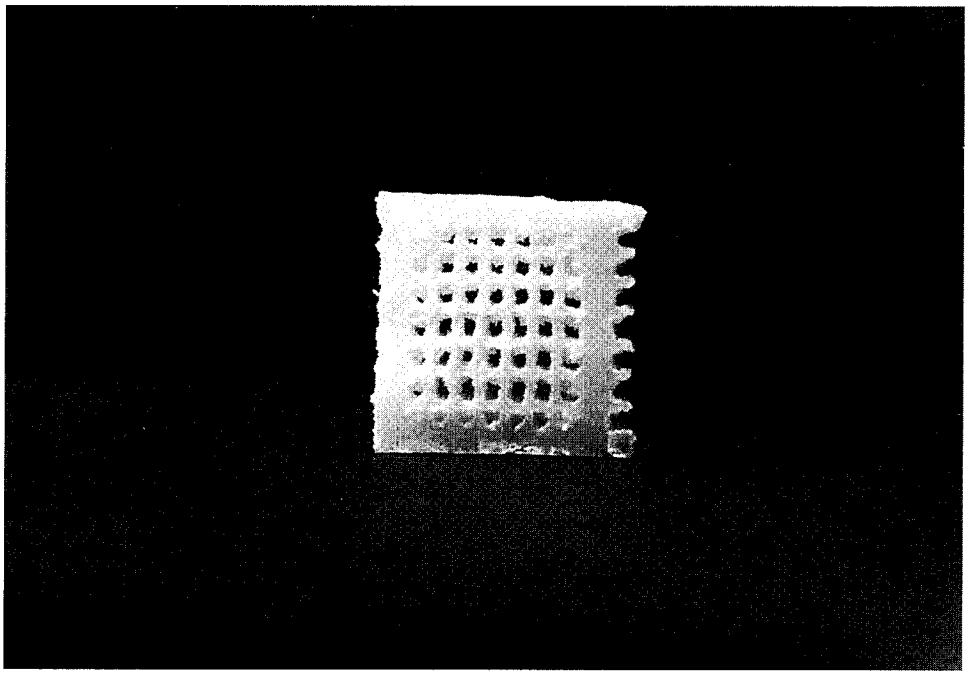

Figure 5: Binder: 26.5 wt% acid modified PCL in chloroform; Binder per Line Length: 3.33 x 10^{-4} cm^3/cm; Powder: PCL 75-150 um; Layer thickness: 250 um; This device was printed horizontally (vertical direction in figure) to produce regions with different density. The figure shows a cross section of this device. Note the outer channels that are not completely open due to bleeding of the binder into those regions.

shown in Figure 3b, the walls are identical in both directions. The difference in release patterns for the two dyes can only be attributed to the difference in spatial distribution of the dyes within the device. This release profile exhibits two maxima in the methylene blue release rate and a relatively constant release rate of alizarin yellow.

Interconnected pores on the order of 50-250 μm within a device provide a structure for cell proliferation, migration, excretion of matrix materials, and blood vessle formation. Pores with width greater than approximately 100 μm can be built directly with the 3DP process. Building a device with smaller pores requires the inclusion of a leachable component. This leachable component can then be removed after printing. An example of the microporosity created by this process is shown in Figure 4. These pores are of the correct size for viable cell function and angiogenisis. The powder bed material, in this case NaCl, has been completely leached out of the final device. Thus, the device is the first 3DP device of any kind to consist only of material delivered through the printhead. Other 3DP devices incorporating natural materials, such as bovine bone, have been constructed. In this case, bone powder was mixed with PCL powder. A solvent polymer solution was used as the binder.

A cross section of a macroscopic device constructed with PCL and polymer solution is shown in Figure 5. All of the interior channels are open, but some of the channels near the dense, high binder delivery regions are obstructed. This is likely due to the bleeding of some of the binder into the void regions.

Final perspective

This brief report represents some of the first experiments to exploit the unusual capabilities of solid-free form fabrication methods. We have already demonstrated unprecedented control of microstructure and local composition using the 3DP method, but other SFF technologies will undoubtedly be used along similar lines. Never before have materials and product designers had the ability to specify structure on the macro *and* micro level. The number of possible applications seems innumerable. Indeed, our most difficult task may be to select applications to develop first. An important consideration for selection of the appropriate process will, however, be the production rate. Components with unique microstructures will only be useful if thousands of parts can be made. 3DP may be uniquely qualified to address this manufacturing issue. Multijet printing is now possible on 3DP machines as has been demonstrated at Soligen[26] and at MIT. This has dramatically increased the production rate of the 3DP process. Commercial ink-jet print heads are available with thousands of individually controlled jets. Thus, future 3DP machines may be closer to production tools rather than tools for prototyping.

Acknowledgments

This work was supported by ARPA/ONR, Johnson & Johnson Development Corp. and Therics Inc. B. Wu acknowledges support from an Institutional Dentist Scientist Award by N.I.H. and Harvard School of Dental Medicine. The authors express their gratitude to J. Serdy and the M.I.T. 3D Printing group for technical assistance. Finally, the authors wish to thank Dr. Walter Flamenbaum and Mr. Tucker Swan for many interesting technical discussions.

References

1. E.M. Sachs, M.J. Cima, P. Williams, D. Brancazio, J. Cornie, "Three-Dimensional Printing: Rapid Tooling and Prototypes Directly from a CAD Model"; J. Eng. Ind., 114 pp. 481-88 (1992).

2. E. Sachs, M.J. Cima, J. Bredt, A. Curodeau, "CAD-Casting: The Direct Fabrication of Ceramic Shells and Cores by Three Dimensional Printing," *Man. Rev.* **5** [2] pp. 117-126, (1992).

3. M.J. Cima and E.M. Sachs, "Three Dimensional Printing: Form, Materials, and Performance," in Proceedings of the Solid Freeform Fabrication Symposium (8/12/91-8/14/91, Austin, TX). Edited by J.J. Beaman, H.L. Marcus, D.L. Bourell, J.W. Barlow, and T. Crawford. University of Texas, Austin, TX pp. 187-94.

4. S. Michaels, E.M. Sachs, M.J. Cima, "Metal Parts Generation by Three Dimensional Printing"; in proceedings of the Solid Freeform Fabrication Symposium (8/3/92-8/5/92, Austin, TX). Edited by J.J. Beaman, H.L. Marcus, D.L. Burrell and J.W. Barlow. University of Texas, Austin, TX, pp. 244-50.

5. J. Yoo, M. J. Cima, S. Khanuja, and E. Sachs, "Structural Ceramic Components by 3D Printing", SFF Symposium Proceedings, Univ. of Texas, p.40-50, 1993

6. S.W. Borland, B.M. Wu, L.G. Cima, R.A. Giordano, E.M. Sachs, and M.J. Cima, "Solid free form fabrication of reticulated structures from biomedical polymers", (submitted for publication in *Biomaterials*)

7. S. Khanuja, J. Yoo, and M. J. Cima, MIT, unpublished results

8. B. Giritlioglu and M.J. Cima, MIT, unpublished results

9. S. Khanuja and M. J. Cima, MIT, unpublished results

10. W. R. Cannon, "Transformation Toughened Ceramics for Structural Applications", Treatise on Mat. Sci. and Tech., 29, p.195-228, 1989.

11. A. G. Evans and R. M. Cannon, "Toughening of Brittle Solids by Martensitic Transformations", *Acta Metall*, **34**, 5, p.761-800, 1986.

12 T.K. Gupta, "Strengthening by Surface Damage in Tetragonal Zirconia", *J. Am. Cer. Soc.* **63**, p.117, 1980.

13. D. J. Green, "A Technique for Introducing Compression into Zirconia Ceramics", *Comm. Am. Cer. Soc.*, C-178, Oct, 1983.

14. R. A. Cutler, J. D. Bright, A. V. Virkar, and D. K. Shetty, "Strength Improvement in Transformation-toughened Alumina by Selective Phase Transformation", *J. Am. Cer. Soc.* **70**, p.714-718, 1987.

15. P. Sarkar, X. Huang, and P. S. Nicholson, "Zirconia/Alumina Functionally Gradiented Composites by Electrophoretic Deposition Techniques", *J. Am. Cer. Soc.* **76**, p.1055-1056, 1993.

16. N. Claussen, "Microstructural Design of Zirconia-Toughened Ceramics (ZTC)", *Science and Technology of Zirconia II*, **12**, p.321-351, 1984.

17. J. Wang, and R. Stevens, "Zirconia-toughened alumina (ZTA) ceramics", *J. of Mat. Sci.*, **24**,p.3421-3440, 1989.

18. M.P. Harmer, H. M. Chan, and G. A. Miller, "Unique Opportunities for Microstructural Engineering with Duplex and Laminar Ceramic Composites", *J. Am. Cer. Soc.*, **75**,p.1715-1728, 1992.

19. B.M. Wu, S.W. Borland, R.A. Giordano, L.G. Cima, E.M. Sachs, and M.J. Cima, "Solid free form fabrication of drug delivery devices". (to be submitted *Biomaterials*)

20. D.S.T. Hsieh, W.D. Rhine, R. Langer, "Zero-order controlled-release polymer matrices for micro- and macromolecules", Journal of Pharmaceutical Sciences. 1983, 72: 17

21. Y.W. Chien, "Polymer-controlled drug delivery systems: science and engineering", in Polymeric Materials in Medication (ed. C.G. Gebelein, C.E. Carraher), Plenum Press, New York, USA. 1985: pp. 27-46

22. C.A. Vacanti, L.G. Cima, D. Ratkowski, J. Upton, and J.P. Vacanti, "Tissue engineering of new cartilage in the shape of a human ear using specially configured polymers seeded with chondrocytes". Tissue-Inducing Biomaterials, L.G. Cima, Editor. 1992, Materials Research Society: 367-374

23. V. Guenard, R.F. Valenti, and P. Aebischer, "Influence of surface texture of polymeric sheets on peripheral nerve regeneration in a two-compartment guidance system". Biomaterials 1991. 12: 259-263

24. U. Ripamonti, S. Ma, and A.H. Reddi, "The critical role of geometry of porous hydroxyapatite delivery system in induction of bone by osteogenin, a bone morphogenetic protein". Matrix (M54), 1992. 12: 202-212

25. A.G. Mikos, G. Sarakinos, S.M. Leite, J.P. Vacanti, and R. Langer, "Laminated three-dimensional biodegradable foams for use in tissue engineering". Biomaterials, 1993. 14: 323-330

26. Soligen Inc., Northridge, CA

Selective Laser Sintering of Calcium Phosphate Powders

Goonhee Lee and J.W.Barlow
Department of Chemical Engineering
The University of Texas at Austin

Abstract

Various forms of calcium phosphate compounds are prepared from hydroxyapatite($Ca_5(OH)(PO_4)_3$) by reacting with phosphoric acid (H_3PO_4) to prepare powders with Ca/P ratio from 1 to 0.5 for the Selective Laser Sintering (SLS) process. These powders are SLS processed using polymer as an intermediate binder. The produced green parts are infiltrated with the calcium phosphate solution and fired to burn out the binder. In this paper, the characterization of the produced parts are examined as consequences of various Ca/P ratio, SLS operating parameters, and post-processing conditions.

Introduction

Since DeJong first observed the similarity between powder X - ray diffraction pattern of the *in vivo* mineral and the hydroxyapatite ($Ca_5(OH)(PO_4)_3$,HA) in 1926, the calcium phosphate ceramics have received attention as a bone substitute material.

Five calcium phosphates which exhibit different X-ray diffraction patterns are known to be precipitated from aqueous solution at normal pressure. [1] These are $Ca(H_2PO_4)_2$, $Ca(H_2PO_4)_2 \cdot H_2O$, $CaHPO_4$, $CaHPO_4 \cdot 2H_2O$, and crystalline precipitate of variable composition of hydroxyapatite with the base formula $Ca_5(OH)(PO_4)_3$. Various forms of calcium phosphate compounds, Ca/P ratio range from 0.5 to 1, are prepared from HA by reacting with phosphoric acid . Thermally dehydrated calcium phosphates are known to form a CaO and P_2O_5 binary system. It is known that for the CaO and P_2O_5 binary system, the chain phosphates appear between the orthophosphate (mole ratio of CaO/P_2O_5 =3) and metaphosphate (mole ratio of CaO/P_2O_5 =1) and ultraphosphate for which mole ratio of CaO/P_2O_5 less than 1. Particularly in the case of metaphosphate, very high degree of polymerization and as a consequence, good mechanical properties are reported. In this binary system, mole ratio of CaO/P_2O_5 less than 55/45 forms a glass-like structure from the melt, and its mechanical properties are known to be nearly same as those of natural teeth.[2]

Materials and Methods

HA was obtained from Monsanto Inc. as Tricalcium phosphate and phosphoric acid was purchased from Fischer Scientific in 85 % concentration. As an intermediate polymeric binder, emulsion poly(methyl methacrylate-co-n-butyl methacrylate) copolymer with a Melt Index of 30.9 g/10min. at 75 psig and 200°C was used.[3]

The mercury porosimeter, Poresizer 9320 from Micromeretics was used to determine the surface area of the powder. The powder samples were heated to expel the absorbed moisture and then stored in desiccator until analyzed. The sample in penetrometer was initially evacuated to 25 *m*Hg. Mercury was then admitted and pressure was increased up to 30,000 psi which is capable of measuring pore size of 0.006 *m*m. Contact angle of 130° was used.

The particle size distributions of powders are measured by a Coulter Multisizer.

1. Powder preparation

(1) calcium metaphosphate ($\{Ca(PO_3)_2\}_n$, CMP)

251 g of HA was reacted with 403g of 85 % phosphoric acid, diluted with 150 g of water according to the following equation.

$$Ca_5(OH)(PO_4)_3 + 7H_3PO_4 \xrightarrow{\text{room Temp}} Ca(H_2PO_4)_2 \cdot H_2O$$

The prepared paste was dried at the room temperature and then heated at 150 °C to drive out the moisture.

$$Ca(H_2PO_4)_2 \cdot H_2O \xrightarrow{150 - 200\ ^\circ C} Ca(H_2PO_4)_2 + H_2O$$

The above equations are not quite exact because of the difficulty in writing a simple formula $Ca_5(OH)(PO_4)_3$ for the HA compositions which does not take into account the variable composition or the amount of hydration. However, the reaction product was confirmed by the X-ray diffraction analysis. Powder that is heated at 150 °C exhibits the X-ray diffraction pattern of mixture of $Ca(H_2PO_4)_2$ and $Ca(H_2PO_4)_2 \cdot H_2O$. This powder is further dehydrated by heating to 900 °C in a porcelain crucible to form stable β -calcium metaphosphate (CMP) which is theoretically composed of 28 wt % of CaO and 72 % of P_2O_5 and reported to have average chain length of 10,000.[4] The X-ray diffraction pattern of CMP made by described method is compared to the standard pattern in Figure 1.

$$Ca(H_2PO_4)_2 \xrightarrow{600 - 700^\circ C} Ca(PO_3)_2 + 2H_2O$$

This thermally coalesced compound is ground by a Szegvary attritor system, type 1HSA to be mixed with polymer for SLS processing.

(2) Calcium pyrophosphate ($Ca_2P_2O_7$, CPP)

CPP was prepared from the 251 g of HA reacted with 196 g of 85 % phosphoric acid by the same way described in the CMP preparation.

$$Ca_5(OH)(PO_4)_3 + 2H_3PO_4 \xrightarrow{150 - 200\ ^\circ C} CaHPO_4\ 2H_2O + H_2O$$

$$2CaHPO_4 \cdot 2H_2O \xrightarrow{700 - 750\ ^\circ C} Ca_2P_2O_7 + 5H_2O$$

(3) Calcium phosphate with 35 wt % of CaO(35CaP)

251 g of HA was reacted with 251 g of 85 % phosphoric acid. X-ray diffraction pattern of this powder, as shown in Figure 1, was identified by JADE X-ray peak identifying program as mixture of major phase of $4CaO3P_2O_5$ and minor phase of CPP.

(4) CPP with 1 wt.% of NaO (1NaCPP)

The prepared CPP powder was mixed with 1 weight percent of NaO to depress the melting temperature in order to study the influence of surface area of the powder on green strength. 1NaCPP was thermally coalesced at 1020°C and then ground in the attritor. The ball milling time was controlled to have different particle size and consequently surface area. Three samples of pore surface area, 1.8 , 1.4, and 1.1 m^2/g, were measured by mercury porosimeter.

2. SLS Processing

CMP powder is mixed with 15 wt.%(30 vol.%) polymer and SLS processed with the following conditions.

Table 1. SLS parameters

Power (W)	Scan Space (mil)	BeamSpeed (ips)	Layer thickness	Bed Temp. (°C)
7.5	5	25	5	90

3. Post processing

(1) Firing The green parts are fired up to sintering temperature to remove the polymer and subsequently to sinter. The temperature was raised at the average rate of 16°C/min up to 500°C and then raised slowly to 880°C. The parts were held at 880°C for 2 hours and cooled down slowly. During the firing, the parts were kept in lightly packed HA powder to help maintain the shape and provide even heat distribution to reduce curling. HA was chosen as packing material due to its low bulk density, less than 0.5 g/cm^3 and high melting temperature. Low density material is critical when fire the complex shape parts because thermal stress create cracks between layers. The fired polymer free parts are then infiltrated with calcium phosphate solution.

(2) Infiltration Infiltration of ceramic cement in a green structure was proposed as an alternative of high temperature sintering.[5] Due to the severe restriction imposed on selection of cement for biomedical applications, the calcium phosphate solution was chosen as the infiltrant. For the effective penetration through the pore, the calcium phosphate have to be dissolved completely in biologically acceptable media. In essence, calcium phosphate paste was prepared by mixing HA and phosphoric acid and then diluted by adding water to form slurry. The prepared slurry is dissolved in boiling water. It is found that 15g of HA with 60 g of 85 % phosphoric acid is good composition when dissolved in boiling water to make about 120 ml of solution. Complete thermal dehydration and condensation of this solution around 600°C forms non porous and transparent ultraphosphate glass that contains of

15.7% CaO. Infiltration is performed mainly by capillary action. After pores are saturated with infiltrant, the parts are allowed to dry and then fired at the appropriate temperature according to the expected final Ca/P ratio. It is found that when pores are saturated upon infiltration, the resulting weight gain is inversely proportional to the initial density.

Results and discussion

The SLS processed CMP green parts have density about 0.91 ±0.03 g/cm^3, 33 % of theoretical density with the fracture strength of 130 ±20 psi which is good enough to permit rough handling of complex bone shapes, such as that shown in Figure 2. This craniofacial image composed of 27 different layers was created from Computed Tomographic scans of a human temporal bone.[6] This part is approximately four inches long and one and half inch thick with very well defined cavities.
However, 35CaP green parts have density of 0.83g/cm^{3}with the fracture strength of 40 ± 10 psi . This relatively low strength of the latter parts are attributed to smaller particle size, consequently higher surface area of powder than that of CMP powder. In the powder preparing step, the firing temperature 900°C was sufficient to coalesce CMP, melting point of 985°C. However, for 35CaP powder, which has a higher melting temperature, 900°C was not high enough to coalesce the powder. The resulting powder has very high surface area. This reasoning is verified when CPP powder, fired at 1300 C for 2 hours, then ground in the attritor and classified to a mean diameter of 30μm, showed good green strength with 15 wt.% polymer whereas the powder fired at 900°C, ground to a mean diameter of 2μm, barely sintered at all. Also, 1NaCPP powder of surface area of 1.8 m^2/g was barely sintered and surface area of 1.4 m^2/g was sintered slightly with loose powder. Whereas the powder of surface area of 1.1 m^2/g showed very good strength.

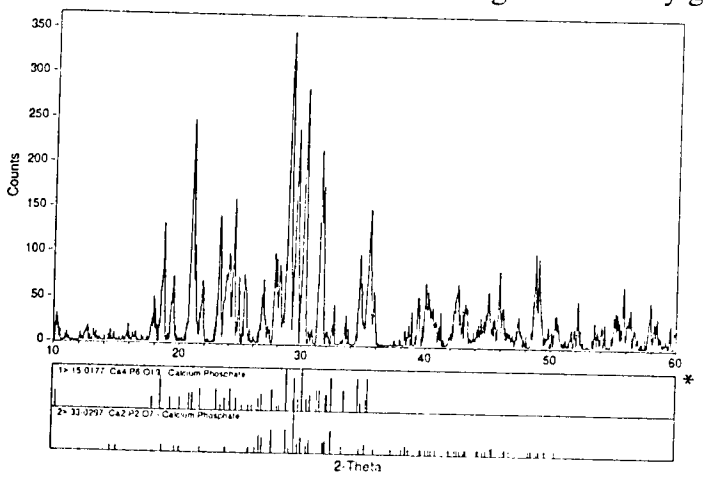

(A)

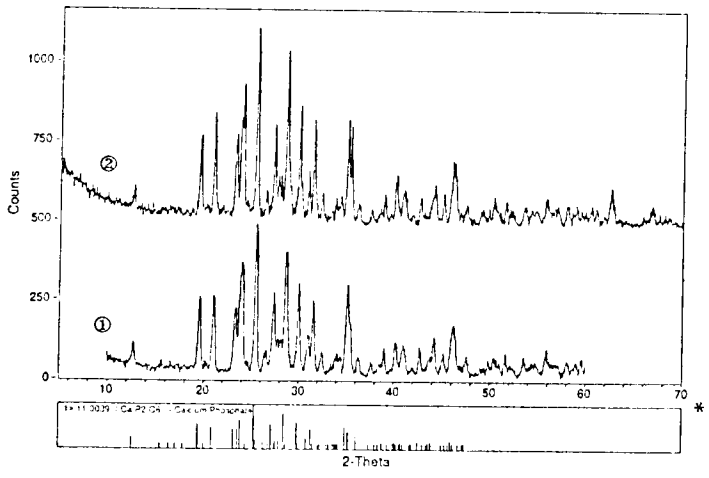

(B)

Figure 1. X-ray diffraction patterns
(A) Pattern for 35CaP powder.
(B) Á Pattern for CMP powder as prepared.
Á Pattern for 35CaP after infiltrated and fired.
* The standard patterns are presented in small box

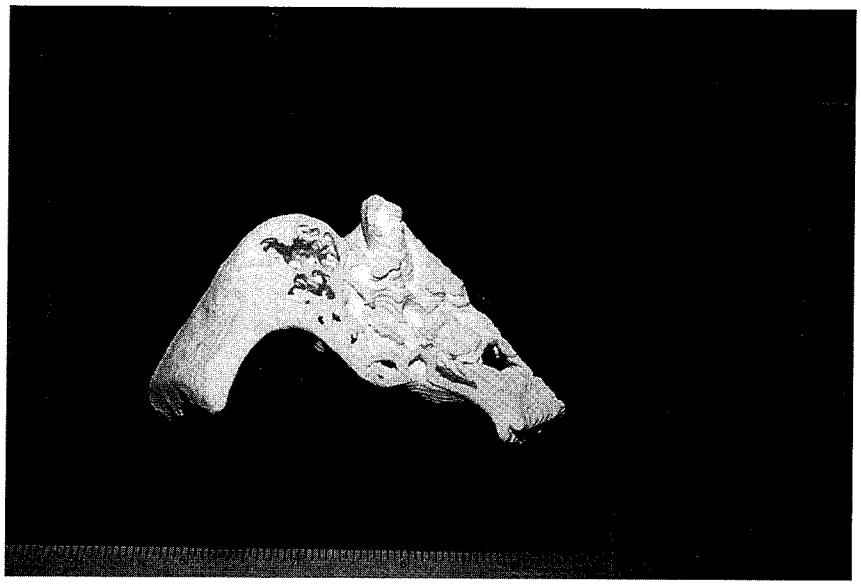

Figure 2. SLS processed craniofacial image from CMP powder.

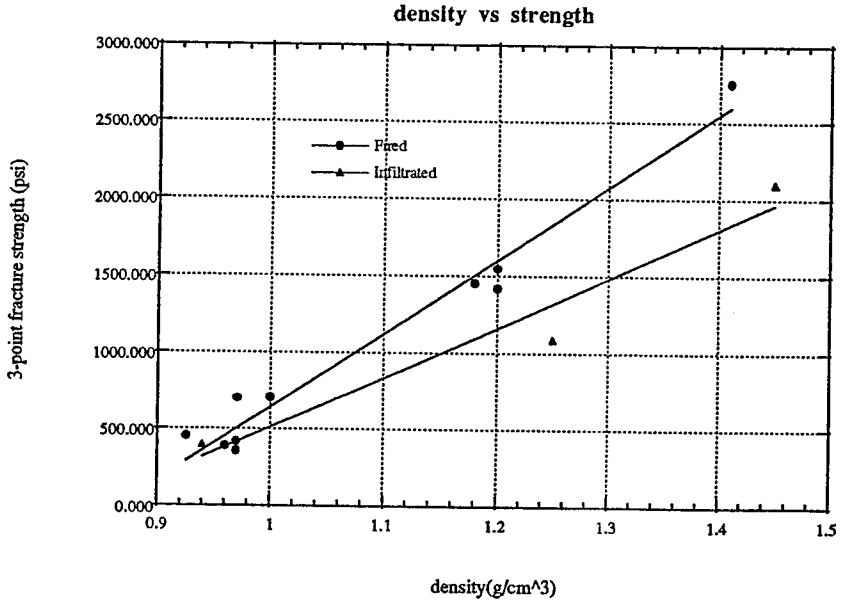

Figure 3. Three point bending strength VS. density of fired part and post processed part

CMP green parts were fired at 880°C for 2 hours. The fired CMP parts showed 3 point bending strength about 400 psi and a density of about 0.97g/cm^3, corresponding to a 17% volume shrinkage. And the strength of about 2700 psi part was obtained by firing at 940°C for 1 hour with a density of about 1.4g/cm^3. The polymer free parts with a density of about 0.97g/cm^3 were infiltrated as described earlier. For the CMP parts, first infiltration resulted in 31±2 % weight gain after firing 725°C and strength of 1100 psi and more infiltration increased the density about 50 % and strength about 1500 psi. Strength vs. density data are shown in figure 3. Further infiltration caused the parts to melt and deform inhomogeneously at 725°C, which

could indicate existence of Ca/P concentration gradient through the part. This even lowered the strength of the part. The fractured surface of this part showed randomly distributed vitrified parts. It is believed that inflitrant, which is ultraphosphate, filled up the pore and formed a phosphate glass. This part were ground back to the powder for the X - ray diffraction analysis. There was no big noticeable difference in X - ray patterns between before and after infiltration. This indicating that no new crystalline phase had been formed. For the 35CaP fired part, the first infiltration caused about 40 % weight gain due to the lower green density, and further infiltration increased the strength to about 3500 psi . X - ray diffraction analysis indicate that

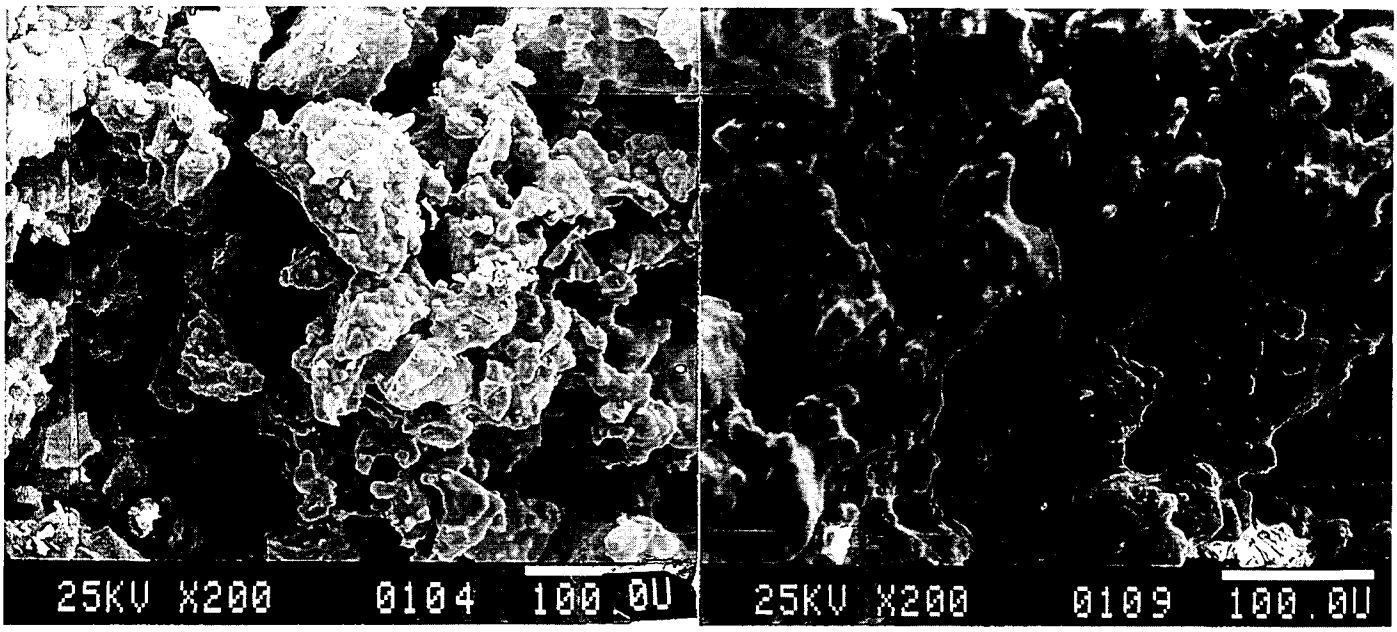

(A) (B)

Figure 4. Scanning Electron Micrographs of porous fractured surface (A) fired. (B) fired and infiltrated. (X 200)

initial powder which was mixture of major phase of $4CaO3P_2O_5$ and minor phase of CPP was converted to calcium metaphosphate after post processing. Figure 1 (B) shows this phase transformation. The morphology of the fired and infiltrated fracture surface are shown in Figure 4. It is noticeable that infiltration make the more necking between the grains. The pores are well interconnected and the pore size is approximately larger than 50 μm.

The firing step causes the part to shrink, which is not desirable because one of the purpose of the SLS for implant material is construction of the accurate facsimile bone structure from the geometric information obtained from patient computed tomography data. Even worse, the shrinkage is not isotropic. Linear shrinkage in thickness is much larger than that in width or length, due to the nature of layer-wise construction of parts in SLS process. In the attempt to avoid the shrinkage, it is proposed that infiltration should be performed on a green part while the polymer present.[7]

Conclusion

It has been shown that complex and delicate bone shape parts can be fabricated from CT data by using selective laser sintering process. It has also been shown that, in order to make denser porous calcium metaphosphate parts, calcium rich powder are SLS processed and calcium phosphate solution are then to be infiltrated to convert the parts to metaphosphate. However, there are still many problems to be investigated. Some of these problems are understanding of effect of the surface area and micro porosity on green strength, controlling the infiltration step to end up with metaphosphate composition according to Ca/P ratio of initial powder, and optimum firing temperature and cycle.

Acknowledgements

This work was carried out as part of a project supported by DARPA / ONP Grant N00014-92-J-1394.

References

1. John R. Van Wazer, Phosphorus and its compounds, Vol.1, Interscience Publisher, 1958, pp 517 - 522

2. Abe Yoshihiro, " Studies of Calcium Phosphate Glass-Ceramic Development of Dental Materials." Shika Rikogaku Zasshi 1975, 16 pp196 - 202.

3 N.K. Vail and J.W. Barlow et al. "Development of a Poly(methyl methacrylate-co-n-butyl methacrylate) Copolymer Binder System," J. Appl. Polym. Sci. Vol. 52,1994,pp 789

4. D.E. Corbridge, Phosphorus : an outline of its chemistry, biochemistry and technology, Elsevier, 1990, pp 224

5. N.K. Vail and J.W. Barlow "Ceramic Structures by Selective Laser Sintering of Microencapsulated, Finely Divided Ceramic Materials", Solid Freeform Fabrication Symposium Proceedings, 3, 1992, pp124 -130

6 Richard A. Levy, " Preliminary Experience with Selective Laser Sintigraphic Models of Human Temporal Bone", Solid Freeform Fabrication Symposium Proceedings, 3, 1992, pp 161-173

7 N.K. Vail and J.W.Barlow, "A Method for Producing High Temperature Parts by Way of Low Temperature Sintering", US Patent. No.5,284,695, Feb.,1994

A Histogram - Based Algorithm for Semiautomated Three-Dimensional Craniofacial Modeling

by Richard A. Levy, M.D.

Department of Radiology

University of Michigan Hospitals

Introduction: Volume averaging artifacts in medical imaging result from voxel occupancy by more than one tissue type and, with anisotropic voxels, may be decreased by changing the imaging plane orientation relative to the target tissue and/or by decreasing slice thickness.[1]

In craniofacial CT imaging, volume averaging artifact becomes significant in areas of thin bone such as the orbital walls and auditory ossicles. These regions are customarily imaged using multiple scan planes and the thinnest slices possible to reduce such artifacts. In three-dimensional craniofacial imaging, these same parameters may be controlled to reduce partial volume averaging, but areas of bone "drop-out" (also called pseudoforamina) are commonly present secondary to a paradoxical inability to lower thresholds without including unwanted background tissues. At present, the optimal solution to this problem is achieved by manually (and often painstakingly) drawing a region of interest around tissues presumed to contain volume averaged target density voxels and lowering thresholds to include these voxels in the 3D reconstruction, one CT slice at a time.

Recently, anatomic modeling technologies have demonstrated the feasibility of assembling particulate hydroxyapatite (synthetic bone) into detailed craniofacial models of high anatomic accuracy, theoretically suitable for in vivo implantation (work in progress with the Department of Mechanical Engineering, University of Texas at Austin.) These modeling systems, such as stereolithography and selective laser sintering, operate as do 3D imaging workstations, using thresholds to

include/exclude pixels from CT data sets in the modeling process. However, the user interactive capabilities of such technologies may be limited such that manual tracing of regions of volume averaged thin bone is not possible. Drop-out artifacts in models so generated would be potentially larger than on corresponding 3D images where user input could reduce these artifacts. To circumvent this inability to manually correct volume averaging artifacts on anatomic modeling systems, and to relieve the intensive operator input required to otherwise achieve this goal on 3D imaging software, a histogram-based algorithm for semiautomated three-dimensional craniofacial modeling was developed.

Materials and Methods: CT data sets from 5 axially and coronally-scanned embryologic craniofacial specimens (aged 18 to 33 weeks) were used to generate one-dimensional histograms of entire imaging volumes. Histograms were constructed with the y-axis representing frequency and the x-axis representing CT number in Hounsfield units. Superimposition of histograms from corresponding orthogonal CT data sets from each case tested the hypothesis that voxel anisotropy produces divergence of corresponding segments of the histograms over ranges of Hounsfield density in which partial volume averaging occurs. These regions of volume averaging were predicted from prior phantom trials based upon 1) divergence of the histograms and/or presence of an asymmetric "tail" in an otherwise symmetric tissue distribution 2) very small numbers of pixels compared to the large populations of bone, soft tissue/water and air and 3) locations intermediate in Hounsfield density to the standard tissue distributions (Figures 1a and 1b). Thresholds based on these assumptions and on prior experimentation with this CT phantom applied to the histograms were compared with CT image-derived operator-selected thresholds. Most bone density pixels were identified using a simple formula obtained from prior phantom trials, $T=0.16|D-Do|+Do$, where

T=threshold, D=mean of bone pixel distribution, and Do=mean of soft tissue distribution.[2] In cases in which volume averaging was predicted from the histograms, the corresponding threshold ranges were expanded and contracted to assess the "uniqueness" of the predicted threshold ranges. All 3-dimensional CT images were generated using a volumetric rendering algorithm. Pathologic correlation consisting of craniofacial specimen photographs was available in some cases.

Results: Only in 1/5 cases (the 33 week specimen) could bone, soft tissue/water and air populations all be identified from the histograms. In the remaining 4/5 cases, only bone and air "peaks" were identified, with soft tissue/water voxels distributed more broadly over less well-defined Hounsfield density ranges. The ability to set thresholds was related to the ease with which the means of these tissue populations could be identified.

In 3/5 cases, inspection of the histograms permitted identification of discrete ranges of Hounsfield density over which partial volume averaging occurred. As anticipated, inclusion of non-osseous volume averaged voxels in the 3D reconstructions also occurred, principally at air-tissue interfaces such as the skin surface and surface of mucous membranes (Figure 2). In all cases in which volume averaging was predicted from the histograms, expansion of the threshold ranges beyond those predicted yielded inclusion of non-osseous tissue in the 3D reconstructions. In 2/3 of these cases, contraction of the threshold ranges caused loss of bone-density voxels from anatomic regions where bone was observed to fill-in using the predicted threshold ranges (Figure 2). In the remaining case, pathologic verification was not available.

Discussion: While volume averaging artifacts may be tolerated in 3D craniofacial imaging, they become more critical in craniofacial modeling, especially with the expectation that biosynthetic (e.g., hydroxyapatite) implants will promote osteoneogenesis.[3,4] Tolerance of "drop-out" artifacts in a craniofacial implant will depend on the size and location of such defects.

The histogram-based thresholding algorithm presented in this essay proposes to diminish volume averaging artifact as well as the operator time involved in the generation of craniofacial implants from CT data. At present, the rate limiting factor is the time required for data transfer from the CT console to the generation of histograms.

Optimally, this process results in a single threshold on the order of 150 HU, as well as a range of lower CT density, e.g., -100 to -400 HU (Figure 2). For the purpose of anatomic modeling, undesired volume averaged tissues such as the skin surface can be dissected from the implant.

A potential pitfall to this method is its dependency upon the presence of well-defined bone, water/soft tissue and air-density histogram populations to permit the initial selection of thresholds. It is likely that the small specimen size used in this experiment contributed to the absence of definable water/soft tissue peaks in most cases, especially since the expected tissue distributions were achieved only with the largest (33 week) specimen. While the utilization of such small craniofacial specimens has the advantage of eliminating (potential positionally-dependent) beam hardening artifacts, it is anticipated that further trials with this method will occur with postnatal and adult subjects.

Another potential pitfall awaiting evaluation in clinical trials of this algorithm arises from the fact that, in the present experiment, the imaging volume encompassing

the entire craniofacial specimen was included in both the paired axial and coronal data sets. In the clinical setting, this may not be possible, making identification of volume-averaged voxels more challenging.

References

1. Levy RA, Edwards WT, Meyer JR, Rosenbaum AE. Facial trauma and 3-D reconstructive imaging: insufficiencies and correctives. AJNR 1992;13:885-892.
2. Levy RA. Semiautomated three-dimensional craniofacial imaging and modeling. Investigative Radiology 1994;29(2):150-155.
3. Damien CJ, Parsons JR, Benedict JJ, Weisman DS. Investigation of a hydroxy-apatite and calcium sulfate composite supplemented with an osteoinductive factor. J Biomed Mater Res 1990 24(6):639-654.
4. Levy RA. U.S. Patent Pending, "Three-dimensional model generation from multiple tomographic scan planes."

Legend to Figures

Figure 1a Superimposition of one dimensional histograms of a polyvinylchloride phantom scanned in water from the axial (→) and coronal (↑) planes. The y-axis indicates frequency. Tcalc = average Hounsfield density of the means of the water and phantom pixel/voxel distributions. Top →, Top ↑ = operator-selected thresholds for 3D reconstructions generated from axial and coronal data, respectively. Note gradual upslope ("tail") as well as slight divergence of the histograms in the intervals defined by Tcalc and Top, with the histogram generated from coronal data (↑) having the larger number of pixels. The intervals defined by Tcalc and Top were demonstrated to contain volume averaged voxels in submillimeter structures in the phantom that "filled-in" using the lower thresholds, Top. These structures were better visualized on 3D imaging using the axial (→) data at a numerically larger Top, consistent with less volume averaging in the axial (→) 2D CT data set.

Figure 1b Superimposed one dimensional histograms generated from axial and coronal 2D CT data sets of a 33 week craniofacial specimen with holoprosencephaly. Note "inversion" of the histograms between -100 and -400 HU, with the coronal data set having the greater number of pixels/voxels. Volume averaged voxels would be expected to appear on 3D reconstruction using an additional threshold of -100 to -400 HU, with greater "fill-in" on the 3D reconstruction generated from coronal data.

Figure 2a Photograph of the 33 week holoprosencephalic specimen. Note intact frontal bones.

Figures 2b,2c 3D reconstructions from axial (2b) and coronal (2c) data using operator-selected thresholds of 183 and 186, respectively. Note better "fill-in" of frontal bone voxels using axial data.

Figure 2d 3D reconstruction from coronal data using the histogram-derived threshold of 130.

Figure 2e 3D reconstruction from coronal data using the combined thresholds of 130 and -100 to -400. Note "fill-in" of frontal bone voxels(*) as well as other volume averaged tissues such as the skin surface (arrow) and mucous membrane surface (double arrows).

Figure 2f Same as in 2e but using axial data, illustrating inclusion of skin surface and mucous membrane volume averaged voxels to a similar extent as with the coronal data set. This indicates that the region of histogram divergence between -100 to -400 HU in Figure 1b where the coronal data set contains a greater number of voxels corresponds to volume averaged frontal bone voxels in the coronal data set. Voxels between -100 to -400 HU are color coded in grey.

Figure 2g Same as in 2e but with lower threshold expanded to -100 to -500 HU. Note appearance of background shroud (arrow). Voxels from -100 to -500 HU are color-coded in grey.

Figure 2h Same as in 2e but with lower threshold contracted to -150 to -250. Note drop-out of bone density voxels from the frontal bones (arrow).

Figure 2i Same as in 2e but with threshold of -100. Note fill-in of soft tissue between skin surface and bone, and drop-out of bone voxels from the frontal bones (*).

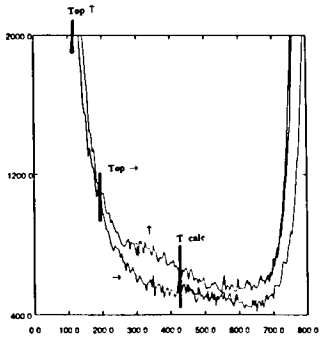
Tep T
2000.0
1200.0
400.0
Tep →
T calc
0.0
100.0
200.0
300.0
400.0
500.0
600.0
700.0
800.0

1a

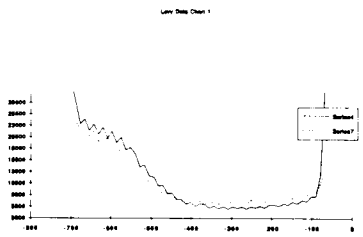

1b

2a

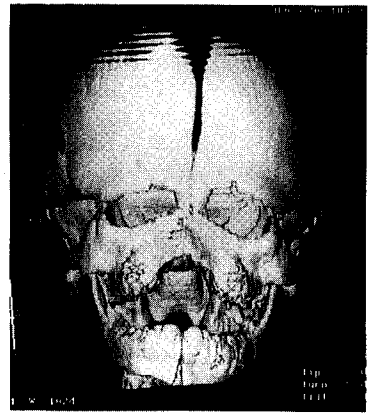

2b

2c

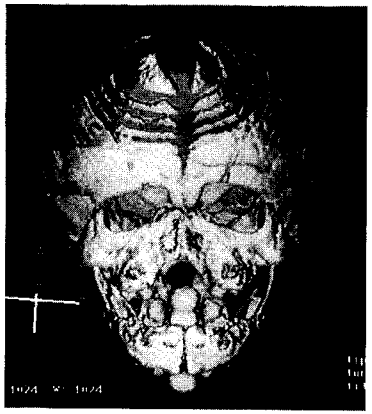

2d

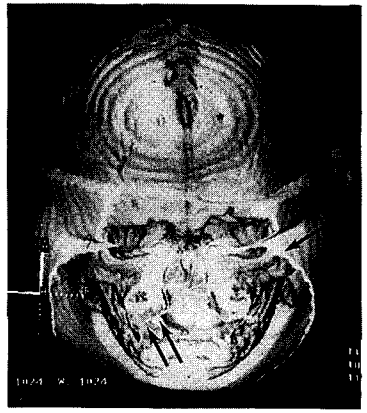

2e

2f

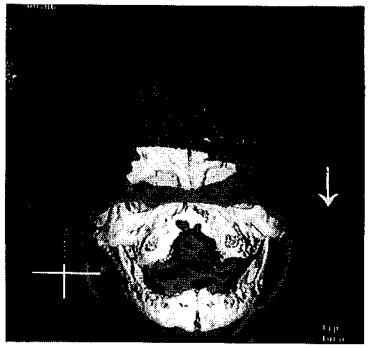

2g

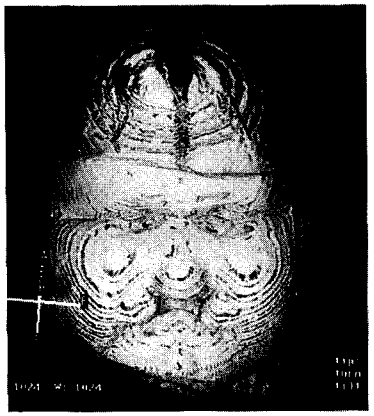

2h

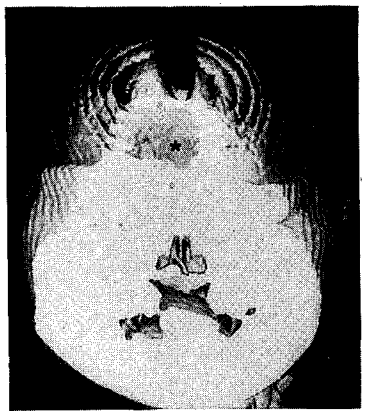

2i

Stereolithography Epoxy Resins SL 5170 and SL 5180: Accuracy, Dimensional Stability, and Mechanical Properties

Dr. Thomas H. Pang
3D Systems Corporation
Valencia, California, U.S.A.

Abstract

Stereolithography (SL) resins based on epoxy chemistry provide significantly improved overall part accuracy, dimensional stability, and mechanical properties relative to the earlier acrylate SL resins. In July, 1993, epoxy-based **SL 5170** resin was introduced for use on the SLA-250 system. In March, 1994, the epoxy-based resin for the SLA-500 system, **SL 5180**, was also released. These epoxy resins have minimal laser-cure and post-cure shrinkage, resulting in extremely low curl and distortion. Overall dimensional accuracy has also improved. Standard User-Parts built in **SL 5170** on the SLA-250, and now, **SL 5180** on the SLA-500, have recently achieved the highest level of dimensional accuracy from a statistically significant number of measurements taken in the x, y, and z directions. Diagnostic test results presented in this paper show that these epoxy-based resins are now capable of producing extremely flat parts when required. SL parts built in these resins also exhibit superb dimensional stability in the laser-cured state, as demonstrated by the "Green" Creep Distortion diagnostic test. Dimensional stability in the laser-cured state is critical, especially for SL parts having the characteristic quasi-hollow internal structure, generated using the QuickCast™ build style. Creep results are presented in this paper. Furthermore, the overall mechanical properties of these epoxy resins were measured according to the ASTM standards for plastics. Tensile, flexural, and impact properties for the epoxy-based and acrylate-based SL resins are presented in this paper. Mechanical properties of thermoplastics, acrylic plastic (PMMA) and medium impact polystyrene, are also presented for comparison. The data shows that the mechanical properties of epoxy-based **SL 5170** and **SL 5180** are comparable to, or exceed those of acrylic plastic and medium impact polystyrene.

For applications that require greater mechanical strengths than **SL 5170** and **SL 5180**, metal parts can be obtained using QuickCast. QuickCast, made possible with the development of these epoxy-based SL resins, is the key to successfully utilizing SL parts for shell investment casting applications, and the generation of precision metal components directly from SL parts. Furthermore, when a "negative" core and cavity pair of a part geometry is produced in metal using QuickCast, tooling is obtained. Prototype, and eventually, production functional parts may then be ultimately injection molded in the QuickCast tooling, using the desired engineering thermoplastic material.

Introduction

In July, 1993, 3D Systems Corporation introduced the first epoxy-based stereolithography (SL) resin, **SL 5170**, developed jointly with Ciba-Geigy, Limited. The epoxy-based SL resin photopolymerizes via cationic chemistry, as opposed to the common free-radical chemistry of acrylate-based resins. The epoxy resin has demonstrated many significant advantages over the conventional acrylate SL resin systems[1]. SL parts built in the **SL 5170** resin showed a high level of overall accuracy, improved flatness, and superior dimensional stability. These properties allow one to generate solid SL parts of exceptional accuracy. However, **SL 5170** resin is only suitable for building on an SLA-190 or 250 machine, which uses the Helium-Cadmium (HeCd) laser. In March, 1994, Ciba-Geigy and 3D Systems released an epoxy-based resin for the SLA-500. The **SL 5180** resin was

developed specifically for use with argon ion laser systems. The dimensional accuracy for this resin also had to be determined, on the SLA-500.

As you will see in this paper, these epoxy resins have major advantages over the conventional acrylate resins. Significant improvements were realized in the overall accuracy, flatness, and dimesional stability of SL parts. Also, parts built in these resins exhibit substantial and reproducible improvements in their mechanical properties, relative to conventional SL acrylate resins systems. These properties, and a number of other properties characteristic of the epoxy resins, were also responsible for achieving QuickCast capability. Finally, the release of epoxy resins **SL 5170** and **SL 5180** culminated with the QuickCast capability, for both SLA-250 and SLA-500 systems.

QuickCast SL parts have continued to succeed in directly generating precision metal parts using **SL 5170** or the **SL 5180** epoxy resins, [2,3] including the generation of QuickCast™ Tooling in A-2 tool steel.[4] Direct functional testing of SL parts built in the solid build style called ACES ™, is also attractive due to the remarkable optical clarity and improved surface finish, in addition to the improved mechanical properties presented in this paper.

This paper focuses on three major dimensional properties, to demonstrate the accuracy achieved by **SL 5170** and **SL 5180** epoxy. Among various diagnostic tests available to characterize SL resins and build processes, the following three methods were chosen. The overall dimensional part accuracy is demonstrated by the statistically significant SL User-Part analysis.[5] Part flatness is determined by the Slab 6X6 flatness test.[6] Finally, the dimensional stability of the laser-cured ("green") SL resins are demonstrated by the Green Creep Distortion test.[1] The latest results are reported in this paper.

In addition, this paper discusses the mechanical properties relevant to SL users including tensile, flexural, and impact properties of various commercially available SL resins, measured according to ASTM (American Standards for Testing and Materials) standards. Mechanical properties of thermoplastics such as acrylic plastic (PMMA) and medium impact polystyrene are also presented for comparison.

Dimensional Properties of SL Resins

Rapid Prototyping and Manufacturing (RP&M) technology will not survive without adequate and repeatable dimensional accuracy necessary for end use applications. To advance the RP&M technology, two simple, but fundamental requirements must be met. On the one hand, the user must have an understanding of the level of accuracy and tolerances required for his application. On the other hand, the RP&M machine supplier has a responsibility to present statistically significant data adequate to define the dimensional accuracy and repeatability that can be achieved by that RP&M machine.

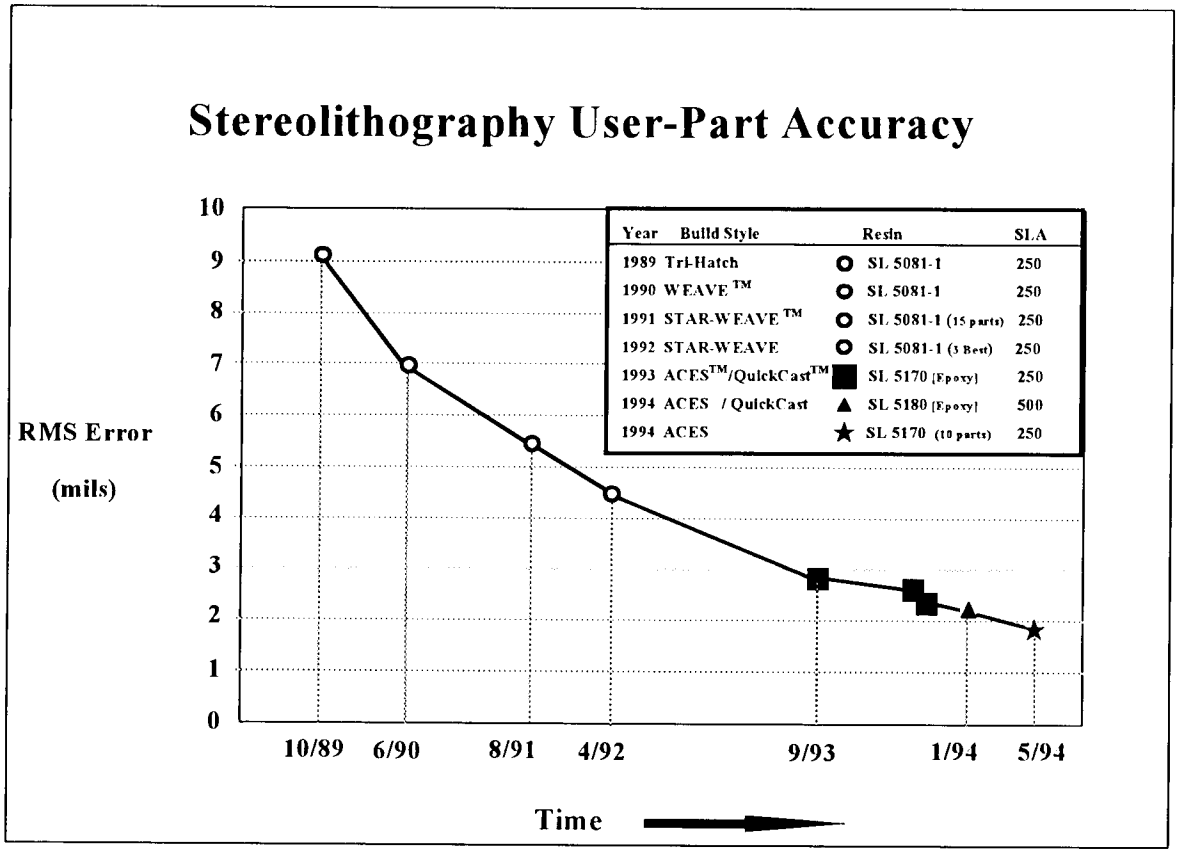

Figure 1

The User-Part Accuracy Test

The User-Part accuracy diagnostic, described in detail elsewhere[5,7] was designed by the North American Stereolithography User Group just for that purpose. The key aspect of this accuracy diagnostic test is the statistical significance of data obtained from accurately measuring 170 dimensions from each User-Part on a coordinate measuring machine (CMM). The statistical significance increases as the number of User-Parts tested increases, therefore multiple parts are built. Multiple User-Parts also determine the repeatability of the process.

The User-Part is 9.5 inches long, 9.5 inches wide, and 1.5 inch tall, and was designed such that it uses almost all of the SLA-250 build area. The measured dimensions of a User-Part include long, medium, and short dimensions spanning almost two orders of magnitude, from 0.100 inch to 9.500 inches, comprising bosses, thin walls, and internal round and square holes.

In the User-Part diagnostic test, a root-mean-square error, or RMS error is reported from the set of 170 dimensional measurements taken for each part. The RMS error is obtained by first generating the Error Distribution Function, and then a Cumulative Error Distribution.[5] If the error distribution is Gaussian, 68% of the dimensional measurements will fall within ± 1.0 RMS error of their CAD value.

The RMS error values measured for Stereolithography User-Parts built in the five-year period from October, 1989 to May, 1994, are presented in figure 1. The figure

clearly shows a significant increase in the accuracy of SL User-Parts over the last five years. Note that SL part accuracy has improved from the RMS error of about ± 9 mils, to about ± 1.8 mils. This represents a *five-fold improvement in dimensional accuracy over a period of only five years.*

The improvement in overall part accuracy was a result of a number of factors. Improvements in hardware, software, process, and resin all contributed incrementally to better SL part accuracy. However, some factors contributed more than others. For example, all of the accuracy data between 1989 and 1992, shown in figure 1, corresponds to User-Parts built with **SL 5081-1** acrylate-based SL resin. Most of the improvements in this time period, resulting in a two-fold accuracy improvement from RMS error of ± 9 mils to ± 4.5 mils, were due to SL process development. SL process includes the appropriate selection of parameters that basically defines the SL part "build style." Some of these parameters include laser scanning speed, drawing sequence, border overcure, hatch spacing, layer thickness, part deep dip distance, etc., as well as, leveling and recoating. In particular, the two-fold improvement of the accuracy data in SL 5081-1 resin was mostly due to build style improvement from Tri-Hatch* , to WEAVE™, to STAR-WEAVE ™ build styles, in the initial period of three years.

However, process alone could not continue to improve part accuracy indefinitely. At that time, in retrospect, there was an inherent limitation due to the SL resin systems. In early 1993, the development program for **SL 5170** was finalizing. At this time, the first User-Part was built in **SL 5170**. The dimensional accuracy immediately jumped from an RMS error of ± 4.5 mils in **SL 5081-1**, to ± 2.8 mils in **SL 5170**, resulting in another nearly *two-fold improvement in accuracy.*

This advance in accuracy was necessary, especially for the QuickCast application, which was also commercially released together with **SL 5170**, in July, 1993. In the QuickCast application, SL pattern generated in the QuickCast build style is converted directly into metal using shell investment casting technique. With the advent of QuickCast, and the subsequent availability of metal prototypes from SL patterns, SL part accuracy requirements have been pushed substantially. The accuracy requirements for a functional prototype are much greater than for parts that are intended mainly for visualization and verification.

In March 1994, the epoxy-based SL resin for the SLA-500, **SL 5180**, was also introduced. With the added help of the hardware and software improvements that culminated with the development of the Orion™ Imaging Technology, as well as the new Diode Laser Leveling system, both developed by 3D Systems, the User-Part built in **SL 5180** was able to achieve an RMS error of ± 2.2 mils.

Furthermore, the latest results from **SL 5170**, built on the SLA-250, produced ***today's record of ± 1.8 mils RMS error***. It is important to note here that this RMS error value is based on, not one, but *ten* User-Parts (viz. 1700 measurements) built on the same

---

* Tri-Hatch is one of the earlier SL build styles that resulted in pockets of liquid resin trapped between walls of cured SL resin. WEAVE and STAR-WEAVE are advanced build styles resulting in minimal internal stress, and maximum volume of laser-cured resin on an SLA. Chapter 8 of reference 5 explains the latter two build styles in great detail.

machine over a period of two months. This demonstrates that SLA has a very high repeatability, when built with the epoxy-based **SL 5170** resin.

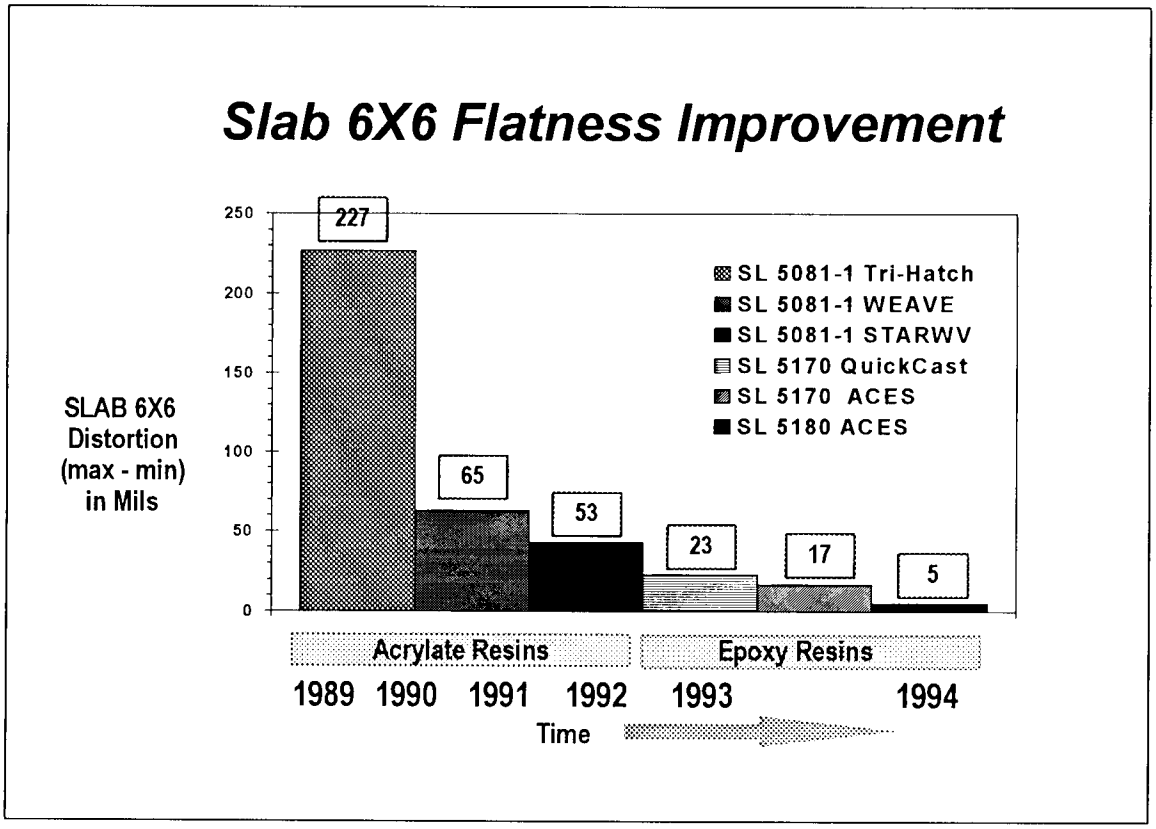

Figure 2

Slab 6X6 Flatness Test

The User-Part is an excellent diagnostic to determine system accuracy from a statistical set of data, especially in the x-y plane (coincident with liquid resin surface). Even though the analysis of each User-Part includes 14 measurements in the z (depth direction) direction, the bulk of the dimensional measurements (156 data points out of 170 measurements) are taken in the x-y plane. In addition, the geometry of the User-Part tends to depress the out-of-plane distortion in the z-direction. Hence, the User-Part analysis is particularly weak in detecting distortion in the z-direction, including the flatness of SL parts.

The Slab 6X6 flatness diagnostic test is suitable for filling that gap. Slab 6X6 is a simple 6 inches long, 6 inches wide, 1/4 inch thick, nominally flat horizontal slab, built flat on an SLA. While this part may seem simple, it is actually one of the most difficult parts to build accurately in SL, or any other layer-additive RP&M method that involves a phase change, or variation in the dimension of the solidifying layer during the building process. It should be stressed that parts that have vertical walls, or other stiffening

features on top of a thin horizontal slab tend to depress distortion. This is due to the increased moment of inertia. The end result is that, in general, a flat slab section with added complex components tends to build flatter than a simple thin horizontal slab. Conversely, a thin slab is an excellent "worst case" diagnostic part to characterize flatness.

In the Slab 6X6 test, the slab is first built on an SLA. Next, the part is taken off the platform and supports are removed. Then, the part is post cured from one side only, to simulate the worst case scenario. Finally, the Slab 6X6 is allowed to sit for seven days, such that any creep distortion during this time would manifest itself in the final measurement. The Slab 6X6, built with acrylate-based resins, usually comes out warped upward (i.e. concave up) after the seven-day period, looking like a shallow bowl.

The distortion range (i.e. highest measurement minus lowest measurement) is established using a CMM on the upper surface. Generally, the highest values occur at the corners and the lowest in the middle of the slab. Additional measurements are actually taken between each process steps in the Slab 6X6 test procedure. However, for purposes of this paper, only the final maximum error value, measured seven days after the build, will be reported.

The Slab 6X6 flatness test results are summarized in figure 2. In 1989, the Tri-Hatch build style was found to build a highly distorted slab 6X6, having a distortion range of 227 mils, or almost 1/4 of an inch. As soon as the newer build styles WEAVE and STAR-WEAVE were introduced in 1991, and 1992, the *flatness improved immediately by more than three-fold*, to 65 mils, and 53 mils, respectively. The best (i.e. smallest) distortion range values in 1992 were achieved by **SL 5081-1** acrylate-based SL resin.

However, further process modifications on the acrylate resin did not yield better results. When the epoxy resin, **SL 5170**, was introduced in 1993, together with the QuickCast build style, *the flatness improved immediately, by more than a factor of two relative to the acrylate resin*. The Slab 6X6 distortion dropped from 53 mils to 23 mils. With further process optimization, and especially with the development of the new ACES ™ build style, the distortion was further reduced to 17 mils.

Now, the Slab 6X6s were finally starting to look like flat slabs. Remember, again, that the Slab 6X6 test involves the absolute worst-case of post curing from one side only. In real applications, such a flat structure would be post cured from both sides such that the part is evenly irradiated, to minimize post cure distortion.

The resin development continued beyond **SL 5170**, resulting in the release of **SL 5180** in 1994, an epoxy-based resin for the SLA-500. The Slab 6X6, built in **SL 5180** in the ACES build style, resulted in a superior flat slab, having a maximum distortion of only 5 mils. ***This Slab 6X6 distortion, obtained in 1994, corresponds to almost 50-fold improvement compared to that of 1989, and 10-fold improvement from the best Slab 6X6 results in 1992***.

Now, the SLA users can build very flat, nearly undistorted parts when required, using the epoxy-based SL resins **SL 5170** and **SL 5180**.

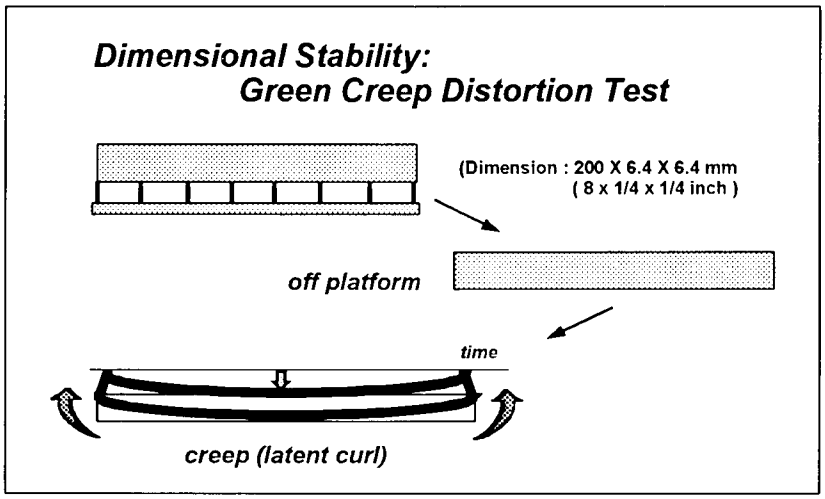

Figure 3

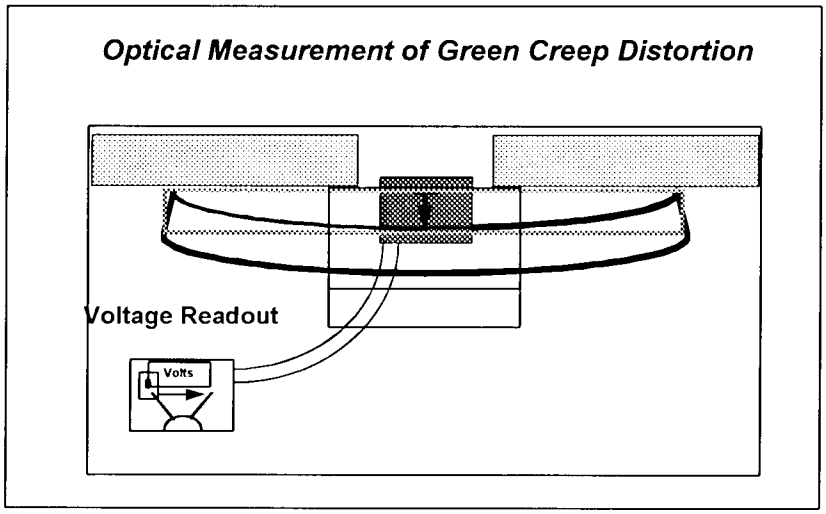

Figure 4

Green Creep Distortion

So far, the User-Part analysis showed the overall part accuracy, obtained from a statistically significant number of dimensional measurements, with emphasis in the x-y plane. The Slab 6X6 test demonstrated the part flatness, indicating accuracy in the z-direction. Both results exhibited great advances in the overall accuracy of the epoxy-based SL resins, **SL 5170** and **SL 5180**. However, both the User-Part and the Slab 6X6 tests involve post-cured parts.

The Slab 6X6 parts are post-cured within one hour after the parts are built. Then the post-cured Slab is allowed to distort over one week. This raises questions about the dimensional properties in the intermediate stage of cure, the so called "green state." Do SL parts creep in the laser-cured, "green" state? How would an SL part behave when left in the green state for an extended period of time?

Some SL parts are complex enough that cleaning and finishing may take many hours. Also, a part may be unintentionally left sitting in the green state before it is post-cured. This may be simply because the part finished building at midnight, or during the weekend, and no one was available to carry out the finishing work. These are both very realistic issues.

In addition, new dimensional requirements for SL resins in the green state became apparent, especially with the development of the QuickCast process. In the QuickCast process, SL parts are built in a quasi-hollow structure. When the QuickCast SL part rises out of the SLA vat, the part is initially filled with liquid resin, trapped in cells between the thin, outer boundary of cured resin. Next, a set of vent and drain holes are generated at appropriate locations either manually, or using the latest QuickCast 1.1 software during SL file preparation, and the uncured liquid resin is drained out of the QuickCast part. In a QuickCast part, the internal volume is "topologically simply connected," allowing liquid resin to flow freely from one internal section of the part to another. This allows complete drainage of the liquid resin before the QuickCast part is further processed for shell investment casting.

Due to the finite viscosity and surface tension of the liquid resin, the draining is certainly not instantaneous. The epoxy-based resins have viscosities of about 200 cps at 30°C, which are already an order of magnitude lower than the viscosity of the earlier conventional acrylate resins. This allows some simple parts to drain in a few minutes, and most parts, in a few hours. However, some complex parts resulting in long, narrow, internal passages, may take several hours to drain. This is a process that is carried out in addition to the normal support removal and finishing processes. During this draining time, what happens to the part dimensions? This is a concern especially because the SL QuickCast parts comprise thin walls, and are left in the laser-cured state, throughout this period.

The Green Creep Distortion (GCD) Test was developed to investigate the dimensional stability of SL parts in the green state. The test procedure, described in detail in reference 1, is schematically described in figure 3. The test involves a 200-mm long, and 6.4 X 6.4 mm (8 X 1/4 X 1/4 inch) square cross-section strip, called the CreepBar. The CreepBar is first built flat on an SLA, in the selected resin. Remember that a long, thin strip, with a high aspect ratio, is one of the most difficult parts to accurately build in layer-additive rapid prototyping methods. The strip is completely supported such that it stays flat on the SLA platform during the building cycle. The part is then removed from the SLA vat. The supports are removed, and the SL strip is placed on an optical measuring device, shown schematically in figure 4. The strip is then intentionally allowed to undergo creep distortion in the green state. To simulate the worst creep distortion, the *strip is not postcured in this test.* Post-cured strips are expected to creep much slower, and to a significantly lesser extent. The maximum deflection at the midpoint of the green CreepBar, or conversely the two ends of the CreepBar, is called the "Green Creep Distortion," (GCD). The GCD, measured optically, is automatically recorded on a computer over a period of 24 hours.

The Green Creep Distortion for the three acrylate-based resins, **SL 5143**, **SL 5149**, **SL 5081-1**, all built in STAR-WEAVE, and the epoxy-based resins, **SL 5170** and

SL 5180, built in the QuickCast build style, are presented in figure 5, as a function of time. The data for the epoxy-based resins built in the solid ACES build style are not plotted in this figure because the results were indistinguishable from the data for QuickCast build style.

Note, from figure 5, that the GCD rate for all resins is quite significant initially, and then the distortion rate slows down very quickly. For all acrylate-based resins shown in figure 5, more than 60% of the absolute GCD measured at an elapsed time of 20 hours occurs within the initial 2 hours. For example, the CreepBar built in **SL 5143** distorts to 48 mils after 20 hours. At 2 hours, the distortion is already about 35 mils, which is about 70% of the final distortion after 20 hours. Among acrylate resins, **SL 5081-1** has the lowest creep distortion. This data suggests that part-cleaning and finishing of acrylate-based SL parts should be performed as quickly as possible once the restraining support structures are removed from the part.

From this data, it is clear that both epoxy resins **SL 5170** and **SL 5180** have very low GCD, hence, they are dimensionally much more stable than the acrylate resins. Both epoxy resins have GCD of less than 4 mils within the 24 hour period.

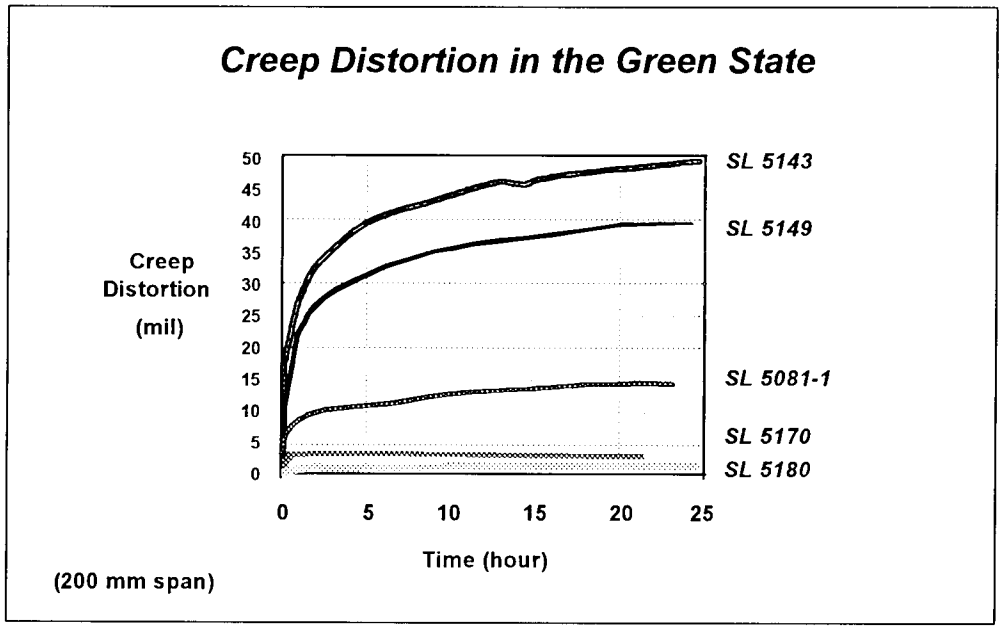

Figure 5

Furthermore, when the GCD data was plotted as a function of the logarithm of time, it was found to be log-linear, as in figure 6. This behavior is due to the viscoelastic nature of cured SL resins. Viscoelastic bodies have been found to behave in a log-linear fashion with time. Using this characteristic log-linear creep behavior, a convenient parameter, called Log Green Creep Rate (GCR), that characterizes the rate at which the SL test part undergoes creep distortion, was defined. It is indicated by the slope of the curve. *This way, a single parameter may be used to describe the creep behavior of SL resins*, and allows one to compare the dimensional stability of various resins, and / or build styles.

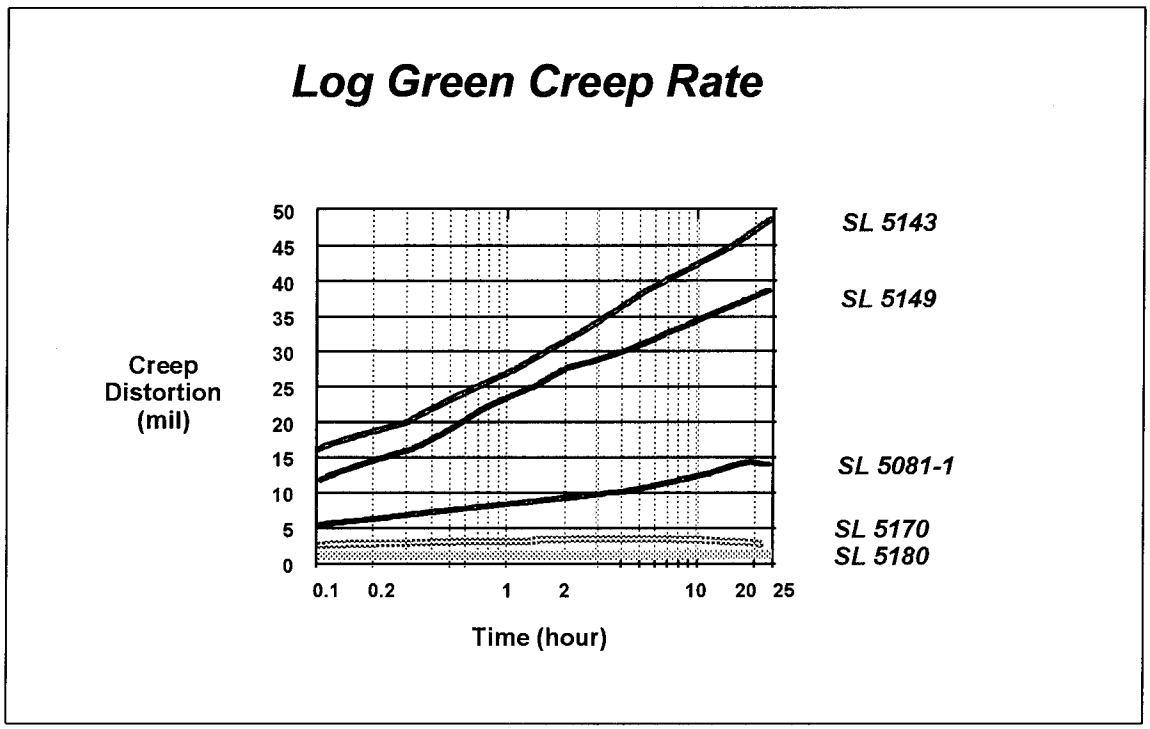

Figure 6

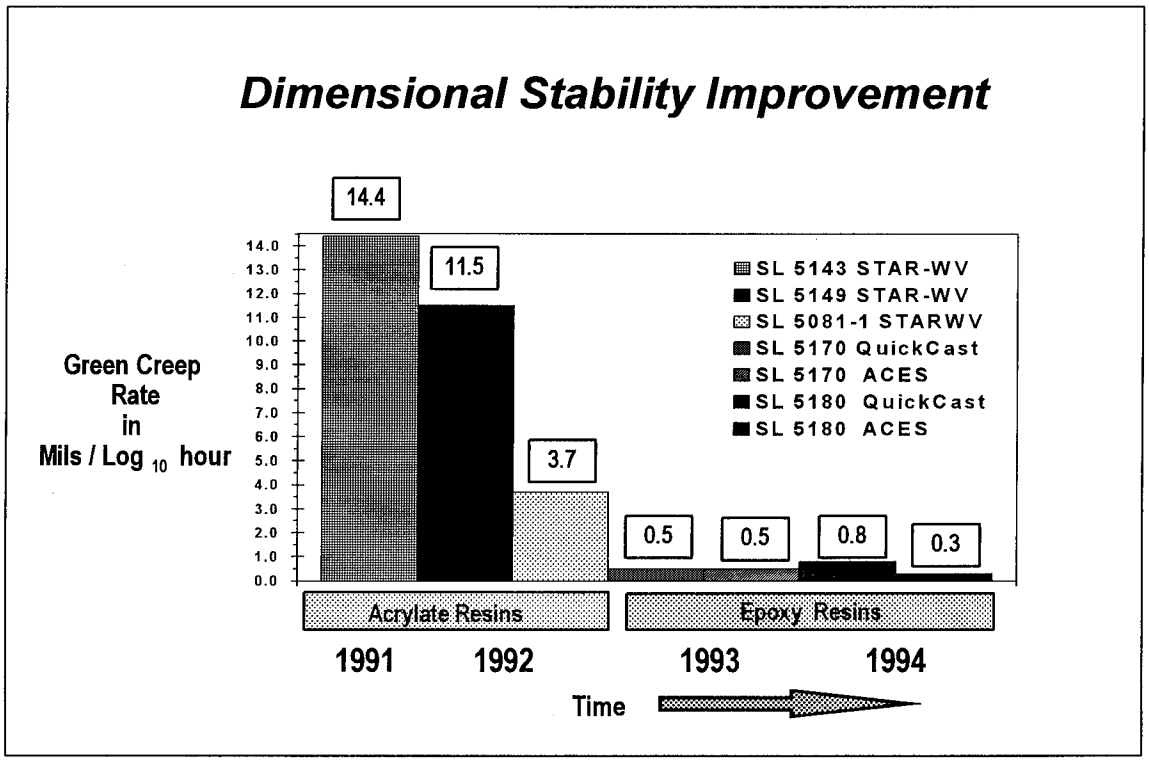

Figure 7

The GCR values for the SL resins tested are shown in figure 7. It is apparent that the epoxy resins have much lower GCR values than the acrylate resins, indicating that the epoxy resins are dimensionally highly stable. The latest result shown in the bar chart of figure 7, indicates that **SL 5180** built in ACES, with the log GCR of 0.3 mils/$\log_{10}$ hour, has the highest dimensional stability in the green state, among the SL resins tested. However, within the error-bar for the experiment, this is comparable to the log GCR of 0.5 mils/$\log_{10}$ hour of **SL 5170**, built in either QuickCast or ACES build styles.

Compared to one of the acrylate-based resins, the *dimensional stability of the epoxy resins improved almost thirty (30)-fold over the period of three years*, from 14.4 mils to about 0.5 mils per every multiple of 10 in time. In summary, the dimensional stability in the green state may be ranked according to the following order, in the descending order of dimensional stability:

SL 5170 & SL 5180 >> SL 5081-1 > SL 5149 > SL 5143.

ASTM Mechanical Properties

At this point, the dimensional accuracy and stability of the epoxy-based resins were demonstrated. Once accurate and stable parts are generated on the SLA, one would also like to know how strong they are. How do the mechanical properties of the epoxy-based resins compare to those of acrylate-based SL resins, and also compared to other thermoplastics?

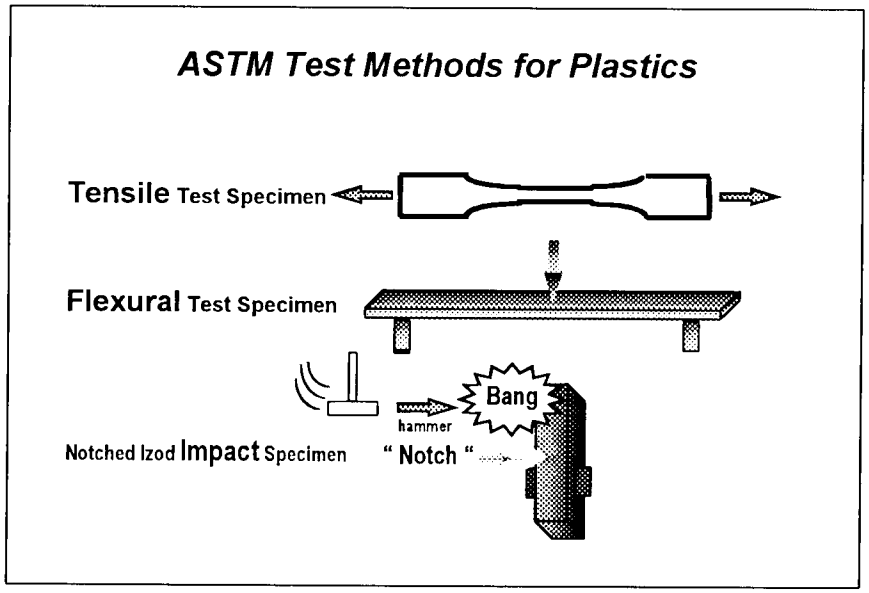

Figure 8

Six types of properties, tensile strength, tensile modulus, elongation to break, flexural strength, flexural modulus, and impact strength, were measured according to the American Standards for Testing and Materials (ASTM) for plastic materials. The results

for the epoxy-based SL resins are compared to the literature values[8] for acrylic plastic (PMMA) and medium impact polystyrene. The mechanical properties for acrylate-based SL resins, in particular, urethane-acrylate-based **SL 5143**, **SL 5149**, **SL 5154**, and epoxy-acrylate-based **SL 5081-1** and **SL 5131**, are also presented for comparison.

As a side note, the description for **SL 5081-1** and **SL 5131**, "epoxy-acrylates," may be misleading. Epoxy-acrylates are a type of acrylates. It should be emphasized that these resins are *not epoxy-based monomers*, and *do not contain epoxies*. The *precursor* molecules for the monomers in the resin was an epoxy. Furthermore, the reaction mechanism for epoxy-acrylates is 100% free-radical polymerization, characteristic of acrylates.

For mechanical testing, the SL resins are all built on the appropriate SLA using the recommended solid build styles, and are post-cured normally. For the epoxy-based **SL 5170** and **SL 5180** resins, ACES build style was used. The other SL resins were built in STAR-WEAVE.

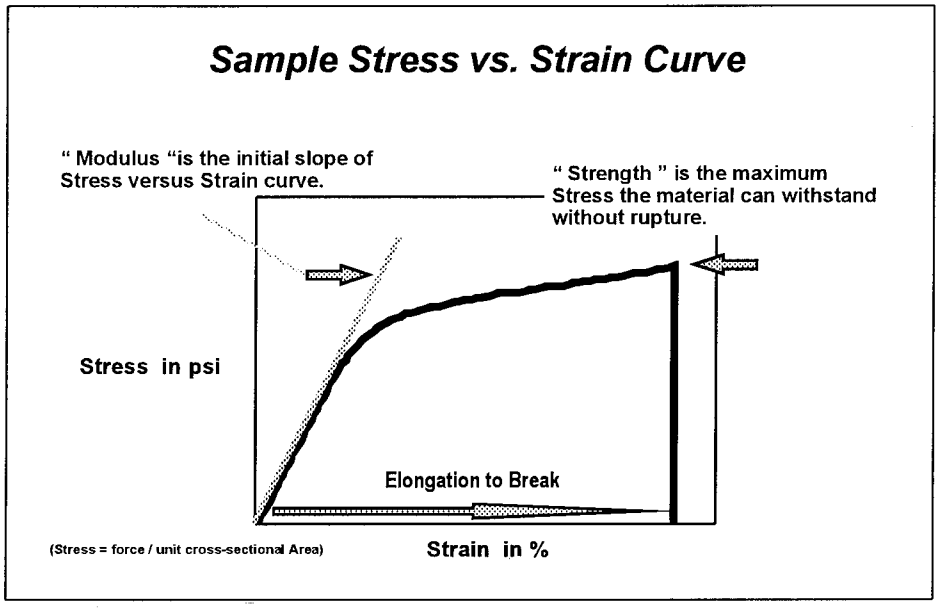

Figture 9

The ASTM mechanical tests are schematically described in figure 8, and a simple definition of modulus, strength, and elongation to break, as applied to tensile testing, is given in figure 9. These are some of the most typical mechanical properties considered in the materials selection process for various prototype and end-use applications in product manufacturing.

The mechanical properties for the SL resins are given in figures 10~16, together with those for acrylic plastic and medium impact polystyrene. The horizontal bars represent the values, and the darkened tips provide the range of values. For the **SL 5170** and **SL 5180** resins, the range is based on the error bar associated with ASTM tests of multiple samples. At least five samples were tested. For the non-epoxy SL resins, the range includes, in addition to the measured range, small, but non-negligible variation

between the SLA-250 and SLA-500 versions of similar resins. For the acrylic and medium impact polystyrene data, the literature values presented include the range of values corresponding to multiple grades of materials available in the market that may be described as "acrylic plastic" and "medium impact polystyrene." Obviously, there are a number of manufacturers as well as a number of grades of these common thermoplastics. For some materials, the range of the mechanical property values may be very large.

Acrylic plastics are used for transparent aircraft enclosures, radio and TV parts, lighting equipment, and goggle lenses. Medium impact polystyrenes are most commonly used for radio and TV cabinets, toys, and containers and packaging applications.

Tensile and Flexural Strengths

Tensile testing for SL resins was performed according to the **ASTM D638** method. The tensile strength data, given in figure 10, demonstrates that the high strength, but relatively brittle resins, **SL 5081-1** and **SL 5131**, have the highest tensile strengths in this group. Their tensile strengths are 7,200~11,500 psi. The urethane-acrylates have the lowest strengths, for both tensile and flexural tests, with strengths of about 5,000 psi. The **SL 5170** and **SL 5180** resins have tensile strengths in the range of 6,000~9,000 psi. These tensile strengths are in the same range as those of acrylic plastic, with 6,000~9,000 psi. The tensile strength of **SL 5180** is comparable to medium impact polystyrene, however, **SL 5170**, with the tensile strength of about 8,800 psi, is almost 50% stronger than medium impact polystyrene.

The flexural strength is defined as the stress measured at fiber strain of 5% as designated by the **ASTM D790** criteria for flexural testing. For most applications, flexural strength is more relevant for SL parts because parts are more often bent than pulled along the long axis. The urethane-acrylates have the lowest strengths, for both tensile and flexural tests.

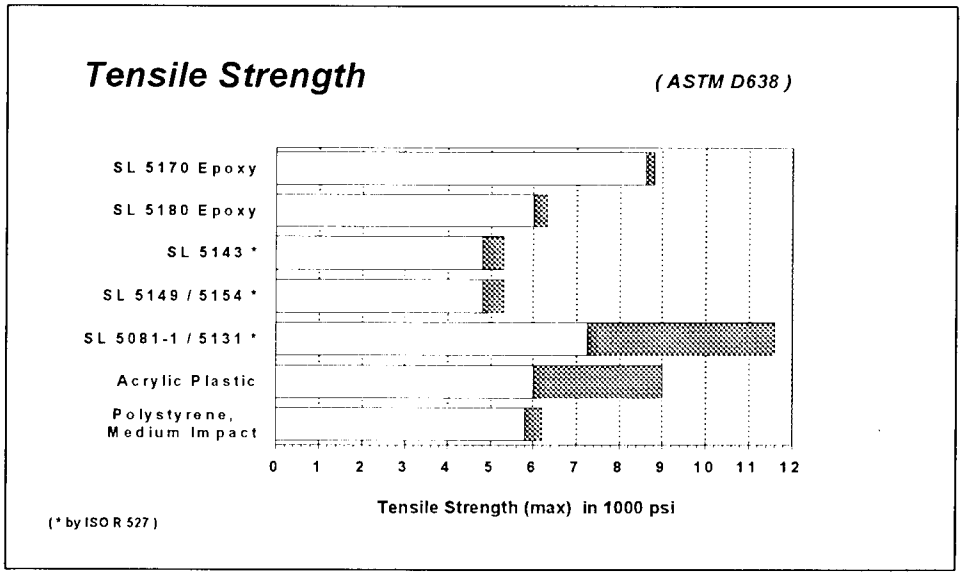

Figure 10

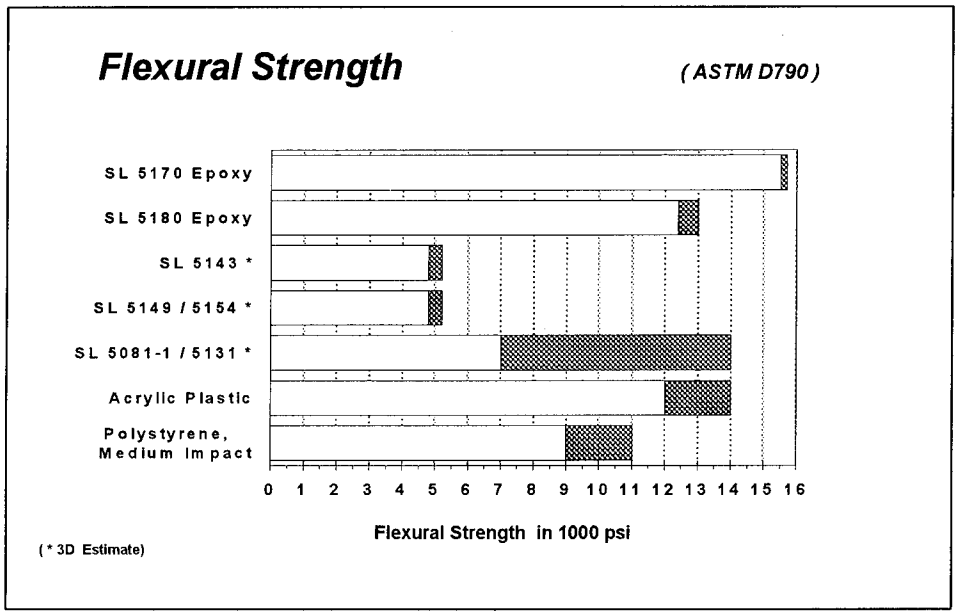

Figure 11

Generally, flexural strength scales with the tensile strength. However, an interesting trend is observed between the acrylate- and epoxy-based resins. In the case of acrylate-based resins, the flexural strengths are equal to, or only slightly greater than their tensile strengths. For example, the maximum tensile strength for **SL 5081-1** is 11,600 psi whereas the flexural value is 14,000 psi, an increase of about 30%. However, epoxy-based resins have significantly higher flexural strengths than the tensile strengths. For example, the flexural strength of **SL 5180** is 12,700 psi, which is more than 100% greater than its tensile strength of 6,100 psi. This tensile strength of **SL 5180** is comparable to that of medium impact polystyrene, however, it is 20% stronger in flexural strength. Similarly, for **SL 5170**, the increase from tensile to flexural strengths is from 8,800 psi to 15,600 psi, an increase of almost 80%. *Furthermore, **SL 5170** has a higher flexural strength than the strongest acrylate SL resin, **SL 5081-1**, and is even stronger than acrylic plastic or medium impact polystyrene.*

Tensile and Flexural Modulus

Modulus is a measure of how much the material elongates, or deforms, when it is subjected to a given load or stress. This is one of the most important parameters that is often referred to as the "rigidity" of the material. The tensile modulus was measured in compliance with **ASTM D638**, and for flexural modulus, with **ASTM D790**.

The tensile modulus, given in figure 12, of **SL 5081-1** resin, is relatively high among the SL resins, with the maximum value approaching 600,000 psi. The urethane acrylates, **SL 5143** and **SL 5149**, have relatively low values, ranging from only 100,000~160,000 psi, compared to the tensile modulus for acrylic and medium impact polystyrene, which is about 390,000~470,000 psi. The epoxy-based resins, however, range from 400,000~600,000 psi. Hence, **SL 5180** is comparable to the thermoplastics.

However, **SL 5170**, on the other hand, has tensile modulus that is almost 30% greater than either acrylic or medium impact polystyrene.

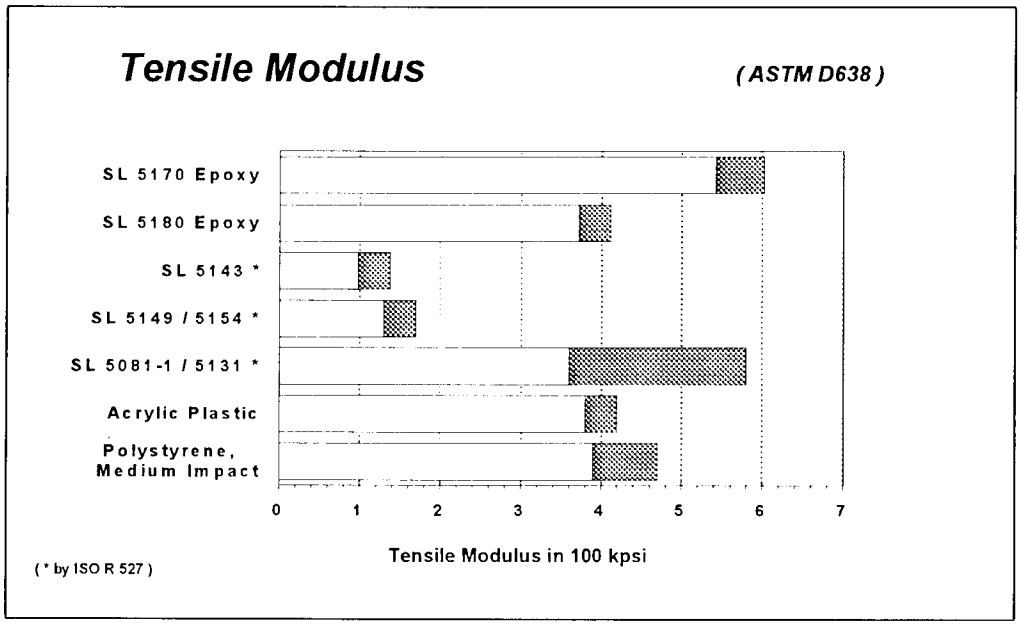

Figure 12

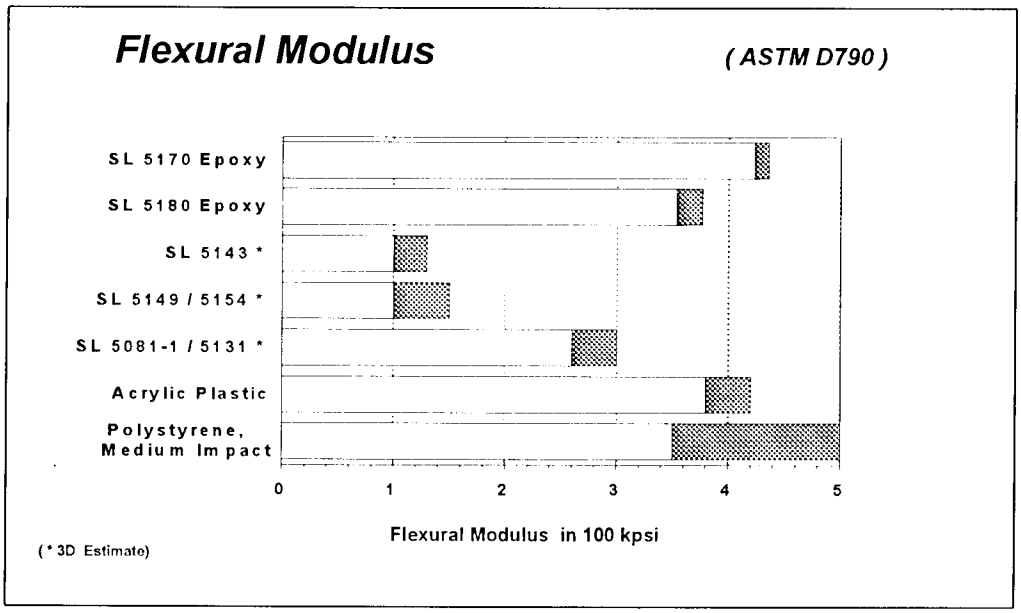

Figure 13

The flexural modulus, shown in figure 13, is a measure of bending, or flexural deformation, when the material is subjected to a stress perpendicular to the long axis of

the test sample. The bending deformation results in shear forces inside the part, and is a common deformation mechanism in complex geometries. The flexural modulus test was carried out pursuant to **ASTM D790** procedure.

The trend for flexural modulus is similar to that for tensile modulus, discussed above. Notice, though, that the epoxy-based resins are more rigid than the acrylate-based resins. Even the high strength acrylate resins **SL 5081-1** and **SL 5131**, have only about 75% of the flexural modulus of **SL 5170** and **SL 5180**. The difference between the urethane acrylate systems **SL 5143** and **SL 5149** is much greater. *The **SL 5170** and **SL 5180** resins are almost three times as "rigid" as those SL resins.* High modulus is the key to improved dimensional stability.

Elongation to Break

The elongation to break data, obtained according to **ASTM D638**, is shown in figure 14. The elongation to break for the flexible urethane-acrylate SL resin, **SL 5143,** is the greatest among SL resins. The range of elongation to break values for medium impact polystyrene is extraordinarily large. The values for medium impact polystyrene may be as small as 3%, or as large as 40%, depending on the grade of material. In contrast, **SL 5081-1** has maximum elongation to break of only 3%, the lowest in the group. The epoxy resins **SL 5180** and **SL 5170**, have elongation to break values of as much as 16, and 19%, respectively. This is substantially greater than the corresponding values for acrylic plastic of 7%, or for the urethane acrylates, **SL 5149** and **SL 5154**, of 11%.

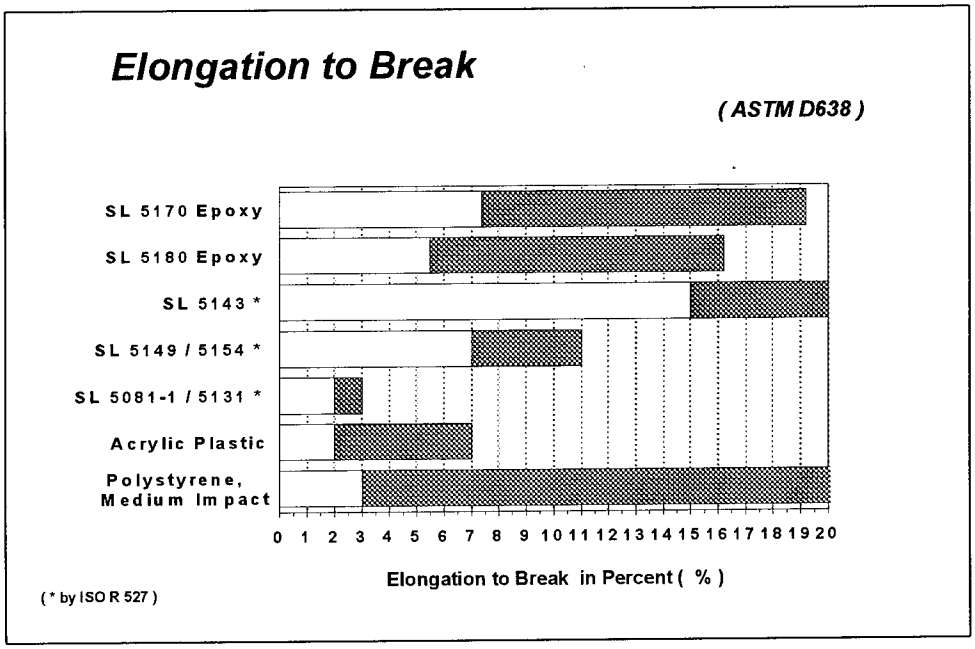

Figure 14

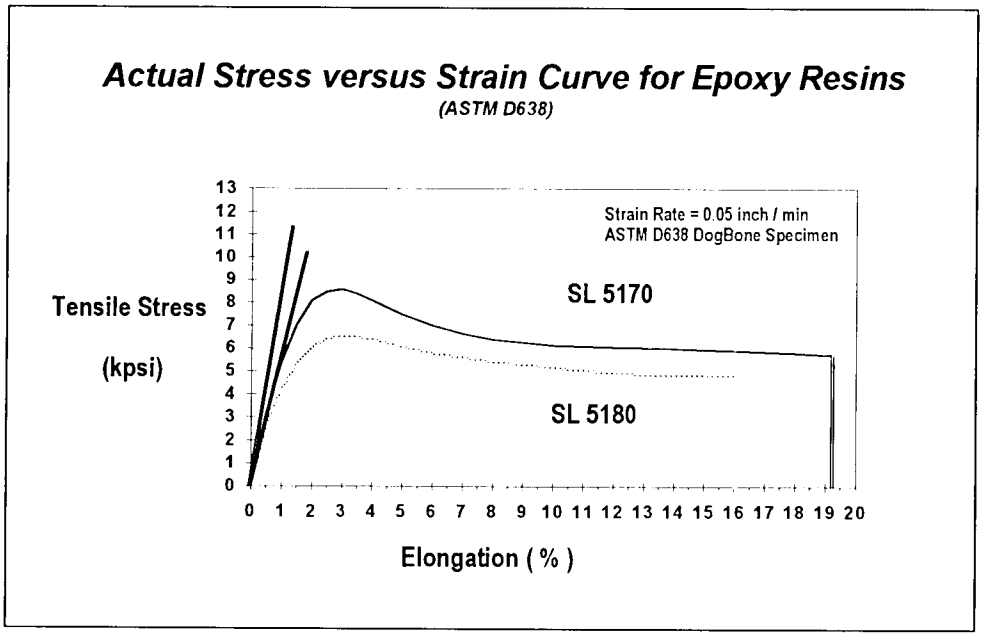

Figure 15

The experimental tensile stress data for **SL 5170** and **SL 5180** is plotted as a function of elongation, in figure 15. The tensile modulus values, defined as the slope of the intial linear portion of the stress vs. strain (elongation) curve, are slightly different between the two epoxy-based resins. **SL 5170** has a greater slope than **SL 5180**, corresponding to the difference in the tensile modulus value of 570,000 psi vs. ~ 400,000 psi. Notice that the measured stress increases as the tensile sample is elongated further, up until an elongation of 3%. Since the stress becomes maximum at this point, in this case, the stress values are assigned as the tensile strengths for the two resins. Then, the curves passe beyond the yield point, and go into *plastic deformation* before it finally breaks at about an elongation of 16~19%. *Plastic deformation is usually not a characteristic of crosslinked polymer systems.* However, these photo crosslinked epoxy-based resins **SL 5170** and **SL 5180** undergo substantial elongation, beyond the yield point. Most other SL resins do not substantially elongate beyond the yield point, except for flexible systems.

Material toughness is defined as the area under the stress vs. strain curve. In this view, the **SL 5170** and **SL 5180** are considered tough materials. Admittedly, there are high-molecular weight engineering thermoplastics that have considerably higher toughness than **SL 5170** and **SL 5180**. However, these epoxy-based SL resins have proven to be extremely rugged and tough for numerous applications, based on SLA user surveys carried out in late 1993. (SL 5180 was not released yet, however, it had been in Beta testing stage.) **SL 5170** and **SL 5180** parts have survived many functional tests that include spinning propellers at high speeds, exposing models to high velocity flow in wind-tunnels, snap-fits for such parts as telephone and computer housings, and fluid flow testing in liquids, to name a few. Some of these functional tests could not be performed with the earlier acrylate-based resins.

Impact Strength

Finally, the impact strengths of SL resins, shown in figure 16, were measured according to the specification of **ASTM D256**. The impact samples were notched in the CAD data, such that no machining was involved, and the SL parts were ready to be tested immediately. The width of the impact test sample was 1/4 inch, a thicker sample, instead of the thinnest allowed, of 1/8 of an inch, by ASTM. This was because thin samples are known to result in higher impact strength values due to the flexing and multi-nodal bending of the sample during the impact, dissipating the energy from the impact much more than for thicker samples. Therefore, such values from thin samples may not be representative of the actual impact strength of the resin. A thicker sample can concentrate the energy of the impact in one direction, and is representative of the material, and not the geometry.

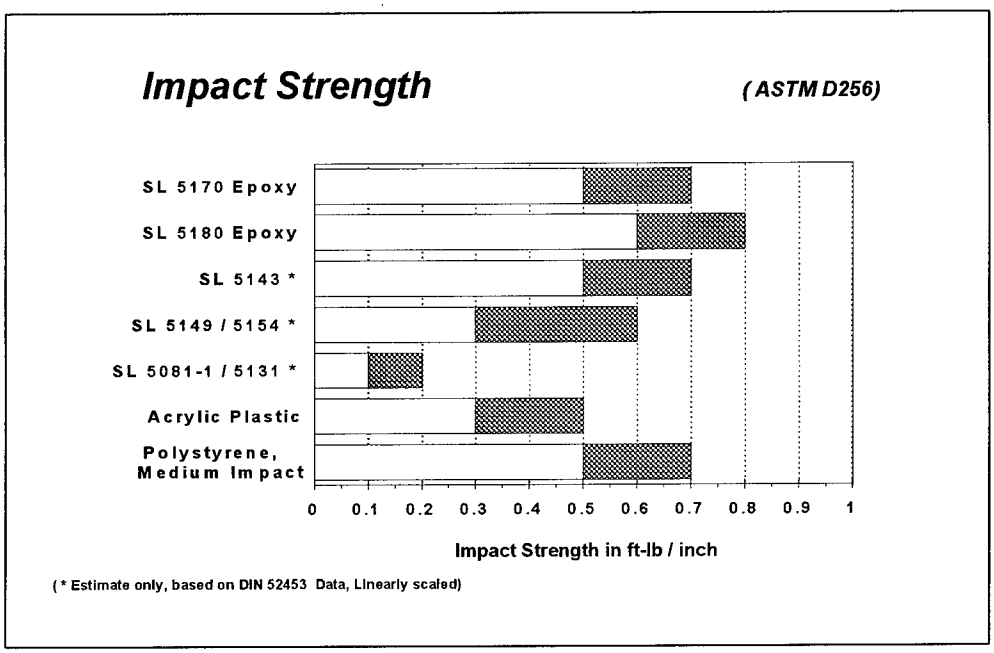

Figure 16

The impact strengths of the epoxy-based resins are comparable to medium impact polystyrene, and are slightly greater than acrylic plastic. In addition, these SL resins, **SL 5170** and **SL 5180**, having impact strengths of 0.5~0.8 ft-lb/inch, are *3~4 times more impact resistant than the earlier acrylate resins **SL 5081-1** and **SL 5131***, which have impact strengths of only 0.1~0.2 ft-lb/inch. **SL 5180**, have the greatest impact strength, with a maximum value of 0.8 ft-lb/inch. Within experimental error, **SL 5170** and **SL 5180** have impact strengths that are comparable to medium impact polystyrene and acrylic plastics.

Precision Metal Prototypes

For applications that require greater mechanical strengths than **SL 5170** and **SL 5180**, metal parts can be obtained by using QuickCast. With QuickCast, *precision* metal components can be directly produced from SL parts.

	Common Plastics	Aluminum	Steel
Tensile Strength (kpsi)	**~10**	**~100**	**~200**
Tensile Modulus (Mpsi)	**~0.5**	**~10.0**	**~30.0**

Table 1.

The mechanical properties of metals, in general, can be orders of magnitude greater than plastic. Some mechanical properties of metals are given in Table 1, for comparison with those of plastics for reference. For example, even aluminum, which is considered a "soft" metal, have tensile strength that is an order of magnitude greater than plastics. The difference is greater for tensile modulus. Metals such as steel is 60 times more rigid than plastics are. Impact resistance, is a measurement available for materials that break and fail. Most ductile and maleable metals do not break and hence impact strength can not be measured. However, if it is measurable, the impact strengths for metals is expected to be orders of magnitude greater than plastics.

Furthermore, when a "negative" core and cavity pair of a "positive" geometry is produced in metal using QuickCast, tooling is obtained. With the metal core and cavity pair, prototype, and eventually production functional parts may be *ultimately injection molded in the desired engineering thermoplastic material*. This allows the user to test his designed object quickly, in the material of his choice.

Conclusion

The dimensional properties of the stereolithography resins based on epoxy chemistry were measured. These resins, **SL 5170** and **SL 5180**, were found to generate parts with significantly improved overall part accuracy, dimensional stability, and mechanical properties relative to the earlier acrylate SL resins. Also, **SL 5170** resin, for the **SLA-250** system, and **SL 5180**, for the **SLA-500** system, have resulted in extremely low curl and distortion.

Overall dimensional accuracy, measured by building not one, but *ten sets of User-Parts* built in **SL 5170** on the **SLA-250** have established the accuracy record to date. The measured RMS error, based on 1700 data points, is ± 1.8 mils, or about ± 45 microns. **SL 5180**, built on the **SLA-500**, is the next most accurate, with RMS error value of about ± 2 mils. The result from ten User-Parts built in **SL 5170** demonstrated, not only high overall accuracy, but outstanding repeatability of the SL process. The accuracy result, based on the 1700 dimensional measurement made by a CMM machine taken in the x, y, and z directions, is statistically significant, and indicates the high level of repeatability achieved by the combination of building parts on an SLA and using the epoxy resin.

The flatness diagnostic Slab 6X6 test showed that these epoxy-based resins are now capable of producing extremely flat parts that were formerly a challenge with the conventional acrylate-based resins. The maximum Slab 6X6 distortion in the epoxy resin, compared to a flat surface, is only +5 mils, even when the Slabs were post cured from one side only, to simulate the worst-case scenario. Now, SLA users can build very flat parts with high confidence.

SL parts built in these resins also exhibit superb dimensional stability in the laser-cured state, as demonstrated by the Green Creep Distortion diagnostic. Green Creep results presented in this paper showed that the log Green Creep Rates (GCR) for **SL 5170** and **SL 5180** are extremely small, with a creep distortion rate of only about 0.5 mils for every decade in time. This is almost a 30-fold improvement over conventional SL acrylate resins. Dimensional stability in the laser-cured state is very important for most SL applications, however, it is critical, for parts generated using the QuickCast™ build style.

Furthermore, the overall mechanical properties of these epoxy resins, measured according to the ASTM standards, were found to be comparable to or exceed those of plastics such as acrylic plastic (PMMA) and medium impact polystyrene.

With respect to the conventional acrylate resins systems, the **SL 5170** and **SL 5180** resins exceed in almost every category of measured mechanical properties. It is worth noting that, in general, the magnitude of these improvements are not incremental, but substantial. For example, flexural strength of the epoxy resins is *two to three times greater*, and the tensile and flexural modulus is more than *four times greater* than the conventional urethane-acrylate-based SL resins. The elongation to break for the epoxy resins is more *than six times greater* than the epoxy-acrylate SL resins. Finally, the impact strength is comparable to the *flexible* urethane-acrylate. However, the impact strength for **SL 5170** and **SL 5180** is *four to seven times greater* than that of the epoxy-acrylate systems, **SL 5081-1** and **SL 5131**. The epoxy resins are considered to possess the best combination of mechanical properties for numerous end-use applications.

Significance of SL 5170 and SL 5180 for SL Users

The improved dimensional and material properties realized by the epoxy-based **SL 5170** and **SL 5180**, bring about numerous advantages. For example, the outstanding strengths, modulus, and dimensional stability makes **SL 5170** and **SL 5180** suitable for building thin walls. Without these tributes, thin walled parts will creep, bend, or, simply collapse if the load is excessive, or distort to the point where the parts become unacceptable. Many successful thin-walled parts such as housings, and custom containers, have been built in the ACES solid build style, by numerous SL users.

Of course, the greatest significance of the epoxy-based resins is associated with the QuickCast application, for which high inherent strength of the resin is essential to prevent premature deformation, especially because QuickCast patterns necessarily require a quasi-hollow internal structure to prevent breakage of the ceramic invesment casting shells during the burn out cycle. The toughness, rigidity, and impact strength of the QuickCast SL patterns made of **SL 5170** and **SL 5180** are much greater than those of waxes commonly used for investment casting. This allowed foundries to shell investment cast

thin walls and delicate features that were once thought to be impossible for patterns made in waxes.

Accuracy, dimensional stability, and good overall mechanical properties are a key to expanding SL into new applications, such as generating prototype and, eventually, production tooling via QuickCast Tooling. Finally, functional parts may be produced by injection molding in the "negative" core and cavity or, QuickCast tooling, to generate parts in the desired engineering thermoplastic material.

---

[1] Thomas. H. Pang. *"Stereeolithography Epoxy Resin Development: Accuracy and Dimensional Stability,"* P. 11, Proceedings of the Solid Freeform Fabrication Symposium. University of Texas at Austin. Austin. Texas. August 8-11. 1993.

[2] Thomas. H. Pang and Paul F. Jacobs. *"Stereolithography 1993: QuickCast™,"* P. 158. Proceedings of the Solid Freeform Fabrication Symposium. University of Texas at Austin. Austin. Texas. August 8-11,1993.

[3] Paul F. Jacobs. 3D Systems. Steve Kennerknecht. Cercast Group. Jeff Smith and Mike Hanslits. Precision Castparts Corporation. and Larry Andre. *"QuickCast™: Foundry Reports,"* 3D Systems Publication. Valencia. California. April 1993.

[4] Karl R. Denton. Ford Motor Company. Paul F. Jacobs. 3D Systems. Inc.. *"QuickCast™ Tooling: A Case History at Ford Motor Company,"* Proceedings of the Rapid Prototyping and Manufacturing Conference. Society of Manufacturing Engineers and the Rapid Prototyping Association. Dearborn. Michigan.. April 26-28. 1994.

[5] Paul F. Jacobs. *"Rapid Prototyping and Manufacturing: Fundamentals of Stereolithography"*,Chapter 11. P. 287. Published by the Society of Manufacturing Engineers. July. 1992.

[6] *ibid*, Chapter 10. P. 263.

[7] Ed P. Gargiulo and D. Belfiore. *"Stereolithography Process Accuracy: User Experience"*, Proceedings of the Second International Conference on Rapid Prototyping. University of Dayton. Dayton. Ohio. pp. 311. June. 1991.

Ed P. Gargiulo and D. A. Belfiore. *"Photopolymer Solid Imaging Process Accuracy ,"* Intelligent Design and Manufacturing for Prototyping. ASME. Vol. 50. Winter Meeting. December 1~6. 1991.

[8] *1994 Materials Selector* Issue. Machine Design. Vol 65.. No(26). December. 1993.

A SIMPLE POLYMER SHRINKAGE MODEL APPLIED TO STEREOLITHOGRAPHY

Lawrance Flach
Department of Chemical and Materials Engineering

Richard P. Chartoff
Rapid Prototype Development Laboratory
and
Center for Basic and Applied Polymer Research

University of Dayton
300 College Park Avenue
Dayton, OH 45469-0246

ABSTRACT

A simple polymer shrinkage model has been successfully applied to the stereolithography process. The shrinkage model, which computes specific volume changes from the degree of conversion of monomer to polymer, incorporates a lag between conversion and shrinkage. An overall process model used to simulate the stereolithography process was modified by inclusion of the shrinkage model. Use of the modified stereolithography process model allows prediction of the shrinkage that might be expected to occur when fabricating a strand of plastic. By varying the lag between conversion and shrinkage it is shown that faster shrinking resins should exhibit lower overall shrinkage than slower shrinking resins. This is a direct result of the fact that less shrinkage occurs after the strand has been scanned for the faster shrinking resins.

INTRODUCTION

The photopolymerization that occurs during stereolithography is accompanied by shrinkage. It is this shrinkage that is responsible for dimensional inaccuracies and warpage in parts produced by the process. The exact amount of shrinkage observed in a strand of plastic manufactured by a stereolithography apparatus (SLA) depends on a number of factors. These factors include the degree of cure achieved during exposure, the polymerization kinetics, the shrinkage kinetics, and also the rate at which the strand is scanned by the laser.

As part of a continuing effort to better understand the complexities of the stereolithography process, we have analysed the shrinkage phenomenon and its relationship to the laser scan rate. In addition, we have modified the general stereolithography process model to include a prediction of the shrinkage that might be expected to occur when using the SLA to fabricate a strand of plastic.

BACKGROUND

An analysis of shrinkage in stereolithography and its relationship to the laser scan rate has been presented elsewhere [1]. It is, however, pertinent to review some of this material at this stage.

The basis for the analysis is that the observed shrinkage is determined by the amount of shrinkage that will occur at each point along the line **at the time the line is completed.** At that time the line is the correct length (due to a scan of the correct length) and any change in length is a result of polymerization and shrinkage that occurs after completion of exposure.

If L is the desired length of a line of plastic drawn by the SLA, then the overall linear shrinkage (fraction) due to cure for the line of plastic will be given by

$$F_c = \frac{1}{L}\int_0^L f_r(y)\, dy \qquad (1)$$

where $f_r(y)$ is the **residual** shrinkage (fraction) at position y along the line, i.e. the amount of shrinkage that will occur at that point after completion of the line.

The residual shrinkage, $f_r(y)$, can be obtained from experimentally determined shrinkage vs. time data, or can be estimated from model-based predictions of the degree of cure along the line of plastic. (The latter approach was adopted here.) If t_s is the time taken for the laser to scan from position y to the end of the line L, and $f_{ts}(y)$ the fractional shrinkage that has occurred up to time t_s at position y, then the residual shrinkage is just

$$f_r(y) = f_\infty(y) - f_{ts}(y) \qquad (2)$$

where $f_\infty(y)$ is the maximum fractional shrinkage that will occur at position y as $t \rightarrow \infty$.

The shrinkage that accompanies the polymerization of diacrylates tends to lag behind the conversion [2,3,4]. The model used for shrinkage should allow for this lag. Bowman and Peppas [3] have presented a method that satisfies this requirement. The method results in a 1st order lag between conversion and specific volume change, and details are as follows:

$$v_\infty = v_m(1-\epsilon_v x) \qquad (3)$$

and

$$\frac{dv}{dt} = \frac{1}{\tau}(v_\infty - v) \qquad (4)$$

Eqn. (3) computes the maximum specific volume change based on conversion, i.e. the specific volume that would be reached as $t \rightarrow \infty$ based on conversion x, and eqn. (4) determines the dynamics of the specific volume change from its present value to v_∞. The contraction factor, ϵ_v in eqn.(3), can be determined from the specific volumes of the monomer and polymer or from

shrinkage data. The lag parameter, τ in eqn.(4), determines the extent of the lag between conversion and shrinkage. Bowman and Peppas change the value of τ as the polymerization proceeds. This allows τ to increase as conversion increases. Initially, at low conversion, shrinkage may occur almost simultaneously with conversion, whereas once vitrification has occurred, there may be a considerable lag between polymerization and shrinkage. Figure 1 illustrates how the model predicts the specific volume change and resultant shrinkage would respond to an instantaneous change in conversion. Results for three different values of the lag parameter are shown.

SHRINKAGE AND THE PROCESS MODEL

The stereolithography process model previously developed [5,6] has the capability of calculating conversion of monomer to polymer as a function of time for a rectangular region around the exposed resin. Conversion information is available at the nodes of a 3-dimensional grid.

In order to estimate the amount of shrinkage that we might expect in a strand of plastic manufactured by the SLA, the following sequence of calculations can be performed:

- Calculate the average conversion, $x_{AV}(y)$, for cross-sections perpendicular to the direction of laser travel at the time the scan is complete. This is necessary because conversion varies somewhat with depth and distance from the scan axis. Any 2-dimensional numerical integration technique can be used to perform this averaging.

- Determine the specific volume, $v_\infty(y)$, that corresponds to $x_{AV}(y)$ from eqn.(3)

$$v_\infty(y) = v_m(1-\epsilon_v x_{AV}(y)) \tag{5}$$

- Convert to a fractional linear shrinkage

$$f_\infty(y) = 1-\left(\frac{V_\infty(y)}{V_m}\right)^{\frac{1}{3}} \tag{6}$$

- Calculate the average specific volume, $v_{AV}(y)$, for cross-sections perpendicular to the direction of laser travel from specific volumes calculated from eqn.(4).

- Convert to a fractional linear shrinkage

$$f(y) = 1-\left(\frac{V_{AV}(y)}{V_m}\right)^{\frac{1}{3}} \tag{7}$$

- Determine the residual shrinkage using the results from eqns. (6) and (7)

$$f_r(y) = f_\infty(y) - f(y) \tag{8}$$

- Perform integration along the strand of plastic to obtain an estimate of the overall linear shrinkage

$$F_c = \frac{1}{L}\int_0^L f_r(y)\, dy \qquad (9)$$

The entire procedure outline above was incorporated into the stereolithography process model. Calculated shrinkage information was included with the other data output by the computer code used to numerically solve the model equations.

RESULTS AND DISCUSSION

In order to verify operation of the shrinkage component of the process model, a number of process simulations were performed. All model parameters were unchanged from those of the previously documented test simulation [5,6], the details of which are not presented here. The results from the shrinkage component of the model are presented below. Tests were performed with shrinkage parameters as follows:

$v_m = 0.885\ cm^3\ g^{-1}$

$\varepsilon_v = 0.0738$

τ = 0.1, 0.2 and 0.3 seconds.

The specific volume and contraction factor parameter values selected were appropriate for the HDDA test simulation performed. The shrinkage lag parameter values, although believed to be of the correct order of magnitude, were selected to illustrate the effect of changing that parameter value.

Plots of average conversion and average specific volume versus y (position along strand of plastic) are shown in Figures 2 and 3. These are time progressions, each curve being the profile at a particular time. As expected the conversion increases to some maximum value as time progresses (the reaction is diffusion limited) and the conversion is accompanied by a decrease in the specific volume of the material. The data shown in Figure 3 were generated using a shrinkage lag parameter of 0.2 seconds. Figure 4 shows the conversion and shrinkage dynamics at the mid-point of the strand of material. The laser passes over this point in the strand at t = 0.5 seconds, half way through the total scan which is of 1.0 second duration. This plot clearly illustrates the lag between the conversion and shrinkage at that point in the strand.

A series of simulations were performed with different shrinkage relaxation times (time constants). For three different values of τ, the overall linear shrinkage in the line of plastic, F_c, was calculated. The results are summarized below.

τ (sec)	% Shrinkage, F_c
0.1	0.078
0.2	0.180
0.3	0.279

The faster shrinking resins (those with the lower τ values) exhibit less overall shrinkage than the slower shrinking resins (those with the higher τ values). This supports the notion that a faster shrinking resin should result in lower overall shrinkage, with less distortion and warpage in the final part.

Figure 5 illustrates the effect of changing the shrinkage lag parameter τ on shrinkage dynamics at the mid-point of the strand of plastic. Higher values of τ result in increased lag between conversion and shrinkage. Residual shrinkage values also increase due to the fact that less shrinkage has occurred at the time the scan is complete. The remainder of the shrinkage occurs after completion of the scan and contributes to the observed linear shrinkage. The change in residual shrinkage with τ is clearly illustrated in Figure 6 where plots of residual shrinkage vs. position along the strand are shown. At higher τ values more of the shrinkage occurs after completion of the scan and as a result contributes to a higher observed linear shrinkage. The overall linear shrinkage values shown above (F_c), obtained from eqn. (9), are the average values of the residual shrinkage along the strand. The residual shrinkage tends to drop towards the end of the strand due to lower conversion of monomer to polymer. This is an "end effect" and becomes fairly insignificant for longer strands of plastic.

CONCLUSIONS

A shrinkage model has been incorporated into the general stereolithography process model. The ultimate amount of shrinkage is determined by the extent of conversion of monomer to polymer. The model allows the shrinkage to lag behind conversion in a 1st order manner.

Successful operation of the stereolithography process model with the shrinkage modification has been verified by performing various simulations. One of the tests performed involved varying the shrinkage lag parameter, and the results obtained confirmed the notion that faster shrinking resins should result in lower overall shrinkage values.

NOMENCLATURE

$f_r(y)$ residual fractional linear shrinkage at position y
$f_{ts}(y)$ fractional linear shrinkage at position y at time t_s
$f_\infty(y)$ maximum fractional linear shrinkage at poistion y ($t \rightarrow \infty$)
F_c overall fractional linear shrinkage due to cure
L length of strand of plastic (cm)
t time (sec)
t_s time for laser to scan from position y to L (sec)

v	specific volume ($cm^3\ g^{-1}$)
v_{AV}	cross-section average specific volume ($cm^3\ g^{-1}$)
v_m	specific volume of monomer ($cm^3\ g^{-1}$)
v_p	specific volume fully polymerized ($cm^3\ g^{-1}$)
v_∞	specific volume at conversion x as $t \rightarrow \infty$ ($cm^3\ g^{-1}$)
x	fractional conversion of monomer to polymer
x_{AV}	cross-section average fractional conversion of monomer to polymer
y	spatial coordinate in direction of laser motion (cm)
ε_v	contraction factor = $(v_m-v_p)/v_m$
τ	relaxation time, 1st order lag constant (sec).

ACKNOWLEDGEMENTS

The authors gratefully acknowledge the financial support of the State of Ohio Edison Materials Technology Center (EMTEC), the United States Air Force, and an industrial consortium of companies.

REFERENCES

1. Flach, L. and R.P. Chartoff, "Laser Scan Rates and Shrinkage in Stereolithography", Proc. 4th Int. Conf. on Rapid Prototyping, Dayton, OH, June 14-17, 1993.

2. Kloosterboer, J.G., G.M.M. van de Hei, R.G. Gossink and G.C.M. Dortant, "The Effect of Volume Relaxation and Thermal Mobilization of Trapped Radicals on the Final Conversion of Photopolymerized Diacrylates", Poly. Comm., Vol. 25, 322-325, 1984.

3. Bowman, C.N. and N.A. Peppas, "Coupling of Kinetics and Volume Relaxation during Polymerizations of Multiacrylates and Multimethacrylates", Macromolecules, Vol. 24, 1914-1920, 1991.

4. de Boer, J., R.J. Visser and G.P. Melis, "Time-Resolved Determination of Volume Shrinkage and Refractive Index Change of Thin Polymer Films During Photopolymerization", Poly. Pap., Vol. 33, No. 6, 1123-1126, 1992.

5. Flach, L. and R.P. Chartoff, "A Process Model for Non-Isothermal Photopolymerization with a Laser Light Source. Part I - Basic Model Development", accepted for publication in **Poly. Eng. & Sci.**

6. Flach, L. and R.P. Chartoff, "A Process Model for Non-Isothermal Photopolymerization with a Laser Light Source. Part II - Behavior in the Vicinity of a Moving Exposed Region", accepted for publication in **Poly. Eng. & Sci.**

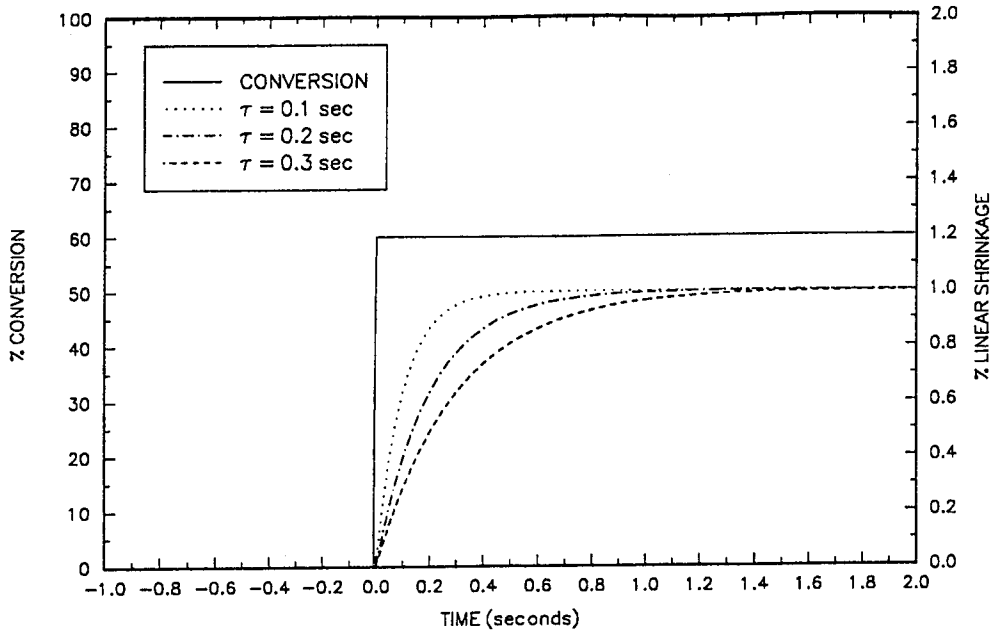

Figure 1: Plot of conversion and shrinkage vs. time. Model predictions for an instantaneous change in conversion for 3 different shrinkage lag parameter values. Ultimate amount of shrinkage determined by shrinkage factor.

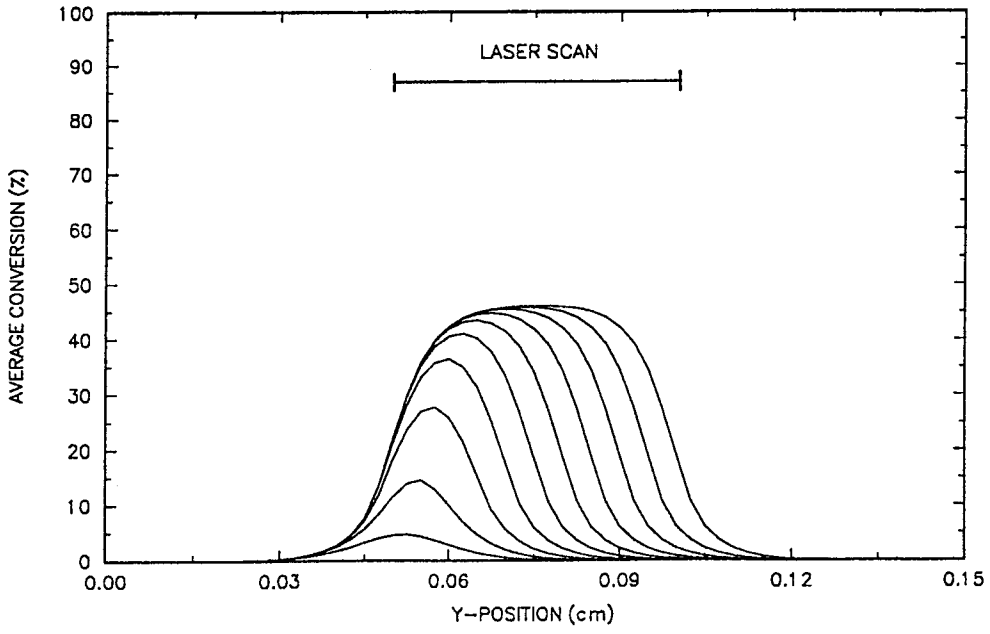

Figure 2: Average conversion vs. position along a strand of plastic. Each curve represents the conversion profile at a particular time. Laser scan duration = 1.0 sec. Plot time increment 0.1 sec.

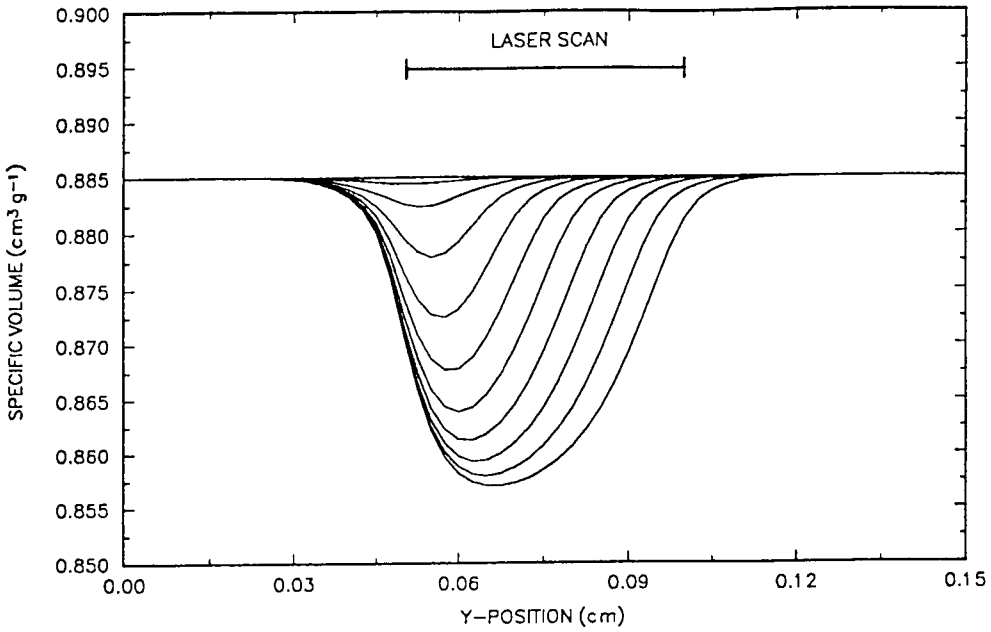

Figure 3: Average specific volume vs. position along a strand of plastic. Each plot represents the specific volume profile at a particular time. Laser scan duration = 1.0 sec. Plot time increment = 0.1 sec. Shrinkage lag parameter τ = 0.2 sec. Data are complementary to Figure 2.

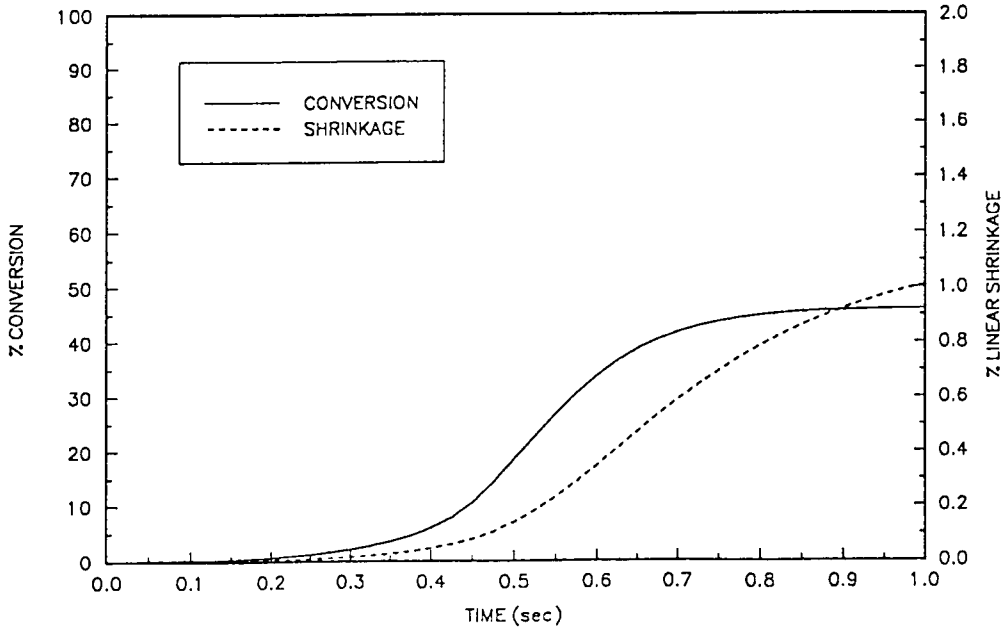

Figure 4: Conversion and shrinkage vs. time at the mid-point of a strand of plastic. Laser passes this point at t = 0.5 sec. Total laser scan time = 1.0 sec. Shrinkage lag parameter τ = 0.2 sec.

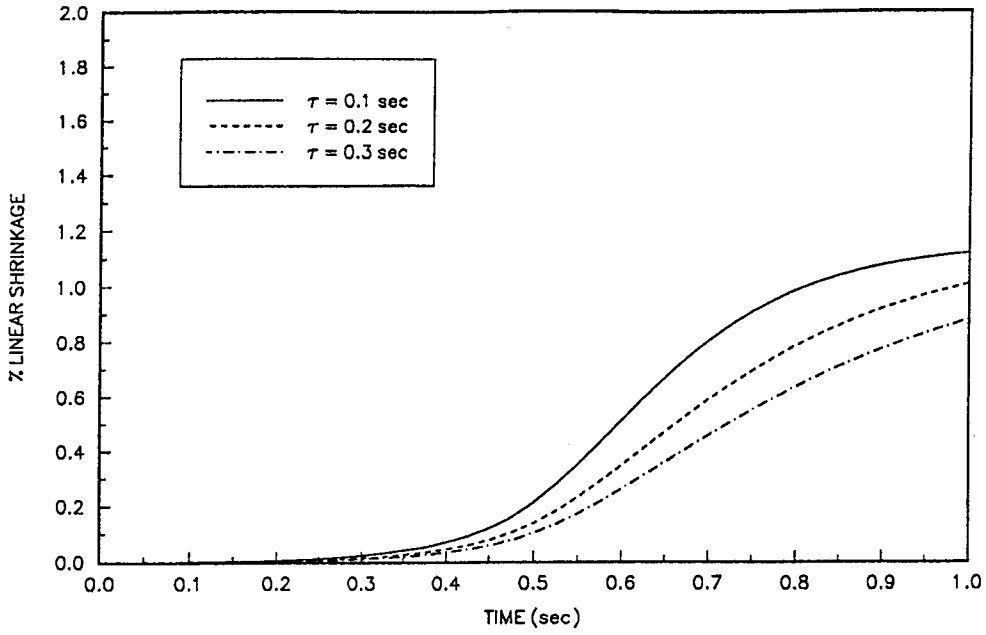

Figure 5: Linear shrinkage vs. time at the mid-point of a strand of plastic for 3 different shrinkage lag parameters. Laser passes this point at t = 0.5 sec. Total laser scan time = 1.0 sec.

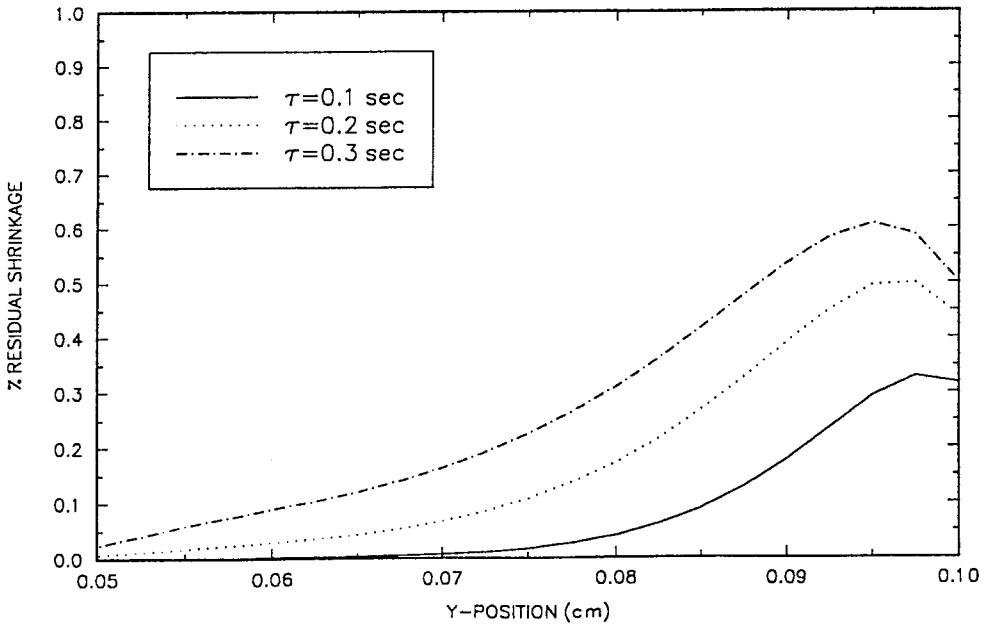

Figure 6: Residual shrinkage vs. position along a strand of plastic for 3 different shrinkage lag parameters. Residual shrinkage calculated from conversion and shrinkage profiles at the end of the laser scan.

MULTI-LAYERED COMPOSITES USING PHOTOLITHOGRAPHY

Amit Bagchi and Robert Beesley, Department of Mechanical Engineering,
Center for Advanced Manufacturing, Clemson University, Clemson, SC 29634

Abstract

The mechanical properties of the parts made using solid freeform fabrication technologies are limited by their resins used. Previous research has shown that the mechanical properties of these parts can be enhanced substantially by using glass and fiber reinforcements. However, all of the published data is for single layered composites, which does not demonstrate its feasibility to manufacture multilayered real objects.

In this paper experiments carried out to build multi-layered parts with glass fiber tow as reinforcement in a matrix of photopolymeric resin are described. These specimens are then tested in uniaxial tension and three point bending to determine their improvement in mechanical properties. The experimental data shows that the tensile strength and tensile modulus increased linearly with the volume fraction of the fiber in the composite, thus demonstrating that the trends observed in single layer composites can be also seen in multi-layered composites.

Introduction

In the past 10 years, solid freeform fabrication (SFF) technologies have allowed the design engineer to produce a working model of a part without the need for tooling, advance planning, and often within hours or days, instead of months. As improvements or revisions are necessary, the part can be redesigned easily before it is prototyped again, and the process can be repeated as many times over a period of days to arrive at the final design.

Many of the SFF technologies utilize polymers to make their parts, either using a certain wavelength of radiation (as in photolithography) or applying localized heat of fusion (as in selective laser sintering). One of the drawbacks of these processes is the compromise in mechanical properties due to those of the pure polymers. These parts are of lower strength than those made using commercially viable processes. One way to strengthen these parts is to re-enforce the parts with high modulus glass, quartz or carbon fibers.

In work done at Clemson University over the past five years [1-6], the process of photolithography has been expanded as a rapid prototyping technology by producing composite parts using glass and quartz fiber as reinforcement. The prototype is generated by reinforcing by selectively laying fibers *in situ* to improve the mechanical properties. These studies have shown that the strength of liquid resin based polymer parts can be increased by up to an order of magnitude. with a very small percent of addition of glass or quartz fibers. Because no real component is made up of a single layer, it is necessary to determine the effect of multiple layers in the build process, and to use more than uniaxial testing to determine the mechanical properties of the parts.

Objective

The objective of this experiment was to build and test multi-layered parts to see if the single layer technology could be applied to manufacture multi-layer, real composite parts. The tensile strength, tensile modulus and modulus of toughness would be studied to measure the enhancement of mechanical properties.

Experimental Work

Specimen Preparation

The multi-layered parts for this research were made from DuPont Somos 3100 photopolymer, and continuous quartz fiber tows (tensile strength 1600 MPa), containing 120 fibers (tensile strength of fibers was 2000 MPa) each 9 microns in diameter. Quartz fibers, with a nearly 100% transmissibility of the ultra-violet (UV) light, allow the UV light to pass through and polymerize even below the fiber tow, thus creating a strong bonding between the resin matrix and the reinforcement.

The specimens were made in a special research test bed developed for producing composite components — the Advanced Desktop Photolithography Unit (ADPU). The ADPU is an emulation of the commercially available stereolithography apparatus, and photopolymerizes the resin and produces parts layer by layer. The ADPU has a two-axis positioning table to move a light source in a pattern just above the liquid resin. The light source is a mercury vapor arc lamp with a fiber optic light pipe to provide the UV radiation (at 325 nanometers) at the desired location. A special fiber dispensing device [7, 8] with three degrees of freedom, two translational and one rotational, lays the fiber bundle onto the resin just ahead of the light. A computer program is used to control the positions of the head of the fiber dispensing device and the light source so that the reinforcement can be provided at the right locations in the specimen. The pencil of light passes over the same regions which were reinforced with the continuous fibers and polymerizes the resin along with the fiber tow. Details of the ADPU can be found elsewhere [6 - 8].

Three layered, rectangular 12.7 mm X 102 mm test specimens were built on the ADPU in accordance with ASTM standards D3039-76 [9]. To grip the ends for carrying out tensile testing, tabs were made of the pure resin and then polymerized onto each end of the finished composite specimen made on the ADPU. A sketch of the specimen is shown in Figure 1.

A program was written in C to generate the path plan for the fiber dispensing device and the light source. This path was provided as input to a machine controller code for the translational and rotational motions of the ADPU necessary to generate the composite specimen. The path of the light source and the fiber dispensing device generated by the program is shown in Figure 2.

A total of 17 specimens passed the initial quality control check for proper construction and tolerances. 13 of these specimens contained fiber strands, spaced 1 mm apart, oriented lengthwise (at 0 degree to the test direction). The other 4 specimens were also three-layered but made of pure resin on the ADPU. The polymerized specimens were found to be wider than the 12.7 mm desired, and were therefore sanded smooth until they were parallel and 12.7 mm wide.

Testing Procedure

Two tests were carried out on the 17 specimens: (i) tensile test; and (ii) three point bend test.

The *tensile test* was carried out on a bench top tensile testing machine, with only the upper grips moving at a constant rate of 2.5 mm/min. The effective length of the specimens was 76.2 mm. The temperature was kept constant at 23.3 degree C, and the relative humidity was 14%. The *bend test* was done in a 3-point bend fixture with a beam length of 57.2 mm, in accordance with ASTM standard D790M-86 [10] for specimens in this range of length to thickness ratio, as shown in Figure 3. The velocity of the loading point was set to 7.6 mm/min, and the maximum displacement was 6.27 mm, when the stress strain relationship became non-linear.

Results

Tensile Test

The tensile specimens displayed a brittle linear-elastic stress-strain behavior for the full range of volume fractions. The pure resin specimens, however, displayed some plastic deformation near the failure point, as shown in Figure 4. The *ultimate tensile strength* (UTS) is plotted against volume fraction in Figure 5. The UTS can be expressed in terms of the volume fraction (VF) by the following relationship: UTS (psi) = 130,041(VF) + 5,047.

The standard error of this least square curve fit is 9.9%, which is quite acceptable because of the inherent variabilities in the specimens in dimensions, surface irregularities, void formation, and volume fraction.

The *tensile modulus* was calculated from the plots of tensile tests. For composite specimens, the slope of the linear portion of the curve in Figure 4 was used to avoid the abrupt slippage shown in the figure. The slippage observed at about 60 lbs. for each composite specimen, upon careful analysis, was found to occur at the grips of the testing machine. For pure resin parts, the slope of the linear portion of the curve in Figure 4 was used, excluding the slippage at the lower end and the non-linear behavior prior to fracture at the end of the test. the tensile modulus (E) can be expressed as a function of volume fraction (Figure 6) as: E (psi) = 2,302,133(VF) + 83,664.

The standard error in this fit was 10%, and was attributed to problems with the building of the composite specimens, similar to that for the tensile strength.

Bend Test

The data from the 3 point bend tests was used to calculate the *bending modulus*. The specimens exhibited linear-elastic behavior in bending as in the tensile tests. The modulii of bending for the specimens calculated using Castigliano's method are shown in Figure 7. The bending modulus results are hard to explain because there appears to be no correlation between volume fraction and modulus. This is attributed to variations in specimen dimensions and compositions. The pure resin specimens have a homogeneous structure, so the results are fairly consistent (Figure 7). However the composite specimens showed large differences in bending modulus even in the same range of volume fraction. Since all of the specimens have three layers of fibers, and yet all have different thicknesses, the variability was attributed to the variation in the manufacturing procedure, and the inability to control dimensions in multi-layer parts.

Another possible explanation could be the location of the fibers within the specimens, which would change the location of the neutral axis, thereby the exact bending characteristics in the specimens. Because the modulus of the fibers is much greater than that of the polymer, their location as in Figure 8a or 8b would influence the behavior of the bending properties. A specimen with configuration (a) in Figure 8 will have a higher modulus in bending than that with (b) because more fibers are located close to the surface, which is the location of the maximum strain, although the two specimens may have the same volume fraction. A similar behavior is not expected in tensile test because the location of the fibers in the matrix is not as critical because the strain is constant throughout the cross section.

It is conjectured that the consistency of the bending modulus data for composite specimens would increase with the number of layers. As the number of layers increased, the specimen would become more homogeneous, and local variations in layer thickness and exact placement of the fibers would not play a dominant role. This hypothesis needs to be investigated in future when the ADPU is improved to produce multi-layered components with repeatable dimensions.

Concluding Remarks

The results from this preliminary study have shown that the mechanical properties continue to improve with the addition of fibers. In tension, the ultimate tensile strength, and modulus increase linearly as the mass fraction increases. The results for bending are not very conclusive at this time, but they do show an increase in the bending modulus with the addition of the fibers. The location of the fibers in bending may be more important than in tension, and will need to be considered in composite specimen design in photolithography based processes.

The ability to produce multi-layered composite parts in this research project demonstrated the possibility of adding fibers *in situ* in a photolithography based machine, such as in stereolithography, stereophotolithography and other similar processes [11]. An important problem to be addressed in the design of fiber dispensation and composite layer fabrication is the control of geometric dimensions, especially layer thickness. Unless the dimensions can be held to tight tolerance for the composite specimens, it will be quite difficult to make the process commercially viable.

Acknowledgment

The authors acknowledge the support of Ford Motor Co. for a grant to support one of the authors (AB). Mr. Rajat Charan, and Drs. Thierry Renault and Amod A. Ogale are thanked for technical discussions and help with the experiments and data analysis.

References

1. T. Renault, A.A. Ogale, R.L. Dooley, A. Bagchi and C.C. Jara-Almonte, "Photolithography for Composites Manufacturing: Continuous Glass Fiber/Polyacrylate Composites," SAMPE Quarterly, 22, 19-225 (1991).
2. A.A. Ogale, T. Renault, A. Bagchi, C.C. Jara-Almonte and R.L. Dooley, "3D Photolithography for Composite Development: Discontinuous Reinforcements," SAMPE Quarterly, 23, 28-38, (1991).
3. R. Charan, A. Bagchi, T. Renault and A.A. Ogale, "Manufacturing of Composite Prototypes Using Stereolithography," Proceedings of 4th International Conference on Rapid Prototyping, Dayton, OH, June, 1993.
4. R. Charan, T. Renault, A. Bagchi and A.A. Ogale, "Design and Fabrication of Selectively Reinforced Prototypes Using Photolithography," Proceedings of 4th Solid Freeform Fabrication Conference, Austin, TX, August, 1993.
5. A. Bagchi and A.A. Ogale, "Manufacturing of Fiber Reinforced Polymer Composite Prototypes," Proceedings of 1st ASME Agile Manufacturing Conference, Albuquerque, NM, October, 1993.
6. R. Charan, T. Renault, A. A. Ogale and A. Bagchi, "Selective Reinforcement of Composite Prototypes Using Photolithography," Proceedings of the 5th International Conference on Rapid Prototyping, Dayton, OH, June, 1994.
7. Thierry Renault, "Processing of Fiber Reinforced Resins by 3-D Photolithography," PhD Dissertation, Clemson University, Clemson, SC, August 1994.
8. Rajat Charan, "Automated Realization of Selectively Reinforced Composite Prototypes Using Photolithography," MS Thesis, Clemson University, Clemson, SC, December 1994.
9. ASTM, Standard No. D3039-76, ASTM, Philadelphia, PA.
10. ASTM, Standard No. D3039-76, ASTM, Philadelphia, PA.
11. Marshall Burns, Automated Fabrication, Prentice Hall, Englewood Cliffs, NJ, 1993.

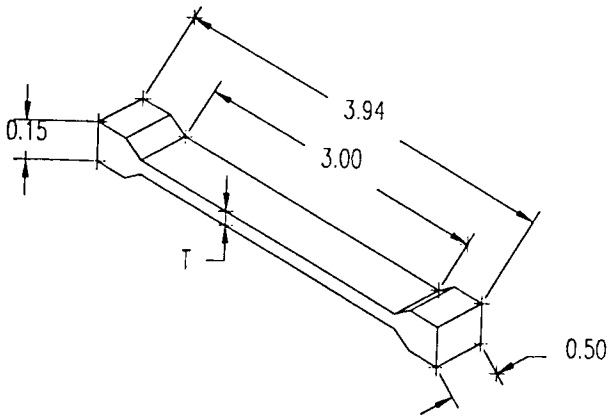

Figure 1. Test specimens used in this study — for both pure resin and composite specimens.

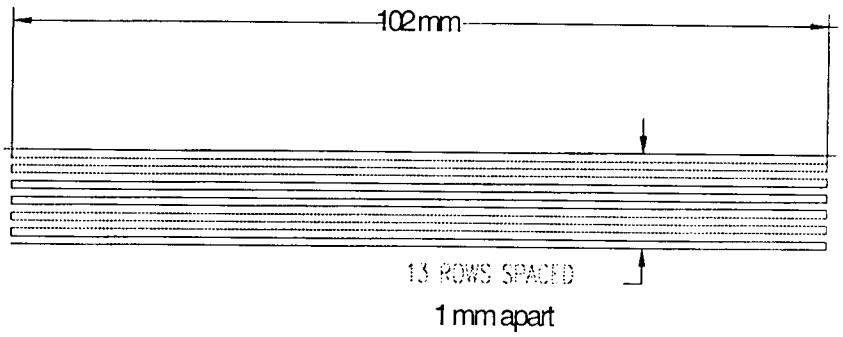

Figure 2. Path of fiber and UV light beam needed to produce a composite (or a pure resin) layer, as generated by the process planning software.

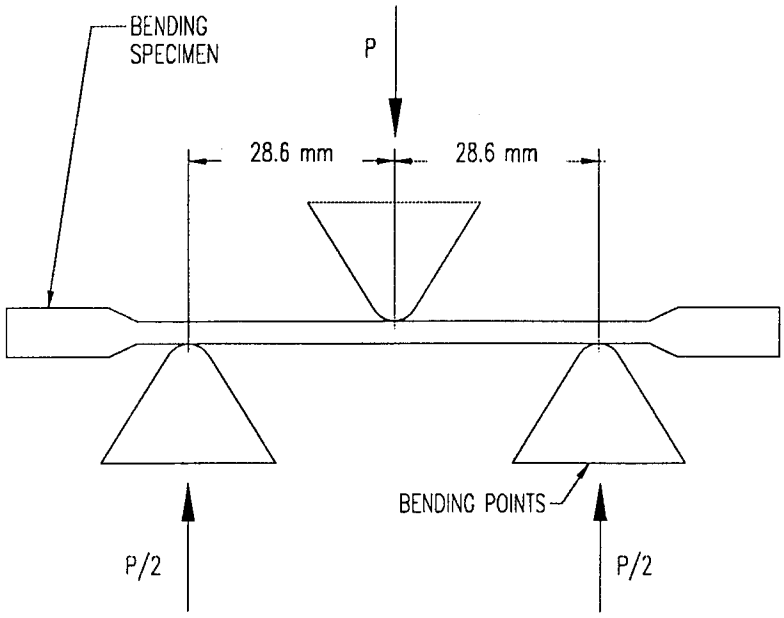

Figure 3. Three point bend test setup, showing the dimensions.

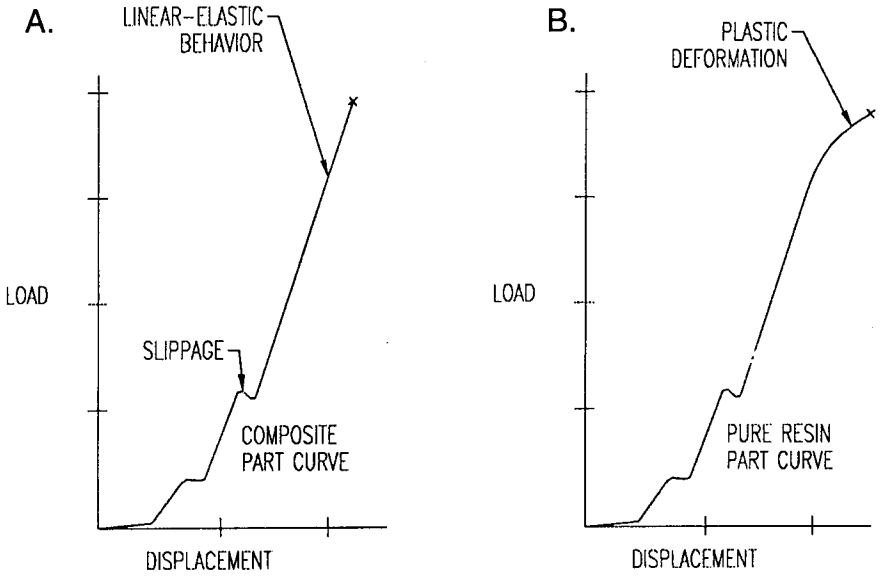

Figure 4. Tensile test results from the experiments; (a) composite specimens, and (b) pure resin specimens. Reinforcement: quartz fiber tows, and resin: Somos 3100.

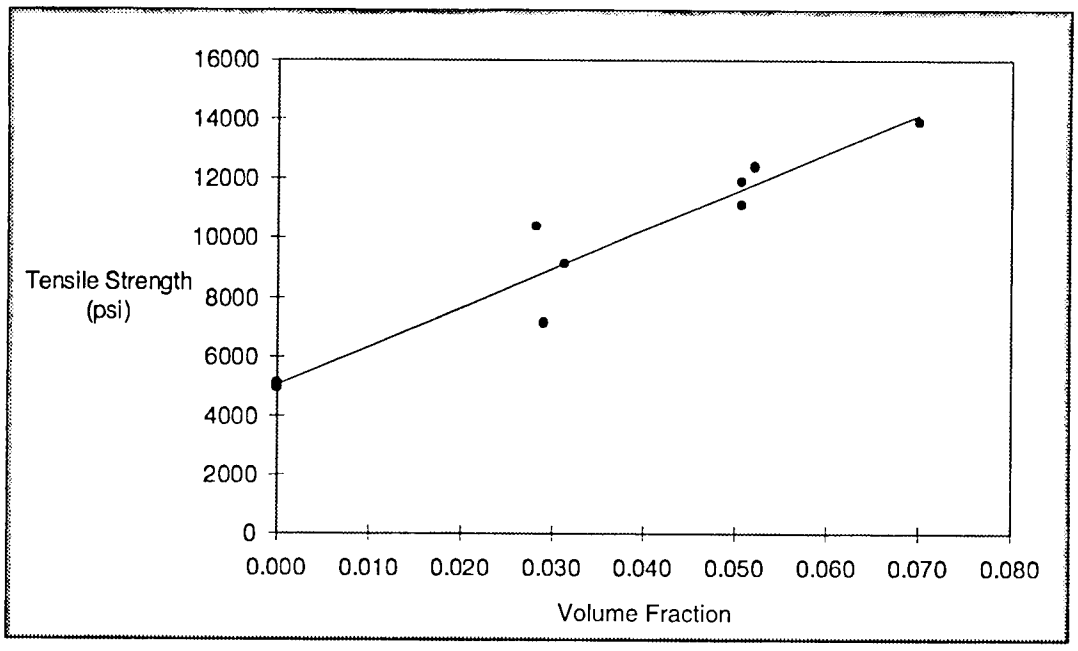

Figure 5. Ultimate tensile strength variation with respect to volume fraction of fiber in the composite specimens. Reinforcement: quartz fiber tows, and resin: Somos 3100.

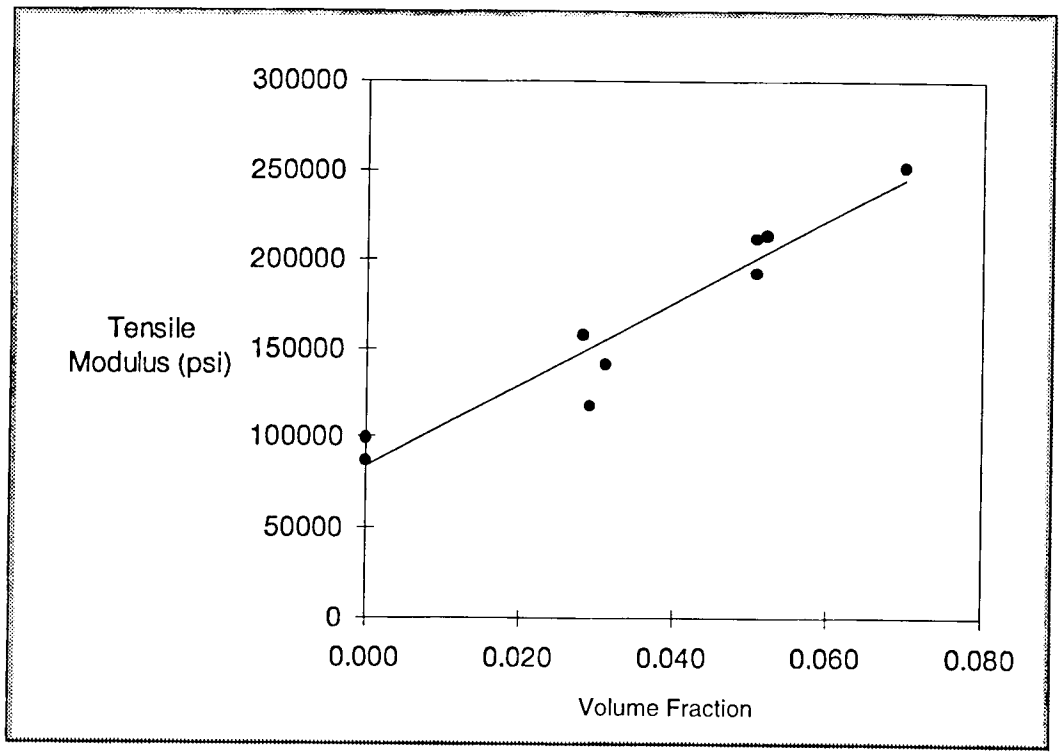

Figure 6. Tensile modulus variation with respect to volume fraction of fiber in the composite specimens. Reinforcement: quartz fiber tows, and resin: Somos 3100.

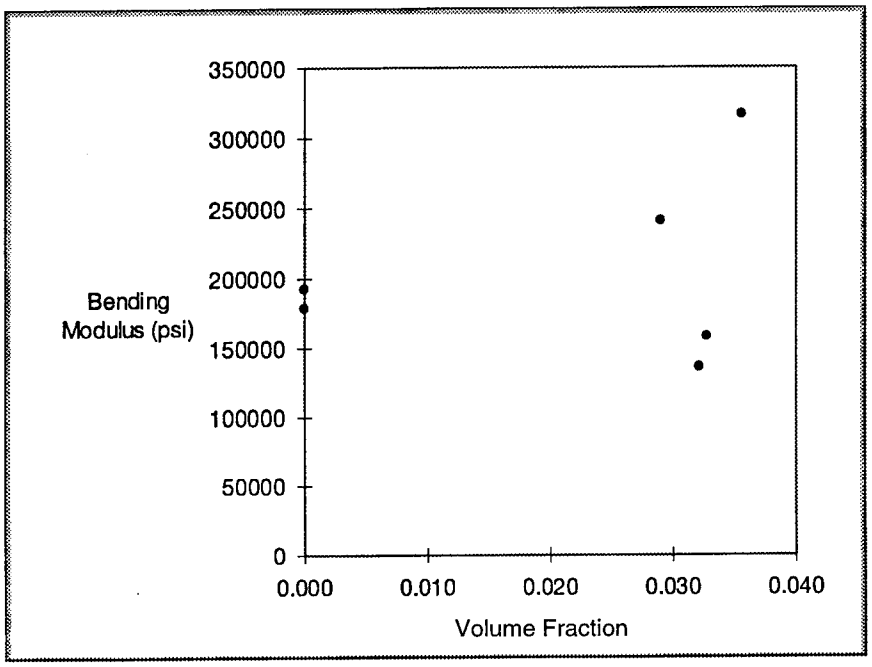

Figure 7. Bending modulus variation with respect to volume fraction of fiber in the composite specimens. Reinforcement: quartz fiber tows, and resin: Somos 3100.

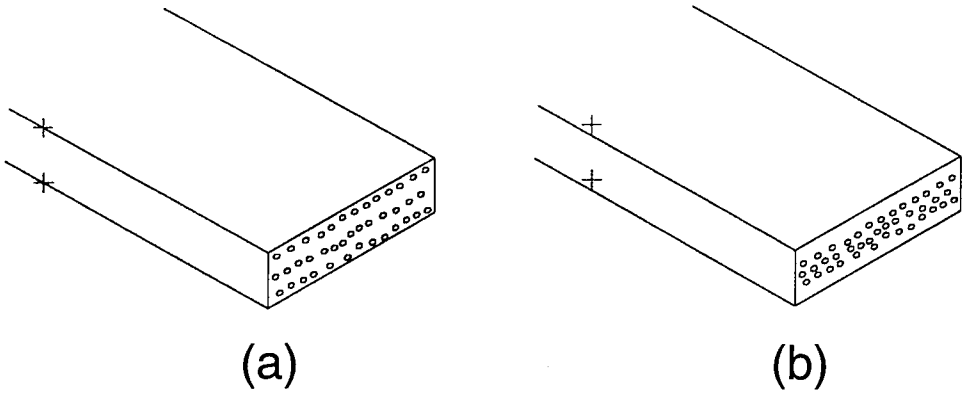

Figure 8. Possibilities of different fiber layouts inside the multilayer composites.

REDUCING WARPAGE IN STEREOLITHOGRAPHY THROUGH NOVEL DRAW STYLES

Jill S. Ullett, Richard P. Chartoff,
Allan J. Lightman, John P. Murphy and Jinghong Li†

The University of Dayton
Rapid Prototype Development Laboratory
and
The Center for Basic and Applied Polymer Research
Dayton, OH 45469-0130, USA

†3D Systems, Inc., Valencia, CA, USA

ABSTRACT

A consistent problem with stereolithography has been part distortion and dimensional inaccuracies caused by resin shrinkage. Resin shrinkage and, thus, warpage occurs during the build process and during the postcure. Build parameters such as draw pattern (the order in which strands are drawn by the laser) and overcure (cure depth minus slice thickness) can affect overall part warpage by minimizing the warpage of individual strands and layers. A software package, PATTERNDRAW, developed at the University of Dayton allows an SLA operator to manipulate vector files and change the pattern by which layers, slices, are filled in. This software was used to study the effects of draw pattern, vector segmentation, and cure depth on warpage of parts of different sizes. All parts were made using Ciba-Geigy 5081-1 resin. Moire analysis was used to measure out-of-plane deflections of part surfaces. Results indicate that significant reductions in warpage can be achieved by the use of novel draw styles.

INTRODUCTION

A consistent problem with stereolithography is part distortion and dimensional inaccuracy. Shrinkage caused by resin-curing unsymmetrically relative to the mid-plane of the strands, layers, and part is the principal cause of warpage. As the resin cures, material properties and shrinkage change with time. Consequently, the order in which the vectors or strands are drawn relative to one another, which is a time-dependent process, affects warpage. Others [1,2] have shown that particular draw styles (such as STARWEAVE™) can reduce warpage and dimensional inaccuracy. This paper shows how further reductions in warpage are possible by considering vector randomization and segmentation.

EXPERIMENTAL

An SLA-250 stereolithography machine was used to make test parts with Ciba-Geigy XB 5081-1 resin. Specific test part geometries are discussed below. Layer thickness was held constant at 0.010" (0.025 cm). Center-to-center vector spacing was also held constant at 11 mils (0.028 cm). This vector spacing was determined to be optimal for the STARWEAVE™ draw style on our SLA-250 machine. Warpage was measured using a moire analysis apparatus. Parts were coated with a thin layer of titanium dioxide powder (nominal diameter 0.2mm) to enhance reflectance for the moire analysis. A description of the particular moire apparatus used is given in [3]. Parts measured in the "green" state were first removed from the platform and supports. Parts to be postcured were also removed from the platform and supports before postcure. Postcure was conducted in three stages: bottom side up for two hours using four lamps (40 watts each) then top side up for two hours using four lamps, and finally, top side up for two hours using eight lamps.

Part Geometries

The following part geometries were tested: 2" x 2" x 0.08" (5.08 x 5.08 x 0.2 cm) plates, 2" x 2" x 0.08" plates with stress concentrators, 6" x 6" x 0.25" (15.24 x 15.24 x 0.64 cm) slabs, and twin cantilevers. Both the 6" x 6" slab and the twin cantilevers are standard 3D Systems test parts and are described in [4]. The dimensions of the twin cantilever specimens are cited below.

The 2" x 2" plate with stress concentrators includes a hole 0.60" in diameter which provides stress concentration, and legs 0.25" x 0.25" x 0.375" in length which pin down the corners and thus promote curl at the edges. Supports for this part did not extend to the outside edge, but to the inside edge of the legs only.

Briefly, the twin cantilever curl test involves building 8 identical parts at one time and measuring the curl deflection in each arm of each part in the "green" state. The cantilever arms are 6 mm thick and 3 mm wide. The unsupported length of each arm is 14 mm. The curl factor C_{f6} is defined as [4]:

$$C_{f6} = (M_6 - M_0)/6 \text{ mm} \bullet 100 \qquad \text{Eq. 1}$$

where M_6 = the thickness of the cantilever arm measured 7 mm away from the base (nearest edge)

M_0 = the thickness of the cantilever arm measured 1 mm away from the base (nearest edge).

The required measurements were made using electronic calipers accurate to 0.001 mm. All measurements were made within 24 hours after building the parts.

Moire Analysis

Moire analysis generates fringe patterns in which the fringes represent out-of-plane deflections similar to the lines on a contour map. The technique is accomplished by projecting a fringe pattern onto the object of interest, then viewing the object from a different direction [5]. Another fringe pattern is placed in the viewing path where it acts as an analyzer, reducing the data interpretation to fringe topography.

The out-of-plane displacement associated with each fringe or contour can be calculated from the expression

$$w = p/(\tan\alpha + \tan\beta) \qquad \text{Eq. 2}$$

where: w is out-of-plane displacement,
p is the grating pitch (1/lines per inch),
α is the angle between the analysis axis and the normal to the reference plane, and
β is the angle between the reference axis and the normal to the reference plane.

For all experiments, p was 0.004, α was 45 degrees and β was 0.0 degrees. Therefore, the fringe-to-fringe (e.g., black-to-black or white-to-white) spacing represented 4 mils (0.10 mm) of deflection. Thus, using interpolation, about 0.5 to 1.0 mil of deflection was measurable. The image is enhanced through the use of a video signal processor. The reconstructed image is displayed on a video monitor and photographed for final analysis. A perfectly flat surface would appear all black. A bowl shaped object would appear as a series of concentric rings with the spacing of the rings proportional to the curvature of the object. Out-of-plane deflection (w) is manually recorded as a function of the x and y (in-plane) dimensions.

Draw Styles

A software package developed by Li [6], called "PATTERNDRAW", allows the operator to manipulate the SLA-250 vector files when building parts. The software both restructures the sequence in which the vectors are to be drawn and permits segmentation of the vectors. Vectors can be drawn in patterns called: Alternating, Centered, or Random. The Alternating pattern draws every other vector from left to right in a first pass and the remaining vectors are drawn in a second pass. With the Centered pattern, vectors are drawn from the center of the part outwards alternating between vectors left of center and vectors right of center. Finally, with the Random pattern vectors are assigned numbers and then a random number generator is used to select the draw order.

In most cases, all vectors in one direction (e.g., x) are drawn before the orthogonal vectors and this order is referred to as X/Y. The specification "Total" groups all vectors (x and y) together. Since strands or vectors are not drawn in a sequential manner, individual strands can shrink independently. Strands can be drawn retracted from the border as is done in STARWEAVE™. The PATTERNDRAW software also allows the border to be drawn last instead of first. This option can minimize the border displacement caused by shrinking fill vectors.

The vector segmentation feature is based on the idea that the maximum deflection of each strand is a function of the curvature (which is material-property-dependent) and the length of the strand. For example, a beam that is fixed at one end and has bending moments applied at both ends has a maximum deflection proportional to the square of the beam length [7]. By reducing strand length, we can reduce net warpage. Vectors can be segmented with or without spaces between. The segments making up a layer can be drawn randomly or sequentially. As a result, pattern style, segment length, and segment spacing all needed to be studied.

Cure depth or overcure is another important parameter to be studied. Overcure affects the overall degree of cure of strands and the cure profile in the depth or z direction. Strands are cured from the top down by the passing laser. Warpage of individual strands occurs because a greater volume of resin above the mid-plane of the strand is cured above the gel point than the corresponding volume of resin below the mid-plane of the strand. The higher the degree of cure the higher the amount of shrinkage. Hence, greater overcure, which causes a greater degree of cure in a strand, should result in more warpage. However, if the cure profile in the z direction can be made more symmetric by curing deeper into the layer below, less warpage should occur. These last two statements are contradictory and, indeed, contradictory results were obtained using overcure depending on the in-plane dimensions of the parts built.

RESULTS AND DISCUSSION

For all part geometries tested, reductions in warpage compared with the standard STARWEAVE™ draw style were achieved. The effects of draw pattern, vector segmentation, and cure depth were evaluated using one or more of the various test geometries, and are summarized below.

Draw Pattern

In addition to STARWEAVE™, three draw patterns were evaluated: Alternating, Centered, and Random. In general, it has been observed that the Alternating pattern is preferable to the others for reducing warpage and improving dimensional accuracy. The Random draw styles can be effective in reducing warpage, however, dimensional inaccuracies may occur with some geometries. When the laser draws vectors in a random order it crisscrosses the vat many times. As a result, holes or open areas in the part may be filled in by the laser movements.

Two geometries were used to compare draw patterns alone. Experiments in which draw pattern was tested in combination with other parameters (e.g., overcure) are discused in subsequent sections.

Slab 6*6. All 6*6 slabs were measured twice, once in the green state after removal from the platform, and once after postcure. The deflection or warpage of the bottom surface was measured. This is an important point. The curvature or deflection of the top surface of a thick part will not reflect the amount of warpage occurring in the vat during part building particularly for high-shrinkage resins like XB5081-1. In fact, from past measurements of 2" x 2" x 0.25" slabs we observed that the greater the warpage in the bottom surface, the less the warpage in the top surface. High warpage in the first few layers creates a "bowl" which is filled in by subsequent layers.

The Alternating X/Y pattern produced a postcured part with 7% less maximum corner deflection than STARWEAVE™ (199 mil versus 215 mil). When Alternating X/Y was used with the Border Last option, the reduction in maximum corner deflection was 16% compared with STARWEAVE™ (180 mil versus 215 mil).

3D Systems Twin Cantilever. Two draw styles were tested, STARWEAVE™ and Alternating X/Y. The average curl factor for the Alternating pattern was measured to be 34% lower than that for STARWEAVE™. The STARWEAVE™ part had a curl factor of

26.4% with a standard deviation of 3.4. The Alternating X/Y part had a curl factor of 17.5 with a standard deviation of 3.4.

Vector Segmentation

In studies of 2" x 2" x 0.08" plates it was found that the optimal segment spacing was zero. That is, leaving no space between the segments minimizes the amount of resin to be cured in the postcure oven and, as a result, minimizes warpage. To use zero spacing and still reap the benefits of segmentation, the vectors cannot be drawn sequentially. Any of the patterns used for whole vectors, such as Alternating, can also be used for segments.

Vector segmentation was used with Alternating X/Y, Random X/Y, and Random Total draw patterns. In most studies, overcure was used in combination with vector segmentation. Only one geometry, Slab 6*6, tested vector segmentation without overcure.

Slab 6*6. Vector segmentation was used in combination with the Alternating X/Y draw style. The segment size used was 0.5". The average corner deflection for the postcure segmented-vector part was 22% less than that for the STARWEAVE™ part; and the maximum corner deflection was 33% less (144 mil versus 215 mil). These improvements are much better than those for the part made using the Alternating X/Y pattern without vector segmentation. It is suggested that the larger the part, the more vector segmentation becomes important.

Overcure

Varying amounts of overcure were tested to evaluate its effects on warpage. For a 2" x 2" part it was found with a 10 mil slice thickness that warpage reduction was maximized with 6 mil of overcure. This was true with and without vector segmentation. For a 2" x 2" part with a 5 mil slice thickness, an overcure of 3 mils also produced flat parts. The difference in out-of-plane deflections between parts made with and without significant overcure was dramatic. As is discussed below, for the 2" x 2" plates maximum corner deflection was reduced by 79% by using 6 mil of overcure for a 10 mil slice thickness. There was some variation in effectiveness of overcure depending on draw pattern, but overcure was overwhelmingly more important in reducing warpage in small (2" x 2") parts than was draw pattern. The exact opposite was observed in large parts made with 6 mils of overcure. For the Slab 6*6 parts, overcure produced very warped parts.

Slab 6*6. The STARWEAVE™ pattern with 6 mils of overcure was compared with the STARWEAVE™ pattern using 0 mil of overcure. The part with overcure had 43% more maximum corner deflection than the standard STARWEAVE™ part. This result is in direct contrast to the results for 2" x 2" plates, suggesting that vector segmentation combined with overcure is necessary for building flat 6" x 6" or larger parts.

2" x 2" x 0.08" plates. A large number of 2" x 2" x 0.08" plates were made using both WEAVE™ and STARWEAVE™ (with and without overcure), Alternating/segmented-vector (with overcure), and the Random/segmented-vector (with overcure) draw patterns. Also, the Border Last option was tried with the above draw patterns. The best results were achieved using 6 mil of overcure. With a 6 mil overcure, the warpage reduction was great regardless of a particular draw pattern. The standard STARWEAVE™ part with no overcure had a maximum edge deflection of 26 mil and a maximum corner deflection of 38 mil. When the STARWEAVE™ pattern was used with 6 mil overcure the maximum edge and corner deflections were reduced to 10 mil and 14 mil respectively. (When the Border Last option was used along with overcure the deflections were 10 mil and 10 mil respectively.) The best overall results were achieved with the

Random/segmented vector draw style (6 mil overcure) which had maximum edge and corner deflections of 7 mil and 8 mil respectively. That is, a 79% reduction in maximum corner deflection was achieved. The best results obtained with the Alternating/ segmented vector draw style (6 mil overcure) were 10 mil of maximum edge deflection and 16 mil of maximum corner deflection using a segment size of 200 mil. Detailed results for these parts are listed in Table 1.

Designations used in the Table are as follows.
R indicates Random X/Y draw pattern
A indicates Alternating X/Y draw pattern
SV-a/b/c indicates segmented vectors having a segment size = a, segment spacing = b, and overcure = c.

Unless otherwise indicated, the parts were made with the border drawn first.

2" x 2" x 0.08" plates with stress concentrators. This part which has been referred to as the "potty seat", has a centered hole and is supported by a short leg at each corner. The standard STARWEAVE™ pattern was used twice, once with the border drawn first, and once with the border drawn last. Two Alternating/ segmented vector parts with overcure (6 mil) were made. The parts with overcure had significantly reduced warpage compared with the STARWEAVE™ parts. Specifically, the overcure part having a segment size of 50 mils had 43% less maximum edge deflection (12 mil versus 28 mil) and 54% less maximum corner deflection (10 mil versus 26 mil) than the STARWEAVE™ (border first) part. The decreased warpage resulted in increased dimensional accuracies for the Alternating/ segmented vector parts. The exception was the hole diameter dimension which was poor in all cases due to faceting errors rather than warpage.The average error measured for the sides designed to be 2.0" in length was 1.5 mil for the segmented vector part with 50 mil segments and 4.2 mil for the STARWEAVE™ border first part. Both STARWEAVE™ parts had delamination at the edges; neither overcure part did. The STARWEAVE™ border last part was not flatter than the border first part.

SUMMARY

Three stereolithography build parameters: draw pattern, vector segmentation, and overcure were studied to find ways to decrease or eliminate warpage. These parameters were tested alone and in combination and compared with the 3D Systems draw style STARWEAVE™. Surface deflections were measured using a projection moire apparatus having a precision on the order of 1 mil. Warpage of parts was typically compared by comparing points of maximum deflection such as at part edges and corners. A variety of test geometries was used. Based on the results discussed in the previous sections the following conclusions are made.

1. Small (< 10%) to moderate reductions in warpage (compared with STARWEAVE™) can be gained by using a novel draw pattern such as Alternating X/Y alone (i.e., without vector segmentation or overcure).
2. Greater reductions (> 30%) in warpage can be realized if vector segmentation is employed. The larger the dimensions of the part in the draw plane the more important vector segmentation becomes.

3. For small parts (e.g., 2" x 2" plates) the use of overcure can produce near flat parts with novel draw patterns as well as STARWEAVE™.

4. Overcure used alone, i.e., without vector segmentation, to build large parts (e.g., 6" x 6" plates) can result in increased warpage compared with no overcure.

5. Drawing the border last may result in significant warpage reduction for thick (e.g., 0.25") parts. Drawing the border last is less effective for reducing warpage in thin parts.

More work needs to be done to determine the relative importance of the build parameters: draw pattern, vector segmentation, and overcure as a function of part size and geometry. In particular, we need to assess whether there is a critical vector length at which vector segmentation becomes necessary to significantly reduce warpage.

ACKNOWLEDGMENTS

This work was sponsored by the Edison Materials Technology Center program CT-31.

REFERENCES

1. E. P. Gargiulo, "Stereolithography Process Accuracy: Further User Experience," in Proceedings of the Third International Conference on Rapid Prototyping, University of Dayton - RPDL, p. 239-243, 1992.

2. J. Richter and P. Jacobs, "The Present State of Accuracy in Stereolithography," in Proceedings of the Second International Conference on Rapid Prototyping, University of Dayton - RPDL, p. 269-294, 1991.

3. J. S. Ullett et al.,"Reducing Warpage in Stereolithography Through Novel Draw Styles," in Proceedings of the Fifth International Conference on Rapid Prototyping, University of Dayton - RPDL, p. 109-125, 1994.

4. P. F. Jacobs, Rapid Prototyping & Manufacturing, Dearborn, MI: Society of Manufacturing Engineers, 249, 1992.

5. K. Harding, "Moire Interferometry for Industrial Inspection," Lasers & Applications, pp. 73-78, November 1983.

6. J. Li, "Improving Stereolithography Parts Quality - Practical Solutions," in Proceedings of the Third International Conference on Rapid Prototyping, University of Dayton - RPDL, p. 171-179, 1992.

7. J. M. Gere and S. P. Timoshenko, Mechanics of Materials, Boston: PWS Publishers, p. 741, 1984.

Note: STARWEAVE and WEAVE are registered trademarks of 3D Systems, Inc.

Table 1. Edge and Corner Deflections for 2" x 2" x 0.08" Plate Specimens

Draw Style	Overcure (mils)	Max. Edge Deflection (mils)	Max. Corner Deflection (mils)
WEAVE™	-1	30	44
STARWEAVE™	-1	26	38
STARWEAVE™ (+6)	6	10	14
STARWEAVE™ (+6) (Border Last)	6	10	10
Random X/Y	0	30	44
Centered X/Y	0	26	38
Centered Total	0	32	50
A-SV-50/0/6	6	10	20
A-SV-50/0/6 (Border Last)	6	14	20
SV-A-100/0/6	6	10	22
SV-A-100/0/6 (Border Last)	6	14	24
SV-A-200/0/6	6	10	16
SV-A-200/0/6 (Border Last)	6	14	30
R-SV-100/10/6	6	20	30
R-SV-200/10/4	4	20	28
R-SV-50/0/5	4	17	22
R-SV-50/0/8	8	8	12
R-SV-100/0/6	6	7	8
R-SV-50/0/6	6	8	10

Studies in Stereolithography : Influence of Process Parameters on Curl Distortion in Photopolymer Models

Suresh Jayanthi
Graduate Assistant

Dr. Michael Keefe
Associate Professor
Dept. of Mechanical Engineering
University of Delaware
Newark, Delaware 19716
(302)831-2421

and

Dr. Edward P. Gargiulo
DuPont Medical Products
Glasgow Business Community # 713
P.O.Box 6101 Newark, DE 19714-6101.

Abstract

To make the stereolithography process more useful in the manufacturing industry, the dimensional accuracy of the parts it creates should be very high. But due to the nature of the polymerization process and the mechanism of laser scanning, distortions are induced in the parts. Curl distortion is a major source of inaccuracy in this photopolymer based technology. This paper approaches the problem from a process related point of view by addressing the major parameters reponsible for curl.The work presented here is a continuation of a similar work presented at the SFF symposium in 1993 [1].

Introduction

The need for stereolithography fabricated parts in areas like form and functional inspection, tooling etc., has made it imperative that the parts

made using this process be of a high degree of dimensional accuracy. To build parts with high levels of accuracy a number of factors need to be closely monitored and controlled. However, models built using stereolithography suffer from curl and other distortions which occur during photopolymerization.

Discussion

Curl distortion in stereolithography parts is a consequence of the stresses induced in the cured material during acrylate polymerization [2]. Curl may be defined as any out-of-plane deflection of a flat layer and is the result of inter layer shear stresses generated during the solidification process . It occurs in a wide range of situations and is dependent mainly on the properties of the photopolymer, the part design, the part building procedures and the post processing methods used. A few empirical criteria have been proposed to minimize curl. They essentially address the inherent material characteristics like the rate of polymerization and the shrinkage behaviour of the polymer.

This study focuses on the problem of curl from a build process point of view. Hence those parameters which determine the build cycle have been identified for experimental investigation. Five essential parameters have been selected based on a similar study done earlier [1]. they include layer thickness, writing style, hatch spacing, hatch over cure and fill cure depth. Layer thickness is controlled by the laser beam intensity and is the thickness of each layer drawn on the liquid surface. It is the thickness used by the slice software to partition the CAD model into layers. Writing styles are primarily distinguished by the methods of printing hatch vectors. They are essentially a combination of border, hatch, fill vectors and overcures used to create a solid imaged part by stereolithography. Hatch spacing is the distance between the centerlines of adjacent parallel hatch vectors used to hatch the interior of the part. Fill cure depth is the depth of the solid layers formed on the upper and lower faces of the solid part. A more detailed discussion on these terms can be found in reference [3]. The rationale behind the parameter selection is better understood by taking a closer look at the way stereolithography process generates three-dimensional parts. There are a few essential building blocks that make part generation possible.

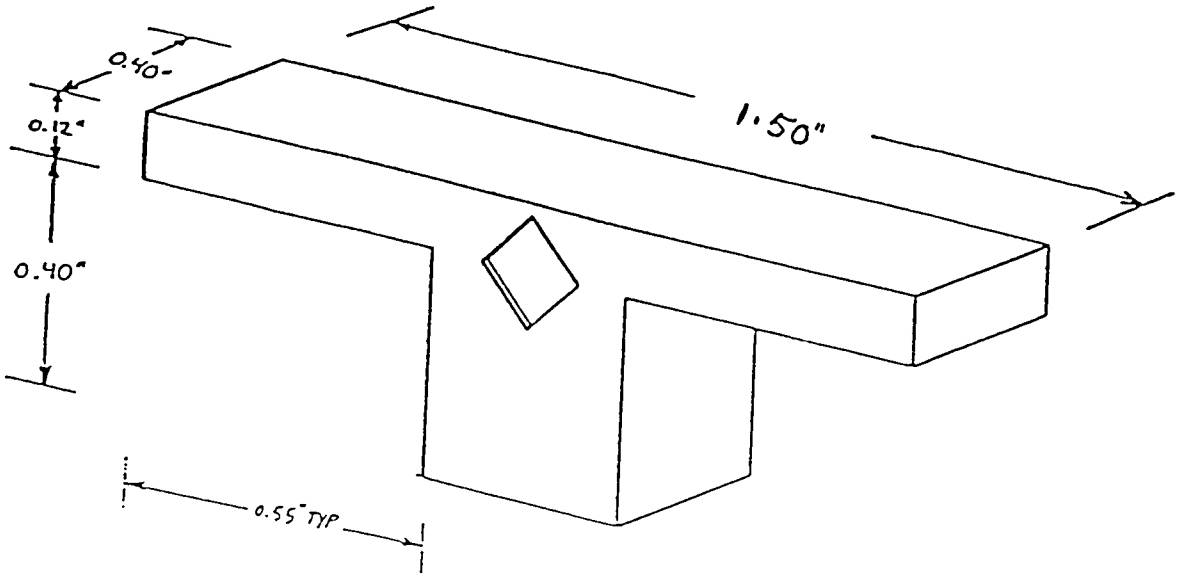

Figure 1: Twin-Cantilever Test-Piece

- a finite set of layers of uniform thickness which make up the three-dimensional object.
- a series of uniformly spaced laser scanned photoploymer strings which constitute the induvidual layers.
- sufficiently thick photoplymer strings which tack successive layers of material to form a laminated object.
- closely drawn top and bottom boundary layers which hold the newly formed part together.

In order to study the influence of variations in the parameters described above on the magnitude of curl, a twin cantilever test-piece has been chosen [4]. The test-piece is illustrated in Fig 1.

The chord height of the distorted twin cantilever surface has been used as a measure of the curl induced. A number of test-pieces were built using different ranges of these parameters. Two different writing styles- Hatch and Weave have been investigated. Table 1 and Table 2 show the ranges of the

Table 1: Ranges of the Process Parameters for Hatch Writing Style

parameter	value
Layer Thickness	10 5 7.4
Hatch Spacing	20 30
Hatch Overcure	-2 2 5 6
Fill Cure Depth	5 15 25

four parameters- layer thickness, hatch spacing, hatch overcure and fill cure depth, used to build parts with hatch and weave styles respectively. In the study the weave writing patterns two more parameters have been included ; namely, retraction (RET) and alternate-staggering (ALTS). All values are in mils (.001 inch).

The choice of these range values was based on the ease of processing the parts and the build time efficiency. It has been found that layer thickness directly controls build cycle times [3]. If thickness of the layers is held below 5 mils, then the recoating process consumes a great majority of the time. If layer thicknesses above 10 mils are chosen, the build cycle efficiency drops because the laser scan velocity needs to be kept low in order to draw thicker layers. Hatch spacing values between 10 mils and 35 mils were chosen because levels lower than 10 mils increase build times while levels above 35 mils leave a considerable fraction of the liquid in the uncured state.

Owing to the nature of the weave patterns, the hatch spacing values have been held low in the weave writing style in order to generate parts with sufficient green strength. The choice of values for hatch overcure was based on the principle of balancing the opposing effects of layer delamination and curl distortion. Earlier studies indicate that the values of fill cure depth between 0 mils and 25 mils produce good results [1].

With these range values a number of test-pieces were built. However, it has been observed that with particular combinations of these various parameters the part building was unsuccessful. For the purpose of analysis a part is considered to have failed if it does not meet the following two conditions:

Table 2: Ranges of the Process Parameters for Weave Writing Style

parameter	value
Layer Thickness	5 10
Hatch Spacing	9 12
Hatch Overcure	0 2
Fill Cure Depth	0 25
Retraction	Off On
Alternating-staggering	Off On

- if it does not have enough green strength to hold togther while being removed from the build platform, or
- if after the postcuring operation, layer delamination occurs and the dimensional integrity of the part is lost.

The material used for the experimental study is the Du Pont SOMOS 3100 solid imaging photopolymer [5]. The test-pieces which have been successfully built were removed from the platform, cleaned in a blast of dry air and postcured in a UV oven for 10 minutes. The postcured parts were then measured for curl by estimating the chord height of the cantilevers using a dial gauge. Next, the resulting data has been statistically analysed. First, an analysis of variance (ANOVA) was performed on the data to test for the relative importance of the parameters. In performing the analysis of variance, a full factorial model was considered and the influence of all the main and interaction effects computed. A factorial experiment is an experiment which extracts information on several design factors more efficiently than can be done by the traditional tests involving the study of the effect of a single factor on some characteristic. The main objective in a factorial experiment is to determine the effect of various factors (independent variables) on some characteristic of a product (dependent variable) of interest. Linear analysis of models can be applied to study these kinds of situations. The principle on which the analysis of variance (ANOVA) works is that, when several sources of variations are acting simultaneously on a set of observations, the variance

in these observations is the sum of the variances of the independent sources. This property makes the application of ANOVA particularly useful in factorial experiments. By this method, the total variation within an experiment can be broken down into variations due to each main factor, interacting factors, and residual (experimental) error. The significance of each variation is then tested.

From this analysis a selection of variables was made depending on contribution of each of these terms to the model sum of squares and their significance, as determined by a F-test. The term **Pr** indicates whether a particular parameter is significant in explaining the variation in the model. A Pr value less than .05 denotes that the parameter is important [6]. Based on the results of this analysis, statistically significant terms have been chosen to describe the model. For the purpose of analysis the hatch and weave styles have been treated seperately.

With the hatch writing style a total of 160 different specimens were successfully built using various combinations of layer thickness, hatch spacing, fill cure depth and hatch overcure. In order to minimize discrepancies during part building and measurement errors, four identical sets of these 160 specimens were built and the mean value of the curl at each combination of these four parameters was used for the analysis. Particular combinations of these four parameters resulted in failed parts. They have not been considered in the data analysis. The results of the data analysis are presented in Table 3.

Table 3 shows the statistically significant terms. DF represents the number of degrees of freedom. SS is the sum of squares of the terms while MS represents the mean sum of squares of the terms. F value is the ratio of the mean sum of squares of the model and the mean sum of squares of the error. F ratio judges the significance of the model as a whoe after fitting the intercept. Pr, which is the significance probability for a particular value of F is a test of the hypothesis that all parameters except the intercept are zero. The significance probability measures the probability that you would get an even larger F value given the hypotheses to be true. This test is usually very significant since most regression models fit better than the simpe intercept model.

A more detailed description of these terms can be found elsewhere [6]. The

Table 3: Results of the ANOVA Procedure- Hatch Writing Style

Source	DF	SS	MS	F value	Pr
Model	24	18933.96	788.91	136.26	0.0001
Error	135	781.60	5.79	-	-
Corrected Total	159	19715.56	-	-	-
LT	2	40.63	20.32	3.51	.0327
HS	1	4010.70	4010.70	692.74	.0001
FCD	2	3210.53	1605.27	277.27	.0001
HOC	2	2067.56	1033.78	178.56	.0001
LT*HS	2	59.02	29.51	5.10	.0073
LT*FCD	4	161.05	40.26	6.95	.0001
HS*FCD	2	3844.02	1922.01	331.97	.0001
LT*HOC	4	141.55	35.39	6.11	.0001

Table 4: Results of the ANOVA Procedure- Weave Writing Style

Source	DF	SS	MS	F value	Pr
Model	10	5628.101	562.81	14.85	0.0001
Error	109	4132.38	37.91	-	-
Corrected Total	119	9760.48	-	-	-
LT	1	570.05	570.05	15.04	.0002
HS	1	953.07	953.07	25.14	.0001
FCD	1	710.61	710.61	18.74	.0001
HOC	1	2375.74	2375.74	62.67	.0001
RET	1	520.29	520.29	13.72	.0003
ALTS	1	8.81	8.81	.23	.6308
HS*RET	1	340.62	340.62	8.98	.0034
HS*HOC	1	254.86	254.86	6.72	.0108
LT*RET	1	272.24	272.24	7.18	.0085
LT*HOC	1	986.65	986.65	26.02	.0001

results of the analysis show that the four main parameters: layer thickness (LT), hatch spacing (HS), fill cure depth (FCD) and hatch over cure (HOC) and the ineractions between LT & HS, LT & FCD, HS & FCD and LT & HOC explain around 95 % of the variation in curl. The mean value of curl for the entire set of observations has been found to be around 3.3 mils. A more detailed presentation of the results can be found in reference [7].

With the weave writing style a total of 120 different specimens were successfully built. Part failures in this style were significantly higher than in the hatch style. The results of the data analysis are presented in Table 4. Analysis of the results obtained for specimens built using weave styles shows that the main parameters: LT, HS, FCD, HOC and RET and the interactions between HS & RET, HS & HOC, LT & RET and LT & HOC are significant. However, The results indicate that these parameters account for only aroud 57 % of the variation in the distortion [7]. Interestingly, the influence of alternate staggering on the curl is not significant. The average value of curl distortion obtained for the entire set of data presented in Table 4 is around 25.3 mils.

From the results obtained so far it is observed that the hatch writing style yields better results than the weave style. It was possible to generate dimensionally more accurate specimens using the hatch style. With regard to the hatch writing style it is possible to define a working domain, wherein consistently good and accurate parts can be built [7]. More experiments need to be conducted to study the high failure rate of the weave specimens and the high magnitude of curl distortion observed in those parts which were successful.

References

[1] An Experimental Study of the Parameters Affecting Curl in Parts Created Using Stereolithography, Leslie Horton, Edward Gargiulo, Michael Keefe. Proceedings of the Fourth Solid Free Form Fabrication Symposium, Austin, Texas, 1993.

[2] E.J.Murphy, R.E.Ansel and J.J.Krajewski, Reduced Distortion in Optical Freeform Fabrication with UV Lasers.

[3] Paul F. Jacobs, Rapid Prototyping & Manufacturing *Fundamentals of Stercolithography* SME McGraw-Hill, Inc. 1992.

[4] Users' Manual for Du Pont SOMOS 2100 and 3100 Solid Imaging Photopolymers, version 1.0, december 1992.

[5] User's Manual for Du Pont SOMOS 3100 Solid Imaging Photopolymers, version 1.3 , February 1993.

[6] A First Course in the Theory of Linear Statistical Models, Raymond H. Myers and Janet S. Milton The Duxbury Advanced Series in Statistics and Decision Sciences PWS-KENT Publishing Company, Boston 1991.

[7] Suresh S. Jayanthi, Studies in Stereolithography : Effect of Process Parameters on the Accuracy of Photopolymer Solid Models, Masters Thesis 1994, University of Delaware (to be published).

ON THE COMPUTATION OF PART ORIENTATION USING SUPPORT STRUCTURES IN LAYERED MANUFACTURING

Seth Allen
Department of Mathematics

Deba Dutta
Department of Mechanical Engineering

The University of Michigan
Ann Arbor, MI 48109

ABSTRACT

During the construction of an object by layered manufacturing, it might be necessary to build external supports either to prevent the object from toppling, or to support floating components and overhanging material. The support structures, if necessary, must be built simultaneously with the object, and hence must be accounted for in the path planning of the laser beam or the deposition nozzle. In this paper, we find the best direction of formation of an object by layered manufacturing process that allows the use of support structures. In the orientation determined by the best direction of formation, the object is constructible with a minimal support structure, is stable, and rests on a planar base. Implementation results are also included.

1. INTRODUCTION

Layered manufacturing is a method of rapid prototyping where objects are constructed layer by layer; see [1] for an overview of various methods and application areas. Many different processes are available for layered manufacturing, but we are concerned only with those processes that might require the use of external support structures during the formation of the object. Two common examples of machines that use this type of process are stereolithography as found in 3D Systems machines and material deposition methods as found in machines built by Stratasys. (To the best of our knowledge, in the layered manufacturing machines of Cubital, Helisys, DTM, and MD* the object is enclosed in material that acts as support, so no external support structure is needed.)

By external support structures, we refer to the scaffolds that have to be built simultaneously with an object in order to prevent it from toppling and to support material that would otherwise droop or fall. Therefore, for some layered manufacturing methods the inclusion of support structures increases the domain of parts that are constructible.

In this paper, we describe a method for determining the best orientation for constructing an object by layered manufacturing. The criteria for choosing the orientation include stability of the object and minimum area of contact with support structures.

2. NEED FOR SUPPORT STRUCTURES

To motivate the need for support structures, we briefly describe the stereolithography process, a popular layered manufacturing technique. The object is

constructed in a vat of photocurable liquid on a platform whose height can be controlled. At first the platform is just below the surface of the liquid at a distance of one layer thickness. A laser 'draws' the first layer of the object on the liquid, causing the liquid to harden. The platform is lowered to expose another layer of liquid on the surface and the laser draws the next layer of the object. This process continues until the object is formed. In material deposition methods, the concept is similar, except here a material laying nozzle plays the role of the laser and liquid. Note, in the current methods, layers of constant thickness are used [2]; a method for determining best orientation for minimizing the number of slices of variable thickness and the total stair-case area see [4].

Consider an object to be built in a given orientation. Support structure will be needed in three different situations. The most common need for support structure occurs when material on one layer overhangs the previous layer by more than a specified amount. In Figure 1 based on the allowable overhang, face B might require a support but not face A. Note, in this case, supports are not required to prevent the object from toppling.

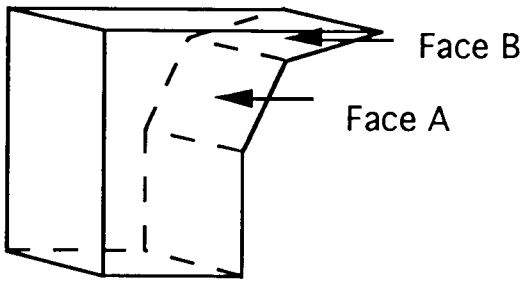

Figure 1. Support required for face B but not for face A.

Including support structure to take care of this case is often sufficient to handle the remaining two cases (and currently in practice the automatic computation of support structure stops here). The second situation where support structures are needed is when a 'floating' component is introduced during the construction. These are parts of the object introduced at a height greater than zero but not joined to the rest of the object until later in the construction; see, for example, Figure 2.

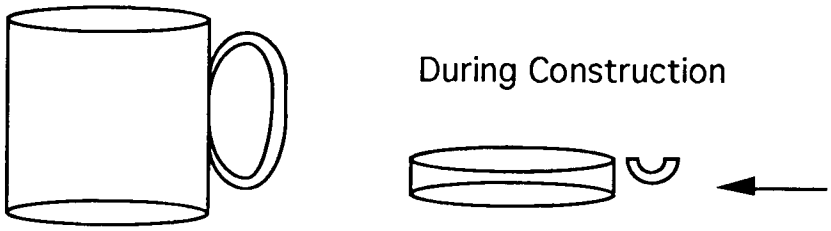

Figure 2. During the construction of the object, support structure is required to carry the floating component.

The third case where external supports might be required is when the object becomes unstable during the construction. In Figure 3, the object will topple if the face indicated by the arrow is not supported. Note, this situation is different from the one illustrated in Figure 1 where the object is in a stable orientation.

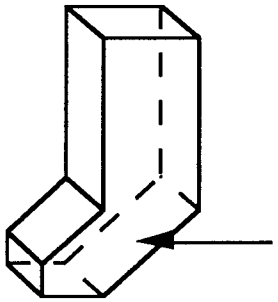

Figure 3. To prevent the object from falling, support structure is needed on the indicated face.

We note, the need for support structures in the third case is somewhat weak if considered in light of the physical process. Factors include the fact that the object's base usually weakly adheres to the platform on which the object is grown, and in the case of stereolithography the liquid in which the object sits adds further stability. However, situations where stability is an issue are conceivable.

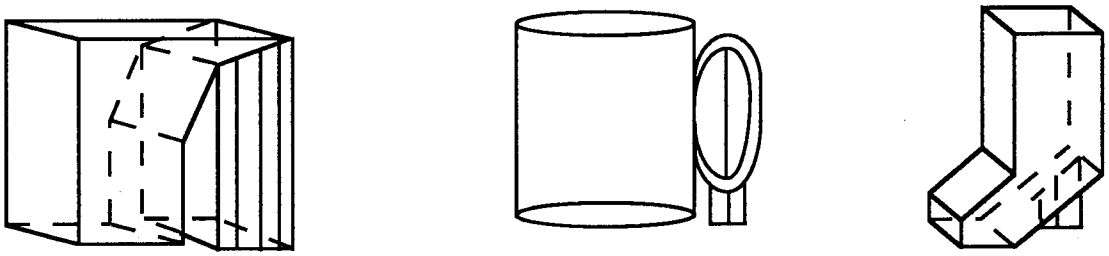

Figure 4. Examples of support structure for the objects shown in the Figures 1, 2, and 3. Notice that the second object needed support structure at the top of the handle because of overhang between layers, and support at the bottom of the handle because of a floating component.

Our approach imposes no restrictions on the geometric domain of objects. In addition to solid objects with or without voids, we also consider the layer manufacture of (thin) surfaces, e.g., a hollow cylinder, sheet metal parts, etc. However, we make the assumption that a curved surface cannot act as a base for the construction. This assumption stems from the observation that whenever a physical object, at rest on some plane P, is in a stable orientation, it has at least a 3-point contact with P. This contact requirement can be met whenever the object has either of the following in contact with P: (i) three distinct non-collinear points, (ii) a line and a point, (iii) a plane, (iv) a non-degenerate planar curve. For example, a sphere resting on a plane will not meet any of the aforementioned requirements, and hence is unstable.

For any object G, every planar face on the convex hull of G will either be an (original) face of G, or will be a (new) face that satisfies the contact criteria. Therefore, our approach to determine stable orientation involves reasoning based on the convex hull of the object. To compute the convex hull of an object we require *sample points* on its surface. We adopt this point based approach due to the difficulties in computing the convex hull of free form objects. In this paper, we first facet (triangulate) the object and then use the vertex set of the faceted object as sample points.

We assume every object to be constructible and every orientation (for construction) to be valid with the addition of sufficient support structures; see Figure 4. The interested reader can compare this use of support structures to the approach taken in [5]. In that paper, polyhedral objects are tested for orientations in which the object has no overhanging material between layers. Any object without such an orientation, according to [5], is not constructible.

The support structures are built, layer by layer, simultaneously with the object. After the object is constructed, the support structure must be removed, often manually. For a complicated object this removal may be difficult, requiring the supports to be dug out of tight spaces, while also reducing the quality of the surface finish. To reduce the time required to manufacture the object and to improve the quality of the surface finish, we wish to minimize the surface area of the support structure that is in contact with the object. Finally, given two orientations of an object with the same amount of support structure, our algorithm will pick the orientation in which the object is more stable, i.e., has lower center of mass.

In addition to [5], the problem of determining optimal orientation in layered manufacturing has been considered in [3] where simulated annealing (SA) is used for selecting the orientation. Orientations are evaluated with respect to the object's height, the total area of the surfaces of the object subject to staircase effect, and the volume of the trapped liquid (specific to SLA process without regard to support structure).

3. DEFINITIONS

We define the following with respect to an object G that is being considered for layered manufacture with a direction of formation along the z-axis.

Up_vector: The up_vector is a unit vector that specifies an orientation of G.

Base: The base of G is the convex hull of the set of points on G whose dot product with the up_vector is minimal.

The orientation of G during formation is obtained by rotating G so that the up_vector is parallel to the positive z-axis and then translating G so that its base rests on the x-y plane. See Figure 5.

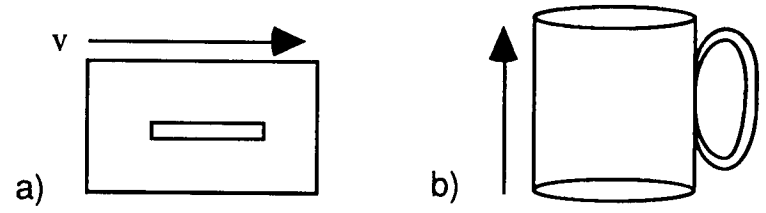

Figure 5. a) An object given in it's initial orientation with an up_vector v, and b) the orientation determined by v.

Supported_Point: A point *p* on the surface of G is a supported_point if the following hold:

i. the outward pointing normal at *p* has a negative z coordinate
ii. *p* lies on the surface of a support structure for G

All other points on G are unsupported_points. Each sample point chosen on G is classified as supported or unsupported. This information is used later to construct an approximation to the necessary support structure.

Extended Base:

An extended base of G is the convex hull of point sets P_1 and P_2 where P_1 contains all sample points of G that lie in the x-y plane and P_2 contains the projection into the x-y plane of all supported_points of G; see also Figure 6.

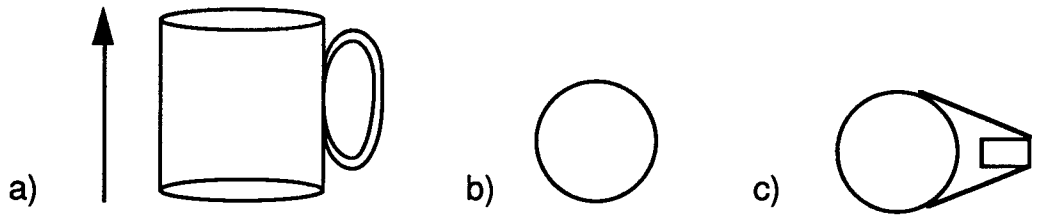

Figure 6. a) An object and its direction of formation. Note that some of the sample points on the handle must be supported, since during the construction a floating component is introduced. b) The base of the object. c) The extended base of the object.

4. THE ALGORITHM

Our method for the determination of the best orientation for the layered manufacture of an object consists of three steps. First, a candidate list of orientations for the object is made. Second, for each orientation in this list, an approximation to a sufficient support structure for the construction of the object is computed. Also, the center of mass of the object in this orientation is found. Finally, the best orientation is selected from the candidate list. The selection criteria includes (i) the surface area of contact between the support structure and the object, which we seek to minimize, and (ii) the stability of the object.

4.1 Determination of Candidate List of Orientations

Consider an object G. The sample points of G are elements of the vertex set of the faceted representation (triangulation) of G. Let CH(G) denote the convex hull of the set of sample points. Note, if G did not contain any planar faces, then CH(G) could possibly contain a large number of faces depending on the coarseness of the triangulation.

The inward pointing normal to each face f of CH(G) corresponds to the up_vector for the orientation of G with f as the base. In order to limit the number of candidate orientations, we use only those up_vectors that correspond to faces of CH(G) with a relatively large area. First, we set a threshold value λ for the surface area of a face. In general, λ is chosen higher than the value for the area of a facet that corresponds to a curved surface region of the original object G. Next, all faces that have surface area less than λ are eliminated. The up_vectors corresponding to the remaining faces of CH(G), with surface area greater than λ, form the list of candidate orientations. In these orientations, G sits on a large base which acts to increase stability and decrease the size of the support structure needed.

4.2 Computation of the Support Structure

Consider an object G and an up_vector v. The computation of the approximate support structure for G in the orientation corresponding to v can be broken down into the following steps. First, G is moved into the orientation corresponding to v. Second, the sample points on G are classified as either supported or unsupported. Third, using the classification of the sample points and normals on G's surface, an approximate support structure is made. We elaborate on the second and the third steps next.

4.2.1 Classification of Sample Points

Initially all sample points in G are classified as unsupported. A sample point *p* will be classified as supported if, after adding support at *p*, either of the following hold:

(i) a floating component introduced during the construction of G is supported
(ii) a component, that would otherwise topple as the object is grown, is stabilized; see Figure 7.

To determine which sample points need to be supported, the growth of G is simulated. This simulation is necessary due to the difficulties in tracking the center of mass of a curved object as the object is formed. We note that if the object domain were restricted to polyhedral objects, such an approach would not be necessary.

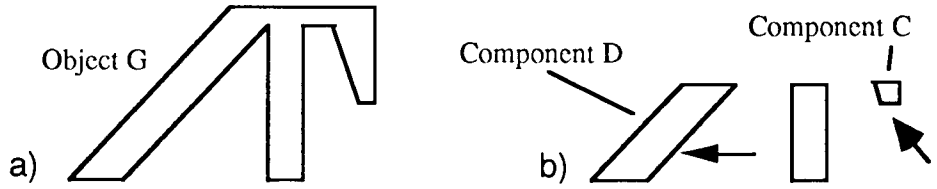

Figure 7. a) The profile of an object G, and b) the connected components of G during formation. The component D is unstable. C is floating. Adding support at the indicated sample points would stabilize these components.

If a new component C is introduced during G's growth, then C is floating since its extended base does not lie on the x-y plane. See Figure 7. To indicate the need for support on C, all sample points in the new component are classified as supported. When the next layer is added, the component is no longer new. Global methods exist for the detection of floating components that do not involve the growth of G. However, since G must be grown to test for unstable components, we make use of this simulation here.

As layers are added, the center of mass of each connected component of the partially formed object is computed. If the center of mass of some connected component D is not directly above its extended base then component D is unstable. D can be stabilized by adding support to G at sample points that lie in D, so that D's center of mass lies above the new extended base. (See Figure 7.)

4.2.2 Computing Approximate Support Structure (Rays Structure)

Assume the object G is in some (candidate) orientation. The approximate support structure for the object in a particular orientation is stored in a (n¥n) array which we refer to as the *rays_structure*. The cells of rays_structure correspond to a grid of rectangles in the

x-y plane. The projection of G onto the x-y plane is contained in the union of these rectangles. Let p_{ij} denote the center of rectangle (i,j) in the x-y plane and let L_{ij} be the half-line originating at p_{ij} and parallel to the z-axis. The points of intersection between the object G and L_{ij} is stored in the cell (i,j) of rays_structure. Note, there can be several points of intersections between L_{ij} and G. These points are stored in the same order as L_{ij} intersects G, i.e., the points have increasing z values.

Next, these points of intersection are classified. The primary classification is based on the direction of the face normal. If the face normal points upwards the corresponding point on G does not require support; all other points may require support. Next, for points that may require support, a classification of *supported* or *unsupported* is done. Initially, support will be added to those points where the angle α, between the face normal and the negative z axis, is smaller than a user specified angle β. Decreasing values of α (down to 0 degrees) correspond to increasing material overhang from the previous layer during the construction; see Figure 8. So, if α is less than the user specified β, the point of intersection is classified as supported; all others are classified as unsupported.

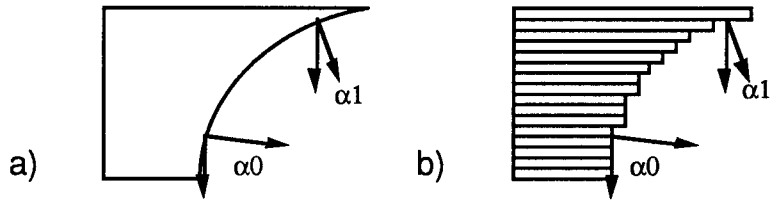

Figure 8. a) An object G and the angles α_0 and α_1 between the normals to G's surface and the negative z-axis. b) The layers added in the formation of G. Note the overhang between layers is greater for the smaller angle α_1.

After the initial rays_structure classification, the support information that was attached to the sample points is used to complete the approximate support structure. A sample point *p* of an object G is classified as supported only when the support structure added at *p* helps stabilize G or carries a floating component of G. So to ensure that adding support at *p* doesn't create a new unstable component, the support structure here is grown from the x-y plane; see Figure 9. With this in mind, let *p* be any supported sample point. Suppose *p* lies above the rectangle in the x-y plane that has center p_{ij}. Then each point of intersection of G and L_{ij} with support type *not_supported* that has z value near or below the z value of *p* is changed to type *supported.* Once each sample point's contribution is included, the approximate support structure stored in rays_structure is a sufficient support for the object during its manufacture.

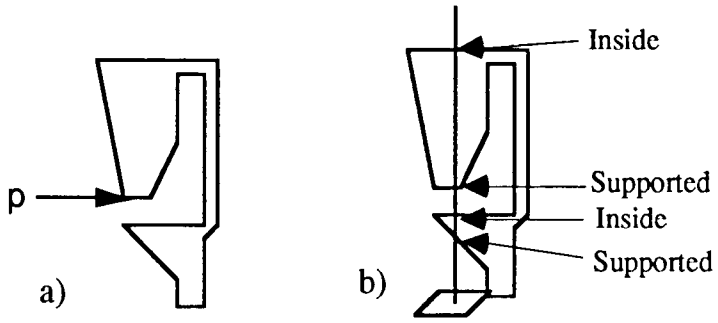

Figure 9. a) Supported sample point *p* on G, and b) the classification of the points of intersection of L_{ij} and G.

By the above process, all points of intersection corresponding to each half-line are classified (as inside, supported, or unsupported). These points break the half-line into several line segments; those segments between consecutive points of intersection along the ray. Since, the points are stored in rays_structure in order of increasing z-values, the points alternate between inside and supported/unsupported; see Figure 9.

Finally, we add the approximate support structures by considering the directed line segments corresponding to each half-line. First, a support structure is added to each line segment l = (u,v) where the endpoints u = point on the x-y base, and v = supported point on G. This corresponds to adding support structures A in figure 10 (b). Next, support structures are added to line segments l = (u,v) where the end points u = inside and v = supported. This step corresponds to adding the support structure B in figure 10 (b). This is required to add support at intermediate levels. Finally, the total surface area of contact between a support structure and the object G is computed as the product of the area of the base of the cell times the number of places where the support touches the object.

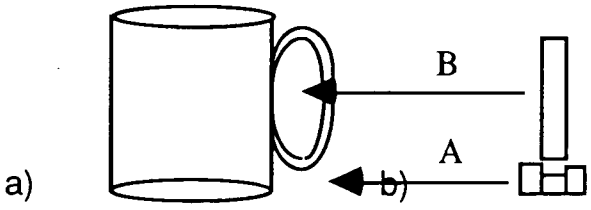

Figure 10. a) An object G, and b) a graphical representation of the support structure approximated by the rays structure for G. Note that support A is added to carry a floating component and support B is added to support overhangs.

Therefore, by using each half line L_{ij} to approximate the support structure needed over the corresponding box in the x-y plane, the information stored in the rays_structure is used to quickly calculate the surface area of the support structure in contact with the object.

The best orientation is chosen from the list of candidate orientations. In this orientation the support structure for G has minimal surface area of contact with G. If two orientations require support structures with equal surface areas of contact, the orientation in which G has a lower center of mass is chosen as best.

5. IMPLEMENTATION AND RESULTS

This algorithm was implemented in C++ with the geometric modeler ACIS. The support types of the sample points on a face of the object are controlled by a height attribute attached to the face. The height signals that all vertices in the faceting of the face with z values less than or equal to the height are supported. Individual control of the support attributes of the sample points is lost, but in most cases the resulting support structure has little excess.

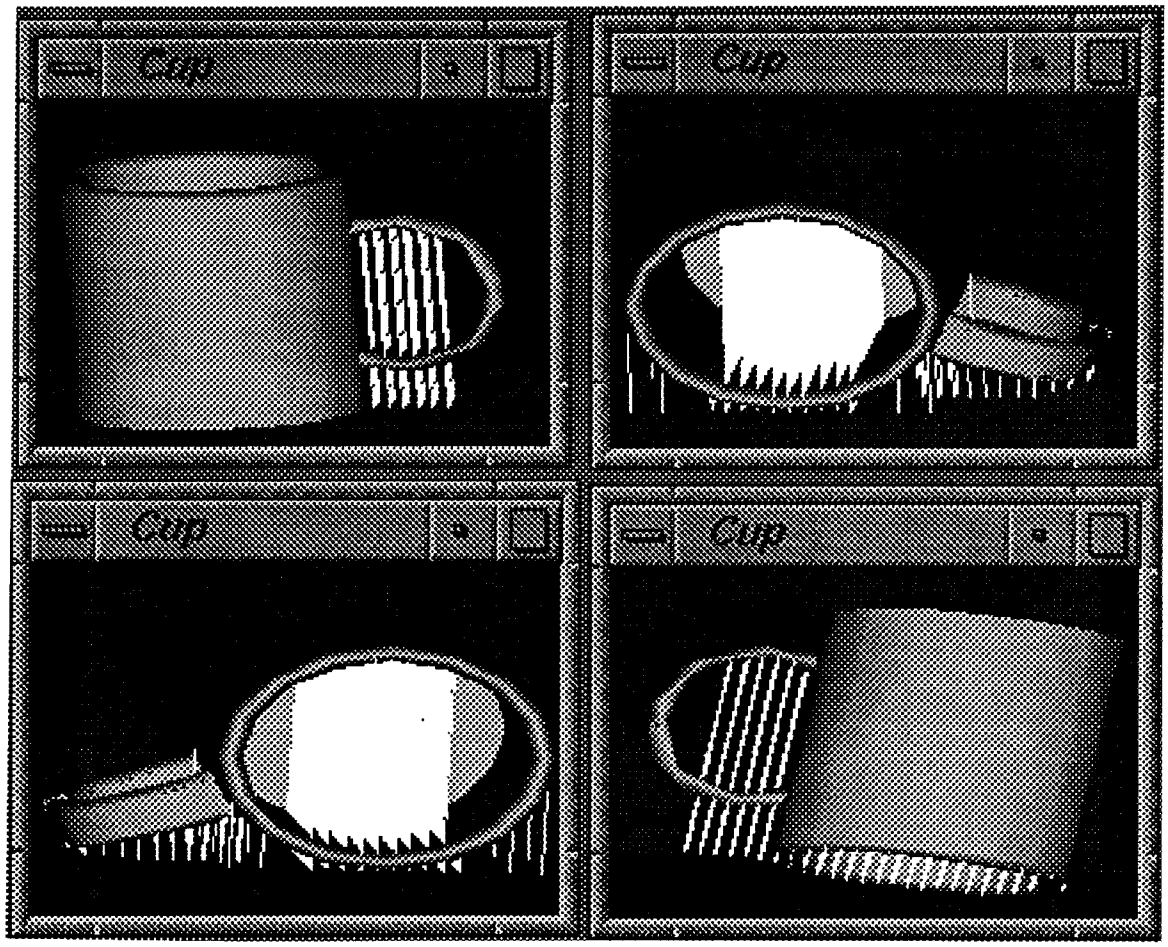

Figure 11. The four candidate orientations for a coffee cup and the support structure necessary for each.

The output as shown in Figure 11 shows the four stable orientations that our program found for a coffee cup and indicates the required support structure for each orientation. The coffee cup is an ACIS model with faces from planes, cylinders, and tori. The first orientation (with the cup opening upward) is the best orientation. The worst is with the cup opening downward, since in this case the flat surface near the top must be supported. The program was run with an overhang threshold of 30 degrees (see Figure 8), a 30x30 rays_structure, and 15 layers in the cups simulated growth. This example took

about 45 minutes to run on a Silicon Graphics Indigo workstation, where most of this time was spent doing the initial rays_structure computation for each orientation.

6. CONCLUDING REMARKS

Layered manufacturing is often described as an attractive rapid prototyping method where CAD models can be simply down loaded and physical prototypes realized, without having to incur "set up" costs. However, the computation of part orientation, support structures, and layer thickness in layered manufacturing are quite complicated and time consuming if done manually. In fact, such tasks are the analogue of set-up functions (i.e., tooling, fixtures, operations sequencing, etc.) in conventional NC machining. We conjecture, the overall efficiency of layered manufacturing as a production tool will depend among other things upon the availability of efficient procedures for tasks such as the one addressed in this paper.

7. REFERENCES

[1] Ashley, S., "Rapid Prototyping Systems" Mechanical Engineering, April 1991, pp. 34-43.

[2] Dolenc, A., and Mäkelä, I., 'Slicing Procedures for Layered Manufacturing Techniques' *Computer Aided Design* Vol. 26, No 2, Feb. 1994, pp. 119-126.

[3] Kim, J. Y., Lee, K., and Park, J.C., "Determination of Optimal Part Orientation in Stereolithographic Rapid Prototyping" *preprint,* July 1994.

[4] Sreeram, P., and Dutta, D., "Determination of Optimal Orientation Based on Variable Slicing Thickness in Layered Manufacturing", Technical Report UM-MEAM-TR-94-14, Department of Mechanical Engineering, University of Michigan, Ann Arbor, MI, July 1994.

[5] Asberg, B., Blanco, G., Bose, P., Garcia-Lopez, J., Overmars, M., Toussaint, G., Wilfong, G., and Zhu, B., 'Feasibility of Design in Stereolithography' *preprint,* January 1994.

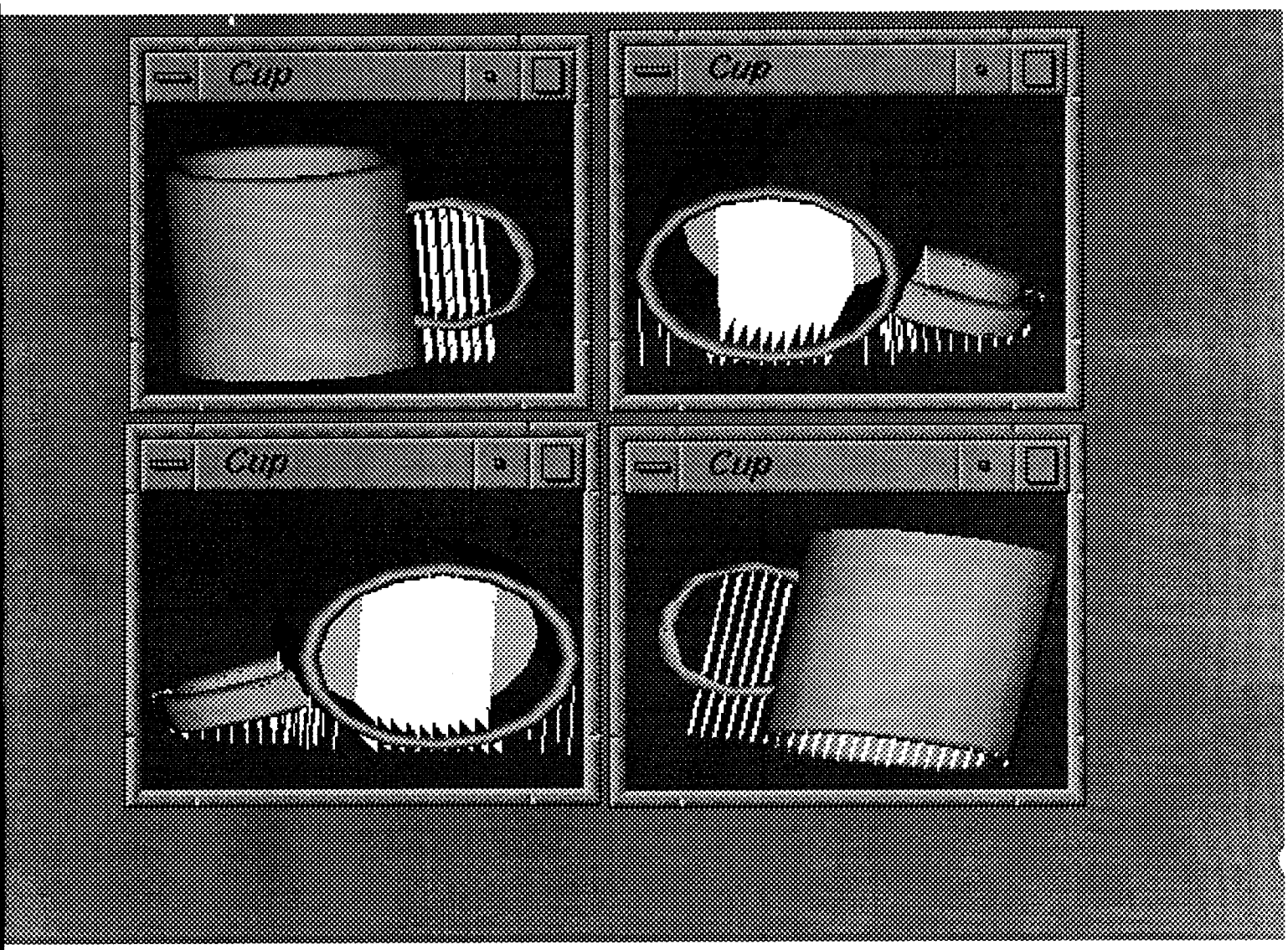
Cup
Cup
Cup
Cup

Product Model Driven Direct Manufacturing

Per Carleberg
Department of Manufacturing Systems
Royal Institute of Technology
Stockholm

Abstract

The input to the freeform fabrication process is essentially geometric data, raw material, material data and process parameters. Optimal process parameters depend upon current material and the part geometry.

This paper describes an research approach in which all necessary input including process parameters are obtained or derived from the product model. The part geometry with its process parameters is transferred as a STEP model to the SFF system. In the SFF system this model is converted to the internal format, coupled to the process parameters. The approach is exemplified with the SLS machine from DTM as SFF system.

Introduction

The product model as the base for different activities, from idea to final product, is the key to successful product realization. The product model as a knowledge base contains of course geometric and technical data but can also refer to company specific information, product background, history, synthesis & analysis results, reasons for decisions etc.

Freeform fabrication gives unique possibilities to really integrate product development, design, process planning and fabrication. In particular the SFF technology is conceptually capable of creating a very direct and fast physical version of the designers intent as given in the product model. This means that product realization with solid freeform fabrication gives new iterative possibilities, Fig. 1. These possibilities put new requirements on our models, our design support and the software for freeform fabrication.

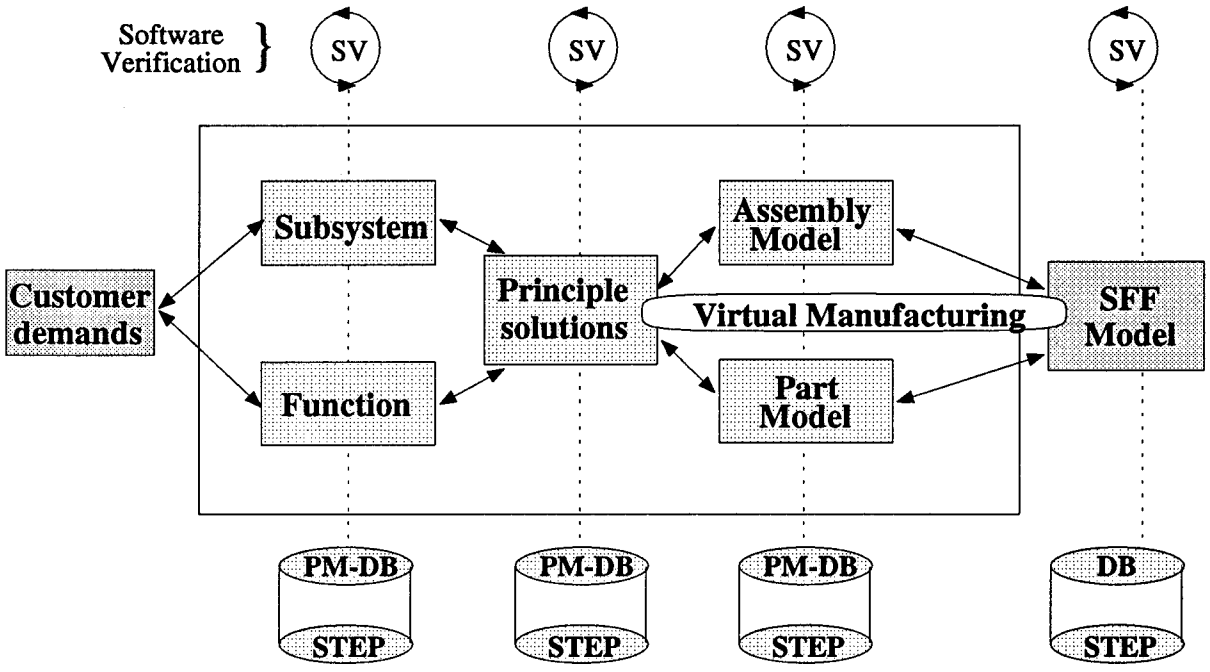

Figure 1 Product Models (PM) in Product Realization

Basis of Research

At the Department of Manufacturing Systems at KTH, research has over the years been conducted on geometric, product and feature modeling etc. In a new research project, Product Model Driven Direct Manufacturing [6], principles and methods for direct manufacturing driven by product model data is being developed, Fig. 2. The product model includes geometry, dimensions/tolerances, functional surfaces, technical data, etc. and the process model is utilized for the simulation and control of a machine tool such as the Selective Laser Sintering (SLS) machine.

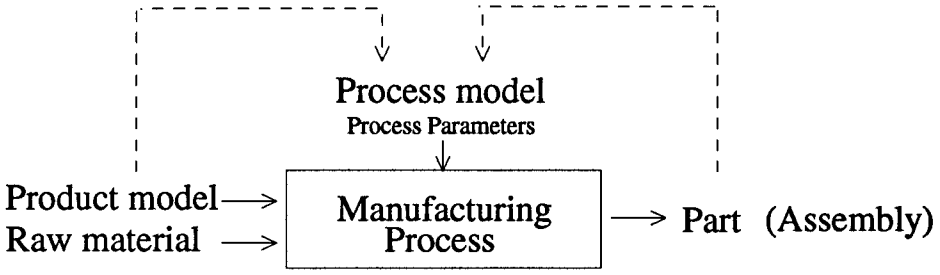

Figure 2 Product Model Driven Direct Manufacturing

In 1993 a SLS machine from DTM [11] was installed at IVF-KTH[1] to serve as a tool for long-term as well as applications research. During this first year we have gained considerable practical experience [5, 9] with the SLS machine. In research collaboration with Swedish manufacturing companies around 150 test parts of various kinds have been produced in the SLS machine. One example is an adjustable wrench, built in nylon with three components and in one operation, Fig. 3.

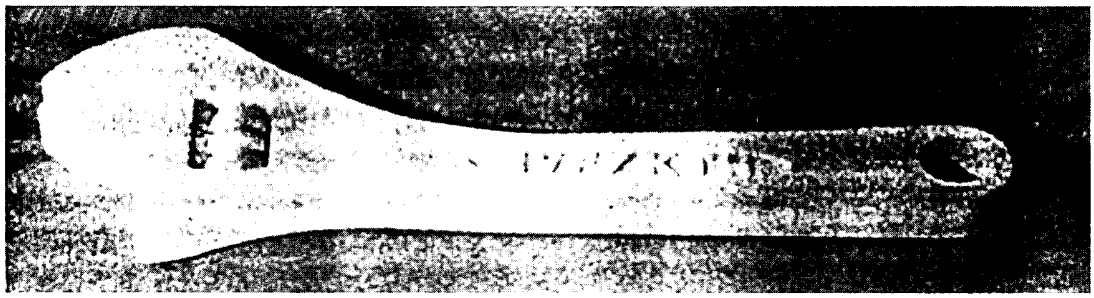

Figure 3 A wrench, built as one assembly in the SLS machine at IVF-KTH

Research approach

The external interface to the SLS software system consists today primarily of the STL-file and process parameters such as laser power and layer thickness. The STL-file is internally sliced into layers from which the scanning patterns are calculated. The process parameters can interactively be modified by the operator. For different materials, predefined material configuration files are used.

Although the present commercially available solution may yield very good results, it is far away from what is conceptually possible, given a product model and a predictable process. Our proposal and research approach is therefore to change the current external interface in order to make product model driven direct manufacturing feasible.

Intelligent scanning is certainly an improvement but in the SLS process we need to have software control of both the laser beam scanning paths and corresponding process parameters, intelligent sintering [3, 13]. This is not only because of the well-known drawbacks with the STL file format [4, 9, 10, 12, 13], like gaps in the faceted model or that the resolution in the STL-file is fixed (which means that for improved resolution the whole STL-file must be recalculated from the original geometric model). It is a combination of process dependent reasons and the STL format that makes the situation problematic. To underline the need for the proposed change, a number of examples of present weaknesses are given:

- In the SLS process we must compensate for *the shrinkage* but as the shrinkage is dependent upon part geometry (~0.3%) it is almost impossible to find *one* correct shrinkage scale factor for the whole part.

[1]The utilization of the equipment is shared by IVF (The Swedish Institute of Production Engineering Research) and KTH (The Royal Institute of Technology).

- The need for compensation for *the thickness of the laser beam* (~0.4 mm), presently done on the STL-file, is also dependent upon material and part geometry. Very thin sections can for example totally disappear or get unnecessary weak. A better solution would be to generate compensated laser beam scanning paths directly from the product model.
- There is also a need to compensate for *the applied energy*. As the build height increases, more and more heat is accumulated in the sintered part (due to the applied laser energy). It is therefore desirable to modify the applied laser power when the build height increases. As the amount of modification is material and part geometry dependent it should preferably be calculated by FEM-like simulation programs [2] and by calculation of applied laser energy to the powder surface [8].
- Another phenomena is that *the temperature distribution is non-uniform* (partly due to the location of the infrared heaters) in the circular build area. Although difficult one possible way to compensate for this is to have a likewise non-uniform scanning pattern.
- The *scanning direction* is uni-axial which gives different accuracy in x and y directions. With software controlled multi-axial scanning patterns this problem would disappear and the surface finish would be improved.

From these examples we can conclude that software control of laser beam scanning paths and process parameters is vital for the optimal generation of accurate and dimensionally stable parts. Although the given examples are specific to the SLS process, similar problems arise in most freeform fabrication processes.

Another problem is the present lack of possibility of having a direct feedback loop in the sintering process [13], today we have to draw our conclusions by examination the final part.

Our research approach now is to compute optimal scanning patterns and process parameters from the product and process model. In this approach the part geometry is connected to process parameters. The STL-file format is not appropriate because it contains no process parameters, no scanning contours and no connections to material data.

We propose the use of a STEP-based[1] format [1]. There is a need to develop an application protocol[2] (AP) for freeform fabrication, [10, 13]. As a first approach we

[1] PDES/STEP (ISO 10303) is an ongoing project and an international effort to specify a series of standards for the unambiguous representation and exchange of computer-interpretable product information throughout the life cycle of a product.

[2] From the user point of view, an implementation of STEP is usually done in the form of an Application Protocol (AP).

intend to utilize the already defined protocol AP204[1] and by extension of that protocol we can include

- process parameters
- scanning patterns and
- material data

and connect it to the part geometry. We call this model a *general SFF model.* In our first approach it consists of a number of strategic discs, Fig. 4. A proper location and thickness of each disc can be calculated by use of a process model and analysis & simulation programs that calculates heat transfer, shrinkage etc. according to simulated scanning patterns and process parameters. The idea is *not* to include all scanning patterns and contours, only *the scanning principle* used by the analysis and simulation programs. As the strategic slice is much thicker than the slices in the fabrication process this would not imply a huge amount of data.

As the STEP standardization efforts in the area of feature modeling [7] improves, we probably will utilize such an application protocol, i.e. how to utilize information about features such as holes etc. in the product model in the final fabrication process.

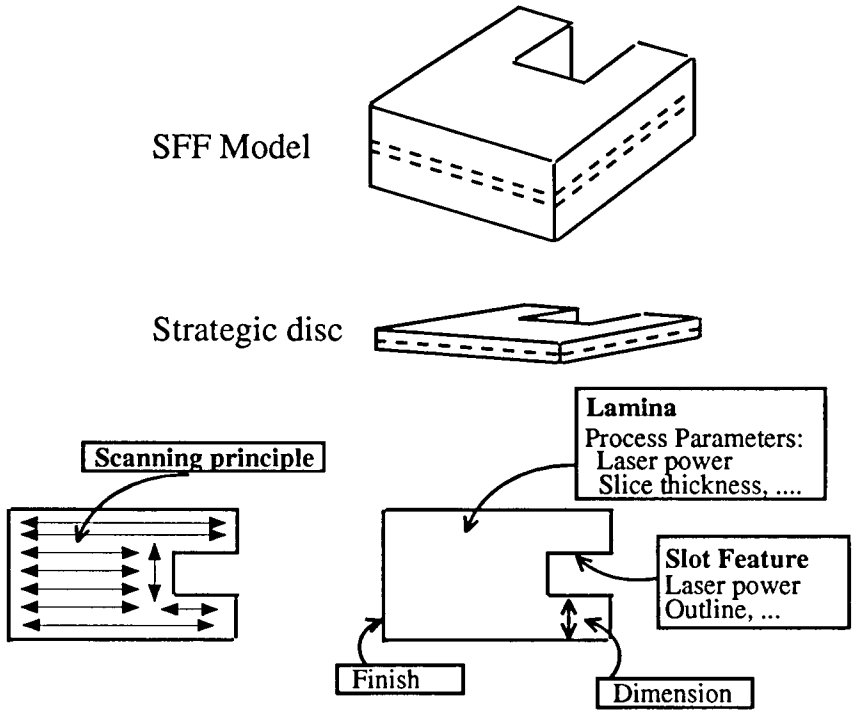

Figure 4 The general SFF model consists of strategic discs accompanied by process parameters and scanning principles.

[1] Application Protocol for Mechanical Design using Boundary Representation

A specific SFF system can now read this STEP based general SFF model and convert it to the systems internal format, a specific SFF model, Fig. 5. To able to convert the general model, the SFF system must be equipped with various software tools such as a STEP interpreter, a boundary geometric modeler, software for contour generation etc.

Our research intent is to investigate more precisely which software tools actually are needed and how they should operate together. The next step is to specify a research implementation.

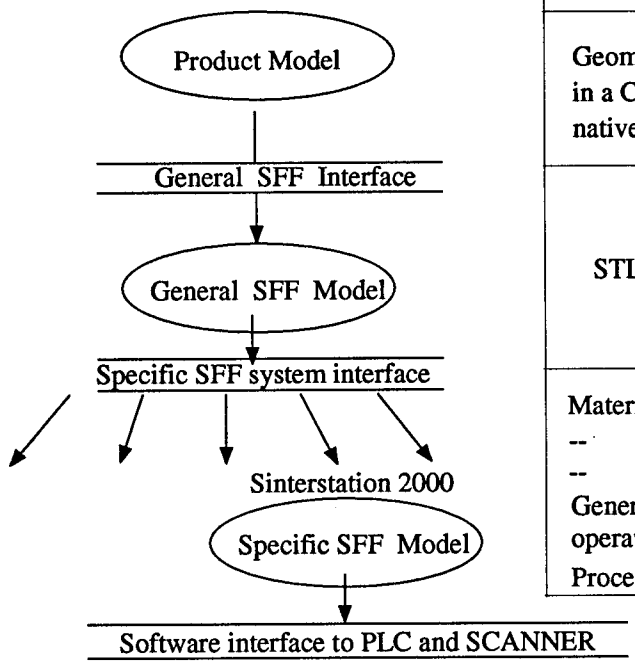

Models in SFF	
Current	Future
Geometry Model in a CAD-systems native format	Product Model in a STEP format
STL file	SFF Model in STEP format
Material data -- -- Generated by operator: Process parameters	Material data Scanning contours Process model Generated automatically: Process parameters

Figure 5 From the product model to a specific SFF model

Summary

We have presented an research approach in which the process parameters and scanning patterns are derived from the product model and from the use of a process model. We have discussed some drawbacks with the STL format and some SLS process weaknesses. We conclude that software control of laser beam scanning paths and process parameters is vital for the optimal generation of accurate and dimensionally stable parts. We also propose the use of a STEP based format and outlines one idea how to create a general SFF model carrying part geometry, process parameters and scanning principles to be used by different SFF systems.

References

[1] Azari M, *Manufacturing Data Systems Based on STEP*, Department of Manufacturing Systems, IVF-KTH, Stockholm, 1994

[2] Brown S, *Simulation of solid freeform fabrication*, Proceedings of Solid Freeform Fabrication Symposium, Austin, Texas, 1993

[3] Crawford R, *Computer aspects of Solid Freeform Fabrication*, Proceedings of Solid Freeform Fabrication Symposium, Austin, Texas, 1993

[4] Dolenc A, *Software Tools for Rapid Prototyping Technologies in Manufacturing*, PhD thesis, Helsinki University of Technology, Helsinki, 1993

[5] Holmer B, Apelskog-Killander L, Palm G, *Some practical experiences of SLS - Selective Laser Sintering*, Proceedings of the 2nd Scandinavian Rapid Prototyping Conference, Aarhus, 1993

[6] Kjellberg T, Carleberg P, *Some thoughts on product model driven direct manufacturing*, Dept. of Manufacturing Systems, KTH, Stockholm, Internal report in Swedish, 1993

[7] Laakko T, *Incremental Feature Modelling: Methodology for Integrating Features and Solid Models*, PhD thesis, Helsinki University of Technology, Helsinki, 1993

[8] Nelson J C and Barlow J W, *Relating Operational Parameters between SLS Machines which have Different Scanner Geometries and Laser Spot Sizes*, Proceedings SFF Symposium, Austin, 1992

[9] Palm G, *Experiences of SLS - Selective Laser Sintering*, Dept. of Manufacturing Systems, IVF-KTH, Stockholm, Internal report, 1994

[10] Steger W, Geiger M, Haller T, *Data models and information technology for the production of prototypes* , IPA, Stuttgart, Germany, 1993

[11] *The Sinterstation 2000 System User's Guide*, DTM Corp., 1993

[12] Vancraen W, Swaelens B, Pauwels J *Contour interfacing in rapid prototyping - Tools that make it work*, Proceedings of the 3rd European Conference on Rapid Prototyping and Manufacturing, Nottingham, 1994

[13] Wozny M, *System issues in solid freeform fabrication*, Proceedings of Solid Freeform Fabrication Symposium, Austin, Texas, 1992

TEMPERATURE-CONTROLLED SELECTIVE LASER SINTERING

J. A. Benda
United Technologies Research Center
East Hartford, CT 06108

ABSTRACT

A control scheme for laser sintering has been developed which maintains sintering powder at constant temperature by actively controlling laser power. It uses a sensor to monitor the temperature of powder at the focus of a moving laser beam. The control scheme corrects for variations of thermal conductivity and powder reflectivity due to the proximity of previously sintered material, as well as for statistical fluctuations. The sensor also serves as a useful diagnostic, and is used to confirm model predictions of the variation of powder temperature with process parameters. A second temperature-controlled laser beam, concentric with the first, but of larger spot size, can be used to locally heat the powder around the sintering powder. This is shown to reduce curling as well as the balling or agglomeration of molten material.

INTRODUCTION

With the advent of stereolithography in 1988, a number of rapid prototyping technologies have been developed. The selective laser sintering process is potentially one of the most versatile [1]. An infrared laser selectively sinters layers of powder, producing a prototype part one layer at a time. Initially developed for wax and plastic materials, current research is directed towards extending the technology to sintering metal and ceramic materials directly [2].

Two problems have been inherent to the SLS process which limits its usefulness. One problem is that the thermal conductivity and reflectivity of powder changes as it is sintered, so that the amount of laser power required to uniformly sinter powder changes depending on the amount and proximity of previously sintered material. Furthermore, heat builds up in the powder bed as material is sintered so that the temperature change and thus the laser power required to sinter is less. Part growth near edges and poor adhesion between layers are possible detrimental effects. One approach to solving the problem is to keep track of the history of the part as it is sintered and passively change the laser power as the part buildup progresses, assuming one knows how to do this. For a complex part, this can be quite complicated.

A second problem is that thermal gradients created during the sintering process cause parts to curl. Previous attempts to control the curling problem have concentrated on heating the entire bed of powder up to some temperature less than that at which it starts to sinter during the time needed to build a part. The approach has been used with success for polymeric powders. For metal and ceramic parts, the approach is much more challenging because of the temperatures involved. Obtaining a uniform temperature distribution for the bed has proven difficult. Also, such powders will begin to sinter on their own at roughly half the melting temperature. Thus, it is not clear there is an operating window in which curling is controlled, but yet the powder bed does not cake up.

To solve the laser control problem, we have developed an active control scheme to keep the

temperature of the powder being sintered at the beam focus constant. A two beam approach to controlling curling was also explored, in which a large beam is used to locally heat the powder around a tightly focused beam which does the actual sintering. Because the heating time is short compared with the build time, it should be possible to achieve more local heating without the powder bed caking than is possible with the approach described above.

ACTIVE CONTROL SCHEME

The key element for the control scheme is a temperature sensor which can monitor the temperature of powder at the focus of a moving laser beam. The sensor is schematically illustrated in Figure 1. A dichroic beamsplitter or a scraper mirror is inserted into the beam path before the scanning mirrors. This optic element allows the infrared laser beam to pass through unattenuated, but reflect thermal emission from the powder in the wavelength range of a detector. In our experiment, a CO_2 laser is used lasing at 10.6 μm, and a germanium detector is used which is sensitive to wavelengths from 1.0 to 1.8 μm. A lens is used to image the powder bed onto the detector. If desired an aperture can be put in front of the detector to insure that only thermal emission at the laser beam focal spot is monitored. Another aperture should be in the system to insure that the solid angle of the thermal radiation reaching the detector does not change as the scanning mirrors are rotated. By putting the sensor before the scanning mirrors, the detector will automatically follow the moving beam.

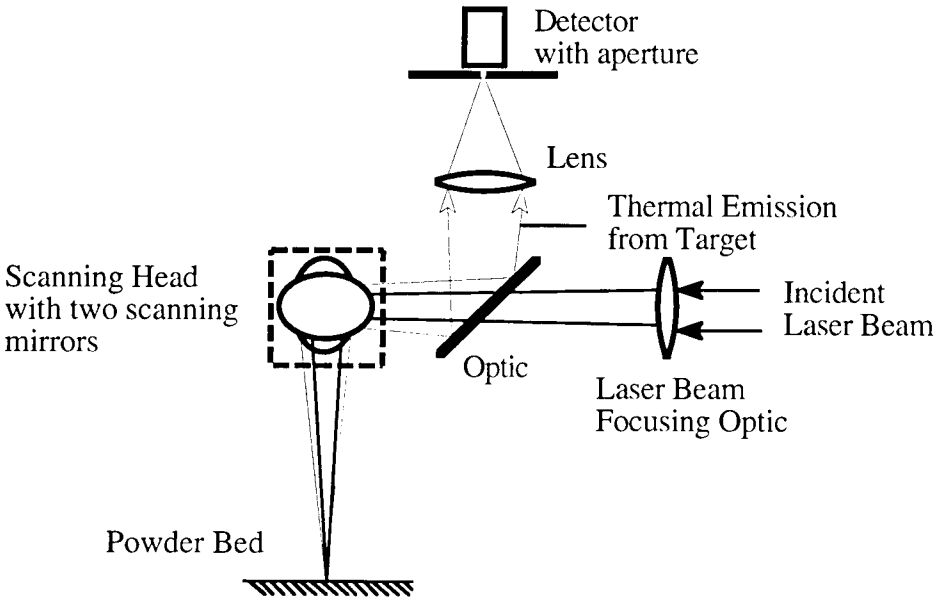

Figure 1. Schematic of thermal sensor.

We have performed tests with a variety of materials and have concluded that primarily thermal emission is seen by our detector. There is no evidence of plasma or a plume being produced at the power levels necessary to sinter powder. The amount of radiation we are seeing as well as the wavelength dependence are consistent with thermal emission. The wavelength dependence of the emission from two ceramic powders was measured with a scanning monochromator and a photomultiplier. The wavelength dependence of the photomultiplier sensitivity, as well as the

grating efficiency of the monochromator, can be normalized out by dividing the signal produced by sintering ceramic materials with that produced by a quartz-tungsten-halogen (QTH) lamp. A QTH lamp approximates a black body source at 3200 °K. The resulting curves were fit assuming thermal emission to derive the temperatures of the ceramic materials, as shown in Figure 2. The temperatures are within a couple of hundred degrees of the melting or sublimation temperatures of these materials as was expected, since some melting or vaporization of material was observed. Although only a few points are plotted, the emission was measured continuously and no structure indicative of anything other than thermal emission was observed.

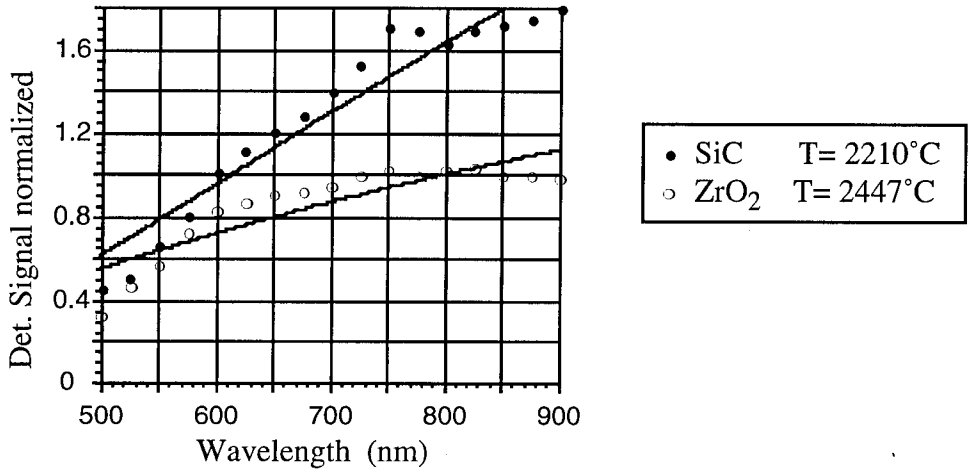

Figure 2. Color Temperature determined by normalizing emission to QTH Lamp.

As a second test, our detector was calibrated and the total irradiance on it agreed with a calculation of thermal emission using the numerical aperture of our collection optics and assuming a reasonable value of emissitivity. This test was done with iron powder and just enough laser power to start melting the iron - implying a temperature of about 1500 °C.

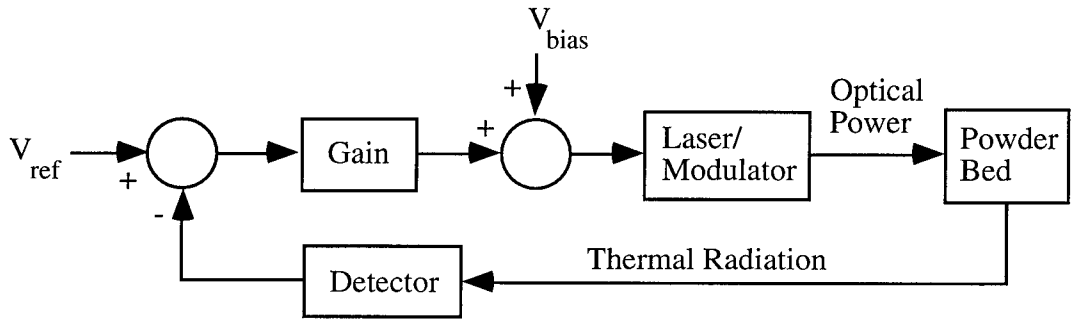

Figure 3. Block Diagram of Control Scheme

The signal from the germanium detector was used to control laser power. Initially this was done with an acousto-optic modulator external to the laser. The modulator uses acoustic waves at rf frequencies to produce a phase grating in a germanium crystal. This grating deflects a portion of the laser beam. Modulating the rf power modulates the beam transmitted directly through the crystal. The laser beam passes first through the modulator, then through a 10X telescope which expands the beam, a concave mirror to focus the beam, and finally two scanning mirrors which

direct the focused beam to the powder. The focused spot size was about 0.3 mm. An analog driver for the AO modulator was used which allowed the laser power to be varied continuously between 10 and 100 per cent of full power. The modulator was initially biased to give about 50% power. A block diagram of our control loop is shown in Figure 3. The control circuit used generated an error signal between the actual detector signal and the desired signal, multiplied it by a variable gain, and used the resulting signal to drive the AO modulator.

A mixture of tungsten and copper powder was used to evaluate the performance of our system. Three adjacent, slightly overlapping scans were made across the initially unsintered powder bed. Figures 4 gives oscilloscope traces comparing the open loop and closed loop performance. The top trace in both plots shows the laser power, which goes to zero between the three successive scans, while the bottom trace shows the germanium detector signal. For open loop operation, the laser power remains constant, but the detector signal is much higher on the first scan and is noisy. For closed loop operation, the detector signal is now constant and the laser power varies, increasing after the first scan by roughly 20%.

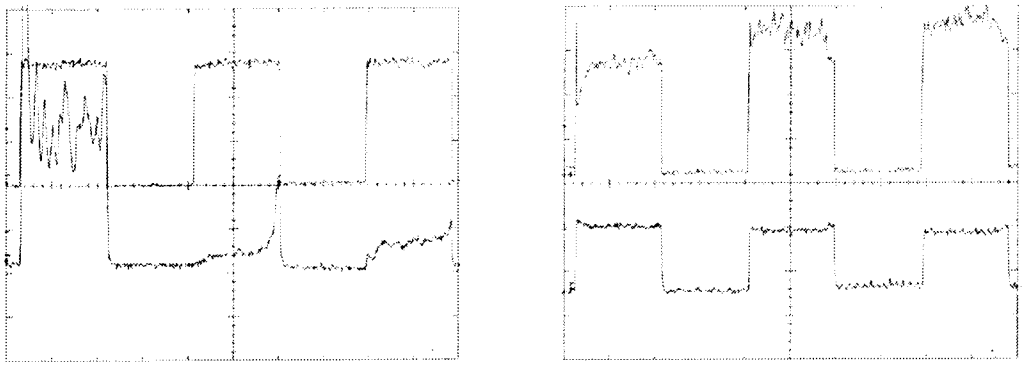

Open Loop Closed Loop

Figure 4. Comparison of open loop and closed loop performance of control scheme with W/Cu mixture. The upper oscilloscope traces are laser power. The lower traces are Ge detector signal. The results from three adjacent scans of the powder are shown.

Examination of the irradiated powder shows that the first open loop scan digs a trench in the powder with molten copper sinking well into the tungsten powder (the power coupled in was too great), while successive scans do not adequately couple into the powder. Under closed loop control, the irradiated powder is uniformly sintered. Examination of the microstructure also reveals that molten copper is more uniformly distributed even within one scan line. This may prove to be as big a benefit for closed loop control as compensating for the previous history of the sintered part. A significant decrease in sensor signal is always noted from the first to the second scan with no feedback control, with the effect more pronounced for the tungsten/copper mixture than for most materials tried.

Recently, we have acquired a 200 W rf-excited laser (SYNRAD model 57-2) and confirmed that it is possible to modulate the laser power directly through pulse width modulation of the rf power supply with performance comparable to that with the AO modulator without its power

limitations. Modulation up to 5 KHz appears possible. Figure 5 shows results on mullite powder (aluminum silicate). The ability to correct for temperature variations is dramatic.

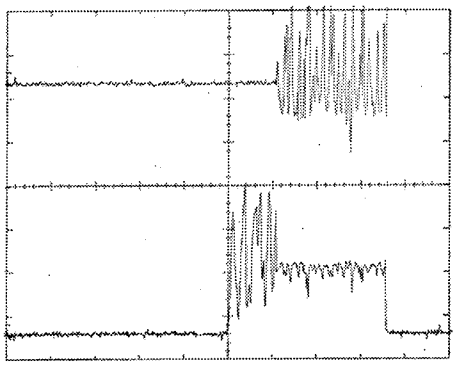

Figure 5. Comparison of open loop and closed loop performance with mullite powder using pulse width modulation. The upper oscilloscope trace is the voltage used to modulate laser power. The lower trace is the Ge detector signal. Closed loop control is turned on part way through a single scan on unsintered powder.

The detector signal is a particularly strong discriminant, varying rapidly with both laser power and scan speed. Measurements of the detector signal as a function of the scan velocity at several laser powers are shown in Figure 6 (using Argon as a cover gas) for sponge iron powder from Pyron Corp. At a detector signal of 15 mv, some of the iron powder is just beginning to melt. So it is reasonable to assume that the powder was near the melting temperature of 1500°C. Using that, it is possible to calculate the temperature rise per watt of laser power for each scan speed.

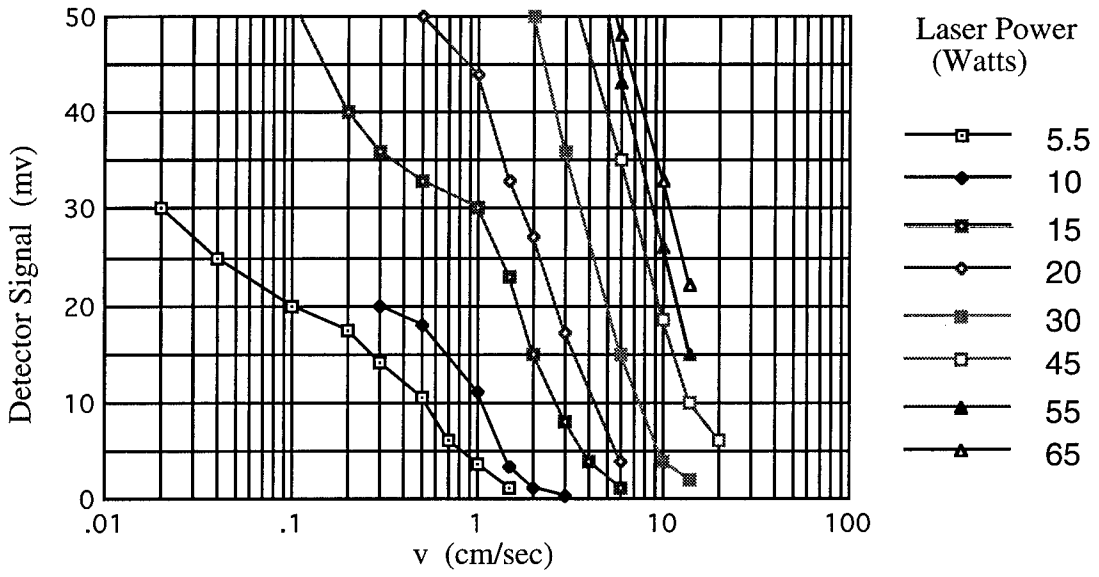

Figure 6. Detector signal versus scan speed for several laser powers.

It is possible to predict the peak temperature rise per watt for a moving Gaussian laser beam fairly simply , if one assumes a constant thermal conductivity. The temperature rise at a given position is given by (derived in a manner similar to results in [3]),

$$\Delta T = \frac{2\varepsilon_S P}{\pi w^2 \rho C_p} \int_0^\infty \frac{w^2/2}{w^2/2 + 4\alpha^2 t'} \exp\left(-\frac{(x+vt')^2+y^2}{w^2/2 + 4\alpha^2 t'}\right) Z(t',z)\, dt' \tag{1}$$

where

$$Z(z,t') = \frac{\beta}{2}\left\{\operatorname{erfc}\left(\left|\beta\alpha\sqrt{t'} - \frac{z}{2\beta\alpha\sqrt{t'}}\right|\right)\operatorname{sgn}\left(\beta\sqrt{t'} - \frac{z}{2\beta\alpha^2\sqrt{t'}}\right)e^{-\beta z} + \right.$$
$$\left.\operatorname{erfc}\left(\left|\beta\alpha\sqrt{t'} + \frac{z}{2\beta\alpha\sqrt{t'}}\right|\right)\operatorname{sgn}\left(\beta\sqrt{t'} + \frac{z}{2\beta\alpha^2\sqrt{t'}}\right)e^{+\beta z}\right\} e^{\beta^2\alpha^2 t'} + \beta\, e^{-\beta z}\, e^{\beta^2\alpha^2 t'}\, \theta\left(\frac{z}{2\alpha^2 t'} - \beta\right)$$

Here ΔT is the temperature rise, P is the laser power, ε_S is the emissitivity of the powder surface, α^2 is the thermal diffusitivity ($k/\rho C_p$), ρ is density, C_p is heat capacity, w is the Gaussian spot size, β is the penetration depth of the radiation into the powder assumed to be exponentially decaying, v is the scan velocity taken to be in the x direction, y is the transverse coordinate on the powder surface, z is the depth into the powder, sgn() is unity with the sign of the argument, and

$$\theta(x) = \begin{cases} 1 & x \geq 0 \\ 0 & x < 0 \end{cases}$$

All coordinates are with respect to the beam center on the surface.

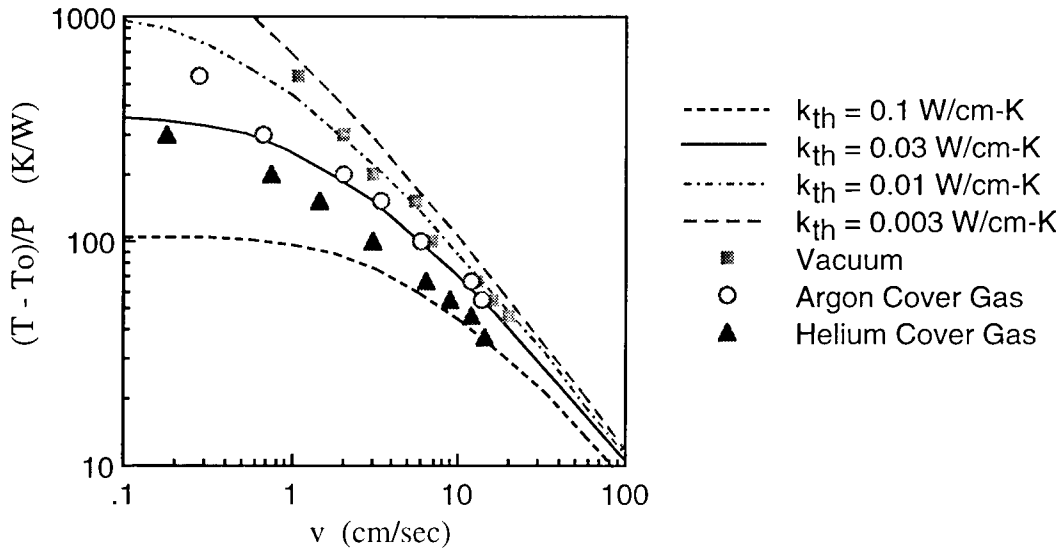

Figure 7. Temperature rise per watt of laser power. Experiment and theory.

The calculated peak temperature rise per watt of laser power is plotted versus scan velocity in Figure 7 for a range of thermal conductivities. Also plotted are experimental curves for iron powder with two different cover gases, helium and argon, and under vacuum. The cover gas modifies the thermal conductivity of the powder with roughly an order of magnitude change predicted in going from vacuum to helium, argon being intermediate [4]. At low scan speeds, thermal equilibrium is established and the temperature rise is independent of speed and varies inversely with thermal conductivity. At high speeds, the power stays where it is deposited during the dwell time of the beam at a given position. Thus the temperature rise varies inversely with scan speed and is independent of thermal conductivity. This behavior is nicely mirrored in the

experimental data, giving some confirmation of the assumption that the radiated power is mainly thermal emission, as well as some confirmation of the theory.

TWO BEAM SINTERING

We first implemented two beam sintering by using the deflected beam from the AO modulator used for feedback control, as shown in Figure 8. The deflected beam was diverted around the 10X telescope and sent directly to the focusing optic. (In the single beam experiments above this beam was blocked.) Because that beam was ten times smaller, its focused spot size is about ten times larger. (The focused spot size varies as $2\lambda f/D$, where f is the focal length, λ is wavelength and D is the initial beam diameter.) The two beams were nominally concentric at focus, although there may be reasons for having one beam lead the other. The modulator was biased so that roughly 80% of the power was in the deflected beam. One drawback of the approach is that if the AO modulator is used for control of the focused beam, any power which is removed from the focused beam is dumped in the defocused beam. But normally the defocused beam is much larger in power, so the percentage change is small.

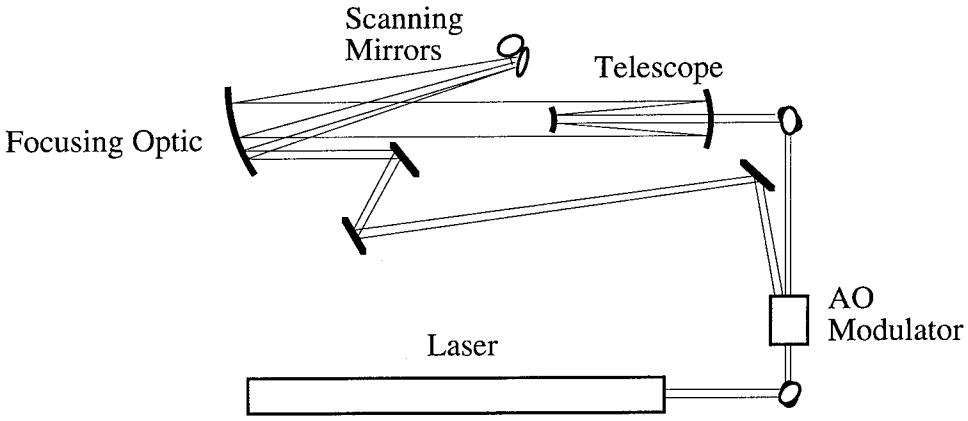

Figure 8. Schematic of two beam sintering experiment.

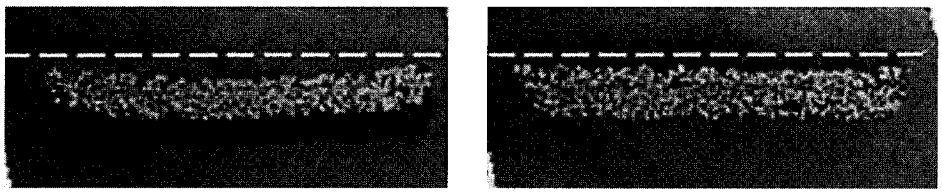

Single Beam Dual Beam

Figure 9. Comparison of curling for two sintered layers of iron/bronze powder using a single laser beam and a dual beam. Sintered material is shown in cross-section perpendicular to scanning direction. Dashed line is for visual reference.

Figure 9 shows the cross section of two layers of an iron/bronze powder mix, sintered with and without the larger beam. The samples were potted in epoxy and ground down to expose the cross section. The powers were adjusted to give the same signal in our germanium detector, so the

actual sintering temperatures used should be close. It is clear that much less curling results with two beam sintering. Without optimization, curling is not always eliminated, but is always observed to be reduced.

Single Beam Dual Beam

Figure 10. Images of selective laser sintering of alumina powder.

As is expected, the sintered material cools more slowly with the second beam. This might be part of its advantage. Figure 10 shows high speed video images of alumina powder being sintered with and without the second beam. The longer tail, as well as the hot powder to the side of the sintered material is clearly evident.

CONCLUSION

Our CO_2 laser, a SYNRAD Duo-Lase™ Model 57-2, has two independent lasers in a single housing with separate controllers and power supplies. A polarization beamsplitter combines the two beams, which are of orthogonal polarization. Each laser can be used to provide one of the two beams for dual beam sintering. We have successfully demonstrated two beam sintering with active control of both beams. A polarization beamsplitter is used to separate the two beams. A separate feedback control circuit is used for each laser. The aperture in front of the detector of figure 1 is now a mirror which is used to reimage the thermal emission from the powder irradiated mainly by the large beam. The second detector is part of the control loop for the large laser beam. Preliminary results indicate that controlling the large laser beam may be more important than control of the focused laser beam. More uniform sintering has been demonstrated. Complete elimination of the curling problem using dual beam sintering alone appears unlikely, at this point, but hopefully the problem can be significantly reduced.

REFERENCES

1. Deckard, C. R., *Part Generation by Layerwise Selective Sintering*, Master's Thesis, The University of Texas at Austin, May 1986.
2. Das, S., McWilliams, J., Wu, B., and Beamon, J. J., *Design of a High Temperature Workstation for the Selective Laser Sintering Process*, Solid Freeform Fabrication Symposium, The University of Texas at Austin, Aug. 12-14, 1991.
3. Rosenthal, D., *The Theory of Moving Sources of Heat and Its Applications to Metal Treatments*, Transactions of the ASME (Nov. 1946).
4. Swift, D. L., *The Thermal Conductivity of Spherical Metal Powders Including the Effect of an Oxide Coating*, Int. J. Heat Mass Transfer **9**, 1061-1074 (1966).

SHAPE AND TOPOLOGY STRUCTURAL REDESIGN BY LARGE ADMISSIBLE PERTURBATIONS

Michael M. Bernitsas, Professor
Danet Suryatama, Research Assistant
Byungsik Kang, Research Fellow
Dale G. Karr, Associate Professor

Department of Naval Architecture and Marine Engineering
The University of Michigan, Ann Arbor, MI 48109-2145

ABSTRACT

The ultimate goal in concurrent engineering of structures is to achieve simultaneously in the design stage the following objectives: (1) A shape that performs its *function*, conforms with the boundary conditions, and can support the external loads. (2) A product with structural *integrity*, i.e. with stress levels remaining below acceptable limits. (3) A product with acceptable *performance*, e.g. modal dynamics, i.e. with natural frequencies and mode shapes that do not amplify external dynamic loads; and static, i.e. acceptable deflection. (4) A composite *microstructure* that can optimally satisfy the above topology/ shape, load, and performance constraints. (5) A microstructure *fabrication* process that efficiently produces the above optimal structure. The purpose of our ONR funded project is to address the complete problem in concurrent structural design by further developing the LargE Admissible Perturbations (LEAP) theory which is being developed at the University of Michigan since 1983, and combining it with micromechanics constitutive equations. At the fabrication end, the Selective Laser Sintering (SLS) process will be simulated so that the SLS variables are defined as the final product of the concurrent structural design optimization process. LEAP theory -- as implemented in Code RESTRUCT (REdesign of STRUCTures) -- produces the final design without trial and error or repeated Finite Element Analyses (FEAs), thus, shortening the redesign process and contributing to rapid prototyping.

1. CONCURRENT STRUCTURAL DESIGN FOR MANUFACTURING

Solid Freeform Fabrication (SFF) techniques enable designers new flexibilities for designing structural components [6]. Microengineered materials can provide seemingly endless possibilities from which a designer might make a selection. In order to realize fully the potential of SFF processes and speed up the rapid prototyping cycle, the structural design should not be decoupled from the material design and the fabrication process. The goal of our research project is to develop structural design methodology which links the macrostructural design with the microengineering of materials and with the material fabrication process. Equivalently, the engineering problem addressed in our research is posed as follows: Given a particular function, what shape should the components have, what should it be made of, and how should it be made? The above concurrent design problem for freeform solids is shown schematically in Figure 1 which indicates the linkage of macrostructural properties and performance with microscale material characteristics and the fabrication process. A global optimization of material and geometry (topology, shape, and size) must address the issues of production efficiency and quality of the product.

As shown in Figure 1, the design process requires establishing the spatial distribution of the material. Thus, the material stiffness which is represented by the elastic modulus E, would be a function of position $E(\bar{x})$. Similarly, the density and strength of the material must be established; $\rho(\bar{x})$ and $\sigma(\bar{x})$ respectively. These parameters are related to the microstructure of the layered material and are described by – for example – porosity $P(\bar{x})$, crack distribution $D(\bar{x})$, and the Lamé elastic constants of material $\lambda(\bar{x})$ and $\mu(\bar{x})$.

In this project, the fabrication process we focus on is Selective Laser Sintering [7, 12]. There has been some work in establishing the effects of process variables such as binder and primary phase volume content on the composite strength. Particle size has also been studied with regard to its influence on strength. These functional relationships are essentially first order approximations which will be developed further during the course of the project. Further analyses will be performed to establish the interrelationship of such parameters on the macrostructure's stiffness, density and strength, etc.

These relations will be employed within the framework of LargE Admissible Perturbations theory to find optimal structural designs. Because the functional relations between the fabrication process, the microstructure, and the macroscale structural parameters are incorporated in the design methodology, an overall optimum design would be established. Accordingly, the five objectives of concurrent engineering of structures are listed in the Abstract and are abbreviated below for future reference:

(1) *Function* = function, boundary conditions, load support
(2) *Integrity* = structural integrity, strength limits
(3) *Performance* = static and modal dynamics performance
(4) *Microstructure* = material properties
(5) *Fabrication* = fabrication process

Several aspects of the concurrent structural design problem have been addressed in design optimization methods [9, 14] and inverse design methodologies that allow for small [13] or large [1-5, 8, 10, 11] structural changes.

2. LARGE ADMISSIBLE PERTURBATIONS APPROACH TO REDESIGN

Several problems in structural analysis and design (see Figure 2) – including the problem of redesign or inverse design – can be cast as two-state problems. State S1 is the initial state which is known and for which all required finite element analyses (modal dynamics, static buckling, etc.) have been performed. It is assumed that State S1 has undesirable characteristics or performance and should be improved to satisfy the designer's specifications. State S2 is the objective unknown state modeled by the same finite element grid but defined by different design variables.

The methodology we have been developing since 1983 for solving two-state problems is based on the LargE Admissible Perturbations theory. This methodology provides several advantages over trial and error, sensitivity methods, iterative techniques, and methods requiring repeated finite element runs. The basic features of our methodology are listed below.

(i) Primarily Two-State Theory is not an optimization methodology. It just uses NPSOL to find a solution to several optimization problems appearing in the process. Two-State Theory is a universal formulation and solution methodology for a plethora of analysis, design, redesign, model correlation (calibration), model reduction, reliability analysis, and monitoring problems related to the entire life of a structure from conception to dismantling. The Large Admissible Perturbations approach to redesign has two parts. The first part PAR (Perturbation Approach to Redesign) is the formulation of a two-state problem. The second uses a large admissible perturbations algorithm to solve the problem.

(ii) The Perturbation Approach to Redesign (PAR) develops the general perturbation equations by relating the two states S1 (known) and S2 (unknown). These are highly nonlinear equations – with implicit and explicit dependence on redesign variables. Nevertheless, they are equations somebody can work with as opposed to dealing only with numerical computations. The generality of the applicability of this methodology is most obvious in the solution it has provided to structural reliability problems where other theories (Stochastic Finite Elements, Structural Systems Reliability, and Response Surface Approach) cannot further progress due to lack of equations describing the failure state.

Some of the general perturbation equations developed in references [1-5, 10, 11] are provided below where unprimed and primed symbols correspond to states S1, S2, respectively. For modal dynamics, where ω is neutral frequency, $\{\psi\}$ is normal mode; k, m are stiffness and mass matrices; and α_e's are fractional change variables, we have:

$$\sum_{e=1}^{p}\left(\{\psi'\}_i^T[k_e]\{\psi'\}_i - \omega_i'^2\{\psi'\}_i^T[m_e]\{\psi'\}_i\right)\alpha_e = \omega_i'^2\{\psi'\}_i^T[m]\{\psi'\}_i - \{\psi'\}_i^T[k]\{\psi'\}_i \ ,$$

$$\sum_{e=1}^{p}\{\psi'\}_j^T[k_e]\{\psi'\}_i\alpha_e = -\{\psi'\}_j^T[k]\{\psi'\}_i \quad ,$$

$$\sum_{e=1}^{p}\{\psi'\}_j^T[m_e]\{\psi'\}_i\alpha_e = -\{\psi'\}_j^T[m]\{\psi'\}_i \quad ,$$

for $i = 1,2,...,n,\ j = i+1, i+2,...,n$ [1, 2] . For static deflections u ,

$$u_i' = \sum_{m=1}^{n}\left\{\frac{\phi_{im}' A_m}{B_m + \sum_{e=1}^{P} C_{me}\alpha_e}\right\} \ ,$$

where $A_m = \sum_{j=1}^{n}\phi_{jm}' f_j$, $B_m = \{\psi'\}_m^T[k]\{\psi'\}_m$,

$C_{m_e} = \{\psi'\}_m^T[k_e]\{\psi'\}_m$, and φ_{jm} represents modal amplitudes.

For static stresses σ ,

$$\sigma_k' = \sum_{i=1}^{g} S_{ki}\sum_{m=1}^{n}\left\{\frac{\phi_{im}' A_m}{B_m + \sum_{e=1}^{p} C_{m_e}\alpha_e}\right\}(1+\alpha_h) \ .$$

For buckling loads P , and modes $\{\psi_b\}$

$$\sum_{e=1}^{p}\{\psi_b'\}_i^T\left([k_{c_e}] - P_i'[k_{\sigma_{0e}}]\right)\{\psi_b'\}_i\alpha_e = \{\psi_b'\}_i^T\left(P_i'[k_{\sigma_0}] - [k_c]\right)\{\psi_b'\}_i \ ,$$

$$\sum_{e=1}^{p}\{\psi_b'\}_j^T[k_{c_e}]\{\psi_b'\}_i\alpha_e = -\{\psi_b'\}_j^T[k_c]\{\psi_b'\}_i \ ,$$

$$\sum_{e=1}^{p}\{\psi_b'\}_j^T[k_{\sigma_{0e}}]\{\psi_b'\}_i\alpha_e = -\{\psi_b'\}_j^T[k_{\sigma_0}]\{\psi_b'\}_i \ ,$$

for i = 1,2,...,n , j=i + 1,i + 2,...,n , where $[k_c] = [k_o] - [k_{\sigma F}]$, $k_{\sigma F}$ includes the body force, and $[k_\sigma] = - P_i[k_{\sigma o}] - [k_{\sigma F}]$.

(iii) The LEAP (LargE Admissible Perturbations) algorithms can solve the general perturbation equations for large changes (about 100%) of both the design variables and structure's specified response. LEAP algorithms are not limited by the 7% increments in sensitivity methods.

(iv) LEAP algorithms do not require repeated FEAs. In fact, for changes of the order of 100% no FEA other than that of the original known structural state S1 is needed.

(v) Code RESTRUCT performs routinely shape optimization as part of all the problems it can solve – see (i) above. The advantage here is that it keeps track of changes in elemental matrices so that the structure produced at the end is real. Some model correlation methods change the mass and stiffness global matrices and do not result in a real structure.

(vi) Code RESTRUCT has been developed for several complex structures; e.g. stiffened plates where the neutral axis and connectivity of stiffness to plate are affected during the redesign process.

(vii) Topology optimization has been achieved by RESTRUCT -- as presented in this paper -- in a very short period of time for 3-D bodies by introducing a brick finite element. The method is equivalent to those developed in [9, 14]. Further, it has all the advantages of large changes, no iterations, and no repeated finite element analyses.

(viii) It postprocesses data of a widely available finite element code MSC/NASTRAN. That is, structural state S1 is analyzed by FEM and RESTRUCT postprocesses these results to produce state S2 from its specifications.

The first step in achieving concurrent design including the five objectives listed in Section 1, is to develop Two-State Theory to formulate and solve (by a LEAP algorithm) the topology/shape optimization problem for concurrent structural integrity, modal dynamics, static deflection, and stress constraints (objectives for state S2). This encompasses objectives (1)-(3) (function, integrity, performance) of concurrent design and can be achieved by: (a) Introducing solid finite elements in code RESTRUCT; producing stiffness and mass, three-dimensional distributions to achieve the optimal topology and material properties; (b) Developing a LEAP algorithm to find the objective state S2 subject to modal dynamic constraints; (c) Developing the LEAP algorithm further to add static deflection constraints; (d) Finalizing the LEAP algorithm to include stress constraints. Actually, since 1983 LEAP algorithms have been developed to solve two-state problems for various finite elements and single or multiple modal dynamics, static deflection and stress redesign objectives. This paper and the following numerical applications provide the first step towards solution of the concurrent design problem defined above for solids.

3. NUMERICAL APPLICATIONS

Development of LEAP algorithms for a new redesign problem usually takes one year. An algorithm is considered fully developed when it can be used to redesign a structure for 100% changes in redesign objectives and large changes in the redesign variables, handle about 100 redesign variables, several simultaneous modal dynamics, static deflection and stress objectives, and about 1000 finite element degrees of freedom. Further development requires only more computational time. Such fully developed algorithms can produce redesign with about 3% error without trial and error or repeated FEAs.

The results presented in this section represent the first attempt to develop a LEAP algorithm for three-dimensional topology redesign for static and modal dynamics objectives. Thus, the error is still above the desired accuracy level of 3%. Improvement of the algorithm will be based on advanced formulation in the prediction phase based on nonlinear approximations of the general

perturbation equations, as well as identification of appropriate extracted modes, admissibility conditions, and selection of redesign variables.

Several numerical applications are presented in Tables 1, 2 and 3 on the redesign of the cantilever beam in Figure 4 and the cantilever plate in Figure 5. In this early stage of development of the LEAP algorithm for solid elements, single frequency redesign is very accurate (cases b1. and d5.). Redesign for static displacement, or simultaneous static displacement and modal dynamics objectives requires further algorithmic development.

Figure 6 shows a simple two-dimensional topology redesign problem which has been used in the literature ([9] and [14]) as a bench mark problem. The results produced by Code RESTRUCT which implements the LEAP algorithm for topology optimization of solid elements are consistent with those published in the literature. The starting structure (state S1) of a solid plate is redesigned to become a multiply connected stucture at state S2.

CONCLUDING REMARKS

Presently, the large admissible perturbations methodology is capable of solving relatively simple three-dimensional redesign problems for static deflection and modal dynamics objectives. After fully developing the topology redesign algorithm for 3-D problems, the large admissible perturbations methodology will be developed further to address concurrent design problems for manufacturing including micromechanics constitutive equations and modeling of the SLS fabrication process.

ACKNOWLEDGMENTS

Research support provided by the Office of Naval Research through Grant No. DOD-G-N00014-90-J-4081 is gratefully acknowledged.

REFERENCES

[1] Bernitsas, M.M. and B. Kang, (1991), "Admissible Large Perturbations in Structural Redesign," *AIAA Journal*, Vol. 29, No. 1, pp. 104-113.

[2] Bernitsas, M.M. and R.L. Tawekal, (1991), "Structural Model Correlation Using Large Admissible Perturbations in Cognate Space," *AIAA Journal*, Vol. 29, No. 12, pp. 2222-32.

[3] Bernitsas, M.M. (editor), (1994), *RESTRUCT: Vol. I - Theoretical Manual, Vol. II - User's Manual, Vol. III - Application Manual*, Report to the University of Michigan/Sea Grant/Industry Consortium in Offshore Engineering, Department of Naval Architecture and Marine Engineering, the University of Michigan, Ann Arbor, September 1994.

[4] Bernitsas, M.M. and C.W. Rim, (1994), "Redesign of Plates by Large Admissible Perturbations," *AIAA Journal*, Vol. 32, No. 9.

[5] Beyko, E. and M.M. Bernitsas, (1993), "Reliability of Large Scale Structures by Large Admissible Perturbations," *Journal of Offshore Mechanics and Arctic Engineering*, ASME Transactions, Vol. 115, No. 3, pp. 167-178.

[6] Bourell, D.L., J.J. Beaman, H.L. Marcus, and J.W. Barlow, (1990), "Solid Freeform Fabrication in Advanced Manufacturing Approach," Solid Freeform Fabrication Symposium, Austin, Texas, August 1990, pp. 1-7.

[7] Bourell, D.L., H.L. Marcus, J.W. Barlow, and J.J. Beaman, (1992), "Selective Laser Sintering of Metals and Ceramics," *Int. J. Powder Met.*, Vol. 28, No. 4, pp. 369.

[8] Hoff, C.J. and M.M. Bernitsas, (1985), "Dynamic Redesign of Marine Structures," *Journal of Ship Research,* Vol. 29, No. 4, pp. 285-295.

[9] Johanson, R., N. Kikuchi, and P. Papalambros, (1993), "Homogenization Design and Layer Manufacturing of a Lower Control Arm in Project MAXWELL," Solid Freeform Fabrication Symposium, Austin, Texas, August 1993, pp. 186-192.

[10] Kang, B., E. Beyko, and M.M. Bernitsas, (1992), "Invariant and Consistent Redundancy by Large Admissible Perturbations, *J. of Marine Structures*, Vol. 5, No. 1, pp. 23-70.

[11] Kang, B. and M.M. Bernitsas, (1994), "Stress Redesign by Large Admissible Perturbations," BOSS '94 Conference, Cambridge, Mass., July 1994, Vol. 3, pp. 201-212.

[12] Lakshminarayan, U. and H.L. Marcus, (1992), "An Experimental Study of the Relationship Between Microstructure and Mechanical Properties of a Ceramic Composite Fabricated by Selective Laser Sintering," Solid Freeform Fabrication Symposium, Austin, Texas, August 1992, pp. 44-53.

[13] Stetson, K.A., (1975), "Perturbation Method of Structural Design Relevant to Holographic Vibration Analysis," *AIAA Journal*, Vol. 13, No. 4, pp. 457-459.

[14] Yang, R.J. and C.H. Chuang, (1992), "Optimal Topology Design Using Linear Programming," CAE Department, Ford Motor Company Research Report, November 1992.

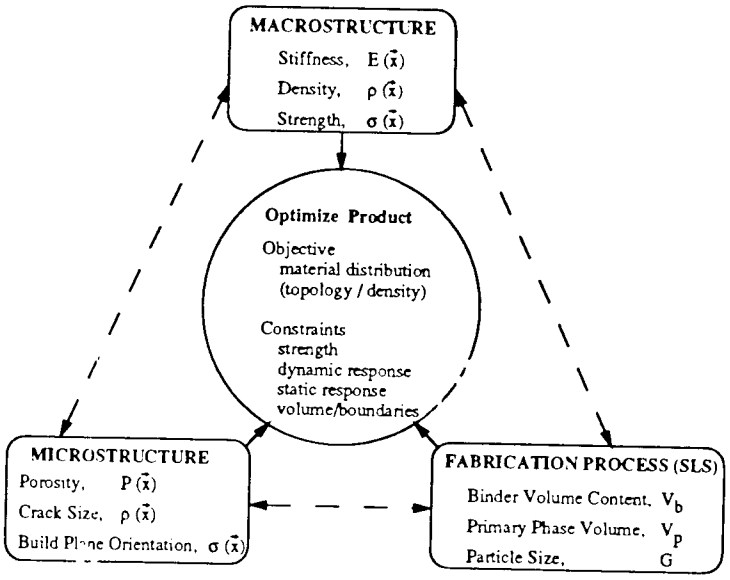

Figure 1. Concurrent design of freeform solids for structural integrity, topology, and microstructure fabrication

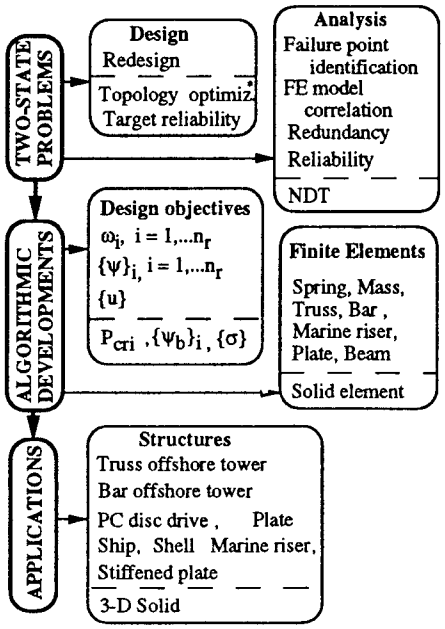

Figure 2. Status of large admissible perturbations theory for solution of two-state problems in structural analysis and design.
* Items below dashed lines are being developed.

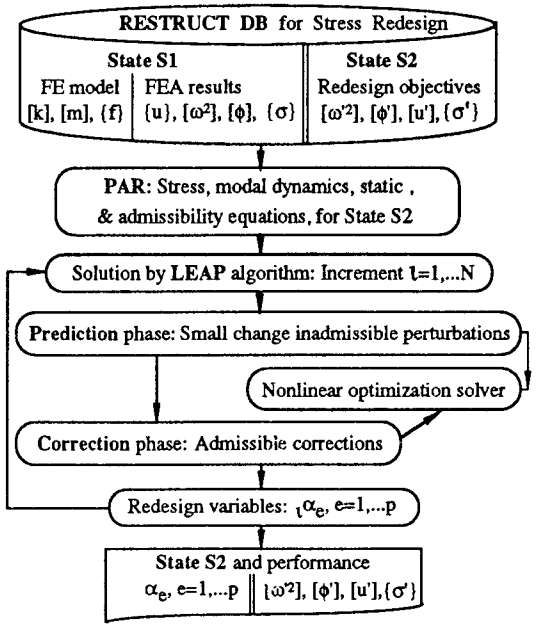

Figure 3. Stress redesign by a large admissible perturbations algorithm

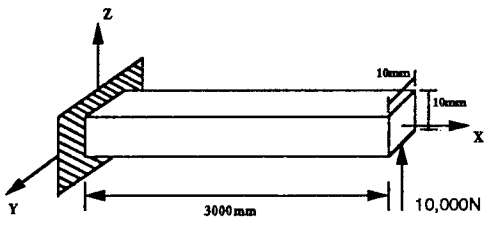

Properties : E = 2.07.10⁵ MPa
ρ = 7.833.10⁻⁹ NSec²/mm⁴
ν = 0.3

Response : f_1 = 9.2778 Hz
w_{42} = w_{82} = 51.6851 mm

Model #a has 10 Hexa elements
Model #b has 30 Hexa elements

Figure 4. 3-D model for redesign of cantilever beam

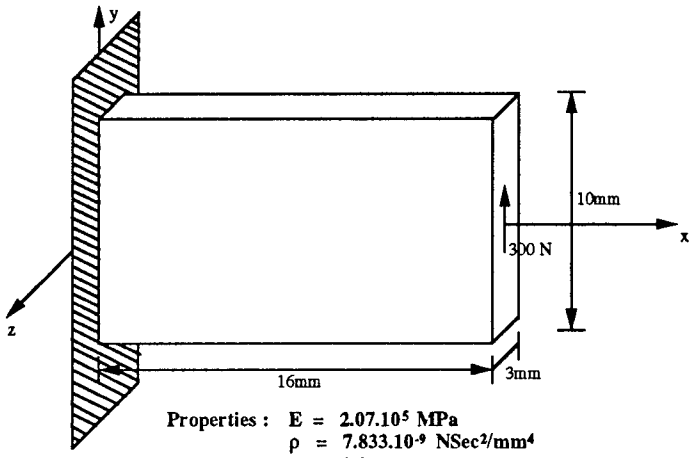

Properties : E = 2.07.10⁵ MPa
ρ = 7.833.10⁻⁹ NSec²/mm⁴
ν = 0.3

Response : f_1 = 9702.04 Hz
v_{289} = v_{102} = 0.01 mm

Model #c has 40 Hexa elements
Model #d has 160 Hexa elements

Figure 5. Solid element model of cantilever plate

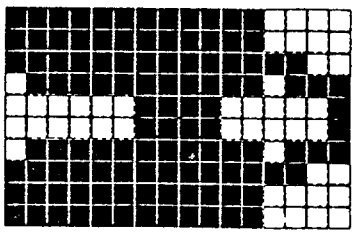

Figure 6. Cantilever plate :
elimination of solid elements with small strain energy (case d4)

Table 1. Redesign of Cantilever Beam

Case #	Redesign Goal			Reanalysis			Error (%)		
	u'_{42}/u_{42}	u'_{82}/u_{82}	$\omega'_1{}^2/\omega_1{}^2$	u'_{42}/u_{42}	u'_{82}/u_{82}	$\omega'_1{}^2/\omega_1{}^2$	u'_{42}/u_{42}	u'_{82}/u_{82}	$\omega'_1{}^2/\omega_1 2$
a1.	0.499	-----	1.068	0.503	-----	1.048	-0.802	-----	1.873
a2.	0.500	-----	-----	0.503	-----	-----	0.600	-----	-----
b1.	-----	-----	3.000	-----	-----	3.000	-----	-----	0.000
b2.	-----	0.500	2.000	-----	0.497	2.233	-----	0.600	-11.65

Case #a1 and a2: Modeled by 10 solid elements; 10 redesign variables (p) for K
Case #b1 and b2: Modeled by 30 solid elements; p = 20 for M in case b_1; p = 20 for K in case b_2
Case #b2: Use of non-linear static prediction equation and NP solver

Table 2. Redesign of Cantilever Plate with 40 Hexa Elements

Case #	Redesign Goal		Reanalysis		Error (%)		$p^{(1)}$	$n_r{}^{(2)}$	n_a	%(3)	incr.
	u'_{53}/u_{53}	$\omega'_1{}^2/\omega_1{}^2$	u'_{53}/u_{53}	$\omega'_1{}^2/\omega_1{}^2$	u'_{53}/u_{53}	$\omega'_1{}^2/\omega_1{}^2$					
c1.	0.750	-----	0.820	-----	-9.333	-----	40	8	0	7	4
c2.	0.750	1.500	0.830	1.529	-10.667	-1.933	40	8	0	7	6
c3.	0.750	-----	0.810	-----	-8.000	-----	40	20	2	7	4
c4.	0.750	1.500	0.820	1.520	-9.333	-1.333	40	20	4	7	6
c5.	0.750	-----	0.797	-----	-6.267	-----	24	20	2	4	9
c6.	0.750	1.500	0.810	1.527	-8.000	-1.800	48	20	0	4	11
c7.	0.750	-----	0.783	-----	-4.400	-----	24	20	2	7	5

Case #c1-c6 calculated using linear static prediction eqn. with QP solver
Case #c7 calculated using non-linear static prediction eqn. with NP solver
(1) p: in all cases except c6, all redesign variables are for K
(2) n_r = number of extracted nodes
(3) % = incremental change to reach redesign goal

Table 3. Redesign of Cantilever Plate with 160 Hexa Elements

Case #	Redesign Goal		Reanalysis		Error (%)		p	n_r	%	incr.
	u'_{289}/u_{289}	$\omega'_1{}^2/\omega_1{}^2$	u'_{289}/u_{289}	$\omega'_1{}^2/\omega_1{}^2$	u'_{289}/u_{289}	$\omega'_1{}^2/\omega_1{}^2$				
d1.	0.755	-----	0.880	-----	-16.556	-----	80	20	7	4
d2.	0.755	1.500	0.880	1.479	-16.556	-1.400	80	20	7	6
d3.	0.755	-----	0.839	-----	-11.126	-----	80	20	7	4
d4.	0.755	-----	0.833	-----	-10.331	-----	80	20	4	7
d5.	-----	1.500	-----	1.500	-----	0.000	80	20	4	7

Case #d1.-d2. calculated using linear static prediction eqn. with QP solver
Case #d3.-d5. calculated using non-linear static prediction eqn. with NP solver

Structural Design for Freeform Fabrication using Composite Materials

Roy Johanson
Noboru Kikuchi
Panos Papalambros

Design and Computational Mechanics Laboratories
The University of Michigan
Department of Mechanical Engineering and Applied Mechanics
Ann Arbor, MI 48109

ABSTRACT

Advances in the development of methods to perform topology optimization offer the ability to design novel structures composed of dense composite materials. These structures, which possess superior mechanical properties, can only be produced through the use of layered manufacturing techniques. In this paper, we demonstrate a technique for the design of layered structures composed of composite materials. In addition, this procedure allows the design of the composite materials used for fabrication of such components on a microstructural level.

INTRODUCTION

Structural optimization has been an active area of research since the early 1970s; see for example Botkin [4]; Fleury [5]; Bendsøe [3]. The two basic optimization problems typically addressed in structural optimization have been sizing and shape optimization. In sizing optimization, variables define local geometric characteristics such as height, width, thickness, and radius of specific portions of the structure. A typical design task is to find the minimum weight shell structure to withstand applied thermo-mechanical loads. In shape optimization, the optimum shape of a structure is sought by varying the boundary shape defined by an appropriate spline function, with the design variables defined in a function form.

In most design problems, the topology of a structure is not known *a priori*. Topology is related to the number of holes in a structure. If the topology is fixed, the configuration is defined easily by spline functions. Significant difficulties are encountered when the topology of a structure must be designed, since its representation with spline-type functions is unwieldy. As a result, design problems involving both shape and topology have not been solved satisfactorily. Several approaches to the topology optimization problem have been proposed: see, for example, Rozvany [9], and the proceedings of a recent NATO Advanced Study Institute [3]. The homogenization method, described by Bendsøe and Kikuchi [2] and used in Project Maxwell, is unique in that it yields the optimal shape and topology at a macro- and micro-level of description.

HOMOGENIZATION DESIGN METHODOLOGY

We can formulate a generalized topology optimization problem by introducing microstructural perforations into the structure, and then minimizing the mean compliance subject to a constraint on the total volume of material used. Formally,

$$\underset{a,b,\text{and }\theta}{Minimize} \sum_i \int_\Omega f_i u_i d\Omega + \sum_i \int_{\Gamma_t} t_i u_i d\Gamma_t \qquad (1)$$

subject to equilibrium equations, and

$$\int_\Omega (1 - ab) d\Omega \le \Omega_s \qquad (2)$$

Here, u is the vector of virtual displacements, f is the applied body force, t is the applied traction on the boundary Γ_t, i is the number of finite elements used to discretize the structure, and Ω_S is the total volume of solid material forming the porous structure. The microstructural model used in this method is shown in Figure 1. There are three design variables per element: void dimensions a and b, and void orientation angle θ. Variables a and b are restricted to values [0,1], i.e., 0 to 1 inclusive.

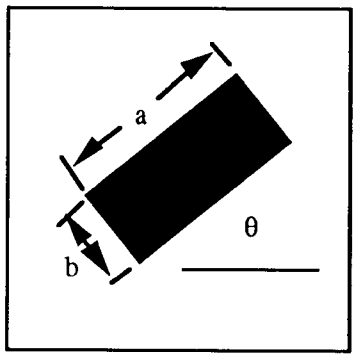

Figure 1: Element Microstructural Model

The equilibrium equation and its associated loading and support conditions, i.e., the structural analysis problem, are solved using the finite element method. The domain for stress analysis is the initial design domain. This domain is discretized into finite elements, with the design variables a, b, and θ for each element evaluated at the centroid. The number of design variables for the present problem is quite large, e.g., five to thirty thousand variables, and it is difficult to apply standard mathematical programming techniques. The optimization method used for this problem is a simple resizing scheme based on the optimality conditions. For details, refer to Bendsøe and Kikuchi [2].

We have demonstrated the applicability of this technique for structural layout design on an extensive and growing body of examples. These examples range from the design of simple plane stress/plane strain structures to the design of automotive body panels, suspension components, and complete vehicle structural layouts. References 1, 7, and 8 contain a variety of these demonstration and validation examples.

MATERIAL DESIGN EXAMPLES

Some recent works by Bendsøe and collaborators [11,12] describe the construction of optimal structures using materials of prescribed constitutitive behavior. In [11], Bendsøe et. al. show that the lower bound on compliance optimization for a single load case is obtained using an orthotropic material with the material directions aligned with the principal stresses and without shear rigidity. The optimal structure thus obtained is stable only under the loads that it was designed for; any other loading condition will cause its collapse. When there are multiple load cases, reference [12] obtains an optimal design using anisotropic materials, with the elastic properties varying along the continuum.

Recently, Sigmund [10] has demonstrated the feasibility of designing materials with prescribed elastic behavior. By using a properly formulated topology optimization model, it is possible to create materials which possess such behavior. Most of Sigmund's structures were realized by using a truss topology optimization model on a material microstructural level. As suggested by Sigmund, it is also possible to develop these materials by using a continuum topology optimization approach, similar to that used for the above examples. Essentially, the optimization problem becomes an inverse homogenization problem: given a particular elasticity tensor E_{ijkl}, determine a material microstructure that possesses such a constitutive matrix. Details of the technical approach can be found in Sigmund [10]. We present two recent examples of the application of such a technique.

Material with Poisson's ratio = 1.0

In this case, we seek to design a material which possesses equal strength in each of the principal directions, and thus possesses a poisson's ratio of approximately 1.0. Note that this material has no shear stiffness. The microstructure of this material is shown in Figure 2. Dark areas indicate areas of solid material in the unit cell, and light areas indicate areas of no material. Note also that this particular microstructure works because of the hinges that are formed in the corner areas. Thus, such a microstructure would be relatively difficult to construct. If we relax the material constraint, and design a material with a Poisson's ratio of 0.8, it is possible to create a microstructure which is physically realizable.

A lattice made of this material resembles an octagonal honeycomb structure. The structural response of this material is similar to that of a more typical honeycomb structure.

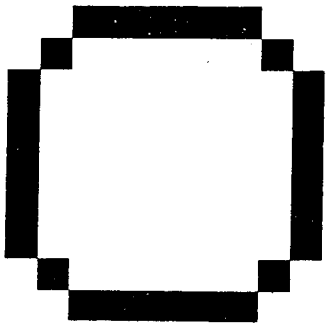

Figure 2: Isotropic Material Microstructure

Orthotropic Material

In this example, we designed an orthotropic material which possesses stiffnesses in the two principal directions in the ratio of 4 to 1. Figure 3 illustrates the microstructural layout of this material. The stiffness in the vertical direction is nearly one-quarter of the stiffness in the horizontal direction. In this case, we have designed a material which also possesses some shear stiffness, and is thus more easily physically realizable than the above example. In this figure, the different grey-scale shading can be interpreted as areas of different material density, where darker shades indicate higher material density and lighter shades indicate less dense material.

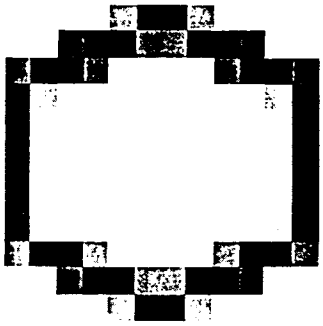

Figure 3: Orthotropic Material Microstructure

Figure 4 shows an example of a material lattice composed of these microstructural unit cells.

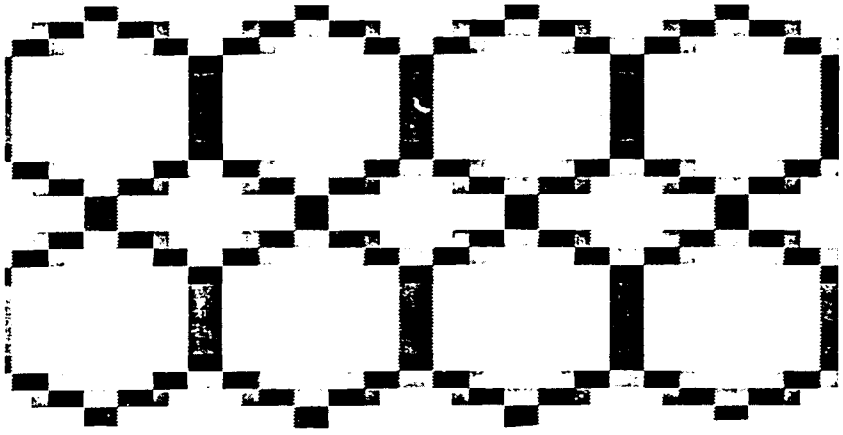

Figure 4: Lattice composed of Designed Material

It is conceptually possible to create structures using this method which possess virtually any physically realizable combination of material properties. Extension to the design of three dimensional material microstructures is underway. Integration of this technique with

advanced fabrication techniques to allow the realization of these novel microstructures is the logical next extension of this research.

CONCLUSIONS

Effective computational tools exist for the structural layout design of typical engineered structures. In addition, these tools offer the potential to design structures which take advantage of the unique possibilities inherent in freeform fabrication technology. It is possible to simultaneously perform layout design and material microstructure design using these techniques. One area of ongoing work involves the integration of the macro- and microscale design procedures. This structural layout design procedure has been extended to the design of multibody welded structures and to problems involving the layout of structures with specified dynamic response characteristics. Additional ongoing work involves extending the methodology to new classes of structures, such as performing layout optimization for structures formed from composite laminates.

ACKNOWLEDGEMENTS

Thanks to Mr. Øle Sigmund and Mr. Jun Fonseca for the development of the material microstructure design examples, and to Ms. Tenny Chang for her assistance with processing the data from the examples. This work was supported in part by NSF grant DDM-9300326, ONR grant N00014-94-1-0022, and TACOM grant DAAE07-93-C-R125. This financial support is gratefully acknowledged.

REFERENCES

1. Ma, Zheng-Dong, N. Kikuchi, and H-C Cheng, (1992) "Topology and Shape Optimization Technique for Structural Dynamic Problem", Recent Advances in Structural Mechanics, Proceedings, ASME Winter Annual Meeting, pp.133-143.

2. Bendsøe, P.M., and Kikuchi, N., (1988) "Generating Optimal Topologies in Structural Design Using a Homogenization Method", *Comp. Meth. Appl. Mech. Eng.*, 71, 197-224.

3. Bendsøe, M.P. and C.A. Mota Soares, (eds)., (1992),*Topology Design of Structures*, NATO ASI, Kluwer.

4. Botkin, M.E. and Bennet, J.A., (1985), "Shape Optimization of Three Dimensional Folded Plate Structures", *AIAA J.*, 23(11) 1804-1810.

5. Fleury, C., and Braibant, V., (1986), "Structural Optimization: A New Dual Method Using Mixed Variables", *Int. J. Num. Methods in Eng.*, 23, 409-428.

6. H. C. Cheng, (1994), The Optimal Shape/Topology Design of Structures for Dynamic Problems Using a Homogenization Method, Doctoral Dissertation, The University of Michigan.

7. Johanson, R. et. al., (1993), "Design of a Lower Control Arm in Project MAXWELL," Proceedings, 1993 Solid Freeform Fabrication Symposium, Austin, TX, pp. 123-129.

8. Johanson, R., N. Kikuchi, and P. Papalambros, (1994) "Computational Tools for Optimal Structural Layout Design," Proceedings, 2nd Annual International Body Engineering Conference, Detroit, September, 1994.

9. Rozvany, G. and M. Zhou, (1993), *Optimality Criteria Methods for Large Structural Systems*, Research Report, Universitat-Gesamthochschule-Essen, March.

10. Sigmund, Øle, (1994), "Tailoring Materials with Prescribed Elastic Properties." Technical Report, Technical University of Denmark, April.

11. Bendsøe, M. P. et. al., (1993) "An Analytical Model to Predict Optimal Material Properties in the Context of Optimal Structural Design," to appear, *J. Applied Mechanics*.

12. Bendsøe, M. P., Diaz, A., Lipton, R., Taylor, J.E. (1993), "Optimal Design of Material Properties and Material Distribution for Multiple Loading Conditions," DCAMM - report No. 469, Technical University of Denmark

Modeling of Selected SFF Process Limits

Patricio Mendez, Stuart Brown

Department of Materials Science and Engineering
Massachusetts Institute of Technology

Abstract

An analytical model of the thermal field for one scan line during SLS is developed. Quantitative relationships between net heat input and beam velocity are stated for sintering at a given distance from the center of the beam and for the case of maximum surface temperature. For the maximum surface temperature, two extreme cases have been analyzed: pure conduction heat transport, and highly convective molten consolidation. It is suggested that a highly convective process allows significantly higher net heat input than pure conduction. It is found that for certain conditions, the relationship between net heat input and beam velocity is independent of the thermal conductivity of the material. Key Words: model, melting, selective laser sintering, thermal, process window.

Introduction

For a reaching a desired sintering depth, the velocity of the laser beam over the surface of the powder layer during SLS depends on the net heat input. It is generally necessary to impose a higher heat input to increase beam velocity while maintaining the same sintering depth. The temperature reached at the surface limits the heat flux. This work focuses on these thermal aspects.

The sintering process is characterized by a sintering temperature (T_s) and sintering time (t_s). These parameters are such that for reaching a desired void fraction or smaller, the powders have to remain at a temperature of at least T_s during at least t_s, and can be estimated with an appropriate sintering model (for example ref. 1 or 2). In the case of melting powders, the sintering time can be considered small and the sintering temperature corresponds to the melting temperature, or the temperature of the peak specific heat in the case of a melting range. In both cases, sintering or melting, the temperature field after the beam passes can be approximated by a thin layer of hot material at the surface.

The mechanism governing consolidation process dictates the maximum surface temperature. For some materials and process conditions, for example polymers or wax, complete melting of the powders occurs under the beam (ref. 3). In other cases a solid phase is always present, for example polymer coated silicon carbide (ref. 2). In the latter case, the physics of the process can be studied as a heat conduction problem, neglecting the presence of some melting. When all the powder is molten, and convective currents help to homogenize the temperature within the liquid, the problem requires a detailed analysis of the effect of flow and the heat conduction with a moving boundary. In this work, the two cases are analyzed. For the melting controlled problem a limiting case is taken, where convective currents completely homogenize the temperature of the liquid, and the deepening velocity of the melting front (V_m in fig. 4) is high.

Modeling the entire SLS process is very difficult due to the many different physical processes involved. For the case of fully molten powder, surface forces change the shape of the sintered line, making it narrower and

convex. This work does not consider these effects and those due to shrinkage and distortion. The geometry of the process will be assumed to be a flat surface throughout the following analysis.

The net heat input is related to the laser power through an optical coupling coefficient (ref. 4). The thermal conductivity of the powders is estimated from that of solid material using the semi-empirical model proposed by Xue and Barlow (ref. 5). For the typical conditions in SLS, the heat transfer problem can be considered one dimensional. (ref. 7). For simplicity of the analytical solutions, the laser beam will be considered as a round uniform surface flux that moves in the direction of x in the moving coordinate frame of Fig. 1. The fact that the heat source can be better described by a gaussian distribution, or that there may be some volume heating in a semi transparent absorbent medium (ref. 4) does not affect the final calculation of the depth, since the temperature field after the beam passed can be approximated by a thin hot surface layer, independent of how the stored energy was added. The surface of the powder layer, with the exception of the zone under the beam will be considered insulated without surface heat losses due to convection or radiation.

Variables not defined within this paper follow the standard definition associated with heat transfer analysis.

Conduction Model

This model considers conduction as the only mechanism of heat transfer. It is assumed that the thermal properties of the body are constant and the heat of melting is negligible. This means that the sintering zone and the powder are considered to have the same thermal properties regardless of temperature.

The one dimensional analytical solution for a moving heat source, like that of Fig. 1, is given by eq. (1) to (4).

$$T(z,t) = \frac{q}{k} 2\sqrt{\alpha t}\,\mathrm{ierfc}\left(\frac{z}{2\sqrt{\alpha t}}\right) \qquad \text{for } t \le \tau \qquad (1)$$

$$T(z,t) = \frac{q}{k} 2\sqrt{\alpha t}\,\mathrm{ierfc}\left(\frac{z}{2\sqrt{\alpha t}}\right) - \frac{q}{k} 2\sqrt{\alpha\,(t-\tau)}\,\mathrm{ierfc}\left(\frac{z}{2\sqrt{\alpha\,(t-\tau)}}\right) \qquad \text{for } t > \tau \qquad (2)$$

$$t = \frac{\sqrt{r^2 - y^2} - x}{V} \qquad (3)$$

$$\tau = 2\frac{\sqrt{r^2 - y^2}}{V} \qquad (4)$$

The temperature profile at the sintering depth and width ($z = d, y = w$), and the isotherm for the sintering temperature at the plane of symmetry ($y = 0$) are shown in Fig. 2 and 3. It can be seen in Fig. 3 that the characteristic length for heat diffusion in the depth direction is much smaller than in the surface direction (axis x and z have different scales).

Eq. (1) gives the temperature field for points under the beam. Eq. (2) represents the diffusion of heat into the bulk of the powder, after the beam has passed. Eq. (3) and (4) connect the one dimensional model and the moving source geometry.

Those points where $T = T_s$ during a time t_s provide the shape of the sintered section in the y = constant plane. For each of these planes we have to find the roots of $T(z,t) = T_s$, and find the depth (z), for which

the difference between the roots is the sintering time t_s. Eq. (2) has no explicit expression for the roots of $T(z, t) = T_s$, so we simplify its form. The first step of this simplification is to consider the process of diffusion of heat into the bulk as diffusion of heat from a thin layer of hot material at the surface. The second step is to approximate the isotherms $T = T_s$ with ellipses.

Eq. (5) corresponds to the thin film simplification. For the representative case analyzed, this approximation is very accurate, as can be seen in Fig. 2 and 3.

$$T(z, t) = \frac{\alpha q \tau \exp\left(\frac{-z^2}{4\alpha t}\right)}{k\sqrt{\pi\alpha t}} \tag{5}$$

Here $t = -x/V$. The corresponding equation for an ellipse approximating the isotherms corresponding to a plane y = constant is:

$$\left(\frac{x+a}{a}\right)^2 + \left(\frac{z}{b}\right)^2 = 1 \tag{6}$$

This ellipse must have the same depth and the same length as the sintering isotherm. The length $2a$ is obtained from eq. (5) solving for x with $T = T_s$ and $z = 0$. This length varies with the y coordinate.

$$a = \frac{\alpha V}{2\pi}\left(\frac{q\tau}{kt_s}\right)^2 \tag{7}$$

The depth of the ellipse (b) is obtained by maximizing eq. (5) with respect to t to find T_{max}, and solving eq. (5) for z with $T = T_s$ and $t = t_{max}$.

$$b = \sqrt{\frac{2}{\pi}} e^{-1/2} \frac{\alpha q \tau}{k T_s} \tag{8}$$

The ellipse corresponding to the representative case analyzed is plotted in Fig. 3. It can be seen that the position of the maximum is shifted, but the distance corresponding to the sintering time remains approximately the same. Taking the desired sintering depth, sintering time, and scan width as d, t_s and $2w$ respectively, in eq. (6) $z = d$, $x + a = Vt_s/2$, and in eq. (4) $y = w$.

For the representative case analyzed, the term containing x in eq. (6) is small up to sintering times of 0.45 s. In the following example we consider the melting of nylon powders, therefore, sintering time is negligible and this term will not be considered. Substituting eq. (7) to (8) in (6), and using the identity $q = Q/\pi r^2$, we obtain the relationship between Q and V for a certain sintering material and geometry:

$$Q = \left(\frac{\pi}{2}\right)^{3/2} e^{1/2} \frac{\rho c T_s r d}{\sqrt{1 - \left(\frac{w}{r}\right)^2}} V \tag{9}$$

Eq. (9) gives the minimum net heat input necessary for sintering a certain depth at a certain speed.

Maximum Surface Temperature Assuming Conduction

There is also a maximum heat input, given by the maximum surface temperature that can be reached before

undesired effects occur (laser ablation (ref. 6), pyrolysis (ref. 3), boiling). For the cases in which conduction is the only heat transfer process (e.g. when there is no melting), the maximum surface temperature is obtained from eq. (1), for $z = 0$, $y = 0$ and $t = \tau$:

$$T_{max} = \frac{1}{\sqrt{\pi}} \frac{q}{k} 2\sqrt{\alpha t} \tag{10}$$

Rearranging eq. (10), we obtain the relationship between net heat input and velocity for a given maximum surface temperature $T_{max} = T_c$.

$$Q = \left(\frac{\pi}{2}\right)^{3/2} \frac{k r^{3/2} T_c}{\sqrt{\alpha}} \sqrt{V} \tag{11}$$

Melting controlled model

When there is complete melting of the powders between the surface and the sintering depth, convective currents can occur, and a pure conduction model is not appropriate. In these cases the sintering temperature corresponds to the melting point.

We analyze the limiting case in which convection current homogenize the liquid temperature (Biot << 1), and the velocity of deepening of the melting front is sufficiently high (Peclet >> 1) to consider that there is no heat lost by conduction (Fig. 4).

This model represents the heating of points under the beam and provides an estimate of maximum surface temperature. Once the beam has passed, the thermal field can be analyzed with eq. (5) as heat diffusing from a thin hot surface layer.

An energy balance for this case is:

$$q\tau = \rho\beta \left[c_{p_p} T_m + \Delta H_m + c_{p_l} (T_l - T_m) \right] + Q_{cond} \tag{12}$$

where we neglect Q_{cond} for high values of the Peclet number.

An energy balance of the heat transfer at the melting front gives:

$$\rho\beta \left(c_{p_p} T_m + \Delta H_m \right) + Q_{cond} = Q_{conv} \tag{13}$$

where

$$Q_{conv} = \int_0^\tau h_t (T_l - T_m)\, dt = h (T_l - T_m)\, \tau \tag{14}$$

Combining eq. (12) and (13), and neglecting Q_{cond}, we obtain the heat input corresponding to a given homogeneous liquid temperature (T_l).

$$Q = \pi r^2 h (T_l - T_m) \frac{c_p T_l + \Delta H_m}{c_p T_m + \Delta H_m} \tag{15}$$

In eq. (15) the heat capacity of liquid (c_{p_l}) and the solid (c_{p_s}) are assumed to be the same.

The Peclet and Biot numbers are estimated using the depth reached at the end of the beam β as the characteristic length, where $\beta = q\tau/\rho\,(c_p T_l + \Delta H_m)$.

Representative Case

The representative case considered is the SLS of Laserite nylon with a velocity of 12.7 mm/s, a sintering depth of 0.317 mm, and a scan spacing of 0.5 mm.

The value of the parameters used are presented in Table 1.

Table 1: Parameters for the Representative Case

Process	Solid Material	Powder
V = 12.7E-3 m/s	T_m =188.7 °C	ε = 0.4
r = 1.5E-3 m	T_c = 1000 °C	ρ = 624 kg/m^3
d = 0.317E-3 m	$T_s = T_m$	k = 0.1 W/m-K
w = 0.25E-3 m	c_p = 1968 J/kg-K	α = 8.14E-8 m^2/s
T_{amb} = 25 °C	ΔH_m = 55688 J/kg	
	ρ_s = 1040 kg/m^3	
	k_s = 0.23 W/m-K	

From eq. (11) we obtain the necessary heat input for sintering: Q = 4 W. Eq. (10) gives the maximum surface temperature T_{max} = 910.6 °C, The dimensions of the ellipse corresponding to the sintering width are $a \approx 11$ mm and $b \approx 0.3$ mm.

The hypothesis of one dimensional heat transfer is valid for all depths (within a 5% error) when $V^2\tau/4\alpha > 4.4$ (ref. 7). For the representative case, this is equivalent to $|y/r| < 0.9993$, i.e., almost all points under the beam approximate 1D heat transfer.

An energy balance indicates that the heat losses by convection and radiation are negligible. During the time it takes to reach the maximum depth at the plane of symmetry (t_{max}), the energy input is $q\tau$ = 134 kJ/m^2. After the beam has passed, the losses by convection account for 0.7%, by radiation 2%; the heat flux by conduction through the sintering isotherm accounts for 32%, and the energy stored between the surface and the sintering isotherm is 68%. In this analysis the heat of melting was neglected; included, it accounts for 12% of the energy stored. An approximate consideration of the heat of melting can be made by increasing the specific heat of the powder by 12%. During the time the beam is over a point, the radiation losses are 7% of the net energy input. This amount must be considered in the overall efficiency of the laser beam.

From eq. (8) it can be inferred that the maximum temperature decreases with increasing depth. A medium is considered semi-infinite when it is deeper than the penetration corresponding to a small temperature increase. For $T = 0.05 \times T_s$, we obtain a depth of $20b$ for the plane of symmetry. In this example, the minimum depth is 6.4 mm (approx. 20 layers).

For the melting controlled model we use representative values for the convection coefficient and for the thermal conductivity of the liquid corrected for convective flow. A typical value for the convection coeffi-

cient in liquids is $h = 1000$ W/m^2-K. A more accurate estimation of h requires a detailed study of the convective flow and liquid properties. The thermal conductivity of the liquid will be estimated as ten times the conductivity of the solid material ($k_l = 2.3$ W/m-K). From eq. (15), for a net heat input $Q = 4$ W, the corresponding liquid temperature is $T_l = 436$ °C. This temperature rise is approximately half of that for the pure conduction model. For a maximum temperature of 1000 °C, the maximum net heat input is 30 W.

The values of β and Pe are 0.25 mm, and 3.2 respectively. The Peclet number is greater than 10 for velocities lower than 4 mm/s. The value of Bi is 0.1, indicating that heat conduction and convective currents act to homogenize the liquid temperature.

Discussion and Conclusions

The analysis described in this article is meant both to provide some physical insight into the SLS process and to guide directions for further analyses including thermal and mechanical effects. Note that many process parameters, such as energy flux, scan rate, and beam radius, enter into the presented relations linearly. In some cases this linearity results from our simplifications in analysis. The actual process obviously contains more nonlinearities and complexities than we represent here. However, we believe that these relatively simple relations represent the first order physics of the process and therefore provide functional guidance on the effect of different process variables.

The relations we derive can also be used to estimate scan rate and heat flux windows for feasible SLS processing. Fig. 5 presents one such process window for Laserite nylon. Note that the thin film solution of heat transfer into the bulk after the beam has passed a given point is common to both the conduction and melting controlled models. The models differ, however, in calculating the temperature field immediately under the beam. The three curves in the figure illustrate the thin film solution and consequences of this difference in temperature field. The lower straight line represents the thin film solution and is a boundary of the process window. The intersecting curve represents the other boundary from the conduction model which is formed by assuming a limiting maximum surface temperature. Together the two boundaries define a process window assuming conduction control of the process. Combining eq. (9) and (11), we obtain the theoretical maximum velocity and heat input that allow sintering to the desired depth and width, without reaching the critical surface temperature.

$$V_{max} = e^{-1}\alpha r\left(\frac{T_c}{T_{sd}}\right)^2\left(1-\left(\frac{w}{r}\right)^2\right) \tag{16}$$

Using the parameters of the representative case, eq. (16) gives $V_{max} = 15$ mm/s. Values of scan rate and incident energy (assuming an optical coupling of 50 percent) taken from a video study provided by the SLS research group at the University of Texas as Austin (ref. 3) are plotted as points in the figure. The video image corresponding to the left point pictured the formation of vapor bubbles. We used the process parameters corresponding to the right point as our representative case for analysis.

The upper line in the figure represents the process boundary assuming melting control, where the molten material is isothermal. It can be seen that the working window in this case is potentially larger, due to a more homogeneous distribution of the thermal energy under the beam. In this case, the molten zone is able to store more energy before reaching the critical temperature. Confirmation of this effect would require a more accurate estimation of the parameters for the convection in the liquid. In the example typical values have been used.

In a sintering process without melting, the model pure conduction model applies. However, when there is melting involved, the process may not be melt controlled. A detailed study of the flow currents is necessary, and depending on its characteristics, the ruling mechanism is melting, pure conduction (for the case in which there are almost no currents), or mixed.

In this model the value of the thermal properties of the body are considered constant, therefore the Fourier equation of heat conduction is linear and it is possible to superimpose solutions. Due to the simplicity of the model, this can be accomplished efficiently and with a moderate computer overhead making it possible to consider the effect of different passes over the same point to calculate a total temperature history. A study addressing the effect of multiple passes could explain the effect of the beam radius on the sintering depth. For the case of multiple passes, increasing the beam diameter increases the depth of sintering (ref. 8). For the case of a single pass, eq. (9) indicates the opposite effect.

Acknowledgments

This work was funded primarily by the Office of Naval Research (grant number N00014-94-1-0181). We would like to acknowledge substantial assistance provided by the research effort in SLS at the University of Texas at Austin, and also the important suggestions and comments of the other students in Professor Brown's research group, G. Trapaga and V. Meli.

References

1. Sun, M., Nelson, J. C., Beaman, J., Barlow, J. 1991 (August). *A Model for Partial Viscous Sintering*. Solid Freeform Fabrication Symposium, Proceedings. University of Texas at Austin, pp. 46-55.

2. Nelson, J. C., Vail, N. K., Barlow, J. W. 1993 (August). *Laser Sintering Model for Composite Materials*. Solid Freeform Fabrication Symposium, Proceedings. University of Texas at Austin, pp. 360-369.

3. Das, S., Pogor, B. *Video Microscopy Experiments on SLS of Polycarbonate, Wax and Nylon*. Unpublished, The University of Texas at Austin, April 25, 1994.

4. Sun, M., Beaman, J. 1991 (August). *A Three Dimensional Model for Selective Laser Sintering*. Solid Freeform Fabrication Symposium, Proceedings. University of Texas at Austin, pp. 102-109.

5. Xue, S., Barlow, J. 1991 (August). *Models for The Prediction of the Thermal Conductivities of Powders*. Solid Freeform Fabrication Symposium, Proceedings. University of Texas at Austin, pp. 62-69.

6. Deng, X., Zong, G., Beaman, J. J. 1992 (August). *Parametric Analysis for Selective Laser Sintering of a Sample Polymer System*. Solid Freeform Fabrication Symposium, Proceedings. University of Texas at Austin, pp 102-109.

7. Festa, R., Manca, O., Naso, V. *A Comparison Between Models of Thermal Fields in Laser and Electron Beam Surface Processing*. Int. J. Heat Mass Transfer. Vol. 31, No. 1, pp. 99-106, 1988.

8. Nelson, J. C. *Selective Laser Sintering: A Definition of the Process and an Empirical Sintering Model*, Ph.D. dissertation, The University of Texas at Austin, 1993.

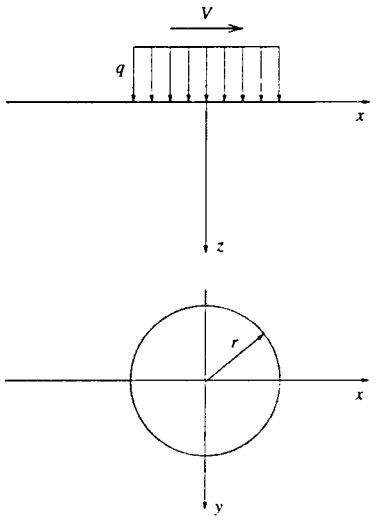

Figure 1

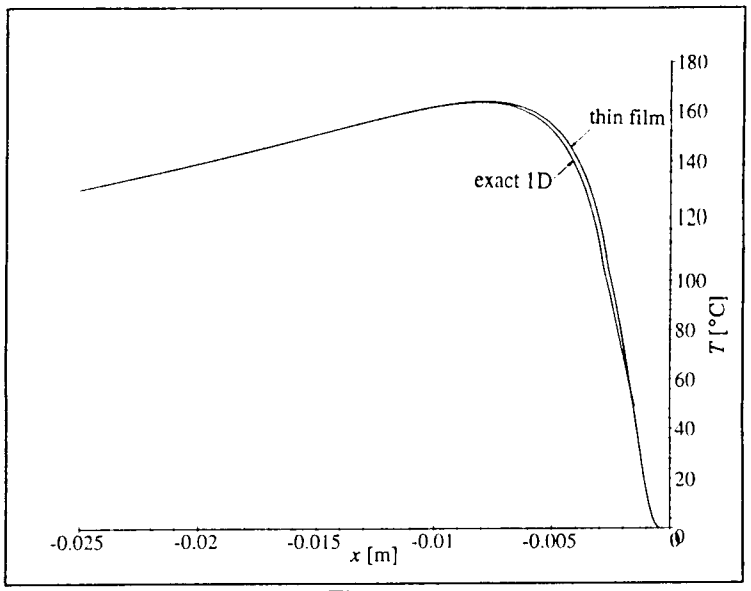

Figure 2

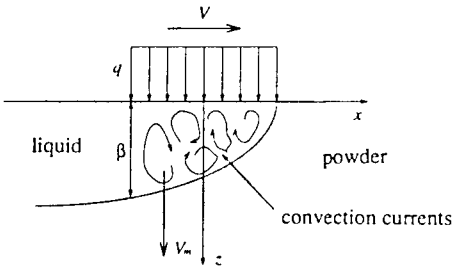

Figure 4

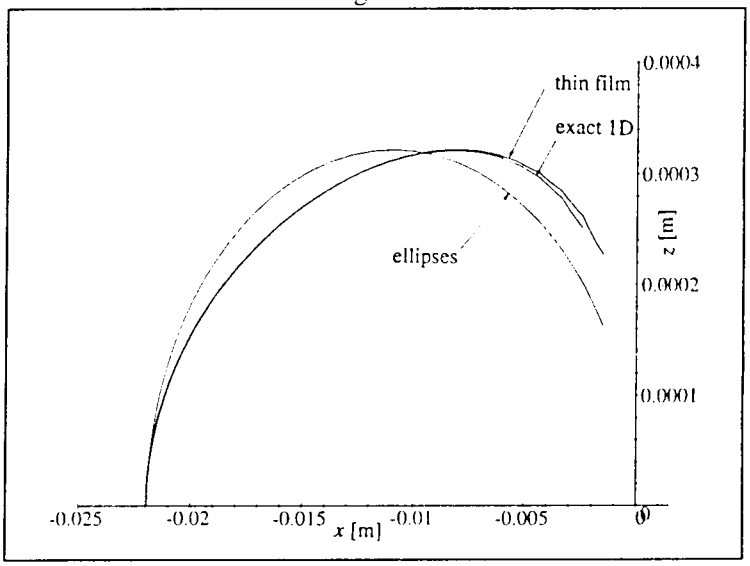

Figure 3

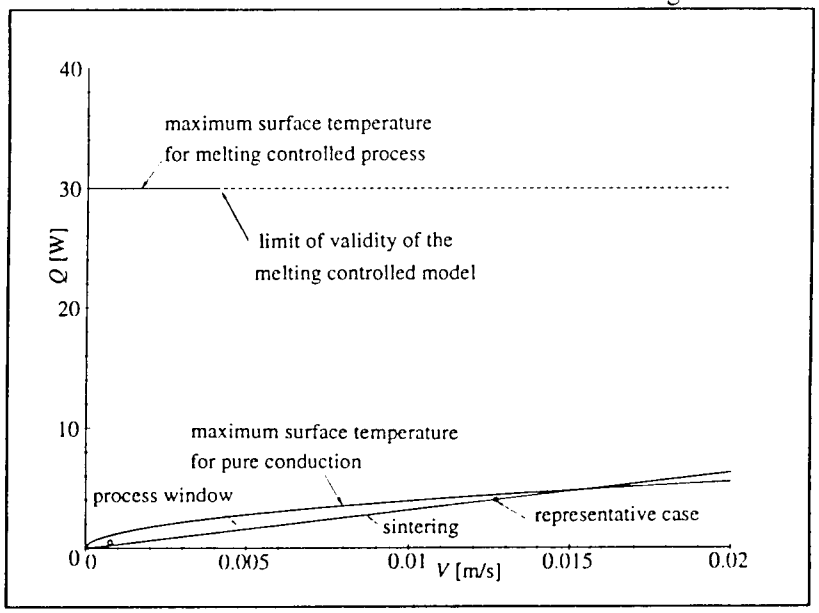

Figure 5

APPLICATIONS OF
3D LASER DIGITIZING AND SURFACING TECHNOLOGIES

Many companies have manufacturing requirements to copy or "reverse engineer" an already existing part for which there is no existing CAD model, print, pattern, or mold. In the past this process has been very tedious requiring weeks and sometimes months to complete. The engineer has to create a CAD model by measuring the physical part with calipers and/or a CMM and then create features and surfaces in CAD. If a 2D print is available, this data must be converted to define the CAD model features. This process is very prone to error and several iterations must be executed before an acceptable completed part is produced.

There is now an available process to support "reverse engineering" applications which greatly reduces the time to complete these projects, provides a complete and accurate CAD model on the first iteration, allows for the programming of tool paths, and is completely compatible with the company's current CAD/CAM procedures. This process includes the integration of the automated 4-axis 3D laser digitizing from Digibotics, Inc. with a complete software environment for point processing, surface generation, and analysis from Imageware. A case study using these technologies was recently completed by Fred Nicholas, CAD/CAM Manager, of InterMotive Technologies, a design and engineering company located in Belleville, MI. This paper describes the entire flow through the digitizing, surfacing, and CAD/CAM processes.

For this case study, Mr. Nicholas selected an automotive thermostat housing which is a part with some complex outer surfaces and an internal cavity. A core stick of the internal cavity was created. The Digibot II 3D laser digitizer from Digibotics, Inc. was used to digitize both the external part and the internal core stick. After editing the 3D digitized data, a point file was imported into the Surfacer software system from Imageware. Surfacer was used to create a network of B-spline curves and surfaces. An IGES NURBS surface file was created and then imported into several CAD/CAM systems to demonstrate the ability to create a surface and tools paths for making the part. For this case study, the Computervision CADDS5 software was used to demonstrate the complete CAD/CAM process.

The Digibotics 3D laser digitizing technology was used for this project because it offers several unique advantages for "reverse engineering" of complex parts. The Digibot II is an automated 4-axis digitizer that provides a simple, accurate, and quick way to copy or inspect complex sculpted surfaces. After fixturing an object, the user specifies a point density and instructs the system to begin. While digitizing, the object

rotates on the platter and the laser translates horizontally and vertically. Vertically spaced cross-sections are digitized starting from the bottom and moving upward. The Digibot Adaptive Scanning Software intelligently follows the contours of the surface acquiring a sequence of adaptively spaced points while keeping the laser beam normal to the surface. Concave surfaces and multiple contours are obtained by pivoting the laser about obstructing surfaces. After digitizing, the object is composed of a stack of cross-sectional contours. The entire object along with individual points and contours can be examined and modified as needed using the Digibot Data Editor. A surface mesh composed of triangular facets is generated by connecting points and contours between cross-sections. The resulting polyline and/or surface mesh can be exported via data formats such as DXF, STL, VDA, or IGES.

The Surfacer software system provides the link between the 3D laser digitized data and the conventional CAD/CAM system. Surfacer accepts point data directly from the Digibot Editor and performs point data analysis and processing such as segmentation, sectioning, filtering, and feature extraction. The NURBS surfaces are then quickly and accurately created from the selected point sections. The quality of the created surfaces are verified by points to surface comparison, reflectance analysis, curvature analysis, and cross-sectional tools. These surfaces can then be edited and/or modified. Point, curve and/or surface geometry can then be exported directly to "downstream" processes such as CAD, CAM, Analysis or Visualization/Animation systems.

The first step of the process was to digitize the thermostat housing using the Digibot II 3D laser digitizer. The housing was attached to the platter of the Digibot II by simply using hot glue. The Digibot II then digitized the entire housing by using Digibotics' patented adaptive scanning procedure. Both the external housing and the internal core stick were digitized. In a post-processing phase, Mr. Nicholas viewed the 120 cross-sections and performed minor editing to guarantee a good clean file of 3D data points. The digitizing and editing process for this housing was completed in 1 1/2 days. Mr. Nicholas also used the Digibotics Triangulator and STL Generation software to create an STL file of the housing. The Accelerated Technologies Inc. DTM rapid prototyping system was used to create a polycarbonate copy of the housing. This is very useful as an intermediate step to demonstrate that the digitizing process was very complete and accurate.

The two files of 3D data points (containing about 20,000 points) were then imported directly into Surfacer for creation of the surfaces. The two data files were first combined to form one complete external and internal object by registering the two

parts to a common axis through the centroid of the part. Surfacer provides a complete set of tools for aligning multiple scans or aligning scan data to CAD data. A "push-button" surface of the entire housing was then created. This one large complex NURBS surface is very useful for visualization, for gross product testing, and for interference checking with other CAD components. Because the Digibot digitized data is created in orderly well-spaced cross sections with no redundant or over-lapping data, this makes it much easier for Surfacer to create surfaces and perform its analysis functions. After the point analysis and registration, individual accurate surfaces were created. This occurs by generating surface patches over different point sections to define unique surfaces. Surfacer provides tools for detecting surface edges and segmenting points to define areas to be surfaced. Surface patches can then be fit to the points, with the user having control over the NURBS smoothness and fitting tolerances. For the housing, 21 different surface patches were created. These patches are stitched to create continuous, "watertight" connections, and different analysis was performed to confirm the accuracy of the surfaces. The 21 surface patches were then converted to an IGES 5.0 NURBS surface file for export into the CAD/CAM systems. This processing time in Surfacer took about two working days.

Mr. Nicholas then imported the IGES file into CADDS5 for processing. The file was also imported into ProEngineer and AutoCAD to demonstrate the IGES compatibility with other CAD systems. In CADDS5, a complete solid model was created by sewing the 21 individual surfaces. With this solid model, physical property analysis can then be performed such as volume and mass calculations. An STL file was created from this solid model, and a prototype was created using the 3D Systems rapid prototyping system. A tool path was created using Computervision's CVNC software. The internal cavity was first isolated from the external part for tool path generation. Then a tool path was generated on the external surface. Finally, a product drawing was generated for documentation of this part. The detailing environment included all radii, dimensions, cutting sections, tolerances, and information for placing the housing in its engine position. The procedures implemented in CADDS5 are very straight forward and utilizes the normal CAD/CAM functions that would be used for any solid model design. The procedures for CADDS5 were executed in two working days.

The processes that are demonstrated in this case study were not available one year ago. There has been tremendous progress during this time in the integration of the digitizing hardware/software and surfacing software for supporting these complex projects. This case study was implemented in about one week, and is at least a four week improvement over uses of other approaches. The Digibotics and Imageware

week improvement over uses of other approaches. The Digibotics and Imageware systems are the only hardware/software combinations that provide automated digitizing and surfacing of complete complex objects. This capability to recreate 3D objects with this process is available now for applications such as creating spare parts, recreating parts where no prints or CAD model exist, and creating a CAD model from a physical model done in clay, foam, or other fragile material.

New Developments in Processing and Control of Selected Area Laser Deposition of Carbon

W. Richards Thissell and H. L. Marcus

Center for Materials Science and Engineering
The University of Texas at Austin
Austin TX 78712

Selected area laser deposition (SALD) has been used to deposit carbon from methane, hydrogen, oxygen, and argon mixtures using a third generation deposition system. The effect of two laser scanning hardware/software designs on the development of morphological instability in the resulting deposit is compared. One method uses programmed I/O using the main process control CPU to calculate and download beam position and desired laser power. Another method is presented which uses dedicated direct memory access (DMA) controllers and a dedicated counter/timer to download the required information. Its improvements to the process include better coordination between laser power and beam speed resulting in an improved beam power delivery uniformity and an improved ability to utilize one CPU for control of more of the SALD process variables.

1. INTRODUCTION

A process being developed at The University of Texas at Austin is solid freeform fabrication (SFF)[1,2] using selected area laser deposition (SALD).[3,4,5] The overall goal of this project is to make arbitrary three dimensional parts from solids deposited out of the vapor phase without human intervention or part specific tooling. The geometry and desired material are defined by a solid modeling computer file. SALD is a mechanism developed here at the University to accomplish this. SALD is accomplished by directing a laser beam normal to a surface and to move this beam relative to the surface. The surface is locally heated where the laser beam impinges upon it. Chemical vapor deposition (CVD) or laser ablation can occur when the surface is at certain temperatures. The physics of the process are extremely complicated. For example, SALD involves the formation of three-dimensional hemispherical boundary layers around the moving deposition regime[6,7] and the substrate heating is a transient, moving boundary value problem.[8,9,10,11,12] Intense photon flux and thermal energy at the substrate surface is known to create plasmas under certain conditions via either a multiphoton induced ionization mechanism or by direct interaction by electrons with the strong electromagnetic fields that exist in focused laser beams via inverse bremsstrahlung, leading to a cascade mechanism.[13]

SALD can be used to achieve very high rates of deposition, when measured in units of length/time. This can be partially explained by the formation of a three-dimensional boundary layer, while a one-dimensional boundary layer exists for large area CVD processes. This three dimensional boundary layer results in much larger fluxes of reactants to the deposition surface and products away from the deposition surface. Carbon rod growth rates of up to 1 mm/s have been measured from 99.6% pure acetylene.[4] SALD deposition rates of this order are desirable for making SFF of structural parts a viable process. However, high deposition rates from SALD may not be required for commercial success using SALD for SFF because SALD can be used to make materials for which there is no current manufacturing process. For example, SALD has the potential to be employed to make arbitrary three dimensional parts out of diamond and diamondlike carbon (henceforth, both diamond and diamondlike carbon will be called sp^3 bonded

carbon). This would allow virtually unlimited applications to employ sp^3 bonded carbon's unexcelled hardness, isotropic modulus, chemical inertness, thermal conductivity, and tribological properties.

This paper documents the current state of the process machine. Preliminary deposition studies are then described. The development of morphological instability as the result of inadequate coordination between laser power control and beam scan velocity is illustrated. An improved controller computer interface and software design results in a great improvement in deposit uniformity and morphological stability.

2. SALD Machine Description

The design of the SALD machine described herein has been described previously in the literature.[14] The process machine is a third generation SALD machine and is the first attempt at computer integration of most of the significant process variables. The design goal of the process machine is to bring the significant process parameters under sufficient control such that SALD may be developed into a viable process for depositing arbitrary three dimensional parts directly from the gas phase from solid model data. Concurrent engineering principles have been utilized in developing the process machine and the process. A schematic overview of the major machine elements is shown in figure 1. A brief description of the laser scanning sub-system follows.

The process laser is a Synrad Duolase 50 and is a 50 W circularly polarized CO_2 laser. A visible HeNe laser (5 mW, 632 nm) is combined with the process beam immediately at its exit to facilitate optical alignment. The combined beams are then immediately expanded by a ten times Galilean beam expander and are then focused about 0.5 m from the exit aperture of the laser by a plano-convex lens of 0.5 m focal length. The beam profile at the focal lens has a profile approximately halfway between the rectangular profile of the beam at the exit aperture of the laser and a fully developed Gaussian profile. The beam is then steered into the process chamber by the galvanometers. Its profile is substantially Gaussian at the beam waist and has a $1/e^2$ diameter of about 250 μm, yielding a composite optical system $M^2 = 1.10$, meaning that the real beam waist is about ten percent larger than the theoretically minimum beam waist.

The laser power is controlled in real time by a combination of a direct memory access (DMA) controlled 12 bit D/A converter and a custom designed electronic circuit that translates the computer controlled analog signal into a 20 kHz pulse width modulated laser control signal. This configuration allows for precise (within the specified ±5 percent output power fluctuation intrinsic to the laser) laser power control that can be coordinated in real time with the galvanometer based scanning setup.

The laser scanning is accomplished with Cambridge Technologies, Inc. 6650 galvanometers and a dedicated analog PID controller from the same manufacturer. The advantage of this scanning system compared to strictly vector based scanning systems is that this system can scan arbitrary curves in the process plane without approximating the curve by a series of vectors where the beam is started and stopped at the corresponding vector line endpoints.[15] Starting and stopping the laser beam movement over the process surface results in uneven power delivery that is difficult to control. Precise beam steering on the process plane at constant velocity is achieved by changing the setpoint in angular position sent to the controller in real time. The desired process plane beam position is readily converted to a mirror angular position exactly by a simple trigonometric expression without the need of a complex calibration procedure or look-up table corrections. The most difficult aspect of the scanning control is calculating and

downloading these points to the controller in real time and coordinating this procedure with real time laser power control.

A first attempt involved a simple digital I/O board that utilized an Intel 8255 controller that is the heart of the floppy drive interface used in industry standard computers. This controller required a programmed I/O under the mode required to interface with the analog PID controller. Both repeatable and random deposition irregularities during the process experimentation indicated that this method was too casual with respect to time for the needs of the SALD process. It also had severe implications on the development of integrated control of other process variables. The scanning algorithm caused a software timer to expire every 250 μs that would result in the main program's event loop to execute a function that calculates and downloads new positions based on

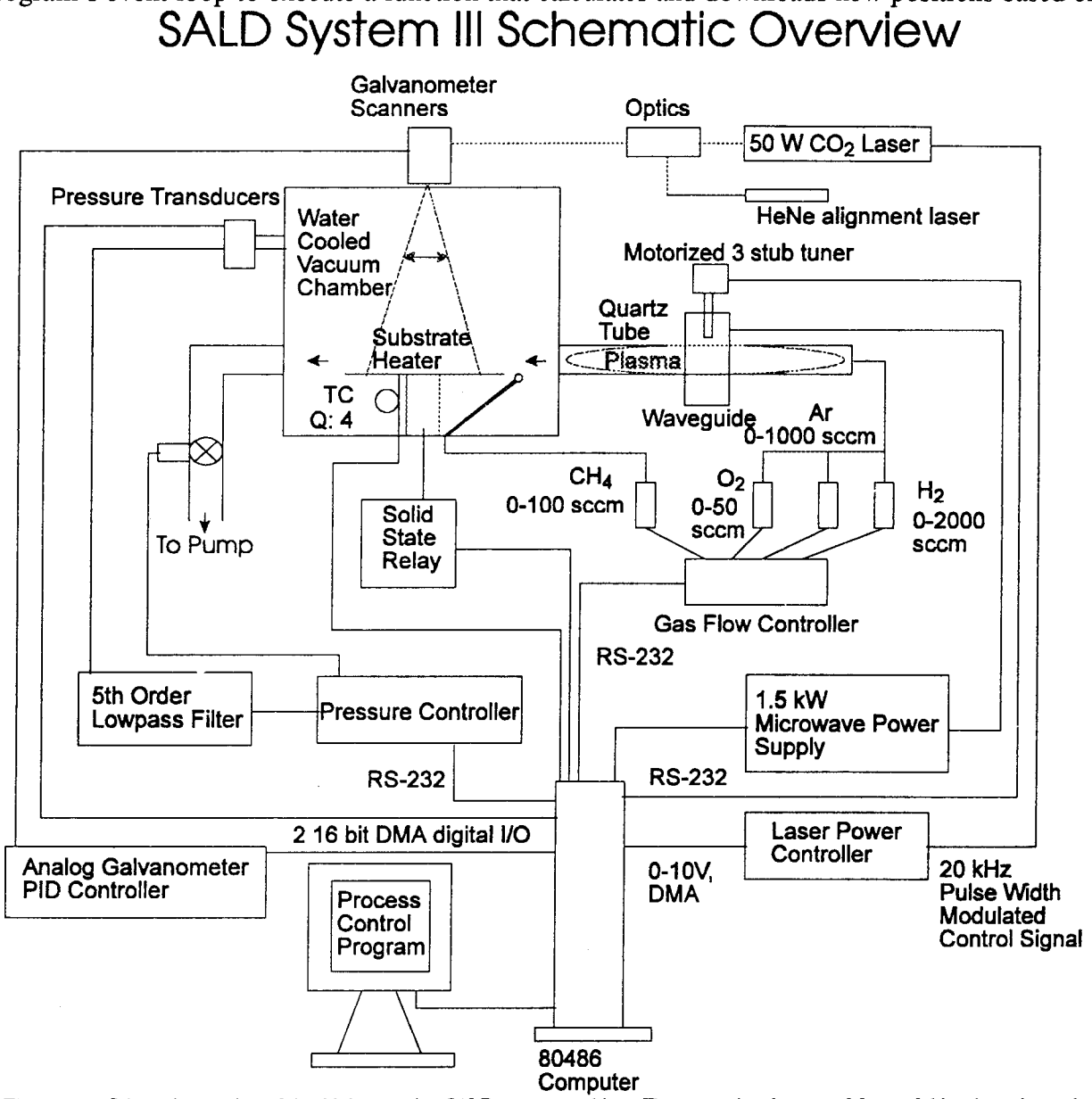

Figure 1: Schematic overview of the third generation SALD process machine. The two major elements of focus of this schematic are the process vacuum chamber and the computer. Control lines fan to and from the computer to various dedicated process controllers, electronic circuits, and modules. Likewise, gases, microwave, laser, and electric heater power flow to the reactor, and sensor information flows from the reactor.

the current time. The stringent real time requirements of the laser beam scanning control precluded other process control modules or GUI operator requests from being executed whilst the beam was on and being scanned. Furthermore, periodic interrupts occur in the process program that can take up to one to two milliseconds to execute which effectively causes the galvanometer mirrors to slow down or stop when these interrupts occur during beam scanning. A practical consequence of the presence of the interrupts is that the DMA laser power array cannot be synchronized with the true end of the scan curve, preventing the utilization of a power ramp down at the end of the scan line. The origins of these interrupts are intrinsic to DOS and the memory managers required to execute the 16 bit protected mode process control program running on an industry standard architecture 33 Mhz Intel 804086 computer with 256 kB of 15 ns cache and 16 MB of 60 ns DRAM. The original programmed I/O configuration turned off the laser when the analog PID control sent a settling signal indicating that the mirrors are within 0.05 degrees mechanical ($\sim 5 \times 10^{-4}$ m on the scan plane) of the setpoint.

A solution to this power delivery problem was engineered by changing the computer interface board to a 32 bit digital I/O board that utilizes two 16 bit DMA channels and a dedicated timer/counter to coordinate data transfers to the analog PID controller. The beam position data transfers are synchronized with the laser power data transfers. The circuitry of the analog controller also had to be modified so that it would accept the data transfer protocol used by the new I/O board. The analog PID controller was further modified so that the settling signal is sent when the mirrors are within 0.0025 degrees mechanical ($\sim 2.5 \times 10^{-5}$ m). The main process control CPU is removed from the stringent real time requirements in the new method, greatly facilitating improved overall process control and user response. The CPU calculates arrays of data for each scan line or arbitrary curve for each mirror axis and the laser power, and three 16 bit DMA channels and a counter/timer handle the transfer of these arrays from system memory across the I/O bus to the process control boards.

Although the new scanning computer interface and software design resulted in much improved laser power delivery uniformity, it is not optimized with our present computer capability. Optimizing the DMA laser scanning software will involve building a 32 bit protected mode program that will decrease the magnitude of the array calculation imposed delays by a factor of two and switching the CPU to a readily available 90 or 100 Mhz Pentium™ processor will approximately decrease the calculation imposed delay by another factor of ten or more. Another optimization will involve changing from the current single DMA buffer for each channel to a dual buffer configuration.

The integration of the SALD machine with solid model data files is a major ongoing goal of the SALD development process. The current state of this development takes industry standard ".STL" files and slices and dices them with two command line filters developed here at the University in a cooperative effort by several researchers. The versions of these programs used for the SALD process development are 32 bit protected mode, virtual memory versions running on top of DOS, Windows, or OS/2. The data file that the second of the filters emits contains laser scan data that can include contours and x and/or y axis laser scan lines for each of the solid model slices. The current contour description implementation is a series of straight line segments due to the intrinsic nature of faceted ".STL" files. The data coordinates represent coordinates on a scan plane as unsigned integers. The process control program takes these data files as input and exactly translates these coordinates to corresponding mirror angular positions. The process

control program is currently implemented as a 16 bit protected mode program using virtual memory and a graphical user interface running under DOS.

3. Deposition Experiments

Silicon wafers were used as substrate materials. Silicon has near zero transmittance at 10.6 μm radiation at temperatures above 400 °C and a normal spectral reflectance of about 0.2-0.25 when doped with impurities less than $2x10^{19}$ cm^{-3} which rises to about 0.7 when doped with impurities of about $7x10^{19}$ cm^{-3}.[16] Graphite has a normal spectral reflectance of about 0.61 at 25 °C and at 10.6 μm radiation and an estimated normal spectral transmittance of about 0.9 under the same conditions, based on trends indicated by data taken at 8 to 9 μm.[17]

Figure 2 shows a cross section of the scanned data file which represents a gear. The laser scanned pattern first traces the contour of the gear and then performs both a x and a y axis vector fill all at a given laser power and scan speed with a beam spacing of $1.0x10^{-4}$ m for each layer. A series of gears were scanned over the wafer, usually under different combinations of scan velocity and laser power holding other parameters constant. A typical grouping of spacings used is shown in figure 3.

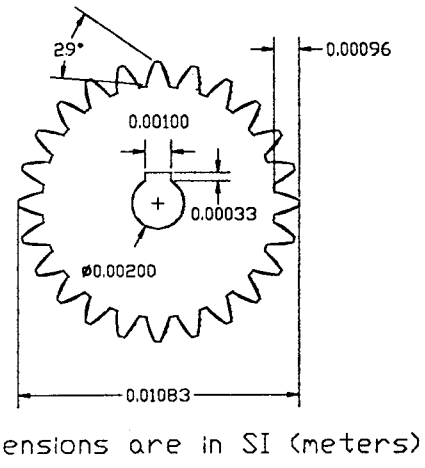

Figure 2: Cross section of a solid model of a the gear used in the heated Si wafer SALD experiments.

Morphological instability refers to increasing topological roughness as growth rates and deposit thickness increase.[18,19,20,21] Several tests were also made to determine the magnitude of the development of morphological instability as the number of scan layers is increased. These tests were initially performed using the initial programmed I/O laser scanning arrangement and demonstrated its inadequacy at controlling morphological instability. The silicon wafer experiments were performed with a substrate bias temperature ranging from 400-800 °C and differing methane and hydrogen flow rates that result in a mole fraction of methane ranging from 1.5 to 14 percent methane in hydrogen, pressures ranging from 66 Pa to 50 kPa (0.5-375 Torr), and several different laser powers, P_l, and scan speeds, v_l, that covered about two orders of magnitude of laser fluence, F_l. The laser power up ramp time is τ_s and the laser power down ramp time is τ_e where negative values indicate a laser power ramp completes when the end of the scan curve is reached and positive values mean the ramp down begins after the the end of the scan curve is reached.

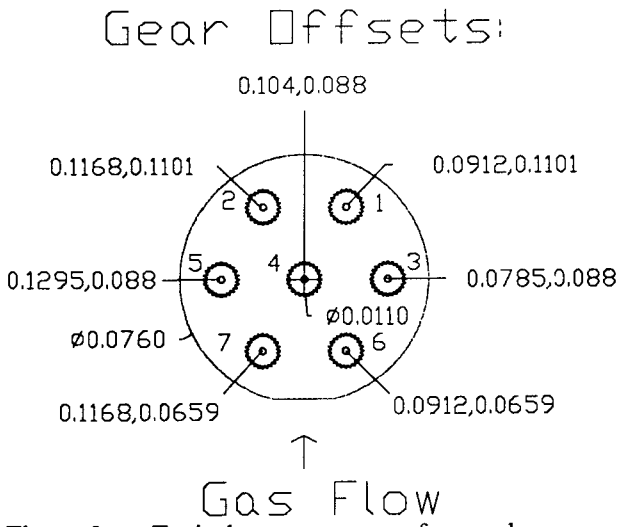

Figure 3: Typical arrangement of gear laser scan patterns on silicon substrate. The listed coordinates are offsets entered into the process control program and are in meters.

Figure 4 is an SEM is an outer surface of a cylindrical deposit that was used prior to the development of the gear model. It illustrates the random and systematic variations in deposition rate that are attributed to the programmed I/O laser scanning configuration.

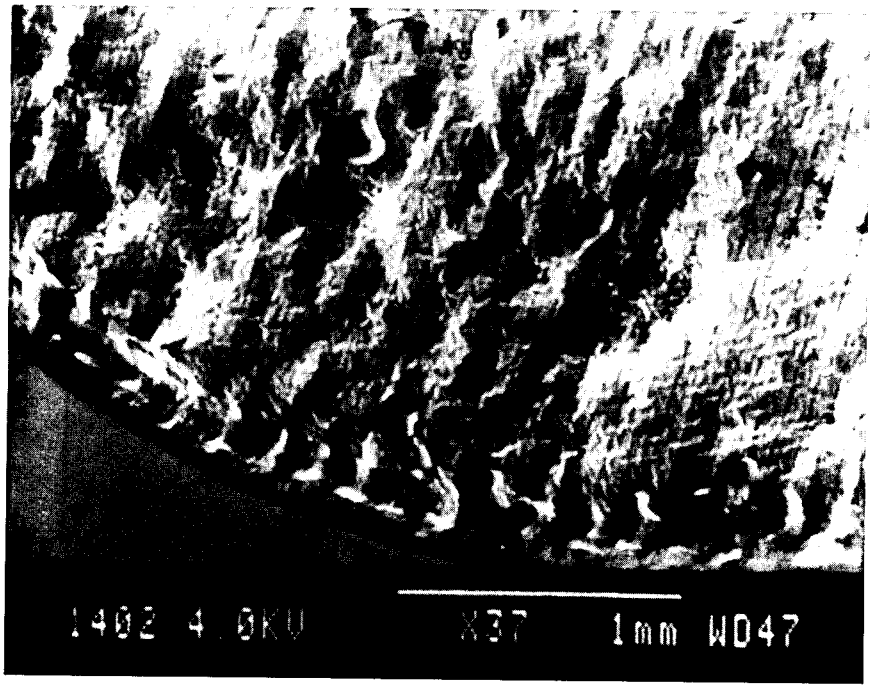

Figure 4: SEM of a laser scanned cylinder, illustrating the random and systematic variation in deposition height resulting from the initial programmed I/O laser scanning configuration. T_s = 700 °C, 14 sccm CH_4, 100 sccm H_2, 50 kPa (375 Torr), v_l= 0.01 m/s, 25 layers, P_l = 40 W (F_l = 2.2x10^7 Ws /m^2), τ_s = 200 μs, τ_s = 0 μs.

Figure 5 is an SEM of a typical SALD gear and shows the variation of deposit thickness that is characteristic of the laser scan pattern. Note the bumps on the beginning and end of each scan line. Figure shows a center of a SALD gear where a nearly vertical contour deposit edge occurs with cone shaped deposits. The vertical wall is about 100 μm high. This systematic deposition irregularity, combined with random deposition irregularities which partially result from the effect of computer interrupts, accumulate as the number of scan layers increases and can result in a process instability.

A dramatic climax to the development of this instability occured during of the morphological instability study. Six gears were scanned with increasing number of scan layers from 25 to 300 under otherwise identical conditions. Five of the gears with 25-150 scan layers appear substantially similar, but the deposition rate of the sixth gear started to take off after about 190 layers, preferentially on the scan line end points and on rod like deposits randomly dispersed over the gear surface. Homogeneous gas phase nucleation took over and a sooty deposit formed The rod like deposits that surrounded the contours of the gear grew to a height of about 1 cm in about 1-2 hours. The laser coupling into deposit the improved sufficiently to result in the melting through of the wafer.

The DMA laser scanning configuration eliminated both the systematic and random variation of deposit thickness across the scanned gear. No morphological indication of the scan

pattern could be observed by SEM, as is shown in figure 6 in the deposited region of the gear. An example of the smoothness of the ends of the scan curve is shown in figure 7. This SEM also shows some webbing between scan lines that occurs due to the power decay associated with the time constant of the laser (τ_l = 150 μs). The lasing decay results in deposition as the beam is steered from the end of one scan line to the beginning of the next. The laser power during this rapid beam steerage is a function of its power during the curve scan, the absolute magnitude of τ_e, and the dwell time provided after each scan line before moving the beam to the beginning of the next. This webbing occurred in both the programmed I/O and DMA laser scanning configurations. The decrease in the beam settling window size made as part of the analog PID controller modifications for implementation of the DMA method facilitated a variable dwell time at each contour end point. The magnitude of this dwell time was increased until the webbing disappeared. Figure 8, to be compared with figure 7, shows a couple of gear teeth where the webbing is almost completely eliminated.

Additional SALD process efficiency will occur when the laser spends a higher fraction of real time lasing. The new DMA scanning method currently calculates the scan and laser power arrays between every scan curve when the laser is not lasing. This time may be significantly decreased by increasing the speed of the processor and changing from 16 bit to 32 bit protected mode operation. Process efficiency may also be improved using a double buffer configuration where one set of arrays are calculated while another set is used to perform a scan. The laser dwell time spent at a laser scan curve endpoint before moving to the beginning of the next curve also

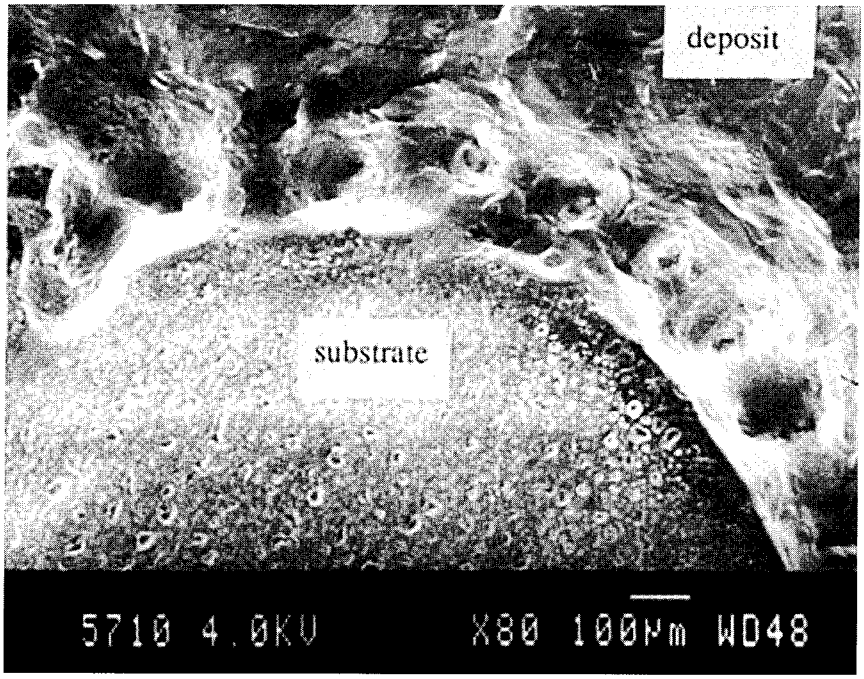

Figure 5: SEM of a laser scanned gear at the gear hole, illustrating the systematic variation in deposition height that results from the initial programmed I/O laser scanning configuration. The deposit rods are nearly vertical and extend about 100 μm above the substrate. T_s = 800 °C, 42 sccm CH_4, 300 sccm H_2, 10 kPa (75 Torr), v_f= 0.025 m/s, 63 layers, P_l = 40 W (F_l = 1.2x10^7 Ws /m^2), τ_s = 200 μs, τ_e = 0 μs.

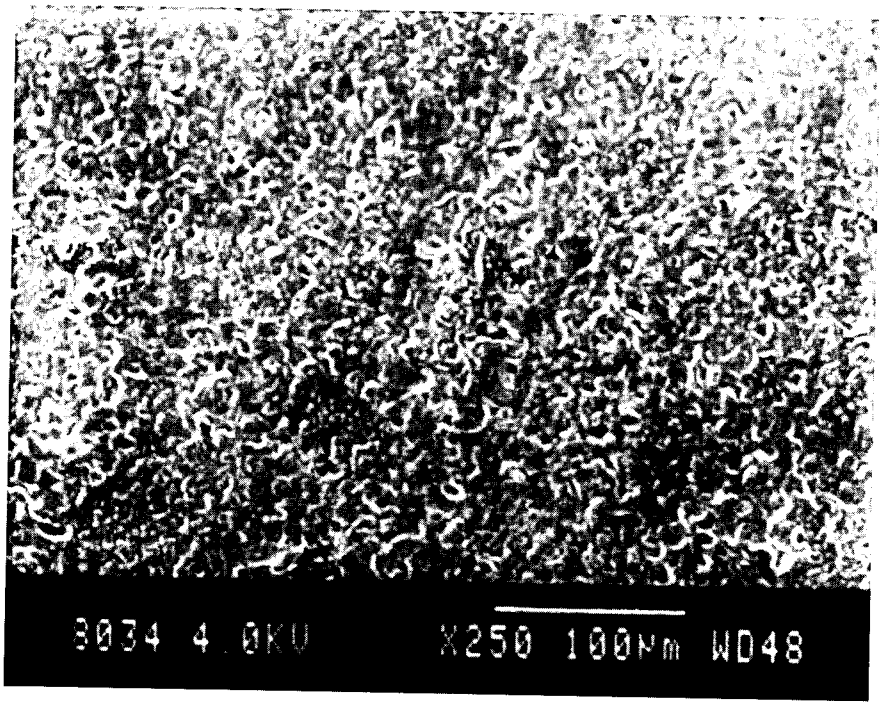

Figure 6: SEM of a laser scanned gear using the DMA laser scanning configuration. No visible indication can be observed by SEM to indicate the laser scanning pattern when this method is properly implemented. T_s = 700 °C, 9 sccm CH_4, 300 sccm H_2, 50 kPa (375 Torr), v_f= 0.025 m/s, P_l = 20 W (F_l = 3x10^6 Ws /m^2), 600 scan layers, τ_s = 2000 μs, τ_e = -1000 μs.

decreases SALD process efficiency. This dwell time may be decreased at the cost of at least fifty percent of the laser power by a photo-acoustical modulator. Alternatively, a high speed shutter may be used to decrease the dwell time without the cost of laser power intrinsic to photo-acoustical modulators.

4. Conclusions

SALD has been used to deposit carbon from methane and hydrogen mixtures using a third generation deposition system. Initial systematic and random morphological instabilities develop as the deposit grows thicker are attributed inadequate laser scan control in the initial programmed I/O scanning configuration. A new DMA based laser scan configuration was designed, prototyped, tested and refined until the systematic and random morphological deposit growth instabilities ceased. This scanning method integrates contour scanning with both x and y axis scanning for each part layer with real time laser power control. This method is applicable to other laser material processes besides SALD.

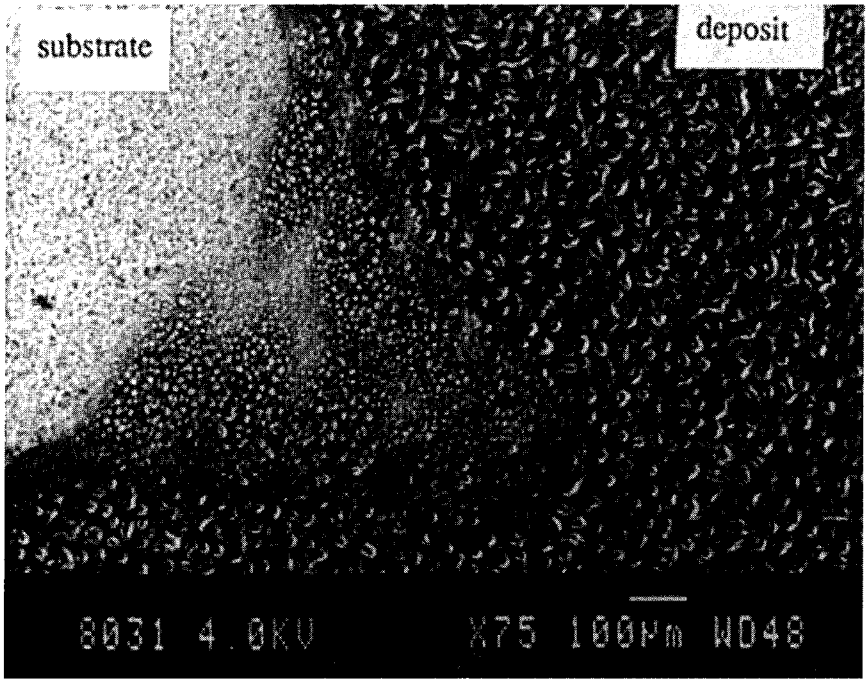

Figure 7: SEM of a laser scanned gear using the DMA laser scanning configuration. T_s = 700 °C, 9 sccm CH_4, 300 sccm H_2, 10 kPa (75 Torr), v_l= 0.025 m/s, P_l = 20 W ($F_l = 3x10^6$ Ws /m^2), 50 scan layers, τ_s = 2000 μs, τ_e = -1000 μs.

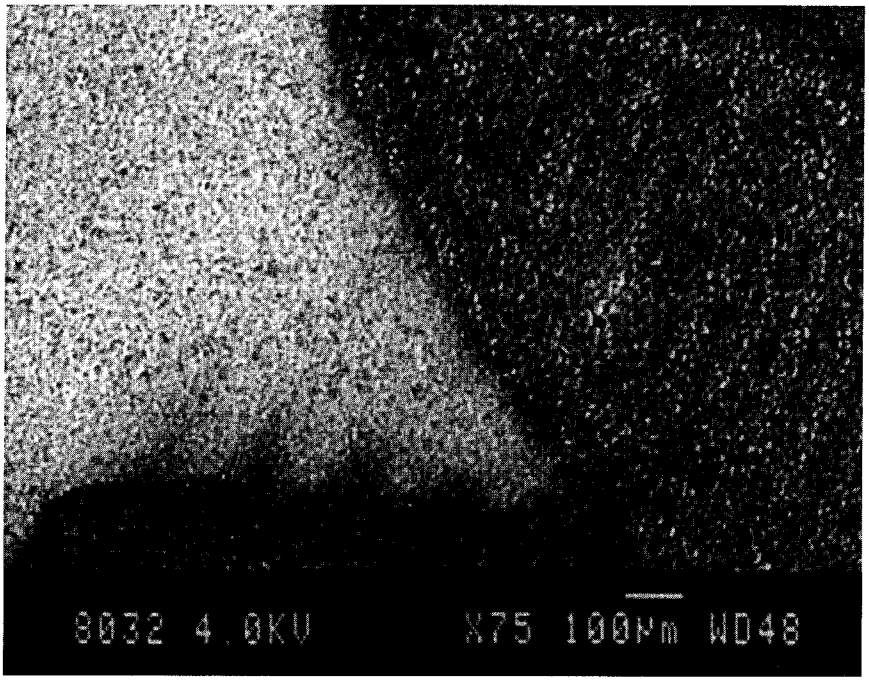

Figure 8: SEM of a laser scanned gear using the DMA laser scanning configuration. T_s = 700 °C, 9 sccm CH_4, 300 sccm H_2, 50 kPa (375 Torr), v_l= 0.025 m/s, P_l = 20 W ($F_l = 3x10^6$ Ws /m^2), 50 scan layers, τ_s = 2000 μs, τ_e = -1000 μs.

5. Acknowledgments

The authors would like to extend their gratitude to Neal Vail and Suman Das whose tutelage in C and assembly languages and sample code greatly facilitated the software development. John Spurgeon of the Mechanical Engineering Electronics Shop provided valuable insight in electronic trouble shooting. This project was sponsored by ONR under contract number: N00014-92-J-1514.

---

[1]Marcus, Harris L., Joseph J. Beaman, Joel W. Barlow, and David L. Bourell, "From Computer To Component In 15 Minutes: The Integrated Manufacture of Three-Dimensional Objects," Journal of Metals, April 1990, 8-10.

[2]Marcus, Harris L., Joseph J. Beaman, Joel W. Barlow, and David L. Bourell, "Solid Freeform Fabrication: Powder Processing," Ceramic Bulletin, 69, 6, 1990, 1030-31.

[3] Zong, Guisheng, Robert Carnes, Harovel G. Wheat, and Harris L. Marcus, "Solid Freefrom Fabrication by Selective Area Laser Deposition," Proceedings of The Solid Freeform Fabrication Symposium, edited by J. J. Beaman, H. L. Marcus, D. L. Bourell, and J. W. Barlow, The University of Texas at Austin, Austin Texas, August 6-8, 1990.

[4]Zong, Guisheng, Yves Jacquot, W. Richards Thissell, and H. L. Marcus, "Solid Freeform Fabrication Using Selective Area Laser Deposition," Plasma and Laser Processing of Materials, edited by Upadhya, Kamleshwar, TMS, 1991, 23-48.

[5]Thissell, W. Richards, Guisheng Zong, James Tompkins, Britton R. Birmingham, and Harris L. Marcus, "Selective Area Laser Deposition - A Method of Solid Freeform Fabrication," The Solid Freeform Fabrication Symposium Proceedings, edited by J. J. Beaman, H. L. Marcus, D. L. Bourell, J. W. Barlow, and Richards H. Crawford, The University of Texas at Austin, Austin Texas, August 12-14, 1991.

[6]Copley, Stephen M., "Mass Transport During Laser Chemical Vapor Deposition," Journal of Applied Physics, 64, 4, August 15, 1988, 2064-8.

[7]Skouby, D. C. and K. F. Jensen, "Modeling of Pyrolytic Laser-Assisted Chemical Vapor Deposition: Mass Transfer and Kinetic Effects Influencing The Shape of The Deposit," Journal of Applied Physics, 63, 1, January 1, 1988, 198-206.

[8]Burgener, M. L. and R. E. Reedy, "Temperature Distributions Produced In a Two-Layer Structure By a Scanning CW Laser Or Electron Beam," Journal of Applied Physics, 53, 6, June 1982, 4357-63.

[9]Moody, J. E. and R. H. Hendel, "Temperature Profiles Induced By A Scanning CW Laser Beam, Journal of Applied Physics, 53, 6, June 1982, 4364-71.

[10]Allen, S. D., J. A. Goldstone, J. P. Stone, and R. Y. Jan, "Transient Nonlinear Laser Heating and Deposition: A Comparison of Theory and Experiment," Journal of Applied Physics, 59, 5, March 1, 1986, 1653-7.

[11]Kar, A. and J. Mazumder, "Three-Dimensional Transient Thermal Analysis For Laser Chemical Vapor Deposition On Uniformly Moving Finite Slabs," Journal of Applied Physics, 65, 8, April 15, 1989, 2923-34.

[12]Jacquot, Yves, Guisheng Zong, and Harris L. Marcus, "Modeling of Selective Area laser Deposition for Solid Freeform Fabrication," Proceedings of The Solid Freeform Fabrication Symposium, edited by J. B. Beaman, H. L. Marcus, D. L. Bourell, and J. W. Barlow, The University of Texas at Austin, Austin Texas, August 6-8, 1990, 74-82.

[13]Radziemski, Leon J., and David A. Cremers, "Laser-Induced Plasmas and Applications," New York: Marcel Dekker, Inc., 1989.

[14] Thissell, W. Richards, James Tompkins, and Harris L. Marcus, "Design of a Solid Freefrom Fabrication Diamond Reactor," Proceedings of The Solid Freeform Fabrication Symposium, edited by J. B. Beaman, H. L. Marcus, D. L. Bourell, and J. W. Barlow, The University of Texas at Austin, Austin Texas, August 6-8, 1990, 48-73.

[15] Wu, Ying-Jeng Engin, and Joseph J. Beaman, "Laser Tracking Control Implementation for Sff Applications," Proceedings of The Solid Freeform Fabrication Symposium, edited by J. B. Beaman, H. L. Marcus, D. L. Bourell, and J. W. Barlow, The University of Texas at Austin, Austin Texas, August 3-5, 1992, 179-87.

[16] Touloukian, Y. S., and D. P. DeWitt, "Thermal Radiative Properties: Metallic Elements and Alloys," in Thermophysical Properties of Matter, Volume 7, Plenum Press, 1972.

[17] Touloukian, Y. S., and D. P. DeWitt, "Thermal Radiative Properties: Nonmetallic Solids," in Thermophysical Properties of Matter, Volume 8, Plenum Press, 1972.

[18] Ravi, K. V., "Morphological Instabilities In The Low Pressure Synthesis of Diamond," Journal of Materials Research, 7, 2, February 1992, 384-93.

[19] C. H. J. Van Den Brekel, and A. K. Jansen, "Morphological Stability Analysis in Chemical Vapour Deposition Processes. I," Journal of Crystal Growth, 43, 1978, 364-70.

[20] Jansen, A. K., and C. H. J. Van Den Brekel, "Morphological Stability Analysis In Chemical Vapour Deposition Processes. II," Journal of Crystal Growth, 43, 1978, 371-377.

[21] Palmer, Bruce, and Roy G. Gordon, "Local Equilibrium Model of Morphological Instabilities in Chemical Vapor Deposition," Thin Solid Films, 158, 1988, 313-41.

MEASUREMENT AND PREDICTION OF THE THERMAL CONDUCTIVITY OF POWDERS AT HIGH TEMPERATURES

Samuel Sumin Sih and Joel W. Barlow
Department of Chemical Engineering
The University of Texas at Austin
Austin, Texas 78712

Abstract

An equation for the prediction of the thermal conductivity of powder beds up to high temperatures is suggested by the authors. The predicted values by the equation are compared with the values of the thermal conductivity of alumina powder, magnesia powder and zirconia powder reported in the literature, and are found to be consistent. The predicted values by the equation are also compared with the measured values of the thermal conductivity of calcium hydroxyapatite powder, at various temperatures, up to 500°C by the laser-heated method.

I. Introduction

The temperatures used during the Selective Laser Sintering process are ordinarily near the fusion points of the powders. The data of the thermal conductivities of powder beds at high temperatures are therefore of importance to this process. For the prediction of the thermal conductivity of powder beds up to high temperatures, a number of equations are found in the literature. The present authors adopted and changed a model (Zehner-Schlünder's model) [1], checked it with the data in the literature, and checked with the data they measured by the laser-heated method [2,3]. They found the consistency of the predicted values with the measured values to be within ±30% relative error..

The measurement of the thermal conductivities of hydroxyapatite powder bed from room temperature up to 500°C was done by the use of the laser-heated method by the authors. A description of the equipment used the authors to collect the high temperature data of the thermal conductivities of powder beds, including diagrams about the construction of the apparatus, was given in an earlier article [2]. The authors have also made preparation for the future use of this apparatus for the measurement of the thermal conductivities of powder beds in vacuum and in other gaseous environments.

II. Predictive Model

A. The Model and Its Derivation. There are some equations in the literature for the prediction of the thermal conductivity of powder beds. Besides Yagi-Kunii's equation [4], Zehner-Schlünder's equation [1] has been noticed to be a comparatively good one [5]. Schlünder's equation [6] considered conduction only. Later, with the cooperation of Zehner, Schotte's equation [7] was adopted for the consideration of the radiation effect. In the derivation of Zehner-Schlünder's equation, the present authors found some mistakes in the original article [1]. We rederived the equations, and suggested the consideration of the radiation by the direct addition of the Damköhler's term to give

$$\frac{k}{k_g} = (1-\sqrt{1-\varepsilon})\left(1+\frac{\varepsilon k_R}{k_g}\right) + \sqrt{1-\varepsilon}\left[(1-\phi)\left(\frac{2}{1-\frac{Bk_g}{k_s}}\left(\frac{B}{\left(1-\frac{Bk_g}{k_s}\right)^2}\left(1-\frac{k_g}{k_s}\right)\ln\frac{k_s}{Bk_g} - \frac{B+1}{2} - \frac{B-1}{1-\frac{Bk_g}{k_s}}\right) + \frac{k_R}{k_g}\right) + \phi\frac{k_s}{k_g}\right]$$

Free fluid — Core heat transfer (incomplete solid contact) — (Complete solid contact)

(1)

where,

k = effective thermal conductivity of the powder bed, W/m-K;
k_g = thermal conductivity of the gas inside the pores of powder bed, W/m-K;
k_s = thermal conductivity of the skeletal solid, W/m-K;
ε = porosity of the powder bed;
k_R = thermal conductivity part of the powder bed owing to radiation, denoted by the Damköler's equation below, W/m-K;
ϕ = flattened surface fraction of particle in contact with another particle; ϕ =0 when there is no contact for the particles; ϕ =1 when there is complete particle contact; and
B = deformation parameter of the particle.

In the heat transfer through powder, the part tranferred by the free fluid, or diffusion and molecular conduction, is $1-\sqrt{1-\varepsilon}$, and the other part, or $\sqrt{1-\varepsilon}$, is for conduction through solid and the fluid entrained in the solid particle interstices. The right-hand side of the above equation is separated into three main parts. The first part is due to the thermal transport done by free fluid, including the conduction part and the radiation part as well. The second and third parts of the above equation are for the heat transfer done by the solid and the fluid entrained in the solid particle interstices. The second part of the above equation is for incomplete solid contact, including heat transfer by conduction and radiation. The third part is for complete solid contact by the conduction of heat only. Heat transfer by convection is not considered here.

For the deformation parameter, B, it has the following ralationship to the cylindrical radius, r, and the z-coordinate of the z-axis in the cylindrical coordinate system.

$$r^2 + \frac{z^2}{[B-(B-1)z]^2} = 1. \qquad (2)$$

We may see that when B=0, it is the z-axis; when B=1, the particle surface is that of a sphere; and, when $B \to \infty$, $r^2 = 1$, or it is a cylinder. So, for B<1, it is a prolonged needle, and for B>1, it is a barrel-like body.

The k_R term, or thermal conductivity part of the powder bed owing to radiation, is calculated by the Damköler's equation [8]. For the prediction of the thermal conductivity of powder beds at high temperatures, the heat transfer effect due to radiation should be considered. Damköhler [8] first proposed the following simple relationship to account for the radiation effect of heat transfer through a powder bed.

$$k_R \Delta T = \xi s d_p e \sigma (T_b^4 - T_l^4) = \xi s d_p e \sigma (T_b^2 + T_l^2)(T_b + T_l)(T_b - T_l) \qquad (3)$$

or: $$k_R = \xi s d_p e \sigma (T_b^2 + T_l^2)(T_b + T_l) \approx 4 \xi s d_p e \sigma T_b^3. \qquad (4)$$

where,

k_R = the thermal conductivity contributed by radiation, W/m-K,
ξ = the area fraction occupied by the canals for the radiation per total unit area,
s = a numerical factor of about 1,
d_p = the diameter of the powder particle m,
e = emissivity,
σ = Stefan-Boltzmann constant = 5.67×10^{-8} W/m^2-K^4,
T_b = the temperature of the powder bed, and
T_1 = the temperature of the surrounding, assumed to be near to T_b

Damköhler suggested that ξs might take the value of 0.3, but he also mentioned that for definite powder beds, one might just measure ξs. In an example in his writing, Damköhler put ξse = 1/3.

B. Comparison of the Predicted Values by the Proposed Equation with the Measured Data Reported in the Literature. We found in the *Landolt-Börnstein: Numerical Data and Functional Relationships in Science and Technology* [9] some high temperature data of the thermal conductivity of powder beds. The numerical data were for alumina (Al_2O_3) powder, magnesia (MgO) powder, and Zirconia (ZrO_2) powder, and they included the temperature, porosity and the particle diameter in the data as well. We also found the thermal conductivity of the alumina, magnesia and zirconia in solid form at the various temperatures (some by interpolations). In calculating, we found the predicted values and the reported values in the literature match in the range of differences of ±30%, . It has been noted that the predicted values of the thermal conductivity of the powder bed (e.g. alumina powder, ε = 0.71) by our equation is much better than by Yagi-Kunii's equation, and also a little better than by Zehner-Schlünder's equation. The following is a graph showing the result.

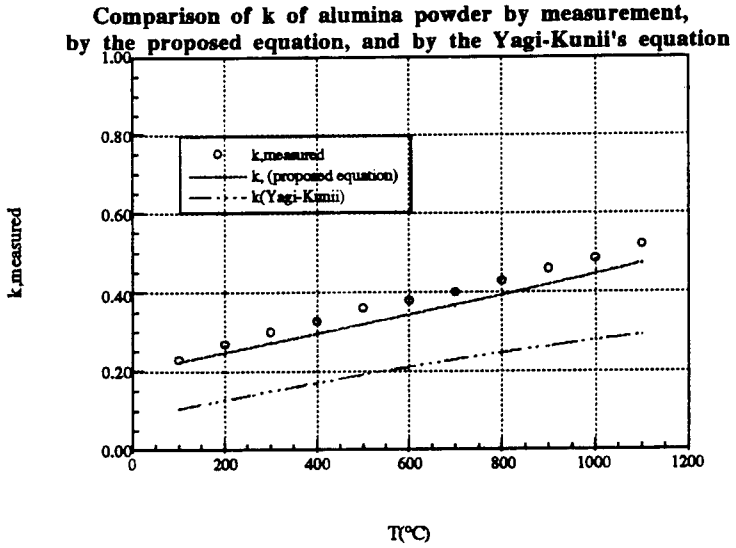

Figure 1. Comparison of k of alumina powder (ε=0.71) (reported) with the predicted values by the authors' equation and Yagi-Kunii's equation.

The following are the graphs showing the comparisons of the predicted values with the reported values of the thermal conductivity of the various powder (alumina, magnesia, and zirconia) beds.

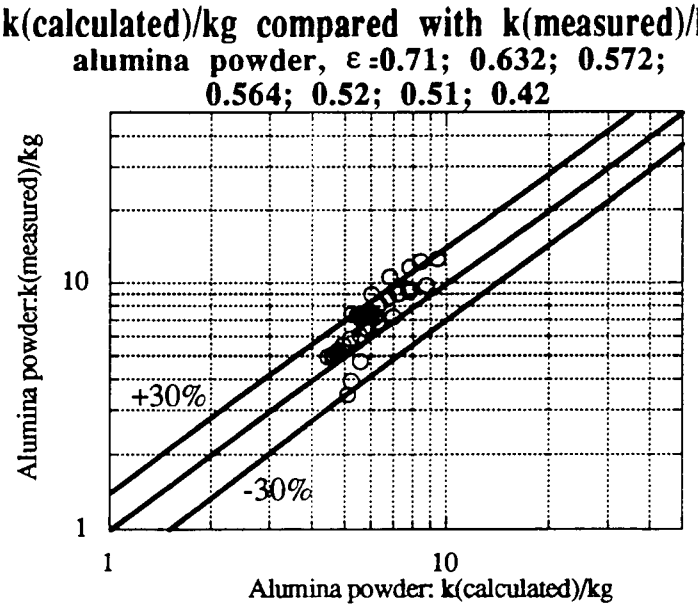

Figure 2. The comparison of the predicted values (calculated values) with the reported values (measured values) of alumina powder beds of various porosities (ε).

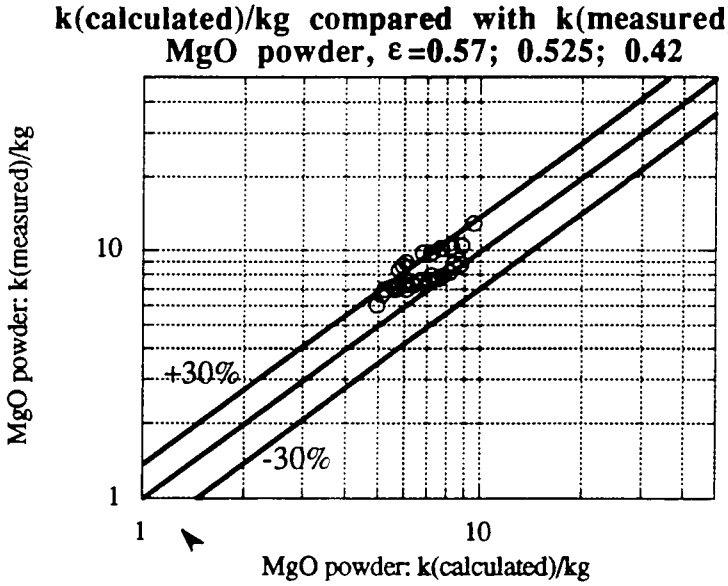

Figure 3. The comparison of the predicted values (calculated values) with the reported values (measured values) of magnesia powder beds of various porosities (ε).

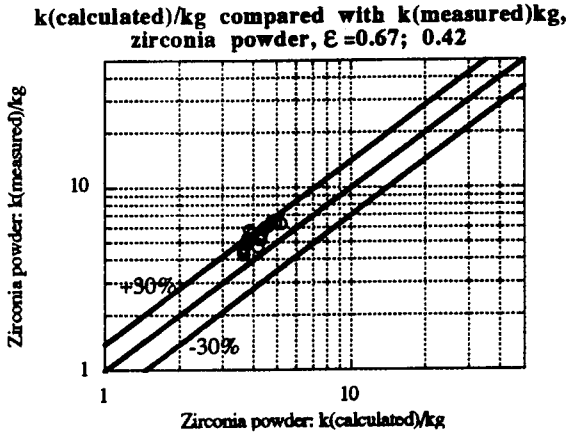

Figure 4. The comparison of the predicted values (calculated values) with the reported values (measured values) of magnesia powder beds of various porosities (ε).

III. Comparison of the Model with Experimental Data for Hydroxyapatite

The authors measured the thermal conductivity of hydroxyapatite powder from room temperature up to 500°C, by the laser-heated method. To obtain the k of a powder bed by the apparatus used by the authors, one must know first the heat capacity of the powder as the measurements by the apparatus only give the thermal diffusivities at the various temperatures. In literature, we found only few references on the heat capacities of hydroxyapatite. [10, 11, 12] In all the cases in the literature, hydroxyapatite samples were preheated to around 1000°C for long hours. Thus, as Kijima and Tsutsumi [10] conceded that the samples that they tested were actually oxyhydroxyapatite. We used the Differential Scanning Calorimeter (Perkin-Elmer DSC-7) for the measurement of the heat capacities of the hydroxyapatite powder (Monsanto Company), starting from room temperature and ending at 500°C, with slow speed for the increase of temperature. The result of our measurement of the heat capacity of hydroxyapatite is shown in the following graph.

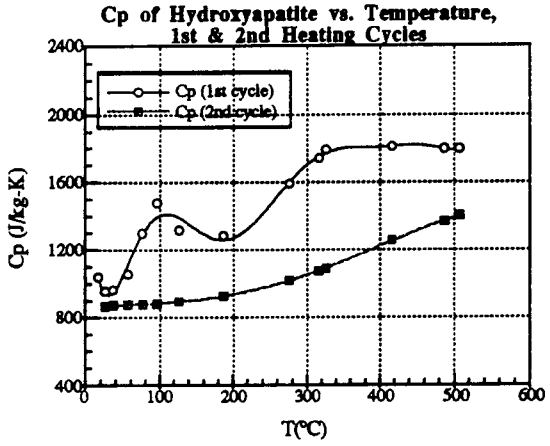

Figure 5. Graph of Cp of hydroxyapatite vs. temperature, 2 heating cycles compared

As the hydroxyapatite powder (Monsanto Company) contained a definite amount of water moisture, it may be seen that around 100°C that was an increase of heat capacity. The second curve in the above graph shows the measured Cp vs. temperature curve of the hydroxyapatite powder which went through a heating cycle from room temperature to 500°C once and cooled down again to room temperature to start for another cycle of the measurement. In heating the powders repeatedly at high temperatures, we found for the second cycle the heat capacities of the powders are lowered and the curve became smoother, with no peak value around 100°C. This was probably owing to the loss of water and change in the chemical structure of hydroxyapatite.

The density of the sample powder bed that we used for the measurement is 0.4004 gm/cm^3. From the relationship of $k = \rho \times Cp \times \alpha$, by measuring the thermal diffusivity, α, we obtained the thermal conductivity of the hydroxyapatite powder bed vs. temperature, from room temperature up to 500°C in 10°C increments, which is shown in Figure 6 below. (C_p of the first cycle was used in the calculations.)

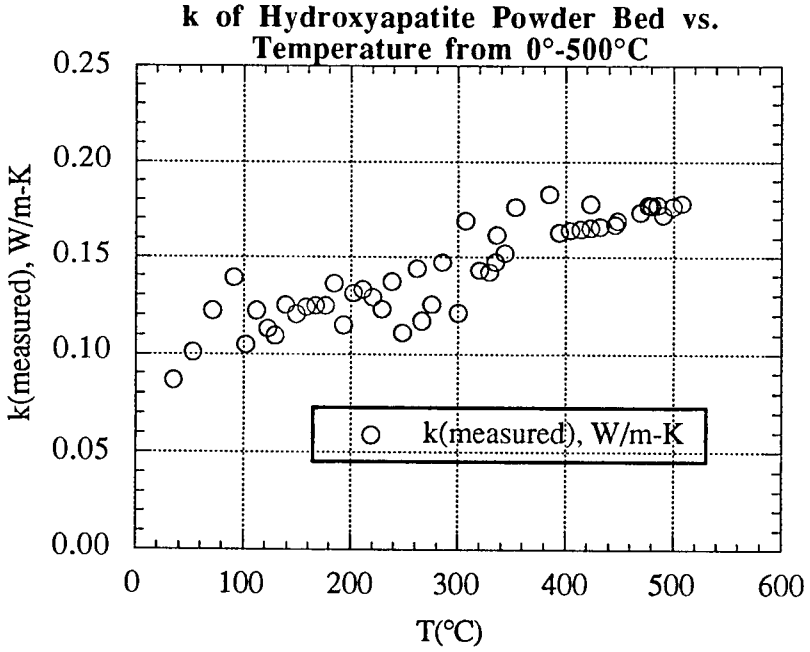

Figure 6. k of hydroxyapatite powder bed vs. temperature, from 0°-500°C

For the application of the above equation to the hydroxyapatite powder bed, we use the following relationship for the calculation of the thermal conductivity of air,k_g, inside the pores of the powder at the various temperatures.

$$k_g = (0.0000586 + 0.00000017639T) \times 418.4 \qquad \text{W/m-K} \qquad (5)$$

In the above equation, T is the temperature in °C. This equation was taken from the Chemical Engineers' Handbook. [13]

For the value of k_S, the thermal diffusivity vs temperature graph of Tsuyoshi Kijima and Masayuki Tsutsumi [10] is referred to by the present authors. Kijima and Tsutsumi heated hydroxyapatite using the range of 1050°-1450°C, with each sample heated for 3 hours. They found that the thermal diffusivity vs. temperature curves for the different sample nearly fell into coincidence. The Figure 8 of their article is reproduced below for reference.

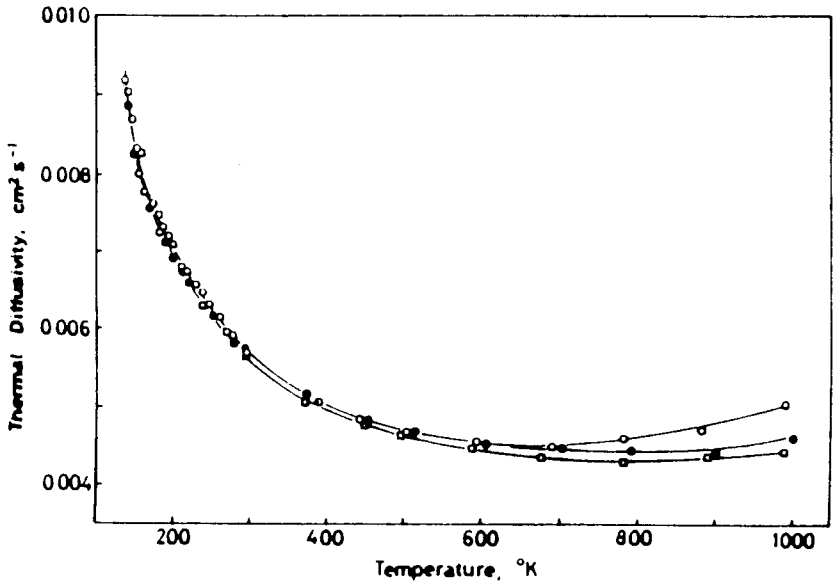

Figure 7. Thermal diffusivity vs. temperature for hydroxyapatite [10] sintered at 1050° (sample S-1, □), 1100° (sample S-2, •), and 1150°C (sample S-3, O).

We assume that hydroxyapatite heated up to 500°C would also have its diffusivity vs. temperature curve of about the same form. With the use of Cp vs. temperature curve of our own measurement (Figure 5 of this article, 1st cycle) again, and the average solid density of hydroxyapatite of 2.4625 gm/cm^3, from the relationship of $k_S = \rho_S \times Cp \times \alpha$, we calculated the k_S vs. temperature values for solid hydroxyapatite. We presumedd ε to be 0.8374 from knowledge of the bulk and solid densities of hydroxyapatite.

We have for porosity, ε,

$$\varepsilon = \frac{\rho_s - \rho_b}{\rho_s} = \frac{2.4625 - 0.4004}{2.4625} = 0.8374.$$

In the above equation, ρ_b is the bulk density of the powder bed.

As the melting point of hydroxyapatite is well above 1000°C, the deformation parameter, B, is assumed to be 1, i.e. the particle are all spherical; and the flattened surface fraction, ϕ, is taken to be zero, i.e. there is no flattened surfaces..

Following Damköhler's suggestion [8], we assumed $\xi se = 0.3$, as we have not yet measured emissivity values to calculate the ξs. For the particle size, d_p, we got a size distribution report of the hydroxyapatite powder from Monsanto Company, the producer of the powder. As radiation is related to a surface area controlling phenomenon, we calculated the mean diameter of the particle by an equation according to the following [14].

$$d_p = D_{20} = \left(\frac{\Sigma N_i D_i^2}{\Sigma N_i} \right)^{1/2} \qquad (6)$$

Through calculation, we got the $d_p = 15.091$ μm.

In substituting the above values into our proposed equation, we found the equation gives predicted values for the thermal conductivity of the powder bed quite well. The following graph shows the nearness of the predicted values by the equation to the measured values of the k of the powder bed. The Yagi-Kunii's equation for the case of the

hydroxyapatite powder bed is shown on the same graph. It may be seen that the proposed equation or ours gives much better predictions than the Yagi-Kunii's equation. The proposed equation of ours gives also a little better predictions than the Zehner-Schlünder's equation.

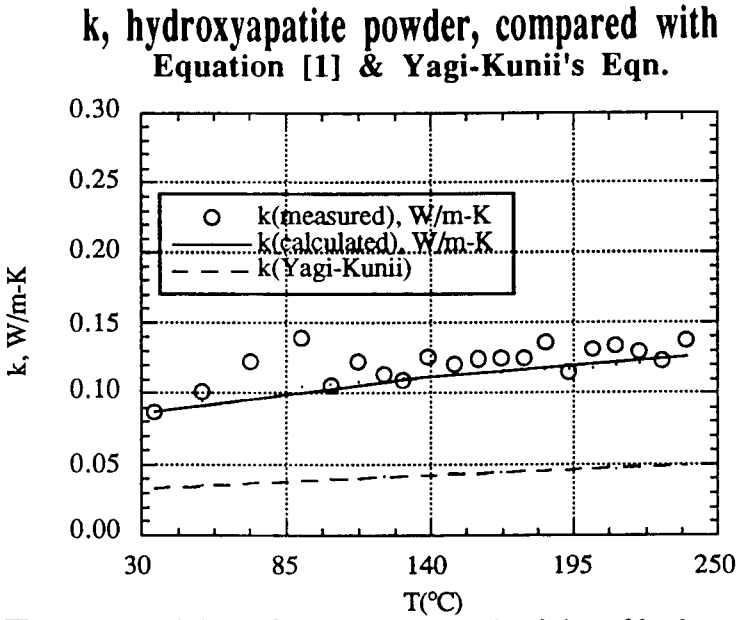

Figure 8. The measured data of the thermal conductivity of hydroxyapatite powder bed compared with the predicted valued of the proposed equation of the authors and the Yagi-Kunii's equation.

In the following graph, the measured values of k/k_g are compared with the values predicted by Equation [1]. It may be seen that the predicted values and the measured values match one another quite well.

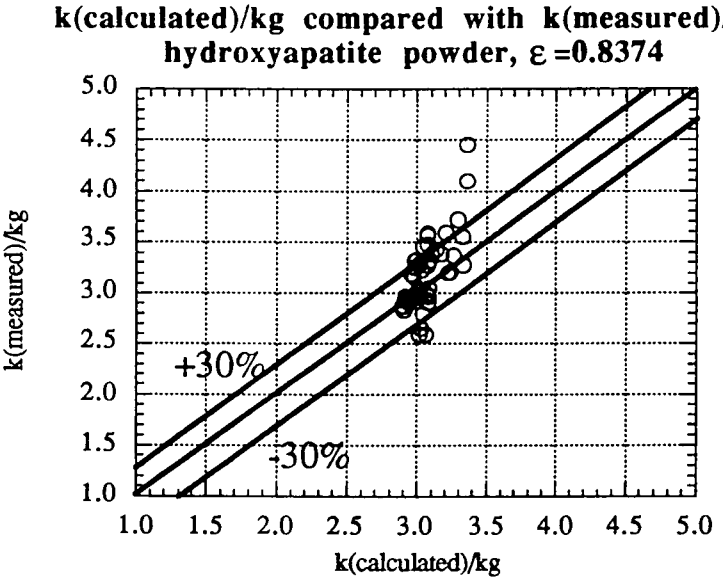

Figure 9. k(calculated)/kg compared with k(measured)/kg for the hydroxyapatite powder bed.

IV. Conclusion

We used a new equation to predict the thermal conductivity of powder beds from room temperature up to high temperatures. The new equation proved to be predicting the thermal conductivity of powder beds to within ±30% of the values reported in literature and the measured values of the thermal conductivity of hydroxyapatite powder from room temperature up to 500°C.

Acknowledgments

The authors gratefully acknowledge support for this work by the University of Texas SFF Industrial Associates Program.

References

1. Zehner, P. and Schlünder, E.U.,'Wärmeleitfähigkeit von Schüttungen bei mäßigen Temperaturen,' *Chemie-Ing.-Techn.*, Vol. 42, No.14, pp.933-941.

2. Sih, Samuel S. and Barlow, J.W., 'Measurement of the Thermal Conductivity of Powders by Two Different Methods,' in the *Solid Freeform Fabrication Symposium Proceedings*, the University of Texas at Austin, Austin, Texas (1993),pp. 370-375.

3. Sih, Samuel S. and Barlow, J.W., 'The Measurement of the Thermal Properties and Absorptances of Powders near Their Melting Temperatures,' in the *Solid Freeform Fabrication Symposium Proceedings*, the University of Texas at Austin, Austin, Texas (1992),pp. 131-140.

4. Yagi,S. and Kunii, D.,'Studies on Effective Thermal Conductivities in Packed Beds,' *A.I.Ch.E. Journal*, September, 1957, pp.373-381.

5. Hahne, E., Song, Y.W., Gross, U.,'Measurement of Thermal Conductivity in Porous Media,' in *Convective Heat and Mass Transfer in Porous Media*, ed. by Kakaç et al., Kluwer Academic Publishers, Netherlands, 1991, pp. 849-865.

6. Schlünder, E.U., *Chemie-Ing.-Techn.*,Vol. 38, pp.967-979, 1966.

7. Schotte, W., 'Thermal Conductivity of Packed Beds,' *A.I.Ch.E. Journal*, Vol.6, p. 63, 1960.

8. Damköhler, G., *Der Chemie-Ingenieur*, Eucken, M. and Jakob, A., eds., Vol. 3, Part 1, Leipzig, Akademischer Verlag GmbH (1937),pp. 359-485.

9. *Landolt-Börnstein: Numerical Data and Functional Relationships in Science and Technology*, edited by Landolt-Börnstein Editorial Staff, 6th ed., 1950-80; New Series 1961- ; Springer-Vertrag, Heidelberg, Germany.

10. Kijima, Tsuyoshi and Tsutsumi, Masayuki, 'Preparation and Thermal Properties of Dense Polycrystalline Oxyhydroxyapatite,' *Journal of the American Ceramic Society*, Vol. 62, No. 9-10, pp. 455-460, 1979.

11. Hopkins, R.H., Damon, D.H., Piotrowski, P., Walker, M.S. and Uphoff, J.H., 'Thermal Properties of Synthetic Fluorapatite Crystals,' *Journal of Applied Physics*, Vol. 42, No. 1, pp. 272-275. 1971.

12. Egan, Edward P. Jr., Wakefield, Zachary T. and Elmore, Kelly L., 'High-Temperature Heat Content of Hydroxyapatite,' *J. Am. Chem. Soc.*, Vol.72, 2418-2421, 1950.

13. Perry, R.H. and Green, Don, *Perry's Chemical Engineers' Handbook*, 6th edition, McGraw-Hill Inc., New York, 1983, p. 3-254.

14. Lefebvre, Arthur H., *Atomization and Sprays*, Hemisphere Publishing Corporation, New York, 1989, p. 91.

Anisotropy in Alumina Processed by SLS.

P. Kamatchi Subramanian, N.K. Vail, J.W. Barlow and H.L. Marcus
Center for Materials Science and Engineering,
The University of Texas at Austin.

Abstract

Alumina powders of 15μm size and 2μm size were processed by SLS using PMMA and a copolymer. The 2μm powders were agglomerated and mixed with the polymer powder before being processed by SLS. SLS bend strength specimens were made with parts built along different orientations. The variation of the strength with incident energy density and with orientation was studied

Introduction

Selective Laser Sintering (SLS) of ceramics is very challenging because of the high melting points of the ceramics. In SLS one of the operating parameters, the energy density is defined as the amount of laser energy input per unit area[1] in each layer. In the case of alumina to form lines of sintered material energy densities of the order of 1000 cal/cm^2 is required. Even at this high energy densities the parts formed do not hold together because of the huge thermal gradients. One solution is to use a low melting temperature second phase material which will melt under the laser and bond the particles together. This second phase may be inorganic[2,3,4] or organic[5,6]. This paper describes some of the SLS experiments of alumina with organic binder. This paper focuses on the variation of properties of the green shapes with processing parameters including the orientation of scanning in the SLS process.

Experiments

Two kinds of alumina powder were investigated in this study. They were i) 2μm powder from Golden Technologies and ii) 15μm powder from Norton Corp. SLS of 2μm as received powder was unsuccessful using a polymer binder even at compositions of 35 Vol % polymer. In an attempt to overcome this problem it was decided to agglomerate the particles. Through a series of experiments of heating to various temperatures for varied lengths of time it was decided that 1400C for 3hrs would give a desirable agglomeration. The 2μm powders were heated in a kiln to 1400C in 12 hrs at a constant heating rate and held at 1400C for 3hrs. The powder was also cooled down in about 12hrs. This produced agglomerates of an average size of 100μm. The flow diagram is shown in Fig.1.

The organic binders used were i) PMMA and ii) a copolymer, Poly[methylmethacrylate-co-butyl methacrylate] (80 mol%MMA/20 mol%BMA). The preparation of these polymers is explained elsewhere[7]. The PMMA had a melt index of 31.5g/10 min and the copolymer had a melt index of 11.6g/10min as measured following ASTM D1238 at 200C with an extrusion pressure of 0.52 MPa (75psi).

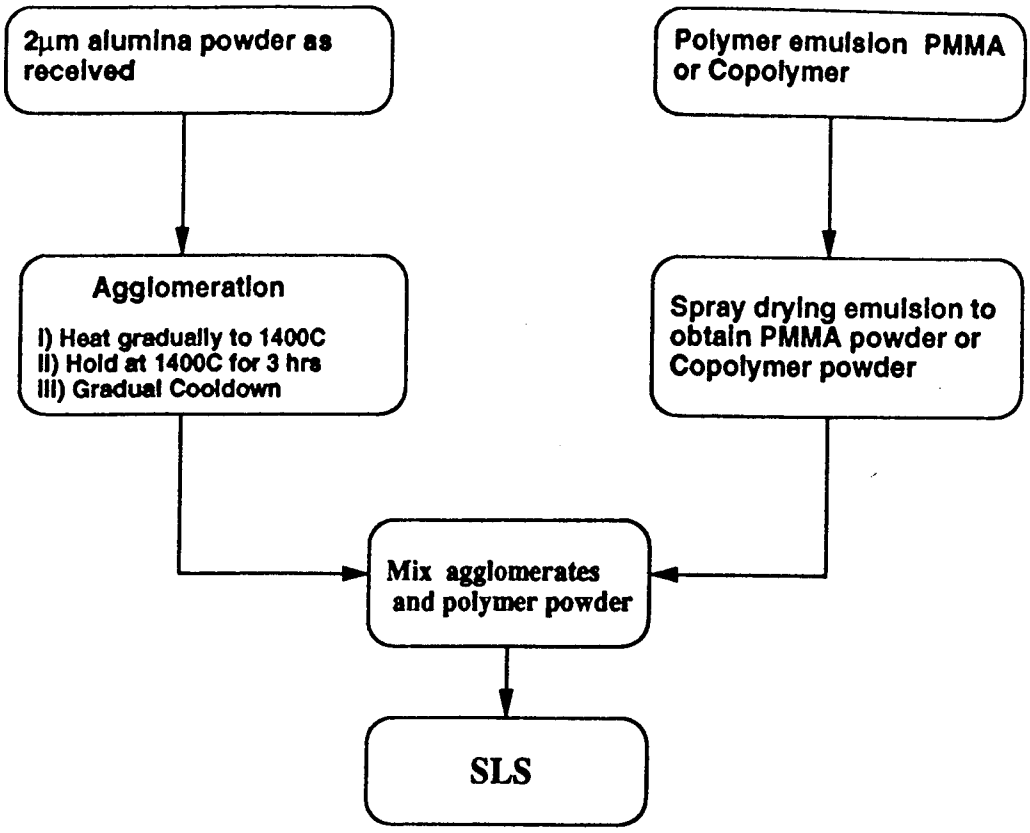

Figure 1. Processing of 2μm Alumina powder

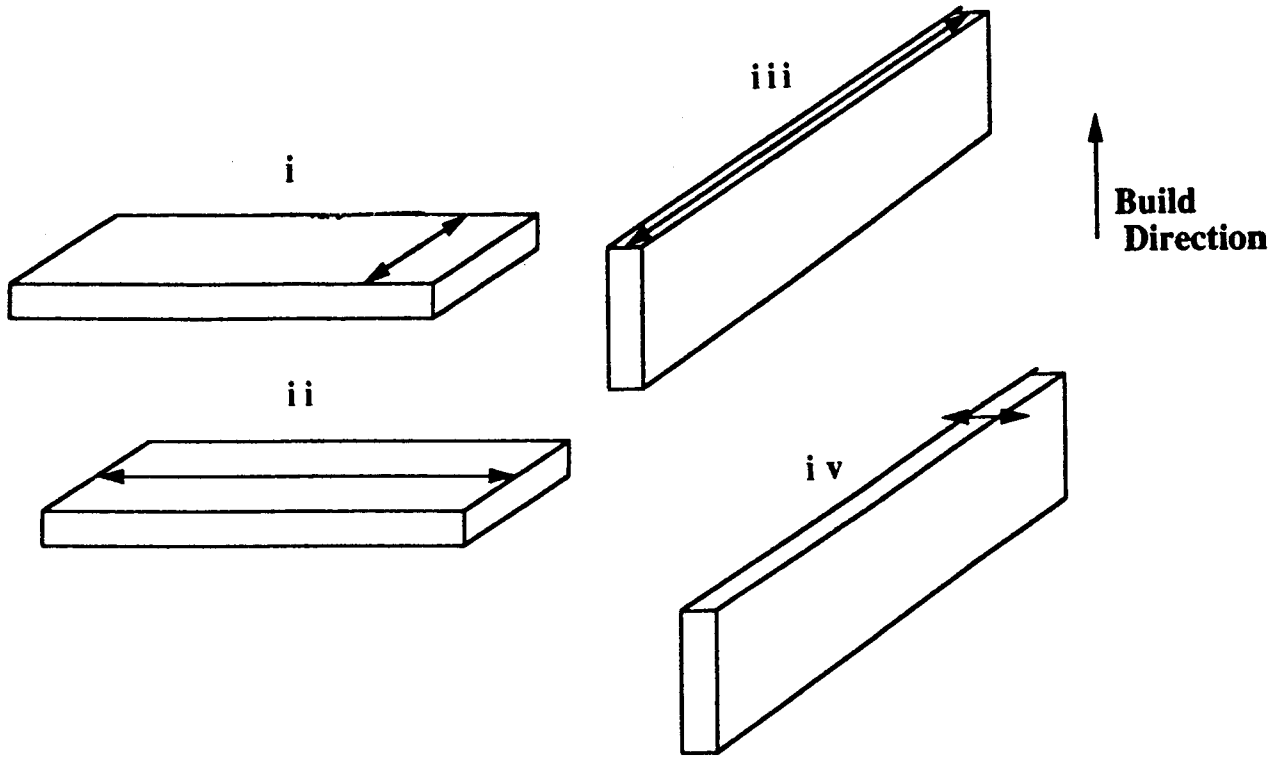

Figure 2. Orientations used in building the bend strength specimens. i:build along thickness, scanning along width ; ii: build along thickness scan along length; iii: build along width with scanning along length; iv: build along width, scan along thickness

The 15μm alumina powders were spray dried with the copolymer in a Anhydro spray drier with inlet temperature of 200C and outlet temperature of 80C. The agglomerates of 2μm alumina were mixed with the polymer powder obtained by spray drying the polymer emulsion. Two mixtures were made, i) the agglomerates of 2μm alumina mixed with the spray-dried PMMA powder and ii)the agglomerates of 2μm alumina mixed with the spray-dried copolymer powder. The spray-dried and mixed powders were then SLS processed.

The layer thickness was kept constant at 175μm. The laser scanning speed and laser scan line spacing were varied along with the power of the laser to change the incident laser energy density. The scan line spacing was varied between 75μm and 125 μm and the scan speed was varied from 30cm/s to 150 cm/s. The laser power was varied between 6 and 14W. The energy density was varied between 2 cals/cm^2 and 8 cals/cm^2. Three point bend strength specimens 0.076mx0.025mx0.00625m (3"x1"x0.25") were made by SLS. The specimens were made in 4 orientations i) built along thickness with scanning parallel to width ii) built along thickness with scanning parallel to length, iii) built along width with scanning parallel to thickness and iv)built along width with scanning parallel to length as shown in Fig.2.

Results and Discussion

SLS of parts from both the spray-dried and mixed powders produced strong green parts. For the case of the spray-dried 15μm powder built along thickness with scanning parallel to width, condition (i), the variation of density with incident energy density is as shown in Fig.3. The density varies little with incident energy density. The variation of bend strength of the green parts with incident energy density is shown in Fig.4. It may be seen that the green strength increases initially with energy density because of better melting and wetting of the alumina by the molten polymer. At still higher energy densities the strength decreases due to decomposition of the polymer.

Scanning along the length while building along thickness, condition (ii) produces a lower green strength at lower energy densities than those scanned along width and built along thickness, condition (i). This anisotropy is due to the region scanned by the laser having longer time for heat transfer between two consecutive scans for condition (ii). At higher energy densities i.e., around 6cals/cm^2 the strength of the samples made by scanning along length has a higher strength due to degradation of polymer for condition (i). Even in the case of scanning along length we have a decrease in strength at higher energy densities. But this decrease occurs at still higher energy densities.

With increase in energy density, higher temperatures are reached in the sample being made. As temperature increases well above the glass transition temperature, the degradation of the polymer increases. Temperatures in the decomposition regime are attained at lower energy densities in the case of samples with shorter scan lines because the time between successive scan overlays is smaller. In the case of samples made with longer scan lines the temperatures in the decomposition regime are attained only at a higher energy density because there is some time for the heat to be dissociated between successive scan overlays.

In the case of parts built along width with scanning parallel to thickness, condition (iv), the green strength increases with energy density at low energy densities, Fig.5. At higher energy

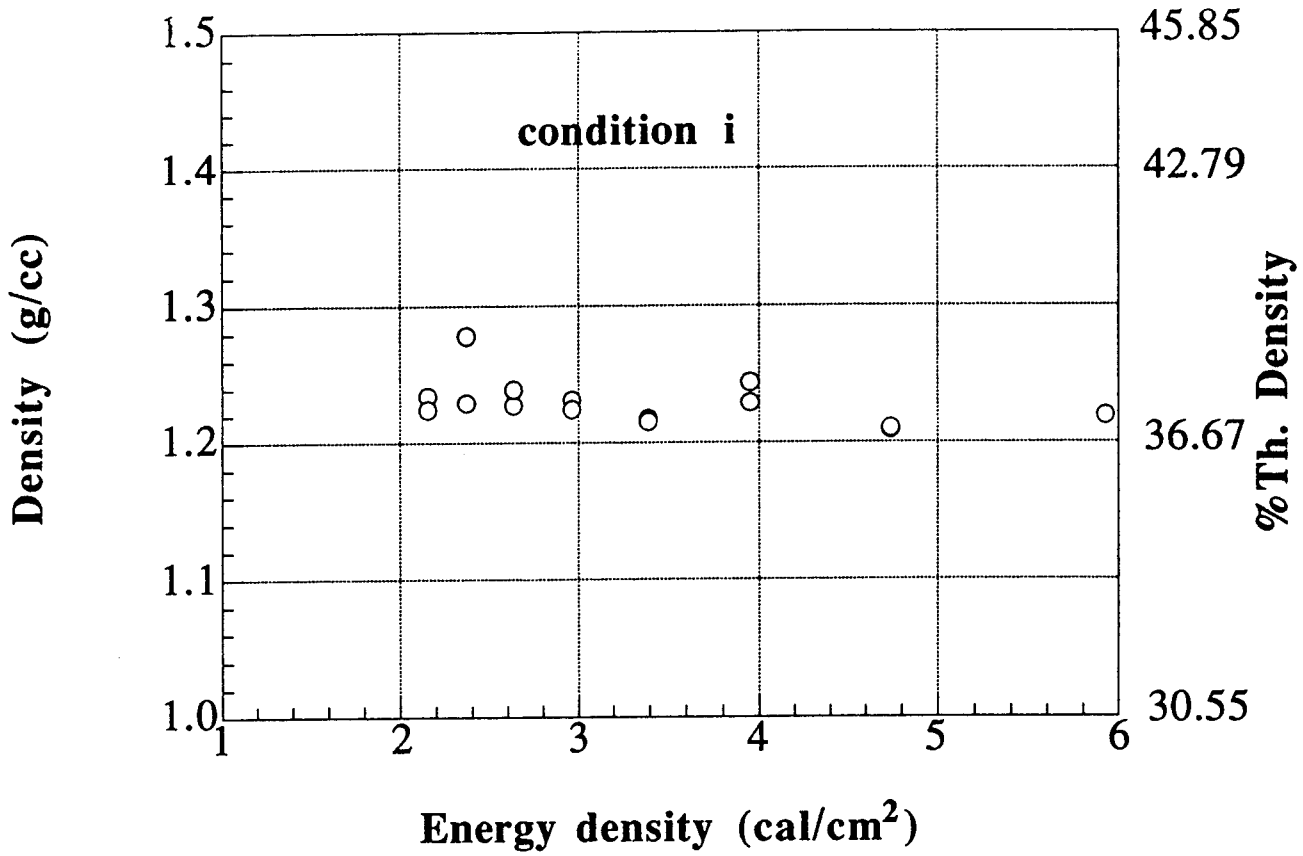

Figure 3. Green density of samples after SLS from 15μm alumina coated with copolymer.

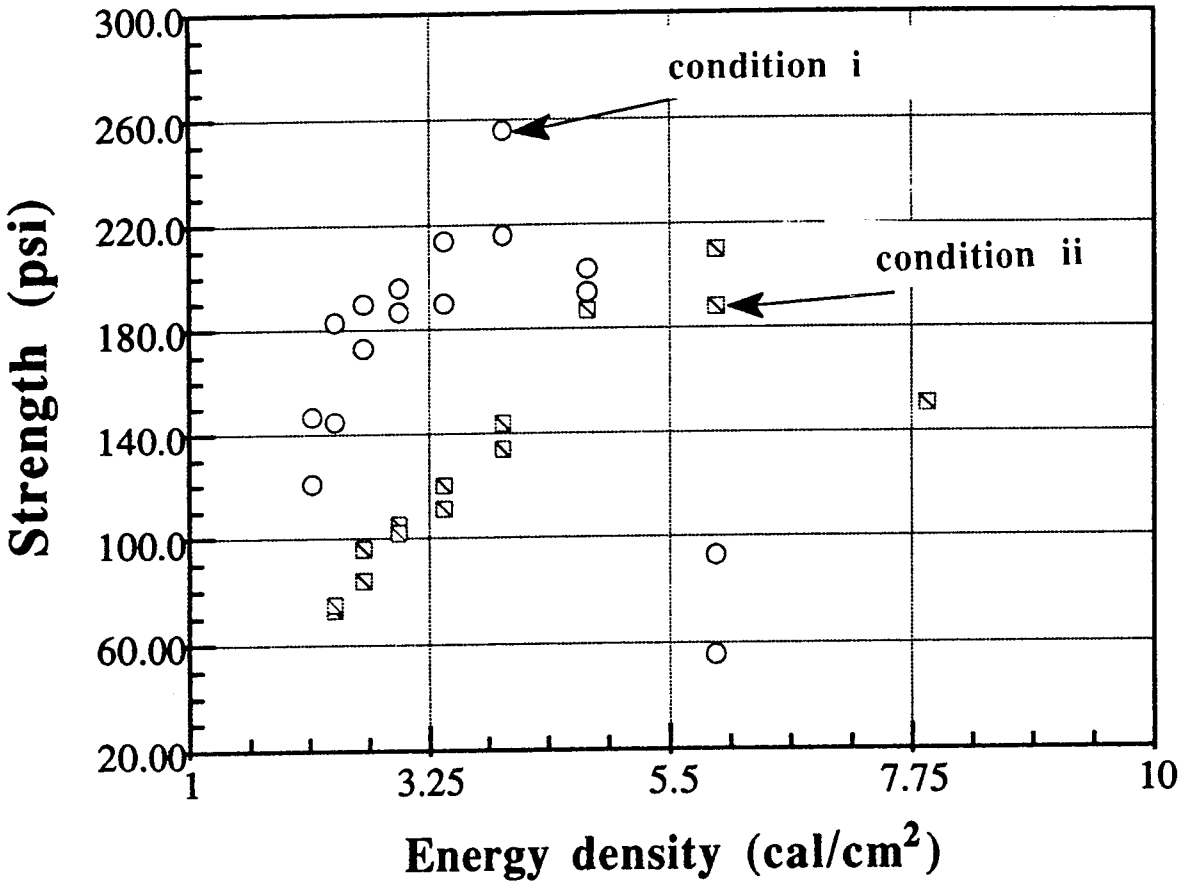

Figure 4. Bend strength of samples from 15μm alumina coated with copolymer built along thickness.

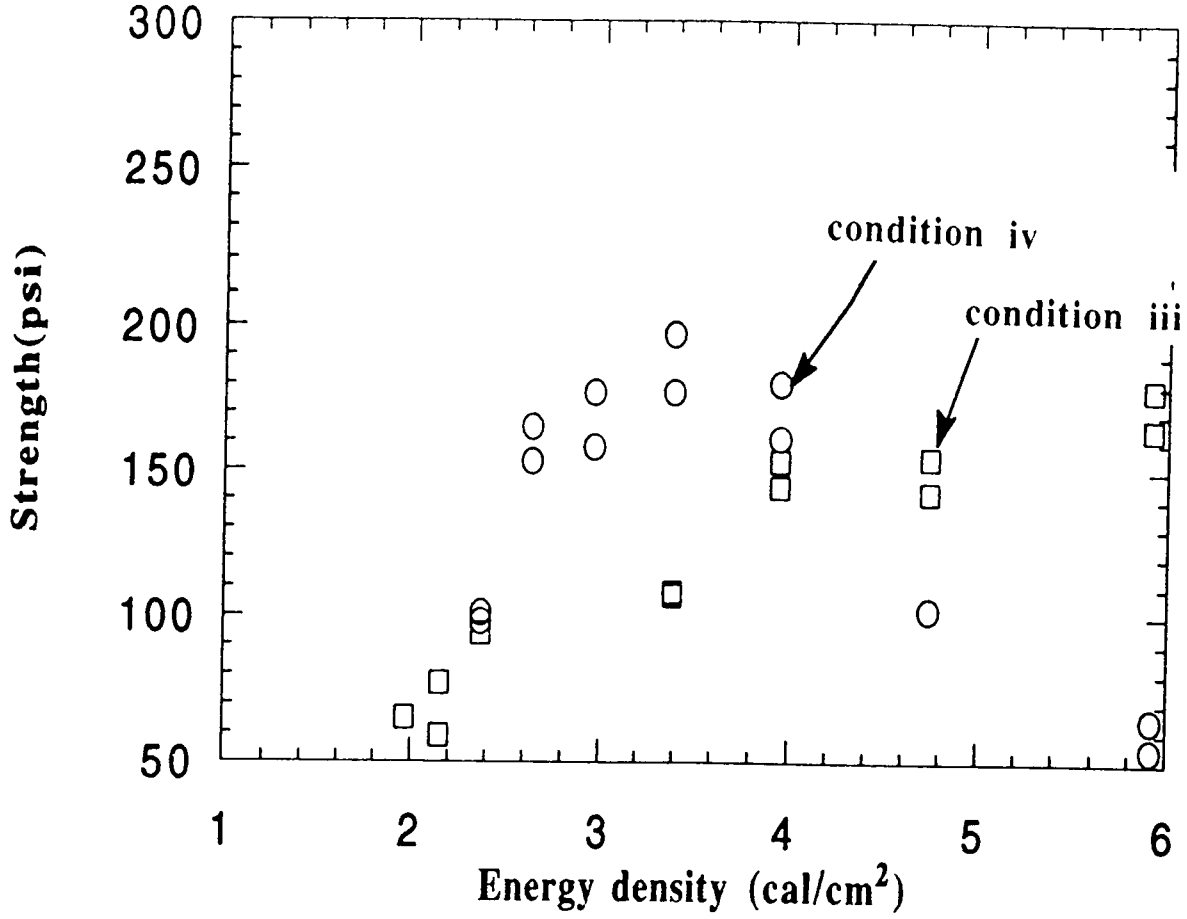

Figure 5. Strength of samples from 15μm alumina coated with copolymer built along width.

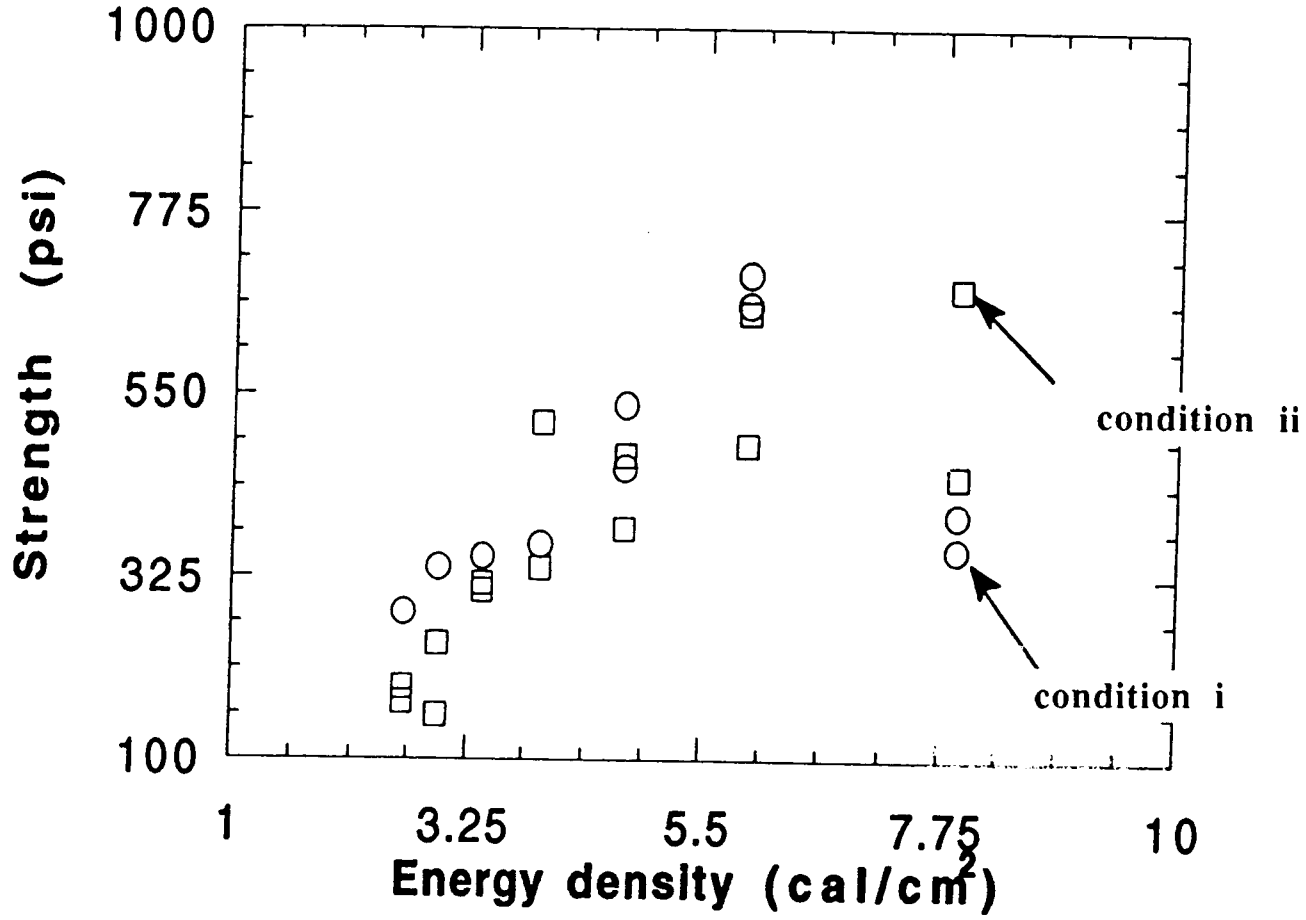

Figure 6. Strength of samples from agglomerated 2μm alumina mixed with PMMA built along thickness.

densities the strength decreases for reasons stated before. Once again it may be seen that when the scan lines are longer the green strength obtained at lower energy densities is lower. Again the peak in the strength vs. energy density plot occurs at a higher energy density for the parts made with longer scanlines.

SLS of agglomerated 2μm alumina mixed with 30 V% PMMA.

Specimens for bend-strength were made from this mixture in the four orientations described above. For specimens built along thickness, conditions (i) and (ii), Fig.6 it may be seen that the maximum strength is higher than that obtained for the 15μm alumina spray-dried with copolymer. This is due to the fact that the alumina agglomerates are much larger than 15μm and hence have a lower surface area to be wet by the polymer. The polymer content is also slightly higher. The variation of green strength with energy density follows similar trend as in the previous case with the strength increasing with energy density at lower energy densities. The peak in the strength vs. energy density plots occurs at a higher value of the energy density for the parts made with longer scan lines.

When specimens were built along the width at low energy densities the parts made with shorter scan lines, condition (iv) had higher green strength, Fig.7. A slight increase in density with increase in energy density may also be observed, Fig.8.

SLS of the mixture of agglomerates of 2μm alumina with 20 V% copolymer.

Specimens for bend strength measurement were made from this mixture by building only along the thickness direction. Three different scanning methods were employed. They were i) scanning along width, ii) scanning along length and iii) scanning alternate layers in length and width. The density increases slightly with increase in energy density, Fig.9. Scanning along the length produces samples of lower density compared to the other two modes at lower energy densities. In this case also it may be seen (Fig.10) that the strengths are lower for scanning along the length at low energy densities, as described earlier. The case of mixed (alternate) scanning results in samples of strength intermediate between the two other modes. This is to be expected since alternate layers will have higher and lower strengths corresponding to scanning in the other two modes.

Summary

Successful SLS was done on 2μm alumina particles by agglomerating the powders and mixing with polymer powder prior to Laser Sintering. Samples were built in different orientations in the SLS process. In all cases the samples that were built using shorter scan lines had a higher strength at lower energy densities. For both longer and shorter scan lines the green strength increases initially with increase in energy density, attains a peak and then starts decreasing with further increase in energy density due to polymer degradation. The peak in the case of samples built with longer scan lines occurs at a higher value of the energy density due to lower temperatures reached under those conditions.

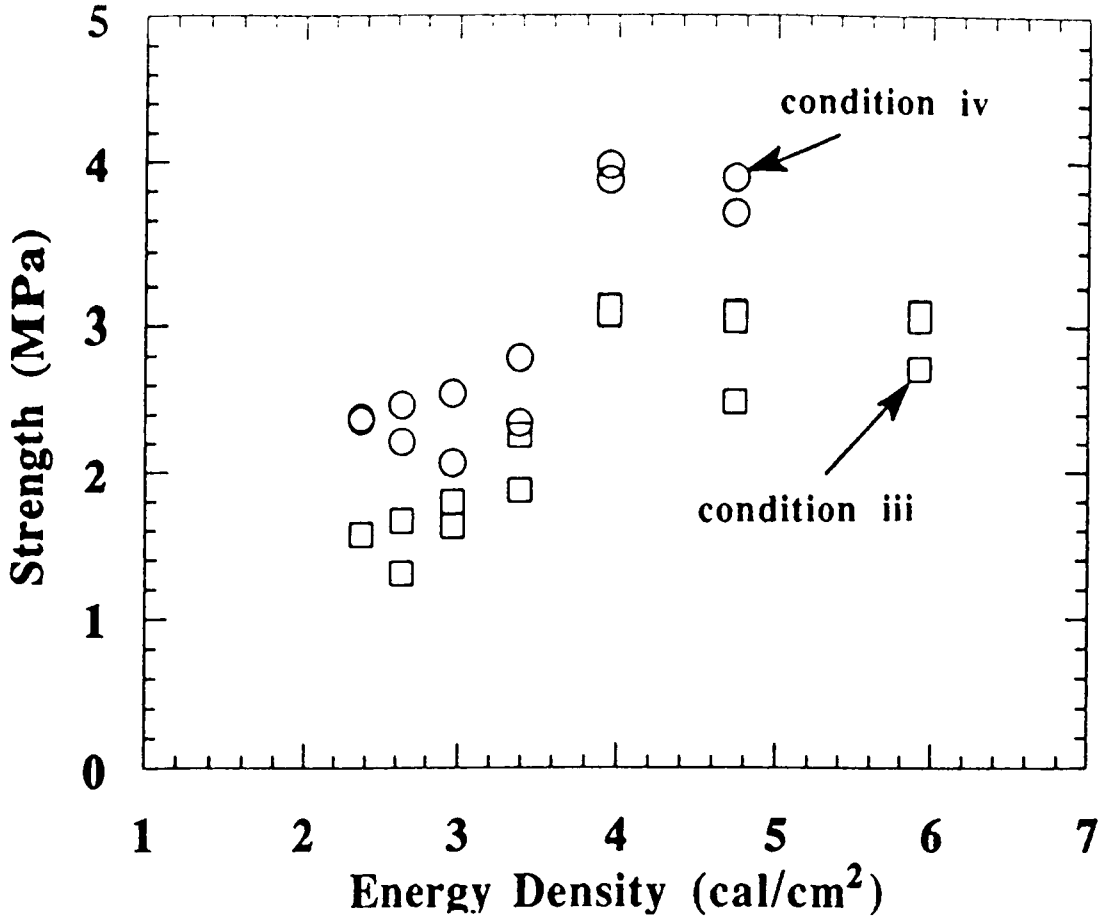

Figure 7. Strength of samples from agglomerated 2μm alumina mixed with PMMA built along width.

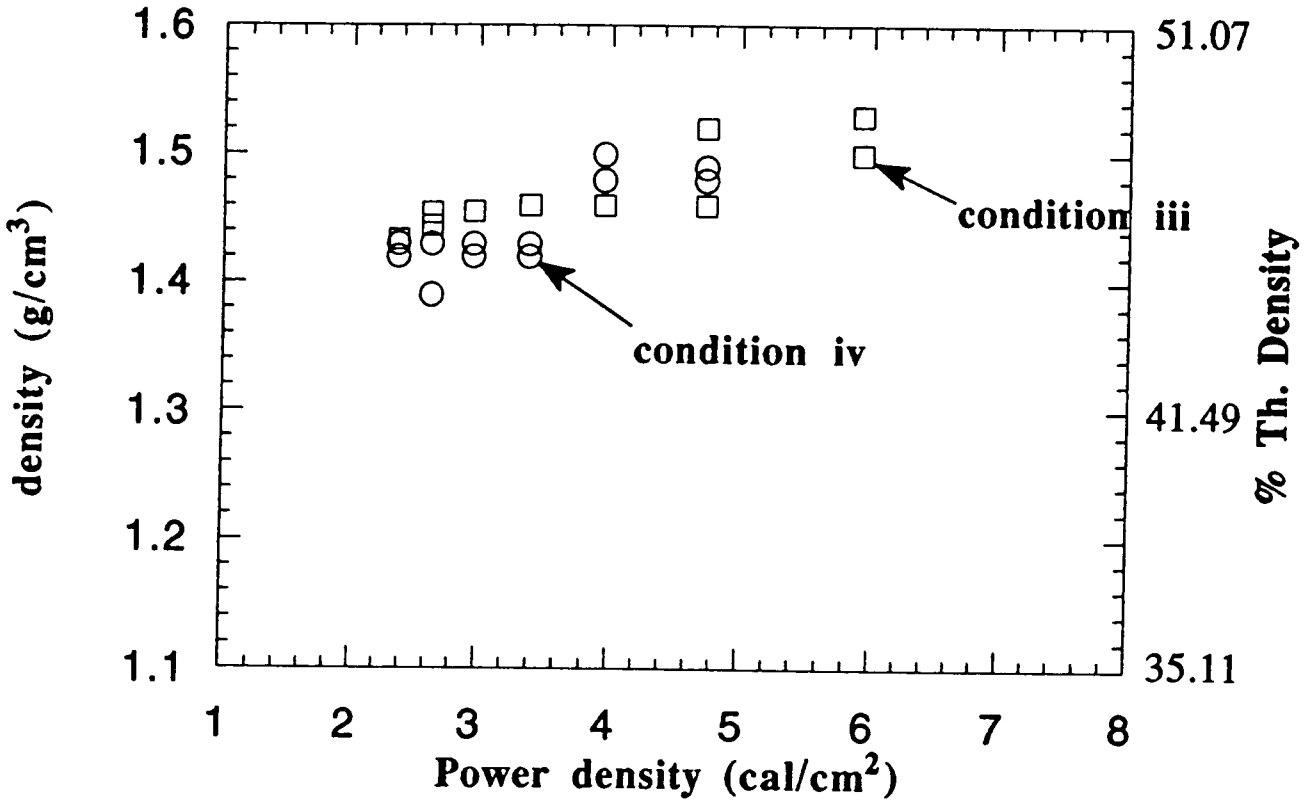

Figure 8. Density of samples as SLS for mixture of 2μm alumina mixed with PMMA.

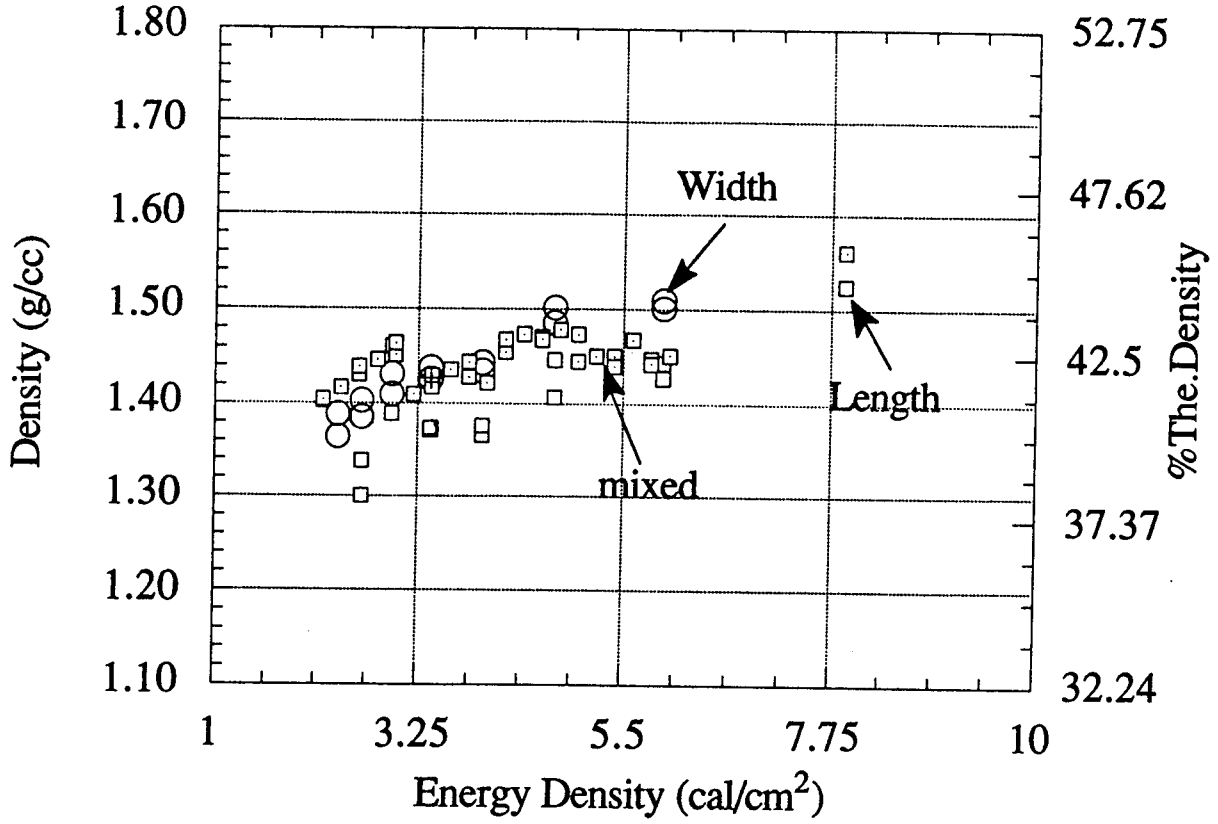

Figure 9. Density of samples from agglomerated 2μm alumina mixed with copolymer built along thickness.

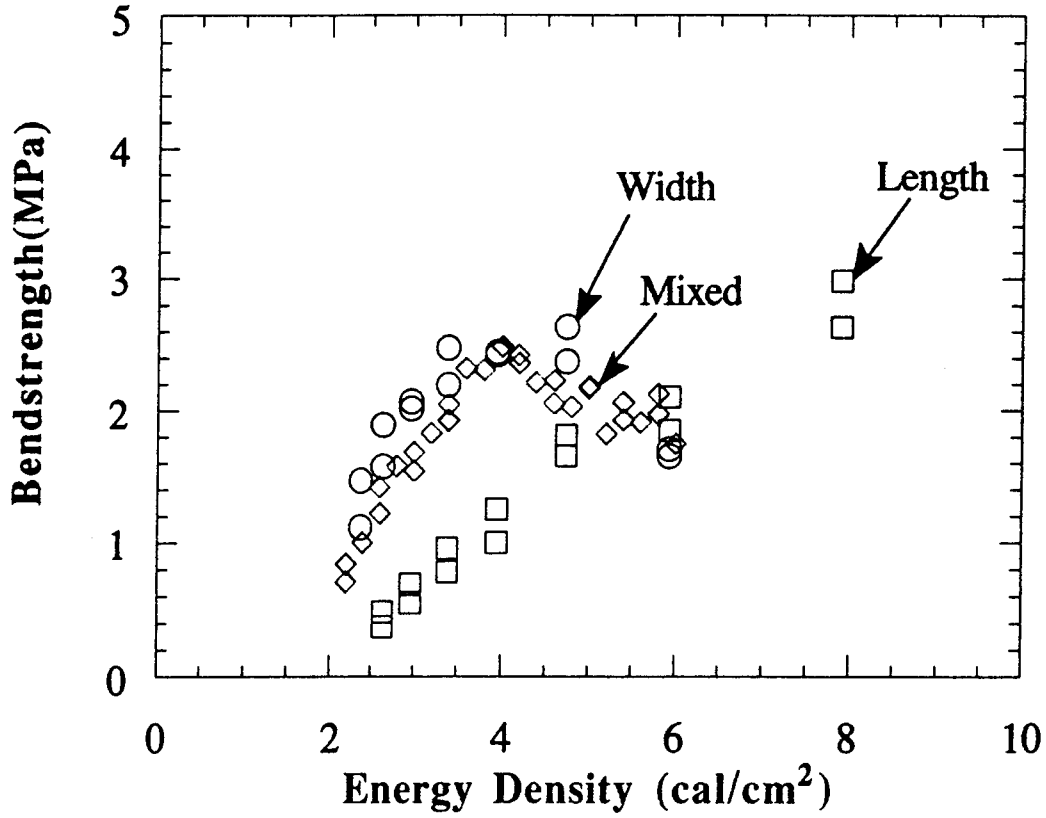

Figure 10. Strength of samples from agglomerated 2μm alumina mixed with copolymer built along thickness.

Acknowledgments

Financial support of this research by DARPA/ONR grant N00014-92-J-1394 is acknowledged.

References

1. J.C. Nelson, Ph.D. Dissertation, The University of Texas at Austin, 1993.
2. U. Lakshminarayan and H. L. Marcus, Proceedings of the Solid Freeform Fabrication symposium, Ed. H.L. Marcus, J.J. Beaman, D.L. Bourell, J.W. Barlow and R.H. Crawford, 1991, p. 205
3. U. Lakshminarayan and H. L. Marcus, Proceedings of the Solid Freeform Fabrication symposium, Ed. H.L. Marcus, J.J. Beaman, D.L. Bourell, J.W. Barlow and R.H. Crawford, 1992, p. 44
4. P.K. Subramanian, G. Zong and H.L. Marcus, ibid. p. 63
5. N.K. Vail and J.W. Barlow, ibid. p. 124
6. P.K. Subramanian, G. Zong, N.K. Vail, J.W. Barlow and H.L. Marcus, Proceedings of the Solid Freeform Fabrication symposium, Ed. H.L. Marcus, J.J. Beaman, D.L. Bourell, J.W. Barlow and R.H. Crawford, 1993, p. 350
7. N.K. Vail, J.W. Barlow, J.J. Beaman, H.L. Marcus and D.L. Bourell, Journal of Applied Polymer Science Vol.52, 1994, p. 789

Selective Laser Sintering of Alumina-Boron Oxide Composites

Insup Lee, A. Manthiram and H. L. Marcus
Center for Materials Science and Engineering, ETC 9. 104
The University of Texas at Austin
Austin, TX 78712

Abstract

The selection of an optimum composite system for selective laser sintering (SLS) is based on materials properties such as the melting point and the wettability between the components in the composite powder. The alumina-boron oxide composite system is attractive for SLS because the presence of the low melting component B_2O_3 (melting point 450° C) can enhance sintering. A better wetting of solid alumina powder by molten boron oxide can also aid densification process. The alumina-boron oxide composite system has been investigated by SLS and selective laser reactive sintering (SLRS). The role of boron oxide content as a binder, laser power density, and secondary heat treatment on the microstructure and mechanical properties is discussed.

Introduction

Solid freeform fabrication (SFF) techniques have recently been developed to overcome some of the barriers of conventional manufacturing techniques, such as difficulties in tooling complex-shaped ceramic parts and long production time in fabricating prototypes [1]. Selective laser sintering (SLS) is a form of SFF technique and employs a focused laser beam which is controlled by a CAD data base to selectively scan the powder bed surface and bind the loose powder [2].

The two-phase powder approach to SLS, which involves binding high temperature ceramics such as alumina and silicon carbide with a low melting inorganic binder, is a promising technology to fabricate ceramic composite parts [3,4,5]. The selection of an optimum materials system for this approach depends on materials properties such as the melting point of the binder material and interparticle wetting between the components in the composite powder [6].

It is known that the role of boron oxide in borosilicate glasses is to reduce the thermal expansion coefficient and to improve workability by decreasing the viscosity [7]. The low viscosity of boron oxide is attributed to its linked ring structure, since there is a high probability that the bonds between rings are more susceptible to failure than the bonds within the rings [8].

The selection of the system Al_2O_3-B_2O_3 for SLS provides an advantage in densification. Boron oxide has a low melting point (450° C) and the liquid generated due to the local melting of B_2O_3 powder during laser beam irradiation can aid the sintering process. In addition, the molten boron oxide completely envelops the neighboring solid alumina particles due to its low viscosity and better wetting.

Materials and Experimental Procedure

High purity, electronic grade 15μm, aluminum oxide powder provided by Lanxide Corporation and a 60 mesh 99% boron oxide powder from Johnson Mathey are the starting materials.

Fig. 1 shows the overall steps associated with SLS process and material characterization. The initial boron oxide powder of 250μm was ground by a Szegvari attritor system and sieved to less than 75μm. Alumina and boron oxide powder blends in various ratios by weight were baked out in a vacuum oven at 120° C for 30 hours. Pre-thermal treatment caused the powder blends to form weak powder cakes, which were subsequently broken and sieved. Baked-out powder blends were immediately sintered in a SLS system of the University of Texas at Austin. Test specimens with

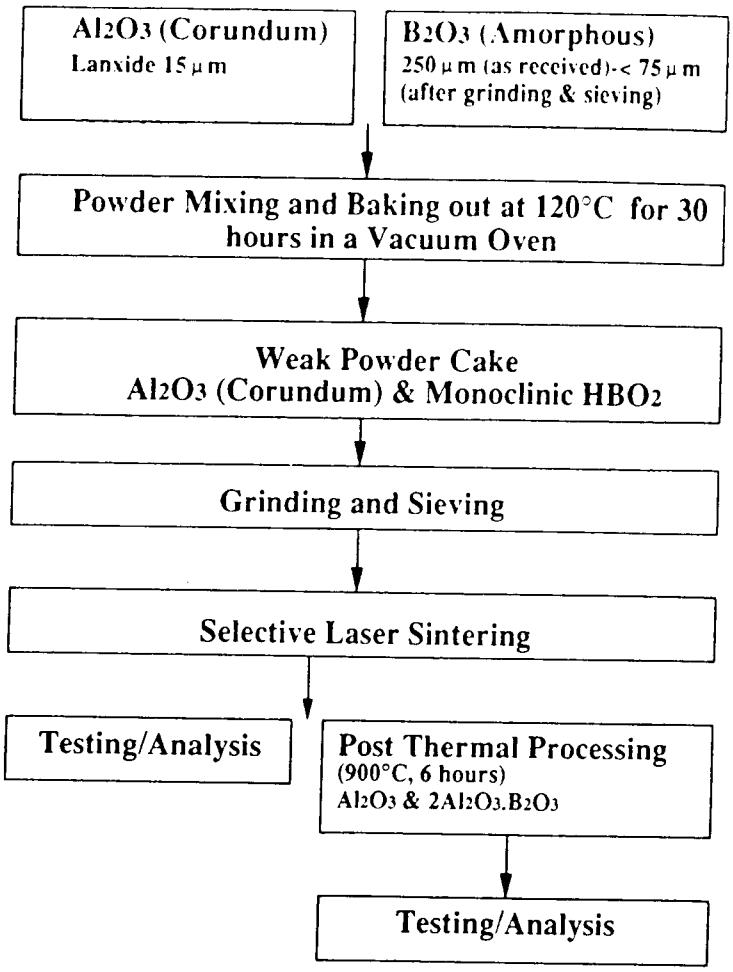

Figure 1. Flow chart for selective laser sintering of alumina-boron oxide composites

dimension of 1"x3"x0.25" were fabricated in an inert nitrogen environment using the operational parameters listed in Table I.

Table I. SLS operational parameters

Laser Power (W)	Bed Temperature (°C)	Scan Spacing (mils)	Layer Thickness (mils)	Scan Speed (inch/sec)
14-16.5	80-100	5	8	12.5-47

The strength of green and samples fired at various temperatures for 6 hours was determined by 3-point bend test using a Instron constant displacement rate machine. Density was obtained by direct measurement of dimension and mass. Identification of phases and microstructural evolution at every step of processing was carried out by x-ray diffraction analysis and SEM.

Results and Discussion

Fig. 2 shows the phase transformation of the initial boron oxide upon reaction with atmospheric water. The as received boron oxide is amorphous. It reacts with moisture in air and transforms into boric acid (H_3BO_3) very quickly. As a result, without baking out before laser sintering, the starting powder blend for laser sintering is a mixture of alumina, amorphous boron oxide and boric acid. Because boric acid has much lower melting point (170°C) than boron oxide (450°C), it causes a weak bed cake through the whole powder bed during SLS process with bed heating

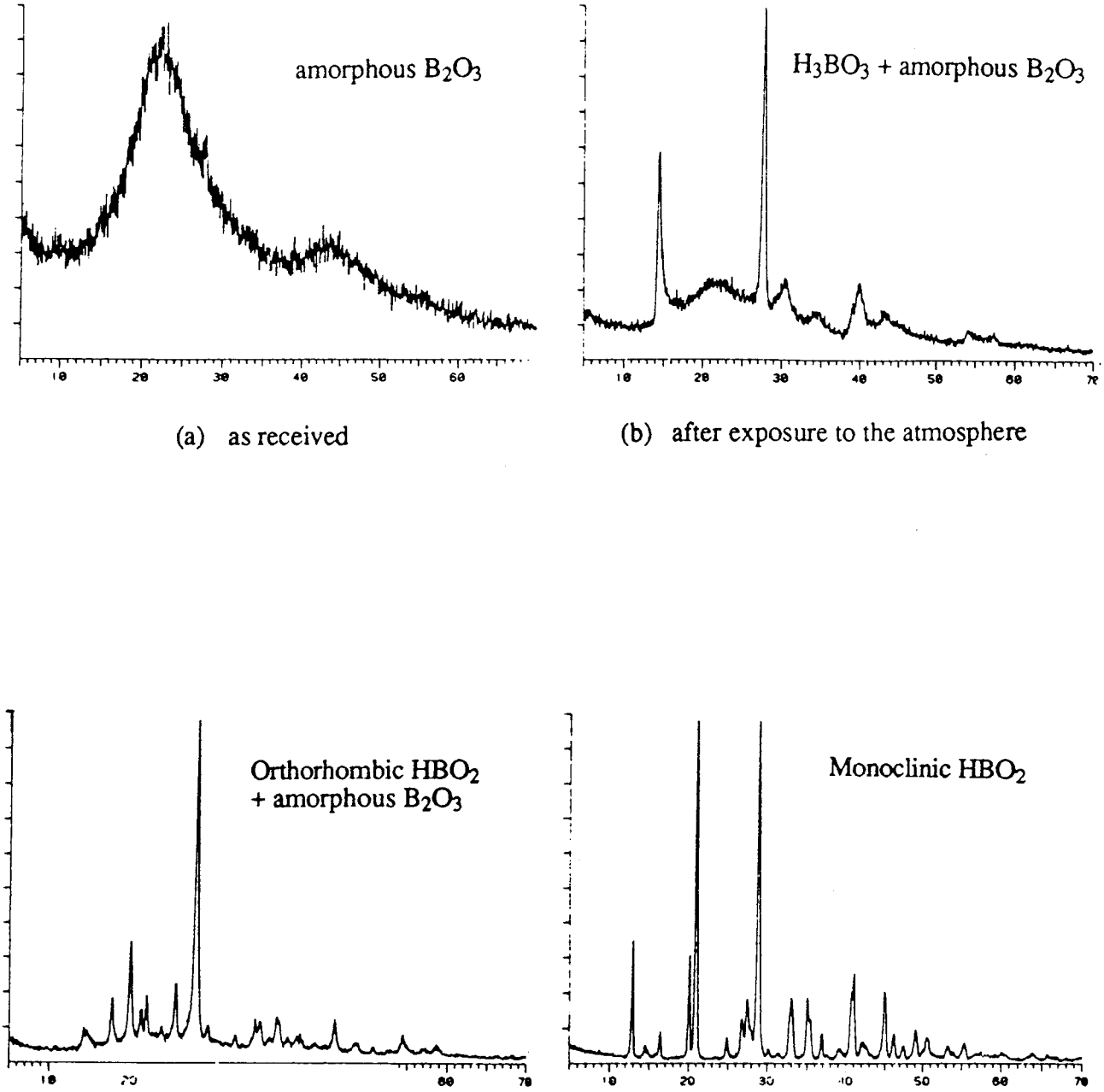

(a) as received

(b) after exposure to the atmosphere

(c) after baking out in a vacuum oven at 120°C for 13 hours

(d) after baking out in a vacuum oven at 120°C for 30 hours

Figure 2. X-ray diffraction analysis showing phase transformation of the initial boron oxide

around 80°C. The cake paralyzes the powder delivery and leveling system. Without employing bed heating system, it was possible to avoid the bed caking. However, curling of the previously sintered layers takes place, making powder leveling difficult due to the displacement of those layers.

In order to overcome bed caking and curling of sintered layers, the boric acid in the initial powder blend must be removed. Dehydration of boric acid gives different forms of metaboric acid HBO_2 or boron oxide B_2O_3 depending on the temperature. Table II shows the physical properties of various forms of metaboric acid HBO_2 [7].

Table II Physical properties of crystalline metaboric acid HBO_2

	CN* of B	Density (g/cm^3)	Melting Point (°C)
Orthorhombic	3	1.784	176
Monoclinic	3 and 4	2.045	201
Cubic	4	2.487	236

* CN refers to coordination number

Careful dehydration of boric acid at 120°C in a rough vacuum oven for 30 hours and slow quenching after bake-out yields monoclinic metaboric acid HBO_2 whose melting point is 201°C. Orthorhombic HBO_2 can be generated after 13 hours of heat treatment under the same conditions. It is found that monoclinic HBO_2 avoids the bed caking phenomenon with powder bed heating at 80°C and reduces the curling problem significantly during SLS process.

Fig. 3 shows the effect of the binder content on bend strength of both green and fired (at 900°C for 6 hours) composites. The bend strength of the composites increases as the binder content increases since all the ceramic interparticle bonds that provide the strength of the composites originate from the melting of the binder and the coating of ceramic (alumina) particles during laser beam irradiation.

The effect of laser power density on bend strength is also shown in Fig. 3. Power density is defined as laser power / (scan spacing x scan speed) [9]. At lower power density, the green composites show poor strength due to insufficient melting and flowing of the binder compared to at higher power density where molten binder coats the ceramic particles completely as revealed by SEM. Similarly, the bend strength of fired parts fabricated with 25 and 20 wt.% boron oxide powder blends is proportional to the power density. Because at higher power density, the laser beam locally melts the binder sufficiently, the binder flows and encapsulates more ceramic particles than at lower power density as revealed by SEM. As a result, the green and fired density increases as the power density increases. Therefore, at higher power density, the fired composites show higher strength due to a higher density (Fig.4). However, bend strength of fired test bars made with 15 wt.% boron oxide is independent of power density. For this system, it was required that the process be done at higher bed temperature (100°C) and at higher power density in order to melt the small amount of the binder completely and bind ceramic particles together. Consequently, there might be a threshold power density to melt the whole binder thoroughly and fabricate green parts which can keep the shape. Above this value, the strength of the fired parts will almost be independent of power density since there is no more additional binder which will coat the ceramic particles.

Fig. 5 illustrates the effect of firing temperature on the mechanical properties of parts fabricated with 25 wt.% boron oxide powder blends. At intermediate firing temperatures at around 800-1100°C, the test bars show higher bend strength due to the formation of aluminum borate ($2Al_2O_3 \cdot B_2O_3$) at the surface of the alumina particles by the reaction of alumina and boron oxide at around 800° C. According to X-ray diffraction analysis (Fig. 6), the amount of $2Al_2O_3 \cdot B_2O_3$ increases relative to that of alumina as the firing temperature increases up to 1100°C. At 1200°C, $9Al_2O_3 \cdot 2B_2O_3$ phase is formed by the reaction: $2\ (2Al_2O_3 \cdot B_2O_3) + 5Al_2O_3 \rightarrow 9Al_2O_3 \cdot 2B_2O_3$ [10]. Below 700°C, it was found that there was no substantial reaction. The bend strength of samples fired at 1300, and 1500°C decreases due to the decomposition of the compound

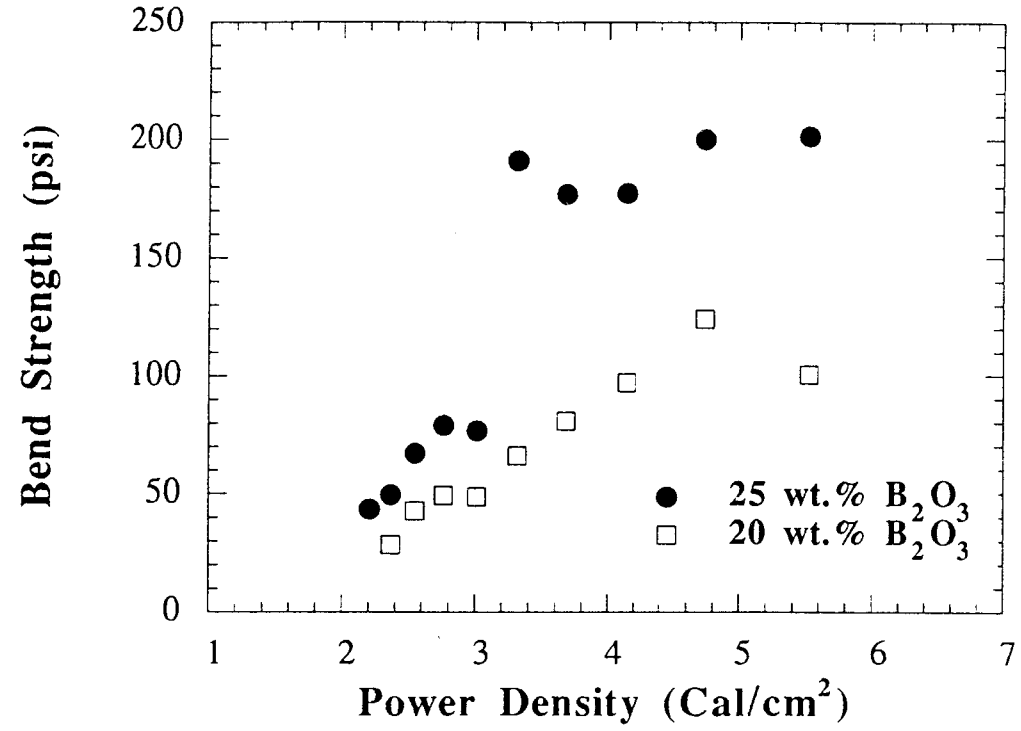

(a) green parts

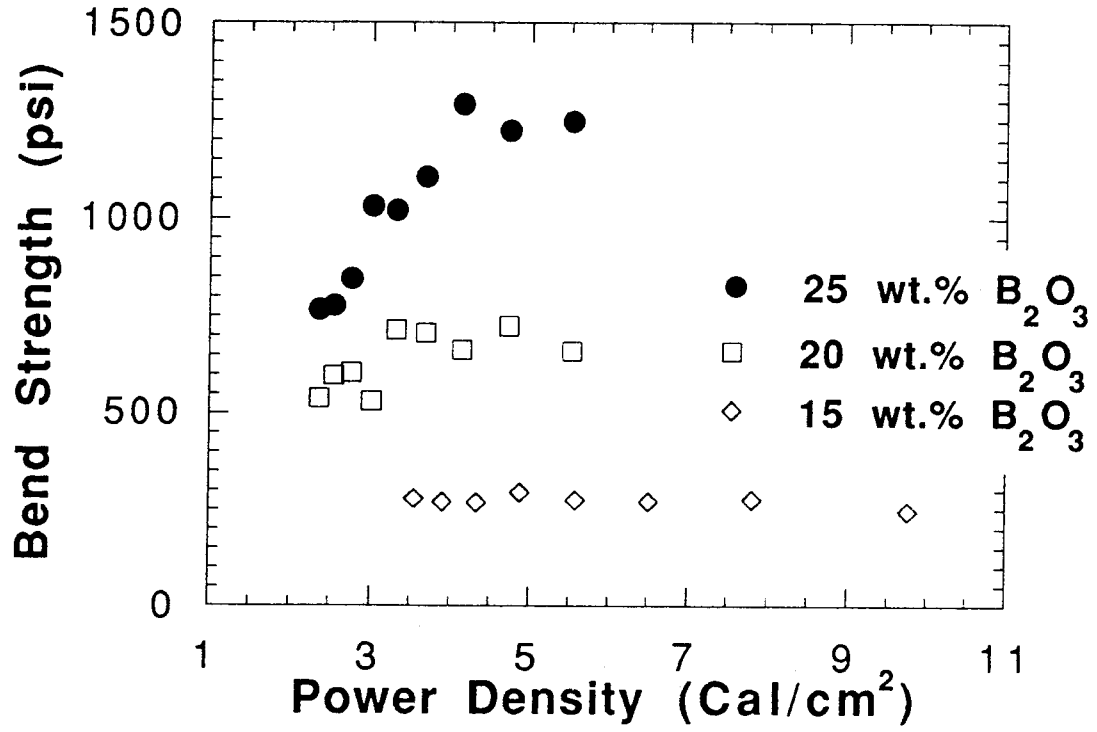

(b) after fired at 900°C for 6 hours

Figure 3. Bend strength of test coupons fabricated with Lanxide 15 μm alumina-boron oxide powder blends

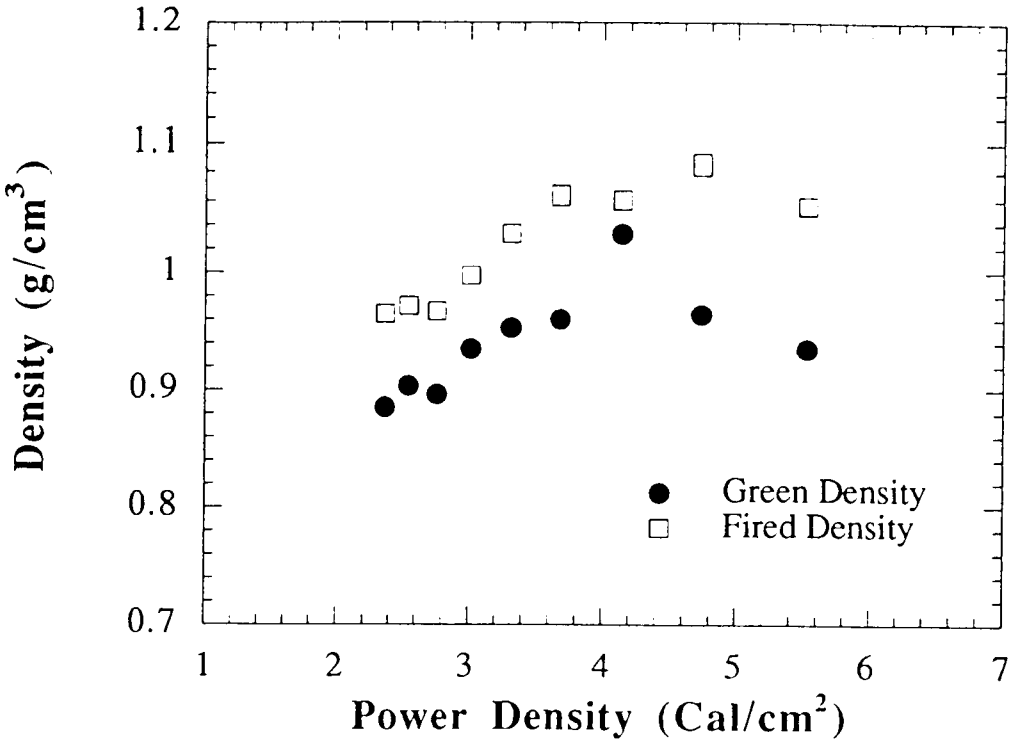

(a) Effect of laser power density on the density

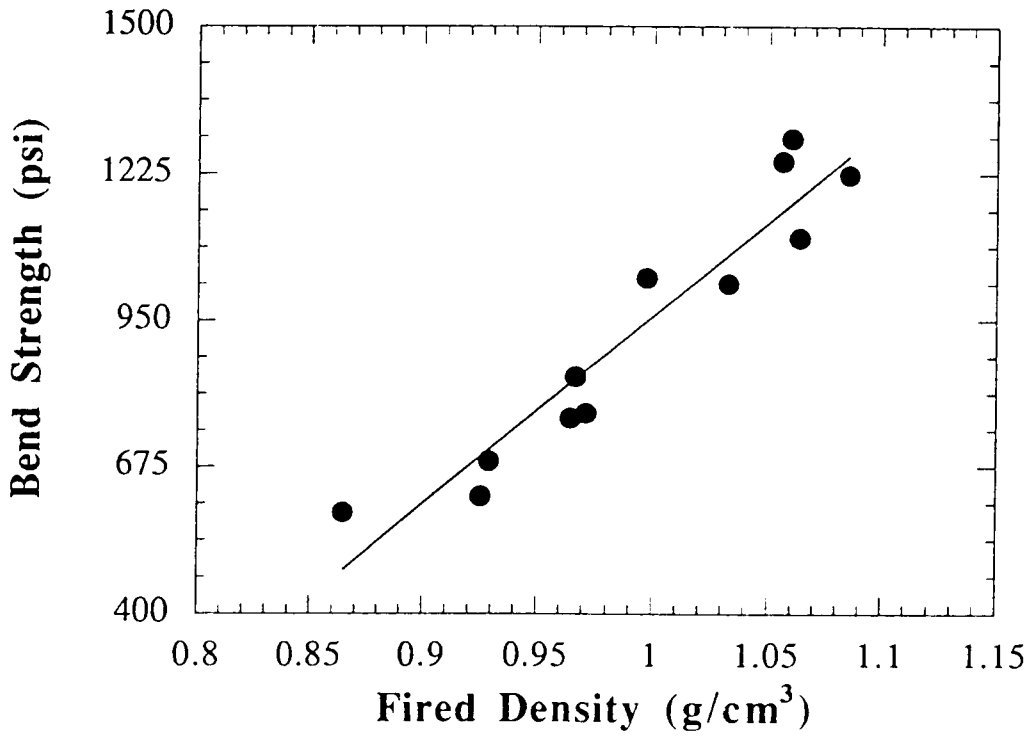

(b) Effect of fired density on the bend strength

Figure 4. Mechanical properties of green samples and samples, fired at 900°C for 6 hours, made from alumina-25 wt.% boron oxide powder blend

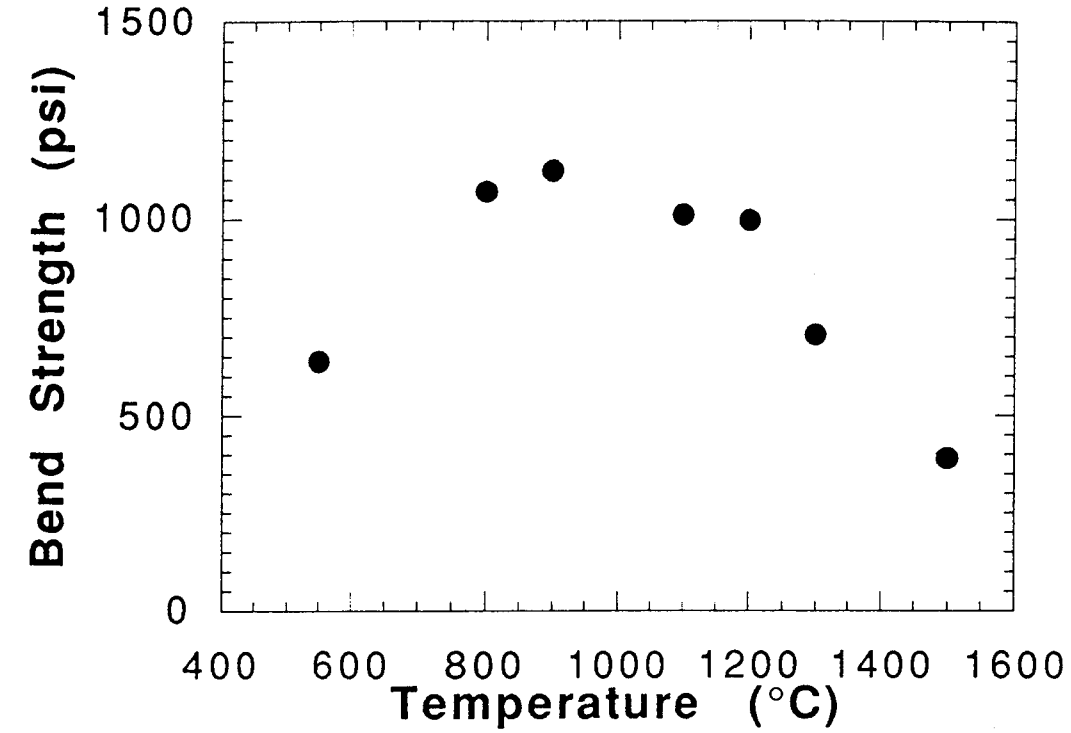

(a) Bend strength

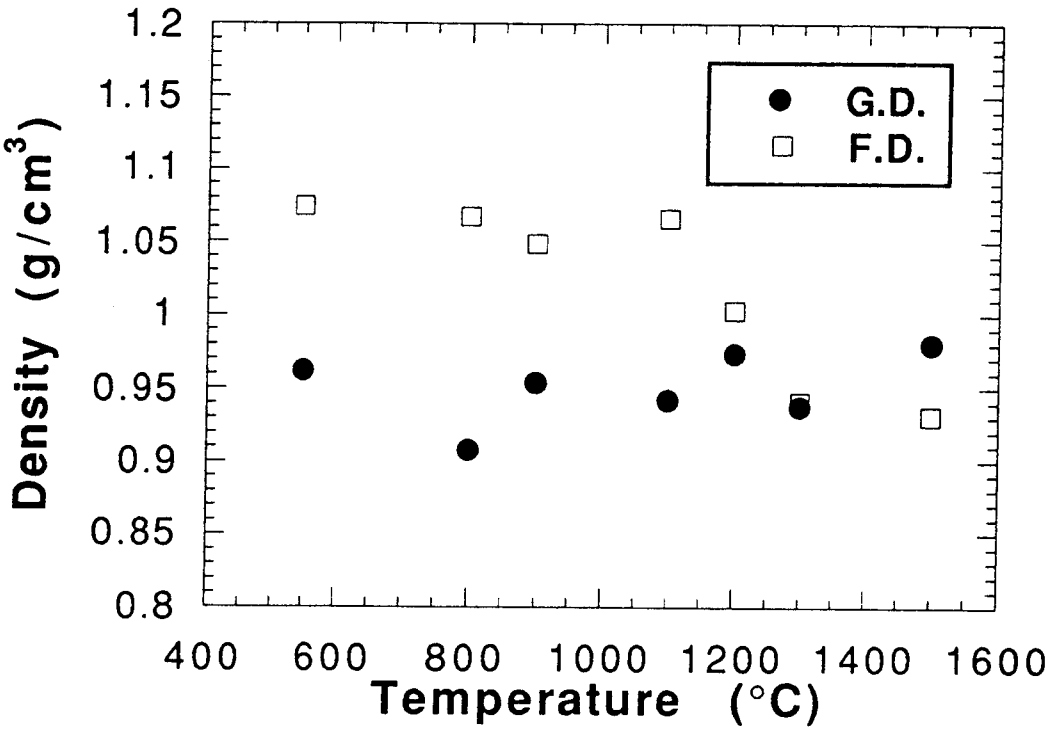

(b) Density

Figure 5. Effect of firing temperature on the mechanical properties of samples made from alumina-25 wt.% boron oxide powder blend

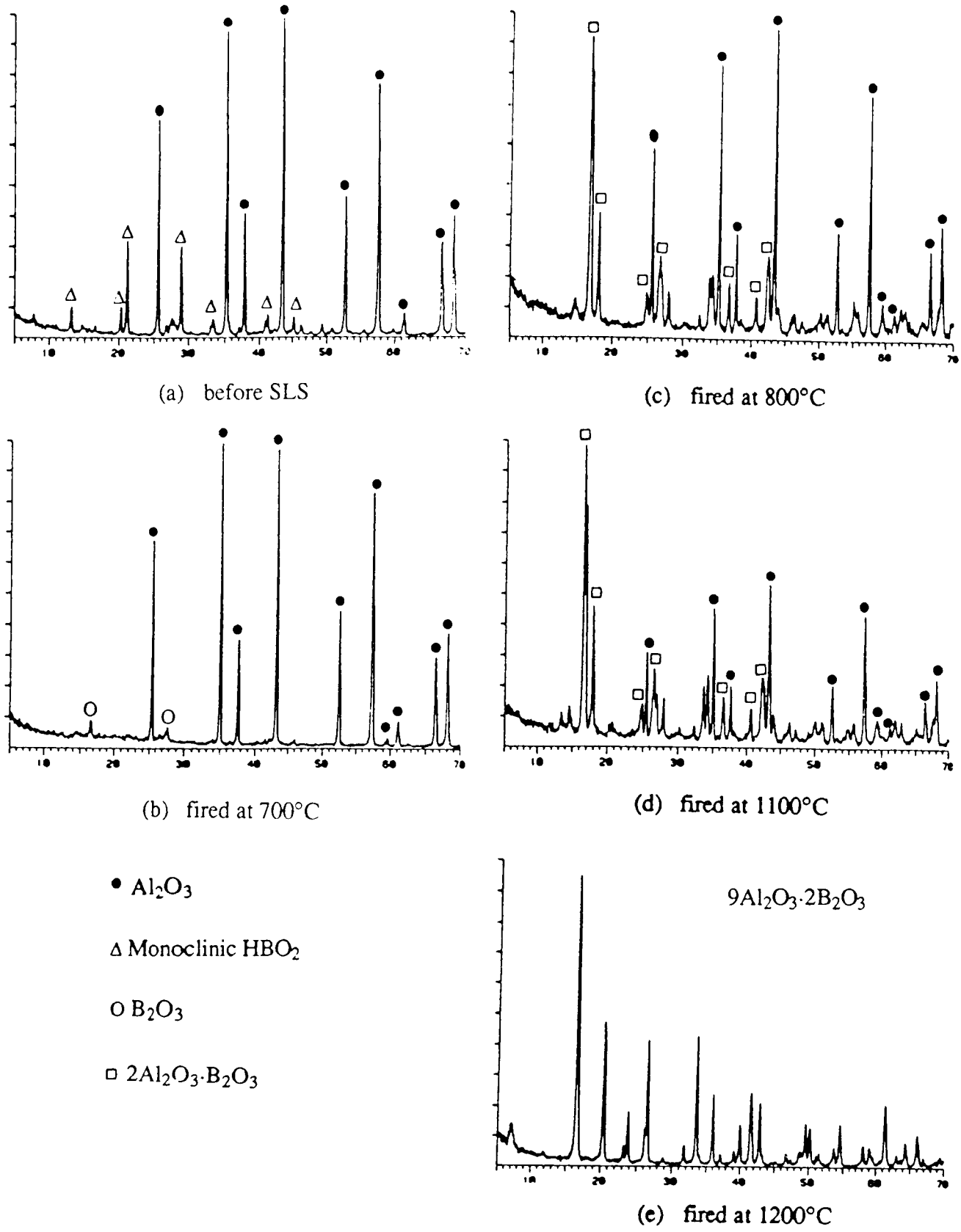

Figure 6. X-ray diffraction analysis of alumina-25 wt.% composites fired at various temperatures for 6 hours

$9Al_2O_3 \cdot 2B_2O_3$ [11]. Below 1300°C, secondary heat treatments increase the density, whereas above 1300°C, fired density is lower than the green density due to the increase in porosity associated with the decomposition of the $9Al_2O_3 \cdot 2B_2O_3$ phase (Fig. 5(b)).

Summary

It was demonstrated that both a composite body Al_2O_3-$2Al_2O_3 \cdot B_2O_3$ and a monolithic material $9Al_2O_3 \cdot 2B_2O_3$ could be successfully fabricated by selective laser sintering and reactive sintering of the material system Al_2O_3-B_2O_3. The bend strength of the composite body increases as the binder content increases. At higher laser power density, the composites show higher bend strength due to higher density. At intermediate firing temperatures around 800-1100°C, test bars show higher bend strength due to the formation of aluminum borate ($2Al_2O_3 \cdot B_2O_3$) at the surface of the alumina particles by the reaction of alumina and boron oxide at around 800°C.

Acknowledgments

Financial support from DARPA-ONR grant N0014-92-J-1394 is gratefully acknowledged.

References

1. Marcus, H.L., Beaman, J.J., Barlow, J.W. and Bourell, D.L. (1990, April) From computer to component in 15 minutes: The integrated manufacture of three dimensional objects. Journal of Metals, pp. 8-10.
2. Bourell, D.L., Marcus, H.L., Barlow, J.W. and Beaman, J.J. (1992). Selective laser sintering of metals and ceramics. The International Journal of Powder Metallurgy, 28, 369.
3. Lakshminarayan, U., Marcus, H.L., (1992, August). An experimental study of relationship between microstructure and mechanical properties of a ceramic composites fabricated by selective laser sintering. In Marcus, H.L., Beaman, J.J., Barlow, J.W., Bourell, D.L. and Crawford, R.H. (Eds.), Proceedings of the Solid freeform fabrication symposium, (pp. 44-53). Austin, Texas: University of Texas Press.
4. Subramannian, P.Kamatchi, Zong, Guisheng and Marcus, H.L.(1992, August). Selective Laser Sintering of Ceramic Composites. In Marcus, H.L., Beaman, J.J., Barlow, J.W., Bourell, D.L. and Crawford, R.H. (Eds.), Proceedings of the Solid freeform fabrication symposium, (pp. 63-71). Austin, Texas: University of Texas Press.
5. Lakshminarayn, U. (1992, May). Ph.D. Dissertation, University of Texas, Austin.
6. German, R. M. (1984). Powder metallurgy science. Princeton, New Jersey: Metal Powder Industries Federation.
7. Greenwood, N. N., Earnshaw, A. (1984). Chemistry of the elements. Oxford: Pergamon Press.
8. Doremus, R. H. (1973). Glass Science. New York. John Wiley & Sons, Inc.
9. Nelson, J.C., Vail, N.K., Barlow, J.W. (1993, August). Laser Sintering Model of Composite Materials. In Marcus, H.L., Beaman, J.J., Barlow, J.W., Bourell, D.L. and Crawford, R.H. (Eds.), Proceedings of the Solid freeform fabrication symposium, (pp. 360-369). Austin, Texas: University of Texas Press.
10. Ray, Siba P. (1992). Preparation and Characterization of Aluminum Borate. J. Am. Ceram. Soc., 75, 2605-609.
11. Rymon-Lipinski, T., Hennicke, H.W., Linaenbera, W. (1985). Decomposition of Aluminum oxide-Boron oxide system at high temperatures. Kerammische Zeitschrift, 37(9), 450-453.

Silicon Carbide Shapes By Selected Area Laser Deposition Vapor Infiltration

Birmingham, B.R., Tompkins, J.V. and Marcus, H.L.
Center for Materials Science and Engineering
The University of Texas at Austin
Austin, TX 78712

Abstract

Selected Area Laser Deposition Vapor Infiltration (SALDVI) is a unique combination of selected area laser deposition, chemical vapor infiltration and layered powder handling techniques that can be used to fabricate silicon carbide (SiC)/SiC composite shapes. This paper discusses a SALDVI process under investigation which selectively infiltrates SiC powder with SiC generated by decomposition of a gas precursor under a scanned laser beam. A general description of the process, including some of its inherent advantages is presented. Experimental results which explore beam interaction, powder size and infiltration time effects are also presented.

Introduction

Selected Area Laser Deposition Vapor Infiltration (SALDVI) is a new solid freeform fabrication (SFF) technique that has the potential to produce both monolithic and composite metal and ceramic shapes. SALDVI uses the selected area laser deposition (SALD) technique [1] to provide material used for simultaneous localized chemical vapor infiltration . The process begins by generating a two dimensional pattern on a powder substrate with a scanned laser. The high temperature at the laser's focal point pyrolitically decomposes a gas precursor(s), and the products of decomposition locally infiltrate and bond the powder particles together. After each two dimensional pattern has been scanned and infiltrated, a fresh layer of powder is spread on top of the previous infiltrated layer using technology developed for selective laser sintering [2]. The process is repeated until the desired three dimensional shape is built. The finished part has a composite structure consisting of the starting powder bonded into a matrix of vapor deposited material.

The SALDVI process has great potential due to several inherent features. These features, discussed below, include the potential to produce fully dense shapes without post processing, a wide materials selection, and the elimination of dimensional constraints associated with traditional chemical vapor infiltration techniques.

High density has been one of the main goals of most SFF processes because of the direct relationship between density and mechanical integrity. Many SFF processes must include secondary heat treatments to produce shapes with satisfactory density. This adds

time and cost to production, and complicates the initial build of the shape by forcing consideration of shrinkage effects [3,4]. The SALDVI process has the potential to make fully dense shapes without post processing because it incorporates vapor deposition, a process that can inherently produce theoretically dense material.

The SALDVI process has the potential to produce shapes from a wide range of materials. Gas precursors have been developed, particularly by the microelectronics industry, for the vapor deposition of a variety of elements and compounds including such useful materials as Al, AlN, Al_2O_3, Si, SiO_2, Si_3N_4, SiC, Ti, TiN, TiO_2, Zr, ZrO_2, Hf, HfC, W, WC, Co, Fe, Ni, Cr and Cu [5]. Many of these precursor systems are candidates for laser deposition, and therefore potential candidates for the SALDVI process. With the proper selection of gas precursor(s) and powder bed material(s), a variety of metal/metal, metal/ceramic, and ceramic/ceramic structures could be produced.

The SALDVI process could also eliminate the dimensional constraints inherent to traditional chemical vapor infiltration (CVI) techniques. Traditional CVI processes are limited to small shapes because the outside of the shapes tend to seal and prevent further infiltration before the interior is fully dense [6]. More complex CVI processes are currently under investigation such as forced flow reverse gradient and microwave heating that impose a reverse temperature gradient on the preform, i.e. heat from the inside out, to improve the infiltration of larger shapes [7,8]. The SALDVI process avoids part size limitations by infiltrating consecutive thin layers to build shapes. This makes possible the production of shapes with dimension limited only by machine size.

Silicon Carbide/Silicon Carbide SALDVI

Initial work characterizing SALDVI has concentrated on producing SiC/SiC composite shapes using SiC powders and a SiC gas precursor. SiC powder was chosen because of the material's desirable engineering properties, and its 2560°C decomposition temperature [9,10]. SiC's high decomposition temperature makes it stable under the laser beam, thereby minimizing any melting or decomposition of the powder that would complicate the vapor infiltration process. Tetramethylsilane (TMS) was chosen as the gas precursor because of its demonstrated ability to produce SiC in a laser deposition process [11], and its ease of handling. TMS is a liquid at room temperature with a vapor pressure that is sufficient for vapor deposition processes.

Preliminary tests were run to establish basic process parameters for use in multi-layer shape fabrication. The effect of beam interactions on power delivered to the surface, the effect of powder size on infiltration behavior and the degree of infiltration versus time are reported on in this paper.

Beam effects

Absorption of laser energy by the precursor gas is an important process consideration because it directly reduces laser power at the powder surface. Organic molecules such as TMS tend to absorb infrared energy through molecular vibration/photon interactions [12]. The absorption coefficient of TMS was determined experimentally by directing the SALDVI CO_2 laser beam through a chamber filled to various pressures of the precursor gas. Laser power leaving the chamber was measured using a standard power meter and compared to the power entering the chamber. Experimental data fit the Beer-Lambert relationship, which describes the transmission of energy through a medium as an exponential function of gas pressure and distance.

$I = I_0 \exp(-\alpha p x)$ = transmitted intensity , in watts

I_0 = initial intensity , in watts

$\alpha = 3.62E-4$ $Torr^{-1}cm^{-1}$ = absorption coefficient

p = pressure, in Torr

x = absorption length, in centimeters

Reflectivity of the surface is also an important process consideration because reflected laser power is not available for powder/infiltrant heating. The reflectivities of SALDVI candidate materials were experimentally determined using the SALDVI CO_2 laser and a standard integrating sphere. The beam was directed onto the test material surface, and the power reflected was collected by the integrating sphere and recorded. The ratio of reflected power to beam power is reflectivity.

Material	**Reflectivity**
0.6 -0.8 μm SiC powder	0.42 - 0.50
12μm SiC powder	0.25 - 0.45
100μm SiC powder	0.20 - 0.50
hot-pressed SiC (solid)	0.16 - 0.60

Table 1: Reflectivity for powder and solid SiC surfaces, CO_2 wavelength energy.

Note that the two reflectivity values reported for each material do not represent a continuous range in the data, but rather the high and low values of a periodic fluctuation observed for all materials tested except the 0.6 - 0.8μm powder. The periodic fluctuations in reflectivity, most apparent in the solid SiC data, see Figure 1, are caused by CO_2 laser mode hopping. An unstabilized CO_2 laser has a nominal output wavelength of 10.6μm, but can periodically mode "hop" through several different modes. At each mode the laser produces

a different wavelength, with wavelengths ranging from 10.55μm to 10.65μm for the SALDVI laser. SiC reflectivity dramatically increases from 0.25 to 0.8 as wavelength increases from 10μm to 11μm [13]. As a result, the reflectivity of the surface changes significantly as the laser output wavelength changes.

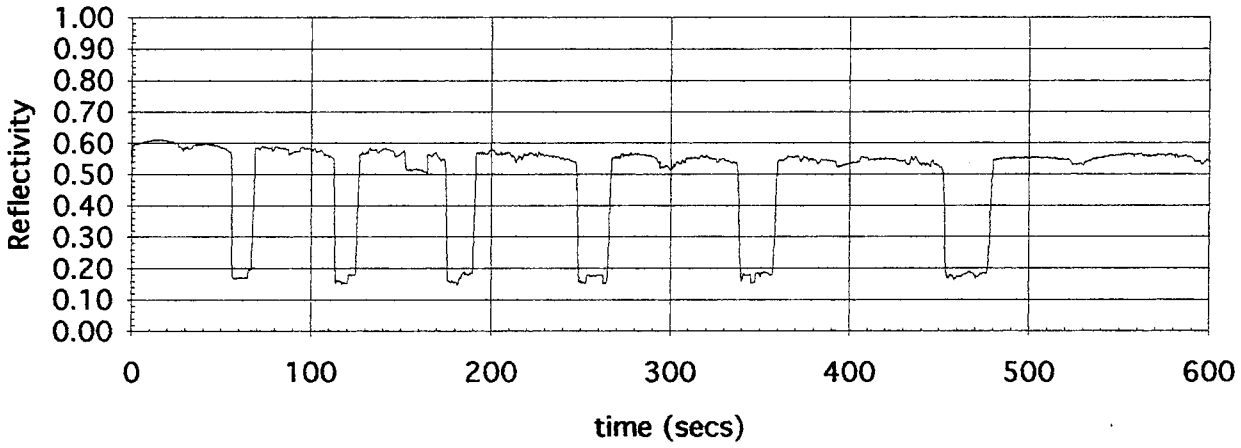

Figure 1: Reflectivity versus time, hot-pressed β-SiC, 10.6μm (nominal) wavelength.

Powder size effect

Figures 2 and 3 are cross-sections of infiltrated 12μm and 100μm powders. A static beam was used with constant laser power and gas pressure.

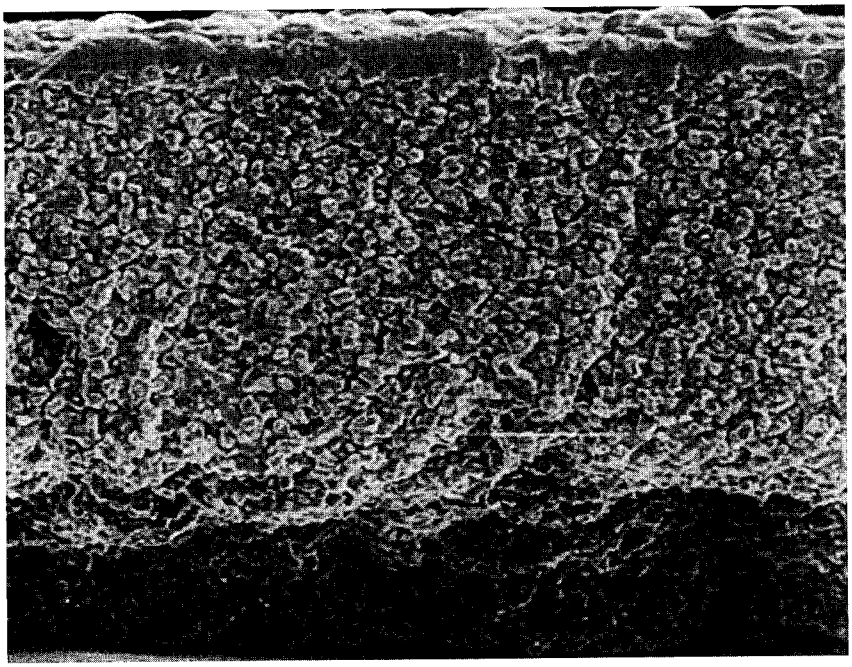

Figure 2: Static beam infiltration - infiltration time 30 seconds, 15μm powder, 25Torr TMS gas pressure, 20watts laser power, cross-section, 200X.

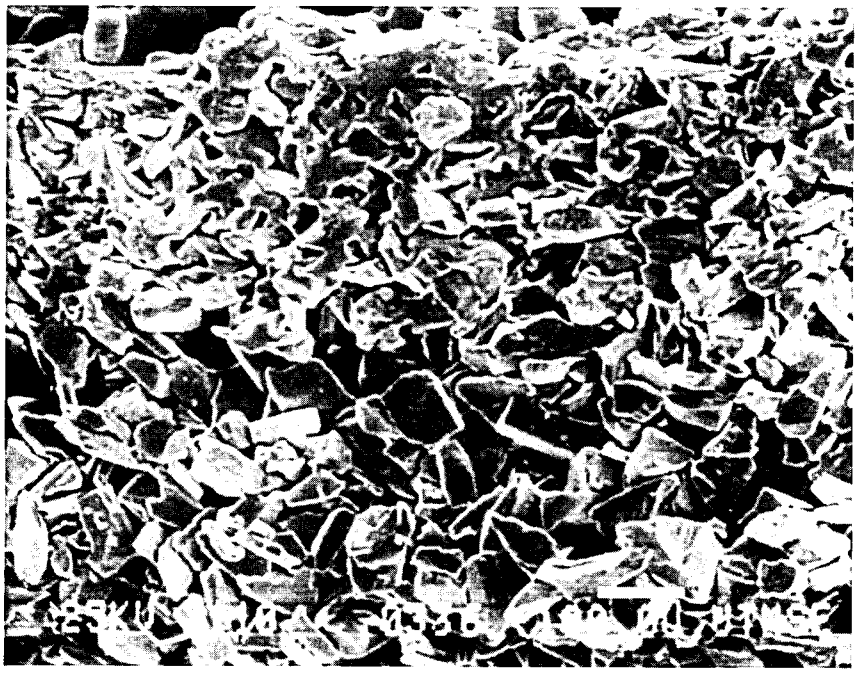

Figure 3: Static beam infiltration - infiltration time 120 seconds, 100μm powder, 25Torr TMS gas pressure, 20watts laser power, cross-section, 150X.

Infiltration time effect

Figures 4 and 5 are cross-sections of material infiltrated different lengths of time. A static beam was used, and gas pressure, laser power and powder size (12μm) were held constant.

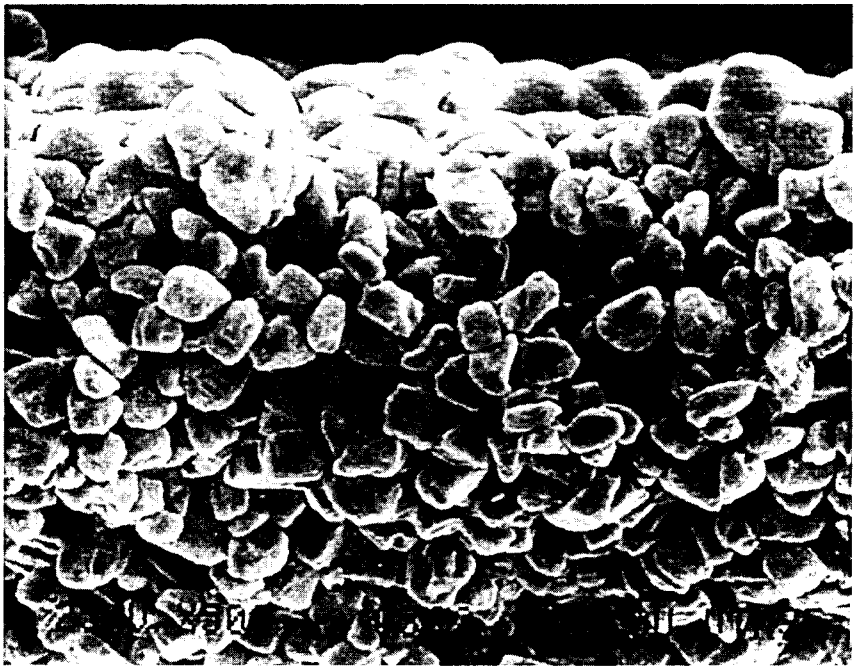

Figure 4: Static beam infiltration - infiltration time 3 seconds, 15μm powder, 10Torr TMS gas pressure, 20watts laser power, cross-section, 500X.

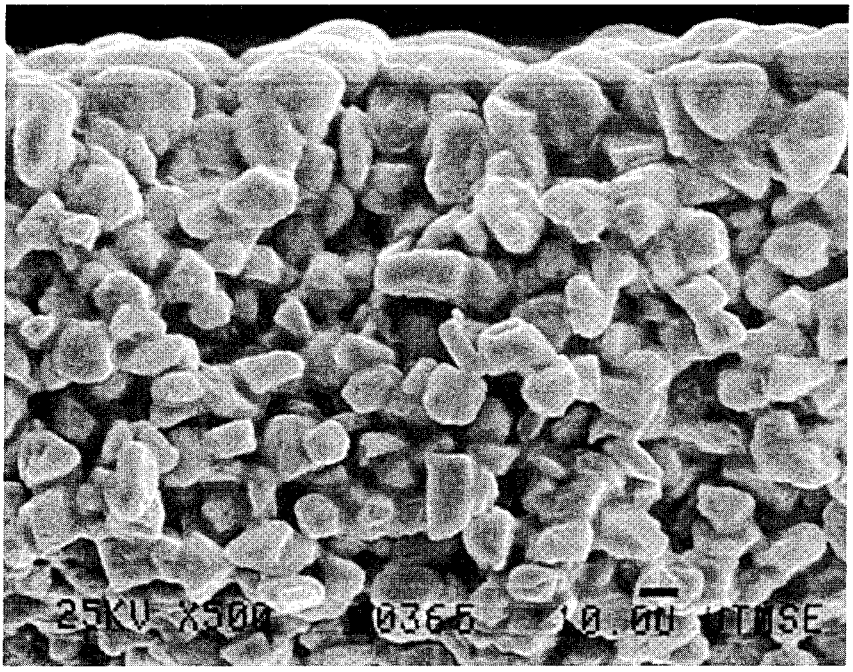

Figure 5: Static beam infiltration - infiltration time 5 seconds, 15μm powder, 10Torr TMS gas pressure, 20watts laser power, cross-section, 500X.

Production of multi-layer parts

Multi-layer tests were run to determine if multiple layers of material could be infiltrated and bonded together to produce a dense multi-layer part. Figures 6 and 7 are cross-sections of one of the test cases.

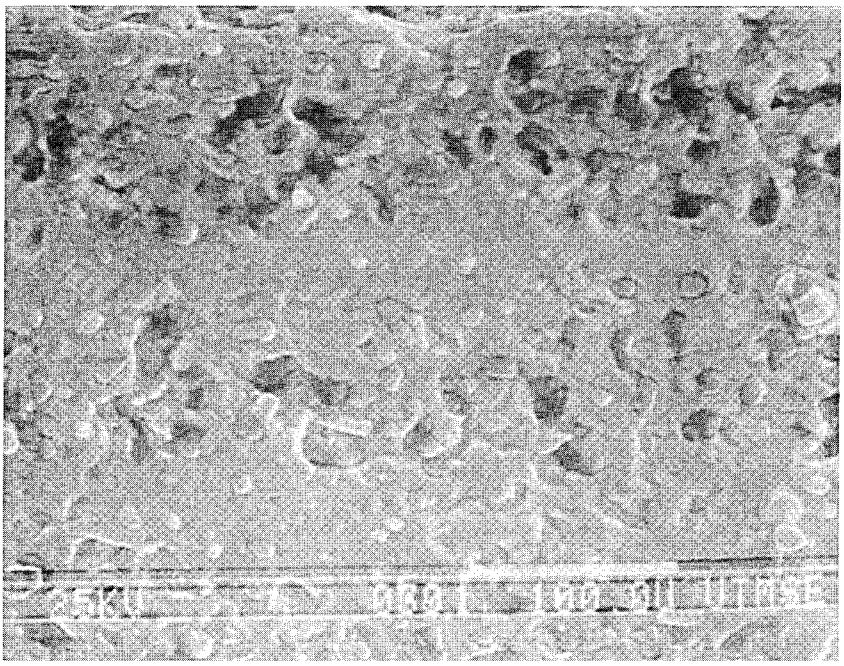

Figure 6: Multi-layer cross-section, top three layers, layer thickness 110μm, 15μm powder, 20Torr TMS gas pressure, 20watts laser power, static beam.

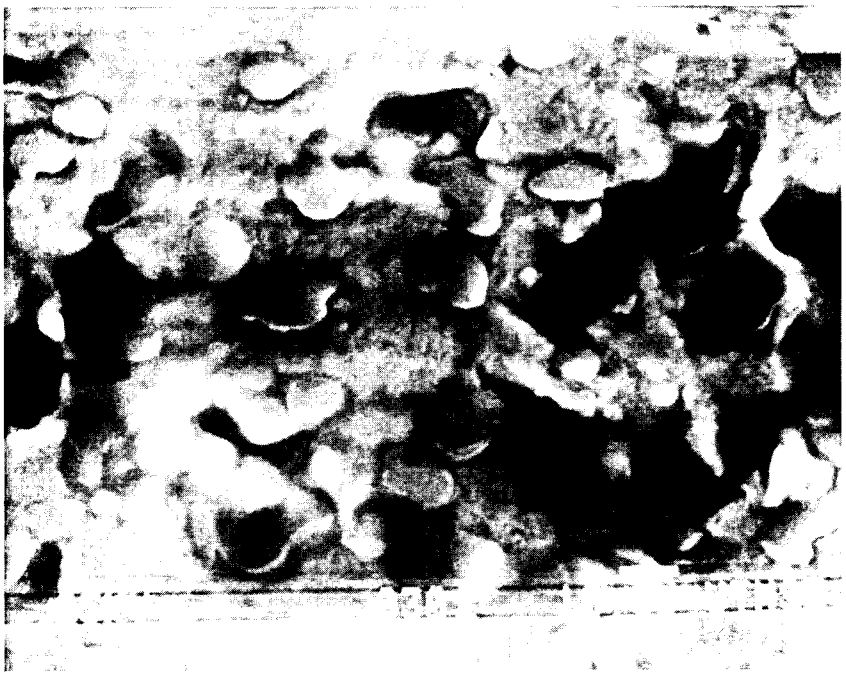

Figure 7: Multi-layer cross-section, top layer including interface, 15μm powder, 20Torr TMS gas pressure, 20watts laser power, static beam.

Discussion

The rapidly changing reflectivity of SiC in the 10.6μm wavelength range makes it difficult to control temperature under the CO_2 laser beam. The immediate solution will be to use a Nd-YAG laser (1.06μm wavelength). This laser should make temperature easier to control because the shorter YAG wavelength is not absorbed by the TMS, and the reflectivity of SiC in this wavelength range is essentially constant. A much more robust solution to the temperature problem will be to use a closed-loop control system like the one currently under development by Benda [14]. That system controls temperature under the beam by measuring surface temperature at the beam focus and then using that information to control laser power. A similar technique using a two colored optical pyrometer is currently under consideration for the SALDVI process.

Powder size has a large effect on infiltration behavior. The smaller powder infiltrates much more rapidly, probably due to increased surface area driving the decomposition reaction. Further testing is required to determine optimum temperature, gas pressure and powder size to achieve maximum infiltration density.

Significant infiltration of the material under the beam occurs in the first five seconds. This represents a part build rate on the order of $2mm^3$/minute, assuming a single 1mm diameter beam is used. It will be possible to speed up the process using variable focus or multiple beam techniques.

Conclusions

Preliminary studies documenting the effects of beam interactions, powder size, and infiltration time have been presented. A multiple layer "proof-of-concept" consisting of a SiC/SiC composite structure produced by the SALDVI process was also presented. Future work will concentrate on maximizing part density and build rate by optimization of gas chemistry, gas pressure, process temperature and powder size. Additional precursors to SiC and other materials will also be investigated.

Acknowledgments

Special thanks to the Office of Naval Research for supporting this work. ONR contract N00014-92-J-1514.

References

1 G. Zong, R. Carnes, H.G. Wheat and H.L. Marcus, "Solid Freeform Fabrication by Selective Area Laser Deposition," *Solid Freeform Fabrication Proceedings*, The University of Texas at Austin, pp. 83-90, (1990).

2 C. Deckard and J. Beaman, in *Advances in manufacture, Integration and Processes, Proceedings of the 15th Conference on Production Research and Technology*, University of California at Berkeley, pp. 623-630, (1989).

3 L. Deckard and T. Claar, "Fabrication of Ceramic and Metal Matrix Composites From Selective Laser Sintered Ceramic Preforms," *Solid Freeform Fabrication Proceedings*, The University of Texas at Austin, pp. 215-222, (1993).

4 J. Yoo, M.J. Cima, S. Khanuja, and E.M. Sachs, "Structural Ceramic Components By 3D Printing," *Solid Freeform Fabrication Proceedings*, The University of Texas at Austin, pp. 40-50, (1993).

5 private communication, K. Jakubenas, The University of Texas at Austin.

6 W.J. Lackey, "Review, Status, and Future of the Chemical Vapor Infiltration Process for Fabrication of Fiber-Reinforced Ceramic Composites," *Ceramic Engineering Science Proceedings*, 10[7-8],pp. 577-584, (1989).

7 S.M. Gupte and J.A. Tsamopoulos, "Forced-Flow Chemical Vapor Infiltration of Porous Ceramic Materials," *Journal of the Electrochemical Society*, 137[11], pp. 3675-3682, (1990).

8 D. Gupta and J. Evans, "A mathematical model for chemical vapor infiltration with microwave heating and external cooling," *Journal of Material Research*, 6[4], pp. 810-818, (1991).

9 D. Richerson, *Modern Ceramic Engineering*, 2nd edition, Marcel Dekker, New York, pp. 162-200, (1992).

10 *Binary Alloy Phase Diagrams*, 2nd edition, T.B. Massalski editor-in-chief, Ohio, ASM International, pp. 882-883, (1990).

11 J. Tompkins and H.L. Marcus, "Selective Area Laser Deposition of Silicon Carbide," *Solid Freeform Fabrication Proceedings*, The University of Texas at Austin, pp. 325-332, (1993).

12 Aldrich Library of Infrared Spectra, edited by C.S. Pouchert, (1970).

13 *Thermophysical Properties of Matter*, edited by Y.S. Touloukian and D.P. DeWitt, Volume 8, I/P Plenum, New York, pg. 65, (1972).

14 J. Benda, "Temperature-Controlled Selective Laser Sintering," to be published in the *Solid Freeform Fabrication Proceedings*, The University of Texas at Austin, (1994).

Selective Laser Sintering of Polycarbonate at Varying Powers, Scan Speeds and Scan Spacings

Childs T. H. C., Cardie S. and Brown J.M.,

University of Leeds, UK

Moving heat source theory has been combined with a sintering model to predict densification in the bulk of and round the edges of a sintered block. The edge effects are related to size errors in sintering. Experiments support the modelling.

INTRODUCTION

A benchmark study (1) has shown selective laser sintering to be the equal of or to have accuracy advantages over other processes for creating parts of size over 10 mm. Experience is needed to achieve best accuracies, as with other processes. This paper is (for us) a first step in understanding the relation between sintering parameters, part size and acuracy.

Work at the University of Texas at Austin (2-4) has established that the sintering of polycarbonate can be understood in terms of a rate model driven by viscous and surface tension effects. Material properties are such that a sharp boundary exists between sintered and unsintered material. When full density is not achieved in a part, density within a single layer varies from fully sintered to totally unsintered; measured part density is thus a mean of widely varying values. Published work (3-4) uses a one-dimensional non-steady state heat flow model to calculate the temperature profile and densification beneath the surface and concentrates on the effects on this of material properties varying with temperature and during sintering. In this paper, these variations are ignored but a three dimensional non-steady heat flow is used to enable edge effects to be estimated. Density gradients at edges are assumed to be responsible for variations of accuracy with sintering parameters, part size, part shape and orientation.

THEORY

The geometry studied is a rectangular block ABCD of width w and length a (figure 1a), sintered by a laser spot of diameter d and power P, travelling at speed U in the x-direction and incrementing in the y-direction by the scan spacing s. The block is made up of layers of thickness z_r (figure 1b) but, because of densification, the thickness of the powder layer being sintered, z_l, is greater than z_r. The calculation has three stages: modelling the heat source, calculating the variation of temperature with time around the heat source, and estimating the density changes caused by the temperature distribution.

Modelling the heat source. Observation of selective laser sintering shows a sintering front to move steadily in the y-direction. In this paper the actual rastering spot is simplified to a strip source of width d, emitting heat q per unit area per unit

time uniformly and moving steadily in the y-direction with speed V. V is found from the time t* to advance the distance s:

$$V = s/t^* \qquad (1)$$

where $t^* = w(1/U + 1/U_r) + t_d$ (2).

U_r is the speed of the returning scan and t_d is the sum of any laser dwell times. By equating the heat put into the block by the simplified source to that put in by the actual rastering spot it is found that q/V, needed later, is

$$q/V = (P/Us) / d \qquad (3).$$

The smearing out of the rastering spot source to a steadily moving strip source is unable to model any periodic density variations that may occur in the y-direction. It must clearly become an oversimplification as s becomes much greater than d, but in practice there is some overlap between successive scans. It is also an oversimplification if heat diffuses further than the source width d in the cycle time t*. When U and U_r are approximately the same and t_d is negligible, it can be shown that for the validity of the approximation

$$U/w \geq 2\kappa/d^2 \qquad (4),$$

where κ is the diffusivity of the material. It will be seen that this is satisfied in typical sintering situations, up to widths w around 100 mm or so.

Temperature calculation. A classical moving heat source result (5) gives the temperature rise T in a semi-infinite body $z > 0$ caused by a rectangular surface source of sides 2l (=d) parallel to y and 2b (=w) parallel to x, moving with speed V in the y direction, and that has been transmitting heat for time t, as

$$T = \frac{\alpha q}{V}\frac{\kappa/k}{2\sqrt{2\pi}}\int_0^{V^2t/2\kappa}\frac{e^{-Z^2/2u}}{\sqrt{u}}\left(\operatorname{erf}\frac{X+B}{\sqrt{2u}} - \operatorname{erf}\frac{X-B}{\sqrt{2u}}\right)\left(\operatorname{erf}\frac{Y+L+u}{\sqrt{2u}} - \operatorname{erf}\frac{Y-L+u}{\sqrt{2u}}\right)du$$

where $X = \frac{Vx}{2\kappa}$, $Y = \frac{Vy}{2\kappa}$, $Z = \frac{Vz}{2\kappa}$, $L = \frac{Vl}{2\kappa}$ and $B = \frac{Vb}{2\kappa}$ (5).

The origin of the axes x, y, z is centred in the heat source, α is the fraction of heat absorbed by the body and k is the thermal conductivity of the body.

Equation (4) has been integrated numerically to provide temperature fields relative to the position of the heat source in four special cases:(i) the steady state temperatures away from the edges of the block; (ii) the steady state temperatures around the edges AC and BD of the block; (iii) the initial temperatures around the edge AB; and (iv), by superposition of (i) less (iii), the final temperatures around the edge CD. κ and k have been taken as constant and to have values appropriate to the unsintered powder. The volume contractions due to sintering during heating have been ignored. These are on the grounds that it is the temperature distribution in the powder around the sintering front that determines the front's spatial extent. The fact that there is a previously sintered layer beneath the current powder layer (with thermal properties of the solid) has also been ignored.

Densification. The simple model of densification used in (4) has been applied:

$$-\frac{d\varepsilon}{\varepsilon} = \int_0^t Ae^{(-E/RT)}dt \qquad (6)$$

where ε is the porosity of the powder. The temperature / time history at a depth z below the surface has been used to integrate the right hand side of (6) and hence obtain the sintered density at that depth. The mean density has been obtained by averaging over the layer thickness. The contractions in z are included at this stage.

Calculations have been performed with thermal data from (4):κ = 0.1 mm^2/s, α = 0.95, k = 0.08 W/m/°K, E/R = 21,000 and A = 8.84×10^{16} s^{-1}; and for d = 0.2 mm, z_r = 0.125 mm and a powder bed ambient temperature of 154°C. Figure 2 shows predicted densities away from the part edges as a function of laser power. For w = 25 mm, density depends only on the energy density parameter P/(Us), but for larger values of w, an effect of cooling between scans is predicted. For P/(Us) = 0.045 J/mm^2, the hatched range for w = 90 mm has been obtained by varying U and s in different combinations. Figure 3 shows predicted edge density variations when w = 25 mm. In figure 3a (for the edges AC and BD) it is noticeable that sinterng occurs outside the geometric boundary. This is not the case, in figure 3b, for the edges AB and CD. For these the density profiles differ from one another as there is no heat in the layer before sintering starts, but heat must diffuse away after the sintering is completed.

EXPERIMENTATION

A standard test piece (figure 4a) was sintered. Pieces were created at positions 1 to 21 in the build zone of a Sinterstation 2000 as indicated in figure 4b. Parts were built with laser powers from 4.5 to 19 W, scan speeds from 517 to 1206 mm/s, scan spacings from 0.08 to 0.406 mm, chosen to surround the manufacturer's recommended settings for polycarbonate of 11 W, 861 mm/s and 0.203 mm. The layer thickness was 0.125 mm. All other variables were held at the manufacturer's recommended defaults. In particular the ambient temperature of the powder bed was 154°C, the nominal beam diameter was 0.2 mm.

RESULTS

In a first test all 21 parts were sintered with P= 11 W, U = 860 mm/s and s = 0.203 mm (P/Us = 0.063 J/mm^2). The slightly lower density of parts 1 to 9 (w = 90 mm) than 10 to 15 and 16 to 21 (w = 25 mm) is seen in figure 5a, but in each group there is one low value. These, from parts 12, 9 and 19, may be caused by a slightly lower bed temperature near to the edge of the build zone (by accident the pattern of parts, figure 4b, was not quite concentric in the zone). These effects combine to give a general scatter of results as shown in figure 5b. In a second test, the full range of P, U and s variables was used to study how density varied with P/Us. Figure 6 (•) is the result. Figure 6 also shows a third test result (o) in which P, U and s were varied, keeping P/Us constant, results derived from figure 26 of reference 4 (+), the theoretical prediction for w = 25 mm from figure 2 and another prediction discussed later. Finally, over- and under-size x and y measurements are presented in figure 7 with theoretical predictions obtained from figure 3 assuming that a density of 650 kg/m^3 marks the boundary of the part.

DISCUSSION AND CONCLUSION

Figure 6 (•) shows that within the scatter of results established in figure 5 density depends mainly on the energy density P/Us. A small influence of w has been found (figure 5), but less than expected from figure 2. Densities (•) are significantly less than the theory. There can be a small variability between runs (results (o) differ from (•)) and it is interesting to note the small differences between the present experimental work and that of reference (4) (+), although the layer thickness used in (4) is not clear. The overprediction of density may result from neglecting the changes in k during sintering. Repeating the calculations using solid material thermal properties gives a better agreement, as indicated in figure 6 ($k = 0.2$ W/m/°K). Perhaps a role of previously sintered material is to conduct heat more rapidly away from the sintering zone.

The under- and over-size measurements of figure 7 are very scattered, perhaps reflecting difficulties of measurement or variablity in breakout and cleaning techniques. Their variation with P/Us is similar to the predicted values. Figure 3 suggests different beam offsets should be used for x and y edges.

These studies are at an early stage. The results encourage further developments to create automatic techniques for controlling sintering conditions and beam offsets for required part densities and accuracies.

ACKNOWLEDGEMENT

Our purchase of a selective laser sintering machine was made possible by participation in a European project EUREKA EU776 and the generosity of the University of Leeds and its Departments of Mechanical Engineering and Applied Mathematics. The experimental studies were developed by undergraduate students J. Bailey, A. Medancos, J. Morris and G. Weaver.

REFERENCES

1. Juster N. P. and Childs T. H. C., A comparison of rapid prototyping processes, Proc. 3rd European Conf. Rapid Prototyping, pp.35-52, Nottingham 1994.
2. Barlow J. W., Sun M. S. M. and Beaman J. J., Analysis of selective laser sintering, Proc. 2nd. Int. Conf. on Rapid Prototyping (Lightman A. J. and Chartoff R. P. eds.), pp. 1-14, Dayton, Ohio 1991.
3. Zong G. et al., Laser processing in solid freeform fabrication, Int. Conf. on Beam Processing of Advanced Materials (Singh J. and Copley S. M. eds.), pp97-110, The Minerals, Metals and Materials Society 1993.
4. Nelson J. C. et al., Model of the selective laser sintering of bisphenol-A polycarbonate, Ind. Eng. Chem. Res., 1993, 32, 2305-2317.
5. Jaeger J. C., Moving sources of heat and the temperature at sliding contacts, Jnl. Roy. Soc. New South Wales, 1942, 76, 203-224.

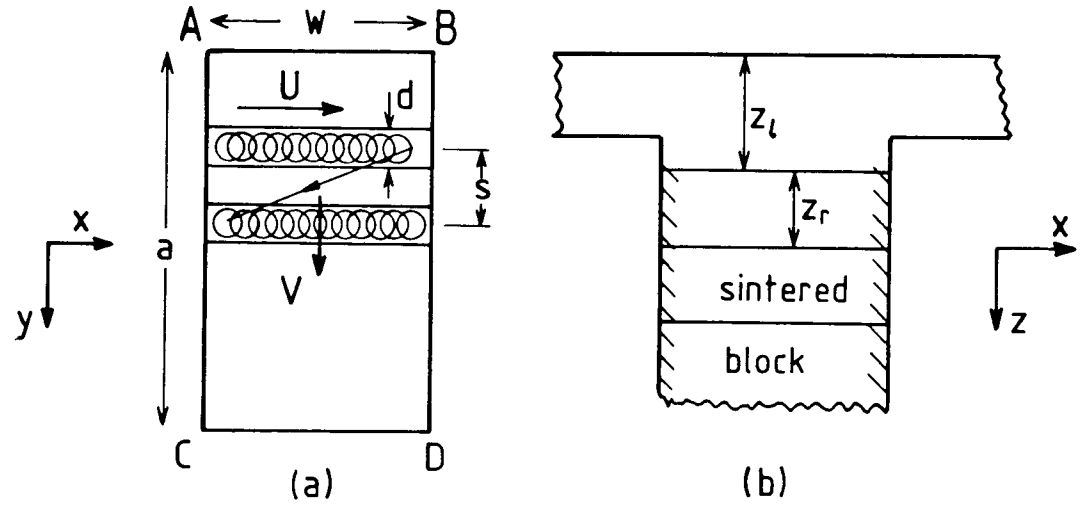

Figure 1. The sintering geometry.

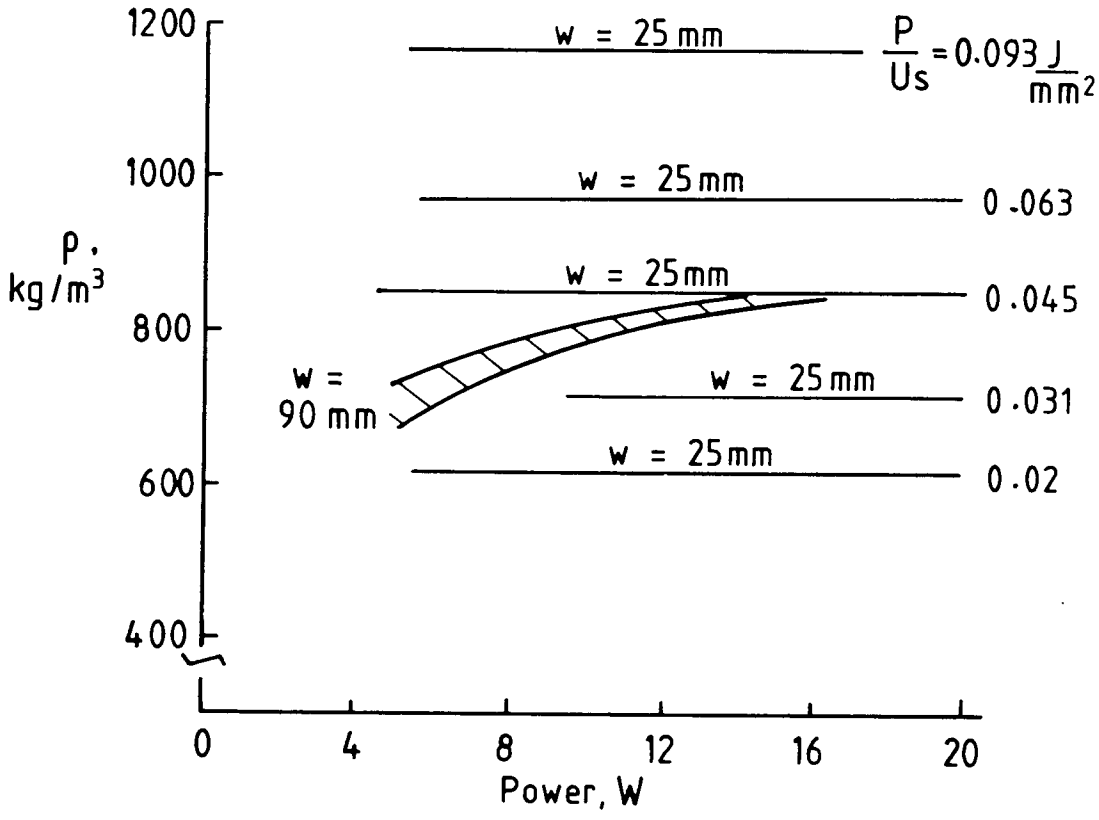

Figure 2. Dependence of density on laser power for a range of scan widths w and energy densities P/(Us).

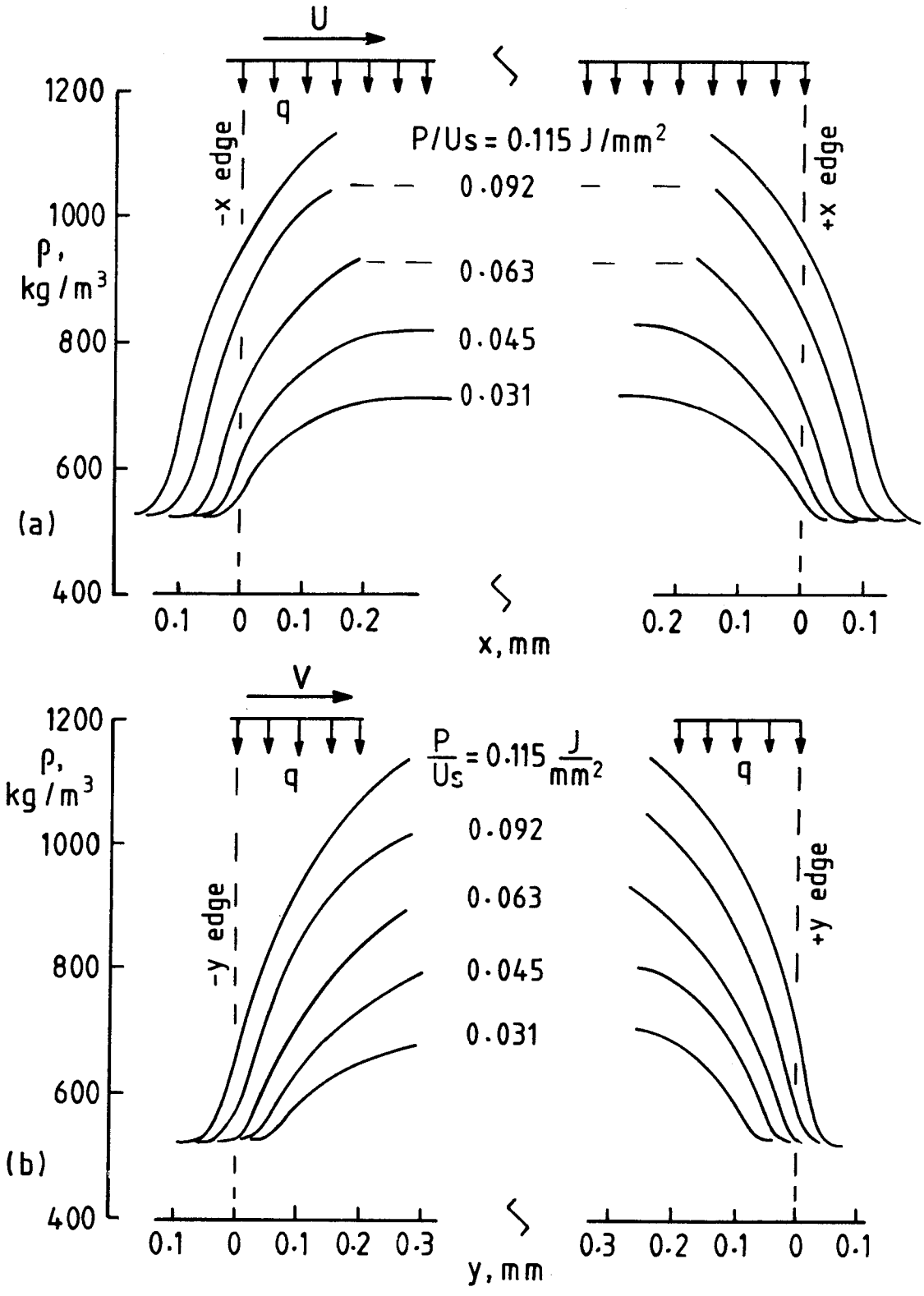

Figure 3. Density variations round the edges of a part: (a) x (side) edges; (b) start and finish (y) edges.

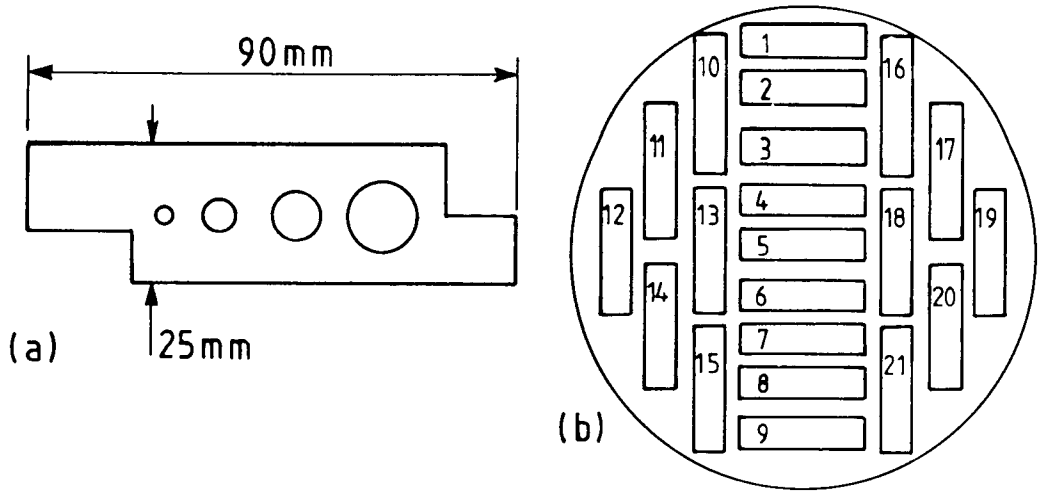

Figure 4. Part geometry (a) and layout (b).

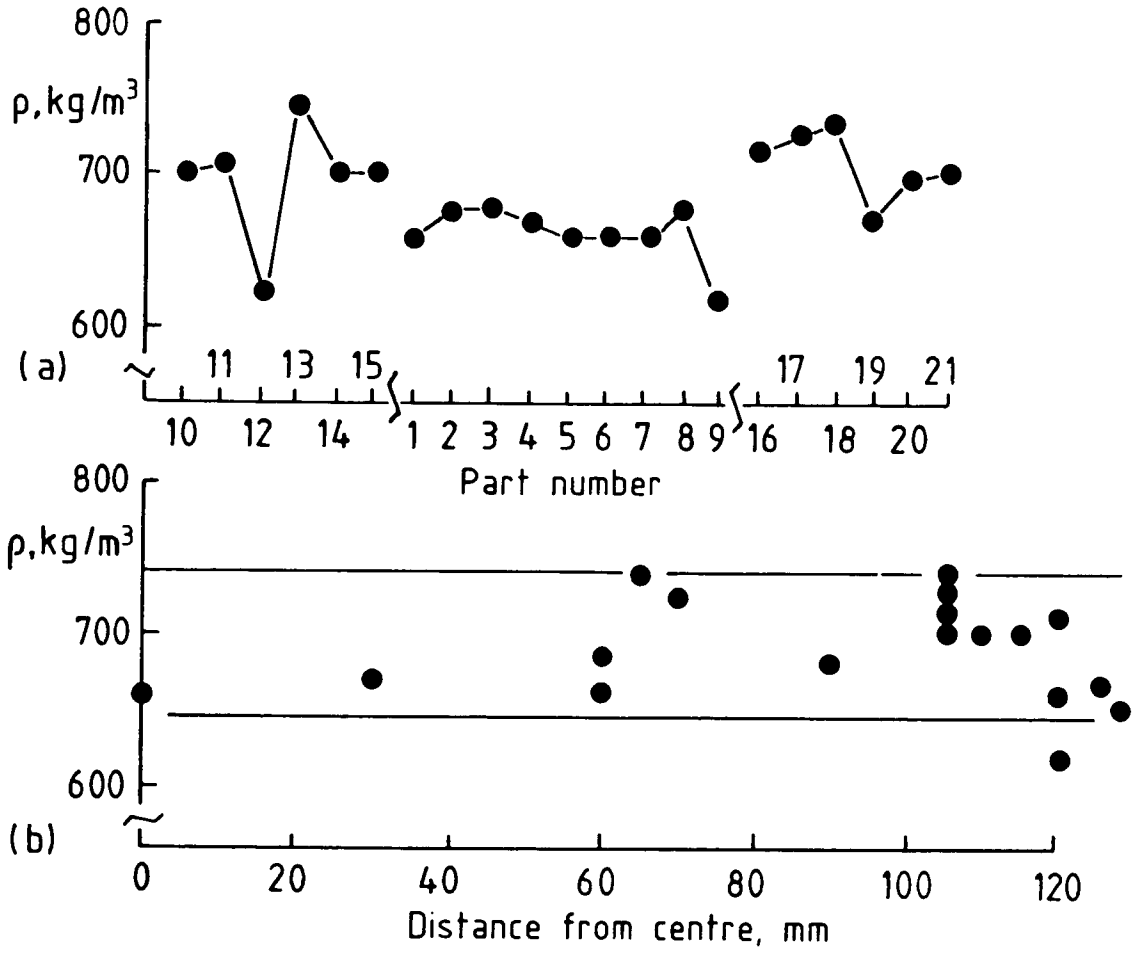

Figure 5. Density variations in nominally constant conditions arranged (a) by part number and (b) by distance from the centre of the build area.

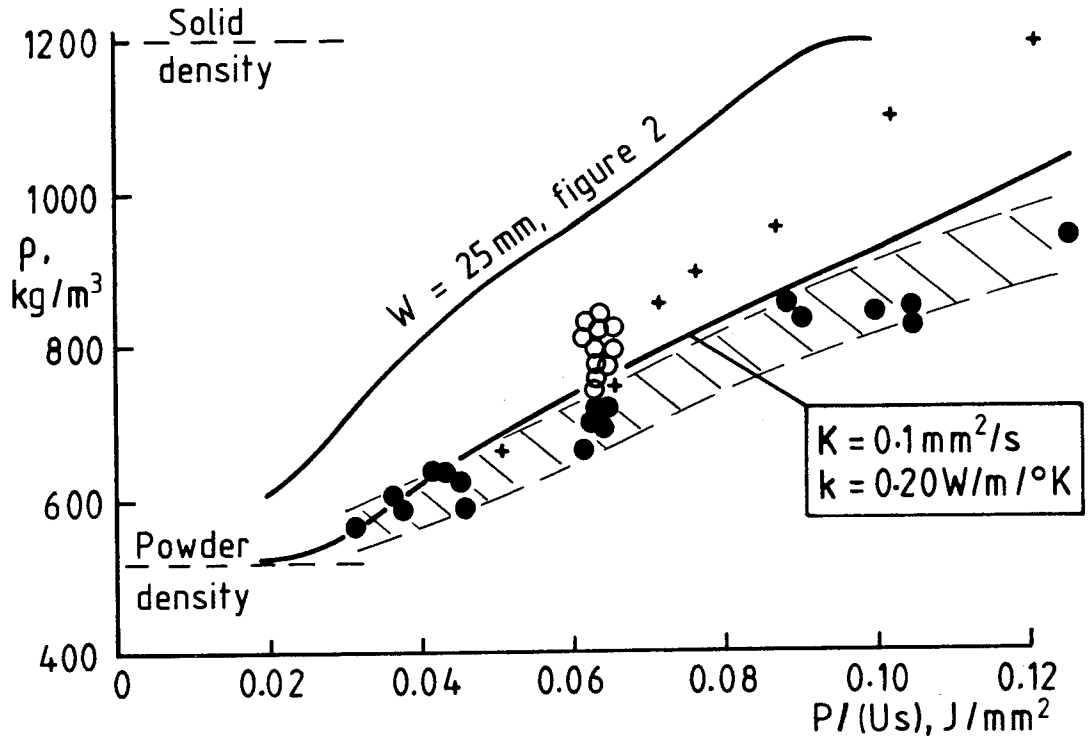

Figure 6. Predicted (—) and experimental (•, o, +) density variations.

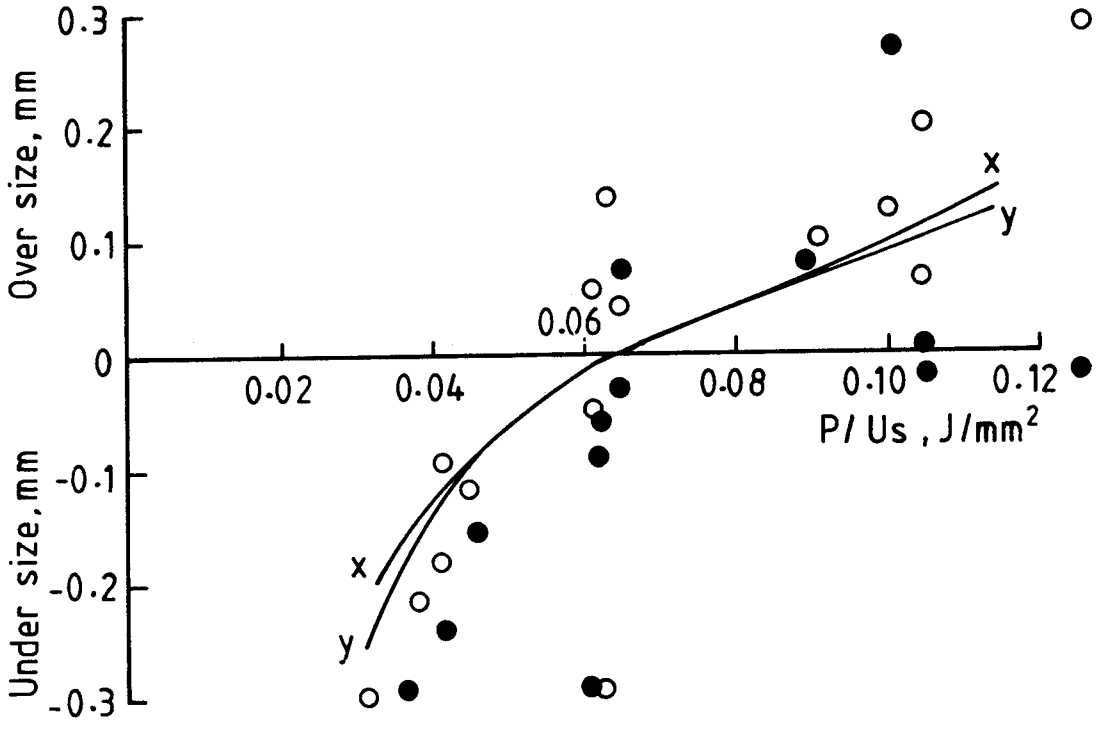

Figure 7. Predicted (—) and experimental x (•) and y (o) out of size, shifted to coincide at P/(Us) = 0.063 J/mm^2.

Selective Laser Pyrolysis for Solid Free-Form Fabrication of Silicon Carbide

K. Jakubenas and H.L. Marcus
Center for Materials Science and Engineering
University of Texas at Austin
Austin, TX 78712

Abstract

Selective laser pyrolysis rapidly decomposes a polymeric precursor to form a cohesive ceramic shape. The considerable shrinkage and porosity during pyrolysis of pure precursor can be modified by the addition of either inert or reactive fillers. With polycarbosilane as the polymeric precursor, the process forms shapes of β-SiC and, by using fillers, composites of β–SiC/Al_4C_3/Al, β-SiC/TiC/Ti, and β-SiC/ZrC/Zr. The technique offers some potential for ceramic shapes with custom designed composition and microstructure including nanometer grain size.

Introduction

Polymeric precursors provide a means for synthesizing and forming ceramics that reduces the need for high temperature processing. Polymeric ceramic precursors contain an inorganic component such as silicon or titanium in an organic polymer chain. Pyrolyzing the polymer results in a residue in which the inorganic component converts to a ceramic such as silicon carbide (or nitride) or titanium carbide. Several researchers have used this approach to produce nano-powders[1-4]; the commercially available Nicalon (SiC) and Tyranno (SiC-TiC) fibers are also formed from pyrolysis of polymeric precursors.[5]

Selective laser pyrolysis seeks to use the relatively low pyrolysis temperature of polymeric precursors to overcome some of the difficulties seen in direct Selective Laser Sintering of ceramics. Polycarbosilane (PCS), the raw material for Nicalon fibers, provided suitable characteristics for the first laser pyrolysis work. Figure 1 compares conventional and laser pyrolysis of PCS and Figure 2 schematically depicts laser pyrolysis of PCS.

Experiments and Discussion

The experimental set-up consists of a vacuum chamber mounted on an x-y table and a 25W cw CO_2 laser. The laser is focused through a ZnSe window, and by moving the chamber, the laser scans across a powder bed of the material to be pyrolyzed. The design of the chamber is discussed in detail in reference 6.

Experiments with laser pyrolysis of PCS were divided into three groups: pure PCS, PCS with inert filler, and PCS with reactive filler.[7] All of the experiments involved

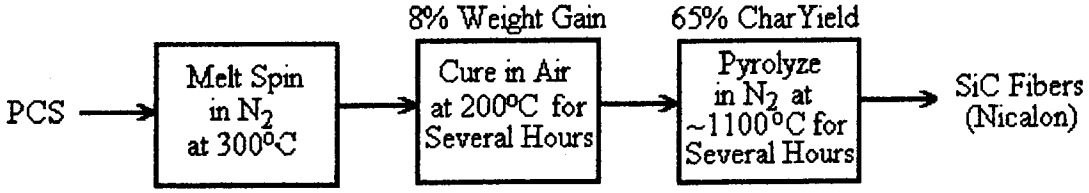

a) Conventional Pyrolysis of Polycarbosilane (PCS)

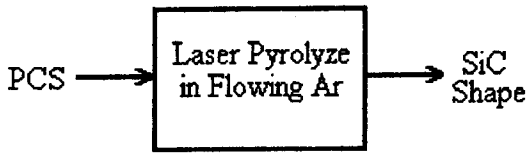

b) Selective Laser Pyrolysis of PCS

Figure 1 Conventional and Selective Laser Pyrolysis of Polycarbosilane

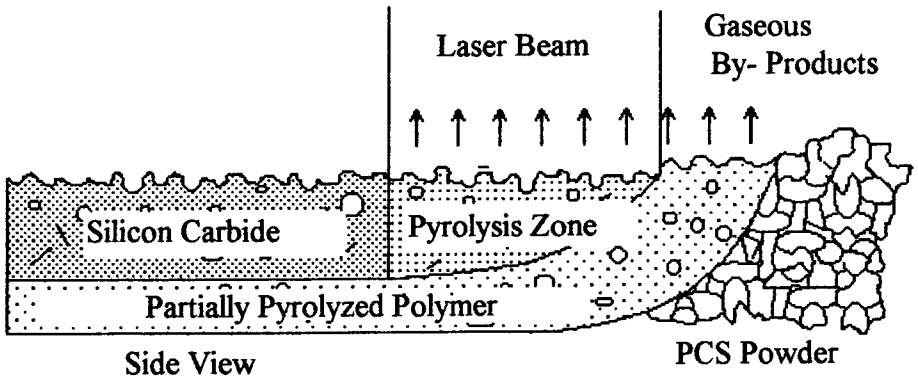

Figure 2 Schematic of Laser Pyrolysis of Polycarbosilane

PCS powder prepared by mortar and pestle grinding. The powder combinations were formed by mechanical mixing.

Pure PCS

The first group of experiments involved pyrolysis of pure PCS. Shapes formed from pure PCS have rough surfaces and are highly porous, but show good cohesion, including between layers. The pores appear evenly distributed both within and across layers. Significant shrinkage occurs during pyrolysis; the surface of the pyrolyzed region of the powder bed is significantly lower than the surrounding non-pyrolyzed regions.

Figure 3 presents the X-ray diffraction spectrum for pure PCS after laser pyrolysis while Figure 4 shows the grain size / laser power relationship. The grain size, as

determined from X-ray diffraction peak widths and the Scherrer equation, shows poor correlation with total energy, but a strong correlation with laser power. Grain size is expected to be independent of laser power but increase with total energy flux (energy flux is proportional to power, scan speed, and scan spacing). The connection of power and grain size here suggests that pyrolysis occurs very rapidly, in less time than the total laser dwell time on a given area (<10 seconds for the scan speed and spacings examined), and that the laser powers examined are too low to raise the temperature enough to cause grain growth after SiC forms. In addition to increasing grain size, higher power also increases cracking and surface roughness.

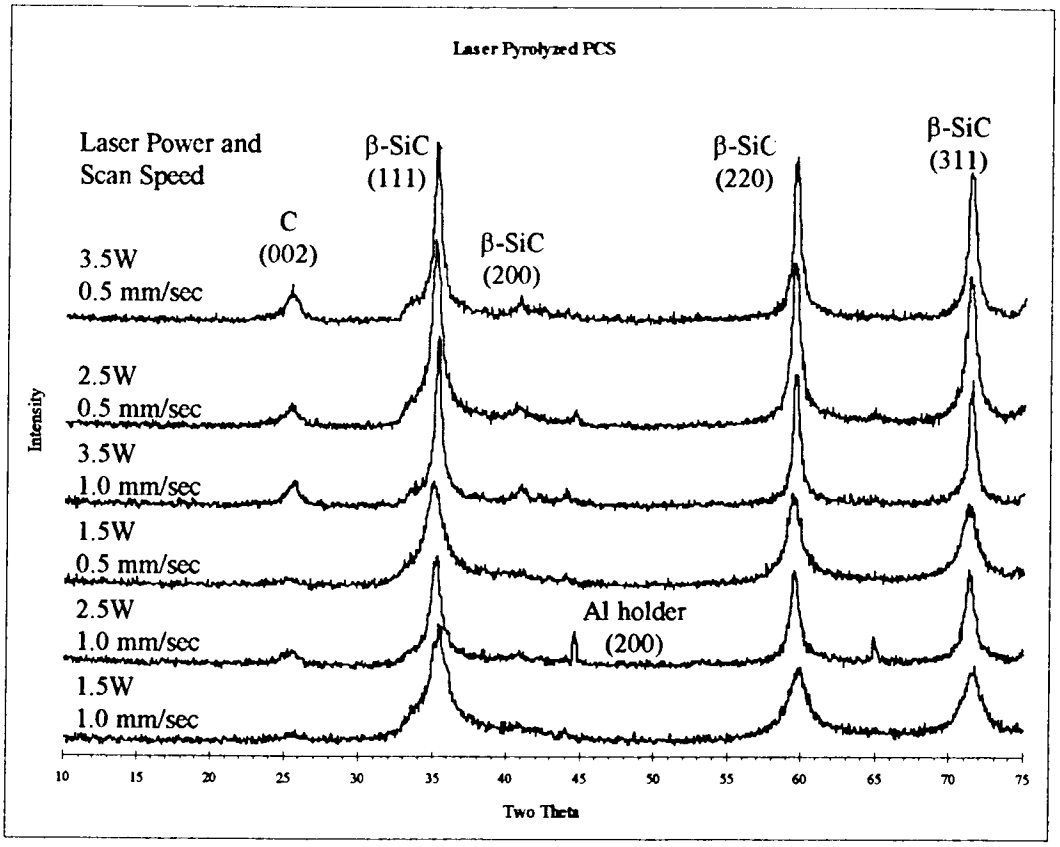

Figure 3 X-Ray Diffraction Spectrum for Laser Pyrolyzed Pure PCS

PCS with Inert Filler

The second group examined consisted of PCS with an inert filler. The filler reduces the shrinkage and porosity seen during pyrolysis of pure PCS. The inert filler simply decreases the volume of PCS needed and therefore the amount of shrinkage during processing. Both silicon carbide and silicon nitride were examined as inert fillers, but none of the silicon nitride mixtures formed cohesive shapes, possibly because of poor bonding

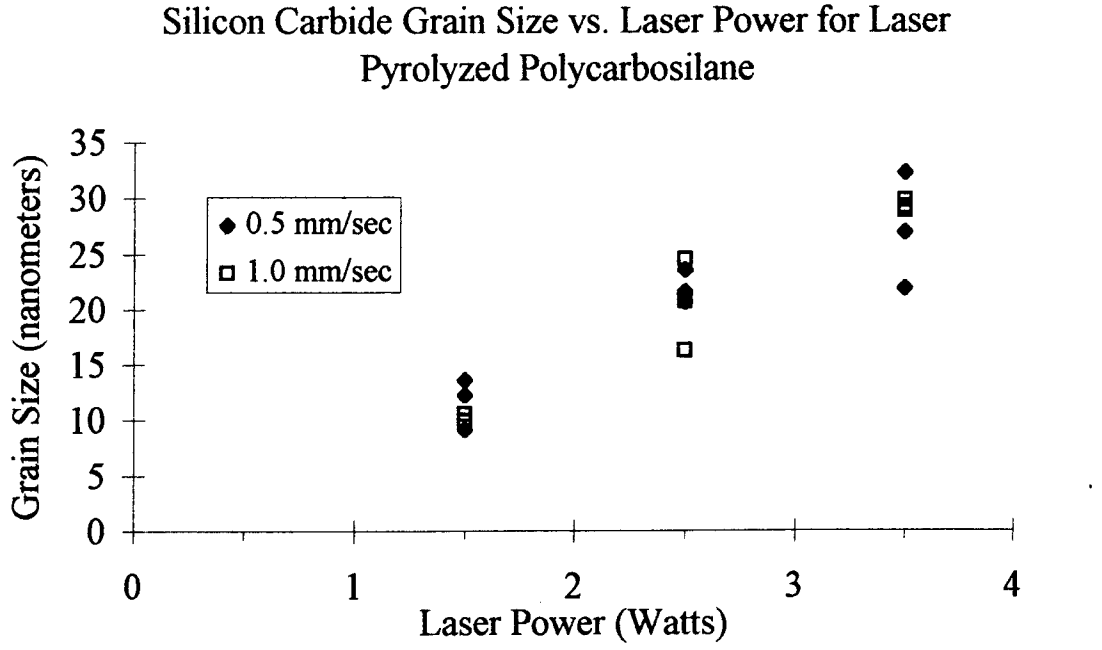

Figure 4 Silicon Grain Size vs. Laser Parameters for Laser Pyrolyzed Polycarbosilane (Grain Size determined from X-ray Diffraction peak widths and the Scherrer Equation).[8]

between the pyrolyzed material and the silicon nitride powder. Silicon carbide filler, however, did show good bonding between pyrolysis product and filler.

PCS with Reactive Filler

Reactive fillers (carbide forming metals) decrease shrinkage and boost yield after pyrolysis by consuming carbon normally lost as gaseous by-products. For all reactive fillers, local porosity appears high, but some regions contain large voids which greatly lowers the overall density of the samples. The compositions resulting from laser pyrolysis of reactive mixtures closely parallels that seen in conventional pyrolysis of such mixtures.[9] Table 1 summarizes the results of the various experiments conducted on PCS with and without fillers.

As an example of the effect of reactive fillers, Figure 5 shows a laser pyrolyzed PCS - Ti mixture. After pyrolysis, the mixture contains β-SiC, TiC, and residual titanium. Although the pre-pyrolysis metal to carbon ratio of the mixture was one to one, two factors prevent complete TiC formation: the large titanium powder size (-100 mesh) and some loss of carbon as gaseous by-products. The pyrolyzed PCS-Ti mixture pictured also shows high local density. Overall density, however, remains low because of isolated, large voids caused by inhomogenities in the original powder mixture.

Conclusions

Selective laser pyrolysis of polycarbosilane successfully produced shapes composed of nano-crystalline β-SiC. A filler approach showed some success in reducing shrinkage and local porosity while also allowing formation of composite materials. Further study, however, is necessary to further decrease overall porosity to more acceptable levels.

Table 1
Results of Laser Pyrolysis of Polycarbosilane

Reactants	Metal: Carbon Ratio	Products	Char Yield	% of Theoretical Density
PCS	0.5 : 1	β-SiC + C	~ 70%	~ 30%
Inert Filler				
50wt% β-SiC (16 μm) + 50 wt% PCS	0.7 : 1	β-SiC + C	~ 70%	~ 35%
Reactive Filler				
29wt% Si (5 μm) + 71wt% PCS	1.0 : 1	β-SiC +Si	~ 85%	~ 25%
50wt% Al (-325 mesh) + 50wt% PCS	1.5 : 1	β-SiC + Al_4C_3 + Al + Si	~ 90%	~ 30 %
34wt% Al (-325 mesh) + 66wt% PCS	1.0 : 1	β-SiC + Al_4C_3 + Al + Si	~ 90%	~ 30%
60wt% Ti (-100 mesh) + 40wt% PCS	1.0 : 1	β-SiC + TiC + Ti	~ 90%	~ 30%
73wt% Zr (-270 mesh) + 27wt% PCS	1.0: 1	β-SiC + ZrC + Zr	~ 90%	~ 30%

Acknowledgments

This material is based upon work supported under a National Science Foundation Graduate Research Fellowship. Further financial support was provided by the Office of Naval Research, ONR Contract N00014-92-J-1514.

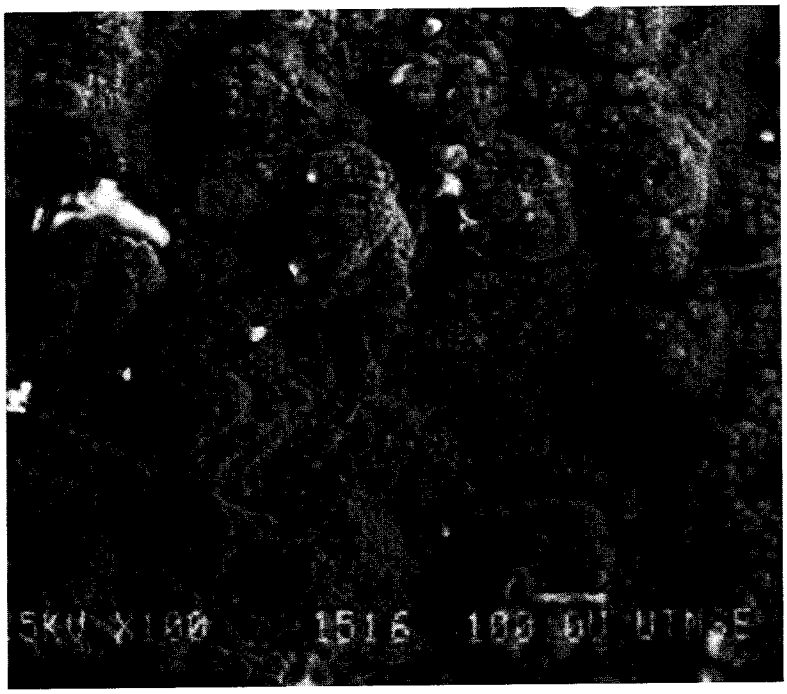

a) Top (Laser Scanned) Surface 100X

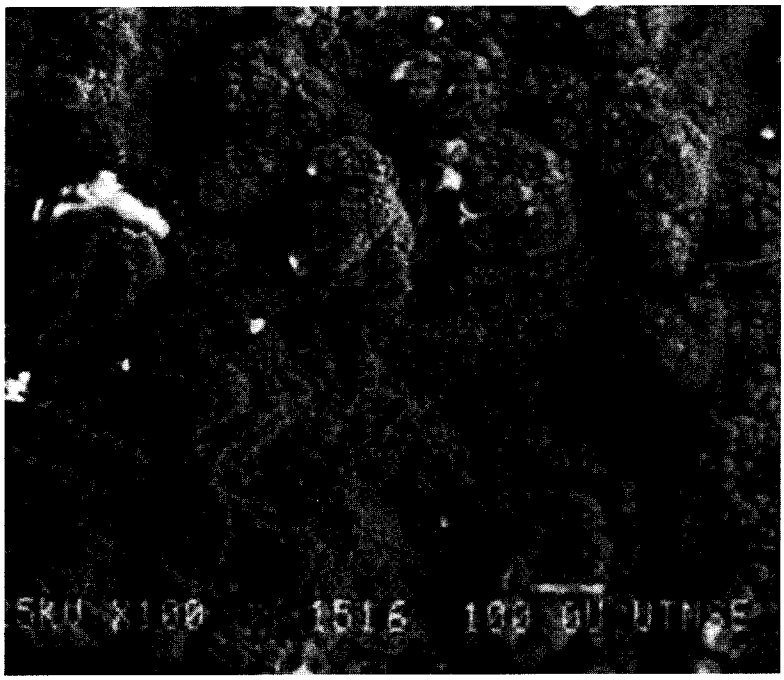

b) Top (Laser Scanned) Surface 500X

Figure 5 SEM Photographs of Laser Pyrolyzed Polycarbosilane / Titanium Mixture
The large nodules are remaining titanium particles (starting size -100 mesh) while the smaller nodules seen at higher magnification likely are aggregates of TiC and SiC.

References

1. M. Suzuki, Y. Maniette, Y. Nakata, T. Okutani, *Journal of the American Ceramic Society*, **76** [5], 1195-1200, (1993).
2. K.E. Gonsalves, P.R. Strutt, T.D. Xiao, P.G. Klemens, *Journal of Materials Science*, **27**, 3231-3238, (1992).
3. G.W. Rice, R.L. Woodin, *Journal of Materials Research*, **4** [6], 1538-1548, (1989).
4. G.W. Rice, *Journal of the American Ceramic Society*, **69** [8], C-183 - C-185, (1986).
5. R. Baney, G. Chandra, "Preceramic Polymers"; pp. 312-344 in *Encyclopedia of Polymer Science and Engineering*, Vol. 13. Editor in Chief J.I. Kroschwitz. John Wiley and Sons, New York, 1988.
6. B.R. Birmingham, J.V. Tompkins, G. Zong, H.L. Marcus, *Solid Freeform Fabrication Proceedings*, The University of Texas at Austin, 147-153, (1992).
7. K. Jakubenas, *Selective Laser Pyrolysis of Polycarbosilane*, The University of Texas at Austin Master's Thesis, December, 1993.
8. Y.-W. Kim, J.-G. Lee, *Journal of Materials Science*, **27**, 4746-4750, (1992).
9. D. Seyferth, N. Bryson, D.P. Workman, C.A. Sobon, *Journal of the American Ceramic Society*, **74** [10], 2687-2689, (1991).

Manufacture Of Injection Molds Using SLS

B.Badrinarayan, and J.W.Barlow
Dept. of Chemical Engineering,
The University of Texas at Austin,
Austin, Texas- 78712,U.S.A.

Abstract

This paper describes the use of SLS technology for the fabrication of injection mold cavities. Green shapes were made from metal - copolymer powder mixtures by SLS. The copolymer was gradually burnt out and the metal was oxidized in an air furnace. The porous oxidized metal part was subsequently infiltrated with an epoxy resin and cured. Effect of process variables in SLS, effect of oxidation cycle, dimensional changes on oxidation and epoxy infiltration of the oxidized metal part are discussed.

Introduction

Selective Laser Sintering comes under the class of Solid Freeform Processes for Rapid Manufacture of parts directly from a CAD model without part specific tooling or human intervention[1,2]. This technology has been developed at the University of Texas at Austin to produce polymer parts as well as indirect metal and ceramic parts that have polymer as an intermediate binder. We have adapted SLS to manufacture indirect oxidized metal molds for injection molding applications. The traditional method for manufacturing injection molds involves precision machining of cast metals. This fabrication process is usually very complex, time intensive, expensive and also requires highly skilled labor. Rapid Prototyping using SLS offers the solution to the problem of fabricating prototypes at low costs and high speed. Time savings due to design refinements are enormous since the prototype can be fabricated in hours as compared to months and changes required can easily be made on the computer and the part rebuilt quickly. The suitability of the material system for mold manufacture has been demonstrated in an earlier paper[3].

Experimental Work

Processing and Post-Processing : The raw material for the SLS process consists of a metal powder and a polymer powder that acts an intermediate binder. Iron powder, -325 mesh in size, was used as the metal and was obtained from Hoeganaes, Riverton, New Jersey. The polymer binder is a copolymer of poly(methylmethacrylate-co-butylmethacrylate) and has an average melt flow index of 28.9g/10min at 75 psi and 200°C[4]. The polymer powder is obtained by spray drying polymer emulsion in a Anhydro Spray Dryer. The iron powder is mixed with polymer and used in SLS for making the green shape. The polymer composition in the mixture was 40 vol % (9.16 wt %). SLS was used to make the green molds as well as bars for strength tests and density cups for measurement of bed density. The mold design was provided by Golden, Colorado. The surface bed temperature in SLS was maintained at 103 °C to prevent powder from caking and also to keep the part from curling. The green part made by SLS was then processed in an air furnace to remove the polymer and oxidize the metal. The effect of firing conditions on oxidized metal part were studied. The effects of processing variables on part strength are described in the following section.

Epoxy Infiltration : The porous oxidized metal preforms were infiltrated with a liquid epoxy resin to increase density and strength of parts. Epoxy resins contain a reactive oxirane structure which is commonly referred to as an "epoxy" functionality. Liquid epoxy resins are converted through these reactive epoxy sites into tough, insoluble, and infusible solids. The main issues in choosing an epoxy infiltration system are :

(i) The epoxy should have low viscosity (of the order of 100 cp) at the operating temperature.
(ii) The epoxy should have good mechanical properties and high heat distortion temperature.
(iii) The gel time of the epoxy at the operating temperature should be large to allow sufficient time for infiltration of parts. If the gel time is short (< 1hr) the epoxy starts crosslinking during infiltration and this increases the viscosity and prevents infiltration. This becomes especially important when one has to infiltrate large parts.

There is usually a compromise between properties. Some of the epoxy infiltration systems that were tried out were : D.E.R. 331 with DEH 24 and D.E.R. 331 with Ac-methyl (anhydride curing agent) from DOW Chemical Company, CGL 1310 resin with RP1520 hardener from Ciba Giegy, and Casting resin CR 00183 from ETI Inc. Typically, the viscosity of the resin drops with temperature. The part to be infiltrated is usually heated to 60 °C and the epoxy system which is also heated to approximately the same temperature is used for infiltration. Infiltration is carried out either by applying the epoxy with a paint brush or by soaking the part in epoxy till all the porosity is filled. Figure 1. shows a resin uptake curve for infiltration of a 68% porous cylindrical oxidized iron preform with D.E.R. 331 resin, Ac-methyl curing agent, and BDMA as cure accelerator at 75 °C. This infiltration was carried out by placing the part in a pond of the epoxy.

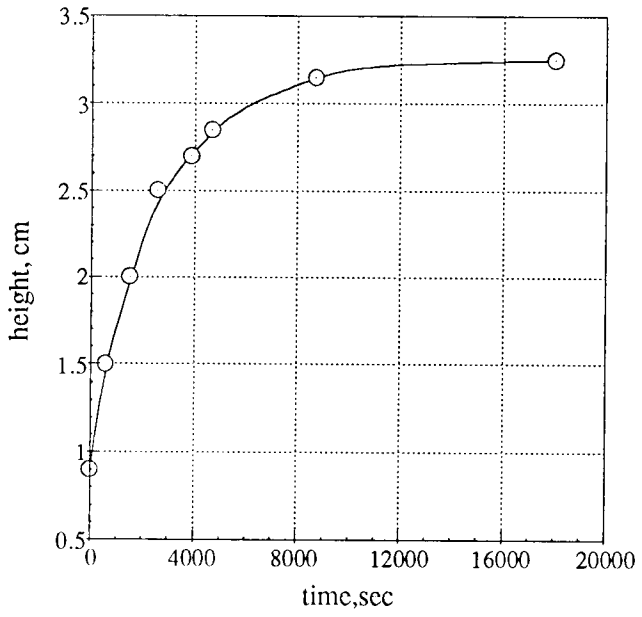

Epoxy System : DER 331 - Ac methyl - BDMA
Infiltration Temperature = 75°C

Figure 1. Resin Uptake Curve For Porous Oxidized Iron Preform

The maximum infiltration height was 3.25 cm. Copper and iron were used as materials for making bars to evaluate strengths.

Results and Discussion

The first task was to select a suitable epoxy infiltration system for infiltration of porous oxidized metal preforms. Three different epoxy resins were evaluated for infiltration using porous oxidized copper preforms fired under the same conditions. The infiltrated strengths are shown in Table 1. Even though the Ciba Giegy system shows higher strength the DOW epoxy with anhydride cure was eventually chosen because of lower viscosity and greater pot life at the operating temperature. Two different metal powders, copper and iron, were used in SLS to make bars to evaluate final strengths of the mold material. Comparison of strengths of epoxy infiltrated oxidized copper and oxidized iron bars are shown in Figure 2. All the bars were processed with identical firing cycles and a maximum firing temperature of 300°C for 15.25 hrs. Epoxy infiltrated oxidized iron bars show much higher strengths than epoxy infiltrated oxidized copper bars and hence iron was chosen as the raw material in SLS for making the mold.

Infiltrant	Avg.preform density (%)	Avg Infiltrated Density (%)	Avg. MOR (psi)
D.E.R. 331	32	98	3841
CGL 1310	32	83	4045
CR 00183	37	89	3103

Table 1. Comparison Of Epoxy Infiltrants

The SLS of iron-copolymer mixture was carried out in a full size DTM Model 125 commercial SLS machine supplied to the University by DTM Corporation. Nitrogen was used as an inert gas during the runs. The variables in SLS manufacture of green parts are the Laser Power, the Scan spacing, the step size and step period, which determine the beam speed, and the layer thickness. These can be coupled together to form an energy term known as the scan density or Andrew number which signifies the amount of heat put in per unit area [5]. Shown below is the equation for Andrew number, A_n :

$$A_n = P*f / (BS*SCSP)$$

Where
A_n = scan density, cal/cm^2
P = Power, Watts
f = conversion factor
BS = Beam Speed, inch/sec
SCSP = Scan Spacing, mils

The scan density was varied by changing the beam speed between 24 and 67 in/sec while keeping the other parameters fixed. The plot of strength with scan density is shown in Figure 2. The effect of density on strength is shown in Figure 4. The strength of a material usually varies as a power law function of the density as given by the equation below :

$$\sigma = A\rho^n$$

The plot of log(σ) with log(ρ) yields the slope "n" and intercept "A". The value of A is 7.025e-03 and n is 11.023 for the iron - copolymer SLS parts.

The effect of Firing cycle on oxidized bar strength was carried out on bars made at a scan density of 3.0. The polymer decomposition and oxidation of the metal preforms were carried out in a conventional air oven . Figure 5 shows the effect of maximum firing temperature on oxidized part strength. Table 2 shows the oxidation cycle used to study the effect of temperature on oxidized part strength.

Furnace Set Point (°C)	Time (Hrs)
200	5
300	1
400	1
500	1
Max Temp	4

Table 2. Oxidation Cycle To Study Effect Of Maximum Firing Temperature on Part Strength.

* Note : For maximum temperatures less than 500°C similar firing cycle is used and the ramp rates are the same.

The effect of firing cycle on strength of epoxy infiltrated oxidized iron bars is shown in Table 3. We see that there is dramatic increase in infiltrated strength as we go from bars oxidized at 300°C to those oxidized at 450°C. This could be a result of higher oxidized strength of the preform fired at 450°C. The epoxy used was D.E.R. 331 with Ac-Methyl as the anhydride curing agent and BDMA as the accelerator. The parts were cured at 100°C for 2hrs and then postcured at 150°C for 6hrs. The tensile strength of the anhydride cured D.E.R. 331 epoxy is reported to be 10,000 psi[6].

Max. Oxidation Temp (°C)	Time (Hours)	MOR (Oxidized part) psi	MOR (Infiltrated Part) psi
300	15.25	1480	5575
450	4.0	2500	9515

Table 3. Effect of Firing Cycle on Infiltrated Part Strength

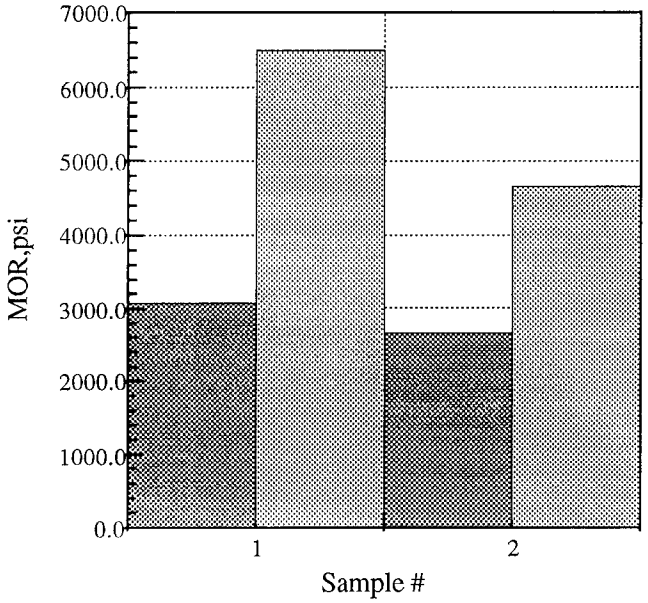

Figure 2. Comparison of Infiltrated Strengths for Oxidized Copper and Oxidized Iron Preforms

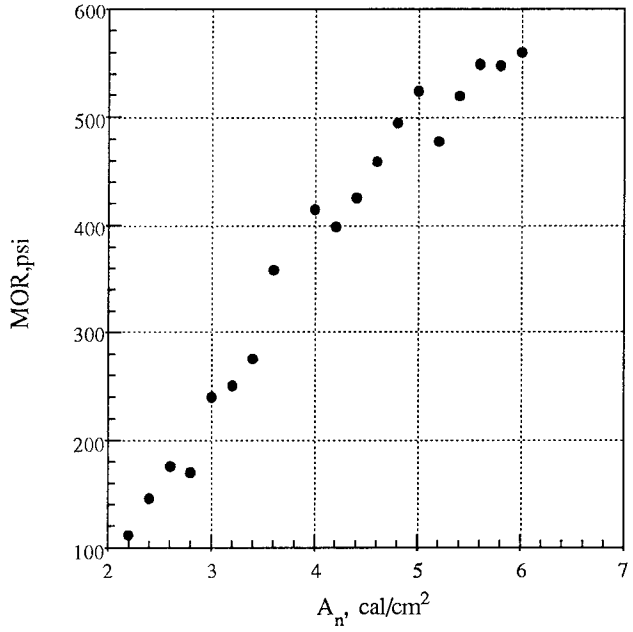

Figure 3. Effect of Scan density on green strength of Fe-copolymer parts.

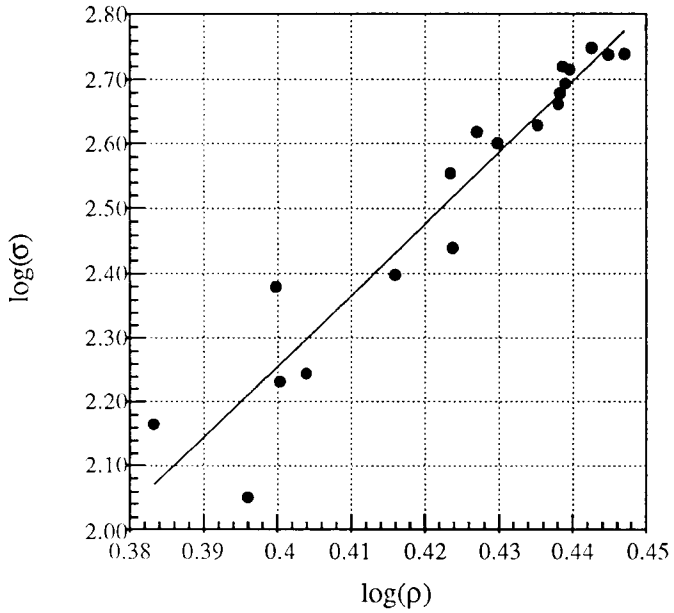

Figure 4. Variation of Part Strength with Part Density

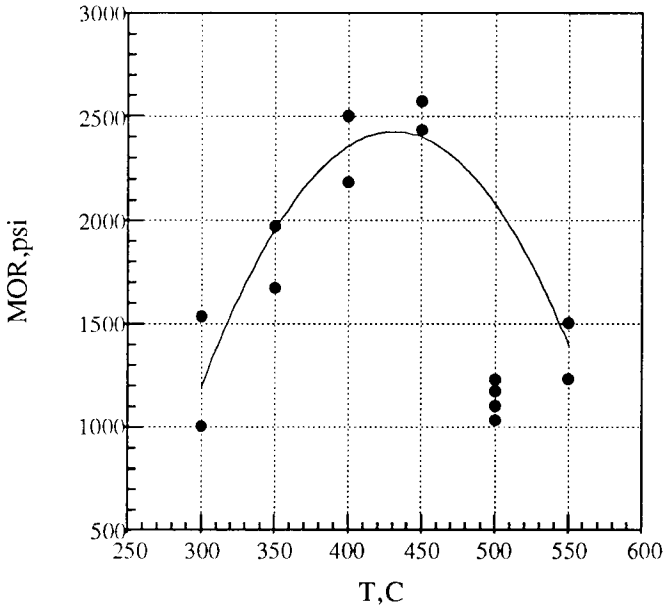

Figure 5. Effect of Maximum Firing Temperature on Oxidized Part Strength

An injection mold for Golden, Colorado, was made using iron-copolymer powder mixture by SLS. The build time for one mold was approximately 10hrs. The mold pieces were fired in an air oven to remove the polymer and oxidize the metal. The porous mold preform was infiltrated with D.E.R. 331 epoxy with Ac-Methyl as the curing agent and BDMA as the accelerator. The dimensional change in going from the drawing to the green part and from the green part to the final infiltrated part is shown in Figure 6. Figure 7 shows the green and infiltrated mold parts. The biggest changes are the associated with going from the drawing to the green part. The difference in dimensionality between the drawing and the green part can be removed using a beam compensating software. Most of the dimensional shrinkages on firing and post-curing are below 4%. The negative value for shrinkage, when going from the green to the infiltrated part, is the result of "growth" due to oxidation of iron during the firing cycle in air.

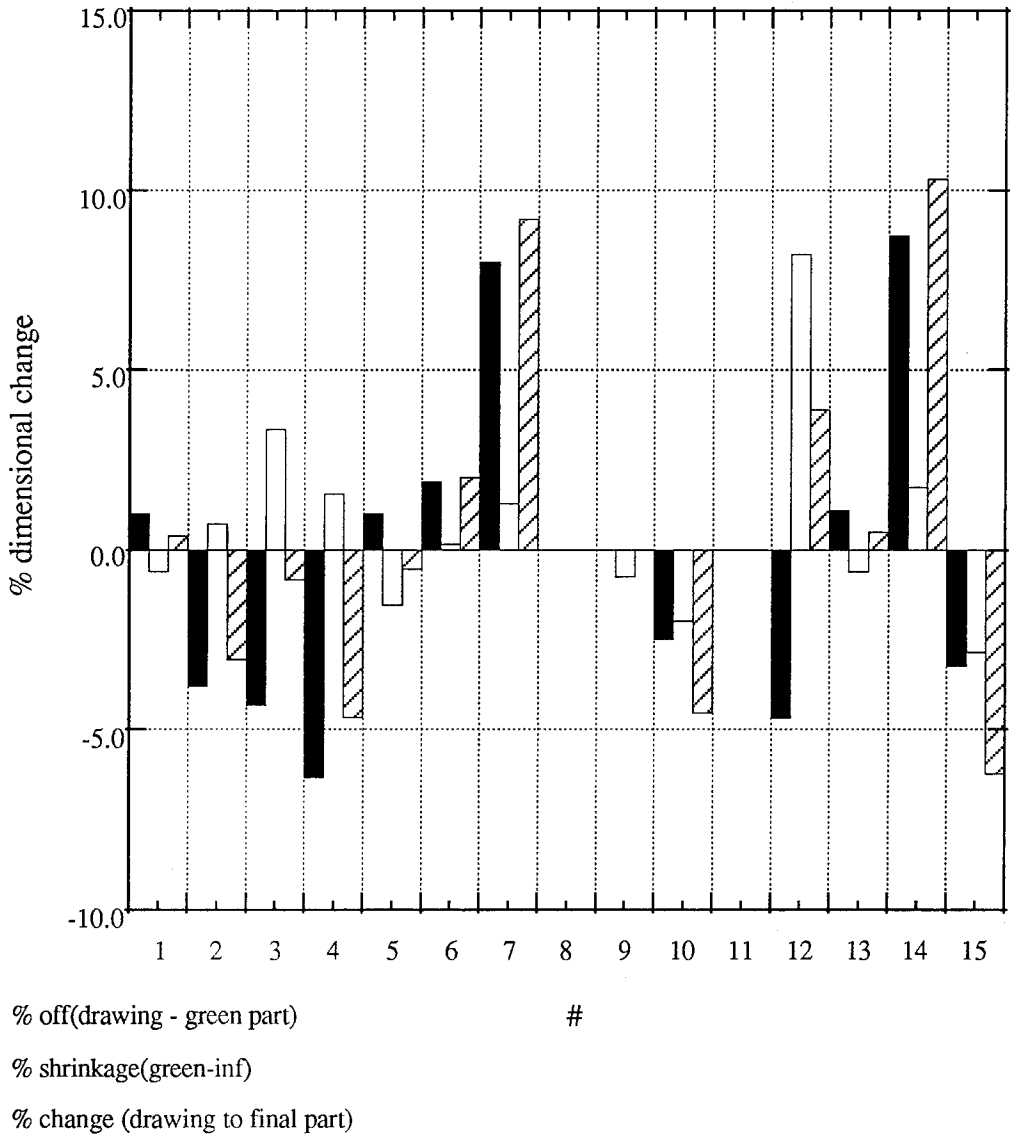

Figure 6. Dimensional Change For Mold Parts

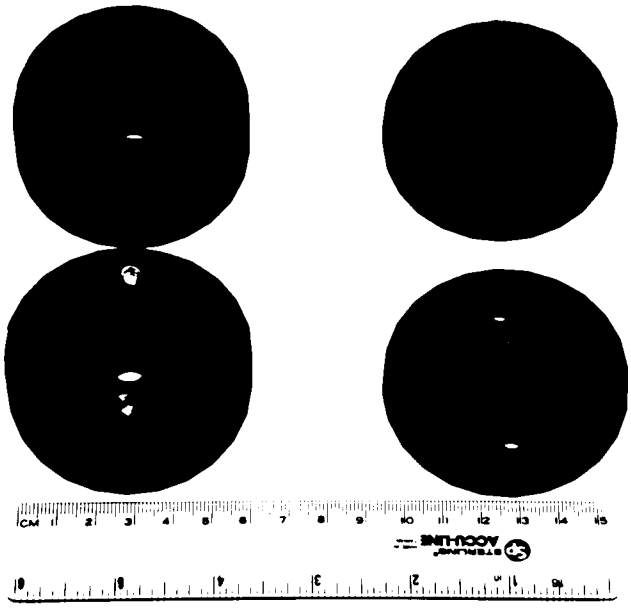

Figure 7. Green And Epoxy Infiltrated Oxidized Metal Molds

Conclusions

Selective Laser Sintering has been used to prepare indirect metal parts that have reasonable strengths. This material system can be used to make injection molds for small scale production runs. Optimization of binder burnout and metal oxidation cycle holds the key to accurate dimensional control which is critical in production of injection molds.

Acknowledgment

The authors gratefully acknowledge support for this work by DARPA / ONR Grant N00014-92-J-1394. The authors also thank N.K.Vail for his invaluable assistance in design of the mold from line drawings and in the machine operation.

References

1. Carl Deckard and Joseph Beaman, *15th Conference on Production Research and Technology*, University of California at Berkeley, p 623 - 630, (1989).
2. Harris L. Marcus, Joseph Beaman, Joel W. Barlow and David L. Bourell, *JOM*, **42**(2), p 8-10, (1990).
3. James R. Tobin, B. Badrinarayan, J. W. Barlow, J. J. Beaman and D. L. Bourell, *Proc. of the Solid Freeform Fabrication Symp.*, p 303 - 307, (1993).
4. N. K. Vail, J. W. Barlow, J. J. Beamean, H. L. Marcus, and D. L. Bourell, " Development of Poly(Methyl Methacrylate - co - n Butyl Methacrylate) Copolymer Binder System," J.Appl. Polym. Sci., **52**, p 789 - 812, (1994).
5. Christian J. Nelson, "Selective Laser Sintering : A Definition Of The Process And An Empirical Sintering Model " Ph.D Dissertation, (1993).
6. "Dow Liquid Epoxy Resins",The Dow Chemical Company, p 26, (1990).

Fundamentals of Liquid Phase Sintering Related to Selective Laser Sintering

D.E. Bunnell, D.L. Bourell, and H.L. Marcus

The Center for Materials Science
University of Texas at Austin

Abstract

Liquid phase sintering is one of the underlying principles that must be modeled and understood when the Selective Laser Sintering (SLS) process is used. This paper describes the initial studies being conducted to measure surface tension of metal alloys used for SLS. A low melting point solder was used to verify the wetting balance and pendant drop techniques and equipment for determining surface tension. The liquid-solid, liquid-vapor, and solid-vapor surface tension of 80 Sn - 20 Pb solder on mild steel was determined to be 245, 417, and 662 dynes/cm.

Introduction

Selective Laser Sintering (SLS) is a process that uses a rastering laser to sinter powder particles into a computer defined shape. Because the laser is typically rastered at speeds of 1 to 10 cm per second, the particles under the laser spot may only be at sintering temperatures for a few seconds. If the particles are to be sintered during this short period, either melting or a chemical reaction must occur to form particle necks. Liquid phase sintering (LPS) differs from conventional sintering in that a liquid phase allows for particle rearrangement and contact dissolution which accelerates the initial shrinkage rate and is the underlying principle of SLS processing of two phase (low and high melting point alloys) systems.

To evaluate the phenomena that control LPS during SLS, several factors must be considered: the rate with which a molten metal will wet a solid metal, the surface tension of liquid-solid and liquid-vapor interfaces, the dissolution rate of the solid phase in the liquid phase, the temperature transition of a powder bed as the laser rasters over it, modeling of the initial particle rearrangement during liquid phase sintering, and applying the model to fabricate a multilayer metal part using SLS. Results of the initial studies of these factors will be presented here.

Liquid Phase Sintering Theory

Kingery proposed three stages for liquid phase sintering[1]. The first stage is the formation of a liquid phase which flows and facilitates the rearrangement of particles. The second stage occurs when the liquid phase dissolves the solids and the compact density increases by solution and reprecipitation. The final phase is the formation of a solid skeleton as the compact become homogeneous and the melting point of the liquid exceeds the processing temperature.

The first stage of liquid phase sintering, particle rearrangement, results in the most rapid and largest extent of densification[2,3]. During SLS, the only part of the powder bed that contains liquid is the small area directly under the moving laser beam and the small area trailing the current position that

has not cooled below the melting point of the liquid phase. These areas will only experience a molten second phase for a short period of time, of the order of seconds, before being cooled to the temperature of the surrounding solid material. Therefore, it behooves us to model the liquid phase sintering particle rearrangement kinetics so as to characterize SLS.

During the initial stage of LPS the mechanism for densification is particle rearrangement driven by surface tension forces[4]. Kingery proposed that the densification of the compact could be modeled by the equation[5]:

$$\frac{\Delta V}{V} = \frac{-27\, C_n\, \gamma_{lv}^2\, t^2}{16\, r^2\, \eta^2}$$

Where V is the volume of the compact, C_n is the coordination number, γ_{lv} is the liquid-vapor surface tension, t is time, r is the particle radius, and η is the melt viscosity. From this equation, we need to find γ_{lv}, the liquid-vapor surface tension, and η, the liquid viscosity.

The driving force for liquid phase sintering is the capillary force that a wetting liquid exerts between two solids[6,7]. The capillary force consists of two components, surface tension and a pressure difference due to the meniscus curvature. To determine the capillary forces, it is necessary to find γ_{ls} and γ_{sv}, the liquid-solid and solid-vapor surface tensions.

The kinetics of wetting are not completely understood. The reactions preceding the advancing liquid front that are responsible for oxide layer removal are complex and involve diffusion of metal vapors through pores in the oxide and changes in surface tension due to surface active elements. Since wetting of metal particles is required for liquid phase sintering during SLS, the kinetics of wetting need to be determined to model this process.

The wetting balance test provides information on the transient wetting characteristics of a liquid-solid couple[8]. Figure 1 is a sketch of the three stages that a solid sample experiences during a wetting balance test. During the initial immersion of the solid into the molten metal, the sample is not wet and is lifted by the surface tension of the liquid. Within a fraction of a second, the liquid starts to react with the surface layer and begins to wet the exposed surface of the solid. The third stage is when the equilibrium meniscus has formed.

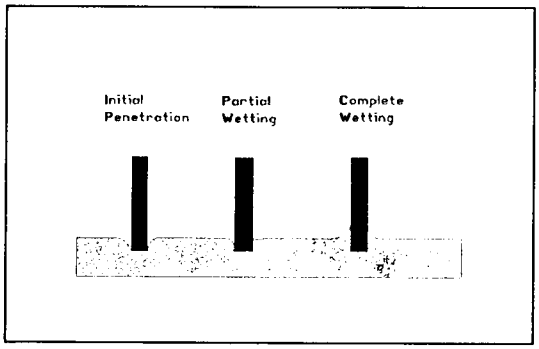

Figure 1. Stages of wetting during wetting balance test.

The value of γ_{ls} (the liquid-solid surface tension) can be determined from a force balance that includes three terms, the weight of the meniscus around the perimeter of the sample, the surface tension that pulls the liquid up, and a buoyancy term related to the volume of liquid displaced:

$$\Sigma F_y = 0 = (\Delta wt \cdot g)/l - \gamma_{ls} / \cos\theta + \Delta\rho \cdot V_d$$

Where Δwt is the weight increase of the sample, g is the gravitational constant, l is the perimeter of the sample, θ is the contact angle of the liquid-solid interface, $\Delta\rho$ is the difference in density between the solid and liquid, and V_d is the volume of liquid displaced.

If the sample penetration into the liquid is small, the buoyancy term can be neglected and from the force balance, γ_{ls} is given by the relationship:

$$\gamma_{ls} = (\Delta wt \cdot g)/l \cdot \cos\theta \qquad (1)$$

The liquid-vapor surface tension (γ_{lv}) can be determined by measuring the weight of a pendant drop[9]. Figure 2 is a sketch of a pendant drop showing the two curvatures. As a drop forms at the end of a rod, two curvatures control when it will separate. If the drop is small, gravity may be neglected and the curvatures of the pendant drop are related to the surface tension by the Laplace equation[10]:

$$\Delta P = \gamma_{lv} 2H$$

where 2H is the Gaussian average curvature and ΔP is the pressure difference. For a symmetrical drop where both curves are revolutions about an axis, the average curvature is given by:

$$2H = (1/R_1 + 1/R_2)$$

In practice, an empirical relationship exists between the diameter of the rod and 2H. The surface tension can be calculated as:

$$\gamma_{lv} = m \cdot g \cdot F/R_1 \qquad (2)$$

where m is the mass of the drop, g is the gravitational constant, F is the correlation factor related to $r/V^{1/3}$ (where V is the volume of the drop after it has separated from the rod), and R_1 is the radius of the solid rod.

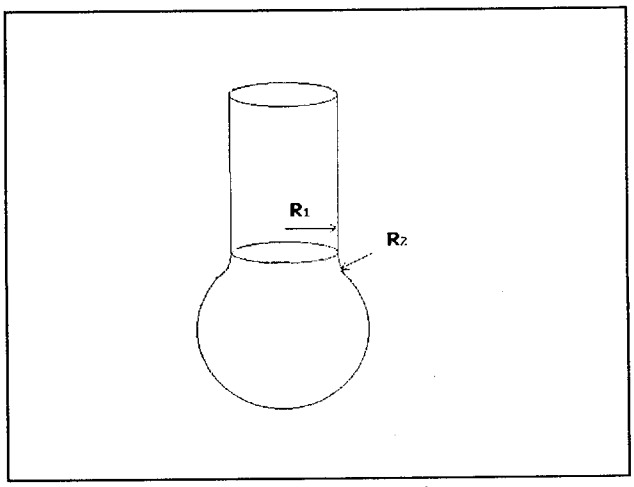

Figure 2. Curvature on a pendant drop

The factor "F" is empirically fitted to the equation:

$$F = 0.14782 + 0.27896(r/V^{1/3}) - 0.166(r/V^{1/3})^2 \quad (3)$$

Where V is the volume of a drop.

To determine the solid-vapor surface tension, γ_{sv}, the contact angle of the solidified metal was measured. At equilibrium, the condition for a liquid to wet a solid is given by Young's equation[11]:

$$\gamma_{sv} = \gamma_{ls} + \gamma_{lv}\cos\theta \quad (4)$$

Since γ_{ls} and γ_{lv} are measured using the wetting balance and the pendant drop tests, to find γ_{sv} all that is needed is the contact angle θ.

Equipment

A "wetting balance" was used to measure the rate of wetting and to provide data used to calculate γ_{ls}, the liquid-solid surface tension. The wetting balance consists of a bottom loading balance accurate to 0.01 gram with a computer interface, a 1000°C top-loading furnace with a graphite crucible, and a lab jack that raises and lowers the furnace. In practice, a sample of the solid is suspended from the bottom of the balance and the liquid metal is melted in the furnace below the balance. When the solid sample and the molten metal are at the correct temperature for the test, the computer interface is activated to record the weight changes and the furnace is raised using the lab jack until the sample touches the liquid surface. At this time, an electrical circuit from the balance to the crucible is closed that deactivates the lab jack motor. This procedure allows for a reproducible (and small) penetration depth of the solid sample into the liquid so that buoyancy effects can be minimized. After 10 seconds the furnace was lowered and the sample was sectioned and metallographically examined to determine the thickness change.

Initial tests were performed to test the suitability of the methods on low melting point materials. Mild steel sheet was the solid sample and the 80Sn-20Pb solder was used as the molten metal. This alloy was chosen since it wets steel and melts at a temperature below 300° C.

The same equipment was use to measure the liquid-vapor surface tension (γ_{lv}) using the drop weight method. A rod of the alloy was suspended vertically from the balance and the furnace was heated to 300°C for the solder alloy. The furnace was raised until just the end of the brazing rod was heated to its melting point and liquid drops formed and fell into the empty crucible. The weight change of the rod, which corresponds to the weight of the drop, was recorded for several drops and from these data, γ_{lv} was calculated.

RESULTS & DISCUSSION

The data from a wetting balance test of steel and Sn80 solder at 300°C are presented in Figure 3. For the first three seconds the weight of steel sample was a constant 1.82 grams as the molten solder was being raised to contact the edge of the sample. The weight decreased rapidly at 3.19 seconds as the steel contacted the liquid solder and pushed down on the surface. There is no initial wetting and the steel formed a depression in the surface of the molten solder. The rate that the weight decreased is related to the speed at which

the solder pot is raised and the rate of wetting. The weight of the sample as it penetrates the surface of the molten solder does not reveal any surface tension data because it is dependent on many parameters such as the velocity of the solder pot and the shape of the solid sample edge.

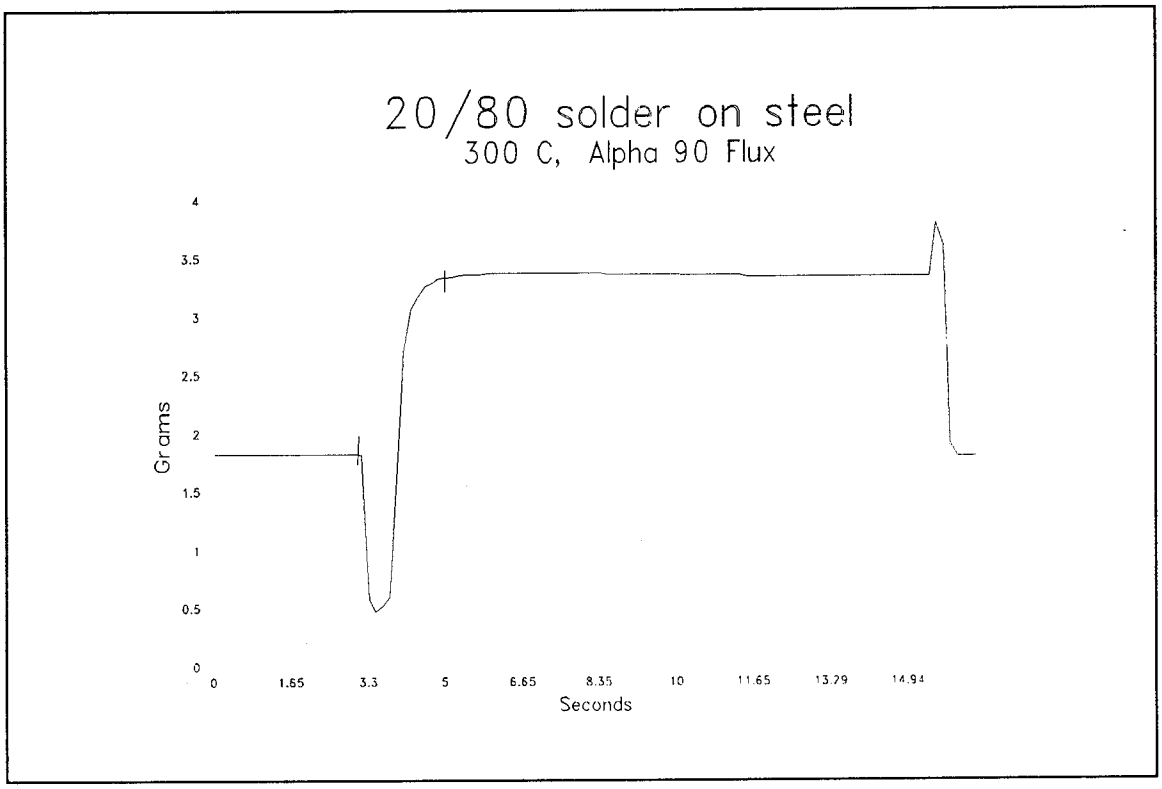

Figure 3. Wetting balance data for 80Sn-20Pb solder

The motor lifting the solder pot stopped when an electrical contact was made between the solder and sample, but inertia allowed the pot to rise a millimeter more after contact. Between 3.2 and 5.04 seconds, the solder wet the sample. During this time the molten metal reacted with any surface films on the steel and wet the solid. After five seconds the equilibrium meniscus formed and the weight leveled off at 3.37 grams and remains there until the solder pot was lowered at fifteen seconds. There is a spike in the weight of the sample as the liquid formed an inverted meniscus. The height of this spike is not relevant because the sample is in motion and equilibrium conditions do not apply.

The plot of weight versus time shows that the wetting time is approximately 2.2 seconds. This time represents the time from when the sheet of steel touched the molten solder surface to the time when the solder meniscus stopped advancing up the sheet. The change in weight due to the solder meniscus rising above the surface of the solder is 1.55 grams. The wetting angle was measured as 0° using an optical microscope at 100x so the value of γ_{ls} was calculated using equation 1 to be 245 dyne/cm.

Figure 4 is a plot of sample weight versus drop number during a pendant drop test. In this test a 80Sn-20Pb solder rod with a diameter of 0.32 cm and dipped in Kester SP-30 solder paste flux was used. The first drop weighed

0.15 grams and was most likely a drop of flux. All the remaining drops weighed between 0.25 and 0.27 grams. From these data, F was calculated from Equation 3 to be 0.2368, and the liquid-flux surface tension was calculated using Equation 2 to be 417 dyne/cm.

This compares with a literature value of 450 dyne/cm[12] but since they were measuring wetting in an inert gas while we were using a zinc chloride based flux, our value should be somewhat lower than the reported value. In a second test where no flux was used and the sample was surrounded by air, the value of γ_{lv} was determined to be 662 dyne/cm.

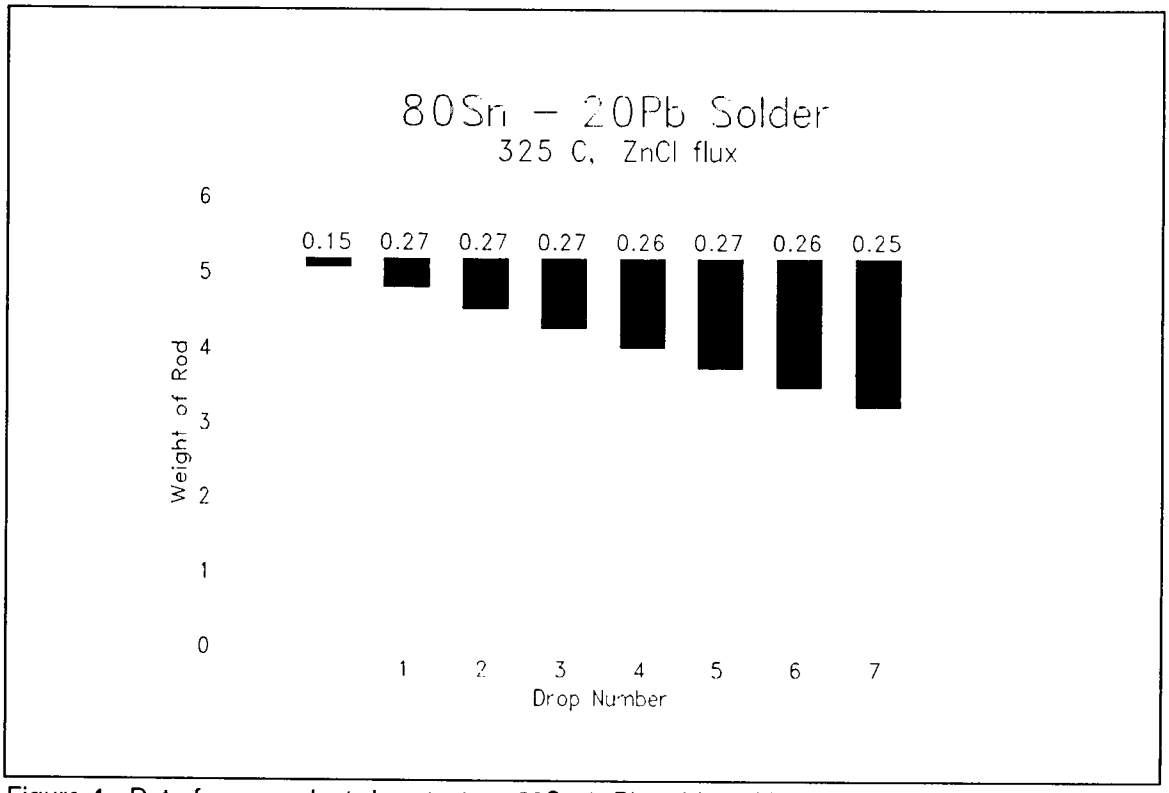

Figure 4. Data from pendant drop test on 80Sn-20Pb solder with flux

Without flux, the solder will not wet steel. Therefore, in order to determine the solid-vapor surface tension from Young's equation the liquid-vapor surface tension obtained using flux was used for this experiment. Because of this, the solid-vapor surface tension is actually the solid-flux surface tension. The contact angle θ was measured from the cross section of the steel, and γ_{sv} was calculated using equation 4 to be 565 dyne/cm.

Summary

These techniques for measuring surface tension (γ) and kinetic data are necessary to model the initial particle rearrangement stage of liquid phase sintering. The pendant drop technique is an accurate and reliable method of determining γ_{lv} and the wetting balance test gives not only γ_{ls}, but wetting kinetics data as well. By using this information we hope to be able to model the particle rearrangement process that occurs as the first stage in LPS. In

turn, the model of LPS will be used to optimize SLS of metal powders to make three dimensional parts.

This work is preliminary, to test the equipment and methods. Future work will include the surface temperature measurement of the brazing alloy in a reducing atmosphere.

Acknowledgements

This study was made possible by support from a State of Texas Advanced Research Project, ATP-116: Selective Laser Sintering: Direct Metal Fabrication and ONR grant #N00014-92-J-1314.

References

1. Kingery, W.D. "Densification during Sintering in the Presence of a Liquid Phase" J. Applied Physics 30 3, 301-306 (1959)

2. Gessinger, G.H., Fischmeister, H.F., and Lukas, H.L.; "A Model for Second-Stage Liquid-Phase Sintering with a Partially Wetting Liquid" Acta Met. 21 5, 715-724 (1974)

3. Courtney, T.H.; "Densification and Structural Development in Liquid Phase Sintering" 15A 6 1065-1074 (1984)

4. Huppmann, W.J. and Riegger, H.; "Modelling of Rearrangement Processes in Liquid Phase Sintering" Acta Met. 23 8, 965-971 (1975)

5. Kingery, W.D. and Berg, M. "Study of the Initial Stages of Sintering Solids by Viscous Flow, Evaporation-Condensation, and Self-Diffusion" J. Applied Physics 26 10, 1205-1212 (1955)

6. Huppmann, W.J. and Riegger, H.; "Modelling of Rearrangement Processes in Liquid Phase Sintering" Acta Met. 23 8, 965-971 (1975)

7. Kingery, W.D. "Densification during Sintering in the Presence of a Liquid Phase" J. Applied Physics 30 3, 301-306 (1959)

8. Vianco, P.T., Hosking, F.M. and Rejent, J.A.; "Solderability Testing of Kovar with 60Sn-40Pb Solder and Organic Fluxes" Welding Journal 6, 230s-240s (1990)

9. Lando, J.L. and Oakley, H.T.; "Tabulated Correction Factors for the Drop-Weight-Volume Determination of Surface and Interfacial Tensions" J. Colloid and Interface Sci. 25 526-530 (1967)

10. Murr, L.E.; Interfacial Phenomena in Metals and Alloys Techbooks p89-105 (1975)

11. Heady, R.B. and Cahn, J.W.; "An Analysis of the Capillary Forces in Liquid-Phase Sintering of Spherical Particles" Met. Trans. 1 1 185-189 (1970)

12. Murr, L.E.; Interfacial Phenomena in Metals and Alloys Techbooks p89-105 (1975)

Modeling of Polymer Degradation in SLS

N.K. Vail and J.W. Barlow
Department of Chemical Engineering
The University of Texas at Austin

Abstract

A simple computer model has been developed to predict the thermal degradation of polymer binders used in the fabrication of composite green shapes from high temperature ceramic materials. Decomposition rate kinetics of the polymer materials were determined and incorporated into the model. The polymer degradation occurring in three separate powder systems was determined as a function of applied laser energy. Agreement between model results and experimental data is quite good.
(Key Words: Polymer, Degradation, Selective Laser Sintering, Composites).

Introduction

The development of polymer coated ceramic and metal materials has provided the capability to Selective Laser Sintering (SLS) to fabricate *green* composite shapes that can be post-processed by conventional means to yield functional objects. Already a great deal of research has been conducted to develop suitable polymer binder materials for SLS[1,2] as well as research that has focused on examining the performance of the developed binders in the fabrication of *green* composites via the SLS process.[3,4]

Still, work is continuing with polymer composite systems to maximize their performance. One problem that is evident from past studies is the occurrence of binder degradation as a result of SLS processing. Measurable amounts of binder loss have been observed in all polymer composite materials studied by these authors. Loss of polymer binder during SLS processing has the obvious consequence of reduced green strength in the fabricated object. As better binder systems are developed that require lesser amounts to yield green objects the effects of binder degradation will become more prevalent. This paper presents preliminary work to model binder degradation in an effort to predict observed results.

Degradation Model

Polymer degradation model development follows closely the modeling of thermoplastic sintering discussed by Nelson.[5] The model derived from the 1-dimensional

heat transfer equation defined as

$$\rho C_p \frac{\partial T}{\partial t} = \frac{\partial}{\partial z}\left(k \frac{\partial T}{\partial t}\right)$$

$$-k\frac{\partial T}{\partial z} = \alpha_R \langle I \rangle - h(T - T_\infty) \quad ; \quad z = 0 \quad t \le \tau$$

$$-k\frac{\partial T}{\partial z} = -h(T - T_\infty) \quad ; \quad z = 0 \quad t > \tau \qquad (1)$$

$$-k\frac{\partial T}{\partial z} = 0 \quad ; \quad z = \infty \quad t > 0$$

where ρ is the bed density, C_p the heat capacity, T the temperature, t the time, k the thermal conductivity, α_R the absorptivity of the material, <I> the laser intensity, h the overall heat transfer coefficient, T_∞ the ambient temperature, and τ the duration of the applied laser energy.

Eq. 1 was solved via a Crank-Nicholson finite difference form that is unconditionally stable with discretization errors $O[(\Delta t)^2 + (\Delta z)^2]$.[6,7] To complete the thermal model several of the physical parameters need to be evaluated. The bed density, ρ, is assumed to be that measured for the green parts with no changes occurring due to polymer sintering and binder loss. Previous data show part densities are very similar to measured bed densities.[3] The specific heat of the bed, C_p, is assumed linear with the mass fraction contribution of the constituents.[8]

$$\overline{C_p} = \sum_1^{\dot{}} x_i C_{p_i} \qquad (2)$$

The effective bed thermal conductivity, k_{eff}, is predicted from the Yagi-Kunii model for packed particle beds[9]

$$\frac{k_{eff}}{k_g} = \frac{\beta(1 - \varepsilon)}{\gamma \frac{k_g}{k_{s,eff}} + \frac{1}{\frac{1}{\varphi} + \frac{D_p h_{rv}}{k_g}}} + \varepsilon \beta \frac{D_p h_{rv}}{k_g} \qquad (3)$$

where ε is the void fraction of the bed, $\gamma \approx 1$ and $\beta \approx 1$ for beds of spherical or cylindrical particles, k_g the thermal conductivity of the gas within the bed, $k_{S,eff}$ the effective thermal

conductivity of the solid, D_p the average particle diameter, h_{rv} and h_{rs} the radiation heat transfer coefficients for void to void and solid to solid, respectively, and φ is a gas-geometry correction factor. For air, Yagi-Kunii give an empirical form of φ as

$$\varphi = 0.1927\,\varepsilon^{1.8544} \tag{4}$$

The effective solid thermal conductivity, $k_{S,\,eff}$, of the composite material was estimated in two steps. The morphology of polymer coated particles used in these studies is such that it is difficult to know their exact makeup. For the purposes here it is assumed the coated particles are of a core-shell geometry thus the thermal conductivity of the coated particle, k_c, is given by[10]

$$\frac{1}{k_c} = \left(\frac{B}{k_1^2} - \frac{2}{k_1}\right)\ln\left(\frac{B - k_1}{B - k_1 t_c / R_1}\right) + \frac{t_c}{R_1 k_2} + \left(\frac{1 - t_c / R_1}{k_1}\right) \tag{5}$$

where

$$B = 2\left(\frac{t_c}{R_1}\right)k_2 + 2\left(1 - \frac{t_c}{R_1}\right)k_1 \tag{6}$$

and k_1 is the thermal conductivity of the core, k_2 the thermal conductivity of the coating, R_1 the radius of the core particle, and t_c the thickness of the coating defined as

$$t_c = R_1\left(\frac{1 - (1 - \phi_p)^{1/3}}{(1 - \phi_p)^{1/3}}\right) \tag{7}$$

and ϕ_p is the volume fraction of the polymer coating. Some of the material systems studied were comprised of coated particles and pure powder substrate. In these cases, $k_{S,\,eff}$ is determined from the rule of mixtures

$$k_{s,eff} = \sum_i^n \phi_i k_i \tag{8}$$

where ϕ_i is the volume fraction of the i-th component. For material systems composed only of coated particles $k_{S,\,eff} = k_c$.

The laser flux, $\alpha_R\langle I\rangle$, was determined based on scanning geometry and is a function of laser power, laser spot size, laser scanning speed, and the distance between adjacent scan vectors. The beam is Gaussian by measurement therefore, the total applied energy to boundary condition is easily modeled as a fixed sequence of discrete pulses occurring at intervals determined from the scan speed for a total time of τ.[5]

Degradation of the binder was determined at each nodal point from kinetic expressions described below. Bed properties were re-evaluated at each time step to reflect changing physical conditions.

Materials and Methods

Two polymer composite material systems were studied. The first consisted of two batches of monodisperse silicon carbide (Norton) coated with a PMMA binder and a methylmethacrylate/*n*-butylmethacrylate (MMA/*n*BMA) copolymer binder. The preparation and evaluation of these coated powders has been described elsewhere.[3] The average particle size of the silicon carbide powder was 12.6±2.9μm (Coulter Multisizer). The second material system was a group of powders that consisted of a series of different molecular weight MMA/*n*BMA copolymer binders coated on to a spheroidized soda-lime glass (Potters Industries). The average particle size of the glass powder was 5.0±2.5μm (Coulter Multisizer).

Test specimens were fabricated from each of the powder materials via SLS. The silicon carbide powders were processed in an SLS™ Model 125 workstation while the glass powders were processed in the academic prototype, Bambi.[11] Operating conditions were maintained constant within limits of the two machines. Test specimens were fabricated using applied energy densities, A_N, over the range 0.5-3.0 cal/cm^2. Two to four specimens were prepared at each scanning condition.

The fabricated specimens were fractured at the midpoint and a powder sample taken from the center of the fracture plane. The polymer content of the powder sample was determined by Thermal Gravimetric Analysis (TGA) (Perkin-Elmer Series 7). The relative mass loss of the samples were measured over the temperature range 50-650°C in a flowing N_2 stream. The polymer content of the sample was evaluated as the difference in relative weight loss at 600°C and 100°C, respectively.

The five copolymer samples of different molecular weights used to coat the glass powder were fabricated by methods described previously.[2] The properties of these polymers are listed in Table 1. The degradation kinetics of these copolymers were also determined by TGA. The normalized weight losses of ~10mg samples of spray dried polymer powder were determined at isothermal conditions while in a stream of pure N_2. Each sample was preheated to 175°C for a period of five minutes before being quickly raised to a predetermined temperature at a rate of 150°C/min. Independent TGA traces showed no appreciable polymer weight loss during the pre-heat period. Weight loss

curves were collected over the temperature range of 290°C-350°C at 10-15°C intervals.

Table 1 Properties of MMA/*n*BMA copolymers used to coat glass powder.

Latex	Density, (g/cm^3)	T_g, (°C)	Melt Flow, (g/10min 200°C 75psi)
M/B -1- S	1.163	97.5	0.104
M/B -2- S	1.163	96.8	0.96
M/B -4- S	1.156	94.1	8.64
M/B -6- S	1.156	91.8	31.1
M/B -8- S	1.156	88.5	74.7

The thermal conductivities and specific heats of the ceramic powders were obtained for the solids from the literature.[12,13,14,15] Similar values for PMMA were also obtained from the literature.[16,17] The thermal conductivity of the MMA/nBMA copolymers was assumed to be that of PMMA. The specific heat of the copolymers has been determined to be[18]

$$C_p\left(\frac{cal}{g\text{-}°C}\right) = 0.319 + 0.802x10^{-3}\,T \;;\; T<90\,°C$$
$$C_p\left(\frac{cal}{g\text{-}°C}\right) = 0.341 + 1.126x10^{-3}\,T \;;\; T\geq 90\,°C \qquad (9)$$

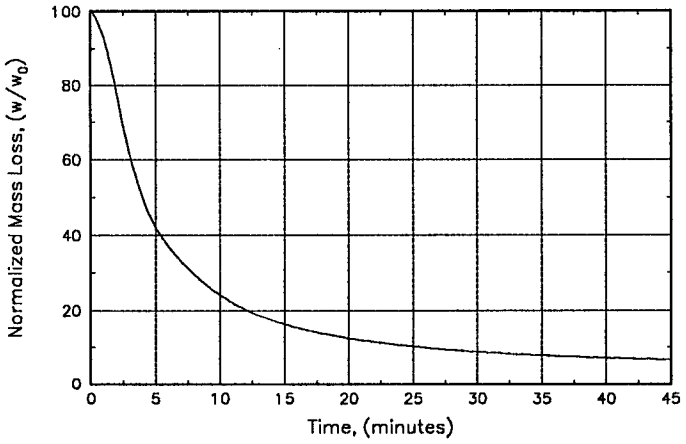

Figure 1 Isothermal decomposition of MMA/nBMA copolymer M/B -4-S at 330°C in N_2.

Results and Discussion

Figure 1 shows a typical weight loss trace for a MMA/*n*BMA copolymer. The traces of all copolymers were first-order to beyond 50% conversion over the temperature range studied. The first order degradation indicates a depolymerization mechanism similar to that of PMMA with reasonably long zip lengths and which is independent of termination reaction order.[19] Degradation rate kinetics were determined from the initial slopes of the relative mass loss curves according to the first-order rate-expression

$$\frac{d}{dt}\left(\frac{w}{w_0}\right) = -k_{DP}\frac{w}{w_0} \tag{10}$$

where w/w_0 is the normalized mass loss of the polymer sample and k_{DP} is the degradation rate constant.

Degradation rates of all the copolymers were similar although a small dependence on molecular weight was noted. An average value of the degradation rate expression was used for prediction of polymer degradation in the model, Eq. 11. The degradation rate expression given by Inaba, *et. al.*,[19] was used for the PMMA coated silicon carbide sample, Eq. 12.

$$k_{DP}(s^{-1}) = 2.631x10^{12}\exp\left(\frac{-21320}{T}\right), \quad T(K) \tag{11}$$

$$k_{DP}(s^{-1}) = 1.182x10^{19}\exp\left(\frac{-32140}{T}\right), \quad T(K) \tag{12}$$

Figure 2 shows the polymer degradation for the PMMA coated SiC material. This material contained ~20 vol. % polymer (8.5 wt. %) and was derived from a polymer coated batch containing ~25 vol. % binder to which raw SiC had been added. The extent of binder loss is significant showing more than a 15% mass loss at the highest energy densities. In this case the model does a reasonable job of predicting the extent of binder loss. Although, the experimental data appear at a glance to be essentially linear this may be more an artifact of error in the data. On the other hand, the model predicts a more gradual development to binder loss, characteristic to the first-order rate dependence, and becomes increasingly dominant at the higher energy densities as would be expected.

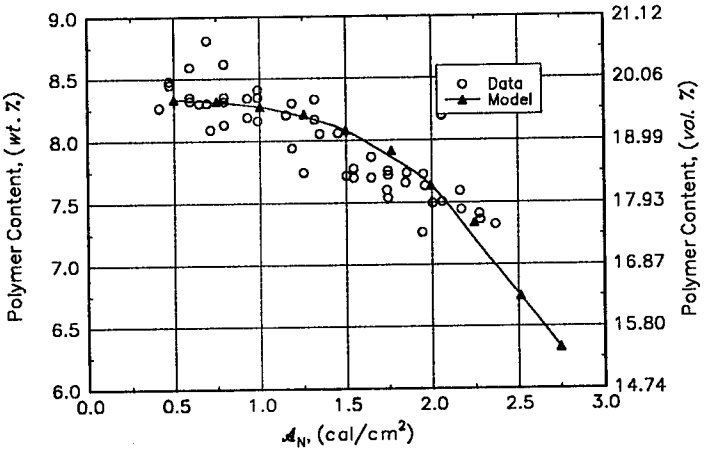

Figure 2 Comparison of predicted polymer degradation to experimental results for PMMA coated Silicon Carbide.

Figure 3 shows the extent of polymer degradation for the MMA/*n*BMA copolymer coated onto SiC. This material system has nearly the same compositional makeup as the PMMA/SiC material discussed above. The extent of degradation is much reduced for this material showing about a 6% wt. loss overall at the highest energy densities. The decreased degradation of the copolymer is consistent with the less rigorous kinetics described by Eq. 11. In this case, the model prediction is quite close to the experimental data. However, at the higher energy densities, the predicted extent of binder degradation may be too severe.

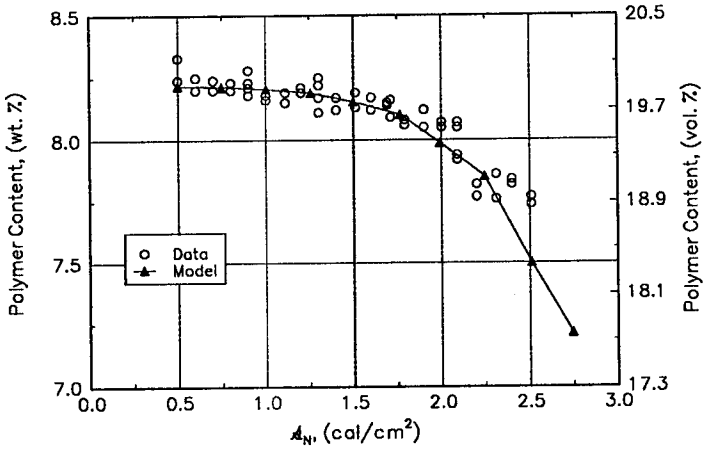

Figure 3 Comparison of predicted polymer degradation to experiment for MMA/*n*BMA copolymer coated Silicon Carbide.

Figure 4 shows the extent of binder degradation for all the copolymer glass powders described above. One set of data corresponding to the M/B -1-S coated glass powder was discarded since the polymer content of this powder was lower (~21% vol) than the remaining powders (~23 vol. %). The remaining data points represent the average of at

least three data points. This system contained only coated powders. The agreement of the model prediction with the experimental data in this case is excellent. This result offers some verification to the validity of the developed model for two reasons. First, the thermal conductivity of the glass powder much lower than for the silicon carbide powder discussed above. SiC has a thermal conductivity similar to that of most metals while that of glass characteristically lower. Second, the makeup of the material systems is altered.

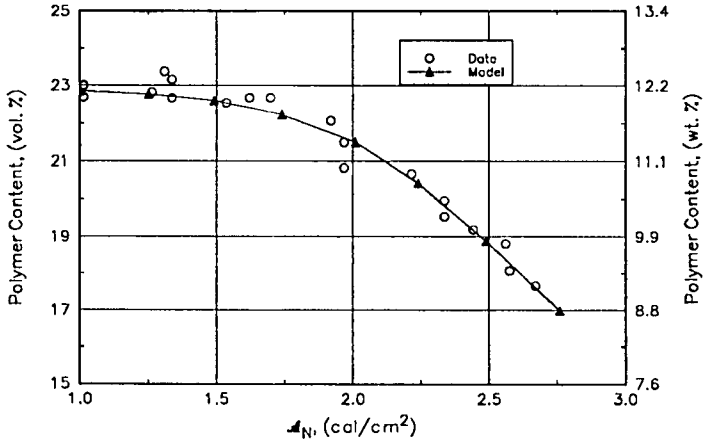

Figure 4 Comparison of predicted polymer degradation for MMA/*n*BMA copolymer coated A-5000 soda-lime glass.

Conclusions and Further Work

The binder degradation model discussed briefly here appears to predict well the extent of binder degradation in the material systems studied. More work is required to verify the validity of the model by comparison to other material systems such as polymer coated metals and material systems of polymer mixed with powder substrates. With further verification of the model it will be simple to use the model to study the effects of SLS processing conditions on the extent of binder loss as possible tool for optimizing process conditions for optimal results.

This research was supported by DARPA/ONR grant N000 14-92-J-1394 and DARPA grant MDA 972-92-J-1026 through Lanxide Corporation.

References

1. N.K. Vail and J.W. Barlow, *SFF Symp. Proc.*, **1**, 8 (1990).

2. N.K. Vail, J.W. Barlow, J.J. Beaman, H.L. Marcus, and D.L. Bourell, *J. Appl. Poly. Sci.*, **52**, 789 (1994).

3. N.K. Vail, J.W. Barlow, and H.L. Marcus, *SFF Symp. Proc.*, **4**, 204 (1993).

4. L. Deckard and T.D. Claar, *ibid. ref. 3*, p. 215.

5. J.C. Nelson, Ph.D. Dissertation, The University of Texas at Austin, 1993.

6. S.C. Chapra and R.P. Canale, *Numerical Methods for Engineers, 2nd Ed.*, McGraw-Hill, New York, 1988.

7. W.F. Ames, *Numerical Methods for Partial Differential Equations, 2nd. Ed.*, Academic Press, New York, 1977.

8. R.M. German, *Powder Injection Molding*, Metal Powder Industries Federation, Princeton, NJ, 1990.

9. S. Yagi and D. Kunii, *J. AIChE*, **3 [3]**, 373 (1957).

10. B. Badrinarayan and J.W. Barlow, *SFF Symp. Proc.*, **1**, 91 (1990).

11. P.A. Forderhase, *Design of a Selective Laser Sintering Machine Intended for Academic Use*, M.S. Thesis, The University of Texas at Austin, 1989.

12. E.S. Dettmer, B.M. Romenesko, H.K. Charles, Jr., B.G. Carkhuff, and D.J. Merrill, *IEEE Trans.*, **12 [4]**, 543 (1989).

13. R.H. Perry and C.H. Chilton, *Chemical Engineers' Handbook, 5th. Ed.*, McGraw-Hill, New York, 1973.

14. Y.S. Touloukian, R.W. Powell, C.Y. Ho, and P.G. Klemens, *Thermophysical Properties of Matter, Vol. 1-4*, IFI/Plenum, New York, 1970.

15. F.P. Incropera and D.P. DeWitt, *Fundamentals of Heat and Mass Transfer*, J. Wiley and Sons, Inc., New York, 1985.

16. V.P. Lohe, *Kolloid-Z. und Z. für Polymere*, **203 [2]**, 115 (1965).

17. J. Brandrup and E.H. Immergut, *Polymer Handbook, 3rd. Ed.*, J. Wiley and Sons., Inc., New York, 1989.

18. N.K. Vail, Ph.D. Dissertation, *to be published.*

19. A. Inaba, T. Kashiwagi and J.E. Brown, *Poly. Deg. and Stab.*, **21**, 1 (1988).

ULTRAVIOLET CURING OF HIGHLY LOADED CERAMIC SUSPENSIONS FOR STEREOLITHOGRAPHY OF CERAMICS

Michelle L. Griffith and John W. Halloran
Materials Science and Engineering Department
The University of Michigan
Ann Arbor, MI

ABSTRACT

Ceramic green bodies can be created using stereolithography methods where a ceramic slip consisting of 45-55 v/o ceramic powder is dispersed within an ultraviolet-curable aqueous acrylamide solution. Two ceramic materials were investigated: silica [SiO_2] for investment casting purposes, and alumina [Al_2O_3] for structural parts. After mixing the powders in the curable solution, the ceramic slip is tape cast onto a substrate for cure under a high intensity ultraviolet lamp (220-450 nm) at different exposure times. The materials systems were evaluated at different solids loadings (10-50 v/o) for cure thickness and viscosity control. Silica had a cure depth of 330 μm at a solids loading of 55 v/o, and at 50 v/o, alumina had a cure depth of 300 μm.

Preliminary work utilizing scattering theory revealed the cure depth is controlled by the particle size and the refractive index difference between the ceramic and ultraviolet solution. The refractive index difference is the dominating factor. Two particle size distributions of alumina were used to more accurately determine the effect of particle size.

INTRODUCTION

Layered manufacturing of ceramics has been accomplished by scanning laser sintering (Lakshminarayan et. al., 1990) and three dimensional printing (Sachs et. al., 1993). The most popular layered manufacturing method, stereolithography (SLA), has not yet been adapted to produce ceramics. For example, the 3D Systems' SLA machine, which use a laser beam to cure a liquid monomer in a line-by-line, layer-by-layer cure sequence (Jacobs, 1993a), is one of the most effective methods for layered manufacturing (Jacobs, 1993b and Burns, 1993), but has only been used for polymeric materials which can be directly produced by photopolymerization. Our goal is to extend the stereolithography method so it can be used for free form fabrication of ceramics such as alumina (Al_2O_3) components, or silica (SiO_2) shells and cores for investment casting refractories. To accomplish this, we are developing techniques for UV curing of a highly loaded suspension of ceramic particles. The UV curable liquid creates the polymer binder to form a ceramic green part. As a preliminary step, we have used the UV curable ceramic suspensions to fabricate single-layer parts with simple masks, but our goal is to develop these suspensions so they can be used to fabricate ceramics by stereolithography. This paper reports our progress at the point of this writing.

A candidate stereolithography system for ceramics must satisfy several requirements. Since a high quality ceramic is the goal, the free form ceramic green body must have a high density, either for its refractory properties or so it can be readily sinterable to form a dense ceramic. To operate in an SLA resin tank, the ceramic SLA suspension must be at least as fluid as

conventional SLA resins (viscosity less than 3000 mPa·s) for proper flow during recoat. The ceramic SLA suspension must also be curable by UV lasers, with useful cure depth and resolution.

To achieve acceptable ceramic quality, the SLA slip must use the same ceramic powders as required by ordinary ceramic processing. Fine-grained structural or electronic ceramics, such as alumina, require very fine powders with 200-700 nanometer particles, while refractories, such as silica-based investment casting cores, have particles ranging from 1-50 micrometers. The alumina is subsequently sintered at high temperature to yield a pore-free body. For successful sintering, the solids volume fraction in the SLA-cured body must be at least 0.50-0.65, similar to conventionally processed ceramic green bodies. Since no shrinkage occurs during curing, the ceramic volume fraction in the solid cured body is the same as the ceramics loading of the fluid SLA suspension before curing. Silica refractory cores do not shrink during sintering, but their fired density is a critical parameter, and control of the density must be exercised in the SLA slip, again requiring high volume fraction loading.

The SLA suspension, at a 0.60 solids volume fraction, is a very highly concentrated suspension, which must have relatively low viscosity with nearly Newtonian flow behavior. These highly loaded suspensions tend to be excessively viscous unless an excellent degree of colloidal dispersion can be achieved. The viscosity [η] of a suspension with a volume fraction solids [ϕ] is greater than the viscosity of the pure liquid [η_O] by a factor modeled by a modified Krieger-Dougherty Equation (1959)

$$\eta = \eta_o \left(1 - \frac{\beta\phi}{\phi_o}\right)^{-2.5\phi_o} \qquad (1)$$

Here ϕ_O represents the volume fraction solids at maximum packing for solid particles, where the system changes from a fluidized suspension into a wet solid. The maximum solids fraction ranges from about 0.63 for uniform spherical particles to about 0.70 for powders with a wide particle size distribution. The term $\beta\phi$ is the effective volume fraction of the suspended solids. If the particles are perfectly colloidally dispersed, β=1, and the suspension has the lowest possible viscosity. Note that the viscosity rises sharply as the solids loading approaches ϕ_O, so fluid suspensions in the 50-60 vol% range are increasingly difficult to prepare. The rise in viscosity is much greater if submicron powder must be used, because dispersion of these fine powders becomes increasingly difficult so the β term is usually significantly greater than 1. Obtaining effective dispersion for submicron powders requires careful design of the colloidal dispersant system. The viscosity of the pure monomer resin, η_O, is extremely important. In this paper, we present results for an aqueous system, so the monomer viscosity is only 1 mPa·s. Low viscosity acrylic systems, based on low molecular weight diacrylates, have been reported elsewhere (Griffith and Halloran, 1994).

This concentrated ceramic suspension must be sufficiently transparent to UV light to permit an acceptable depth of cure. Powder suspensions can have a very high turbidity due to light scattering, even if the ceramic itself is transparent to UV. The scattering-induced turbidity limits the distance of penetration of the UV light into the suspension, and largely determines the depth of cure, D_{cure}, for a ceramic suspension. The depth of cure can be modeled by assuming it to be the depth at which the UV beam is attenuated from the incident intensity (I_O) down to the minimum intensity required to achieve photocuring (I_{cure}) for the particular photoinitiator/monomer system. This can be derived from a standard expression for turbidity of suspensions (van de Hulst, 1957), to give:

$$D_{cure} \approx \left[\frac{d}{Q}\right]\left(\frac{1}{\phi}\right)\ln\left[\frac{I_o}{I_{cure}}\right] \qquad (2)$$

where Φ is the volume fraction of ceramic, d is particle size, and Q is the efficiency factor for the extinction coefficient for the ceramic-resin system. The term Q is not a simple quantity, and in

general must be numerically calculated for a specific situation (Barber and Hill, 1990). However, for many cases relevant to ceramics, it can be modeled by the Raleigh-Gans equation (van de Hulst, 1957)-

$$Q \approx \left[\frac{\Delta n}{n_o}\right]^2 \left(\frac{d}{\lambda}\right)^2 \qquad (3)$$

where Δn is the refractive index difference between the ceramic (n_p) and the UV curable resin (n_o) and λ is the UV wavelength. Notice the strong dependence which the refractive index difference has on the depth of cure.

One final feature is the absorption range of the photoinitiator system. As with other particle -filled systems, such as UV-cured pigments (Dorfner, 1991), the absorption range of the photoinitiator must be adjusted to avoid interference from the particles.

MATERIALS SYSTEMS

We are investigating an aqueous system which gels upon UV irradiation, to transform the fluid suspension to a rigid solid. The liquid phase is a 30 wt% solution of acrylamide, a monofunctional monomer which can be polymerized with a free radical initiator to create water-soluble polyacrylamide. Addition of the crosslinking monomer methylene bis-acrylamide creates a rigid aqueous gel upon curing. After evaporation of the water, about 15 vol% of dry polyacrylamide remains in the green ceramic. This is sufficient to impart adequate strength to the green ceramic, but is easily removed during binder burnout. The aqueous acrylamide solution has a refractive index of 1.35 at 366 nm. This system is based upon an Oak Ridge National Laboratory "gel casting" technique for injection molding (Janney, 1990 and Young et. al., 1991), which uses thermal polymerization of acrylamide to solidify a suspension into a polyacrylamide gel.

Two ceramic materials were investigated. Silica is a typical example for low refractive index ceramics. It also is of great technological interest, as silica is a workhorse refractory material for shells and cores in the investment casting industry. The particle size range is broad, averaging 1.5 micron, which is similar to the finer components in silica refractories. Alumina was investigated as an example of a high strength structural ceramic. Alumina has a higher refractive index, and most applications demand a submicron particle size. Two grades of alumina were investigated to help determine the effect of particle size on the UV cure depth. Table 1 contains the refractive index (Palik, 1985) and particle size information for these three powders and the aqueous UV curable solution.

TABLE 1: PROPERTIES OF CERAMIC AND UV CURABLE LIQUID.

Material	n (366 nm)	d (μm)	ηo (mPa·s)
aqueous UV	1.35		1
silica	1.56	1.5	
alumina (15)	1.70	0.7	
alumina (50)	1.70	0.2	

Two photoinitiators (PI) were used. One is a phosphine oxide which has an absorption range up to 400 nm with photobleaching properties. A ketone derivative with an absorption to 400 nm was also used. Two photoinitiators were needed for the aqueous system due to the low solubility of commercial PIs in water.

EXPERIMENTAL

We used a medium pressure mercury ultraviolet lamp (UV Laboratory System, Hanovia) to examine the UV curing properties of the ceramic suspension. This lamp has three power outputs: 300, 200, 125 W/in, which corresponds to irradiance densities of 2.51, 1.69, and 1.02 W/cm^2, and emits a broad spectrum of ultraviolet wavelengths ranging from 220 to 450 nm. This lamp is part of a conveyorized system where the suspension, applied as a film onto a substrate, moves under the lamp. The time of cure is controlled by the speed of the conveyor belt.

The UV curable suspensions were prepared by adding ceramic powder incrementally, and then mixing in a high shear mixer for 1-5 minutes per increment of powder. After the chosen solids loading was reached, the suspension was homogenizing by conventional ball milling for 2-12 hours, depending on the solids loading.

The UV suspension was either put in a petrie dish or tape cast onto a glass slide, depending on viscosity, and subsequently exposed to the UV light. Afterwards, the cured film was lifted off the substrate. The thickness of the cured film was measured using optical or scanning electron microscopy, and used to infer depth of cure.

RESULTS

I. Silica

Due to the larger particle size and surface chemistry of silica powder (Iler, 1979), it was easy to disperse silica in the aqueous UV curable liquid. The approximate viscosity of a 50 v/o SiO_2 suspension was 200 mPa·s. Note the refractive index term, $[\Delta n/n_o]^2$ is 0.024 for this system, reflecting the similar refractive indices of powder and the aqueous solution. Both photointiators were used in the formulation: 0.4 w/o phosphine oxide and 0.7 w/o ketone derivative, which is the maximum solubility of the PIs in the aqueous system.

Figure 1 shows the depth of cure versus volume percent silica added to the aqueous system. All materials were cured at 2.51 W/cm^2 for times of 2.4 and 9.6 seconds corresponding to exposures of 6.01 and 24.06 J/cm^2 to the UV light. At low volume fraction silica, the exposure time or dose is important, as cure depth increases with exposure dose. By 50 v/o, the exposure time has much less effect upon cure depth. Note that 55 v/o SiO_2 suspensions, which are sufficiently concentrated for ceramic use, have a cure depth of 330 μm, which is large enough for effective use in stereolithography.

Figure 2 shows the depth of cure, at 2.51 W/cm^2, versus time for short exposures to the UV light. There seems to be no incubation time for cure of these highly loaded ceramic suspensions, which is expected due to the photoinitiator and polymerization reactions occurring rapidly (Decker and Moussa, 1990, and Hoyle and Trapp, 1990). The depth of cure gradually saturates within about 0.75 seconds for the 50 v/o suspension and after about 2 seconds for the 40 v/o suspension. In the previous figure, the ceramic suspensions were cured for 9.6 seconds. The same result would be achieved for a cure time of 1-2 seconds for a 50 v/o suspension.

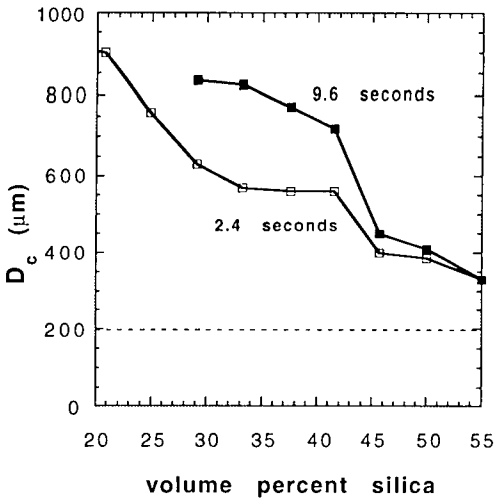

FIGURE 1: DEPTH OF CURE VERSUS VOLUME PERCENT SILICA IN AQUEOUS UV CURABLE SLIP FOR EXPOSURE TIMES OF 2.4 AND 9.6 SECONDS AT 2.51 W/CM^2.

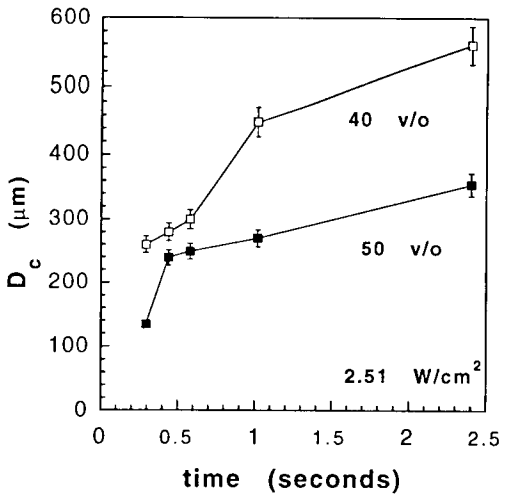

FIGURE 2: DEPTH OF CURE VERSUS TIME, AT 2.51 W/CM^2, FOR 40 AND 50 V/O SILICA IN THE AQUEOUS UV SUSPENSION.

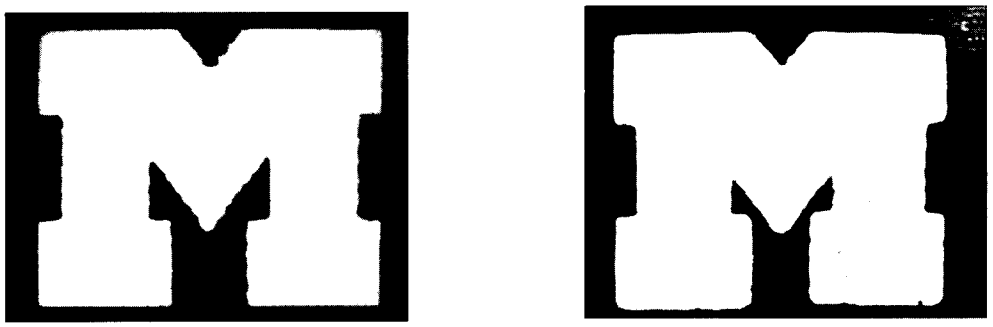

(A) (B)

FIGURE 3: A) MICHIGAN "M" MASK [1.0 CM X 0.75 CM], B) SILICA GREEN BODY REPLICA FROM UV CURING 50 V/O SLIP FOR 2.4 SECONDS AT 2.51 W/CM^2.

Now that the depth of cure was determined for the silica aqueous suspension, a simple dimensional test was performed. A University of Michigan "M" mask was made, as shown in Figure 3a. This was placed over the 50 v/o silica suspension and cured for 2.4 seconds at 2.51 W/cm^2. The resulting part is shown in Figure 3b. Notice the mask has a jagged edge in the top 'v' which is replicated in the green body. The dimensionality between the green body and the mask is quite exact, since at 50 v/o SiO_2, the amount of shrinkage due to UV cure is negligible.

II. Alumina

Figure 4 shows the depth of cure for two grades of alumina dispersed in the aqueous UV curable solution. As expected, the smaller particle size alumina (d=0.2μ) had the larger depth of cure at high volume percent solids since D_C is inversely proportional to the particle size. At 50 v/o, the 0.2μ alumina had a D_C=400 μm, whereas the 0.7μ alumina had a D_C=300 μm. Both materials were easy to disperse in the aqueous solution, resulting in viscosities of 200 and 500 mPa·s for the 0.7 and 0.2 micron powders, respectively.

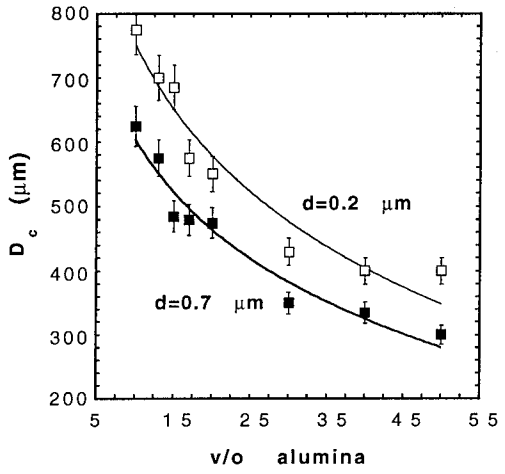

FIGURE 4: DEPTH OF CURE VERSUS VOLUME PERCENT ALUMINA IN THE AQUEOUS UV CURABLE SLIP FOR EXPOSURE TIME OF 2.9 SECONDS AT 2.51 W/CM^2.

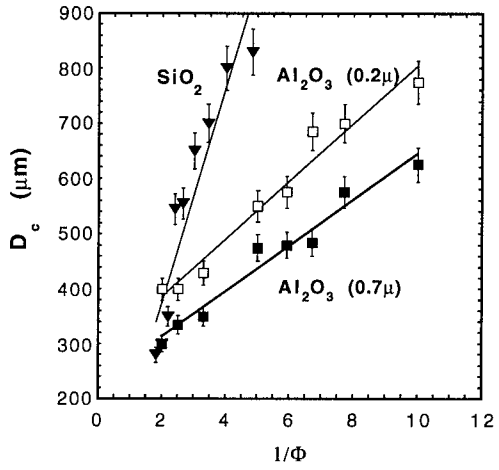

FIGURE 5: PLOT OF CURE DEPTH VERSUS INVERSE IN CONCENTRATION OF SOLIDS FOR AQUEOUS SILICA AND ALUMINA SLIPS UV EXPOSURE TIME WAS 2.9 SECONDS AT AN IRRADIANCE DENSITY OF 2.51 W/CM^2.

The turbidity expression, in Equation 2, suggests a linear relationship between the depth of cure, D_{cure}, and the inverse of the concentration of ceramic, 1/Φ. Figure 5 is a graph of the experimental depth of cure versus 1/Φ for silica and alumina in the aqueous suspension. As expected, there is a linear fit for all ceramic suspensions.

Since Equation 2 is consistent with the data, a value for the efficiency factor, Q, can be obtained from the slopes of Figure 5. Assuming the I_{cure} value is not affected by the dispersed powder, silica and alumina should have a slope ratio between 3 and 4 since the Raleigh-Gans model for Q is proportional to the refractive index difference term squared. Figure 5 shows a slope ratio of 3.7, roughly in accord. Particle size dependence predicted by the Raleigh-Gans equation anticipates a large difference in slopes between the two grades of alumina, which is not observed. We are not clear if this indicates that the Raleigh-Gans formula is not applicable, because the two alumina particle distributions overlap and cannot be quantified by a simple particle size.

Depth of cure could be greatly modified by changing the refractive index term in Equation 3. Unfortunately, refractive indices of materials are not variable for the ceramic or the monomer. Over the ultraviolet wavelength range, most monomers have refractive indices around 1.5, and ceramics have refractive indices that vary from 1.56 for silica to 2.6 for silicon carbide. Currently, we are researching acrylate formulations (Griffith and Halloran, 1994) to increase the depth of cure by modifying n_o. With further understanding of the terms in Equation 2, it should be possible to predict the cure depth for any ceramic powder in any UV curable resin.

CONCLUSIONS

Ultraviolet curing of highly loaded ceramic suspensions is achievable, and appears to be practical for stereolithography of ceramics. Silica in an aqueous acrylamide liquid is most promising because of the large depth of cure at high volume fractions. For 50 v/o silica, cure depths of 300 μm for ~2 seconds of exposure can be achieved. Simple patterns have been made by exposure through a mask. Alumina with a refractive index of 1.7 achieved acceptable depths of cure (D_C=300μm for 0.7μ), and showed that decreasing the particle size increases the depth of cure (D_C=400μm for 0.2μ). Depth of cure is controlled by the refractive index difference, Δn, and particle size, d.

ACKNOWLEDGMENT

This research was supported by the Office of Naval Research under grant N00014-93-1-0302.

REFERENCES

Barber, P. W. and Hill, S. C., 1990, *Light Scattering by Particles: Computational Methods*, World Scientific Publishing, NJ, pp. 187-254.

Burns, M., 1993, *Automated Fabrication: Improving Productivity in Manufacturing*, Prentice Hall Publishing, Englewood Cliffs, NJ, pp. 40-43, 49-53.

Decker, C. and Moussa, K., 1990, "UV-Radiation and Laser-Induced Polymerization of Acrylic Monomers", *Proceedings of the 197th National Meeting of the American Chemical Society*, vol. 417, American Chemical Society, Washington D.C., pp. 439-456.

Dorfner, K., 1991, "UV Photoinitiators in Pigmented Systems", in *Radiation Curing of Polymers II: The Proceedings of the Third International Symposium of the Royal Society of Chemistry*, The Royal Society of Chemistry, Science Park, Cambridge, pp. 216-243.

Griffith, M.L. and Halloran, J. W., 1994, "Ultraviolet Curable Ceramic Suspensions for Stereolithography of Ceramics", *Proceedings of the Symposium on Non-Traditional Design and Layered Manufacturing*, American Society of Mechanical Engineers, Annual Meeting, Nov. 1994

Hoyle, C. E. and Trapp, M. A., 1990, "Laser-Initiated Polymerization of Multifunctional Acrylates", *Proceedings of the 197th National Meeting of the American Chemical Society*, vol. 417, American Chemical Society, Washington D.C., pp. 429-438.

Iler, R. K., 1979, *The Chemistry of Silica*, John Wiley and Sons Publishing, NY, pp. 622-729.

Jacobs, P. F., 1993a, *Rapid Prototyping and Manufacturing: Fundamentals of Stereolithography*, Society of Manufacturing Engineers, Dearborn, MI, pp. 1-23

Jacobs, P. F., 1993b, "Stereolithography 1993: Epoxy Resins, Improved Accuracy and Investment Casting", *Proceedings of the Fourth International Conference on Rapid Prototyping*, University of Dayton, Dayton, OH, pp. 249-262.

Janney, M. A., 1990, "Method for Molding Ceramic Powders", U. S. Pat. No. 4 894 194, Jan. 16.

Krieger, I. M. and Dougherty, T. J., 1959, "A Mechanism for Non-Newtonian Flow in Suspensions of Rigid Spheres", *Society of Rheology Transactions*, vol. 3, pp. 137-152.

Lakshminarayan, U., Ogrydiziak, S., and Marcus, H. L., 1990, "Selective Laser Sintering of Ceramic Materials", *Proceedings of the Solid Free Form Fabrication Symposium*, University of Texas at Austin, Austin, TX, pp. 16-26.

Palik, E. D., 1985, *Handbook of Optical Constants of Solids*, Harcourt Brace Jovanovich Publishing, NY, pp. 749-764, 771-774.

Sachs, E., Cima, M., Cornie, J., Brancazio, J.D., Bredt, J., Curodeau, A., Fan, T., Khanuja, S., Kremmin, K., Lauder, A., Lee, J., Michaels, S., Milner, J., and Tuerck, H., 1993, "Micro-Constructive Manufacturing by Three Dimensional Printing", *Proceedings of the 1993 Design and Manufacturing Systems Conference*, Society of Manufacturing Engineers, Dearborn, MI, pp. 1657-1666.

van de Hulst, H. C., 1957, *Light Scattering by Small Particles*, John Wiley and Sons Publishing, NY, pp. 85-102, 131-134.

Young, A. C., Omatete, O. O., Janney, M. A. and Menchofer, P. A., 1991, " Gel Casting- A New Ceramic Forming Process", *Journal of the American Ceramic Society*, vol. 74, no. 3, pp. 612-618.

Adaptive Slicing of Solid Freeform Fabrication Processes

Yong Seok Suh and Michael J. Wozny*
Rensselaer Polytechnic Institute
Troy NY 12180

Abstract

The Solid Freeform Fabrication (SFF) process significantly reduces part specific setup manufacturing lead time. This process has been primarily used in fabricating prototypes for design visualization and verification. However, the major impact of this process on the future of manufacturing technology would be the possibility of fabricating functional parts for end use. One of the obstacles to this goal is the insufficient accuracy of the final physical part produced by the process. From the software point of view, the major sources of the inaccuracy come from the inappropriate data transfer format and the *3D aliasing' or Stair-stepping'* problem.

The `3D aliasing' problem can be reduced by adapting the layer thickness to the geometry of the part. In this paper, the procedure of adaptive slicing from the exact representation of the part model is described. This will improve part accuracy and minimize building time especially for the parts with highly curved surfaces. The procedures are implemented and a comparison to the conventional uniform layer thickness method will be discussed.

1. INTRODUCTION

The primary application of the SFF process has been to fabricate prototypes of new designs for their quick visualization and verification. For this purpose only, high part accuracy is not generally required. However, as the process is improved, fabrication of final functional parts is becoming more interesting. To fabricate functional parts, two major obstacles to the goal must be overcome. The first is the fact that most of the processes build parts made of limited special materials only. The second is an accuracy problem: the process has a relatively loose tolerance, in general, compared to others such as NC machining[1].

In building a part using the SFF process, part accuracy is usually the most important consideration. The major sources of inaccuracy in the process are part shrinkage, approximation of CAD models during data transfer with CAD systems, and the *stair-stepping* or *3D aliasing* problem[2]. A tessellated model is transferred to the SFF process from a CAD system via a file format that stores an unordered list of vertices which comprise triangular facets. Even though a part is modeled with exact geometries in a CAD system, valuable geometric and topological information is lost during the data transfer[3]. The finite thickness of layers of physical material produces 3D aliasing effects that cause the inaccuracy of the final physical part[4]. This is illustrated in Figure 1.

---

* Currently at National Institute of Standards and Technology

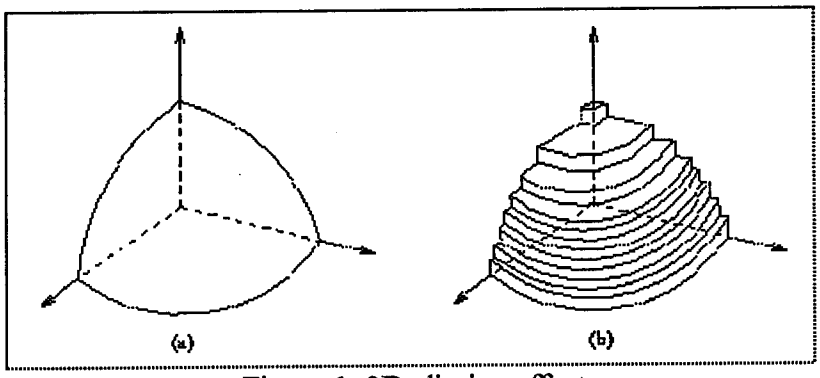

Figure 1. 3D aliasing effect

It is not possible to eliminate 3D aliasing completely because of the process characteristics. However, it can be reduced by varying the thickness of the slices. The thickness must be adaptive to the shape of the surface of the part in order to guarantee that the deviation between the final part surface and the ideal part surface lies within a certain tolerance limit.

In this research, the issue of accuracy is concerned primarily with focusing on reducing the 3D aliasing problem by optimizing the layer thickness. The exact model is transferred from CAD systems through high-level data exchange standards such as STEP/PDES[5].

2. OVERALL SYSTEM ARCHITECTURE

For a fully automated SFF process, a system architecture shown in Figure 2 is currently being developed and tested at Rensselaer Polytechnic Institute. A solid modeling kernel is built as a part of the process software to store model information and perform geometric reasoning. Exact model representation can be exchanged between the kernel modeling system and other CAD systems at the designers' side through a high-level data exchange format such as STEP/PDES. In the near future, the STEP/ACIS Husk[6] being developed at Rensselaer Polytechnic Institute will be integrated for the data transfer. The interface between the modules is via API (Application Protocol Interface) routines to conform to the idea of the standardized application interface[7].

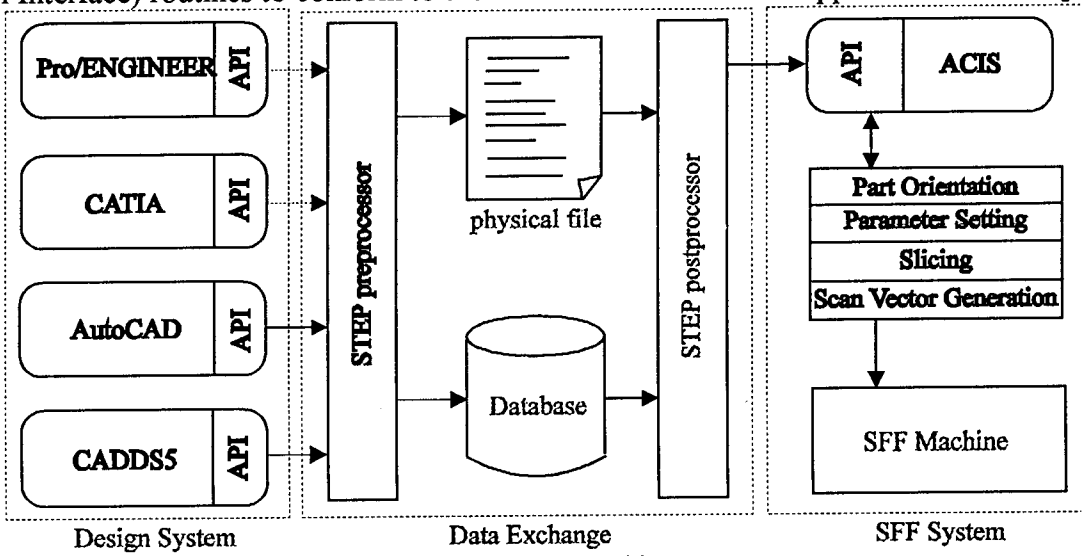

Figure 2. System Architecture

3. ADAPTIVE SLICING PROCEDURE

The purpose of the adaptive slicing is to fabricate geometrically accurate parts. The reference of the part accuracy is the solid model with mathematically defined surfaces. Many attempts have been made successfully to manufacture parts directly from CAD models: the automatic NC machine tool path generation is an example of the attempts.

The 3D aliasing causes the deviation of the part surface from the true surface definition, and the deviation is defined by the maximum gap measured in the normal direction of the surface as shown in Figure 3. The cusp height tolerance is set by designers or SFF process operators based on the functionality of the part to be built. Each surface of a part may be set with different tolerance values according to its functionality. The following subsections will discuss the procedure of adaptive slicing in sequence based on the assumption that a cusp height tolerance and a range of allowable layer thickness are given with a properly oriented part model.

3.1 Finding Slicing Sub-regions

Some special features must be considered when slicing a part for accuracy. Those features include flat areas, peak points and edges, and horizontal edges and the slicing plane must pass through those features for accurate fabrication. The inaccuracies caused by ignoring those features are illustrated in Figure 4. These features will be called *peak features* throughout this paper.

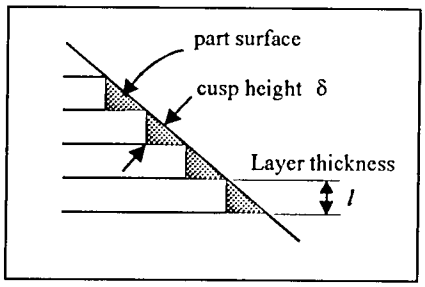

Figure 3. Cusp height

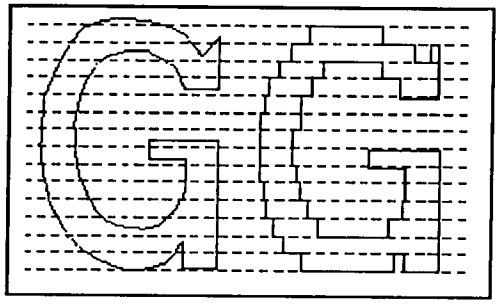
Figure 4. Inaccuracies due to peak features

Once all the peak features are identified in a model, the height of the features is sorted in the order of vertical direction, then the whole part can be subdivided into several sub-regions so that no peak features are within a region except its boundaries. An adaptive slicing algorithm, which will be discussed in the next section, is applied to each subregion. The peak features are identified from the vertices, edges and faces of the model, as described in the following three subsections.

3.1.1 Vertex peak features

All the vertices are basically considered as peak features. However, two types of vertices are excluded from the peak feature list.

- **topological vertex** Some vertices exist only to fulfill the B-rep data structure requirements of a solid modeling system. Several examples are shown in Figure 5. Usually, only one or two faces are adjacent to the topological vertex.

The part orientation is important because it affects the build time, dimensional acccuracy and post-processing complexity.

• **smooth vertex** If a vertex lies on the intersection of surfaces that meet smoothly at the vertex, the vertex is excluded from the peak feature list. Figure 6 shows an example of such vertices.

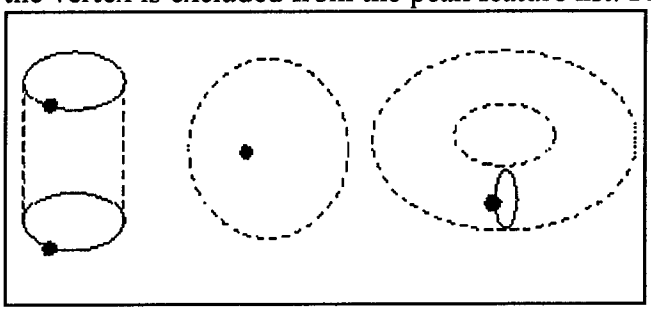

Figure 5. Topology vertices

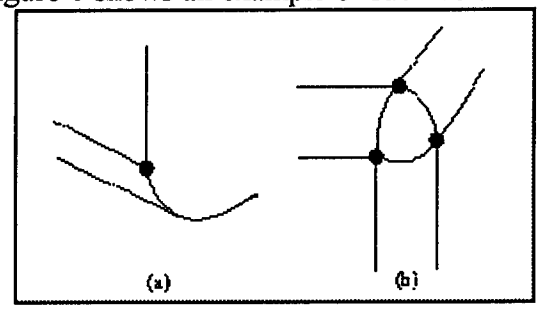

Figure 6. Smooth vertices

3.1.2 Edge peak features

• **horizontal edge** If the geometry of an edge is a planar curve and the edge lies horizontally, the edge is considered as a peak feature as shown in the Figure 7(a). However, if the adjacent surfaces meet smoothly at the edge as illustrated in Figure 7(b), the edge is excluded from the peak feature list.

• **extreme point** If an edge is not linear, the extreme points in the vertical direction must be found to be included in the peak feature list as shown in the Figure 8.

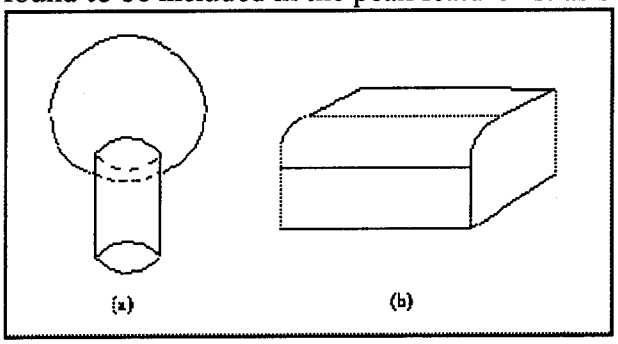

Figure 7. Horizontal edges

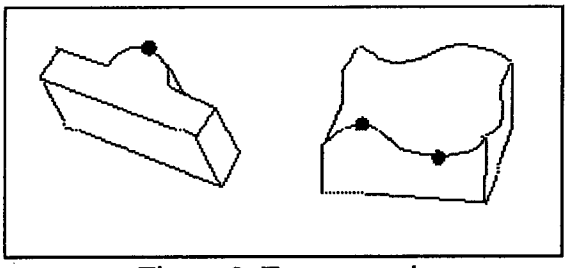

Figure 8. Extreme points

3.1.3 Face peak features

• **horizontal planar face** The slicing plane must pass through the horizontal planar face.

• **extreme point** Extreme points of curved surfaces in vertical direction.

Once these features are found and the part is divided into regions, the procedures in the following sections are applied to each region to generate a series of slicing planes.

3.2 Calculation of the Next Slice Height

Within each slicing region found at the previous section, a set of slicing planes is generated, considering a cusp height tolerance. Let Z^i_L and Z^i_H be the height of the lower and higher boundaries of the i_{th} slicing region respectively, and $Z^i_L < z^i_1 < z^i_2 < ... < z^i_j < ... < Z^i_H$ be an ordered sequence of height of the slicing planes. The height of a slicing plane, z_{j+1}, is determined from the contours (intersection curves) generated by the previous slicing plane at the height of z_j, based on the geometry of the part.

The procedure is basically similar to that of NC tool path generation for curved surfaces[8,9]. Let C_j be the contour at the height of z_j and C_{j+1} be the next contour to be found. In calculating

the next layer thickness, $d = z_{j+1} - z_j$, a set of sampling points are selected along the previous contour, C_j, and the next layer thickness is calculated at each sampling point considering the geometry of the surface at that point. The minimum value is selected as the next layer thickness among those values calculated at every sampling point. The method for selecting a set of sample points will be discussed in the next section.

3.3 Determination of the sampling points

Assume that a sample point, P_i, on a contour curve is obtained. The next sampling point, P_{i+1}, can be calculated from the Figure 9 and Eq.(1). The contour curve is approximated by an arc with the radius of $\rho=1/\kappa$ where κ is the curvature of the curve at the sampling point P_i. The Eq.(1) calculates an arc length to the next sampling point so that the maximum deviation, δ, is less than or equal to the cusp height tolerance.

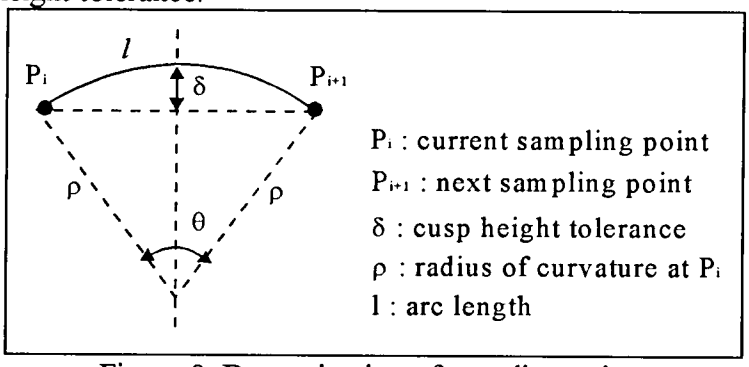

Figure 9. Determination of sampling points

$$l = \begin{cases} \infty & \text{if } \rho = 0 \\ 2\rho\cos^{-1}(1-\rho/\delta) & \text{otherwise} \end{cases} \quad (1)$$

3.4 Calculation of layer thickness at a sampling point

In this section, a method for calculating the next layer thickness at a sample point will be discussed.

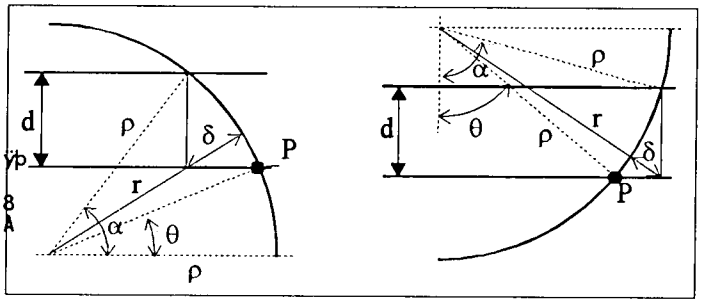

Figure 10. Calculation of next slicing plane

Let ρ be the radius of curvature of the part surface in the vertical direction at the sampling point, P. Then the part surface can be approximated by a sphere with the radius of ρ as shown in Figure 10. This is a good approximation because the layer thickness is much smaller than the radius of curvature of the surfaces of most mechanical parts. The next layer thickness, d, can be calculated from the Figure 10, with the given cusp height tolerance, δ. It is assumed that the laser

beam radius is compensated at the border of the part to allow for the laser line width. The cross-sectional shape of a curved line is approximated by a rectangle[2].

If ρ is infinite, the next layer thickness, d, is calculated using Eq.(2),

$$d = \begin{cases} \infty (= l_{\max}) & \text{if } n_k = 0 \\ \delta/\cos\theta = \delta/n_k & \text{otherwise} \end{cases} \tag{2}$$

where n_k is a vertical component of the normal vector of the surface at the point P. Note that the layer thickness, d, must be bounded by the maximum and minimum layer thicknesses, l_{max} and l_{min}.

If r is not infinite, it is required to check the location of the sampling point, P, relative to the center of the sphere. If the point is on the northern hemisphere, the layer thickness, d, is calculated using Eq.(3). The Eq.(4) is for the case where the point is on the southern hemisphere of the sphere.

$$d = -\rho \sin\theta + \sqrt{\rho^2 \cos^2\theta - 2\delta\rho - \delta^2} \tag{3}$$

$$d = \begin{cases} \rho\cos\theta - \sqrt{\rho^2\cos^2\theta - 2\delta\rho - \delta^2} & \text{if } \rho^2\cos^2\theta - 2\delta\rho - \delta^2 > 0 \\ \rho\cos\theta & \text{otherwise} \end{cases} \tag{4}$$

3.5 Layer Contour Generation at Region Boundaries

Care must be taken when generating contours of a layer that pass through a region boundary. All the pathological cases of surface intersection problems may occur because of the peak features. Another concern is the removal of the contours generated by downward planar faces. As pointed out by Dolenc and Makela[10,11], if a slicing plane passes through a down-facing flat surface, the corresponding contour area must be discarded.

These problems can be eliminated by lowering the slicing plane by an infinitesimal amount which is far less than the minimum layer thickness, but greater than the tolerance value used in surface intersection procedure.

4. IMPLEMENTATION AND EXAMPLES

A prototype program has been implemented that includes the features discussed in this paper. Based on the ACIS®[3] solid modeling kernel, the system is built on a Sun Sparc workstation with an X-window based user interface.

To compare the adaptive slicing with the uniform slicing, a sphere with the diameter of 10" is modeled and sliced with various cusp height tolerances as shown in Figure 11. The minimum and maximum layer thickness is set to be 0.001" and 0.020" respectively. The results are summarized in the table below.

Adaptive Slicing		Uniform Slicing
Cusp Height (in.)	Number of Layers	Number of Layers Thick. cusp height
0.006	909	1667
0.007	803	1429
0.008	726	1250

[2] The shape of a cured line is better approximated by a parabolic cylinder 2.

[3] ACIS is a registered trademark of SPATIAL TECHNOLOGY Inc., Boulder, CO

0.009	669	1112
0.010	626	1000
0.011	593	909
0.012	658	834
0.013	548	770
0.015	533	715

With the cusp height of 0.01", the number of layers is 626. If the uniform thickness method is used, the number of layers is between 500 and 10,000 according to the layer thickness chosen. For the uniform thickness method, the deviation error (cusp height) will vary according to the latitude of the sphere and the maximum error will occur around the north and south poles. For the uniform layer thickness of 0.011", for example, the number of layers will be 909 and the cusp height at the angle of 80 degrees from the equator will be 0.0109", which can be achieved with only 593 layers by using the adaptive slicing method.

From this experiment, we can conclude that, in many parts with highly curved surfaces, a part can be fabricated by using the adaptive slicing method, not only more accurately but also more rapidly. Figure 12 and 13 show more examples.

5. CONCLUSION

The Solid Freeform Fabrication process is a promising new manufacturing method that can fabricate a product with lot size of 1 with minimum cost. In order to serve this goal, however, further development of the process is required. From the software point of view, the part accuracy is the major area to be tackled first. The sources of inaccuracy is identified to be from the approximate model data caused by the data exchange format and '3D aliasing' problem. In this paper, a new system architecture was proposed to exchange exact model representation with CAD systems. And adaptive slicing procedure for reducing the 3D aliasing problem was also discussed.

The procedures has been implemented and tested on several example parts. The results show that the adaptive slicing assures part accuracy and minimizes the number of layers for minimal build time.

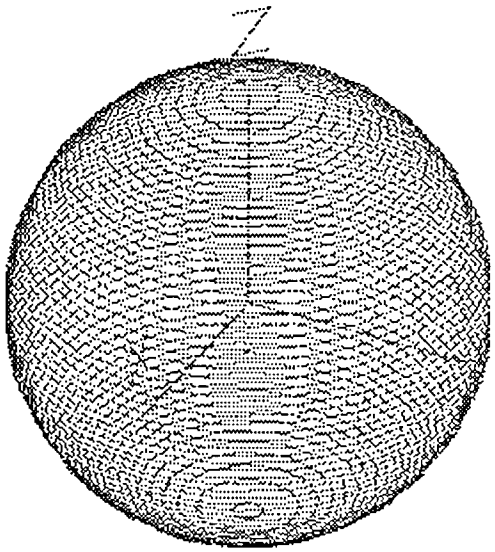

Figure 11. Adaptive slicing of a sphere

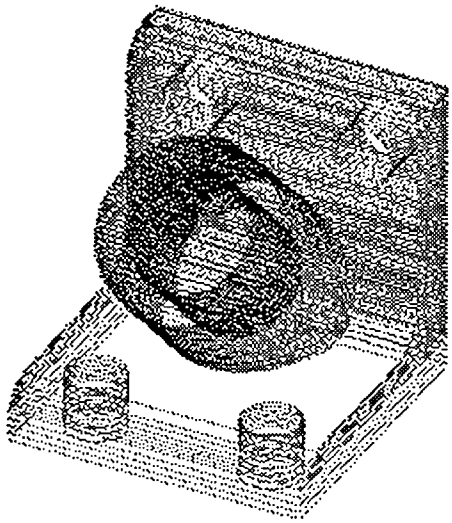

Figure 12. Adaptive slicing of a CAM-I part

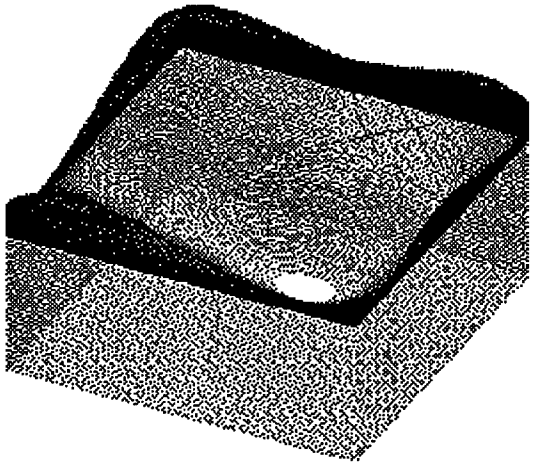

Figure 13. Adaptive slicing of a NURB surface

6. REFERENCES

[1] B. E. Hirsch and H. Muller. "StereoLithography - fields of application and factors influencing the accuracy.", In D. Kochan (Ed), *Complex Machining and AI-Methods*, pages 219-233, Elsevier Science Publishers B.V. (North-Holland), 1991

[2] Paul F. Jacobs, *Rapid Prototyping & Manufacturing, Fundamentals of StereoLithography*, Society of Manufacturing Engineers, first edition, 1992

[3] Marshall Burns, *Automated Fabrication - Improving Productivity in Manufacturing*, PTR Prentice Hall, Englewood Cliffs, New Jersey, 1993

[4] Michael J. Wozny, "Systems Issues in Solid Freeform Fabrication", Technical Report 92023, Rensselaer Polytechnic Institute, Troy, NY 12180, September 1992

[5] *Product Data Exchange Specification (PDES) Testing Draft.* National Institute of Standards and Technology, Gaithersburg, MD, 1988

[6] The STEP/ACIS HUSK, *User's Guide*, STEP Tools Inc., Troy, NY

[7] Spencer P. Magleby and David B. Jackson, "A Standardized Application Interface for Geometric Modelers", in J. Turner, J. Pegna, and M. Wozny (Ed), *Product Modeling for Computer-Aided Design and Manufacturing*, pages 227-243, Elsevier Science Publishers, 1991

[8] I. D. Faux and Michael J. Pratt, *Computational Geometry for Design and Manufacture*, Chichester, England: Horwood; New York: Halsted Press, 1981

[9] Yong Seok Suh and Kunwoo Lee, "NC Milling Tool Path Generation for Arbitrary Pockets Defined by Sculptured Surfaces", *Computer-Aided Design*, 22(5):273-284, June 1990

[10] A. Dolenc, R. Hovtun, and I. Makela, "Better Software for Rapid Prototyping with INSTANTCAM", In G. J. Olling and F. Kimura (Ed), *Human Aspects in Computer Integrated Manufacturing*, pages 449-456, Elsevier Science Publisher B.V. (North-Holland), 1992

[11] A. Dolenc and I. Makela, "Slicing Procedures for Layered Manufacturing Techniques", *Computer-Aided Design*, 26(2):119-126, February 1994

Advances in Selective Area Laser Deposition of Silicon Carbide

J. V. Tompkins, R.. Laabi, B. R. Birmingham, H. L. Marcus
Center for Materials Science and Engineering
The University of Texas at Austin

Abstract

Selective Area Laser Deposition (SALD) is a Solid Freeform Fabrication (SFF) technique which uses a scanning laser beam to produce solid material by locally decomposing a gas precursor. In this work, a focused CO_2 laser beam strikes a substrate in the presence of tetramethylsilane (TMS) or diethylsilane (DES), producing silicon carbide objects with high density and no binder phase. Recent investigation has yielded growth rates up to 2.7mm/min in the beam area, and has eliminated previously noted contamination of the optics by a byproduct which mass spectroscopy identifies as silicon dioxide. This paper reviews a cause of non-uniform growth and demonstrates the addition of hydrogen and reduced scan speeds to make multilayer parts. In addition, it presents a method for in-situ measurement of height of deposited material.

Introduction

Selective Area Laser Deposition [1] describes a rapid prototyping process in which a moving laser beam causes localized decomposition of a precursor gas, creating solid material. A computer containing specifications for a three dimensional object controls the motion of an x-y table, which moves the beam relative to a substrate surface. The moving area heated by the beam dictates where material will be added, building up solid material (metal, ceramic, glass, etc.) in the desired shape for either prototype or structural parts.

This paper reviews recent progress in SALD employing tetramethylsilane ($Si(CH_3)_4$) and diethylsilane ($H_2Si(C_2H_5)_2$) to produce silicon carbide. Pyrolysis of tetramethylsilane has been investigated by Figueras et al in the growth of silicon carbide films [2]. Tetramethylsilane decomposes according to the following overall reaction:

$$Si(CH_3)_4(g) \Rightarrow SiC + 3\ CH_4(g)$$

The reaction proceeds exothermically, with an enthalpy change of -73.75 kcal/mole [3].

We also considered an alternative precursor, diethylsilane. The molecular formula for diethylsilane suggests the following overall reaction:

$$Si(C_2H_5)_2H_2(g) \Rightarrow SiC + C_2H_6(g) + CH_4(g) + H_2(g)$$

Diethylsilane offered the possibility of lower deposition temperatures, as both the hydrogen and ethyl groups display less electronegativity and should ease decomposition relative to the methyl groups in tetramethylsilane.

A previous paper reports the fabrication of single layer silicon carbide objects from tetramethylsilane by Selective Area Laser Deposition [4]. Thermal shock and uneven growth posed the greatest obstacles to the production of larger, more general shapes. The investigation of rod growth with a stationary beam produced growth rates of up to 1.6 mm/min. The following describes the most recent advances in producing more complex, multilayer silicon carbide objects, including increased growth rates, more even growth, and reduction in the effects of residual oxygen on the process.

Apparatus

The equipment setup (Fig. 1) varies somewhat from early SALD work [5]. Vapor drawn from a flask containing liquid tetramethylsilane (vapor pressure 755 Torr) or diethylsilane (85 Torr) at ambient temperature fills a vacuum chamber. A computer controlled x-y table supports a CO_2 laser and associated optics which produce a focused beam passing through a ZnSe window into the chamber. A firmly packed powder bed within the vacuum chamber serves as a substrate. Movement of the table scans the beam over selected areas of the substrate, where

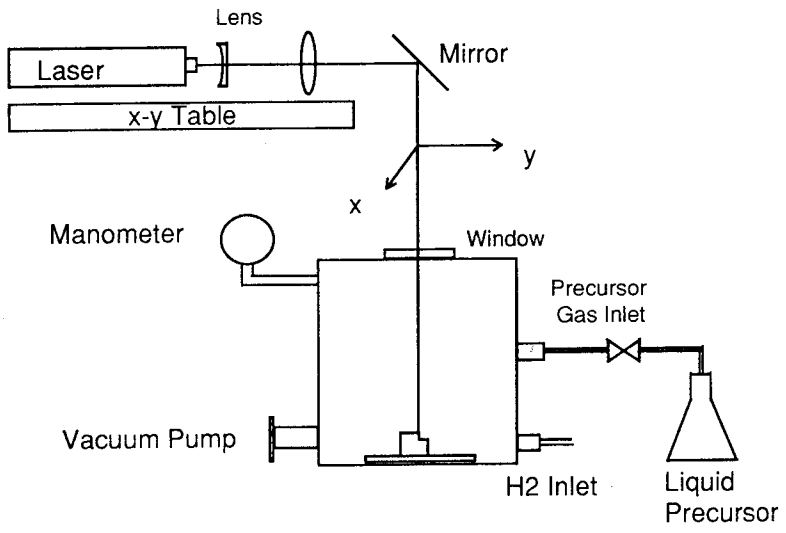

Fig. 1 SALD System Schematic

pyrolysis of the tetramethylsilane or diethylsilane produces silicon carbide. In a departure from the earlier system, we have added a small fan with a brushless DC motor inside the chamber to provide forced convection to the deposition area similar to that in a flowing gas system.

Experimental Procedure

The vacuum chamber underwent multiple cycle purges with nitrogen to base pressures of less than 10^{-2} Torr. The system did not undergo a bakeout between trials. The substrate consisted of firmly packed 16um silicon carbide powder. Powder provides greater absorption of the beam, as well as less conduction of heat away from the deposition point, assisting in initiation of the SALD process.

Precursor gas pressure ranged from 20-140 Torr for tetramethylsilane. The upper limit reflects previous problems experienced with fogging of the ZnSe window by decomposition products at higher pressures. An equilibrium vapor pressure of 85 Torr at room temperature limited diethylsilane pressures to 85 Torr or less. Where indicated below, we also added chromatograph grade hydrogen gas at pressures up to 100 Torr.

Two successive ZnSe lenses acted to focus the beam from the CO_2 laser, producing an estimated 400um spot size (1/e2). Previous measurements of absorption by tetramethylsilane provided a pressure/absorption correction factor to achieve a constant intensity at the substrate surface of six watts regardless of pressure. Trials for diethylsilane represent the first investigation for this precursor, and considerations outlined below prevented the acquisition and use of correction curves for uniform power at the surface.

Scanning of the laser beam typically took place at 80-100 um/sec. We have not thoroughly investigated a full range of scan speeds, and future work will address the determination of an optimal scan speed. All scanning patterns consisted of parallel lines with a spacing of 100 um.

Results

As seen in Fig. 2, we observed growth rates as high as 2.7 mm/min. The previous maximum rate of 1.6mm/min occurred at 80 Torr of TMS. Rates had previously decreased at pressures over 80 Torr, due in part to clouding of the ZnSe window by precipitation of a reaction byproduct. The data shown apply to rods grown with a stationary beam for 5 minutes in pure tetramethylsilane.

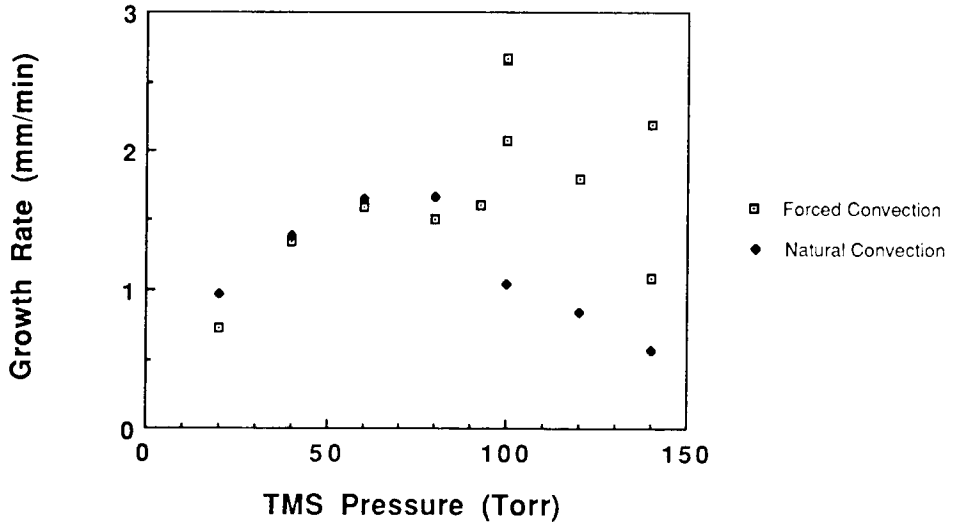

Fig. 2 Growth rate vs. TMS pressure

The improvement in the rate may have resulted from the addition of a forced convection component in the mass transport mechanism. The variation seen in growth rates probably results from an irregular flow pattern from the small fan; for example, a small lateral displacement relative to the fan might greatly affect the flow velocity. The difficulty of exactly reproducing the positioning of the deposition point relative to the small fan used in these experiments

probably accounts for much of the scatter observed in rate data. Mode hopping in the laser, resulting in fluctuations in output power as described later in this paper, may represent an additional source of variation.

Airflow from the fan offers an additional benefit: in previous SALD experiments, natural convection from the heated area carried a relatively undiluted stream of heated reaction byproducts upward along the beam path, ultimately striking surfaces on optical components such as the ZnSe window. At these surfaces, a solid material precipitated from the gas, leading to absorption of the beam. The addition of forced convection dispersed this stream of waste gas leaving the deposition site, greatly reducing clouding of the optical path.

Trials with diethylsilane did not show significant growth except at very low pressures. Observation of the substrate showed no heating of the surface even at the highest available laser settings (30 Watts). Only at pressures below 10 Torr did the beam have a noticeable effect on the surface, and at 10 torr a small amount of growth occurred. We interpret this as an indication of very strong absorption of the 10.6 um wavelength, requiring further investigation. Although the laser could not deliver the desired six watts to the substrate surface, growth of silicon carbide at pressures below 10 Torr suggest that solving the absorption problem may allow diethylsilane to serve as a suitable precursor.

The issue of growth rate represents a critical concern in the development of SALD technology. The data shown above for tetramethylsilane represents nearly a doubling of the growth rate over that previously reported. Fig.3 shows an example of a 3-D silicon carbide object. The scale of the object, approximately one inch, indicates the capability of SALD in its current state. The three horizontal appendages contain a 1mm thick layer of deposited silicon carbide. This material has a durable and solid feel, but definitive density and strength data require further investigation.

As mentioned above, previous work had revealed a problem with contamination of the optics in the chamber due to a byproduct of the deposition reaction. Mass spectroscopy using electron impact ionization identified the solid byproduct precipitating on the reactor walls as well as on the ZnSe window as pure SiO_2. Based on this information, three steps have eliminated the contamination problem: drying the substrate in vacuum for 24 hours prior to deposition, redesigning the precursor flask to eliminate exposure to oxygen-bearing vacuum grease, and adding hydrogen gas. Hydrogen acts to getter any available oxygen to form water, which adsorbs onto the chamber wall. Adding hydrogen to the tetramethylsilane has dramatically reduced the formation of silicon dioxide, and experiments involving up to twenty hours of deposition have not resulted in any visible fogging of the optical components. However, hydrogen slows the deposition rate significantly: 100 Torr of hydrogen reduces the rate by approximately a factor of five. Future work will investigate the minimum pressure of hydrogen needed as a function of tetramethylsilane pressure to prevent silicon dioxide formation.

Although silicon carbide generally has excellent thermal shock resistance for a ceramic material, thermal shock also presented difficulties in SALD, specifically in the growth of multiple layers of material. Scan rates of 400 um/sec produced solid single layers of material, suitable for analysis by XRDS, SEM, scanning auger spectroscopy, or for annealing experiments in a furnace. However, deposition of a second layer resulted in severe thermal shock caused by the steep, moving thermal gradient, fracturing the original layer. Reducing the scan speed to 80-100 um/sec reduces this problem. Two separate contributions may account for this: first, the initial layer of material has greater thickness and therefore greater strength; and second, the

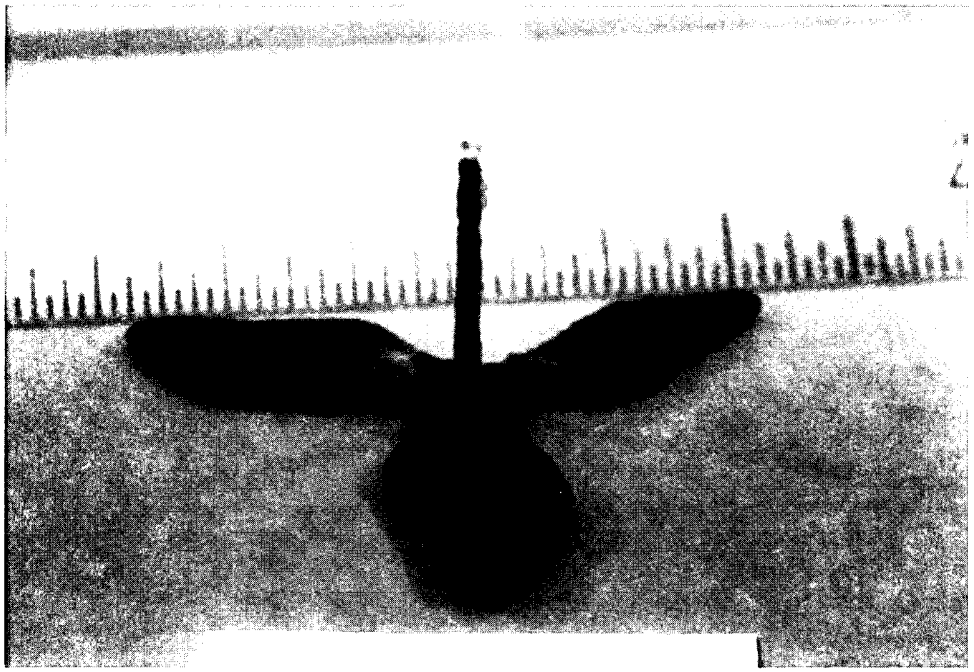

Fig. 3 "Stirrer" created in 3 hours 15 minutes from tetramethylsilane.

slower scan rate induces a proportionately lower thermal shock on the material. Thermal shock under current conditions no longer interferes with growth of multiple layers of silicon carbide.

The requirement to heat the deposition surface from above with laser radiation as opposed to heating the substrate from below as in conventional CVD creates a unique challenge in SALD: any projection above the planar surface of the material suffers less conduction into the underlying solid, causing it to retain more of the incident energy. This causes it to grow faster, and an unstable situation exists which we refer to as preferential growth. An instability in deposition rate identified during rod growth compounds the problem by actually initiating projections along the deposition path. During growth rate measurements using a stationary beam, an unexpected periodic variation appeared in rod diameter, referred to hereafter as "beading". Fig. 4 shows an extreme case of this. This instability may also exhibit itself in the growth of single or multiple layers of material, but became directly observable during the growth of rods. Beading results from several physical phenomena. Birmingham [6] identified small periodic fluctuations in the CO2 laser, and later showed that the associated shift in wavelength caused by mode hopping created a dramatic shift in absorption by the gas. Further, he showed that reflectivity of the silicon carbide powder and deposit also varied sharply in the region in which the CO_2 laser's mode hopping occurred. The period of the beading events corresponds very closely with the established period of mode hopping in the CO_2 laser.

We employ two approaches to minimize the problem of localized growth: reducing the scan rate reduces the thermal gradient between the substrate surface and the underlying material, reducing heat flow into the substrate. Also, the addition of hydrogen increases the rate of

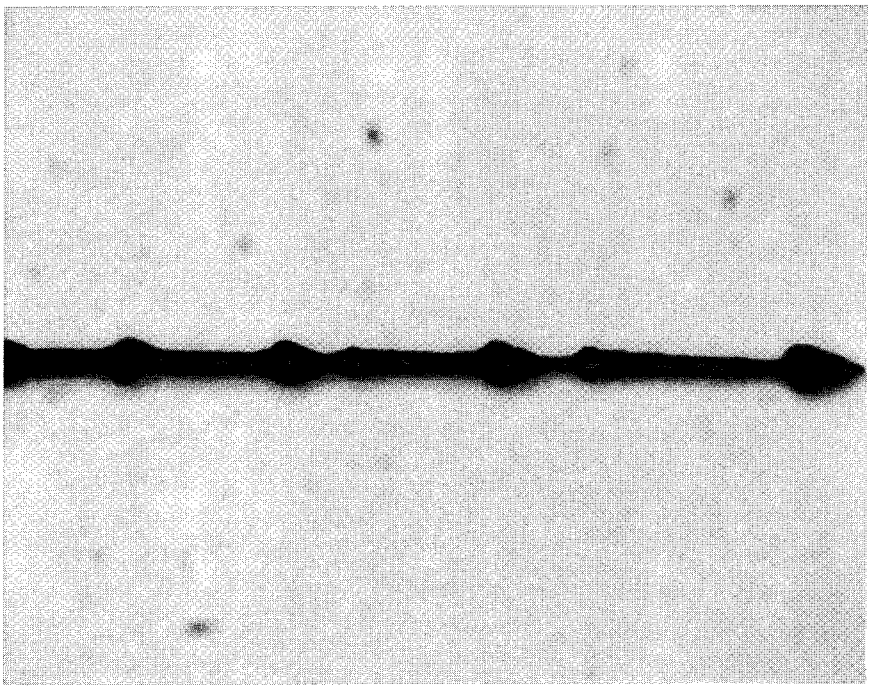

Fig. 4 Example of "beading" occurring during rod growth

etching (reverse reaction) of silicon carbide at the higher temperatures experienced by projections on the surface. Although these approaches reduce preferential growth, the answer ultimately lies in the use of precursors with lower deposition temperatures to further reduce the thermal gradient in the material, and hence conduction into the substrate. Such precursors exist but require complex and critical handling procedures. In addition, SALD requires a laser with a wavelength appropriate to the chemical and physical properties of the material produced.

In-situ deposition thickness measurement approach

Development of an in-situ deposition thickness measurement technique is critical to control the height of the different shapes built up by the SALD process. One method consists of using the scattered energy of the He-Ne laser focused beam to make an image of the spot. This method is easier than the interferometric methods and does not require polished surfaces, nevertheless its sensitivity may approach that of medium accuracy interferometry. This system is shown schematically in Fig. 5.

Measuring principles

The He-Ne laser beam is focused onto the surface of the growing object by the lens L1. When the surface is exactly at the focal plane of the lens, a large fraction of specular reflection light is backscattered and collected by the lens L2 to project the spot image onto the position-sensitive detector (PSD). When the deposit grows, the spot image moves along the detector which is an optoelectronic sensor that provides continuous position data of a light spot traveling over its surface. An aperture is used in front of L2 to improve the resolution by decreasing the

spotsize. Knowing the displacement d along the detector we can estimate the growth G by the following formula:

$$G=(X\sin\alpha/X')*d$$

(Xsinα/X') is a ratio associated with the position of the lens L2.

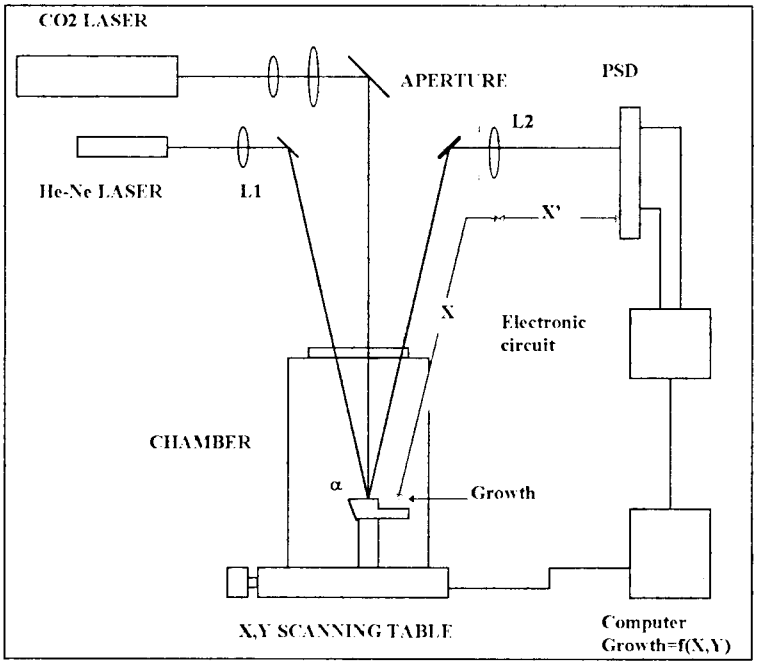

Figure 5
Schematic of the deposition thickness measurement system

The Detection

When a light spot falls on the PSD, an electric charge proportional to the light energy is generated at the incident position (Fig.6). This electric charge is driven through the resistive P-layer and collected by the electrodes. Since the resistivity of the P-layer is uniform, the photocurrent collected by an electrode is inversely proportional to the distance between the incident position and the electrode.

The following formulas give us an estimation of the incident position depending on the two outputs I1 and I2.

$$I1 = I0(L-d)/2L$$
$$I2 = I0(L+d)/2L$$

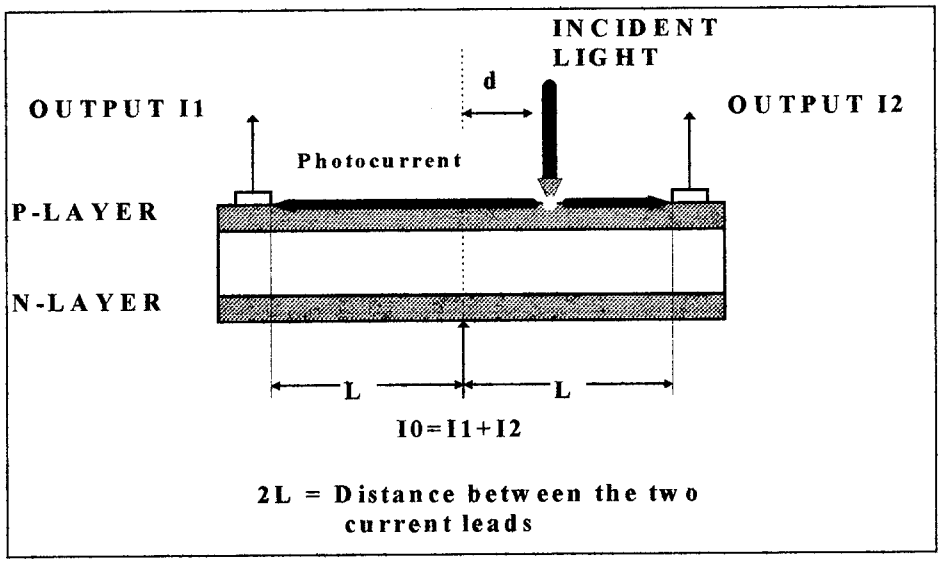

Figure 6
Schematic of the position-sensitive detector

One of the most important problems that we met is the specular reflection on the rough surface of the silicon carbide, which causes a variable incident intensity of the spot image (I0 variable). To avoid that problem an operating electronic circuit was built in order to calculate the ratio: (I2-I1)/(I2+I1) = d/L which is independent of the reflected light intensity.

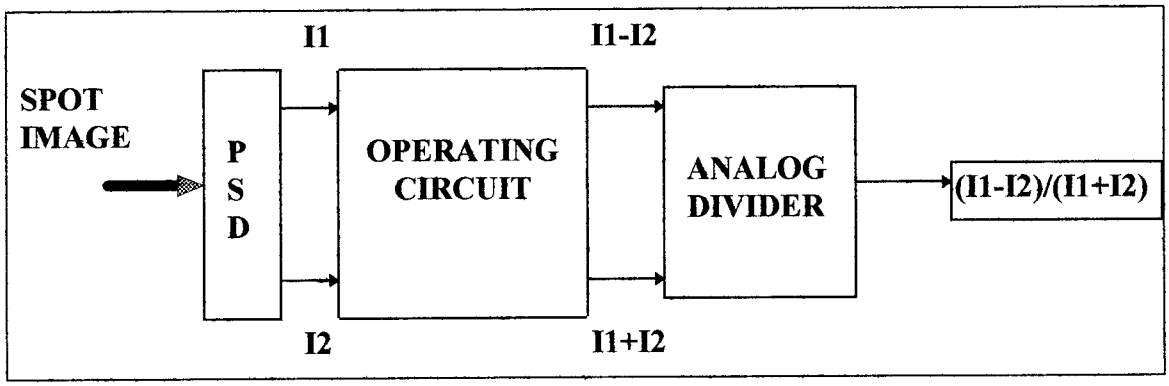

Finally we have :

$$G = (X\sin\alpha/X')*L*(I2-I1)/(I1+I2)$$

Results

Initially, different measurements were made by changing the ratio (Xsinα/X'). The spot was directly projected onto a fluorescent screen. The smallest displacement d resolvable was d = 0.5 mm which corresponds to 30 μm of growth with a ratio of (Xsinα/X') = 0.06. The PSD will be used to improve the position resolution of the spot image. A detected spot displacement of 150 μm is possible with such a detector which corresponds to a resolvable 10 μm of growth for the same ratio (Xsinα/X')=0.06. The dynamic range linearity (Fig.7) and errors (Fig.8) were estimated by placing a sample that was a flat surface of silicon carbide at the plane G = 0 and moving the sample in the Z direction.

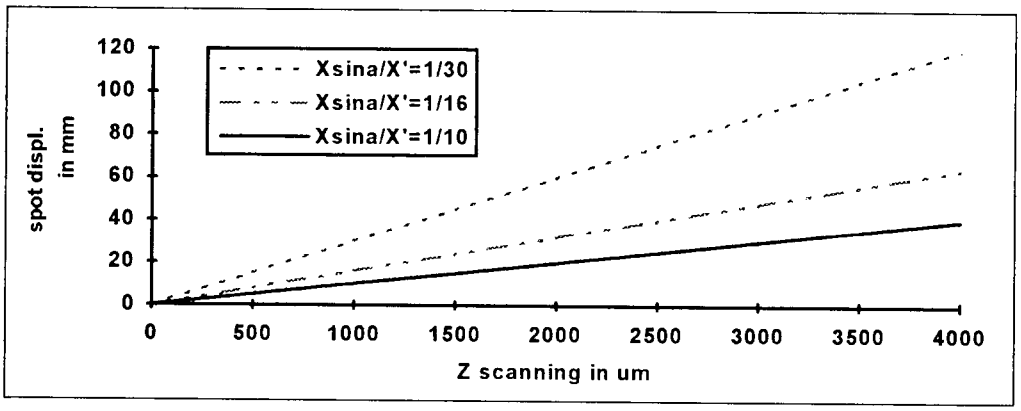

Figure.7
The displacement of the spot (mm)
function of the Z-scanning

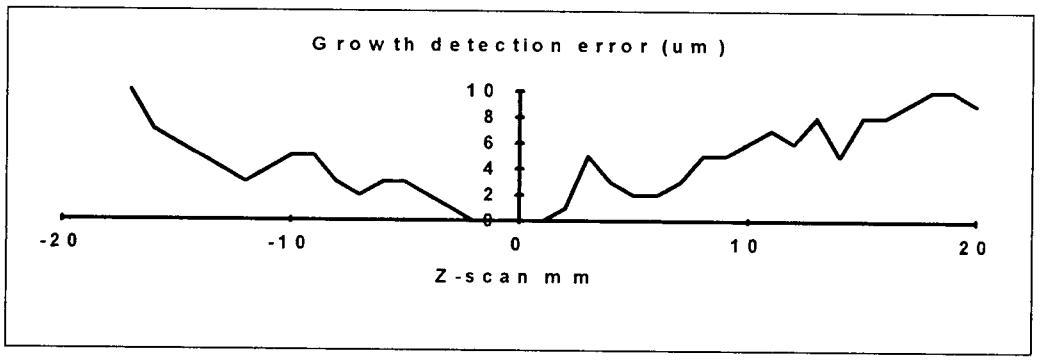

Figure.8
Growth detection error in um

Conclusion

The above paper describes continuing progress toward a SALD technology capable of producing prototype as well as structural parts. The current process already yields dense silicon carbide free of the glassy binder phases which typically compromise high temperature resistance. The alternative precursor, diethylsilane, shows incompatibility with CO_2 lasers, but growth at low pressures with a greatly attenuated beam indicates its potential for lower deposition temperatures. The process continues to produce higher growth rates, and thermal shock and contamination of the optical path no longer pose significant obstacles in the practical matter of producing large scale parts. Additionally, an in-situ method for measuring height of the material following deposition represents a step toward actively controlling the uniformity of deposition height in spite of variations in deposition rate. The ability to produce solid objects on a useful scale (approximately 1 inch) in a matter of hours represents a substantial advance in the area of SALD.

ACKNOWLEDGEMENTS

The authors gratefully acknowledge the support of ONR grant N00014-92-J-1514 and Texas ATP grant 351.

REFERENCES

1. Zong, G., Yves Jacquot, W. Richards Thissell, and H. L. Marcus, "Solid Freeform Fabrication Using Selective Area Laser Deposition", Plasma and Laser Processing of Materials, edited by K. Upadhya, The Minerals, Metals, and Materials Society, 1991.

2. Figueras, A., S. Garelik, J. Santiso, R. Rodroguez-Clemente, B. Armas, C. Combescure, R. Berjoan, J. M. Saurel, R. Caplain, "Growth and Properties of CVD-SiC Layers Obtained by LPCVD Using Tetramethylsilane", Journal de Physique IV, Colloque C2 Supple. au Journal de Physique II, Volume I, September 1991, pp C2225-232.

3. JANAF Thermochemical Tables, 2'nd ed., Stull, D. R. and H. Prophet, U. S. Government Printing Office, Washington, D. C., June, 1971.

4. Tompkins, J. V. and Harris L. Marcus, "Selective Area Laser Deposition of Silicon Carbide", Proceedings of the Solid Freeform Fabrication Symposium, edited by Harris L. Marcus, Joeseph J. Beaman, David L. Bourell,and Richard H. Crawford, The University of Texas at Austin, Austin, Texas, August 9-11, 1993.

5. Zong, G.S., R. Carnes, H. G. Wheat, and Harris L. Marcus, "Solid Freeform Fabrication by Selective Area Laser Deposition", Proceedings of the Solid Freeform Fabrication Symposium, edited by J. J. Beaman, Harris L. Marcus, David L. Bourell, and J. W. Barlow, The University of Texas at Austin, Austin, Texas, August 6-8, 1990.

6. Birmingham, B. R. and Harris L. Marcus, " Silicon Carbide Shapes by Selective Area Laser Deposition Vapor Infiltration" , Proceedings of the Solid Freeform Fabrication Symposium, edited by Harris L. Marcus, J. J. Beaman, David L. Bourell, and J. W. Barlow, The University of Texas at Austin, Austin, Texas, August 8-10, 1994.

KEYWORD INDEX

3D aliasing' (404)
3D laser digitizing (307)
3D Systems (154)
accuracy (356)
acousto-optic modulator (277)
active feedback control (277)
adaptive scanning (307)
adaptive slicing (404)
alumina (17, 330)
alumina powder (321)
Aluminum borate $2Al_2O_3 \cdot B_2O_3$ (339)
Aluminum borate $9Al_2O_3 \cdot 2B_2O_3$ (339)
amorphous B_2O_3 (339)
anatomic modeling (198)
anisotropy (65, 330)
ANOVA (250)
bead deposition (110)
benchmark (118)
benchmarking (146)
bending modulus (234)
bendstrength (330)
biomedical devices (181)
Boric acid H_3BO_3 (339)
boron oxide B_2O_3 (339)
calcium phosphate compounds (191)
carbon (311)
carbon fiber (50)
ceramic molds (56)
ceramic powder (277)
ceramic precursors (364)
ceramics (396)
ceramics processing (17)
Chemical Vapor Deposition (CVD) (311)
chemical vapor infiltration (348)
CNC machining (1)
composite materials (293)
composite microstructure (285)
composite powders (175)
composites (50, 234, 364, 387)
computer derived-microstructures (181)
copper-based powder (82)
core and cavity (154)
creep (146)
curl (146, 250)
curling (277)
CVD (311)
Damköhler's equation (321)
degradation (387)
dense composite materials (293)
densification (65, 356)
densification maps (65)
density (65, 330)
depth of cure (396)
design visualization (404)
diffusion bonded (74)
dimensional accuracy (242)
dimensional stability (204)
Direct Memory Access (DMA) (311)
direct laser sintering of metals (175)
direct metal prototyping (9)
DMA (311)
draw pattern (242)
dual beam laser sintering (277)
elastomeric (42)
encapsulation (65)
epoxy chemistry (204)
epoxy infiltration (371)
epoxy resin (154)
external supports (259)
extrusion (50)
FDM" (42)
filament (42)
firing cycle (371)
Ford (154)
Ford Explorer (154)
fracture surfaces - sprayed metal (74)
free-form fabrication (17)
function (285)
Fused Deposition Modeling (FDM") (42)
galvanometers (311)
geometric data (270)
government initiatives (110)
hard tool (154)
heat capacity (321)
homogenization (65)
Hot Isostatic Pressing (HIP) (65)
hydrogen (311)
hydroxyapatite (191, 321)
IGES NURB Surfaces (307)
IMS Test Case (118)
in situ reinforcement (50)
infiltration (175)
information processing (9)
injection molding (154)
injection molds (371)
ink-jet printhead (56)
integration of modeling with RP (94)
investment casting (94, 154)
laminate (25)
LAPS (Laser Aided Powder Solidification) (82)
laser (225)
laser deposition (348)
laser forming (25)
laser fusion (110)
laser machining (25)
laser scanning (311)
laser sintering (94, 356)
laser sintering/melting (82)
laser welding (25)

laser-heated method (321)
layered deposition (74)
layered manufacturing (259)
layered structures (293)
liquefier (42)
Liquid Phase Sintering (65, 82, 379)
LMT (82)
magnesia (321)
material data (270)
material extrusion (9)
MD* (1)
mechanical properties (74, 175, 204)
melting (299)
metal (371)
metal melt infiltration (175)
metal parts (1)
metal powder (82, 175, 277)
metallurgical bonding (74)
microcasting (1)
microstructure fabrication (285)
model (225, 299)
moire analysis (242)
Monoclinic HBO_2 (339)
morphological instability (311)
Multiphase Jet Solidification (9)
Nickel Vapor Deposition (NVD) (154)
novel structures (293)
numerical modeling (94)
Nylon 6 (50)
nylon (34)
nylon-based materials (102)
Orthorhombic HBO_2 (339)
overcure (242)
part accuracy (204, 404)
part registration (307)
part specific setup (404)
particle size (396)
path planning (259)
pendant drop techniques (379)
photo polymerization (110)
photolithography (234)
photopolymerization (225, 250)
photopolymers (250)
plaster block moulding (82)
polyamide (42, 82)
polycarbonate (34, 356)
polycarbosilane (PCS) (364)
polymer (225, 330, 371, 387)
polymer powder (82)
polymer powder mixture (94)
polyolefin (42)
polypropylene (154)
polystyrene (82)
post-processing (191)
prediction (225)
printing parameters (181)
process control (277, 311)
process modelling (25, 277)
process parameters (270)
process window (299)
product model (270)
pulse width modulation (277)
Quartz fiber (234)
QuickCast (154, 204)
QuickCast Tooling (154)
Rapid Prototyping (17, 110, 154)
Rapid Tooling (154)
rapid prototyping technologies (118)
real time (311)
repeatability (146)
reverse engineer (307)
reverse engineering (9)
review of research (110)
SALD (311)
scattering (396)
Selective Area Laser Deposition (SALD) (311)
Selective Laser Sintering (SLS) (34, 65, 175, 191, 277, 299, 371, 379, 387)
selective laser pyrolysis (364)
Shape Deposition (1)
sheet lamination (110)
shot-peening (1)
shrinkage (65, 146, 225)
silica (50)
silicon carbide (348, 364)
SLA-250 (154)
slice formats (9)
SLS (330)
SLS process (102)
solid freeform manufacturing (348)
Somos 3100 (234)
sprayed metal (74)
sprayed steel (74)
sprayed tooling (74)
Stair-stepping' (404)
Standard for the Exchange of Product Model Data (STEP) (9)
steel tooling (154)
STEP model (270)
stereolithography (204, 225, 234, 242, 250, 396)
structural ceramics (17)
structural integrity (285)
structural materials (181)
structure optimization for castings (94)
support structure (259)
surface creation (307)
surface structures (56)
surface textures (56)
surface tension (379)
system development (9)
temperature modelling (356)
temperature sensor (277)
tensile strength (146, 234)

tetramethylsilane (348)
thermal (299)
thermal conductivity (321)
thermal control (102)
thermal diffusivity (321)
Three Dimensional Printing (3DP) (56, 181)
thresholding algorithms (198)
tooling (74)
topology optimization (293)
triangulation (307)
ultraviolet (396)
video microscopy (34)
viscosity (396)
volumetric flow rate (42)
warpage (146, 242)
wax (34)
wetting balance (379)
Wiper Module Cover (154)
worldwide assessment (118)
zirconia (321)

Author/Attendee List (Starting page numbers of papers contributed are listed in parenthesis

Mukesh Agarwala
(65)
The University of Texas at Austin
Center for Materials Science & Engineering
C2201
Austin TX 78712

Seth Allen
(259)
413 Third Street #2
Ann Arbor MI 48103
313 668-1584/ fax: 747-3170
swallen@math.lsa.umich.edu

Daniel Anderson
DePuy
700 Orthopaedic Drive
Warsaw IN 46581-0988
219 372-7360 fax: 267-6003
dla@depuy.com

Jim Anderson
Mesa Technical College
824 West Hines
Tucumcari NM 88401
505 461-4413 fax: 461-1901

Timothy Anderson
MIT
35-231
77 Massachusetts Avenue
Cambridge MA 02139
617 253-2606/ fax 617 253-2123

Clint Atwood
Sandia National Laboratories
P.O. Box 5800, M.S. 0958
Albuquerque NM 87185
505 844-0816 fax: 505 844-5589
clatwoo@sandia.gov

Dick Aubin
(118)
United Technologies Research Center
411 Silver Lane, M/S 129-48
East Hartford CT 06108
203 727-1697/fax 203 727-7880
rfa@utrc.utc.com

B. Badrinarayan
(371)
Department of Chemical Engineering
The University of Texas at Austin
C0400
Austin TX 78712
512 471-5838

Amit Bagchi
(146,234)
Mechanical Engineering Department
Clemson University
Box 340921
Clemson SC 29634-0921
803 656-5641/ fax: 803 656-4435

Clifford Ballard
Allied Signal Inc.
101 Columbia Road
PO Box 1021
Morristown NJ 07962-1021
201-455-2963/Fax 201-455-3008
ballard™allied.com

Clifford Bampton
Rockwell Science Center
1049 Camino Dos Rios
Thousand Oaks CA 91360
805-373-4453 / fax 805-373-4775

Joel Barlow
(191,321,330,371,387)
Department of Chemical Engineering
The University of Texas at Austin
Austin TX 78712
512 471-1271/fax 512 471-7060

Chester Barry
U.S. Patent Trademark Office
4809 8th Road North
Art Unit 1304
Arlington VA 22203
703-308-1916 /fax 703-305-3601

Joseph Beaman
(34, 65)
The University of Texas at Austin
Mechanical Engineering
C2200
Austin TX 78712
512 471-3058 fax: 512-471-8727
jbeaman@mcl.cc.utexas.edu

Gerald J. Beck
3M Austin Center
Bldg. A141-2S-03
6801 River Place Blvd.
Austin TX 78726
512 984-3907 fax: 984-3989

John A. Benda
(277)
United Technologies Research Center
411 Silver Lane MS 129-39
East Hartford CT 06108
203 727-7215 fax: 203 727-7852

Michael M. Bernitsas
(285)
University of Michigan
Department of Naval Architecture & Marine Engr.
2600 Draper Road
Ann Arbor MI 48109-2145
(313) 764-9317/ fax: 936-8820
BERNITSAS@um.cc.umich.edu

Britton R. Birmingham
(348,412)
Center for Materials Science & Engineering
The University of Texas at Austin
C2201
Austin TX 78712

Paul Blake
Texas Instruments
P. O. Box 405, MS 3428
Lewisville TX 75067
214 462-3015/ fax: 214 462-2684

Jack Boudreaux
NIST/ATP
Bldg. Admn., Room A 421
Gaithersburg MD 20899
301 975-3560

David L. Bourell
(65,379)
The Center for Materials Science and Engr.
The University of Texas at Austin
Austin TX 78712
512 471-3170 fax 512-471-7681
dbourell@mcl.cc.utexas.edu

Harold Brashears
Mississippi Polymer Institute
University of Southern Mississippi
Box 10003
Hattiesburg MS 39406-0003
601 266-4607 fax: 266-5504

David Bunnell
(379)
The University of Texas at Austin
Center for Materials Science & Engineering
C2201
Austin TX 78712
512 471-3578

Larry Burkholder
Deere & Co. Technical Center
3300 River Drive
Moline IL 61265
309-765-3798 /fax 309-765-3807

Marshall Burns
ENNEX Fabrication Technologies
549 Landfair Avenue
Los Angeles CA 90024
310 824-5185 (voice & fax)
marshall@ennex.com

Dan Cain
Lockheed Corporation
86 S. Cobb Drive
D/48-11 Z/0150
Marietta GA 30063
404 494-1671/ fax: 404 494-1436

Salvatore Caldarise
(56)
Johnson & Johnson Professional
325 Paramount Drive
Raynham MA 02767-0350
508-880-8449/fax 508-880-8144

Ian Campbell
(110)
Dept. Man. Eng. & Ops. Mangmt.
The University of Nottingham
University Park
Nottingham, NG7 2RD UNITED KINGDOM
44 602 514 015/ fax: 0602 514 000
IanCampbell@vme.ccc.nottingham.ac.uk

Per Carleberg
(270)
Department of Manufacturing Systems
KTH
Brinellvagen 81
10044 Stockholm SWEDEN
46 8 790 7095 / fax:46 8 20 22 27
pc@caccam.kth.se

Carlos A. Chacon
Marquette University
1515 W. Wisconsin Avenue
Milwaukee WI 53233
414 288-7080/ fax: 288-7082

Richard P. Chartoff
(225,242)
University of Dayton
Rapid Prototype Development Laboratory
300 College Park Avenue
Dayton OH 45469-0130
513 229-2517/ fax: 229-3433

Bruce Chiangi
EDS /NAO Prototype Shops
30001 Van Dyke Room 134-42
Warren MI 48090
810 575-8564

Tom Childs
(356)
The Department of Mechanical Engineering
The University of Leeds
Woodhouse Lane
Leeds LS2 9JT ENGLAND
44 0532 332 165/ fax: 44 0532 332 150
thcc@lera.leeds.ac.uk

Michael J. Cima
(56,181)
Ceramics Processing Research Laboratory
MIT
77 Massachusetts Ave.
Room 12-011
Cambridge MA 02139
617 253-6877 fax: 612 258-6936
mjcima@mit.edu

William Coblenz
Materials Science Division
Advanced Research Projects Agency
3701 N. Fairfax Dr.
Arlington VA 22203-1714
703 696-2288/ fax: 696-2201
wcoblenz@arpa.mil

Richard H. Crawford
The University of Texas at Austin
Department of Mechanical Engineering
C2200
Austin TX 78712
512 471-3030/ fax 512 471-7682
rhc@bianchi.me.utexas.edu

Robert Crockett
(50)
University of Arizona
4715 E. Ft. Lowell Road
Tucson AZ 87512
602 322-2968/ fax 322-2993
rcrocket@ccit.arizona.edu

Alain Curodeau
(56)
Massachusetts Institute of Technology
77 Massachusetts Avenue
Room 35-136
Cambridge MA 02139-4307
617 253-5381 fax 253-0209

Stephen C. Danforth
Rutgers University
Center for Ceramic Research
P. O. Box 909
Brett and Bowser Roads
Piscataway NJ 08855-0909
908-445-2211 fax: 445-3258
danforth@alumina.rutgers.edu

Suman Das
(34)
Department of Mechanical Engineering
The University of Texas at Austin
C2200
Austin TX 78712

Carl Deckard
Department of Mechanical Engineering
Clemson University
PO Box 340921
Clemson SC 29634-0921
803-656-5642/ fax 803-656-4435
carl.deckard@eng.clemson.edu

Karl R. Denton
(154)
Ford Motor Company
20000 Rotunda Drive
P. O. Box 2053
Body Engineering Bldg. ROOM 2019
Dearborn MI 48121
313 322-0960 fax: 390-0652
kdenton@engrg1.pms.ford.com

P. M. Dickens
(110)
Dept. Man. Eng. & Ops. Mangmt.
The University of Nottingham
University Park
Nottingham NG7 2RD UNITED KINGDOM
44 602 514063/ fax: 602 514000

Mike Durham
Accelerated Technologies
12919 Dessau Rd.
Austin TX 78754
512-990-7199/ Fax 512-990-9726

Deba Dutta
(259)
Mechanical Engineering Department
University of Michigan
2250 G. G. Brown Labs
Ann Arbor MI 48105
313 764-2694/ fax: 747-3170
dutta@engin.umich.edu

Ingo Ederer
Lehrstuhl Für Feingeratebau (FGB)
Arcisstraße 21 80230 München
Munich GERMANY
006 832405 2441
ederer@tgb.mw.tu-muenchen.de

Donald L. Erich
Concurrent Technologies Corp.
1450 Scalp Avenue
Johnstown PA 15904
814 269-2727 fax: 269-2799

Domenic Fazio
Polaroid Corporation
1 Upland Road
Mail Stop N-4
Norwood MA 02060
617 446-5440 fax: 446-5246

Terry Feeley
Laserfare Adv. Tech. Gp.
70 Dean Knauss Drive
Narragansett RI 02882
401 783-9559 fax: 789-1932
73060,205@COMPUSERVE.COM

Steven G. Fishman
Program Manager
Office of Naval Research
800 N. Quincy St.
Arlington VA 22217-5000
703 696-0285/ fax: 696-0934
fishmas@onrhq.onr.navy.mil

Paul Forderhase
(102)
DTM Corporation
1611 Headway Circle, Bldg. 2
Austin TX 78754
512 339-2922 fax: 339-0634

Paul S. Fussell
(74)
Alcoa Labs
100 Technical Drive
Alcoa Center PA 15069-0001
412 337-2721/ fax:337-5944
fussell@atc.alcoa.com

Martin Geiger
(9)
Fraunhofer-Institut fur Produktionstechnik
und Automatisierung
Nobelstrasse 12
D-7000 Stuttgart 80 GERMANY
49 711 970 1835 or 1837
mrg@qt.ipa.fhg.de

Dan Girouard
DTM Corporation
1611 Headway Circle, Bldg. 2
Austin TX 78754
512 339-2922/ fax: 512 339-0634

Damian Gray
DTM Corporation
1611 Headway Circle, Bldg. 2
Austin TX 78754
512 339-2922 fax: 339-0634

Alair Griffin
Lone Peak Engineering
12660 S. Fort Street
Draper UT 84020
801 553-1732 fax: 553-1734

Curtis W. Griffin
(17)
Lone Peak Engineering
1270 West 2320 South/Suite F
West Valley UT 84119
801 975-7979/ fax: 972-9207

Michelle Griffith
(396)
University of Michigan
MS & E Department
2300 Hayward Street
Ann Arbor MI 48109-2136
313 936-0177 fax: 313 763-4788

Richard Hague
University of Nottingham
Manufacturing Engineering Dept.
University Park 2RD
Nottingham NG7 2PH ENGLAND
44-602-514033/Fax 44-602-514000

Jill Paulick Heddleson
ALCOA
100 Technical Drive
Alcoa Center PA 15069
412 337-3103 fax: 337-5944
heddlesson jp@atc.alcoa.com

Tim Heller
Stratasys, Inc.
14950 Martin Drive
Eden Prairie MN 55344
612 937-3000/ fax 612-937-0070

William Hong
Institute for Defense Analyses
1801 N. Beauregard Street
Alexandria VA 22311
703 5782826/ fax: 703 578-2877
whong@ida.org

K. David Howard
Ford Motor Company (Box 26)
36200 Plymouth Rd
Livonia MI 48150
313 523-5006 fax: 525-2090

Kevin Jakubenas
(364)
The University of Texas at Austin
Center for Materials Science & Engineering
C2201
Austin TX 78712

Michael James
Director, Materials Science
Rockwell Science Center
1049 Camino Dos Rios
Thousand Oaks CA 91360

Suresh Jayanthi
(250)
University of Delaware
126 Spencer Lab.
Academy Street
Newark DE 19711
301 831-2421/ fax 302 831-3619
jayanthi@me.udel.edu

Anand Jog
Department of Mechanical Engineering
The University of Texas at Austin
C2200
Austin TX 78712

Roy Johanson
(293)
2212 G.G. Brown
Dept. of Mechanical Engineering
University of Michigan
Ann Arbor MI 48103
313 936-2624/ fax 313-747-3170
rpjrim@caen.engin.umich.edu

Lars Karlsson
Lulea University of Technology
Institute for CIM
S-97752 Lulea SWEDEN
46 920 72004/fax: 46 920-91047
lasse@cad.luth.se

Bernd Keller
(82)
University of Stuttgart
Institut für Kunststoffprüfung
Pfaffenwaldring 32
7000 Stuttgart 80 GERMANY

Ron Knight
Loral Vought Systems
P. O. Box 650003 M/S WT-21
Dallas TX 75265-0003

Martin Koch
(25)
Industrial Engineering Dept.
Cal. Polytechnic State University
San Luis Obispo CA 93407
805-756-1114 /fax 805-765-5439
mkoch@oboe.calpoly.edu

Bruce Kramer
National Science Foundation
4201 Wilson Blvd
Arlington VA 22230
703-306-1330 /fax 703-306-0298
bkramer@nsf.gov

Rashid Laabi
(412)
Center for Materials Science and Engineering
The University of Texas at Austin
Austin TX 78712

Uday Lakshminarayan
DTM Corporation
1611 Headway Circle, Bldg. 2
Austin TX 78754
512 339-2922 fax: 339-0634

Thomas S. Latham
United Technologies Research Center
411 Silver Lane
East Hartford CT 06140
203 727-7409 / fax: 203 727-7880

Goonhee Lee
(191)
The University of Texas at Austin
Department of Chemical Engineering
C0400
Austin TX 78712
512 471-5828

Insup Lee
(339)
Center for Materials Science & Engineering
The University of Texas at Austin
C2201
Austin TX 78712

Richard Levy
(198)
Department of Radiology
The University of Michigan Medical Center
1500 E. Medical Center Drive
Ann Arbor MI 48109-0030
313 936-9878 fax: 764-2412
Levy,Richard@med.umich.edu

Marc Lipman
Office of Naval Research
800 North Quincy Street
Arlington VA 22217
703-696-4310/fax 703-696-2611
lipmanm@onrhq.navy.mil

John Lombardi
(50)
University of Arizona
Arizona Materials Labs
4715 East Ft. Lowell Road
Tucson AZ 85712

Subhas Malghan
National Institute of Standards & Technology
Powder Characterization & Proc. Ceramics Div.
Matls. Bldg. 223/A256
Gaithersburg MD 20899
301 975-6101 fax: 975-2129
malghan@enh.nist.gov

Arumugam Manthiram
(339)
The University of Texas at Austin
Center for Materials Science & Engineering
C2201
Austin TX 78712
512 471-1791 fax: 471-7681

Harris Marcus
(311,330,339,348,364,379,412)
The University of Texas at Austin
Center for Materials Science & Engineering
C2201
Austin TX 78712
512 471-3188 fax: 471-7681
hmarcus@mcl.cc.utexas.edu

Nicholas Martin
Concurrent Technologies Corporation
1450 Scalp Ave.
Johnstown PA 15904
814 269-2559/ fax 269-2666

Kevin McAlea
(102)
DTM Corporation
1611 Headway Circle, Bldg. 2
Austin TX 78754
512 339-2922/ fax: 512 339-0634

Dennis Medler
DTM Corporation
1611 Headway, Bldg. 2
Austin TX 78754
512 339-2922 fax: 339-0634

Lawrence Melvin III
(34)
Department of Mechanical Engineering
The University of Texas at Austin
C2200
Austin TX 78712

Patricio Mendez
(299)
MIT
Dept. of Materials Science & Engineering
77 Massachusetts Ave., Room 8-103
Cambridge MA 02139
617 252-1632/ fax: 253-8669
PAT@MIT.EDU

Robert Merz
(1)
Carnegie Mellon University
5000 Forbes Avenue
Pittsburgh PA 15213
412 268-3788 fax: 412 268-5229

David Miller
Laurel Vought Systems
PO Box 650003 M/S:SK-03
Dallas TX 75265-0003
214-603-0258/ fax 214-603-0419

Steve Miller
GE, CRD
Bldg. K-1, 2C7M
P. O. Box 8
Schenectady NY 12301
518 387-6296/ fax 387-5576

Tony Mulligan
Advanced Ceramics Research
841 E. 47th Street
Tucson AZ 85713
602 792-2616/ fax: 602 792-2635

Kesh Narayanan
National Science Foundation
Program Director
4201 Wilson Blvd.
Arlington VA 22230
703 306-1328 fax:703 306-0298
knarayan@nsf.gov

Christian Nelson
1611 Headway Circle
Bldg. 2
Austin TX 78729
512 339-2922/ fax: 512 339-0634
nelson@bga.com

Garth M. Nelson
GE CR & D
P. O. Box 8, River Road
Schenectady NY 12301
518 387-5739 fax: 387-5752
nelsongm@diane.crd.ge.com

Dennis Nohns
Delco Electronics
700 E. Firmin Street
MS 9159
Kokomo IN 46904-9005
317 451-8644/ fax:451-7151

Olli Nyrhila
(94)
Electrolux Rapid Development
Aholantie 17
FIN-21290
Rusko FINLAND
358-21-819-600, fax 358-21-819-620

Kurt O'Connor
Delco Electronics
700 E. Firmin Street
Mail Stop 9159
Kokomo IN 46904-9005
317 451-9309 fax: 451-7151

John O'Kelly
(50)
University of Arizona
4715 E. Ft. Lowell Road
Tucson AZ 85712
602 322-2302/ fax 322-2993
jao@bigdog.engr.arizona.edu

Sean O'Reilly
(146)
Ford Motor Company
Manufacturing Development Center
Operations Engineering
24500 Glendale Avenue
Detroit MI 48239
fax 313 592-2381

Sung Pak
Helisys, Inc.
24015 Garnier St.
Torrance CA 90505
310 891-0600 fax: 310 891-0626

Ioannis Pandelidis
The Gillette Company
One Gillette Park
Boston MA 02127-1096
617 463-3543/ fax 463-4448

Thomas Pang
(204)
3D Systems
26081 Ave. Hall
Valencia CA 91355
(805) 295-5600/ fax: 805 257-0249

Frank Paul
Clemson University
Mechanical Engineering
Clemson SC 29634-0921
803 656-3291 fax: 656-4435

Elaine Persall
308 Rhodes Research Center
Product Realization Lab
Clemson University
Clemson SC 29634
803-656-0321

Theo Pintat
(94,175)
Fraunhofer-IFAM
Lesumer Heerstraße 36
28717 Breman GERMANY
49 4216383153/ Fax: 421-6383190
sl@ifam.fhg.de

Gopalakrishna Prabhu
The University of Texas at Austin
Center for Materials Science & Engineering
C2201
Austin TX 78712
512 471-3170 fax: 471-7681

Fritz Prinz
(1,74)
Director, EDRC
Carnegie Mellon University
5000 Forbes Avenue
Pittsburgh PA 15213
412 421-1941, 415-723-0089 fax: 412 268-5229
fbp@aandsow.cmu.edu

Tim Pruitt
DePuy
700 Orthopaedic Drive
Warsaw IN 46581-0988
219-372-7114, Fax 219-269-9516
tjp@depuy.com

Keith Ramthun
Howmet Corporation
Products Technology-Operhall Rsch. Ctr.
1500 So. Warner Street
Whitehall MI 49461
616 894-7984

Fred D. Raniere
Rockwell Science Center
1049 Camino Dos Rios
Thousand Oaks CA 91360
805 373-4619/ fax: 373-4775

R.C. Reuter
Department of Energy, DP-14
1000 Independence Ave. SW
Washington DC 20585
202-586-9876/ fax 202-586-1057
robert.reuter@mailgw.er.doe.gov

Vincent Reymond
Centre de Transfert de Technologie du Mans
Technopole Université
20 Rue Thalés de Milet
22000 Le Mans FRANCE
33 43 39 46 23/ fax 33 43 39 46 29

Paul Rivard
U.S. Patent & Trademark
2042 Peach Orchard Dr. Apt. T4
Falls Church VA 22043
703 308-1917 fax: 305-3601

Ernie Rodriguez
Sr. Dev. Engineer
3M
6801 Riverplace Blvd.
Austin TX 78726
512 984-7188/ fax: 984-7258

Emanuel Sachs
(56,181)
MIT
35-231
77 Mass Avenue
Cambridge MA 02139
617 253-5381/ fax 617 253-0209
sachs@mit.edu

Sunity Sharma
SRI International
333 Ravenswood Avenue PS 253
Menlo Park CA 94025
415 859-3036 fax: 859-2316

Christopher Shutts
Massachusetts Institute of Technology
77 Massachusetts Avenue
Room 35-136
Cambridge MA 02139-4307
617 253-5381 fax 253-0209

Samuel Sumin Sih
(321)
Department of Chemical Engineering
The University of Texas at Austin
C0400
Austin TX 78712

Manfred Sindel
(9,94,175)
Fraunhofer-IFAM
Lesumer Heerstraße 36
28717 Breman GERMANY
49 421-6383 249 Fax: 421-6383790
sl@ifam.fhg.de

Jean Smith
DTM Corporation
1611 Headway Circle, Bldg. 2
Austin TX 78754
512 339-2922 fax: 339-0634

John E. Smugeresky
Sandia National Labs
7011 East Avenue
MS 9402 (Dept. 8714)
Livermore CA 94551-0969
510 294-2910/ fax 294-3410
smug@CCSMTP.sandia.gov

Brent Stucker
Texas A & M University
Department of Mechanical Engineering
College Station TX 77843

Kevin Stuffle
(50)
Advanced Ceramics Research
841 E. 47th Street
Tucson AZ 85713
602 792-2616/ fax: 602 792-2635

P. Kamatchi Subramanian
(330)
Center for Materials Science & Engineering
The University of Texas at Austin
C2201
Austin TX 78712

Richard Sudduth
Mississippi Polymer Institute
University of Southern Missippi
Box 10003
Hattiesburg MS 39406
601 266-4607 fax: 266-5504

Yong Seok Suh
(404)
Rensselaer Polytechnic Institute
110 8th Street
Troy NY 12180
518 276-6751 fax: 276-2702

Jean Claude Tasse
Centre de Transfert de Technologie du Mans
Technopole Université
20 Rue Thalés de Milet
22000 Le Mans FRANCE
33 43 39 48 03/ fax 33 43 39 48 04

Leo Tentoni
U.S. Patent and Trademark Office
14527 Skipton Court
Centreville VA 22030
703 308-3834 fax: 305-3601

Rich Thissell
(311)
The University of Texas at Austin
Center for Materials Science & Engineering
C2201
Austin TX 78712

David Thompson
Department of Mechanical Engineering
The University of Texas at Austin
C2200
Austin TX 78712
512 471-3030

Andy Tkach
Concurrent Technologies Corporation
Mgr. Industrial Operations
1450 Scalp Avenue
Johnstown PA 15904
814 269-6421/ fax: 814 269-6480

James R. Tobin
Procter and Gamble
6110 Center Hill Ave
Mail Stop FB1B42
Cincinnati OH 45224
513 634-2392 fax: 513 634-4588

N.K. Vail
(330,387)
Department of Chemical Engineering
The University of Texas at Austin
C0400
Austin TX 78712
512 471-5838

Douglas van Putte
Eastman Kodak Company
Kodac Park, Building 604
Rochester NY 14652-4102
716-477-1492/fax 716-722-0810

Steve Yencho
Stanford University
Rapid Prototyping Lab
Dept. of Mechanical Engineering
Stanford CA 94305-4021
915-723-0234/ fax 915-723-3521

Ralph Wachter
Office of Naval Research
Computer Science Division, Code 1133
800 N. Quincy Street
Arlington VA 22217-5660
703-696-4304/ fax 703-696-0934
wachter@itd.nrl.navy.mil

Craig T. Wadham
DTM Corporation
1611 Headway Circle, Bldg. 2
Austin TX 78754
512 339-2922 / fax: 512 339-0634

Gary Waite
Vertical Dimensions
630 So. 4th St. Suite 100
Las Vegas NV 89101
702 387-6453 fax: 702 382-0365

Lee Weiss
(1)
Carnegie Mellon University
5000 Forbes Avenue
Pittsburgh PA 15213
412 268-7657 / fax: 412 621-1970
lew@cs.cmu.edu

Christian Wilkening
(94,175)
EOS GmbH
Pasinger Str. 2
82152 Planegg GERMANY
89-899-13132/fax 89-859962

Martin Wohlert
Center for Materials Science & Engineering
University of Texas at Austin
C2201
Austin TX 78712
512 471-1504

John Wooten
Rockwell International Corp.
Rocketdyne Division
6633 Canoga Ave., MS IB15
P. O. Box 7922
Canoga Park CA 91304
818-586-0464/ fax: 818-586-0575
jrwooten@rdyne.rockwell.com

Michael J. Wozny
(404)
NIST/MEL
Building 220 Room B322
Gaithersberg MD 20899
301-975-3400 Fax 301-948-5668